ISSN 2188-5001

MATERIALS DESIGN AND CHARACTERIZATION LABORATORY

SUPERCOMPUTER CENTER

ACTIVITY REPORT
2015

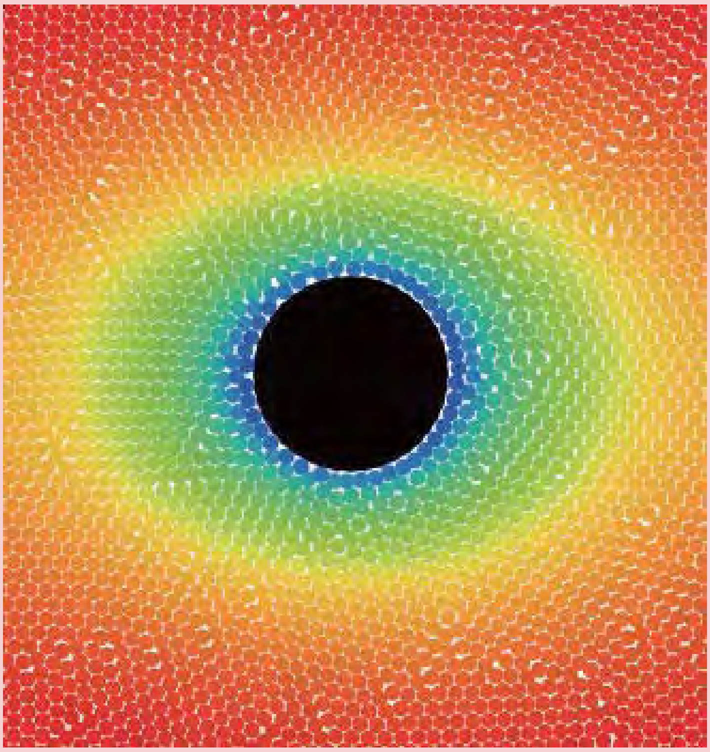

INSTITUTE FOR SOLID STATE PHYSICS

THE UNIVERSITY OF TOKYO

Materials Design and Characterization Laboratory (MDCL)

The MDCL was established as the third research facility of the Institute for Solid State Physics (ISSP) when the latter was reorganized in May 1996. Its aim is to promote material science with an emphasis on the “DSC cycle”, where DSC stands for design, synthesis and characterization, three processes for developing new materials.

The MDCL consists of two sections, Materials Design (MD) section and Materials Synthesis and Characterization (MSC) section. The Supercomputer Center of the ISSP (SCC-ISSP) is placed in the MD section, while in the MSC section there are six laboratories for joint use; Materials Synthesis Laboratory, Chemical Analysis Laboratory, X-ray Diffraction Laboratory, Electron Microscope Laboratory, Electromagnetic Measurement Laboratory, and Spectroscopy Laboratory.

Almost all the facilities of the MDCL are open to scientists in Japan through the User Programs conducted by two steering committees of the MDCL. One is the steering committee of the SCC-ISSP, under which the Supercomputer Project Advisory Committee is placed for reviewing proposals. The other is the steering committee of the MSC facilities. More than half of the members of these committees are from the outside of ISSP.

PREFACE

The Supercomputer Center (SCC) is a part of the Materials Design and Characterization Laboratory (MDCL) of ISSP. Its mission is to serve the whole community of computational condensed-matter physics of Japan providing it with high performance computing environment. In particular, the SCC selectively promotes and supports large-scale computations. For this purpose, the SCC invites proposals for supercomputer-aided research projects and hosts the Steering Committee, as mentioned below, that evaluates the proposals.

The ISSP supercomputer system consists of two subsystems: System B, which is intended for more nodes with relatively loose connections. In July, 2015, the SCC replaced the two supercomputer subsystems (SGI Altix ICE 8400EX and NEC SX-9) to one new system (System B, SGI ICE XA/UV hybrid system). The system B consists of 1584 CPU nodes, 288 ACC nodes, and 19 FAT nodes. The CPU node has 2CPUs (Intel Xeon). The ACC node has 2CPUs (Intel Xeon) and 2GPUs (NVIDIA Tesla K40). The FAT node has 4CPUs (Intel Xeon) and large memory (1TB). The system B have totally 2.6 PFlops theoretical peak performance. System C - FUJITSU PRIMEHPC FX10 was installed in April, 2013. It is highly compatible with K computer, the largest supercomputer in Japan. System C consists of 384 nodes, and each node has 1 SPARC64TM IXfx CPU (16 cores) and 32 GB of memory. The system C have totally 90.8 TFlops.

The hardware administration is not the only function of the SCC. The ISSP started hosting Computational Materials Science Initiative (CMSI), a new activity of promoting materials science study with next-generation parallel supercomputing. This activity is financially supported by the MEXT HPCI strategic program, and in CMSI, a number of major Japanese research institutes in various branches of materials science are involved. The SCC supports the activities of CMSI as its major mission.

All staff members of university faculties or public research institutes in Japan are invited to propose research projects (called User Program). The proposals are evaluated by the Steering Committee of SCC. Pre-reviewing is done by the Supercomputer Project Advisory Committee. In school year 2015 totally 239 projects were approved.

The research projects are roughly classified into the following three (the number of projects approved):

First-Principles Calculation of Materials Properties (123)
Strongly Correlated Quantum Systems (31)
Cooperative Phenomena in Complex, Macroscopic Systems (85)

All the three involve both methodology of computation and its applications. The results of the projects are reported in 'Activity Report 2015' of the SCC. Every year 3-4 projects are selected for “invited papers” and published at the beginning of the Activity Report. In the Activity Report 2015, the following three invited papers are included:

"Capacitance of Nanosized Capacitors Investigated using the Orbital-Separation Approach --Dead Layer Effect and Negative Capacitance",

Shusuke KASAMATSU, Satoshi WATANABE, Seungwu HAN, and Cheol Seong HWANG

"Correlation Effects in Topological Insulators",

Norio KAWAKAMI

"Multiscale Simulation Performed on ISSP Super Computer: Analysis of Entangled Polymer Melt Flow”,

Takahiro MURASHIMA

June 3, 2016

Hiroshi Noguchi
(Chairman of the steering committee, SCC, ISSP)

CONTENTS

PREFACE

1 Outline

1.1 Supercomputer System

Before SY 2015, the ISSP supercomputer center provided users with three supercomputer systems: NEC-SX9 (System A), SGI Altix ICE 8400EX (System B), and FUJITSU PRIMEHPC FX10 (System C). At the beginning of SY 2015, Systems A and B were replaced by SGI ICE XA/UV hybrid system, and this system will be called System B for the next five years. The (new) System B and System C are installed in the main building of ISSP.

System B - SGI ICE XA/UV hybrid system is a massively-parallel supercomputer with three types of compute nodes: 19 “Fat” nodes, 1584 “CPU” nodes, and 288 “ACC” nodes. “Fat” nodes are each comprised of four Intel Xeon E5-4627v3 CPUs (10 cores/CPU) and 1 TB of memory. “CPU” nodes have two Intel Xeon E5-2680v3 CPUs (12 cores/CPU) and 128 GB of memory. “ACC” nodes have two nVIDIA Tesla K40 GPUs in additon to two Xeon E5-2680v3 CPUs and 128 GB of memory. System B achieves 2.6 PFLOPS in theoretical peak performance with high power efficiency. The subsystem comprised of only CPU nodes ranks 61st on the November 2015 Top 500 List, which is a ranking based on total performance measured by the HPL benchmark. The subsystem of ACC nodes ranks 104th on the Top 500 List, and it also ranks 23rd on the Green 500 List, which is a ranking based on performance per watt of electrical power consumption. The compute nodes communicate to each other through FDR Infiniband. The Fat nodes are interconnected in fat tree topology, while the CPU and ACC nodes are connected in enhanced hypercube topology. System B entered official operation on Aug. 21, 2015.

System C - FUJITSU PRIMEHPC FX10 has been in service since April, 2013. It is highly compatible with K computer, the largest supercomputer in Japan. System C consists of 384 nodes, and each node has 1 SPARC64TM IXfx CPU (16 cores) and 32 GB of memory. The total system achieves 90.8 TFlops theoretical peak performance.

For further details, please contact ISSP Supercomputer Center (SCC-ISSP).

[Correspondence: center@issp.u-tokyo.ac.jp]

1.2 Project Proposals

The ISSP supercomputer system provides computation resources for scientists working on condensed matter sciences in Japan. All scientific staff members (including post-docs) at universities or public research institutes in Japan can submit proposals for projects related to research activities on materials and condensed matter sciences. These proposals are peer-reviewed by the Advisory Committee members (see Sec. 1.3), and then the computation resources are allocated based on the review reports. The leader of an approved project can set up user accounts for collaborators. Other types of scientists, including graduate students, may also

Figure 1: Supercomputer System at the SCC-ISSP

be added. Proposal submissions, peer-review processes, and user registration are all managed via a web system.

The computation resources are distributed in a unit called “point”, determined as a function of available CPU utilization time and consumed disk resources. There were calls for six classes of research projects in SY 2015. The number of projects and the total number of points that were applied for and approved in this school year are listed in Table 1.

In addition, from SY 2010, ISSP Supercomputer is providing 20% of its computational resources for Computational Materials Science Initiative (CMSI), which aims at advancing parallel computations in condensed matter, molecular, and materials sciences on the 10-PFlops K Computer. The points for projects run by CMSI are distributed in accord with this policy. Computer time has also been alloted to Computational Materials Design (CMD) workshops run by CMSI, as well as for Science Camps held in ISSP for undergraduate students.

1.3 Committees

In order to fairly manage the projects and to smoothly determine the system operation policies, the Materials Design and Characterization Laboratory (MDCL) of the ISSP has organized the Steering Committee of the MDCL and the Steering

Table 1: Classes of research projects in SY 2015

Class	Maximum Points		Application	# of Proj.	Total points			
					Applied		Approved	
	Sys–B	Sys–C			Sys–B	Sys–C	Sys–B	Sys–C
A	100	100	any time	13	1.3k	1.3k	1.3k	1.3k
B	1k	500	twice a year	57	43.8k	8.6k	26k	7.8k
C	10k	2.5k	twice a year	162	1394.8k	181.3k	475k	147.8k
D	10k	2.5k	any time	2	18k	4k	14k	2.5k
E	30k	2.5k	twice a year	5	150k	7.5k	79k	6.2k
S	–	–	twice a year	0	0	0	0	0
CMSI				33	125k	139k	125k	139k

- Class A is for trial use by new users; proposals for Class A projects are accepted throughout the year.

- Proposals for projects in Classes B (small), C (mid-size), E (large-scale), and S (exceptional) can be submitted twice a year. Approved projects in Classes A, B, C, and E continue to the end of the school year.

- In Class D, projects can be proposed on rapidly-developing studies that need to perform urgent and relatively large calculations. An approved project continues for 6 months from its approval.

- Class S is for projects that are considered extremely important for the field of condensed matter physics and requires extremely large-scale computation. The project may be carried out either by one research group or cooperatively by several investigators at different institutions. A project of this class should be applied with at least 10,000 points; there is no maximum. We require group leaders applying for Class S to give a presentation on the proposal to the Steering Committee of the SCC-ISSP. Class S projects are carried out within one year from its approval.

- Project leaders can apply for points so that the points for each system do not exceed the maximum point shown in this table.

Committee of the SCC-ISSP, under which the Supercomputer Project Advisory Committee (SPAC) is formed to review proposals. The members of the committees in SY 2015 were as follows:

Steering Committee of the MDCL

HIROI, Zenji	ISSP (Chair person)
KATO, Takeo	ISSP
KAWASHIMA, Naoki	ISSP
MORI, Hatsumi	ISSP
NAKATSUJI, Satoru	ISSP
NOGUCHI, Hiroshi	ISSP
SUGINO, Osamu	ISSP
SUEMOTO, Toru	ISSP
KIMURA, Kaoru	Univ. of Tokyo
YOSHIMOTO, Yoshihide	Univ. of Tokyo
HASEGAWA, Tadashi	Nagoya Univ.
MIYASAKA, Hitoshi	Tohoku Univ.
MORIKAWA, Yoshitada	Osaka Univ.
OKAMOTO, Yuko	Nagoya Univ.
OTSUKI, Tomi	Sophia Univ.
TAKEDA Mahoto	Yokohama Natl. Univ.

Steering Committee of the SCC-ISSP

NOGUCHI, Hiroshi	ISSP (Chair person)
HARADA, Yoshihisa	ISSP
KAWASHIMA, Naoki	ISSP
SUGINO, Osamu	ISSP
TAKADA, Yasutami	ISSP
TSUNETSUGU, Hirokazu	ISSP
KASAMATSU, Shusuke	ISSP
MORITA, Satoshi	ISSP
SHIBA, Hayato	ISSP
WATANABE, Hiroshi	ISSP
HATANO, Naomichi	Univ. of Tokyo
IMADA, Masatoshi	Univ. of Tokyo
NAKAJIMA, Kengo	Univ. of Tokyo
TSUNEYUKI, Shinji	Univ. of Tokyo
YOSHIMOTO, Yoshihide	Univ. of Tokyo
MOHRI, Tetsuo	Tohoku Univ.
MORIKAWA, Yoshitada	Osaka Univ.
ODA, Tatsuki	Kanazawa Univ.
OKAMOTO, Yuko	Nagoya Univ.
OTSUKI, Tomi	Sophia Univ.

SUZUKI, Takafumi	Univ. of Hyogo
YATA, Hiroyuki	ISSP
FUKUDA, Takaki	ISSP

Supercomputer Project Advisory Committee

NOGUCHI, Hiroshi	ISSP (Chair person)
HARADA, Yoshihisa	ISSP
KATO, Takeo	ISSP
KAWASHIMA, Naoki	ISSP
OZAKI, Taisuke	ISSP
SUGINO, Osamu	ISSP
TAKADA, Yasutami	ISSP
TSUNETSUGU, Hirokazu	ISSP
KASAMATSU, Shusuke	ISSP
MORITA, Satoshi	ISSP
SHIBA, Hayato	ISSP
WATANABE, Hiroshi	ISSP
AOKI, Hideo	Univ. of Tokyo
ARITA, Ryotaro	Univ. of Tokyo
HATANO, Naomichi	Univ. of Tokyo
HUKUSHIMA, Koji	Univ. of Tokyo
IKUHARA, Yuichi	Univ. of Tokyo
IMADA, Masatoshi	Univ. of Tokyo
IWATA, Jun-Ichi	Univ. of Tokyo
MIYASHITA, Seiji	Univ. of Tokyo
MOTOME, Yukitoshi	Univ. of Tokyo
NAKAJIMA, Kengo	Univ. of Tokyo
OGATA, Masao	Univ. of Tokyo
OSHIYAMA, Atsushi	Univ. of Tokyo
TODO, Synge	Univ. of Tokyo
TSUNEYUKI, Shinji	Univ. of Tokyo
WATANABE, Satoshi	Univ. of Tokyo
YOSHIMOTO, Yoshihide	Univ. of Tokyo
NEMOTO, Koji	Hokkaido Univ.
AKAGI, Kazuto	Tohoku Univ.
KAWAKATSU, Toshihiro	Tohoku Univ.
KURAMOTO, Yoshio	Tohoku Univ.
MOHRI, Tetsuo	Tohoku Univ.
SHIBATA, Naokazu	Tohoku Univ.
KIM, Kang	Niigata Univ.
ISHIBASHI, Shoji	AIST
MIYAMOTO, Yoshiyuki	AIST
OTANI, Minoru	AIST
KOBAYASHI, Kazuaki	NIMS

TATEYAMA, Yoshitaka	NIMS
HATSUGAI, Yasuhiro	Univ. of Tsukuba
KOBAYASHI, Nobuhiko	Univ. of Tsukuba
OKADA, Susumu	Univ. of Tsukuba
YABANA, Kazuhiro	Univ. of Tsukuba
ODA, Tatsuki	Kanazawa Univ.
SAITO, Mineo	Kanazawa Univ.
HIDA, Kazuo	Saitama Univ.
NAKAYAMA, Takashi	Chiba Univ.
FURUKAWA, Nobuo	Aoyama Gakuin Univ.
MATSUKAWA, Hiroshi	Aoyama Gakuin Univ.
TAKANO, Hiroshi	Keio Univ.
YAMAUCHI, Jun	Keio Univ.
YASUOKA, Kenji	Keio Univ.
TOMITA, Yusuke	Shibaura Inst. Tech.
OTSUKI, Tomi	Sophia Univ.
OBATA, Shuji	Tokyo Denki Univ.
ANDO, Tsuneya	Tokyo Tech.
TADA, Tomofumi	Tokyo Tech.
HOTTA, Takashi	Tokyo Metropolitan Univ.
TOHYAMA, Takami	Tokyo Univ. of Sci.
WATANABE, Kazuyuki	Tokyo Univ. of Sci.
HAGITA, Katsumi	National Defense Academy
KONTANI, Hiroshi	Nagoya Univ.
OKAMOTO, Yuko	Nagoya Univ.
SHIRAISHI, Kenji	Nagoya Univ.
TANAKA, Yukio	Nagoya Univ.
KAWAKAMI, Norio	Kyoto Univ.
MASUBUCHI, Yuichi	Kyoto Univ.
YAMAMOTO, Ryoichi	Kyoto Univ.
YANASE, Yoichi	Kyoto Univ.
KAWAMURA, Hikaru	Osaka Univ.
KUROKI, Kazuhiko	Osaka Univ.
KUSAKABE, Koichi	Osaka Univ.
MORIKAWA, Yoshitada	Osaka Univ.
OGUCHI, Tamio	Osaka Univ.
SHIRAI, Koun	Osaka Univ.
YOSHIDA, Hiroshi	Osaka Univ.
YUKAWA, Satoshi	Osaka Univ.
HARIMA, Hisatomo	Kobe Univ.
SAKAI, Toru	Univ. of Hyogo
SUGA, Seiichiro	Univ. of Hyogo
SUZUKI, Takafumi	Univ. of Hyogo
TATENO, Masaru	Univ. of Hyogo
HOSHI, Takeo	Tottori Univ.

YASUDA, Chitoshi	Univ. of the Ryukyus

1.4 Staff

The following staff members of the SCC-ISSP usually administrate the ISSP Supercomputer.

NOGUCHI, Hiroshi	Associate Professor (Chair person)
KAWASHIMA, Naoki	Professor
SUGINO, Osamu	Associate Professor
WATANABE, Hiroshi	Research Associate
KASAMATSU, Shusuke	Research Associate
NOGUCHI, Yoshifumi	Research Associate
SHIBA, Hayato	Research Associate
MORITA, Satoshi	Research Associate
YATA, Hiroyuki	Technical Associate
FUKUDA, Takaki	Technical Associate
ARAKI, Shigeyuki	Technical Associate

2 Statistics (School Year 2015)

2.1 System and User Statistics

In the following, we present statistics for operation time taken in the period from April 2015 to March 2016 (SY 2015). In Table 2, we show general statistics of the supercomputer system in SY 2015. The total number of compute nodes in System B, and C is 1891 and 384 respectively. Consumed disk points amount to about 1% and 7% of the total consumed points in System B and C respectively. Roughly 20% of the total points in System B 60% of that in System C were consumed by CMSI projects. This means that about 20% of the total computational resources in this school year were actually used by CMSI projects.

In the left column of Fig. 2, availabilities, utilization rates, and consumed points in each system are plotted for each month. Throughout the school year, the utilization rates were very high. Especially in System B, they were exceeding 90% throughout most of the year.

The user statistics are shown in the right column of Fig. 2. The horizontal axis shows the rank of the user/group arranged in the descending order of the execution time (hour×nodes). The execution time of the user/group of the first rank is the longest. The vertical axis shows the sum of the execution time up to the rank. From the saturation points of the graphs, the number of “active” users of each system is around 250, and 70 for System B and C respectively. The maximum ranks in the graphs correspond to the number of the users/groups that submitted at least one job.

Table 2: Overall statistics of SY 2015

	System-B	System-C
total service time ($\times 10^3$ node·hours)	9728.4	3363.8
number of executed jobs	183721	22278
total consumed points ($\times 10^3$ point)	337.1	113.84
CPU points ($\times 10^3$ point)	334.6	106.0
disk points ($\times 10^3$ point)	2.5	7.9
points consumed by CMSI ($\times 10^3$ point)	63.3	59.5
total exec. time ($\times 10^3$ node·hours)	8803.1	2464.4
availability	96.0%	96.3%
utilization rate	90.5%	76.1%

2.2 Queue and Job Statistics

Queue structures of System B and C in SY 2015 are shown in Table 3. In System B, users can choose from three types of compute nodes; jobs submitted to queues with “cpu”, “acc”, and “fat” at the end of their queue names are submitted to CPU, ACC, and Fat nodes, respectively. See Sec. 1.1 for a description of each type of compute node. The user then has to choose the queue according to the number of nodes to use and the duration of their calculation jobs. Queue names starting with “F” are for jobs taking 24 hours or less, while those starting with “L” can run much longer up to 120 hours. More nodes are allotted to “F” queues in order to maximize the turnaround time of user jobs. The queue names starting with “i” are used for interactive debugging of user programs and the elapsed time limit is 30 minutes. The number following “F”, “L”, or “i” correspond to the number of nodes that can be used by one user job.

In System C, the “F” and “L” queues are set up similarly to System B. In addition, a debug queue is set up for short debugging jobs utilizing 1 to 4 CPUs, and an interactive queue that can use 1 to 4 CPUs is also available.

To prevent overuse of the storage, points are charged also for usage of disk quota in the three systems, as shown in Table 4. Disk points are revised often for optimal usage of the resources by examining usage tendencies each year.

Although we do not mention here in detail, to promote utilization of the massively parallel supercomputer, background queues (“B4cpu”, “B36cpu”, “B144cpu”, “B18acc”, “B72acc”, and “B2fat”) which charge no points for the jobs have also been open in System B.

The number of jobs, average waiting time, and total execution time in each queue are shown in Table 5. In both System B and C, a large portion of jobs have been executed in “F” queues. The largest amount of the execution time has been consumed in the large-scale “F144cpu” queue, but substantial number of jobs were run in every queue, suggesting that a wide variety of user needs are met by this queuing scheme. In most of these queues, the queue settings meet the user’s tendencies in that the waiting times are on the order of the elapsed-time limit.

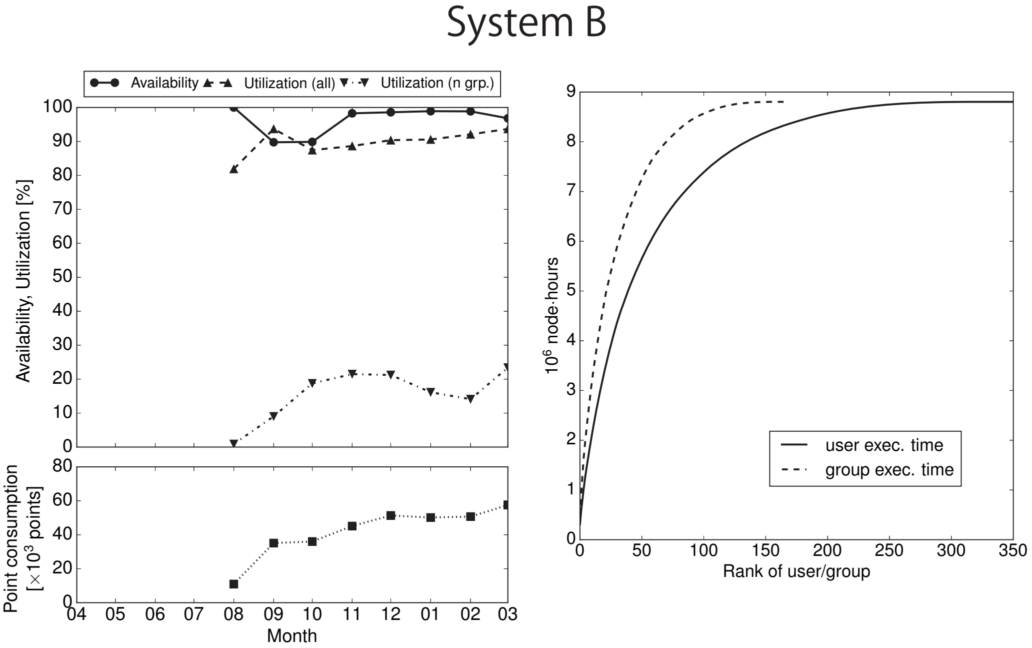

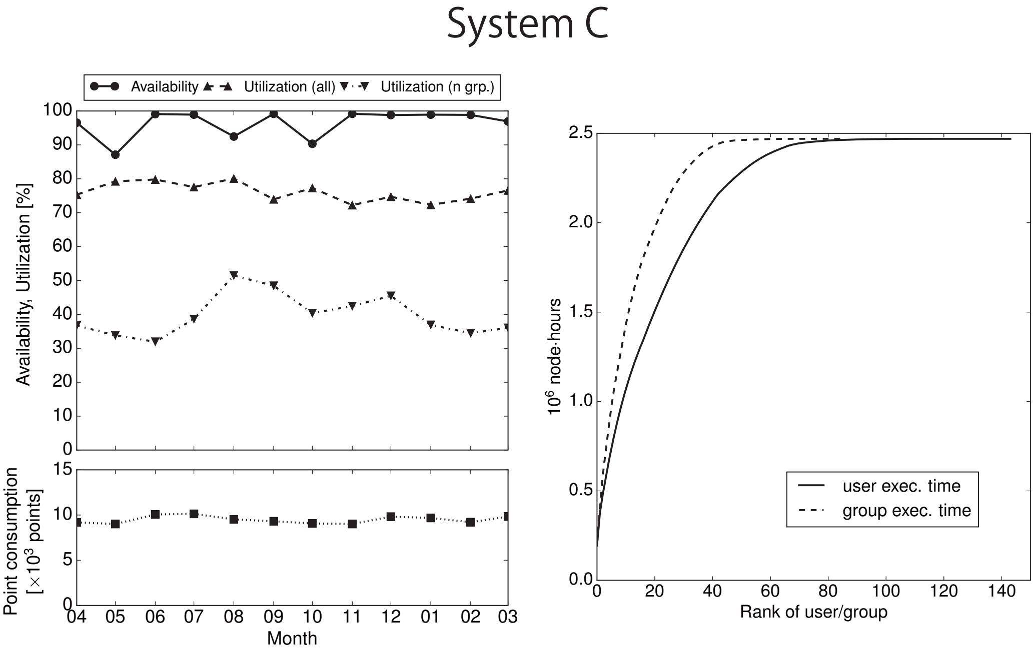

Figure 2: Left: Availabilities, utilization rates and point consumptions of each month during SY 2015. The utilization by CMSI projects (denoted by "n grp.") is plotted in addition to the total utilization (denoted by "all"). Right: User statistics. The horizontal axis shows the rank of the user/group arranged in the descending order of the execution time (hour×nodes). The vertical axis shows the sum of the execution time up to the rank.

Table 3: Queue structures in SY 2015

System–B

queue name	Elapsed time limit (hr)	# of nodes /job	# of nodes /queue	Memory limit (GB)	job points /(node·day)
F4cpu	24	1–4	216	120/node	1
L4cpu	120	1–4	108	120/node	1
F36cpu	24	5–36	288	120/node	1
L36cpu	120	5–36	144	120/node	1
F144cpu	24	37–144	1008	120/node	1
L144cpu	120	37–144	144	120/node	1
i18cpu	0.5	1–18	72	120/node	1
F18acc	24	1–18	108	120/node	2
L18acc	120	1–18	54	120/node	2
F72acc	24	19–72	144	120/node	2
i9acc	0.5	1–9	36	120/node	2
F2fat	24	1–2	17	1000/node	4
L2 fat	120	1–2	6	1000/node	4
i1fat	0.5	1	2	1000/node	4

System–C

queue name	Elapsed time limit (hr)	# of nodes /Job	# of nodes /queue	job points /(node·day)
debug	0.5	1-4	24	1
interactive	0.5	1-4	24	1
F12	24	2-12	60	1
F96	24	2-12	288	1
L12	120	24-96	24	1
L96	120	24-96	192	1

* In System C, the available memory size is limited to 28 GB per one CPU.

Table 4: Disk points of System B and C

		point/day
System B	`/home`	$0.001 \times \theta(q - 300)$
	`/work`	$0.0001 \times \theta(q - 3000)$
System C	`/home`	$0.05 \times \theta(q - 10)$
	`/work`	$0.005 \times \theta(q - 100)$

* q is denoted in unit of GB.

* $\theta(x)$ is equal to the Heaviside step function $H(x)$ multiplied by x, i.e., $xH(x)$.

Table 5: Number of jobs, average waiting time, total execution time, and average number of used nodes per job in each queue.

System-B

queue	# of Jobs	Waiting Time (hour)	Exec. Time ($\times 10^3$ node·hour)	# of nodes
F4cpu	60680	20.14	667.69	1.92
L4cpu	5524	59.70	307.34	1.99
F36cpu	18095	31.29	955.91	10.24
L36cpu	2673	53.33	471.42	8.75
F144cpu	7965	15.28	3812.97	88.29
L144cpu	177	136.37	580.61	117.15
i18cpu	19750	0.54	33.35	6.66
F18acc	22329	14.14	288.57	2.09
L18acc	6097	39.16	111.13	1.41
F72acc	1617	5.69	188.79	43.99
i9acc	2436	0.58	2.68	4.14
F2fat	4243	8.53	24.22	1.11
L2fat	311	23.84	16.90	1.14
i1fat	1142	0.26	0.20	1.00

System-C

queue	# of Jobs	Waiting Time (hour)	Exec. Time ($\times 10^3$ node·hour)	# of nodes
F12	8029	14.69	399.99	5.89
L12	64	85.11	10.72	5.59
F96	5180	43.50	2037.12	41.24
L96	6	555.42	15.15	96.00
debug	6966	0.16	1.87	2.61
interactive	1017	0.00	0.22	1.33

Table 6: List of supported software and project proposers for the GPGPU support service for SY 2015.

Software	Project Proposer	Affiliations
LargeScaleBoidsSimulator	Takashi Ikegami	The University of Tokyo
MDACP	Hiroshi Watanabe	The University of Tokyo
MODYLAS	Yoshimichi Andoh	Nagoya University
pTensor	Satoshi Morita	The University of Tokyo
RSCPMD	Yasuteru Shigeta	University of Tsukuba

The acc queues have relatively short waiting times, but we expect that to change as more users get accustomed to using GPGPUs.

2.3 GPGPU Support Service

As noted in Sec. 1.1, ACC nodes with graphics processing units (GPU) were introduced in System B in School Year 2015. Since GPUs were introduced in the ISSP Supercomputer center for the first time, many programs developed or utilized by users of this center have not been programmed for GPU computing. To help users take advantage of GPUs, the supercomputer center has started a service for porting users' materials science software to General Purpose GPUs (GPGPU)[1]. After a call for proposals (which will usually be in December), target programs for the next school year are selected by the Steering Committee of SCC. The porting service is carried out on each program for about two months; the coding is performed by engineers from the computer vender suppling the ISSP supercomputer system, and ISSP staff oversee the progress of the project and manage necessary communications with the proposer. Copyrights of the resulting software basically belong to the proposers, but the supported contents might be published under agreement with the proposer.

Since 2015 was the first year of the operation of System B with ACC nodes, the call for proposals was announced in May and target programs shown in Table 6 were selected in July. To determine the specific support contents and schedule, we first held kickoff meetings for each selected proposal from August to September.

In the actual service, analysis of the program was first performed to judge whether the target problems being solved can be accelerated using GPUs. After the analysis, the following support was carried out. For MDACP, MODYLAS and RSCPMD, parallelization using OpenACC or CUDA was performed on hotspots. For pTensor, matrix-matrix multiplication, which originally used BLAS, was rewritten to use cuBLAS[2]. For LargeScaleBoidsSimulator, parallelization with multiple GPUs on a single process was extended to that with multiple GPUs on multiple processes. The contents and results of the porting service of MODYLAS and pTensor were presented in ISSP joint-use supercomputer/CCMS symposium in 2016. Details on the porting service can be found on the ISSP supercomputer center web page[1].

References

[1] http://www.issp.u-tokyo.ac.jp/supercom/rsayh2/gpgpu

[2] cuBLAS, http://docs.nvidia.com/cuda/cublas/

Acknowledgments

The staffs would like to thank Prof. Takafumi Suzuki (now at University of Hyogo) for developing WWW-based system (SCM: SuperComputer Management System) for management of project proposals, peer-review reports by the SPAC committee, and user accounts. We also thank Ms. Reiko Yamaji for creating and maintaining a new WWW page of the ISSP Supercomputer Center.

3 RESEARCH REPORTS

3.1 Invited Articles

Capacitance of nanosized capacitors investigated using the orbital-separation approach–dead layer effect and negative capacitance

Shusuke KASAMATSU
The Institute for Solid State Physics, the University of Tokyo
5-1-5 Kashiwa-no-ha, Kashiwa-shi, Chiba 277-8581, Japan

Satoshi WATANABE
Department of Materials Engineering, the University of Tokyo
7-3-1 Hongo, Bunkyo-ku, Tokyo 113-8656, Japan

Seungwu HAN and Cheol Seong HWANG
Department of Materials Science and Engineering, Seoul National University
Seoul, 151-742, South Korea

Abstract

As the characteristic lengths in nanoelectronics devices approach the nanometer and subnanometer regimes, it is becoming increasingly clear that device properties at the nanoscale cannot be interpolated straightforwardly from bulk properties. To aid in understanding and controlling such nanoscale properties, first-principles simulation based on the Kohn-Sham (KS) formalism of density functional theory (DFT) [1, 2] has now become a go-to method. However, conventional KS-DFT is a ground-state method and cannot simulate devices operating under bias voltage. To this end, we developed what we now call the orbital-separation approach, which is capable of simulating metal/insulator heterostructures with different Fermi levels in each of the metallic parts. In this report, we review this method and its application to investigation of the interesting phenomena of negative capacitance that has been reported in ferroelectric heterostructures.

1 Orbital-separation approach for finite-bias simulations from first principles

1.1 Introduction

Advances in process technologies have made possible fabrication and observation of devices at nanometer or even subnanometer scales. Such nanodevices sometimes exhibit peculiar properties that cannot be understood from bulk properties of the constituent materials.

In this work, we concentrate on the capacitance, which determines the amount of charge Q that can be induced by application of bias voltage V ($C = dQ/dV$), which is a fundamental property in the design of all semiconductor devices. Classically, the capacitance per unit area of a parallel-plate capacitor is determined from the permittivity ϵ and thickness d of the dielectric film as

$$\frac{C}{A} = \frac{\epsilon}{d}. \tag{1}$$

Continuation of the scaling-down of semiconductor device design rule requires increasing

C/A. This is because the basic idea for achieving higher computation power and data storage density is to cram more device elements onto a chip, and this translates to decreasing real-estate per device element. For capacitors and transistors to function properly, the capacitance has to be maintained despite the decreasing area assigned to each device, which translates to higher capacitance per unit area. To obtain higher capacitance density, it is apparent from Eq. (1) that one should employ high-permittivity dielectric (the so-called high-k materials) films that are made as thin as possible while still being thick enough to suppress tunneling current between electrodes. However, it has been found that in many cases, the capacitance degrades rather significantly compared to that predicted from Eq. (1) in nanometer-thin dielectrics. This has been explained by so-called interfacial "dead layers" having a degraded permittivity compared to bulk. First-principles simulations have indicated that this is an intrinsic effect that remain even in perfectly epitaxial metal/dielectric interfaces, although the amount of the effect depends on the screening capabilities of the metal as well as the specifics of the chemical bonds at the interface [3, 4]. On the other hand, experiments report varying capacitance values depending on processing conditions, which indicate that various types of defects and interface chemistry are also at play. The dead layer problem is a significant bottleneck towards realizing further scaling in the semiconductor industry [5].

To assist in the understanding and design of such interface effects for future nanoelectronics, it may be natural nowadays to resort to atomistic simulations based on the Kohn-Sham (KS) formalism of density functional theory (DFT). However, since the capacitance is the response of the metal/insulator heterostructure to external bias voltage, it is not straightforward to utilize KS-DFT, which is conventionally a ground state theory, for such simulations. Linear-response type methods such as density functional perturbation theory (DFPT) [6] are applied routinely to calculate bulk permittivities, but it cannot be applied to metal/insulator heterostructures. One may also be interested in nonlinear regimes such as polarization reversal in ferroelectric systems under bias. To this end, many finite-bias methods have been developed [7, 8, 9, 10, 11, 12, 13, 14, 15, 16], but none of them are perfect; each have limitations in efficiency, accuracy, geometric constraints, and/or difficulty in implementation and use. We have given a somewhat thorough discussion on these methods in Ref. [17]. To overcome many of these limitations and to provide an efficient KS-DFT-based methodology for simulation of metal/insulator heterostructures under bias, we developed what we now call the *orbital-separation approach* (OSA) [17, 18]. This method will be briefly discussed below.

1.2 Orbital-separation approach

In conventional KS-DFT [2], the N-electron Schrödinger equation is rewritten as a set of single-particle KS equations

$$\left(-\frac{\hbar^2}{2m}\nabla^2 + v_{\mathrm{eff}}(\mathbf{r})\right)\phi_i(\mathbf{r}) = \epsilon_i\phi_i(\mathbf{r}), \qquad (2)$$

where v_{eff} is the KS effective potential containing the external potential (usually from the nuclei), the electrostatic (Hartree) potential, and the exchange-correlation potential that contains all remaining many-body effects

$$v_{\mathrm{eff}} = v_{\mathrm{ext}}(\mathbf{r}) + \int d^3r' \frac{\rho(\mathbf{r}')}{|\mathbf{r}-\mathbf{r}'|} + v_{\mathrm{xc}}(\mathbf{r}). \qquad (3)$$

$\rho(\mathbf{r})$ is the electron density that is constructed from KS orbitals $\{\phi_i\}$ as

$$\rho(\mathbf{r}) = \sum_i f_\sigma(\epsilon_i - \epsilon_{\mathrm{F}})|\phi_i(\mathbf{r})|^2, \qquad (4)$$

where $f_\sigma(\epsilon-\epsilon_{\mathrm{F}})$ is the occupation function and ϵ_{F} is the Fermi level determined from charge conservation

$$\int \rho(\mathbf{r})d\mathbf{r} = N. \qquad (5)$$

Since ρ appears in Eq. (2), which in turn determines ρ through its solutions $\{\phi_i\}$, these equations are solved iteratively until self-consistency is reached. Note that Brillouin zone integration over **k**-points is necessary in periodic systems but have been omitted in the above equations for simplicity. In the OSA, the occupation scheme for constructing the density ρ is modified to simulate systems under external bias voltage. The self-consistency iterations are carried out in exactly the same manner as in conventional KS-DFT.

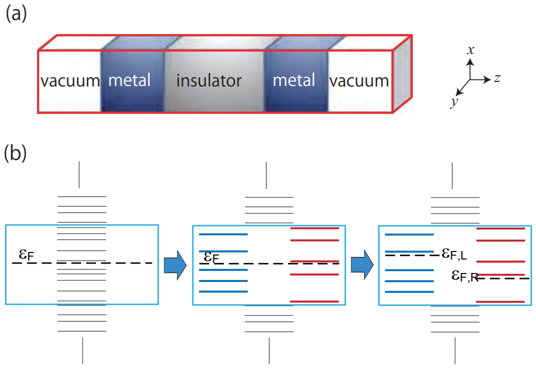

Figure 1: (a) Schematic of the metal-insulator-metal slab model considered in this study. The red lines indicate the boundaries of the periodic boundary condition. (b) Schematic of the orbital separation procedure around the Fermi level. Adapted from Ref. [17].

As a demonstration, we consider a metal/insulator/metal capacitor slab structure shown in Fig. 1. We employ the widely-used dipole correction procedure for canceling the electrostatic interaction between adjacent unit cells across the vacuum [8]. When the metallic parts are well-separated by insulating parts, the KS orbitals with eigenenergies near the Fermi level can be separated out into each of the electrodes because there are no eigenstates within the band gap of insulators. The separation is performed by examining the real-space extent of the KS orbitals within a preset energy window around the ground state Fermi level in each step of the self-consistency iterations. It is also possible to perform the separation in reciprocal space [19]. When employing symmetric electrodes, degeneracy between states in two electrodes may cause KS orbitals to have finite amplitude in both electrodes; in such cases, it is possible to perform a unitary transformation to separate the orbitals. In practice, we start the self-consistency loop from a slightly perturbed initial electron density by applying a sawtooth potential, for example, to lift the degeneracy. Once the KS orbitals are separated and grouped into each electrode, the occupation numbers are determined by applying different Fermi levels to each group of orbitals, and the density $\rho(\mathbf{r})$ is constructed accordingly. This density is then used in constructing the KS effective potential for the next step of the self consistency loop. Generalizing to two or more electrodes well separated by insulating parts, the occupation in the OSA is given as

$$f_{i,\mathbf{k}} = \begin{cases} 1, & \epsilon_{i,\mathbf{k}} < \epsilon_{\mathrm{win}}^{\mathrm{lower}} \\ 0, & \epsilon_{i,\mathbf{k}} > \epsilon_{\mathrm{win}}^{\mathrm{upper}} \\ f_\sigma(\epsilon_{i,\mathbf{k}} - \epsilon_{\mathrm{F},\alpha(i,\mathbf{k})}), & \epsilon_{\mathrm{win}}^{\mathrm{lower}} \leq \epsilon_{i,\mathbf{k}} \\ & \leq \epsilon_{\mathrm{win}}^{\mathrm{upper}}, \end{cases} \tag{6}$$

where $\epsilon_{\mathrm{win}}^{\mathrm{upper\ (lower)}}$ is the upper (lower) bound of the energy window, and $\alpha(i,\mathbf{k})$ specifies to which electrode the KS orbital $\phi_{i,\mathbf{k}}$ belongs (note that we have resurrected the **k**-point notation for Brillouin zone integration). The Fermi levels in each electrode are determined so as to maintain total charge neutrality

$$\int \rho(\mathbf{r})d\mathbf{r} = \int d\mathbf{r} \sum_{\mathbf{k},i} w_{\mathbf{k}} f_\sigma(\epsilon_{i,\mathbf{k}} - \epsilon_{\mathrm{F},\alpha(i,\mathbf{k})}) \times |\psi_{i,\mathbf{k}}(\mathbf{r})|^2 = N \tag{7}$$

where $w_{\mathbf{k}}$ is the **k**-point weight, while also maintaining specified bias voltages with respect to one reference electrode

$$\begin{aligned}\epsilon_{\mathrm{F},1}-\epsilon_{\mathrm{F},0}&=eV_1\\ \epsilon_{\mathrm{F},2}-\epsilon_{\mathrm{F},0}&=eV_2\\ &\vdots\\ \epsilon_{\mathrm{F},\alpha_{\max}}-\epsilon_{\mathrm{F},0}&=eV_{\alpha_{\max}}.\end{aligned} \tag{8}$$

The above procedure makes possible constant voltage (closed-circuit) simulations, but one may also desire to perform constant charge (open-circuit) simulations, which are especially useful for examining ferroelectric systems as pointed out in Ref. [20]. As long as nothing drastic occurs at the interface (e.g., chemical reactions involving atoms belonging to the metallic slab), the bias voltage has minimal effect on the KS orbitals of the electrodes. Thus, it is possible to calculate the free charge by comparing the occupation before and after bias application, and it is straightforward to determine the bias voltages that result in a preset free charge. Details on this constant charge scheme are given in Ref. [18].

It is worth pointing out that the OSA can be understood as a variant of the ΔSCF approach for simulating excited states of molecules [21, 22]. In the ΔSCF approach, electron-hole pairs are introduced by transferring an electron from an occupied to an unoccupied KS orbital, and performing the self consistency procedure with this occupation scheme. Although this method seems, at first sight, to be unjustified within the framework of KS-DFT, a formal basis was put forth in Ref. [23] as an approximation to an exact excited-state KS formalism.

We also note that the Hellman-Feynman forces acting on the nuclei can be calculated with no modification in conventional KS-DFT codes [17]. Thus, it is possible to simulate the dielectric response originating from ionic polarization, and it is also possible to perform molecular dynamics simulations using OSA.

The only clear limitation of the OSA is that it cannot handle situations where there is non-negligible electronic current between electrodes, because in such cases, the KS orbitals cannot be separated unambiguously into each electrode. This means that the amount of voltage that can be applied is limited by the band gap and the band offset at the metal/insulator interfaces. It can be applied as long as KS orbitals are employed in the calculations, which means that it can be implemented in codes employing any type of basis set (plane wave, wavelet, pseudoatomic orbitals, etc.).

Finally, we list a few useful equations for calculating capacitance and the local permittivity in a metal-insulator-metal model. The differential capacitance can be evaluated from the definition $C = dQ/dV$, but it can also be calculated from the total energy as [17]

$$C=\frac{1}{V}\frac{dE}{dV}. \tag{9}$$

This can come in handy when one wants to avoid the overhead (and possible complications) in calculating the free charge Q. The inverse local permittivity between the electrodes can be calculated from the capacitance and the local macroscopically-averaged electrostatic potential $\bar{V}_{\mathrm{H}}$ as (see supplementary material of [24])

$$\frac{1}{\epsilon_{\mathrm{r}}(z,V)}=-\frac{\epsilon_0 A}{C(V)}\frac{\partial^2[\Delta\bar{V}_{\mathrm{H}}(z,V)]}{\partial V\partial z}. \tag{10}$$

The above quantities calculated while fixing the positions of the nuclei correspond to optical frequency response, while those calculated by fully relaxing the nuclear positions correspond to static frequency response of the system.

1.3 Test on typical capacitor: Au/MgO/Au

To confirm the validity of this method, we implemented the OSA in Vienna ab-initio Simulation Package [25, 26] and performed finite bias simulations on the Au/MgO/Au capacitor shown in Fig. 2 (a) [17]. As shown in Fig. 2 (b), the electronic states near the Fermi level have virtually zero amplitude in the middle of the insulating MgO slab, although there are some metal-induced gap states penetrating within

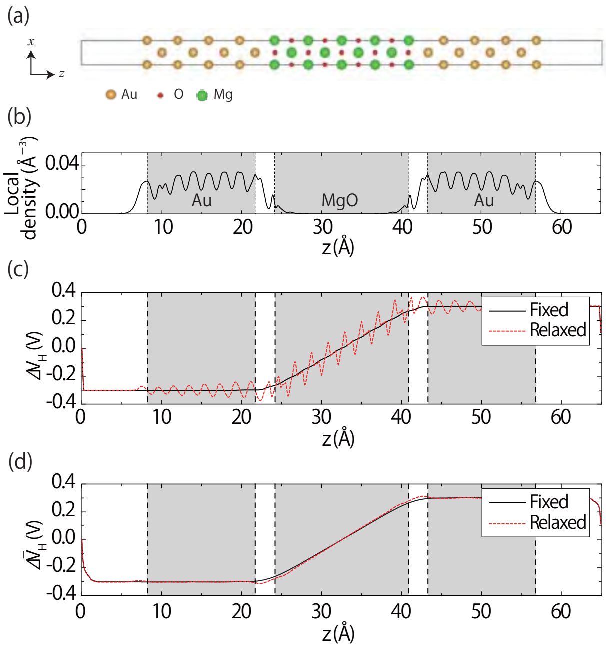

Figure 2: (a) Schematic of the Au/MgO/Au slab model considered in this study. (b) The local density of states within ±1 eV around the Fermi level. (c) The bias-induced change in the local electrostatic potential calculated with ions fixed (solid line) and after full ionic relaxation under 0.6 V. (d) The macroscopic average of (c). Adapted from Ref. [17].

a few angstroms from the interface. Thus, the OSA is applicable to this system. When the finite- bias calculations are performed with atoms fixed to their zero-bias relaxed positions, the induced potential ΔV_{H} is flat in the electrodes and drops linearly in the insulator as expected from classical electrostatics. The difference in ΔV_{H} between the Au electrodes equals the applied Fermi level difference (Fig. 2 (c)), implying that the self-consistent procedure is working as expected. When the atoms are allowed to relax under bias (corresponding to static frequency response), ΔV_{H} oscillates due to local ionic polarization, but the classical picture still holds if one performs macroscopic averaging of the potential (Fig. 2 (d)).

The total energy vs. the applied bias is a parabolic curve within numerical error, and

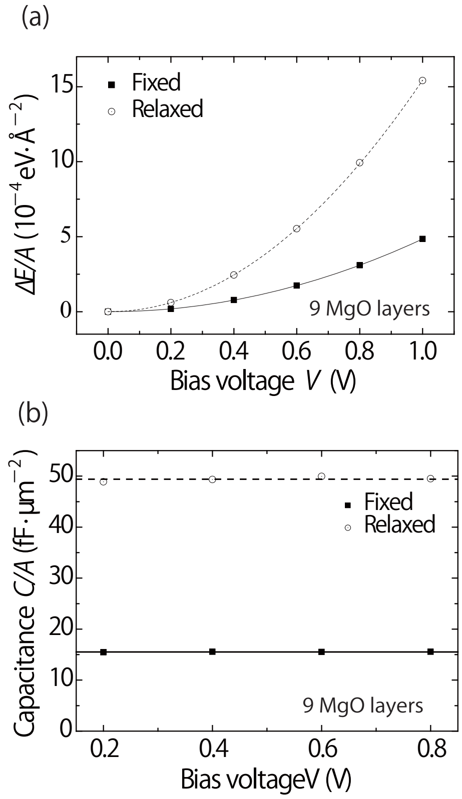

Figure 3: The calculated energy (a) and capacitance (b) as a function of applied bias. Adapted from Ref. [17].

the capacitance evaluated from Eq. (9) is virtually constant (Fig. 3). It is notable that the energy increases with relaxation; although this may seem strange at first sight, it is actually reasonable because ionic polarization allows further charging of the capacitor when a battery is connected at constant bias.

The calculated capacitance and induced potential can be used to calculate the local permittivity from Eq. (10) as shown in Fig. 4. The permittivities in the middle of the metal slabs diverge, while the values in the middle of the MgO slab for optical and static response correspond almost exactly to bulk values calculated using DFPT. The numerical consistency with DFPT results indicate the high reliability of the OSA. The small oscillations near the interface originate from the chemical details of the interface, giving rise to an interfacial ca-

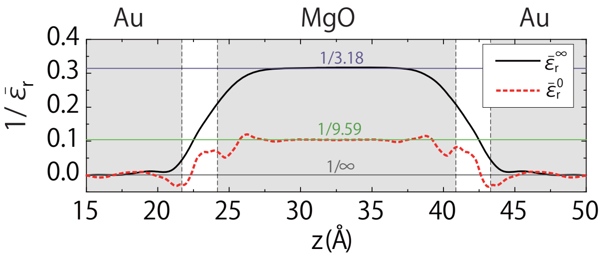

Figure 4: The calculated inverse permittivity profile of the Au/MgO/Au capacitor.

pacitance component that adds in series to the bulk capacitance.

1.4 The intrinsic dead layer effect: $SrRuO_3/SrTiO_3/SrRuO_3$

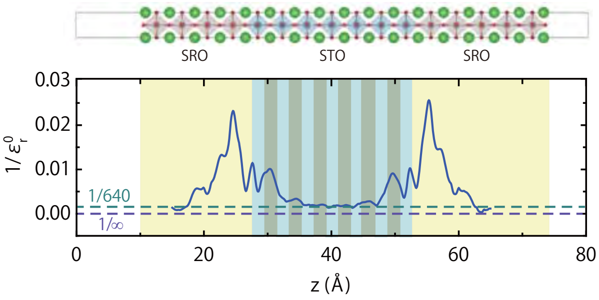

Figure 5: The calculated inverse permittivity profile of the SRO/STO/SRO capacitor.

Next, we apply the OSA to a system with much more prominent interfacial capacitance component; we reexamine the intrinsic dead layer effect in the $SrRuO_3$ (SRO)/$SrTiO_3$ (STO)/SRO capacitor that was reported in Ref. [3]. A different finite-bias approach based on maximally-localized Wannier functions [15] was used in Ref. [3], but we obtain essentially the same results here (Fig. 5). The dielectric constant is severely decreased at the interface, amounting to an interfacial capacitance component of 610 fF/μm^2. This translates to an upper limit of 305 fF/μm^2 on the capacitance that can be attained by simple scaling-down of dielectric thickness, since for very thin high-ϵ_r dielectrics, the total capacitance will be dominated by the interfacial component. In the 6-layer STO capacitor shown here, the calculated capacitance is 270 fF/μm^2, which is very close to this intrinsic limit. The severity of this dead layer problem is not limited to such ultrathin cases. Even for a capacitor with STO as thick as 54 nm, the total capacitance would have only 74% of the nominal capacitance calculated using the bulk dielectric constant $\epsilon_r = 640$ and Eq. (1).

1.5 Quantum capacitance of graphene

In certain situations, quantum effects can have a large impact on the total capacitance. One such known situation is when using graphene as the electrode [27, 28]. Due to its conical band dispersion with zero DOS at the Fermi level, the Fermi level position has to be displaced significantly to charge graphene. The bias voltage does not match the potential difference as depicted schematically in Fig. 6, and this results in a bias-dependent quantum capacitance component that adds in series to the geometric capacitance of Eq. (1). To test whether the OSA can treat this effect, we performed calculations on the graphene/vacuum/graphene capacitor shown in Fig. 7 (a) [17]. The electrostatic potential difference between the electrodes is predicted to be smaller than the applied voltage in line with the above-mentioned picture (Fig. 7 (b)). The calculated capacitance (Fig. 8) can be fitted decently with an approximate analytical formula for the quantum capacitance in this system [17, 27]. Thus, we can judge that the OSA can be used to calculate quantum capacitance effects.

1.6 Summary

We developed the orbital-separation approach for simulating the effect of applied bias on metal/insulator heterostructures within the Kohn-Sham formalism of density functional

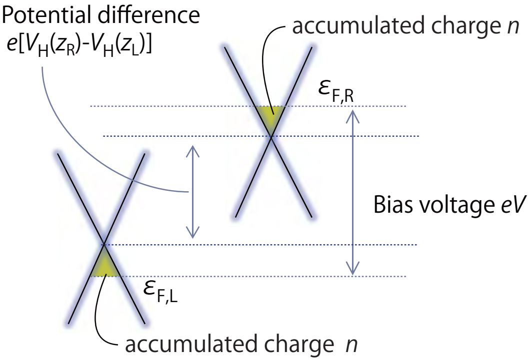

Figure 6: Schematic of the situation in graphene giving rise to the quantum capacitance.

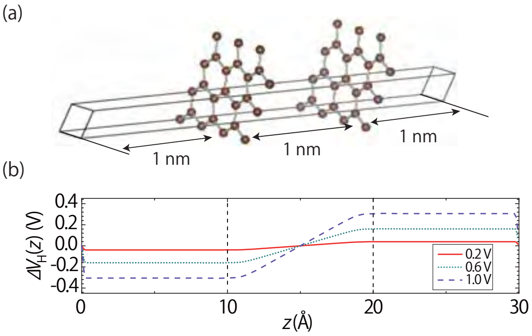

Figure 7: (a) Schematic of the graphene/vacuum/graphene capacitor and (b) xy-plane average of the electrostatic potential difference with respect to zero bias. The dashed vertical lines correspond to the position of the graphene sheets. Adapted from Ref. [17].

theory. The method is shown to be robust, efficient, and reliable. We showed that the method can be applied to examination of the dead layer effect as well as the quantum effects on the capacitance. Finally, we note that the application of the OSA is not limited to calculation of the dielectric response; it also holds much future promise for applications in a wide range of problems where bias voltage is an important factor such as electrochemical devices and scanning probe microscopy.

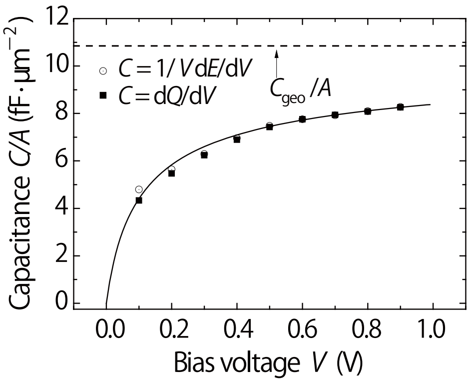

Figure 8: The capacitance calculated from voltage vs. energy (white circles) and voltage vs. induced charge (black squares). The dashed line indicates the geometric capacitance obtained from the fitting to analytical formula (see Ref. [17] for details). Adapted from Ref. [17].

2 Negative capacitance of multi-domain ferroelectric-paraelectric bilayer capacitor under bias

2.1 Introduction

As mentioned above, the difficulty to increase the capacitance due to the dead layer effect is a significant bottleneck that must be overcome for future nanoelectronics. One possibility that has been gaining attention recently is the utilization of negative capacitance. Since series capacitance adds up as $C^{-1} = C_1^{-1} + C_2^{-1}$, negative capacitance implies that its addition to a capacitor in series results in capacitance enhancement without further thinning of the dielectric layer. Recently, experimental works have reported capacitance enhancement in two-dimensional electron gas near depletion [29], as well as in ferroelectric thin films [30, 31, 32, 33, 34]. Here, we focus on the latter.

According to elementary electrostatics, the inverse capacitance is proportional to the curvature of the internal energy vs. electric displacement curve, i.e.,

$$C^{-1} = \frac{d^2U}{dD^2}. \tag{11}$$

Thus, negative capacitance is attained in the middle region of the double-well energy landscape of ferroelectric materials. Of course, this region is unstable and bulk ferroelectrics spontaneously polarize. However, it has been suggested that depolarizing field effects can suppress the polarization [35], resulting in stabilization of the near-zero polarization negative capacitance state. Such effects can be introduced by placing a paraelectric material in series with the ferroelectric, or it can also take the form of polarization stiffening due to the interfacial dead layer. Indeed, uniform spontaneous polarization in metal/ferroelectric/metal heterostructures was found to be suppressed when the ferroelectric was thinned down to a few unit cells as a result of the interfacial dead layer effect [36, 4].

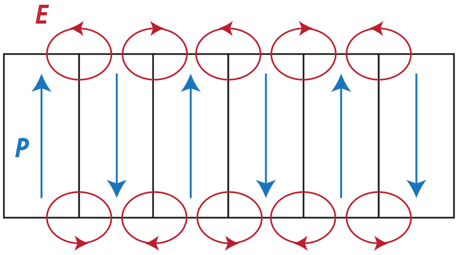

Figure 9: Schematic of the confinement of depolarizing field to the surface region by stripe domain formation.

The above discussion has been criticized for overlooking the fact that ferroelectrics usually form polarization domains to decrease the depolarization energy [37, 38, 39, 40, 41, 42]. By forming 180° domains, the surface polarization charge of adjacent domains cancel each other and the depolarizing field is confined near the surface of the film (Fig. 9). This allows the ferroelectric to polarize and lower the energy of the system, so the magnitude of the negative capacitance effect would be severely limited [43]. On the other hand, works on various heterostructures containing ferroelectric films have shown that the domain structure does not always appear, and that the domain formation in thin films depends on the film thickness, electrical boundary conditions, and the specific ferroelectric material [44, 45, 46, 47, 48, 49]. We also recall that capacitance enhancement has indeed been measured by several workers as mentioned above.

In Ref. [24], we set out to clarify this situation using first-principles simulation. We employed the orbital-separation approach to simulate the ferroelectric thin film system under bias, focusing on the response of the polarization domain structure to applied bias voltage and the resulting capacitance. We give a somewhat shortened version of the work presented in Ref. [24] and refer the reader to the original paper for more in-depth discussion with various subtleties in translating the simulation results to experimental systems.

2.2 Method and Model

We employ the orbital-separation approach implemented in VASP for finite bias calculations. We consider a metal-ferroelectric (FE)-paraelectric (PE)-metal bilayer capacitor where $\mathrm{SrRuO_3}$ (SRO) is used as the metallic electrodes, $\mathrm{BaTiO_3}$ (BTO) is used for the ferroelectric layer, and $\mathrm{SrTiO_3}$ (STO) is used as the paraelectric layer. The model consists of 1 × 4 in-plane perovskite unit cells for consideration of 180° striped domains. We also consider a model with only one in-plane unit cell to constrain the system to be monodomain; this model will serve as a reference to compare to the above multidomain model and elucidate the effect of domain formation. We also calculate a metal-PE-metal capacitor with the same number of PE layers to single out the effect of the FE layer. The in-plane unit cell size is constrained to that of bulk cubic STO to implicitly model the epitaxial growth of the multilayer structure on STO substrate. The capacitor models are relaxed under finite biases to simulate the static (DC) dielectric response and examine the stability of the polarization domain structure.

2.3 Results and Discussion

2.3.1 Formation of striped domains

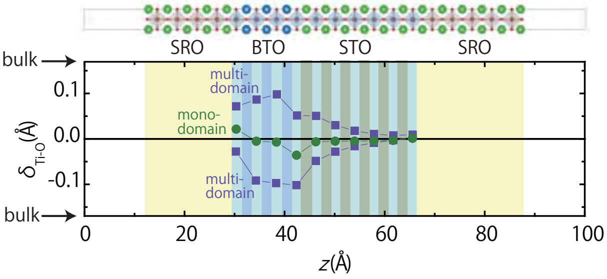

Figure 10: Anion-cation displacement in the TiO_2 layers of BTO and STO at zero bias. Results in monodomain and multidomain FE-PE capacitor models are compared. The value in bulk $BaTiO_3$ is indicated by arrows.

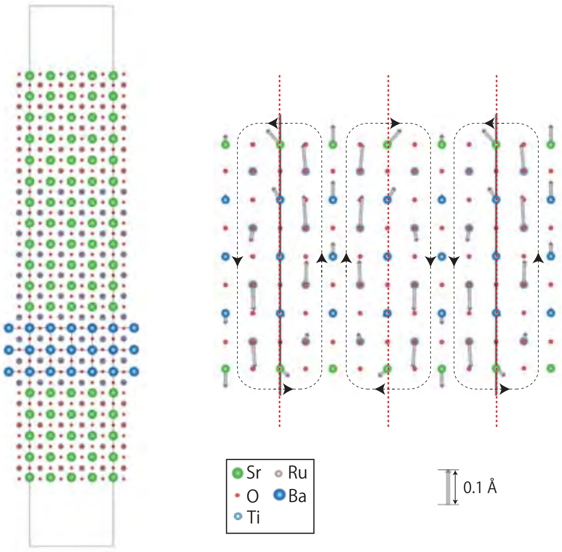

Figure 11: The local cation displacements in the BTO part of the stripe domain FE-PE capacitor model. Adapted from Ref. [24].

Figure 10 compares the local polarization perpendicular to the interface of the relaxed bilayer capacitor model with four in-plane unit cells and that with only one in-plane unit cell. The polarization is suppressed in the single unit cell model, but the four-unit cell model shows finite polarization in two directions due to striped domain formation (Fig. 11). The energy gain by domain formation is ∼ 20 meV per in-plane unit cell; this means that indeed, it is more favorable to break up into domains to lower the depolarization energy. However, the magnitude of the polarization is smaller than bulk, implying that there is some remaining depolarizing effect due to the combination of epitaxial strain and interface effects.

2.3.2 Bias dependence of the capacitance and domain structure

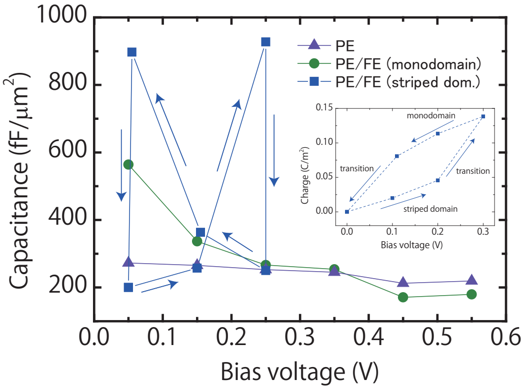

Figure 12: The calculated capacitance as a function of applied bias for PE (triangles), monodomain PE-FE (circles), and striped domain PE-FE capacitors. The calculated free charge for the striped domain PE-FE system is shown in the inset. From Ref. [24].

Figure 12 shows the calculated differential capacitance dQ/dV of the metal-FE-PE-metal bilayer capacitor with and without polarization domains compared to the metal-PE-metal capacitor. Near zero bias, the monodomain FE-PE bilayer capacitor shows capacitance enhancement over the monolayer PE capacitor, implying that the FE layer shows negative ca-

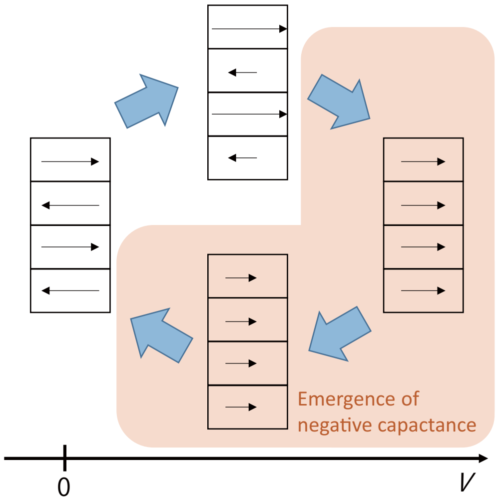

Figure 13: Schematic of the antiferroelectric-like evolution of the polarization domains under bias. Negative capacitance is observed within the shaded region.

pacitance due to the suppression of polarization. On the other hand, the more realistic multidomain model shows lower capacitance than the PE capacitor, indicating that domain formation indeed inhibits the emergence of the negative capacitance effect. However, once we turn on the bias voltage and examine the voltage dependence, we find that the capacitance shows hysteretic behavior with a large enhancement over the monolayer PE capacitor. This behavior is due to the antiferroelectric-like domain evolution summarized in Fig. 13. At low bias, the striped domain state is stable and no negative capacitance effect is observed. At higher biases, the monodomain state becomes stable and remains so until the bias is lowered below 0.1 V. The negative capacitance effect is seen within this monodomain regime, and the multidomain-monodomain transition also contributes to a huge capacitance enhancement.

2.4 Summary

We employed our newly-developed orbital separation approach to examine the possibility of the emergence of negative capacitance in ferroelectric ultrathin films. Although several experimental works had reported rather large negative capacitance effects, it was not clear how such an effect was viable when considering domain formation. In this work, we showed that at least when the ferroelectric film is thinned down to a few unit cells, a not-so-large bias of ~ 0.2 V is sufficient to turn the system into a monodomain state with significant capacitance enhancement due to the negative capacitance effect. Further experimental and theoretical studies are necessary to clarify the effects of non-idealities not taken into account in this work such as finite-temperature, defects, and nucleation.

References

[1] P. Hohenberg and W. Kohn, Phys. Rev. **136**, B864 (1964).

[2] W. Kohn and L. J. Sham, Phys. Rev. **140**, A1133 (1965).

[3] M. Stengel and N. A. Spaldin, Nature **443**, 679 (2006).

[4] M. Stengel, D. Vanderbilt, and N. A. Spaldin, Nature Mater. **8**, 392 (2009).

[5] S. K. Kim *et al.*, Adv. Funct. Mater. **20**, 2989 (2010).

[6] X. Gonze and C. Lee, Phys. Rev. B **55**, 10355 (1997).

[7] J. Neugebauer and M. Scheffler, Phys. Rev. B **46**, 16067 (1992).

[8] L. Bengtsson, Phys. Rev. B **59**, 12301 (1999).

[9] Y. Gohda, Y. Nakamura, K. Watanabe, and S. Watanabe, Phys. Rev. Lett. **85**, 1750 (2000).

[10] N. Nakaoka, K. Tada, S. Watanabe, H. Fujita, and K. Watanabe, Phys. Rev. Lett. **86**, 540 (2001).

[11] M. Brandbyge, J.-L. Mozos, P. Ordejón, J. Taylor, and K. Stokbro, Phys. Rev. B **65**, 165401 (2002).

[12] K. Burke, R. Car, and R. Gebauer, Phys. Rev. Lett. **94**, 146803 (2005).

[13] M. Otani and O. Sugino, Phys. Rev. B **73**, 115407 (2006).

[14] K. Uchida, H. Kageshima, and H. Inokawa, Phys. Rev. B **74**, 035408 (2006).

[15] M. Stengel and N. A. Spaldin, Phys. Rev. B **75**, 205121 (2007).

[16] B. Lee, C.-K. Lee, S. Han, J. Lee, and C. S. Hwang, J. Appl. Phys. **103**, 24106 (2008).

[17] S. Kasamatsu, S. Watanabe, and S. Han, Phys. Rev. B **84**, 085120 (2011).

[18] S. Kasamatsu, S. Han, and S. Watanabe, Phys. Rev. B **92**, 115124 (2015).

[19] S. Watanabe and S. Kasamatsu, First-principles calculations on the dielectric properties of oxide heterostructures, in *ISSP Materials Design and Characterization Laboratory Supercomputer Center Activity Report 2012*, pp. 56–57, 2013.

[20] M. Stengel, N. A. Spaldin, and D. Vanderbilt, Nature Phys. **5**, 304 (2009).

[21] R. O. Jones and O. Gunnarsson, Rev. Mod. Phys. **61**, 689 (1989).

[22] A. Hellman, B. Razaznejad, and B. I. Lundqvist, J. Chem. Phys. **120**, 4593 (2004).

[23] A. Görling, Phys. Rev. A **59**, 3359 (1999).

[24] S. Kasamatsu, S. Watanabe, C. S. Hwang, and S. Han, Adv. Mater. **28**, 335 (2016).

[25] G. Kresse and J. Furthmüller, Phys. Rev. B **54**, 11169 (1996).

[26] G. Kresse and D. Joubert, Phys. Rev. B **59**, 1758 (1999).

[27] T. Fang, A. Konar, H. Xing, and D. Jena, Appl. Phys. Lett. **91**, 092109 (2007).

[28] J. Xia, F. Chen, J. Li, and N. Tao, Nat. Nanotechnol. **4**, 505 (2009).

[29] L. Li *et al.*, Science **332**, 825 (2011).

[30] A. I. Khan *et al.*, Appl. Phys. Lett. **99**, 113501 (2011).

[31] G. A. Salvatore, A. Rusu, and A. M. Ionescu, Appl. Phys. Lett. **100**, 163504 (2012).

[32] W. Gao *et al.*, Nano Lett. **14**, 5814 (2014).

[33] A. I. Khan *et al.*, Nat. Mater. **14**, 182 (2015).

[34] D. J. R. Appleby *et al.*, Nano Lett. **14**, 3864 (2014).

[35] S. Salahuddin and S. Datta, Nano Lett. **8**, 405 (2008).

[36] J. Junquera and P. Ghosez, Nature **422**, 506 (2003).

[37] C. Kittel, Phys. Rev. **70**, 965 (1946).

[38] E. V. Chenskii and V. V. Tarasenko, J. Exp. Theor. Phys. **56**, 618 (1982).

[39] D. D. Fong *et al.*, Science **304**, 1650 (2004).

[40] T. Nishimatsu, U. Waghmare, Y. Kawazoe, and D. Vanderbilt, Phys. Rev. B **78**, 104104 (2008).

[41] P. Aguado-Puente and J. Junquera, Phys. Rev. Lett. **100**, 177601 (2008).

[42] E. Glazkova, K. McCash, C.-M. Chang, B. K. Mani, and I. Ponomareva, Appl. Phys. Lett. **104** (2014).

[43] A. Cano and D. Jiménez, Appl. Phys. Lett. **97**, 133509 (2010).

[44] D. D. Fong *et al.*, Phys. Rev. Lett. **96**, 127601 (2006).

[45] V. A. Stephanovich, I. A. Luk'yanchuk, and M. G. Karkut, Phys. Rev. Lett. **94**, 047601 (2005).

[46] M. Dawber *et al.*, Adv. Mater. **19**, 4153 (2007).

[47] P. Zubko, N. Stucki, C. Lichtensteiger, and J.-M. Triscone, Phys. Rev. Lett. **104**, 187601 (2010).

[48] L. Kim, J. Kim, U. Waghmare, D. Jung, and J. Lee, Phys. Rev. B **72**, 214121 (2005).

[49] C.-L. Jia *et al.*, Nature Mater. **6**, 64 (2007).

Correlation Effects in Topological Insulators

Norio Kawakami
Department of Physics, Kyoto University, Kyoto 606-8502

1 Introduction

Recent years have witnessed a surge of interest in topological insulators (TIs), which provide a new research platform in condensed matter physics. TIs have nontrivial band structures due to the spin-orbit coupling. A striking feature in TIs is that they host gapless edge states at boundaries, which are protected topologically. The notion of TI was originally proposed for graphene [1] and also for HgTe/CdTe quantum wells [2]. The latter TI was confirmed experimentally [3]. Also, many examples of TIs in three dimensions have been found in bismuth-based compounds, etc.[4, 5]. Although theory for TIs has been mainly devoted to non-interacting systems so far, correlation effects on them have attracted much attention, since novel aspects of electron correlations would emerge under topologically nontrivial conditions. This issue has further been stimulated by the fact that there are a variety of candidates for correlated TIs [6, 7, 8, 9], such as SmB_6 [10, 11], etc. In spite of extensive studies, understanding of topological phases in correlated systems[12, 13, 14, 15, 16, 17, 18, 19, 20], especially a topological Mott insulator, is still not sufficient. As mentioned above, gapless edge modes which are a source of exotic and rich physics are induced by bulk nontrivial properties in free fermion systems. Even in correlated systems, the nontrivial band structure would lead to novel gapless edge states; for example, edge states composed only of spin excitations in topological Mott insulators.

Here, we report our recent studies on the correlated TIs[21, 22]. We first discuss a topological Mott insulator in one dimension (1D) in Sec.2 to address how the edge Mott states emerge due to the interplay of topology and correlation [21]. We demonstrate, based on DMRG calculations with high accuracy, that the topological Mott insulator accompanied by the edge Mott states is indeed stabilized. In Sec.3, we then address a similar question for a two-dimensional (2D) correlated TIs [22]. In this case, we find a remarkable property caused by the interplay of topology and correlation: the topological properties emerge with increasing temperature in the presence of strong correlations. We demonstrate that the above counterintuitive properties are not specific to the model employed here but rather generic for correlated TIs. In Sec.4, we briefly explain some related topics we have studied in recent years [23, 24, 25, 26]. Brief summary is given in Sec.5.

2 Topological Mott insulator in 1D

We start with a fundamental question: whether a topological Mott insulator really emerges in correlated system, and if so, how the edge states behave in the presence of the interaction. To address this question, we here investigate a prototypical TI with Hubbard interaction in 1D [21]. By examining the bulk topological invariant and the entanglement spectrum of the correlated electron model, we elucidate how gapless edge states in a non-interacting TI evolve into Mott edge states in a topological Mott insulator. Furthermore, we propose a topological Mott transition, which is a new type of topological phase transition. This unconventional transition occurs in spin liquid phases in the Mott insulator and is accompanied by zeros of the single-particle Green's function and a gap closing in the spin excitation spectrum.

We consider a 1D correlated Su-Schrieffer-Heeger (SSH) model, which describes a bond-alternating tight binding model with electron correlation. The Hamiltonian reads,

$$\begin{aligned} H_{SSH} &= \sum_{i\sigma}(-tc^{\dagger}_{i+1a\sigma}c_{ib\sigma} + Vc^{\dagger}_{ia\sigma}c_{ib\sigma} + h.c.) \\ &+ U\sum_{i\alpha} n_{i\alpha\uparrow}n_{i\alpha\downarrow} + J\sum_{i} \mathbf{S_{ia}}\cdot\mathbf{S_{ib}} \quad (1) \end{aligned}$$

with $n_{i\alpha\sigma} = c^{\dagger}_{i\alpha\sigma}c_{i\alpha\sigma}$, where $c^{\dagger}_{i\alpha\sigma}(c_{i\alpha\sigma})$ is a creation (annihilation) operator for an electron at site i and in orbital $\alpha = a, b$ and spin $\sigma =\uparrow,\downarrow$ state. We introduce the third term representing the ferromagnetic spin exchange interaction, which is crucial for a topological phase transition induced by electron correlations. We recall that in the non-interacting case, in the region of $-t < V < t$, the system is in a TI phase protected by chiral symmetry, which is characterized by a nonzero winding number. Note that the symmetry is essential for determining the topological properties, and our analysis is valid generically for the 1D chiral-symmetric class. We employ the density-matrix renormalization group (DMRG) method, which provides a powerful tool to compute the ground-state quantities with high precision. In what follows, we choose the hopping integral t as the energy unit.

(a) *Topological Mott phase with spinon edge states*

Let us start with a Topological Mott insulator by setting $J = 0$ in the model Hamiltonian [21]. The obtained results are shown in Fig. 1. It is seen from Fig. 1(a) that even in the presence of U, the winding number takes $N_1 = 1$, implying that the system is always in a topological phase. Although the noninteracting TI continuously changes to the Mott insulator in the bulk with keeping $N_1 = 1$, the edge site shows a discontinuous change at $U = 0$; namely as seen from Fig. 1(b), the double occupancy abruptly decreases once the interaction U is introduced. This implies the formation of a local spin around the edges. This abrupt change signals the emergence of topological edge-Mott states, where electron correlations play a crucial role. Namely, the emergent local spin is not completely free, but still screened even after the abrupt change, implying that the edge states are strongly correlated. As seen from Fig. 1(c), this abrupt change is accompanied by a gap formation for the single particle excitations at the edges, while the collective spin excitations are still gapless. The latter may be referred to as gapless "spinon edge states". These observations lead us to the conclusion that at $U = 0$ a correlated edge-Mott state with gapful charge (gapless spin) excitations is induced at each edge, while the bulk behaves as a correlated band insulator. Although the single particle excitation spectrum is gapped at edges, degeneracy in the entanglement spectrum is maintained, giving rise to gapless edge modes in the spin excitation spectrum (Fig. 1(d)). Furthermore, the analysis with the entanglement spectrum

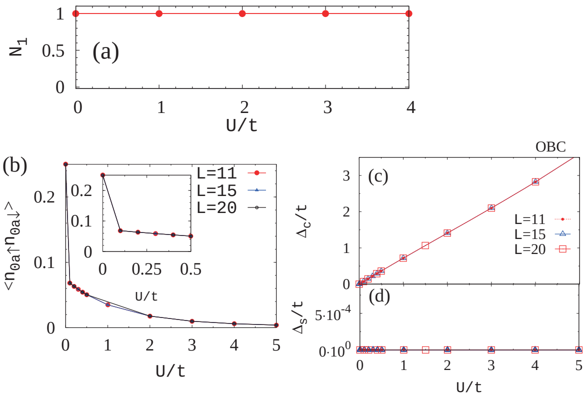

Figure 1: Results obtained for the parameters $(J, V) = (0, -0.4)$ [21]: (a) winding number N_1 for chain length $L = 11$, (b) double occupancy of orbital a at the edge site for several choices of L, (c) ((d)) single particle (spin) excitation gap under open boundary conditions.

(not shown here [21]) elucidates the above-mentioned fragility of edge states upon introduction of U.

Summarizing the results obtained for the correlated SSH model with $J = 0$, we have a topological Mott insulating phase where the bulk is always in a correlated TI insulator characterized by the Chern number $N_c = 1$, while the edge state is changed from a gapless electron mode to a topological edge Mott mode having gapful charge (gapless spin) excitations. We believe that this gives the first unambiguous example of topological Mott insulators.

(b) *Topological phase transition*

We now consider a topological Mott transition, which is a new type of topological phase transition characterized by zeros of the single-particle Green's function and a gap closing in the spin excitation spectrum [21]. To address this problem, let us switch on the exchange interaction J in the Hamiltonian (1), which can induce an intriguing phenomenon never observed in free fermion systems. If the interaction is ferromagnetic, a topological transition is induced by correlation effects; for example, for $J = -1.5$, the winding number changes from $N_1 = 0$ to $N_1 = 1$ with increasing the interaction U, as shown in Fig. 2(a). Therefore, the trivial insulator changes into a nontrivial one. In contrast to the non-interacting case, the topological properties are changed without a gap closing; as seen in the right panel of Fig. 3, the single particle excitation gap remains finite even at the transition point. Thus, zeros of Green's function are required at this point. Indeed we can see that a zero appears at the transition point (right panel of Fig. 2); at $U = 0$, a locus of the Green's function $G(i\omega = 0, k)$ does not wind the origin, but as the interaction U is increased, the locus approaches the origin and finally crosses it.

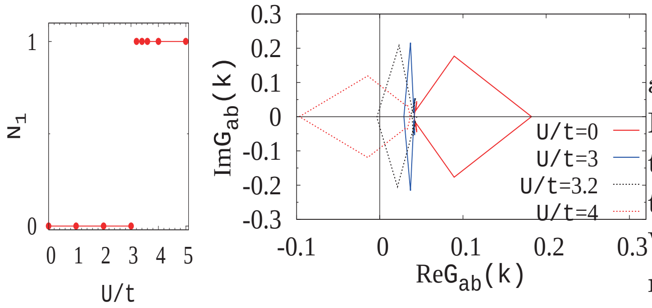

Figure 2: Left panel: Winding number for $(J, V) = (-1.5, -1.6)$ and $L = 11$ as a function of U [21]. Right panel: locus of the Green's function G_{ab}. As the momentum k is increased, $G_{ab}(k)$ draws its locus clockwise. In a trivial phase, at $k = k_{min}$, $G_{ab}(k)$ is positive and real and draws its locus clockwise.

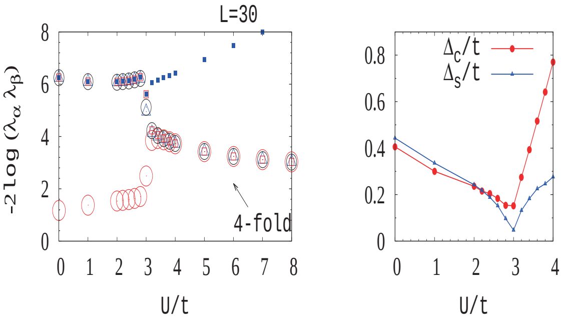

Figure 3: Left panel: Plots of lowest five entanglement spectra as functions of U under periodic boundary conditions for $(J, V) = (-1.5, -1.6)$ [21]. Right panel: Plots of spectral gap for the same parameters; single particle excitation (spin excitation) is denoted as Δ_c (Δ_s). These values are extrapolated to thermodynamic limit with scaling L^{-1}

The above-mentioned topological properties are confirmed by the entanglement spectrum. Namely, topological properties described by the winding number are also characterized by the structure of the entanglement spectrum. We can observe in Fig. 3 that the entanglement spectrum becomes degenerate for $3.2 < U$. Note that a change in the degeneracy of the entanglement spectrum requires a gap closing at the transition point, although the single particle gap remains finite at this point. Therefore, the only way to satisfy the condition for this topological Mott transition is to close a gap in a collective excitation spectrum, which corresponds to the spin excitation spectrum in our case. Therefore, we generally expect that a collective excitation spectrum becomes gapless at the topological Mott transition point where the Green's function has zeros.

3 Temperature-induced topological properties in 2D

We now investigate how topologically nontrivial phases evolve at finite temperatures. Specifically, we study a Kane-Mele Kondo lattice shown below at finite temperatures with dynamical mean field theory (DMFT) [22]. We find an intriguing phenomenon: restoration of topological properties at finite temperatures, which is caused by the interplay between topology and correlation. These phenomena are uncovered by analyzing the bulk as well as edge properties: in the bulk, the spin-Hall conductivity which is almost zero around zero temperature increases with increasing temperature, while at the edge, the gapless edge modes emerge with increasing temperature. We thus elucidate that the interplay of the topological nature of the system and the Kondo effect is essential for the restoration of topological properties.

In order to demonstrate the above-mentioned phenomena explicitly, we here employ a topological Kane-Mele Kondo model on a two-dimensional (2D) honeycomb lattice. The Hamiltonian reads

$$
\begin{aligned}
H_{KMK} &= H_{KM} + J\sum_i \mathbf{s}_i \cdot \mathbf{S}_i, \\
H_{KM} &= -t \sum_{\langle i,j\rangle\sigma} c^\dagger_{i,\sigma} c_{j,\sigma} \\
&+ it_{so} \sum_{\langle\langle i,j\rangle\rangle} \mathrm{sgn}(i,j)\mathrm{sgn}(\sigma) c^\dagger_{i,\sigma} c_{j,\sigma}, \quad (2)
\end{aligned}
$$

with $\mathbf{s}_i = \frac{1}{2} c^\dagger_{i,s}\sigma_{s,s'}c_{i,s'}$ and $\mathrm{sgn}(\sigma) = 1$ (-1) for $\sigma = \uparrow$ $(\downarrow)$. Here $c^\dagger_{i,s}$ creates an electron with spin $s = \uparrow, \downarrow$ at site i. $\mathbf{S}_i$ denotes a localized moment of spin $S = 1/2$ at site i on the honeycomb lattice. The effect of spin-orbit coupling is incorporated in $\mathrm{sgn}(i,j)$, which takes 1 (-1) when the electron hops clockwise (counter clockwise), respectively.

At $J = 0$, conduction electrons on the Kane-Mele lattice are completely decoupled from localized spins, and therefore the conductivity takes a finite quantized value at zero temperature, which is proportional to the topological invariant. At finite temperatures, it takes a finite but not quantized value. Nevertheless, if the temperature is smaller than the bulk gap, we have a spin-Hall conductivity close to the quantized value. This temperature region is regarded as a "topological insulator region" approximately, although the quantization is not well defined at finite temperatures.

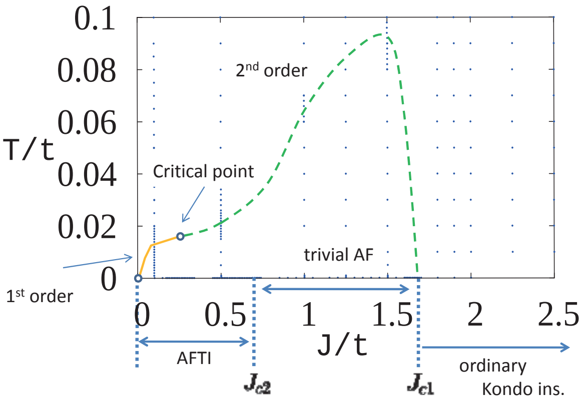

Figure 4: Phase diagram of temperature (T) vs. the antiferromagnetic coupling (J) [22]. A first order transition (solid orange line) is observed in the weak-coupling region while it becomes second order (dashed green line) with increasing J. For $J < 0.683t$ a topological antiferromagnetic phase (AFTI) is stabilized. This phase changes to a trivial antiferromagnetic phase and an ordinary Kondo insulator with increasing J. The topological structure is well-defined only at zero temperature.

Before addressing the topological properties, let us briefly summarize the obtained phase diagram shown in Fig. 4. For weak exchange interaction J, there is an antiferromagnetic topological phase, which is induced by the RKKY interaction. With increasing J, this phase changes to a trivial antiferromagnetic phase. Further increase in J stabilizes an ordinary (trivial) Kondo insulator. When the temperature increases, the antiferromagnetic order disappears via a first (second) order transition for weak (strong) interaction strength J. We find that the system shows the topologically nontrivial properties for $J < 0.683t$, while the increase in J induces a topological transition. At this continuous topological transition point, gap-closing in the density of states is observed.

In the following, we reveal that the interplay between electron correlations and topological properties leads to an intriguing crossover behavior; topological properties are restored at finite temperatures in the region where the topological structure of the ground state is destroyed. We confirm these intriguing properties in the following two steps: we start with the nonmagnetic phase then move to the antiferromagnetic phase.

In order to capture the essence, let us first restrict ourselves to paramagnetic solutions. The calculated conductivity is plotted in Fig. 5(a). At low temperatures, the spin-Hall conductivity is zero for $J = 0.5t$ since the topological invariant is no longer well-defined due to the Kondo effect; the singlet formation between electrons and localized spins leads to zeros of the Green's function (i.e., divergence of the self-energy) [see Fig. 5(b)]. With increasing temperature, the Kondo effect is suppressed, and the conductivity increases. For $T > 0.03t$, the conductivity approaches the values of $J = 0$ which are almost quantized. The increase of the spin-Hall conductivity is also observed for $J = 0.7t$, even though increasing the coupling strength J suppresses the conductivity at finite temperatures due to enhancement of the Kondo effect.

This increase of the conductivity is interpreted as a restoration of gapless edge modes. Our real-space dynamical mean-field theory (R-DMFT) calculations using the ribbon geometry reveal how finite temperatures affect the edge modes. From the results (not shown here [22]), we can see that edge modes are destroyed due to the Kondo effect at low temperatures, but are restored with increasing temperature, leading to an increase of the spin-Hall conductivity.

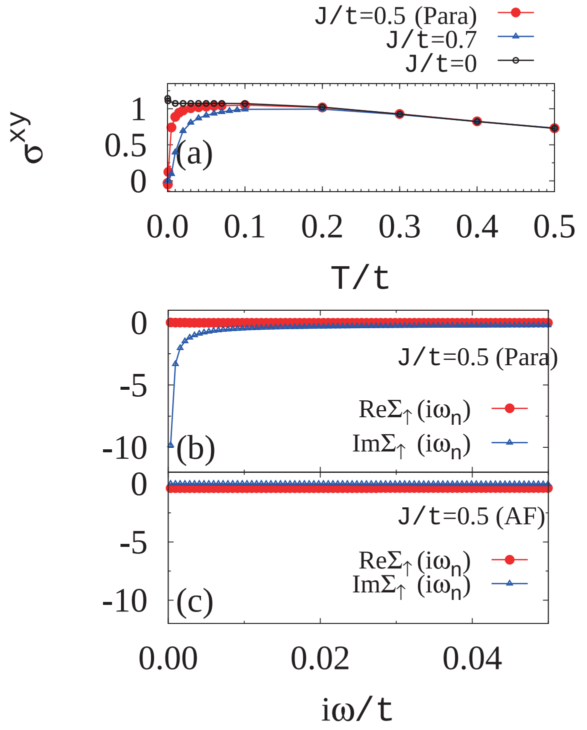

Figure 5: (a): Spin-Hall conductivity at finite temperatures. (b) ((c)): Self-energy of up-spin state in the paramagnetic (antiferromagnetic) phase [22]. For $t_{so} = 0$, the spin-Hall conductivity is zero even in the high temperature region.

Therefore, we conclude that the origin of this crossover is the competition of the Kondo effect and the topological properties. In the low temperature region, the Kondo effect governs the low energy properties and destroys the topological structure. On the other hand, topological properties (i.e., the conductivity and edge states) are restored if the temperature is higher than the Kondo temperature but smaller than the energy scale of the band gap of the noninteracting topological insulator.

It should be noted that the restoration of topological properties occurs even in the anti-

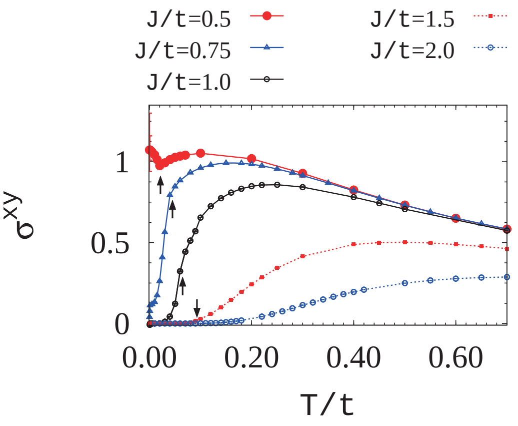

Figure 6: Spin-Hall conductivity for several values of J [22]. The error bars at low temperatures are due to extrapolation to the $\omega \to 0$ limit. At high temperatures these error bars are smaller than symbols. Arrows denote antiferromagnetic transition points.

ferromagnetic phase; the increase of the spin-Hall conductivity is observed in the antiferromagnetic phase. The conductivity in the antiferromagnetic phase is shown as a function of T in Fig. 6. At $J = 0.75t$, where the ground state is topologically trivial, the spin-Hall conductivity vanishes at zero temperature, but increases with increasing temperature. Note that the ground state is an antiferromagnetic topological phase for $J < 0.683$. As seen in Fig. 5(c), the magnetic order removes the pole of the self-energy, and the ground state possesses nontrivial properties. This leads to a dip structure in the temperature dependence of the conductivity for $J = 0.5t$; with decreasing temperature the Kondo effect firstly decreases the conductivity for $0.021t < T < 0.03t$, but with entering the antiferromagnetic phase ($T < 0.021t$), the conductivity increases again because the ground state is the antiferromagnetic topological insulator.

Summarizing this section, we have observed an intriguing crossover behavior due to the interplay between electron correlations and topological properties. At low temperatures, the Kondo effect destroys the topological structure. However, the topological properties are restored if the temperature is higher than the Kondo temperature but smaller than the band gap of the topological insulator. The restoration of topological properties can be observed in the bulk and the edge. The spin-Hall conductivity rapidly increases even if it is almost zero at low temperatures. Edge modes, destroyed by the Kondo effect in the low temperature region, appear with increasing temperatures. The crossover behavior is observed in both of the paramagnetic and the antiferromagnetic phases.

4 Related issues

We have also studied some interesting issues related to topological phases, which we briefly summarize below.

(a) *Topological phase transitions in periodically driven systems* [23, 24]: Recently, concepts of topological phases of matter have been extended to nonequilibrium systems. In particular, periodically driven systems described by Floquet theory have been a topic of intensive studies. We propose a model which shows non-equilibrium topological phase transitions in cold-atomic systems. Namely, we demonstrate that the Rabi oscillation plays an important role to tune the band structure in fermionic optical lattices, driving a non-equilibrium topological phase transitions from the trivial insulator to a time-reversal symmetric (Z_2) TI.

(b) *Hidden topological properties of quantum walks*[25]: Quantum walks provide a unique platform to realize Floquet TIs in a nonequilibrium systems driven by a time-periodic field. So-called discrete quantum walks consists of two operators, i.e. shift and coin operators, which respectively play a similar role of particle hopping and spin-rotation due to spin-orbit coupling. We can thus realize various topological phases in quantum walks for cold atomic systems, photonic systems, etc. We here obtain the phase diagrams of the topological numbers for the 1D discrete quantum walks. This accounts for a hidden topological phase of the 1D photonic quantum walk studied in recent experiments, in which edge states were observed, even though the parameter space was considered to be topologically trivial.

(c) *Topological properties of quasiperiodic correlated systems* [26]: We analyze a quasiperiodic Bose lattice system in 1D, which we call Harper-like Bose-Hubbard model. We compute the Chern number and observe a gap closing behavior as the Hubbard interaction U is changed. Also, we discuss the bulk-edge correspondence in the system. Furthermore, we explore the phase diagram as a function of U and a continuous deformation parameter between the Harper-like model and another important quasiperiodic lattice, the Fibonacci model. We numerically confirm that the incommensurate charge density wave (ICDW) phase is topologically non-trivial and it is topologically equivalent in the whole ICDW region

5 Summary

We have reported our recent studies on correlated TIs and some related topics. We have established the emergence of 1D topological Mott insulator, which is accompanied by edge Mott states carrying only spin currents. This was done by applying the DMRG method to the calculation of the winding number as well as the entanglement spectrum. We have also shown an intriguing topological phase transition from a trivial to nontrivial phase, which is characterized by zeros of Green's function.

We have addressed a similar question for two-dimensional TIs by using a DMFT approach. As a typical example of correlated topological phase in two dimensions, we have considered a Kane-Mele Kondo lattice model, where the Kondo effect becomes dominant, leading to a topologically trivial singlet ground state. However, a remarkable phenomenon is induced by temperature effects, reflecting strong competition between topology and correlation, i.e. topological properties are restored by raising the temperature. We have confirmed that this kind of temperature induced topological properties are not specific to the present model, but applicable more generically to correlated TIs [27].

We have also summarized some other topics related to topological phases, which we studied recently. This includes laser-induced TIs in nonequilibrium conditions, hidden topological properties in quantum walks, and topological properties of correlated quasi-periodic systems.

This work was partly supported by a Grand-in-Aid for Scientific Research on Innovative Areas (KAKENHI Grant No. 15H05855) and also KAKENHI (No.25400366). This report is based on the recent studies done in collaboration with T. Yoshida, R. Peters, S. Fujimoto, M. Nakagawa, F. Matsuda and M. Tezuka.

References

[1] C. L. Kane and E. J. Mele, Phys. Rev. Lett. **95** 146802 (2005).

[2] B. A. Bernevig, T. L. Hughes, and S. C. Zhang, Science **314** 1757 (2006).

[3] M. König, S. Wiedmann, C. Brüne, A Roth, H. Buhmann, L. W. Molenkamp, X. L. Qi, and S. C. Zhang, Sience**318** 776 (2007).

[4] M. Z. Hasan and C. L. Kane: Rev. Mod. Phys. **82** (2010)3045.

[5] X.-L. Qi and S. C. Zhang: Rev. Mod. Phys. **83**(2011)1057.

[6] A. Shitade, H. Katsura, J. Kunes, X.-L. Qi, S. C. Zhang, and N. Nagaosa, Phys. Rev. Lett. **102**, 256403 (2009).

[7] S. Chadov,X-L. Qi, J. Kubler, G. H. Fecher,C. Felser, and S-C Zhang, Nature Materials **9**, 541-545 (2010).

[8] H. Lin, L. A. Wray, Y. Xia, S. Xu, S. Jia, R. J. Cava, A. Bansil, and M. Z. Hasan, Nature Materials **9**, 546-549 (2010).

[9] B. Yan, L. Müchler, X.-L. Qi, S.-C. Zhang, and C. Felser, Phys. Rev. B **85**, 165125 (2012).

[10] M. Dzero, K. Sun, V. Galitski, P. Coleman: Phys. Rev. Lett. **104** (2010) 10.

[11] M.-T. Tran, T. Takimoto, and K.-S. Kim: Phys. Rev. **B85** (2012) 125128.

[12] S. Raghu, Xl. L. Qi, C. Henerkampp, and S. C. Zhang, Phys. Rev. Lett. **100** (2008) 156401.

[13] Y. Zhang, Y. Rau, and A. Vishwanath, Phys. Rev. **B79** 245331 (2009).

[14] M. Kurita, Y. Yamaji, and M. Imada, J. Phys. Soc. Jpn. **80** 044708 (2011).

[15] M. Hohenadler, T. C. Lang, and F. F. Assaad, Phys. Rev. Lett. **109** (2012) 229902.

[16] D. A. Pesin and L. Balents, Nature Physics **6** (2010) 376.

[17] Y. Yamaji and M. Imada, Phys. Rev. **B83**, 205122 (2011).

[18] T. Yoshida, S. Fujimoto and N. Kawakami: Phys. Rev. **B85** (2012) 125113; **B87** (2013) 085134; **B87** (2013) 165109.

[19] Y. Tada, R. Peters, M. Oshikawa, A. Koga, N. Kawakami and S. Fujimoto: Phys. Rev. **B85** (2012) 165138.

[20] See for a review, M. Hohenadler, F. F. Assaad, J. Phys.: Condens. Matter **25**, 143201 (2013) and references therein.

[21] T. Yoshida, R. Peters, S. Fujimoto and N. Kawakami: Phys. Rev. Lett. **112** (2014) 196404.

[22] T. Yoshida, R. Peters and N. Kawakami: Phy. Rev. **B93** (2016) 045138.

[23] M. Nakagawa and N. Kawakami: Phys. Rev. **A89** (2014) 013627.

[24] M. Nakagawa and N.Kawakami, Phys. Rev. Lett. **115** (2015) 165303.

[25] H. Obuse, J. K. Asboth, Y. Nishimura and N. Kawakami: Phys. Rev. **B92** (2015) 045424.

[26] F. Matsuda, M. Tezuka and N. Kawakami: J. Phys. Soc. Jpn. **83** (2014) 083707.

[27] T.Yoshida and N. Kawakami: arXiv:1604.00122.

Multiscale Simulation Performed on ISSP Super Computer:Analysis of Entangled Polymer Melt Flow

Takahiro Murashima
Department of Physics, Tohoku University
Aramaki-Aza-Aoba, Aoba-Ward, Sendai, Miyagi 980-8578

Abstract

Multiscale simulation of entangled polymer melt flow has been developed based on the smoothed particle hydrodynamics model and the dual slip-link model. A kernel gradient free method and a particle shifting method were implemented to improve the accuracy of the macroscopic fluid dynamics and stabilize the multiscale simulation. We have investigated an effect of the polymer chain length on the fluid dynamic behavior. Since the longer chain has the longer correlation time, the non-linearity in the macroscopic field is enhanced in the longer chain case.

1 Introduction

Flow prediction of polymer melt is important for industrial processing [1–3]. Microscopic polymer dynamics has a long correlation time between a past state and the current state, and the flow histories of polymer chain affect the macroscopic flow dynamics. The microscopic polymer dynamics should be considered to predict the macroscopic flow dynamics of polymer melt. It is, however, difficult to include the microscopic polymer dynamics into the macroscopic flow dynamics because there are large scale differences on space and time between microscopic polymer dynamics and the macroscopic flow dynamics.

Micro-macro bridging approaches have been done by several groups in two decades and they have succeeded to treat simple viscoelastic fluids without entanglements of polymer chains [4–10] and also with entanglements [11]. We have proposed a multiscale simulation technique to treat the entangled polymer melt flow using a different approach [12–15]. Our multiscale simulation is based on the fluid particle simulation and the coarse-grained entangled polymer dynamics simulation. Each fluid particle has a polymer simulator, where the states of polymer chains are different from those in the other fluid particles. At each position, the stress tensor $\boldsymbol{\sigma}$ is calculated from the polymer simulator in the fluid particle. The macroscopic flow field $\boldsymbol{v}$ is updated through the momentum balance equation, and then the velocity gradient tensor $\boldsymbol{\kappa} = (\boldsymbol{\nabla}\boldsymbol{v})^{\mathrm{T}}$ is calculated at each fluid particle. Under the renewed velocity gradient tensor $\boldsymbol{\kappa}$, polymer dynamics simulation is performed and the stress tensor is renewed. The macroscopic states and the microscopic states are updated alternately in the multiscale simulation. This way is same with the heterogeneous multiscale method that the several time steps of molecular dynamics simulation fits to the one time step of fluid dynamics simulation [16–21].

To consider the flow history of polymer chain, the macroscopic fluid dynamics is solved using the fluid particle simulation. The smoothed particle hydrodynamics (SPH) method is widely used to simulate the fluid dynamics of simple liquids and polymer melts [22–28]. However, SPH is defective to calculating the spatial gradient of physical variables near wall boundaries and surfaces. To correct the gradient of field variables in SPH, a corrective SPH method [29,30], a modified SPH (MSPH) method [31], and a finite particle method (FPM) [32] have been developed. These methods have succeeded in calculating the gradient of field variables more accurate than the original SPH method. Very recently, a kernel gradient free (KGF) method has been developed [33]. This new method does not need to calculate in literally the kernel gradient. KGF improves the gradient of field variables and KGF is more stable than MSPH and FPM. Since the spatial homogeneity of fluid particles affects the accuracy of fluid particle simulation, we use a particle shifting method (PSM) [34] to correct and distribute the fluid particles equally at every time steps. KGF and PSM improves the accuracy of the multiscale simulation.

The correlation time of entangled polymer chains with length ℓ is proportional to $\ell^{3.5}$ and is larger than of the order of milliseconds. Such a long time scale is not accessible with the conventional coarse-grained molecular dynamics simulation, so called Kremer-Grest model [35]. Based on the reptation theory with the some extensions [36–39], several entangled polymer dynamics simulators have been developed [40–47]. In our multiscale simulation, we use the dual slip-link model [44]. The merit to use the dual slip-link model is that the model can predict the rheological properties of the standard polymer chains, such as polyethylene and polystyrene, the algorithm is simple to simulate the entangled polymer dynamics, and the model does not require much computation time.

We investigate the effect of the polymer chain length to the macroscopic field. In the next section, we review the procedure of the multiscale simulation, the kernel gradient free method, the particle shifting method, and the dual slip-link model. Then, we discuss on the flow dynamics around a obstacle. This problem is same with the previous works [13, 15]. We discuss the effect of the polymer chain length difference using the revised multiscale simulation method.

2 Multiscale Simulation

The multiscale simulation is based on the fluid particle simulation and the polymer dynamics simulation. Polymer melt flow is described with the dynamics of fluid particle according to the following equations.

$$\frac{\mathrm{d}\boldsymbol{x}}{\mathrm{d}t} = \boldsymbol{v}, \tag{1}$$

$$\rho\frac{\mathrm{d}\boldsymbol{v}}{\mathrm{d}t} = \boldsymbol{\nabla}\cdot\boldsymbol{\sigma} + \rho\boldsymbol{g}, \tag{2}$$

where $\boldsymbol{x}$ is the position, $\boldsymbol{v}$ is the velocity, ρ is the density, $\boldsymbol{\sigma}$ is the stress tensor, and $\boldsymbol{g}$ is the external force. The density $\rho(\boldsymbol{x})$ is obtained using the kernel function $W(|\boldsymbol{x}'-\boldsymbol{x}|, h)$ to interpolate the particle $\boldsymbol{x}$ and the neighboring particles $\boldsymbol{x}'$,

$$\rho(\boldsymbol{x}) = \int \mathrm{d}\boldsymbol{x}' m W(|\boldsymbol{x}'-\boldsymbol{x}|, h), \tag{3}$$

where m is the mass of fluid particle. We use the following kernel function,

$$W(r,h) = \begin{cases} \frac{A_d}{(h\sqrt{\pi})^d}\left[e^{-r^2/h^2} - e^{-4}\right], & r \le 2h, \\ 0, & r > 2h, \end{cases} \tag{4}$$

where d is the dimension of the system, and the normalization coefficient A_d is calculated from $\int \mathrm{d}\boldsymbol{r} W(|\boldsymbol{r}|, h) = 1$, and found to be $A_1 = 1.04823$, $A_2 = 1.10081$ and $A_3 = 1.18516$. The half value of width of kernel function h is set to $1.5\delta_0$ where δ_0 is the initial distance between fluid particles. The stress tensor $\boldsymbol{\sigma}$ consists of the hydrostatic pressure term, the viscous stress term, and the polymeric stress term:

$$\boldsymbol{\sigma} = -p\boldsymbol{I} + \boldsymbol{\sigma}_{\mathrm{s}} + \boldsymbol{\sigma}_{\mathrm{p}}. \tag{5}$$

The hydrostatic pressure p is determined from the density deviation:

$$p - p_0 = C^2(\rho - \rho_0), \tag{6}$$

where C is the sound velocity, p_0 and ρ_0 are the reference pressure and density, respectively. The viscous stress coming from the molecular vibration ignored in the coarse grained polymer dynamics simulation is assumed to $\boldsymbol{\sigma}_{\rm s} = \eta_s \left\{(\boldsymbol{\nabla v})^{\rm T} + \boldsymbol{\nabla v}\right\}$ where η_s the viscous constant. The polymeric stress $\boldsymbol{\sigma}_{\rm p}$ is obtained from the coarse grained polymer dynamics simulation. The polymeric stress $\boldsymbol{\sigma}_{\rm p}$ depends on the polymer chain conformation in the fluid particle.

2.1 Kernel Gradient Free Method

The original SPH method uses the following approximation for calculating the gradient of field variable:

$$\langle \boldsymbol{\nabla} f(\boldsymbol{x})\rangle = \int \mathrm{d}\boldsymbol{x}'(\boldsymbol{\nabla}_{\boldsymbol{x}'} f(\boldsymbol{x}'))W \tag{7}$$

$$= \int \mathrm{d}\boldsymbol{S} f(\boldsymbol{x}')W - \int \mathrm{d}\boldsymbol{x}' f(\boldsymbol{x}')\boldsymbol{\nabla}_{\boldsymbol{x}'} W \tag{8}$$

$$\simeq \int \mathrm{d}\boldsymbol{x}' f(\boldsymbol{x}')\boldsymbol{\nabla}_{\boldsymbol{x}} W, \tag{9}$$

where $W = W(|\boldsymbol{x}' - \boldsymbol{x}|, h)$ is the kernel function interpolating fluid particles. From eq. (7) to eq. (9), we use the partial integral and the change of variables. The surface integral in eq. (8) is assumed to be zero because the kernel function is zero at the kernel boundary. When the fluid particles exist near the boundaries, e.g. the wall boundary or the free surface boundary, this assumption fails since the kernel boundary does not correspond to the boundary of integral. When the surface integral is not equal to zero, the original SPH method can not calculate the gradient of field variables accurately.

The kernel gradient free (KGF) method has succeeded in calculating the gradient of field variable accurately when the surface integral is not equal to zero. The KGF method is based on the Taylor expansion of field variable:

$$f(\boldsymbol{x}') = f(\boldsymbol{x}) + \boldsymbol{r}\cdot\boldsymbol{\nabla} f(\boldsymbol{x}) + \frac{1}{2}\boldsymbol{rr} : \boldsymbol{\nabla\nabla} f(\boldsymbol{x}) + O(|\boldsymbol{r}|^3), \tag{10}$$

where $\boldsymbol{r} = \boldsymbol{x}' - \boldsymbol{x}$. Multiplying $W(|\boldsymbol{r}|, h)$ to eq. (10) and integrating over $\boldsymbol{x}'$, we get

$$\int \mathrm{d}\boldsymbol{x}' f(\boldsymbol{x}')W = f(\boldsymbol{x})\int \mathrm{d}\boldsymbol{x}'W + \boldsymbol{\nabla} f(\boldsymbol{x})\cdot\int \mathrm{d}\boldsymbol{x}'\boldsymbol{r}W + \frac{1}{2}\boldsymbol{\nabla\nabla} f(\boldsymbol{x}) : \int \mathrm{d}\boldsymbol{x}'\boldsymbol{rr}W. \tag{11}$$

Substituting W to $\boldsymbol{r}W$ and $\boldsymbol{rr}W$ in eq. (11), we get

$$\int \mathrm{d}\boldsymbol{x}' f(\boldsymbol{x}')\boldsymbol{r}W = f(\boldsymbol{x})\int \mathrm{d}\boldsymbol{x}'\boldsymbol{r}W + \boldsymbol{\nabla} f(\boldsymbol{x})\cdot\int \mathrm{d}\boldsymbol{x}'\boldsymbol{rr}W + \frac{1}{2}\boldsymbol{\nabla\nabla} f(\boldsymbol{x}) : \int \mathrm{d}\boldsymbol{x}'\boldsymbol{rrr}W, \tag{12}$$

and

$$\int \mathrm{d}\boldsymbol{x}' f(\boldsymbol{x}')\boldsymbol{rr}W = f(\boldsymbol{x})\int \mathrm{d}\boldsymbol{x}'\boldsymbol{rr}W + \boldsymbol{\nabla} f(\boldsymbol{x})\cdot\int \mathrm{d}\boldsymbol{x}'\boldsymbol{rrr}W + \frac{1}{2}\boldsymbol{\nabla\nabla} f(\boldsymbol{x}) : \int \mathrm{d}\boldsymbol{x}'\boldsymbol{rrrr}W. \tag{13}$$

The eqs. (11) - (13) can be summarized to matrix equation $\boldsymbol{A}\cdot\boldsymbol{X} = \boldsymbol{B}$;

$$\boldsymbol{A} = \begin{pmatrix} \langle 1\rangle & \langle \boldsymbol{r}\rangle & \langle \boldsymbol{rr}\rangle \\ \langle \boldsymbol{r}\rangle & \langle \boldsymbol{rr}\rangle & \langle \boldsymbol{rrr}\rangle \\ \langle \boldsymbol{rr}\rangle & \langle \boldsymbol{rrr}\rangle & \langle \boldsymbol{rrrr}\rangle \end{pmatrix}, \tag{14}$$

$$\boldsymbol{X} = \begin{pmatrix} f \\ \boldsymbol{\nabla} f \\ \frac{1}{2}\boldsymbol{\nabla\nabla} f \end{pmatrix}, \tag{15}$$

$$\boldsymbol{B} = \begin{pmatrix} \langle f\rangle \\ \langle \boldsymbol{r}f\rangle \\ \langle \boldsymbol{rr}f\rangle \end{pmatrix}, \tag{16}$$

where $\langle O\rangle = \int \mathrm{d}\boldsymbol{x}'O(\boldsymbol{x}')W$. We can solve the matrix equation $\boldsymbol{A}\cdot\boldsymbol{X} = \boldsymbol{B}$ using LU decomposition and obtain $\boldsymbol{\nabla} f$ not $\langle\boldsymbol{\nabla} f\rangle$. Note that the kernel gradient $\boldsymbol{\nabla} W$ does not appear in eqs. (14) - (16). That is why this method is called as the kernel gradient free method.

In the simulation, $\langle O\rangle$ is computed using the following discrete form.

$$\langle O(\boldsymbol{x}_i)\rangle = \sum_{j\in\Omega_i} \frac{m_j}{\rho_j} O(\boldsymbol{x}_j) W(|\boldsymbol{x}_{ij}|, h), \tag{17}$$

$$\begin{aligned} \rho_i &= \rho(\boldsymbol{x}_i) \\ &= \sum_{j\in\Omega_i} m_j W(|\boldsymbol{x}_{ij}|, h), \end{aligned} \tag{18}$$

where Ω_i represents the cutoff region with the radius $2h$ from the i-th particle $\boldsymbol{x}_i$, and $\boldsymbol{x}_{ij} = \boldsymbol{x}_j - \boldsymbol{x}_i$.

2.2 Particle Shifting Method

When the fluid particles get closer, tensile instability occurs, where the particles make a string like structure and these strings repel each other [48]. The tensile instability affects the simulation results and should be suppressed. The pressure between the fluid particles does not disturb the tensile instability because the force acting on the fluid particles is the pressure gradient and the pressure gradient is zero between these close fluid particles. We need an extra trick to correct the particle positions to distribute uniformly.

The particle shifting method is one of the choices to suppress the tensile instability. The following direction vector $\boldsymbol{n}$ represents the direction of the nonuniform distribution of the fluid particles around $\boldsymbol{x}$.

$$\boldsymbol{n}(\boldsymbol{x}) = \int \mathrm{d}\boldsymbol{x}' \widehat{\boldsymbol{r}} W, \tag{19}$$

$$\widehat{\boldsymbol{r}} = \frac{\boldsymbol{r}}{|\boldsymbol{r}|}. \tag{20}$$

When we shift the particle at $\boldsymbol{x}$ to the direction $\boldsymbol{n}$, the particle distribution closes to uniform one. Using the direction vector $\boldsymbol{n}$, we define the shift vector $\Delta\boldsymbol{x}$:

$$\Delta\boldsymbol{x} = \epsilon\delta_0\boldsymbol{n}, \tag{21}$$

where ϵ is the shift parameter. After the position and velocity of fluid particle is updated from $(\boldsymbol{x}_{\mathrm{old}}, \boldsymbol{v}_{\mathrm{old}})$ to $(\boldsymbol{x}^*, \boldsymbol{v}^*)$, according to (1) and (2), respectively, we apply the particle shifting method:

$$\boldsymbol{x}_{\mathrm{new}} = \boldsymbol{x}^* + \Delta\boldsymbol{x}, \tag{22}$$

$$\boldsymbol{v}_{\mathrm{new}} = \boldsymbol{v}^* + \Delta\boldsymbol{x}\cdot\boldsymbol{\nabla}\boldsymbol{v}. \tag{23}$$

Eq. (23) is obtained from the Taylor expansion of $\boldsymbol{v}(\boldsymbol{x} + \Delta\boldsymbol{x})$ around $\boldsymbol{x}$. When ϵ is less than 0.001, the tensile instability appears. On the other hand, when ϵ is larger than 0.1, the fluid particles make a crystalline structure and the dynamics of fluid particles shows stick-slip motion. The shift parameter ϵ should be set between 0.001 to 0.1.

2.3 Polymer Dynamics Simulation

The dynamics of entangled polymer chains is handled with the dual slip-link model. The dual slip-link model is placed on each fluid element and undergoes flow history that is nonuniform flow changing at each position and time.

In the dual slip-link model, the number of entanglements on a polymer chain in equilibrium state is proportional to the polymer chain length. The polymer chain with length L is separated to Z sub-vectors $\boldsymbol{r}_i, (i = 1, \cdots, Z)$ with unit length a representing the constraint tube between two entanglement points, or slip-links, and two free end segments s_1 and s_2: $L = s_1 + s_2 + \sum_{i=1}^{Z} |\boldsymbol{r}_i|$. Each slip-link has a pair of slip-link on the other polymer chain. The entangled polymer chain can move along the constraint tube.

When a shear flow applied to a chain, the tube segments are affinely deformed:

$$\frac{\mathrm{d}\boldsymbol{r}_i}{\mathrm{d}t} = \boldsymbol{\kappa}\cdot\boldsymbol{r}_i, \tag{24}$$

$$\boldsymbol{\kappa} = (\boldsymbol{\nabla}\boldsymbol{v})^{\mathrm{T}}, \tag{25}$$

where $\boldsymbol{\kappa}$ is obtained from the macroscopic fluid dynamics simulation. The length of polymer chain is assumed to follow the differential equation with Gaussian white noise $g_1(t)$:

$$\frac{\mathrm{d}L}{\mathrm{d}t} = -\frac{1}{\tau_\mathrm{R}}(L - L_0) + g_1(t) + \left(\frac{\mathrm{d}L}{\mathrm{d}t}\right)_\mathrm{affine}, \qquad (26)$$

$$\tau_\mathrm{R} = \tau_0 Z^2, \qquad (27)$$

$$L_0 = Z_0 a^2, \qquad (28)$$

where τ_R is the Rouse relaxation time corresponding to the relaxation time of non-entangled polymer chain, τ_0 is the unit time of the slip-link model, L_0 is the equilibrium length. $\left(\frac{\mathrm{d}L}{\mathrm{d}t}\right)_\mathrm{affine}$ represents the difference of chain length between before and after affine deformation in eq. (24). The thermal fluctuation of polymer chain causes the center of mass motion along the tube segments. This is called as reptation. The reptation is achieved through updating the free end segments with Gaussian white nose $g_2(t)$:

$$\frac{\mathrm{d}s_1}{\mathrm{d}t} = \frac{1}{2}\left(\frac{\mathrm{d}L}{\mathrm{d}t}\right) + D_\mathrm{R} g_2(t), \qquad (29)$$

$$\frac{\mathrm{d}s_2}{\mathrm{d}t} = \frac{1}{2}\left(\frac{\mathrm{d}L}{\mathrm{d}t}\right) - D_\mathrm{R} g_2(t), \qquad (30)$$

where the first term represents the contribution from the chain difference from eq. (26) and the second term represents the reptation motion. $D_\mathrm{R} = \sqrt{2a^2/3\pi^2\tau_\mathrm{e} Z}$ is the diffusion constant of Rouse chain. Note that

$$\langle g_i(t)\rangle = 0, \qquad (31)$$

$$\langle g_i(t) g_j(t')\rangle = \delta(t - t')\delta_{ij}. \qquad (32)$$

When s_1 or s_2 is less than 0, the end of entanglement point and the pair of it disappear. On the other hand, when s_1 or s_2 is larger than a, the new entanglement point is created on the free end segment and the pair on the other polymer chain, selected randomly, are created. The stress tensor $\boldsymbol{\sigma}_\mathrm{p}$ is obtained from the dyadic of the tension of polymer chain and the direction of the tube segment averaging over the all chains in the fluid particle:

$$\boldsymbol{\sigma}_\mathrm{p} = G_0 \langle \sum_{i=1}^{Z} \frac{\boldsymbol{r}_i \boldsymbol{r}_i}{a|\boldsymbol{r}_i|} \rangle, \qquad (33)$$

where $G_0 = (15/4)k_\mathrm{B}T/V$ is the unit shear modulus, k_B is the Boltzmann constant, T is the temperature, V is the unit volume.

2.4 Simulation Conditions

We consider 2-dimensional polymer melt flow around an cylindrical obstacle as same as the previous works [13, 15]. The cylinder with the radius R is made of particles fixed on the space. To disturb penetration of the fluid particles into the inside of the cylinder, the spaces between wall particles are smaller than δ_0. Since the density of the wall particles is higher than the bulk fluid, fluid particles are difficult to penetrate into the cylinder. At initial condition, fluid particles are placed at regular intervals with space δ_0 and polymer chains in the fluid particles are equilibrium states.

We impose the periodic boundary condition to the macroscopic system. The mass center of polymer chains in the microscopic system corresponds to the position of the macroscopic fluid particle. Since the polymer chains in the dual slip-link model are in the virtual space, we can ignore the diffusion of polymer chains between fluid particles.

We can obtain the zero-shear viscosity of dual slip-link model from the Green-Kubo formula.

$$\eta_\mathrm{p} = G_0^{-1} \int_0^\infty \mathrm{d}t \langle \sigma(t+\tau)\sigma(\tau)\rangle_\tau. \qquad (34)$$

In the multiscale simulation, the zero-shear viscosity is modified to include the dissipation from the molecular vibration less than the tube:

$$\eta = \eta_\mathrm{p} + \eta_\mathrm{s}. \qquad (35)$$

η_s represents the viscosity coming from the dissipation. We choose η as a characteristic viscosity in the multiscale simulation.

The time units of macroscopic simulation and microscopic simulation are set to the same. The velocity gradient obtained from the macroscopic simulation is used to the microscopic simulation without any conversion factor. The stress unit of macroscopic simulation is normalized so that the characteristic viscosity η is equal to one.

Number of fluid particles in the system is 3,548 and each fluid particle has 1,000 polymer chains. Since the polymer simulators on each fluid particle are independent from the others, parallel computing is effective for the multiscale simulation. Using 3,456 cores on supercomputer systems at the SCC-ISSP for 24 hours, we can run the simulation sufficiently larger than the relaxation times of the short and long polymer chain melts.

We discuss the low Reynolds number flow where the flow around cylinder is expected to be symmetric. The Reynolds number is $\mathrm{Re} = \rho U R/\eta$ where ρ is the density of fluid, U is the maximum velocity of the flow, R is the radius of the cylinder, and η is the characteristic viscosity. Polymer melt has the relaxation time τ that the polymer chain stretch and orientation persist after cessation of applying the deformation. The polymer melt flow is characterized with the two dimensionless numbers, the Weissenberg number and the Deborah number. The Weissenberg number $\mathrm{Wi} = \tau\dot{\gamma}$ is the ratio of the viscous force and the elastic force. The Deborah number $\mathrm{De} = \tau/\tau_{\mathrm{o}} = \tau U/R$ is defined as the ratio of the relaxation time τ and the characteristic time scale of observation τ_{o}. We expect that the shear viscosity η_{p} decreases when the Weissenberg number is larger than one, and the non-symmetric flow field is observed when the Deborah number is larger than one.

3 Nonlinear Flow Behavior

We compare the results of a short polymer melt with $Z = 10$ and a long polymer melt with $Z = 20$. The relaxation time of $Z = 10$ is about 530 and that of $Z = 20$ is about 6400, obtained from the correlation function of the end-to-end vector of polymer chain. The relaxation time of the long polymer melt is $2^{3.5}$ times larger than that of the short polymer melt. We use the normalized viscosity η and apply the same external force $\boldsymbol{g}$ to the fluid particles so that the Reynolds number is much less than one.

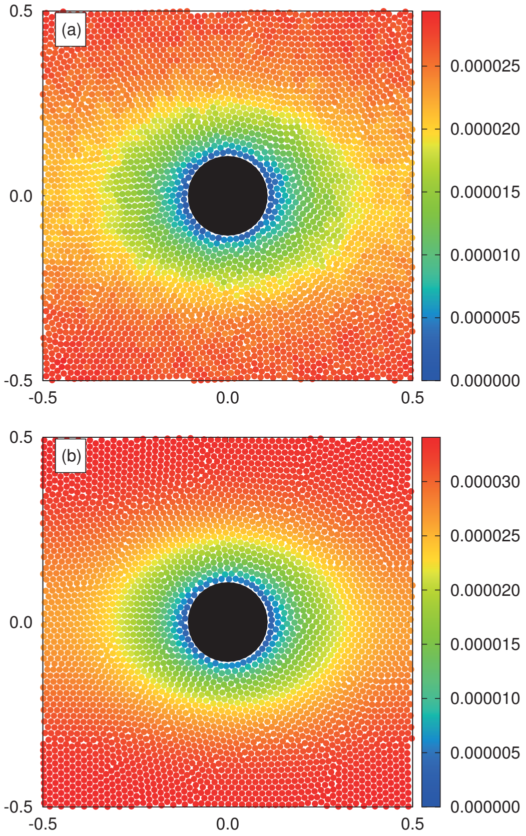

Figure 1: Velocity fields of (a) short chain melt and (b) long chain melt at steady state.

The velocity fields at steady state are summarized in Fig. 1. The Reynolds number is less than 0.1 in this condition. The maximum velocity of the long polymer melt is higher than that of the short polymer melt. We expect that the viscosity coming from the polymeric stress decreases in the long polymer melt because of the shear thinning phenomena.

The reason why the maximum velocity of the long chain melt is larger than that of the short chain melt will be found from comparing the stress tensors. Since each component of the stress tensor is not rotationally invariant, we obtain the eigen values and vectors of the stress tensor, and compare them.

The largest eigen value and vector of the stress tensor are shown in Fig. 2 and Fig. 3, respectively. The eigen value field is almost symmetric among the upstream and downstream in the short polymer melt, while that is clearly not symmetric in the long polymer melt.

The asymmetry of the eigen value field is coming from the Deborah number. The Deborah number is higher than one in the long polymer melt and is less than one in the short polymer melt. The eigen vectors both in the short and long polymer melts are aligned to the same direction in the vicinity of the cylinder where the Weissenberg number is larger than one. In the short polymer melt, however, the orientation is random away from the cylinder where the Weissenberg number is less than one. Polymers are extended and aligned in the long polymer melt rather than the short polymer melt, resulting in the shear thinning phenomena.

4 Summary

We have reviewed the multiscale simulation that is composed of the fluid particle simulation and the polymer dynamics simulation. The fluid particle simulation has been solved using the kernel gradient free method and the particle shifting method. These two methods stabilize the fluid particle simulation. The dual slip-link model has been used as the polymer dynamics simulation in the multiscale simulation. This model has a full chain picture and can treat the entanglement between the polymer chains. We have shown a flow around a cylinder in cases of the short and long polymer melts. The long polymer melt has shown the shear thinning phenomena while the short polymer melt has not. The asymmetric fields of the largest eigen value and the corresponding eigen vector of the stress tensor have suggested the polymer chain stretch and orientation around the obstacle. Especially in the long polymer chain melt, the asymmetry is clear because the relaxation time or the correlation time of the long polymer chain melt is $2^{3.5}$ times longer than that of the short polymer chain melt.

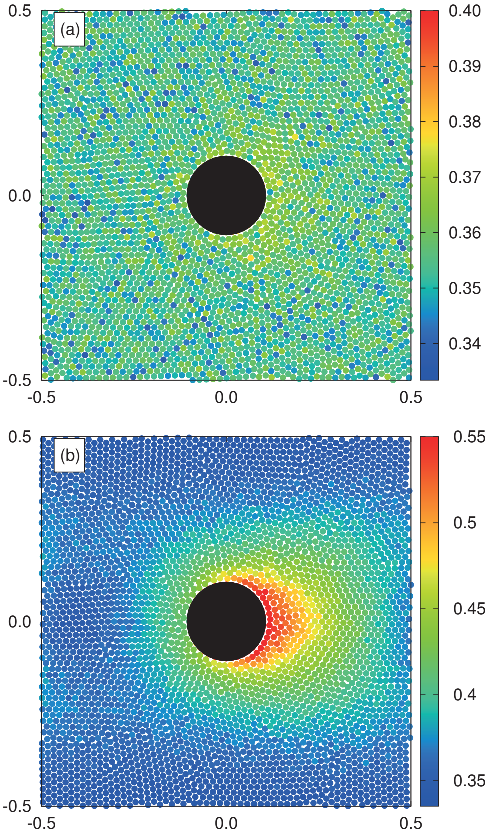

Figure 2: The largest eigen values of the stress tensor of (a) short chain melt and (b) long chain melt at steady state.

To decrease the noise, the number of polymer chains in the polymer dynamics simulation should be increased from the point of view of the central limit theorem in probability theory. We have developed the ensemble average method using several replica simulation boxes for a fluid particle to obtain the stress tensor averaging over the replica [49]. This method needs 10 to 100 times larger super computer than that we used here and has been only applied to one dimensional problem. We will apply the noise reduction technique to the multiscale simulation of two or three dimensional problem in the future using a super computer

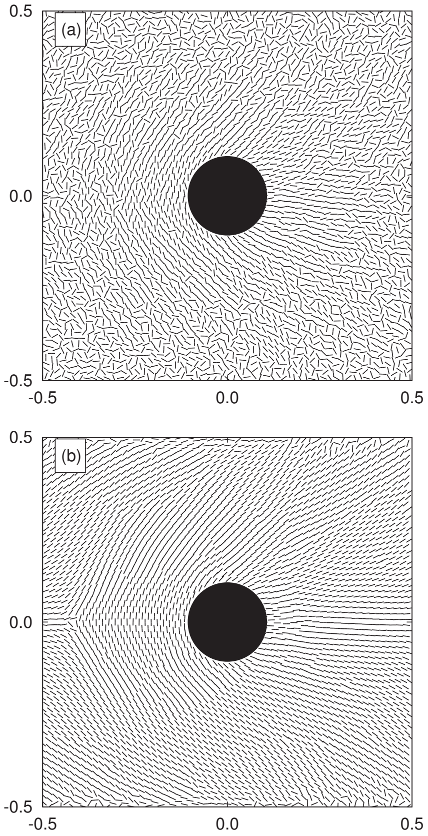

Figure 3: The eigen vectors (corresponding to Fig. 2) of the stress tensor of (a) short chain melt and (b) long chain melt at steady state.

with more than 1,000,000 cores.

Acknowledgment

This work was supported by JSPS KAKENHI Grant Number 15K17733. The computation in this work was done using the facilities of the Supercomputer Center, Institute for Solid State Physics, University of Tokyo.

References

[1] C. W. Macosko, "*Rheology*", Wiley-VCH, Inc. (1994).

[2] R. G. Larson, "*The Structure and Rheology of Complex Fluids*", Oxford University Press (1999).

[3] R. G. Owens and T. N. Phillips, "*Computational Rheology*", Imperial College Press (2002).

[4] M. Laso and H. C. Ottinger, J. Non-Newtonian Fluid Mech., **47** (1993) 1.

[5] H. K. Rasmussen and O. Hassager, J. Non-Newtonian Fluid Mech., **56** (1995) 65.

[6] H. A. Hulsen et al., J. Non-Newtonian Fluid Mech., **70** (1997) 79.

[7] P. Halin et al., J. Non-Newtonian Fluid Mech., **79** (1998) 387.

[8] A. P. G. van Heel et al., J. Rheol., **43** (1999) 1239.

[9] E. A. J. F. Peters et al., J. Rheol, **44** (2000) 811.

[10] H. A. Hulsen et al., J. Non-Newtonian Fluid Mech., **98** (2001) 201.

[11] C. C. Hua and J. D. Schieber, J. Rheol., **42** (1998) 477.

[12] T. Murashima and T. Taniguchi, J. Polym. Sci. B, **48** (2010) 886.

[13] T. Murashima and T. Taniguchi, Europhys. Lett., **96** (2011) 18002.

[14] T. Murashima and T. Taniguchi, J. Phys. Soc. Jpn., **81** (2012) SA013.

[15] T. Murashima et al., J. Phys. Soc. Jpn., **82** (2013) 012001.

[16] W. Ren and W. E, J. Comp. Phys., **204** (2005) 1.

[17] S. De et al., Phys. Rev. E, **81** (2010) 030801(R).

[18] S. Yasuda and R. Yamamoto, Phys. Fluid., **20** (2008) 113101.

[19] S. Yasuda and R. Yamamoto, Europhys. Lett., **86** (2009) 18002.

[20] S. Yasuda and R. Yamamoto, Phys. Rev. E, **81** (2010) 036308.

[21] W. E, "*Principles of Multiscale Modeling*", Cambridge University Press (2011).

[22] J. J. Monaghan, Rep. Prog. Phys., **68** (2005) 1703.

[23] M. Ellero et al., J. Non-Newtonian Fluid Mech., **105** (2002) 35.

[24] M. Ellero and R. I. Tanner, J. Non-Newtonian Fluid Mech., **132** (2005) 61.

[25] J. Fang et al., J. Non-Newtonian Fluid Mech., **139** (2006) 68.

[26] X.-J. Fan et al., J. Non-Newtonian Fluid Mech., **165** (2010) 219.

[27] H. Zhu et al., J. Non-Newtonian Fluid Mech., **165** (2010) 362.

[28] T. Jiang et al., Appl. Math. Model., **35** (2011) 3833.

[29] J. K. Chen et al., Comput. Mech., **23** (1999) 279.

[30] J. K. Chen et al., Comput. Mech., **24** (1999) 273.

[31] G. M. Zhang and R. C. Batra, Comp. Mech., **34** (2004) 137.

[32] M. B. Liu et al., Appl. Math. Model., **29** (2005) 1252.

[33] C. Huang et al., Int. J. Numer. Meth. Fluids, **78** (2015) 691.

[34] R. Xu et al., J. Comp. Phys., **228** (2009) 6703.

[35] K. Kremer and G. Grest, **92** (1990) 5057.

[36] P. G. de Gennes, J. Chem. Phys., **55** (1971) 572.

[37] M. Doi and S. F. Edwards, "The Theory of Polymer Dynamics", Oxford University Press, (1986).

[38] G. Marrucci, J. Non-Newtonian Fluid Mech., **62** (1996) 279.

[39] G. Ianniruberto and G. Marrucci, J. Non-Newtonian Fluid Mech., **65** (1996) 241.

[40] D. W. Mead et al., Macromol., **31** (1998) 7895.

[41] C. C. Hua and J. D. Schieber, J. Chem. Phys., **109** (1998) 10018.

[42] J. T. Padding and W. J. Briels, J. Chem. Phys., **115** (2001) 2846.

[43] Y. Masubuchi et al., J. Chem. Phys., **115** (2001) 4387.

[44] M. Doi and J. Takimoto, Phyl. Trans. R. Soc. Long. A, **361** (2003) 641.

[45] A. E. Likhtman, Macromol., **38** (2005) 6128.

[46] R. Khaliullin and J. Schieber, Macromol., **42** (2009) 7504.

[47] T. Uneyama, J. Soc. Rheol. Jpn. (Nihon Reoroji Gakkaishi), **39** (2011) 135.

[48] J. P. Morris, arxiv:astro-ph/9503124 (1995) (unpublished).

[49] T. Murashima et al., AIP Conf. Proc., **1518** (2013) 436.

3.2 First-Principles Calculation of Material Properties

Atomic Structures and Electronic Properties of Hard- and Soft-Nanomaterials

Atsushi Oshiyama
Department of Applied Physics, The University of Tokyo
Hongo, Tokyo 113-8656

Main purpose of this project is to develop the density-functional approach which enables us to perform more accurate and larger scale static and dynamical calculations on massively parallel architecture computers, to clarify underlying physics and chemistry in phenomena in nano-materials and structures, and to predict new phenomena in nano-world. The following is an example which we have achieved in 2015 fiscal year [J.-I. Iwata, C. Shinei and A. Oshiyama, Phys. Rev. B **93**, 125202 (2016)].

Magic Numers in Nano-size of Multivacancies in Silicon Carbide

Point defects inevitably exist in semiconductors and play important roles both in technology and science. Such point defects as lattice vacancies or interstitial atoms generally induce electron states localized around the defects, their energy levels being in the fundamental energy gap (deep levels). Those deep levels act as carrier traps. Hence structural identification of the deep levels is highly demanded from technology viewpoints. Scientifically, the deep localized state brings forth intriguing properties: It enhances electron-lattice interaction and then occasionally constitute Anderson negative U system with Jahn-Teller type local relaxation.

SiC is a promising material due to its attractive properties such as the high dielectric breakdown voltage and the high melting temperature. It is a tetrahedrally bonded covalent semiconductor and exists as many polytypes called 2H (wurtzite), 3C (zincblende), 4H, 6H and so forth. The most experimentally common polytype is 4H, which is corroborated by our density-functional calculations: The calculated cohesive energy with the generalized gradient approximation (GGA) by Perdew, Burke and Ernzerhof (PBE) in the density-functional theory (DFT) of the 4H polytype is the largest, followed by 6H, 3C, 2H with the cohesive-energy decrease of 0.1 meV, 1.0 meV and 8.0 meV per SiC unit, respectively.

Thermal treatment inevitably required in device fabrication causes diffusion of point defects and thus point defects are likely to segregate to be of complex forms. Some deep levels are indeed argued to be the divacancy or the trivacancy. However detailed investigation of energetics and electron states of such complex defects is lacking.

We have performed the density-functional calculations that clarify the atomic structures, the energetics and the electron states of the multivacancy V_n consisting of n_{Si} silicon vacant sites and n_{C} carbon vacant sites ($n = n_{\mathrm{Si}} + n_{\mathrm{C}}$) in the most stable silicon carbide polytype 4H-SiC. The calculations with the generalized gradient approximation (GGA) for the monovacancy, V_{Si} and V_{C}, have clarified the significantly lower formation energy of the C vacancy accompanied with the efficient pairing relaxation of the surrounding Si dangling bonds. Based on this structural characteristics and the energetics for the monovacancy, we have proposed an extended dangling-bond counting (EDBC) model to discuss the stability of the multivacancy. The EDBC model predicts a new stable next-neighbor $V_{\mathrm{C}}V_{\mathrm{C}}$ divacancy (Fig.) which is lower in the formation energy than the usual nearest-neighbor divacancy $V_{\mathrm{C}}V_{\mathrm{Si}}$ discussed in the past. Our calculations with PBE functional and also with the hybrid functional (HSE06) have indeed clarified that the $V_{\mathrm{C}}V_{\mathrm{C}}$ is more stable than the $V_{\mathrm{C}}V_{\mathrm{Si}}$ under C-poor condition. Even under C-rich condition, the next-neighbor divacancy $V_{\mathrm{C}}V_{\mathrm{C}}$ is more stable than the nearest-neighbor $V_{\mathrm{C}}V_{\mathrm{Si}}$ when the Fermi level is located in the lower half of the energy gap. The next-neighbor divacancy is possible to be detected with its peculiar hyperfine coupling constants by

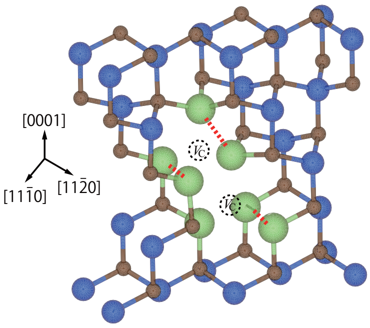

Figure 1: Geometry optimized structure of the divacancy $V_\mathrm{C}V_\mathrm{C}$ composed of a next-neighbor pair of two carbon vacancies. Blue (large) and brown (small) spheres depict Si and C atoms, respectively. The nearest neighbor Si atoms around $V_\mathrm{C}V_\mathrm{C}$ are marked by Green (large) spheres. The vacant sites are depicted by the dashed circles. The two of the nearest neighbor Si atoms connected by the red dashed line form the pairing relaxation.

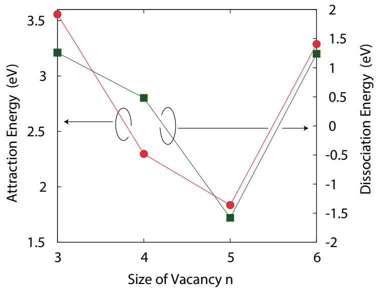

Figure 2: Dissociation energy ζ (squares) and the attraction energy η (circles) of the multivacancy V_n obtained from GGA calculations. Right and left axes represent ζ and η, respectively. Here the dissociation energy ζ_n is defined as $\zeta_n = E_\mathrm{f}(V_\mathrm{n+1}) + E_\mathrm{f}(V_\mathrm{n-1}) - 2E_\mathrm{f}(V_\mathrm{n})$ using the formation energies of each vacancy. The attraction energy is defined as $\eta_n = E_\mathrm{f}(V_\mathrm{n-1}) + E_\mathrm{f}(V_1) - E_\mathrm{f}(V_\mathrm{n})$.

the electron paramagnetic resonance (EPR) measurements.

The EDBC model has been also applied to larger multivacancy and revealed the energetically favorable pair (n_Si, n_C) and the topological network for the multivacancy V_n. As a result, V_n with $n = 6$, 9, 10, 14 has been shown to have relatively lower formation energies: the magic numbers of the stable multivacancy. We have also performed GGA calculations for the multivacancy V_n and clarified that V_3 and V_6 is energetically favorable (Fig.). The stable V_3 is a nearest neighbor complex of V_C-V_Si-V_C, whereas the V_6 is the high symmetry V_5 (the central V_Si surrounded by 4 V_C) plus symmetry breaking next-neighbor V_C.

We have performed the GGA calculations for electronic structure of thus obtained stable V_3 and V_6 and discussed the possibility of detecting these multivacancies. We have clarified the existence of various charge states for V_3 and V_6, for which high-spin and low-spin states are possible depending on the charge states (Fig.). In particular, the EPR detected ANN1 center has been provisionally identified as the doubly positive trivacancy V_C-V_Si-V_C. The present calculations provide a firm theoretical frame work to identify the multivacancies generated by heat treatments of SiC and discuss their physical properties.

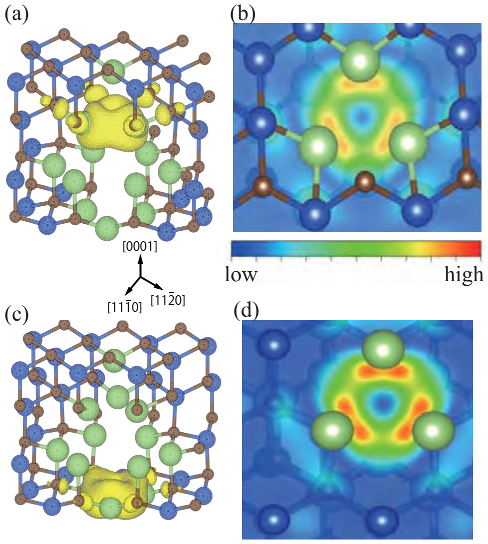

Figure 3: Spin densities for the doubly positive [(a) and (b)] and doubly negative [(c) and (d)] charge states of the hexavacancy. In (a) and (c), the iso-surfaces at the value of 20 % of the maximum value are shown, and (b) and (d) are the contour plots. The large (blue and green) spheres and the small (brown) spheres depict Si and C atoms, respectively. The green spheres depict the under-coordinated Si atoms.

First-principles statistical thermodynamics simulations on the structure and reactivity of heterogeneous catalysts

Fahdzi MUTTAQIEN, Shiro TORII, Yuji HAMAMOTO, Kouji INAGAKI,
Hidetoshi KIZAKI, and Yoshitada MORIKAWA
Department of Precision Science and Technology,
Osaka University, Yamada-oka, Suita, Osaka 565-0871

In our research project, we have investigated several systems including CO_2 adsorption and hydrogenation on Cu surfaces, Bathocuproine-metal interactions, naphthalene on graphite surfaces, ligand-free Suzuki-Miyaura cross coupling reactions in aqueous solutions, and stability of Pd atoms dissolved into $LaFeO_3$ perovskite oxides. In the present report, we explain some of our recent progresses.

Adsorption and decomposition of formic acid on Cu surfaces are attracting considerable attention because of their fundamental importance in catalysis and also applications experimentally reported that the formic acid decomposes to formate species upon adsorption on Cu(100)[1], and Cu(110)[2]. On the other hand, it was pointed out that formic acid does not dissociate at room temperature on the Cu(111) surface, At low temperature, the formic acid decomposition can be induced on Cu(111) from polymeric structures[3,4]. The hydrogen bonding network in polymeric structure is responsible to stabilize the formic acid and enhance its decomposition [4].

In the present works, we carried out self-consistent van der Waals density functional (vdW-DF) study of formic acid decomposition on the single crystal Cu(111) surface. We implemented vdW-DF based functionals (vdW-DF1 [5], rev-vdW-DF2 [6], and optB86b-vdW [7]) to describe the interaction between molecule-surface and molecule-molecule in the system more accurate [8]. To calculate self-consistent potential for vdW-DFs accurately

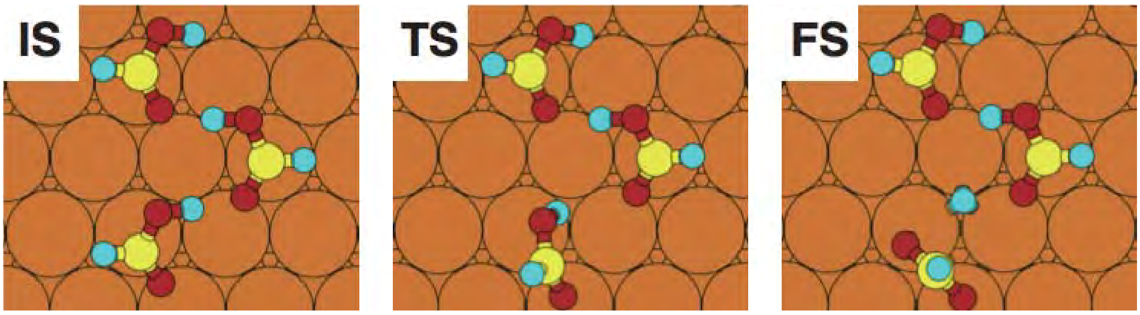

Fig. 1: Schematic of formic acid decomposition in the polymeric structure on the Cu(111) surface.

and efficiently, we employed separable form of vdW kernel proposed by Roman-Perez and Soler [9] with a modification by Wu and Gygi to suppress the divergence of the kernel [10]. Our results showed that isolated single formic acid is easily desorbed rather than decomposed on the Cu(111) surface. While, the polymeric structure of formic acid is more stable on the Cu(111) surface, and easily decomposed into formate species (Fig.1). We also noticed that the formate product tends to form bidentate formation on the surface. We clarified the mechanism for the enhancement of formic acid decomposition by the formation of polymeric formic acid.

References

[1]. B.E. Hayden, K. Prince, D.P. Woodruff, and A.M Bradshaw, *Surf. Sci*. **133**, 589 (1983).

[2] A. E. Baber, K. Mudiyanselage, S. D. Senanayake, A. Beatriz-Vidal, K. A. Luck, E. C. H. Sykes, P. Liu, J. A. Rodriguez, and D. J. Stacchiola, *Phys. Chem. Chem. Phys*. **15**, 12291 (2013).

[3] Y. Shiozawa, T. Koitaya, K. Mukai, S. Yoshimoto, J. Yoshinobu, *J. Chem. Phys*. **143**, 234707 (2015).

[4] F. Muttaqien, Y. Hamamoto, K. Inagaki, and Y. Morikawa, *J. Chem. Phys.* **141**, 034702 (2014).

[5] M. Dion, H. Rydberg, E. Schröder, D.C. Langreth, and B.I. Lundqvist, *Phys. Rev. Lett.*, **92**, 246401 (2004).

[6] I. Hamada, *Phys. Rev. B* **89**, 121103 (R) (2014).

[7] J. Klimeš, D.R. Bowler, and A. Michaelides, *Phys. Rev. B* **83**, 195131 (2011).

[8] Y. Hamamoto, I. Hamada, K. Inagaki, and Y. Morikawa, *Phys. Rev. B*, submitted.

[9] G. Román-Pérez and J.M. Soler, *Phys. Rev. Lett.*, **103**, 096102 (2009).

[10] J. Wu and F. Gygi, *J. Chem. Phys*. **136**, 224107 (2012).

First-principles calculation of interactions between extreme pulse light and matter

Kazuhiro YABANA
Center for Computational Sciences,
University of Tsukuba, Tsukuba, 351-8577

Interaction between intense and ultrashort laser pulse and solid is one of active subjects in current optical sciences. Employing a few-cycle femtosecond laser pulses, a number of intriguing phenomena reflecting extremely nonlinear light-matter interactions have been observed. We have been developing a first-principles computational method to describe electron dynamics in solids under irradiation of a pulsed electric field based on time-dependent density functional theory, solving time-dependent Kohn-Sham equation in real time for electron orbitals in a unit cell of crystalline solids.

For a quantitative description of light-matter interactions, it is important to employ a potential in the Kohn-Sham equation that describes the band gap of the material adequately. As is well known, a simple local density approximation underestimates the band gap systematically. Recently, a few potentials that describe band gaps reasonably have been proposed. We have investigated computational methods to use such potentials in our code and examined optical responses of dielectrics in both linear and nonlinear regimes [1].

We implemented two potentials in our code, a meta-GGA potential developed by Tran and Blaha and a hybrid functional of Heyd, Scuseria, and Ernzerhof. For the meta-GGA potential, we have found that a predictor-corrector step is essential for a stable time evolution. Since a computation of nonlocal exchange potential in the hybrid functional requires heavy computational costs, we have developed a code that efficiently utilizes GPU.

We applied the code to various optical phenomena. One of such applications is the nonlinear photogalvanic effect [2]. It was found that an extremely intense and ultrashort laser pulse produces a current in dielectrics of wide band gap. We have found that the induced current in such dielectrics shows complex behavior, changing its direction depending on the maximum intensity of the pulse.

References

[1] S.A. Sato et.al, J. Chem. Phys. **143**, 224116 (2015).

[2] G. Wachter et.al, New J. Phys. **17**, 123026 (2015).

Development of first-principles electronic-structure and transport calculation method based on real-space finite-difference approach

Tomoya Ono
Center for Computational Sciences, University of Tsukuba
Tennodai 1-1-1, Tsukuba, Ibaraki 305-8577

1 Introduction

SiC is attracted much attention due to its excellent physical properties, such as a high thermal conductivity, high breakdown strength, and large band gap. However, unlike Si metal-oxide-semiconductor (MOS) field-effect transistors (FETs), SiC MOSFETs suffer from unacceptably low carrier mobility. Large amount of defects at SiC/SiO$_2$ interface, which are generated in oxidation process, is expected to be one of the origins for the low carrier mobility. Therefore, understanding and precise control of the atomic structure of SiC/SiO$_2$ interface are vital to increase the carrier mobility of SiC MOSFETs. SiC has many different polytypes, determined based on their stacking along the [0001] direction. Si and C atoms can occupy one of three positions along the $[1\bar{1}00]$ direction, normally labelled ABC. Stacking ordered ABCAB... is called cubic whilst that ordered ABABA... is called hexagonal. The most commonly used polytype for electronic devices is 4H-SiC, which consists of four repeated SiC bilayers, ordered ABCBAB.... Within these four bilayers, there are two inequivalent lattice sites, usually known as h (hexagonal) and k (quasi-cubic) based on the site occupied by the Si atoms in the neighboring bilayers. h sites are equivalent to A or C stacking positions and k sites are equivalent to B stacking positions. The local structure around the SiC/SiO$_2$ interface will change depending on which of this stacking at the SiC surface. In this study, we have conducted density functional theory (DFT) calculations for the relation between the electronic structures at the interface and the local atomic structures which appear in the oxidation process.

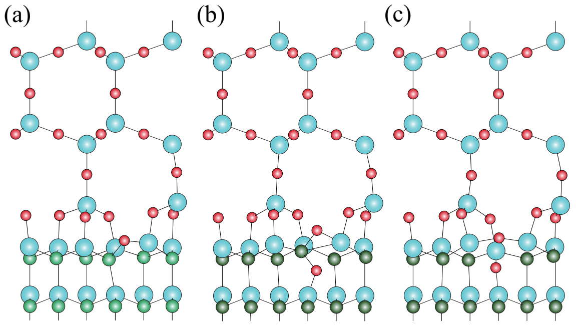

Figure 1: 4H-SiC(0001)/β-tridymite SiO$_2$ interface model. (a) O$_{\rm if}$, (b) O$_{\rm if+sub}$, and (c) V$_{\rm C}$O$_2$. White, green (large dark gray), red (small dark gray), and blue (light gray) circles are H, C, O, and Si atoms, respectively.

2 Computational Methods

DFT calculations are performed using RSPACE code.[1] The lateral size of the supercell is the $(3 \times \sqrt{3})$ 4H-SiC(0001) surface and the substrate contains four Si-C bilayers. Dangling bonds at the bottommost Si-C bilayer as well as those at the topmost layers of SiO$_2$ are terminated by H atoms. The top bilayer of SiC shown in Fig. 1 is hexagonal

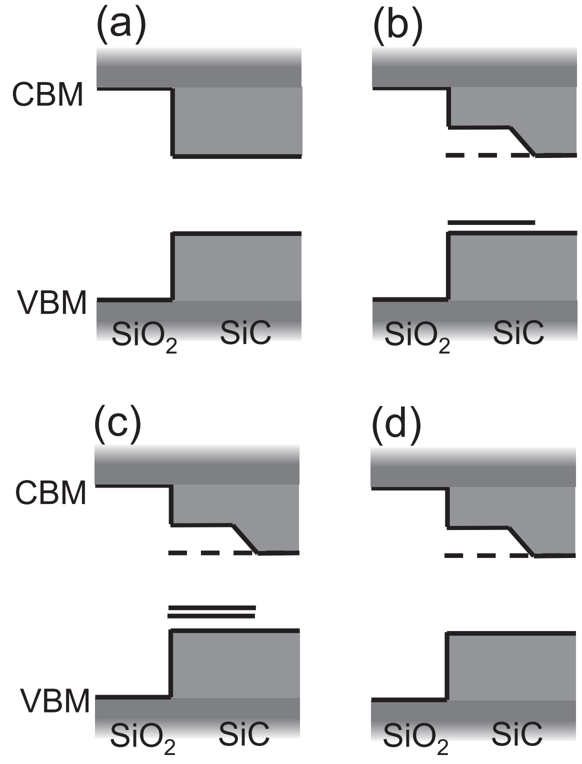

Figure 2: Band alignment of *h* type. (a) clean interface, (b) O_{if}, (c) O_{if+sub}, and (d) V_CO_2.

surface, in which the stacking sequence is ABCBA ... from the top bilayer. The details of the computational procedure are explained elesewhere.[2] The typical computational models for the oxidation are shown in Fig. 1(a), 1(b), and 1(c), which are obtained by our previous study.[3]

3 Results and Discussion

We examine the local density of states (LDOS) for the clean interface. Figure 2 shows the schematic image of LDOS at the interface. There are no significant changes at the valence band edge (VBE) between two types. On the other hand, the most interesting results are along the valence band edge (CBE), the location of which changes with interface type. The *h* type has CBE at the first bilayer of the interface, whereas one does not appear until the second bilayer for the *k* type. The states which contribute to the CBE are the previously noted floating states,[4] which only appear at the CBE in the cubic stacking regions (ABC or CBA) and are blocked by the hexagonal stacking regions.

We examine the LDOS for each structure, noting how it changes compared to the clean interfaces. We start with O_{if}. Notably, the CBE of the *h* type changes, while that of the *k* type does not. Next we examine O_{if+sub}. The same changes are observed at the CBE as before, with the CBE removed for *h* type. Finally, we consider the V_CO_2 structure, which looks similar to the clean interface. Although one CO molecule is removed from the vicinity of the Si-surrounded tetrahedron, there still remains two O atoms. Therefore, the CBE does not recover for the *h* type. For the *k* type, the CBE is not changed because the tetrahedron is located deep inside the substrate.

Since recent SiC-based MOSFETs mainly use the conduction band as a channel, the behavior of the CBE might play an important role in the performance of these devices. In the future we want to do more complete calculations for all of these structures, to get a fuller picture of how the scattering properties of the interface change with defect type using first-principles transport calculations.

References

[1] K. Hirose et al., First-Principles Calculations in Real-Space Formalism (Imperial College Press, London, 2005).

[2] T. Ono and S. Saito, Appl. Phys. Lett. **106**, 081601 (2015).

[3] C. Kirkham and T. Ono, J. Phys. Soc. Jpn. **85**, 024701 (2016).

[4] Y. Matsushita et al., Phys. Rev. Lett. **108**, 246404 (2012).

First-principles study of quantum transport in nanostructures

NOBUHIKO KOBAYASHI
Institute of Applied Physics, University of Tsukuba
1-1-1 tennodai Tsukuba Ibaraki 305-8573

1 Introduction

The aim of this project is to reveal charge and heat transport in materials using atomistic theory. Quantum nature is essential in nanoscale systems, and atomistic analysis based on detailed electronic states calculations are indispensable to discuss the transport property. In order to analyze transport properties, we have developed the nonequilibrium Green's function (NEGF) method, and the time dependent wave-packet diffusion (TD-WPD) method. Using these methods, we have investigated charge and heat transport properties of nanostrucures, organic molecules and so on.

2 Charge Transport

The recent progress in the fabrication technology of organic single-crystal semiconductors and thin-film field-effect transistors with very high carrier mobility up to 40 cm^2/Vs requires us to elucidate the mechanisms of carrier transport in organic semiconductors, which are assemblies of p-conjugate molecules weakly bonded by van der Waals interactions. Observations of the crossover from the hopping transport of localized carriers to bandlike transport with a diffusive nature are expected to provide us with clues allowing us to reveal the carrier transport mechanisms.

We show evidence of a strong correlation between the carrier coherence factor α and the thermally induced fluctuations of transfer energies with neighboring molecules. The thermal fluctuation effects of molecular motion have been discussed for transport properties of organic semiconductors. We present numerical data of transfer energy fluctuations of pentacene at various temperatures and pressures, and we compare them with experimental observations of α. As a result, we find a strong correlation between these two factors. We apply this method to other organic semiconductors and obtain consistent results with those of transport experiments. [1, 2]

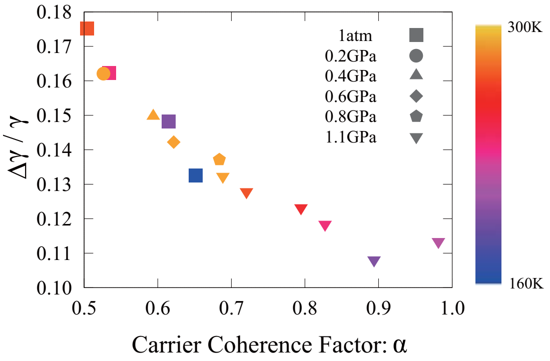

Figure 1: Correlation between carrier coherence factor α obtained from experimental data and calculated thermal fluctuation $\Delta\gamma/\gamma$. The data are taken at various temperatures and pressures.

3 Thermoelectricity

The thermoelectric properties of TiN/MgO superlattices have been analyzed using first-principles calculation techniques. The Seebeck coefficients, the electrical conductances, the thermal conductances, and the figure of merit are investigated employing electrical and thermal transport calculations based on density functional theory combined with the nonequilibrium Green !s function and nonequilibrium

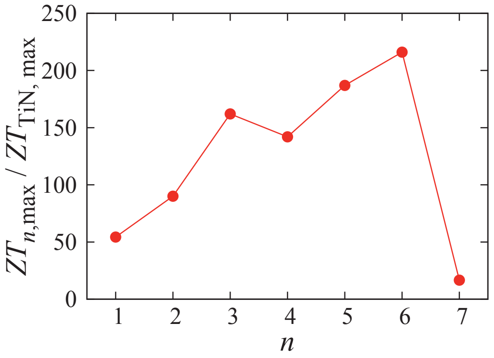

Figure 2: Maximum figure of merit ZT in the calculated configurations normalized by $ZT_{\mathrm{TiN,max}}$.

molecular dynamics simulation methods. The TiN/MgO superlattices with a small lattice mismatch at the interfaces are ideal systems to study the way for an enhancement of thermoelectric properties in artificial nanostructures. We find that the interfacial scattering between the two materials in the metal/insulator superlattices causes the electrical conductance to change rapidly, which enhances the Seebeck coefficient significantly. We show that the figure of merit for the artificial superlattice nanostructures has a much larger value compared with that of the bulk material and changes drastically with the superlattice configurations at the atomistic level. [3]

4 O(N) Method

We have also developed the O(N) TD-WPD method for the quantum transport calculation of huge systems of up to 100 million atoms.We calculated the conductance and the mobility of the system with micron-order lengths at room temperature based on the Kubo-Greenwood formula. Using this method we can study the transport properties from diffusive to ballistic regimes including the effect of realistic electron-phonon scattering, and determine the mean free path and relaxation time from an atomistic viewpoint. We performed DFT calculations of electronic structures and interactions between molecules of pentacene and rubrene single-crystal organic semiconductors including the effect of the van der Waals interaction, and applied the TD-WPD method to the analysis of transport properties of the organic semiconductors.

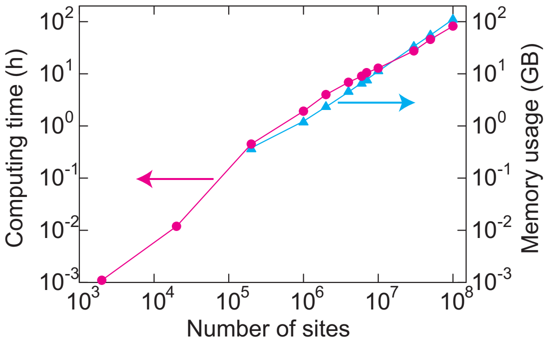

Figure 3: Computing time (red circles) and memory usage (blue triangles) per one initial wave packet as a function of site number of the lattice.

We have analyzed relationships between charge transport properties and disorder in rubrene single crystals. We take into account two different types of disorder, namely, intrinsic dynamical disorder due to intermolecular vibrations and extrinsic static disorder. Then we evaluate the transport properties using our wave-packet dynamical approach which gives us a unified theoretical description from hopping to band transport behavior. We show that the mobilities are completely changed from the intrinsic power-law temperature dependence to the thermally activated behavior by introduction of the extrinsic trap potentials. [4, 5]

References

[1] T. Fukami, H. Ishii, N. Kobayashi, T. Uemura, K. Sakai, Y. Okada, J. Takeya, and K. Hirose, Appl. Phys. Lett. 106 (2015) 143302.

[2] K. Sakai, Y. Okada, T. Uemura, J. Tsurumi, R. Hausermann, H. Matsui, T. Fukami, H. Ishii, N. Kobayashi, K. Hirose and J. Takeya, NPG Asia Materials, 8, e252 (2016).

[3] H. Takaki, K. Kobayashi, M. Shimono, N. Kobayashi, and K. Hirose,
J. Appl. Phys. 119 014302 (2016).

[4] H. Ishii, H. Tamura, M. Tsukada, N. Kobayashi, K. Hirose,
Phys. Rev. B 90 (2014) 155458 (1-5).

[5] H. Ishii, N. Kobayashi, K. Hirose, Mol. Cryst. Liq. Cryst. 620 (2015).

First-principles meta-dynamics analysis of Catalytic Referred Etching method (Analysis of atom removal process)

Kouji INAGAKI

Precision Science and Technology & Applied Physics, Graduate School of Engineering

Osaka University, Yamada-oka 2-1, Suita, Osaka 565-0871

We investigated reaction mechanisms of chemical etching processes in a surface smoothening technique named Catalyst Referred Etching (CARE)[1], in which etching is invoked by bringing the material surface (e.g. wide band-gap semiconductors) into contact with a catalyst (e.g. Pt) in an etching solution (e.g. aqueous HF solution for SiC etching or pure water for GaN etching). In SiC-HF system, we have already obtained findings in the previous study with respect to SiC back-bond cleavage and simultaneous dissociative adsorption of HF molecule as the first step of etching process. The reaction barrier is clarified to be strongly lowered by the existence of Pt catalyst [2]. In this project, we analyzed Pt position dependence particularly in distance between Pt and SiC [3]. It is clarified that the initial, medium metastable and final states in the reaction path are all destabilized by approaching Pt to SiC, but the initial state become relatively most unstable [3]. This means the dissociative adsorption is enhanced when Pt approaches to SiC surface. As for GaN, we firstly find that a spontaneous dissociative adsorption onto OH terminated kinked-GaN surface occurs in the presence of Pt catalyst (Fig. 1). This reaction strongly depends on the initial hydrogen-bond network configuration of the surface OH-termination groups. The accurate reaction barrier can be evaluated by thermal average molecular dynamics methods such as the blue moon ensemble or the meta-dynamics. To reduce the huge calculation costs in such kind of analysis, we proposed a new meta-dynamics method in which the shape of the penalty potential is controlled by the momentum along the corresponding reaction coordinate. The basic behavior of the method is confirmed and it will be applied to realistic models in the next project.

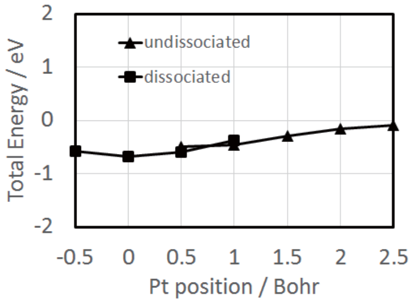

Fig. 1: Pt position dependence in GaN/H_2O/Pt initial state.

References

[1] H.Hara, et al., J.Electron.Mater. 35 (2006) L11.

[2] P. V. Bui, et al. Curr. Appl. Phys., 12 (2012) S42.

[3] P. V. Bui, et al. Appl. Phys. Lett. 107 (2015) 20160.

Quantum effects of hydrogen and oxygen reactions on solid surfaces, Investigations of hydrogen and oxygen reactions on oxide surfaces and interfaces

Hideaki Kasai

1) Department of Applied Physics, Osaka University, Suita, Osaka 565-0871, Japan

2) Center for International Affairs, Osaka University, Suita, Osaka 565-0871, Japan

3) National Institute of Technology, Akashi College, Japan, Akashi, Hyogo 674-8501, Japan

4) Institute of Industrial Science, The University of Tokyo, Meguro, Tokyo 153-8505, Japan

We have studied various surface reactions with a focus on hydrogen and oxygen reactions [1,2] using supercomputer system at ISSP.

Our original code “NANIWA” has allowed us to investigate various quantum states appeared in the reactions. In addition to electronic states, which can be calculated by conventional methods, NANIWA can simulate motions of nuclei based on quantum theory. Therefore, this method is applicable to analyze quantum effects like tunneling, and has been successful to reveal hydrogen reactions at low temperatures.

In this project, we clarified the quantum states of hydrogen atom on Pd(110) [1]. Based on the potential energy surface (PES), obtained from first principles calculations, we calculated the wavefunction of hydrogen atom on the surface. The ground quantum state shows localization of the wavefunction at the pseudo-threefold (P3F) site, which is the energetically most favorable adsorption site. However, the 1st excited state exhibits the localization at the short-bridge (SB) site, although the secondary favorable adsorption site is long-bridge (LB) site. This finding clearly indicates an importance of consideration of quantum behavior in the case of hydrogen reactions.

We also investigated effects of O-vacancies on O_2 adsorption on anatase TiO_2(001) [2]. Although the stoichiometric surface does not bind an oxygen molecule, the introduction of O-vacancies, that induces redistribution of excess electrons, results in strong promotion of O_2 binding. The view obtained in this study provide us a basic understanding of chemical reactivity of anatase TiO_2(001) and clues for designing novel materials.

References

[1] A.A.B. Padama, H. Nakanishi, H. Kasai: App. Surf. Sci. **359** (2015) 687-691.

[2] N.H. Linh, T.Q. Nguyen, W.A. Diño, H. Kasai: Surf. Sci., **633** (2015) 38-45.

Analyses on atomic structure, magnetism, and electronic structure in spintronics materials and molecular magnets

Tatsuki ODA[1,2], Daiki YOSHIKAWA[2], Hiroto NAKANO[2], Naohiro KITAGAWA[2],
Yosuke FUNATO[2], Masao OBATA[2]
Institute of Science and Engineering, Kanazawa University, Kanazawa, Ishikawa 920-1192
Graduate School of Natural Science and Technology, Kanazawa University, Kanazawa, Ishikawa, 920-1192

We studied the several topics involved with this project; Rashba's effect of surface, magnetic anisotropy and its electric field effect in the thin film related with spintronic devices, and magnetic effects in molecular system. We also developed a method of van der Waals density functional (vdW-DF) approach for magnetic systems. These investigations have been done by employing the home-made density functional code, which has run efficiently in the architectures in Systems B and C in ISSP.

Rashba's effect of surface

The heavy-element-covered semiconductor surfaces show a giant Rashba-type spin splitting and many experiments have been reported for spintronics applications. In particular, the surface of Tl/Si(111) has been known to show out-of-plane spin textures in the surface bands. This is novel, compared with a normal Rashba spin texture, in which the spin lies within the surface plane. However, the vertical spin configuration may be useful, because of the suppressed spin scattering. The silicon based materials are still recommended as a new material in the next generation electronics (spintronics). In these contexts, it is important to clarify electronic structures in the surface.

Rashba's effects were investigated in the systems of both PbTl/Si(111) and Tl/Si(110). The calculation of the former revealed the electronic structure and spin.

We also revealed that the surface in Tl/Si(110) has vertical spin textures at around the parts of momentum space, which corresponds to the K-bar points in the 1st surface Brillouin zone. We calculated the distribution of the surface states given at constant energies. These results agreed well with the corresponding experimental result.

Magnetic anisotropy and electric field effect

Magnetic anisotropy energy (MAE) and its EF effect were investigated in the MgO/Fe/MgO and Fe/SrTiO$_3$(STO) systems. We also investigated under layer effects of Cr on the Fe/MgO.

The Fe/STO system was found to have a perpendicular magnetic anisotropy at zero EF and the MAE was estimated be 1.12 mJ/m^2. This is less than those of the interfaces of Fe/ MgO (around 1.5 mJ/m^2). Such perpendicular magnetic anisotropy is commonly observed in the interface consisting of an two-dimensional alignment of Fe-O bonds.

In the STO system, we obtained an decrease of perpendicular MAE under the positive EF caused by electron depletion at the interface. This property on MAE is different from those of theoretical data and available experimental data of the Fe/MgO interfaces and their family systems. Such difference may be devoted to a future research work for clarifying the origin on the response of EF. The interface Ti atom was found to play an important role in the electronic structure, where the orbital hybridization forms between 3d orbitals on Fe and Ti atoms. These effects never exist in the Fe/MgO systems. We discussed effects of in-plane lattice constant in both electronic structure and MAE, by comparing them with those of Fe/MgO.

The slope against for the external EF variation was estimated to be －7.28 fJ/Vm. Using the dielectric constant ε_r of STO, the MAE may be evaluated with the formula of －7.28 ε_r fJ/Vm for the present case. If one can keep a large ε_r in a real device under a large bias-voltage, the EF effect on MAE becomes very large and a candidate of materials for the EF driven magnetization. This is because the ε_r possibley amounts to 30－300.

Charged six-coordinate Fe porphyrin complex

Properties on electronic structure in an Fe-porphyrin (FeP) complex with the proximal imidazole (Im) ligand, a model of active moiety of hemeprotein for analyzing bonding- and separating-processes of dioxygen molecule (O_2), were studied with the spin-polarized density functional theory. It was found that in the ionized model, the bonding stability of O_2 was reduced by one order in energy compared with that of the neutral model, implying existence of the state having a large fluctuation between bonded and separated configurations [1]. We proposed a microscopic scenario on O_2 dissociation phenomenon in terms of spin-crossover and allosteric mechanism.

Van der Waals density functional approach

The van der Waals density functional (vdW-DF) approach was developed for the spin polarized system. The development was tested in the oxygen systems of molecules and solids [2,3].

In the calculations of H-type oxygen molecular pair, the potential curve dependence of the functional parameters defined in a van der Waals density functional with spin-polarization-dependent gradient correction (vdW-DF-SPDGC) was investigated. These parameters were introduced to reduce the stability of antiferromagnetic interaction between oxygen molecules, so that using the set of optimal choices the resulting magnetic interaction was found to give more improved structural parameters in solid oxygen, compared with the functionals developed in the previous work. The finding in this work farely enabled to tune the magnetic interaction between ferromagnetic and antiferomagnetic interactions in density functional approach.We discussed general features of the functionals. The structural parameters of solid oxygen were improved in some choices of the potential parameters. It was also found that our treatment reduced both the binding and magnetic energies in the solid oxygen, indicating that the energy functional was improved for describing the energetics of spin-polarized vdW systems. Although the new approach developed in this work has parameters in the present stage, further investigation on the correlation energy functional may reveal applicability and limitation for an application range on real material.

[1] N. Kitagawa et al., Chem. Phys. Lett. **643** (2016) 119.

[2] M. Obata et al., JPS Conf. Proc, **5** (2015) 011011.

[3] M. Obata et al., Phys. Procedia. **75** (2015) 771.

DFT study on electron transfer and ionic transport at solid-liquid and solid-solid interfaces

Yoshitaka TATEYAMA

International Center for Materials Nanoarchitectonics (WPI-MANA), National Institute for Materials Science (NIMS), 1-1 Namiki, Tsukuba, Ibaraki 305-0044; Elements Strategy Initiative for Catalysts & Batteries (ESICB), Kyoto University, Goryo-Ohara, Nishikyo-ku 615-8245.

Transformation of energy management systems via success of efficient utilization of renewable energy and CO_2 zero emission is an urgent challenge in our society. To step toward its realization, development of larger batteries and next-generation solar cells has been extensively addressed. However, establishments of high-efficiency techniques as well as high reliability are not satisfactory yet for practical implementation. In the field of batteries such as lithium ion battery (LIB), safer electrolyte and high-performance film at the electrolyte-electrode interface to prevent the thermal runaway, in addition to the higher energy density, have been crucial issues. Perovskite solar cell (PSC) emerging quite recently still has problems such as the poor durability for its practical use. Due to the difficulty in experimental observations, these atomistic mechanisms are still open questions.

We addressed such issues with well-optimised first-principles calculations. In the studies on LIB, we demonstrated the reductive decomposition mechanism of electrolyte molecules and the subsequent processes of the decomposed products for solid electrolyte interphase (SEI) films formation, which overturns the conventional understandings. (Fig. 1a) [1]. Furthermore, we theoretically elucidated the electrochemical stability of highly-concentrated lithium salt electrolyte solution and the origin of its excellent transport characteristics3). In the studies on PSC, the stability of surface and interface of the perovskite material and the probable cation diffusion in addition to the anion were theoretically demonstrated for the first time. Then, the possible degradation mechanism and how to control it was proposed as well (Fig. 1b) [2]. We are still keeping intensive collaborations with the experimentalists as well as the industries, and solving crucial issues for fundamental science and industrial application on the atomic scale. In the near future, our computational researches may play a decisive role in the transformation of energy management in our society.

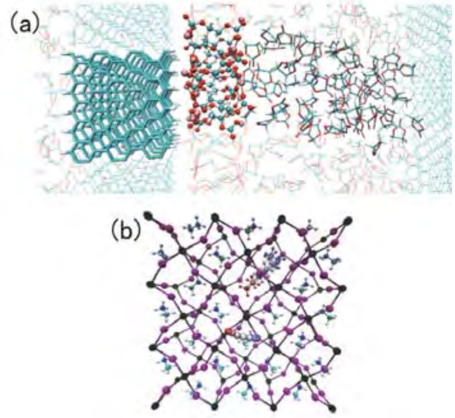

Fig. 1 (a) SEI film model in LIB. (b) Diffusion processes of anions & cations in PSC.

References

[1] K. Ushirogata, K. Sodeyama, Z. Futera, Y. Okuno, Y. Tateyama: J. Electrochem. Soc. **162** (2015) A2670-2678.

[2] J. Haruyama, K. Sodeyama, L. Han, Y. Tateyama: J. Am. Chem. Soc. **137** (2015) 10048-10051.

.

Materials design toward spin-valleytronics by using ferroelectric oxides

Kunihiko YAMAUCHI
ISIR-SANKEN, Osaka University, Ibaraki, Osaka 567-0047

When the bulk inversion symmetry us broken, spin-orbit coupling lifts the spin degeneracy of the electronic bandstructure, as leading to spin-splitting of bands known as Dresselhaus and Rashba effects. This phenomenon is typically realized at surface of interfaces where its structure breaks inversion symmetry. Alternatively, it has been recently proposed that bulk Rashba effect can be induced in ferroelectric structure, additionally providing a non-volatile ferroelectric functionality. In this case, the spin polarization is strongly bound to spin polarization and, as such, allows for its full-electric control.

Recently, the spin-valley coupling has been studied in graphene and transition-metal chalcogenide such as MoS_2, where the valleys at the corner K points of the Brillouin zone is coupled with the spin degree of freedom. The coupling could be used in future valleytronic devices in which both the valley and spin polarized carriers have information. In order to propose new spin-valley-coupling system, we designed a new ferroelectric oxide heterostructure $BiAlO_3/BiIrO_3$ grown along the [111] direction. In this system, $BiIrO_3$ forms a bilayer, where Ir^{3+} ion is aligned in a corrugated graphene-like honeycomb lattice. Between a wide energy gap made by $BiAlO_3$, Ir-d^6 state is split into $P3$ crystal field states, as pushing up $3z^2 - r^2$ orbital level just below the Fermi energy. Since the orbital state is $m = 0$, it is further split into $j_z = \pm\frac{1}{2}$ states under spin-orbit coupling. This band is strongly spin-polarized at K point, because the three-fold rotation at K point allows the s_z state as the basis. Finally, we confirmed that the spin polarization is coupled with the structural ferroelectric distortion, which enables the control of the spin polarization by the external electric field. Interestingly, it is also found that the in-plane spin texture of Ir d state is transformed by flipping electric polarization. This is because the heterostructure has two different distortion, i.e. polar distortion and tilting of oxygen octahedra. The former is responsible for the out-of-plane spin polarization, whereas the latter modifies the in-plane spin polarization significantly.

We proposed a prototype of the ferroelectric spin-valley material by ab-initio materials design approach. We hope that the phenomenon will be confirmed by experiments and the spin-valley coupling property will be optimized by future works. The detail of the present work will be found in a reference[1].

References

[1] K. Yamauchi, P. Barone, T. Shishidou, T. Oguchi, and S. Picozzi: Phys. Rev. Lett. **115** (2015) 037601.

Theoretical Study on Electronic Structure of Bathocuproine: Renormalization of the Band Gap in the Crystalline State

Susumu Yanagisawa
Department of Physics and Earth Sciences, University of the Ryukyus
1 Senbaru, Nishihara, Okinawa, Japan 903-0213

Bathocuproine (BCP) is a well-known organic material of a hole blocking layer in organic light-emitting diodes and an electron buffer layer in organic photovoltaics (Fig. 1). The nature of the unoccupied electronic states is a key characteristic of the material, which play vital roles in the electron transport. In terms of the molecular orbital or the band structure, the roles played by the frontier energy levels such as the highest occupied molecular orbital (HOMO) and the lowest unoccupied molecular orbital (LUMO) levels are of importance, by which the carriers are transported in the solid or across the organic-organic or organic-inorganic interfaces.

To elucidate the electronic properties of the molecular or crystalline BCP, we use the *GW* approximation for calculation of the crystalline band gap[1]. We obtain the fundamental gaps of the gas and the crystalline phases with the one-shot self-energy correction denoted by G_0W_0 using the *GW* space-time method[2]. We use PBE eigenfunctions and eigenvalues as a zeroth-order starting point. For the band energies of the crystalline BCP, we use the plane wave cutoff energies of 60 Ry and 24 Ry for the static Hartree-Fock exchange (Σ_x) and the dynamical *GW* correlation (Σ_c), respectively. For the sum over unoccupied bands in the calculation of the Green's function required to calculate the *GW* correlation, we employ 4,852 unoccupied bands for the crystalline band energy (102 eV above the middle of the band gap). By the estimation of the convergence with respect to the number of the summed bands (N_b) based on the fit to a linear polynomial of $1/N_\mathrm{b}$, we confirm that the calculated band gap is deviated from the extrapolated infinite N_b limit by 0.1–0.2 eV. We determine the GGA-PBE orbital energies of the gas phase relative to the vacuum level using the dipole correction, align the PBE band gap of the single crystal to the center of the PBE gas phase gap, and thus obtain the crystalline ionization potential (IP) and electron affinity (EA) within GGA-PBE. For the EA and the IP at the G_0W_0 level of theory, the fundamental gap is aligned to the center of the gap obtained with GGA-PBE. In other words, we assume that the self-energy corrections to the HOMO and LUMO levels with GGA-PBE are the same.

It is found that the band gap of the crystalline BCP is 4.39 eV. The result is in agreement with the experimental band gap of 4.58 eV, which is estimated using the experimental IP and EA measured with the photoemission yield spectroscopy (PYS) and low-energy inverse photoemission spectroscopy (LEIPS) techniques, respectively[3]. The theoretical gap for the single crystal, which is smaller by 0.2 eV than the experimental, is reasonable, given that the polarization energy in the single crystal may become larger than in thin film and noncrystalline phases fabricated in experiments, with their lower molecular packing den-

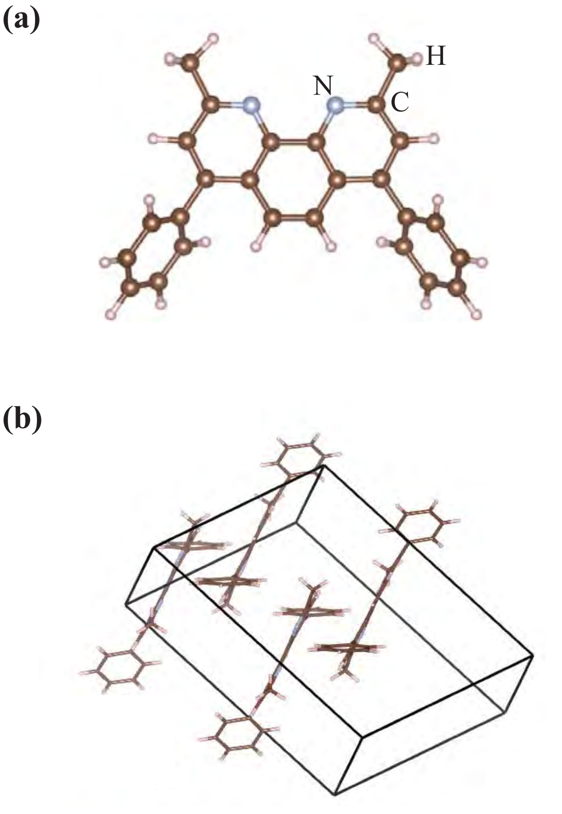

Figure 1: Schematics of (a) BCP molecule, and (b) the single crystal with the monoclinic c2/c symmetry

sity than single crystals.

The polarization energy, obtained as the average of the polarization energies on HOMO and LUMO levels, is estimated to be 1.05 eV, demonstrating the large polarization effects induced by the electronic clouds surrounding the injected charge (Fig.2). The polarization energy of 1.05 eV is reasonable in organic solids, given a body of the polarization energies of the similar magnitude determined experimentally or theoretically, and that may be elucidated in terms of the organic crystal represented by a linear dielectric medium and the charged molecule by a hollow sphere, with a point charge put at its center[4].

The calculated IP (6.00 eV) and EA (1.61 eV) of the single crystal are in fair agreement with experimental IP (6.47 eV[3]) and EA (1.89±0.04 eV[3]). The theoretical IP is reasonably smaller than the experimental values, given that the calculation describes larger polarization in the single crystal than that in the thin-film or non-crystalline phases in the experiment. However, the calculated EA is not reasonable, in that it is smaller than the experimental value measured with the LEIPS technique[3]. We feel that the the IP and the EA should be calculated separately, rather than assume the polarization energies to be the same. Such a work is in progress.

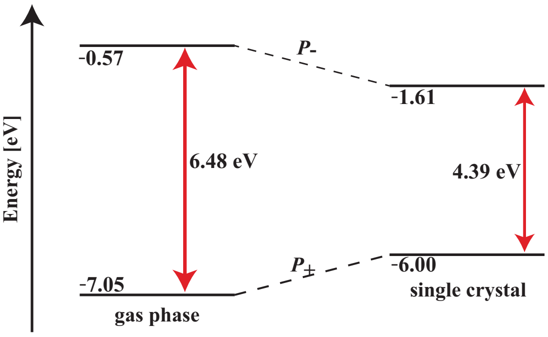

Figure 2: Frontier energy levels of the gas and the single crystal phases of BCP. Polarization energies on the HOMO and LUMO levels (P_+ and P_-, respectively) were assumed to be the same (1.05 eV).

References

[1] S. Yanagisawa, S. Hatada and Y. Morikawa: J. Chin. Chem. Soc. (Special Issue), *in press*.

[2] M. M. Rieger et al.: Comput. Phys. Commun. **117** (1999) 211; L. Steinbeck et al.: *ibid.* **125** (2000) 105; C. Freysoldt et al.: *ibid.* **176** (2007) 1.

[3] H. Yoshida and K. Yoshizaki: Org. Electron. **20** (2015) 24.

[4] N. Sato, K. Seki and H. Inokuchi: J. Chem. Soc., Faraday Trans. 2 **77** (1981) 1621.

DFT Investigations on the Electronic State Changes of Ferrocene-Terminated Self-Assembled Monolayers by Coadsorbed Species

Ken-ichi FUKUI

Department of Materials Engineering Science, Graduate School of Engineering Science,
Osaka University, Machikaneyama, Toyonaka, Osaka 560-8531

Ferrocene(Fc)-terminated self-assembled monolayers (SAMs) have been widely studied in the last quarter century to reveal the electrochemical properties of chemically modified electrodes. It has been well known that the formal potential of the system strongly depends on the local environment of the Fc moiety [1]. Although electronic states of the Fc-terminated SAMs should directly affect the electrochemical properties, knowledge concerning electronic structures with respect to different local environment is very limited. In this study, we performed density functional theory calculations of Fc-terminated SAMs with different coadsorbed species to reveal the relationship between the electronic structures and the local environment of Fc moieties [2].

All calculations were carried out by using DFT as implemented in the STATE (simulation tool for atom technology) code. In a unit cell a Fc-terminated thiol molecule (C5Fc) was coadsorbed with three matrix thiols possessing different terminal functional groups (C4 and C4X: X= OH, CN, and -Br) on Au(111) consisting of 12 Au atoms at the surface as shown in the inset of Fig. 1.

After structure optimization for the mixed SAMs, the HOMO level localized on Fc moiety, work function (W) of the SAM, and electrostatic potential at the Fc moiety (V_{ES}(Fe)) were analyzed and the results are summarized in Fig. 1.

Whereas ΔW is positively correlated with $\Delta\mathrm{HOMO}_{\mathrm{SAM}}$, we found that only the C5Fc-substituted C4CN system increases the overall deviations from a dotted line. It is because the contribution of negative charge of the nitrogen atom to modulate the local electrostatic potential is compensated by the positive charge of the carbon atom. On the other hand, the fact that the average height of the nitrogen atom is higher than that of the carbon atom by 0.63 Å results in the large increase of the W value.

Instead, the $\mathrm{HOMO}_{\mathrm{SAM}}$ values have excellent correlation with V_{ES}(Fe). This analysis indicates that the energy shifts of the HOMO-related state are practically determined by V_{ES}(Fe) felt by the central iron atom in the Fc moiety.

While the structures of these systems are practically indistinguishable, HOMO-related states were found to largely shift due to the difference of the local electrostatic potential at the central iron atom in the Fc moiety.

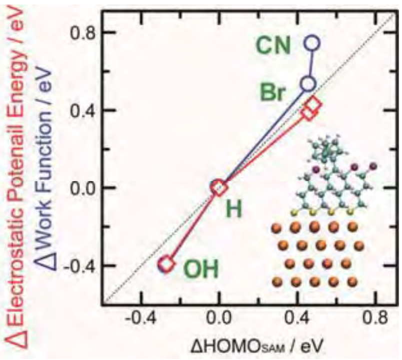

Fig. 1: Comparisons between electronic properties and $\mathrm{HOMO}_{\mathrm{SAM}}$ of C5Fc-substituted SAMs with various coadsorbed molecules.

References

[1] Y. Yokota, Y. Mino, Y. Kanai, T. Utsunomiya, A. Imanishi, M. Wolak, R. Schlaf , K. Fukui: J. Phys. Chem. C **118** (2014) 10936.

[2] Y. Yokota, S. Akiyama, Y. Kaneda, A. Imanishi, K. Inagaki, Y. Morikawa, K. Fukui: J. Phys. Chem. C, in press.

Spin-orbit coupling parameters at surfaces and interfaces of semiconductors: first-principles study

Fumiyuki ISHII
Faculty of Mathematics and Physics, Institute of Science and Engineering,
Kanazawa University, Kanazawa, 920-1192, Japan

Spin-orbit coupling is key ingredient in the spintronics applications. The examples includes the Rashba-type spin-orbit coupling in the Datta-Das type spin field effect transistor (Spin-FET) where the spin direction of the electrons participating in the electric current could be controled by the gate voltage. The Rashba coefficient is an important parameter that determines the performance of the Spin-FET. In addtion, in recent years, the Rashba spin-orbit coupling is also quite important for the conversion between charge and spin currents.

In this study, by using OpenMX code[1], we have performed first-principles calculations on Zincblende structure III-V semiconductors and its heterostructures such as GaAlAs/GaAs and InAlAs/InAs with different orientations, (001) and (110).

Table I shows calculated Rashba parameters of valence band top for III-V semiconductors, its heterostructures and ZnO[2]. The calculated values are in the same order of magnitude compared to the experimental one, 90 meV·Å for InAs/GaSb, 40 meV ·Å for InGaAs/InAlAs and 72 meV ·Å for $In_{0.53}Ga_{0.47}As/In_{0.52}Al_{0.48}As$. The origin of Rashba parameters is the strength of atomic spin-orbit coupling constant ruled by atomic numbers.

We have also evaluated spin distribution in momentum space by using our developed post-processing code for OpenMX code, SOfield[3]. The origin of spin textures is built-in electric field, i.e., electric polarization. In order to analyze the electric polarization in the heterostructures and superlattice system, we have calculated the layer polarization evaluated by one-dimensional Wannier functions.

Table 1: Calculated Rashba paraemters α_R for III-V semiconductors, its (001) orientation heterostructures, and ZnO[2].

Materials	α_R(meVA)
AlP	–
AlAs	0.27
AlSb	1.22
GaP	14.66
GaAs	19.24
GaSb	9.42
InP	79.51
InAs	43.47
InSb	41.81
$(InP)_4/(GaAs)_4$	206.29
$(InP)_4/(InAs)_4$	795.57
ZnO	1.15

References

[1] T. Ozaki et al., http:// www.openmx-square.org/

[2] M.A.U. Adhib, H. Kotaka, F. Ishii and M.Saito, Appl. Phys. Express, **7**, 053002 (2014).

[3] H. Kotaka and F. Ishii, `http://cphys.s.kanazawa-u.ac.jp/~lab-ishii/SOField/index.html`

First-Principles Calculation of Spin-Orbit Field and Thermopower

Fumiyuki ISHII
Faculty of Mathematics and Physics, Institute of Science and Engineering,
Kanazawa University, Kanazawa, 920-1192, Japan

We are interested in how to achieve much higher thermoelectric (TE) conversion efficiency by effectively manipulating electron-spin degree of freedom. As one possibility, we have been studying the contribution of the anomalous Hall conductivity (AHC) in TE power. Previously, we have shown quite large effect of AHC in a massive Dirac fermion model [1]. While seeking for novel systems that exhibit much larger AHC, hopefully leading to a favorable TE performance, we have noticed recent reports illustrating large AHC in some crystals of whirling spin textures, among which we taget the 2D skyrmion type case“ *skyrmion crystal* ” (SkX) here. We have performed first-priciples calculations of TE properties of some model SkXs, evaluated via an efficient method based on the interpolation of the ab-initio electronic band structure with Wannier functions (localised orbitals) realized by employing two open-source packages, namely, OpenMX[2] and Wannier90[3]. Our findings[4] include: (i)Larger size of unit skyrmion makes AHC larger [e.g. exceeding $12 \times e^2/h$ for 6×6 size, while limited up to $6\times e^2/h$ for 4×4]. (ii) The larger AHC leads to larger transverse (anomalous Nernst) voltage in some filling (Fermi-level) range. As our future task, we hope to find good TE materials among skyrmion systems, by applying the above ab-initio method to realistic crystals.

We also studied thermoelectric properties of pyochlore iridate system as follwoing. Candidates for the ground state of pyrochlore iridates $A_2\mathrm{Ir}_2\mathrm{O}_7$ include various phases of metals, normal insulators, topological insulators and Weyl semimetals[5], accompanying diverse magnetic structures originating from the $4f$-electrons of A-ion and Ir $5d$-electrons. Regarding the transitions between some of these phases and transport properties there, discrepancies exist between the findings of different research groups. As a basic step in solving those problems and better understanding this series of compounds, we have investigated their electronic structures from first-principles using OpenMX package[2]. We have revealed, for the case of A=La, how its band-structure evolves as one of the structural parameters x (oxygen Wyckoff position) is varied. In addition, the behavior of its thermopower, a band-structure-sensitive quantity, is revealed. Since the variation of x and also the other one, i.e., lattice constant) can be viewed, for example, as corresponding to different A-ion species, our results give us information on how the A-ion affects each compound's band structure.

References

[1] Y.P. Mizuta and F. Ishii, JPS Conf. Proc. **5**, 011023 (2015).

[2] T. Ozaki et al., http:// www.openmx-square.org/

[3] A.A. Mostofi et al., Comput. Phys. Commun. **185**, 2309 (2014).

[4] Y.P. Mizuta and F. Ishii, arXiv:1601.03510.

[5] F. Ishii et al., J. Phys. Soc. Jpn. **84**, 073703 (2015).

Development and Application of First-Principles Simulation of Material Structure and Electronic Properties

Shinji TSUNEYUKI
Department of Physic, School of Science, The University of Tokyo
Hongo 7-3-1, Bunkyo-ku, Tokyo 113-0033
Institute for Solid State Physics, The University of Tokyo
Kashiwanoha 5-1-5, Kashiwa, Chiba 277-8581

First-principles electronic structure calculation based on the density functional theory (DFT) has been successfully used not only in the analysis of material structures and their electronic states but also for theoretical prediction of material properties, yet there are many problems remaining: (1) accuracy and reliability of the calculation, (2) calculable system size, (3) treatment of non-equilibrium dynamics, (4) exploration of complicated structure like amorphous or interfaces, etc. We have developed various simulation methods with or beyond DFT calculation to solve the parts the problems. Our achievements in FY2015 are summarized below.

Lattice thermal conductivity is a key parameter for thermoelectric materials, while its estimation needs accurate calculation of anharmonic force constants responsible for phonon-phonon scattering. Previously we developed a general method of calculating anharmonic force constants efficiently with first-principles molecular dynamics simulation, with which we calculated lattice thermal conductivity of various materials [1, 2]. We improved the method by the sparse modeling technique to obtain reliable results. Furthermore, we introduced the self-consistent-phonon approach to treat highly anharmonic lattice: the method is applicable even when the material has imaginary phonon modes with ordinary harmonic approximation. With the method, we succeeded in quantitative calculation of the temperature dependence of the soft phonon mode and the lattice thermal conductivity of $SrTiO_3$ in the high-temperature cubic phase (Fig.1) [3].

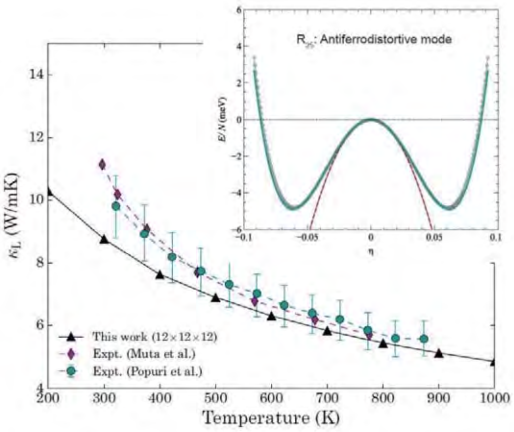

Figure 1: Temperature dependence of the lattice thermal conductivity of cubic $SrTiO_3$. The computational result is compared with experimental values reported by Muta et al.(J. Alloys Compd. 392, 306 (2005)) and Popuri et al. (RSC Adv. 4, 33720 (2014)). Lines are shown to guide the eye. (Inset) Potential energy surface for the deformation of the soft mode. The dotted line is the harmonic potential fitted at the symmetry center.

Development of the first-principles electronic structure theory for strongly correlated electrons is also one of our important activities, for which we have long investigated the first-principles transcorrelated (TC) method for periodic systems. We newly implemented an iterative scheme for the solution of the TC self-consistent equation and succeeded in drastic speed-up of the calculation. With the new code, we examined the effect of atomic core states to the valence band structure by including the highly localized core orbitals [4].

Computational time of the DFT calculation usually scales as N^3 with N being the number of atoms in the system. So-called Order-N methods, in which the system is somehow divided into small fragments, enable us to calculate total energy and atomic force with the computational cost of order N, while the energy spectrum and wavefunctions of the whole system are not accessible directly. Borrowing an idea from the linear combination of the molecular orbitals (LCMO) scheme for the fragment orbital (FMO) method [5], based on the lean divide-and-conquer method [6], we developed an efficient method to derive one-electron Hamiltonian of the whole system from the orbital energies and orbital wavefunctions of each fragment of the system [7]. We implemented the method to xTAPP, a plane-wave DFT code, to find the energy spectrum of a large system with reasonable accuracy.

Finally, we developed a method to find activation barrier for the diffusion of an impurity in semiconductors considering the change in its charge state. The method is based on the nudged elastic band (NEB) method but potential energy hypersurfaces for different charge states are considered. With the method, we discussed the stability of hydrogen impurity (H^0, H^+, H^-) in SiO_2 [8].

References

[1] T. Tadano, Y. Gohda, and S. Tsuneyuki, J. Phys.: Condens. Matter **26**, 225402 (2014).

[2] T. Tadano, Y. Gohda, and S. Tsuneyuki, Phys. Rev. Lett. **114**, 095501 (2015).

[3] T. Tadano and S. Tsuneyuki, Phys. Rev. B **92**, 054301 (2015).

[4] M. Ochi, Y. Yamamoto, R. Arita, and S. Tsuneyuki, J. Chem. Phys. **144**, 104109 (2016).

[5] S. Tsuneyuki, T. Kobori, K. Akagi, K. Sodeyama, K.Terakura, and H. Fukuyama, Chem. Phys. Lett. **476**, 104 (2009).

[6] F. Shimojo, S. Hattori, R.K. Kalia, M. Kunaseth, W. Mou, A. Nakano, K. Nomura, S. Ohmura, P. Rajak, K. Shimamura and P. Vashishta, J. Chem. Phys. **140**, 18A529 (2014).

[7] Y. Yamada, R. Akashi and S. Tsuneyuki, in preparation.

[8] Y. Yamamoto, R. Akashi and S. Tsuneyuki, in preparation.

Atomic-Scale Structure and Local Chemistry of CoFeB-MgO Magnetic Tunnel Junctions

Mitsuhiro Saito[1,2], Keith P. McKenna[3], Yuichi Ikuhara[1,2]
[1]*Advanced Institute for Materials Research, Tohoku University, Sendai, Miyagi, 980-8577*
[2]*Institute of Engineering Innovation, The University of Tokyo, Yayoi, Tokyo, 113-8656*
[3]*Department of Physics, University of York, Heslington, York YO10 5DD, United Kingdom*

Magnetic tunnel junction(MTJ)s are the most important in random access memory and spintronics-based integrated circuits. The fundamental element of a MTJ consists of an atomically thin insulating tunnel barrier sandwiched in between two ferromagnetic electrodes. A giant tunneling magnetoresistance was identified in a (001)-oriented MgO MTJ with (001) CoFe electrodes due to coherent electron tunneling of the Δ_1 Bloch states. Clarifying how each species of atom diffuses and structure changes via annealing is critical in designing optimal stacks for the fabrication process.

We employed first-principles calculations combined with advanced electron microscopy to unravel atomic-scale structure and local chemistry of confined stacking layers in the CoFeB-MgO based MTJ which could offer direct evidence of how B diffused in the MTJs via annealing. Such combined techniques allowed us to demonstrate that B diffused out of the crystalline CoFeB into Ta interstitial sites rather than into the MgO tunnel barrier after annealing, and CoFe atomically bonded to the textured MgO grains with an epitaxial orientation relationship by forming Fe(Co)-O bonds yet with no Co or Fe incorporation in MgO [1].

Calculations were performed with the Vienna ab initio simulation package within the framework of density function theory. The projector augmented wave method was employed and the generalized gradient approximation of Perdew-Burke-Ernzerhof was used to describe exchange and correlation. The $2s$ and $2p$ electrons of O and B, $2p$ and $3p$ electrons of Mg, and $3d$ and $4s$ electrons of Co and Fe were treated as valence electrons and expanded in a plane wave basis with a cutoff energy of 400 eV. A Monkhorst-Pack grid of $9\times9\times9$ k-points was adopted on primitive unit cells and equivalent k-point densities were used for supercells (up to 513 atoms). Interface models consisted of a 10-layer Fe_3Co (001) slab connected to a MgO (001) slab of six layers. A vacuum gap of 10Å was included in the supercell to avoid unwanted interactions between the slab and its periodic images. All atoms in the slabs were fully relaxed until the magnitude of the force on each atom fell below 0.05eV/Å. We also employed a first-principles thermodynamics method to assess the tendency for B, Co, and Fe to incorporate in MgO and Ta. The B incorporation in MgO turns thermodynamically favorable only for very high or very low Fermi energies. Such capability of direct spatial and chemical analysis of the buried polycrystalline stacking layers in MTJs will deepen our understanding of the physics of MTJs.

References

[1] Z.C. Wang, M. Saito, K.P. McKenna, S. Fukami, H. Sato, S. Ikeda, H. Ohno, and Y. Ikuhara: Nano Lett., **16** (2016) 1530.

First-Principles *GW*+Bethe-Saleter Calculation for a 160 Atom System

Yoshifumi NOGUCHI
Institute for Solid State Physics,
The University of Tokyo, Kashiwa-no-ha, Kashiwa, Chiba 277-8581

Green's function is a powerful method that is capable of determining the excited energy spectra of real materials from first-principles. However, the required computational cost is much higher than that of a conventional density functional theory (DFT)-based first-principles method. For example, a GW approximation (GWA), in which the one-electron self-energy operator (Σ) is expressed as the simple product of a one-particle Green's function (G) and a dynamically screened Coulomb interaction (W), requires a computational cost that scales as O(n^4), and the Bethe-Salpeter method needs the computational cost that scales as O(n^6) (note that the computational cost required when using DFT scalses as O(n^3)). Therefore, there is a strong limitation in treatable system size.

This year, we improved our original first-principles GW+Bethe-Salpeter program of hybrid parallel version to handle 288 Intel Xeon processors (=3456 CPU cores) on a new system B and to simulate systems of 100-200 atoms without the need to further reduce theoretical accuracy. By using our program, indeed, we succeeded in simulating the UV-Vis absorption spectra of [16]CPP ($C_{96}H_{64}$, see Fig. 1, the atomic geometry optimized for the ground state by B3LYP/cc-pVTZ). The simulated spectra were compared with the available experimental spectra. The agreement is fairly good, in particular, in terms of peak position and overall peak shape. Indeed, we newly introduced a method for exciton analysis that is based on a two-particle picture beyond the independent particle approximation and analyzed first dark (S_1) and bright (S_n, n >1) excitons. These results will be published soon [1].

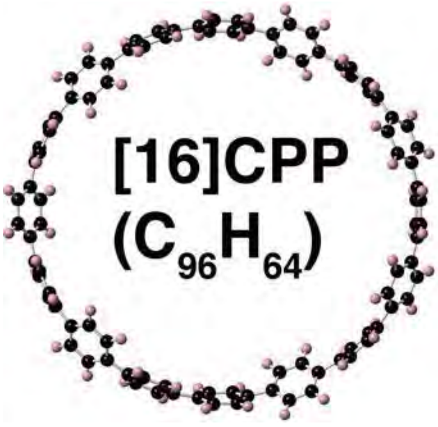

Fig. 1. Atomic geometry of [16]CPP optimized for ground state by using B3LYP/cc-pVTZ.

References

[1] Y. Noguchi and O. Sugino., in preparatio

First-principles calculation for device application of wide gap semiconductors

Mineo SAITO

Institute of Science and Technology, Kanazawa University

Kakuma, Kanazawa, 920-1192 Japan

GaN, which has a wide gap, has been attracting scientific and technological interests because of its device applications.

Hydrogen impurities have crucial effects on GaN. It is well known that hydrogen passivates acceptors. However, the understanding of mono-hydrogen impurities is still insufficient. A study based on a μSR experiment indicated that the neutral muonium in GaN induces a shallow donor level, suggesting that hydrogen should be a shallow donor [1]. On the other hand, first-principles study concludes that the mono-hydrogen has a negative-U property [2]. Theoretical analysis of the μSR experiment is necessary for clarifying the origin of the inconsistency,

The μSR spectroscopy exhibits strong anisotropy in the hyperfine structure and its origin is still unclear. In this study, we carry out first-principles calculations to clarify the origin of the anisotropy.

We find that the most stable site of hydrogen is in the trigonal channel. This stable site in the wurtzite structure is in sharp contrast with bonding and antibonding sites which were discussed in studies of diamond and zinc blend structures. We clarify that the spin density is large not only in the hydrogen site but also in the six near N sites. As a result, the spin density has a strongly anisotropic distribution in space, which is expected to be the origin of the observed anisotropic hyperfine constant.

Then, we carry out calculation of the hyperfine constant and find that the dipole-dipole interaction term induces strong anisotropy, i.e., this term is positive when the magnetic field is applied in the same direction as the c axis and is negative when the magnetic field is perpendicular to the c axis. These results are consistent with the experimental results [1].

References

[1] K. Shimomura et al., Phys. Rev. Lett., 92,135505 (2004).

[2] C. G. Van de Walle et al., Nature, 423, 626 (2003).

First Principles Study of Planar Pt Clusters Supported on Defective Graphene

Yuji HAMAMOTO
Department of Precision Science and Technology, Osaka University
Yamada-oka, Suita, Osaka 565-0871

Graphene, atomically thin two-dimensional material composed of a honeycomb lattice of carbon atoms, has drawn keen attention since its experimental realization, due to the peculiar electronic and structural properties. Nowadays, the applications of graphene to various industries have been explored extensively, among which one of the most promising candidates is the usage of graphene as a support material of metallic cluster catalysts. Experiments have demonstrated that Pt clusters deposited on graphene exhibit higher catalytic activity than on other carbon substrates such as carbon black and carbon nanotubes [1]. Similar phenomena have been observed for Pt clusters supported on highly-oriented pyrolytic graphite (HOPG) [2], in which the enhanced catalytic activity is attributed to planar cluster structures observed with scanning tunneling microscopy. Although the adsorption structures of Pt clusters on graphene has also been studied theoretically so far, such a planar cluster structure has never been reproduced on (undoped) graphene.

To explore possible planar cluster structures, we investigated Pt clusters on graphene with the Stone-Wales (SW) defects using the first principles calculation code State [6]. We first investigated adsorption of a Pt atom on the defective graphene with a SW defect. While the adsorption energy E_{ads} on a C–C bond of pristine graphene is -1.54 eV, we found that a C–C bond closer to the SW defect gives larger E_{ads} and we obtained $E_{\mathrm{ads}} = -2.85$ eV at the center of the SW defect. This suggests that, at finite temperature, Pt atoms diffusing on graphene are drawn into SW defects and form Pt clusters.

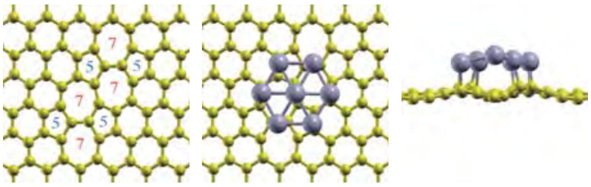

Figure 1: Planer Pt cluster structure obtained on a SW defect dimer in graphene.

To confirm whether this scenario leads to the planar cluster structure on graphene, we next examined the stability of a planar Pt_7 cluster adsorbed on SW defects. When the Pt_7 cluster was adsorbed on a single SW defect, it could not sustain the planar structure and was distorted after structure relaxation. On the other hand, the adsorption on a SW defect dimer shown in Fig. 1 was considered, it was found that the Pt_7 cluster remains planar in agreement with the experiments on HOPG [2]. Similar planar cluster structures were also obtained on a lattice completely consisting of five- and seven-membered rings, which indicates the importance of SW-type defects for the stabilization of planar cluster structures. However, these planar Pt clusters were found to be metastable and convert into spherical structures by using the finite-temperature molecular dynamics. Moreover, the dangling bonds of the planar cluster strongly bind CO molecules on the edges, which could result in the reduction of catalytic activity of the Pt cluster. This strongly suggests that the support effect due to SW defects is not strong enough to stabilize the planar structure and enhance its catalytic activity.

References

[1] E. Yoo, T. Okata, T. Akita, M. Kohyama, J. Nakamura, and I. Honma, Nano Lett. **9**, 2255 (2009).

[2] T. Kondo, K. Izumi, K. Watahiki, Y. Iwasaki, T. Suzuki, and J. Nakamura, J. Phys. Chem. C, **112**, 15607 (2008).

[3] Y. Okamoto, Chem. Phys. Lett. **420**, 382 (2006).

[4] K. Okazaki-Maeda, Y. Morikawa, S. Tanaka and M. Kohyama, Surf. Sci. **604**, 144 (2010).

[5] T.-u. Park, Y. Tomita and T. Nakayama, Surf. Sci. **621**, 7 (2014).

[6] Y. Morikawa, K. Iwata, and K. Terakura, Appl. Surf. Sci. 169, 11 (2001).

Development and application of first-principles electron-transport simulator based on time-dependent density functional theory

Yoshiyuki EGAMI
Division of Applied Physics, Faculty of Engineering, Hokkaido University
Kita 13, Nishi 8, Kita-ku, Sapporo, Hokkaido 060-8628

Recently, numerical simulations have attracted much interest not only in fundamental science but also in industrial applications. For example, in the research and development of high-performance and high-integrated electronic devices, the electron-transport simulations of nanoscale materials play important roles. So far, many remarkable results have been reported using first-principles calculations. However, most of the calculations estimete the static characteristics of electrons in the steady state, and there remains a lot of uncertainty on the dynamic behavior of electrons flowing across the materials.

In order to examine the dynamic transport properties of the nanoscale materials, we developed the impulse response (IR) method [1] based on the real-space finite-difference approach [2] within the framework of the time-dependent density functional theory. The conventional IR method employs an algorithm for enabling efficient calculations on the assumption that the electrodes are imitated by the structureless jellium. In this subject, we attempted developing a new algorithm to treat the models sandwiched between semi-infinite crystalline electrodes. In the calculation, the time-evolution operation for an incident wave constructed by the propagating Bloch waves in the crystalline electrode is repeatedly performed. To reuse the algorithms in the conventional method, the Bloch waves are expanded by the plane wave basis set consisting of the Bloch waves in the jellium electrode.

To demonstrate the performance of the improved IR method, we carried out the time-dependent electron-transport simulations for the BN-dimer embedded graphene connected to semi-infinite graphene electrodes, where the calculations were performed with a few hundred cores on FUJITSU PREMEHPC FX10 in System C. As the results, we observed the time-dependent behavior of electrons flowing through the graphene and being scattered by the impurity potential of BN dimer. However, the flowing electrons exhibit unphysical behavior, where the time-evolved wave function is largely different from the scattering wave function in the steady state even if a sufficiently long time is passed. Challenges to resolve this problem are in progress.

References

[1] Y. Egami and K. Hirose: JPS Conf. Proc. **1**, 016012 (2014).

[2] K. Hirose *et al.*: *First-Principles Calculations in Real-Space Formalism*, (Imperial College Press, London, 2005).

Computational Design of SiC-Based Future Power Devices

Kenji SHIRAISHI

Institute of Materials and Systems for Sustainability,
Nagoya University, Furo-cho, Chikusa-ku, Nagoya, Aichi 464-8603

We clarify the intrinsic problems of SiC/SiO_2 interfaces by the first principles calculations.

We first discuss the oxidation induced C-C bond formation. O incorporation causes large bond rearrangement. Two Si-O bonds and one C-C bond are formed by breaking two Si-C bonds as shown in Fig. 1. A C-C bond causes local strain around it and it modifies the shape of internal space of NFE states. This results in the lowering of conduction band by about 100 meV, leading to the formation of interface states near conduction band bottoms.

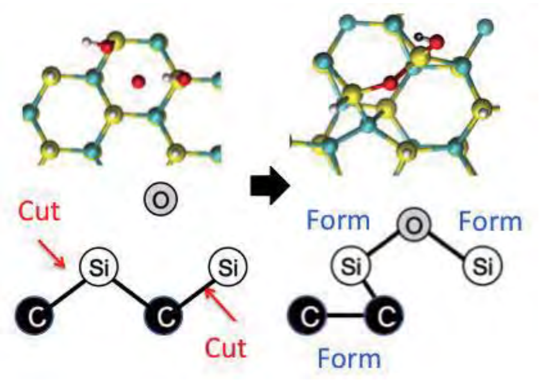

Fig.1: (a) Initial and (b) oxidized structure. O atom incorporation induces large bond rearrangement and forms C-C defects with large energy gain.

Next, we comment on the Vth instability of SiC-MOSFET caused by proton [1] It has been reported that C impurity in SiO_2 can form CO_3^- like ions [2] If proton forms complex with CO_3^- in SiO_2 as shown in Fig.2, hopping from one CO_3^- ion to another CO_3^- ion can cause Vth instability since proton act as positively charged mobile ions. This consideration coincides with recent experimental finding which indicate the existence of mobile ions in SiC-MOSFET [3].

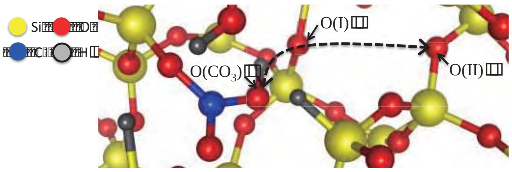

Fig.2:Atomistic structure of proton and CO_3^- ion complex and proton diffusion path.

References

[1] H. Shirakawa, M. Araidai, K. Kamiya, H. Watanabe, and K. Shiraishi, Appl. Phys. Exp. in press.

[2] Y. Ebihara, K. Chokawa, S. Kato, K. Kamiya, and K. Shiraishi, Appl. Phys. Lett., **100**, (2012) 212110.

[3] A. Chanthaphan et al. Appl. Phys. Lett. **102**, (2013) 093510.

Development of Measurement Technique of Local Optical Property and Analysis of Hydrogen Embrittlement Properties of Steel and Aluminum

Yuji KUNISADA

Center for Advanced Research of Energy and Materials, Faculty of Engineering,

Hokkaido University, Sapporo, Hokkaido 060-8628

We studied the new measurement technique of local optical property and analysis of hydrogen embrittlement properties of steel and aluminum, with the aid of the first principles calculation based on the density functional theory (DFT).

At first, we investigated the optical properties of Al_2O_3 using scanning transmission electron microscopy (STEM). The dielectric function can be calculated from through Kramers-Kronig analysis of experimentally obtained electron energy-loss spectra (EELS). We have to take into account the effect of kinetic momentum transport from the incident electron beam to the electron in materials in the optical property analysis with STEM-EELS. Therefore, we calculated the electronic structure of Al_2O_3. We performed the band structure calculations using VASP code. [1] We installed parallelized VASP with Intel® MPI Library and Intel® Math Kernel Library. We found that the calculated band gap of Al_2O_3 with GGA-PBE and hybrid HSE06 functional are 6.0 and 7.4 eV, respectively. We also clarified that the effect of kinetic momentum transport is negligible because the corresponding valence band structures of Al_2O_3 near Fermi level are almost flat.

We also investigated the hydrogen atom behaviors in Fe(111) and Al(111) subsurfaces. [2] We obtained the most stable adsorption sites from the corresponding potential energy surfaces. We found that hydrogen atoms negatively charge and weakly adsorbe in both of Fe(111) and Al(111) subsurfaces through ionic bonding between hydrogen atoms and surface atoms.

References

[1] G. Kresse and J. Hafner: Phys. Rev. B **47** (1993) 558. G. Kresse and J. Hafner: Phys. Rev. B **49** (1994) 14251. G. Kresse and J. Furthmüller: Comput. Mater. Sci. **6** (1996) 15. P. E. Blöchl: Phys. Rev. B **50** (1994) 17953. G. Kresse and J. Furthmüller: Phys. Rev. B **54** (1996) 11169.

[2] Y. Kunisada and N. Sakaguchi: J. Japan Inst. Met. Mater. **79** (2015) 447.

First-Principles Calculation of Transition-Metals and Their Alloys and Compounds

Tamio OGUCHI, Masayuki TOYODA, Kunihiko YAMAUCHI,
Hiroyoshi MOMIDA, Masayuki FUKUICHI, Tetsuo TANAKA, Hiroshi KATSUMOTO
Institute of Scientific and Industrial Research, Osaka University, Ibaraki 567-0047

In this project, we study the electronic properties of several transition metals and their alloys and compounds and explore their chemical trends and effects associated with structure and symmetry. In addition, continuing developments of numerical methods related to the first-principles calculations are also pursued. In FY2015, we theoretically investigated the magnetism of the A-site ordered perovskite-type transition-metal oxides, the mechanical properties of hard materials such as WC, and the x-ray optical activity in noncentrosymmetric materials. Among them, results of first-principles electronic-structure calculations for the A-site ordered perovskites [1] are summarized below.

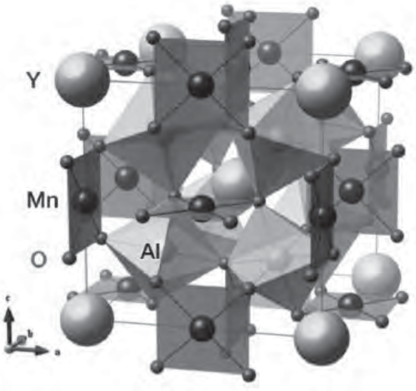

Figure 1: Crystal structure of $YMn_3Al_4O_{12}$.

$YMn_3Al_4O_{12}$ (YMAO) is one of the A-site ordered perovskite oxides (Fig. 1) and its magnetic ordering is a G-type antiferromagnetic (G-AFM) arrangement of Mn^{3+} (spin S=2) determined by a neutron powder diffraction measurement. Magnetic coupling parameters between neighboring Mn ions are estimated by using total-energy calculations for several magnetic configurations. It is found that the G-AFM is stabilized by the nearest-neighboring exchange coupling J_1 mainly originating form a superexchange mechanism, not direct exchange, and exchange interactions between farther neighboring Mn ions J_2 and J_3 are also AFM but relatively small, being in consistent with the neutron experiment. Calculated mean-field Néel temperature 53.5 K is slightly higher than the experimental value (35K) and the overestimation may be partially due to the mean-field approximation. This dominant nature of J_1 over J_2 and J_3 is in striking contrast with the situation of competing J_1 and J_2 leading to the stability of the E-AFM in $LaMnO_3$, showing a difference of Mn^{3+} ions between the A' and B sites. This also sharply contrasts with the other G-AFM A-site ordered perovskite $CaCu_3Ti_4O_{12}$ (CCTO) previously studied [2]. In CCTO, J_1 between Cu ions is ferromagnetic and the stability of G-AFM originates from the third neighbor J_3 via long-range superexchange paths realized by strong Ti-3d and O-2p hybridization. In YMAO, on the other hand, the relevant Al states are far in energy from the O-2p preventing from sizable hopping integrals in the superexchange couplings.

References

[1] M. Toyoda, T. Saito, K. Yamauchi, Y. Shimakawa, and T. Oguchi, Phys. Rev. B **92**, 014420 (2015).

[2] M. Toyoda, K. Yamauchi, and T. Oguchi, Phys. Rev. B **87**, 224430 (2013).

DFT study of excess electrons introduced by Ti interstitials in rutile TiO_2 (110) surface

Kenji Yasuoka
Department of Mechanical Engineering,
Keio University, Kohoku, Yokohama, Kanagawa 223-8522

As a model surface of transition metal oxide, rutile TiO_2 (110) surface have been studied intensively by experiments and theories. Excess electrons are known to be important in considering the surface chemistry of TiO_2. Until recently, surface bridging-oxygen vacancy was considered to be the main source of these excess electrons, however an experimental result suggested that subsurface Ti interstitial is the main source of these excess electrons [1]. Following this result, theoretical works have revealed that Ti interstitial in bulk TiO_2 can introduce excess electrons to the surface [2, 3]. However, the behavior of these excess electrons on the surface is still unclear.

In this work, we have studied the stability of these excess electrons in rutile (110) surface theoretically using static density functional theory (DFT) and Born-Oppenheimer molecular dynamics (BOMD). It was difficult to explicitly calculate all the possible combination of Ti sites that excess electrons localize. So we performed BOMD to find Ti sites where the excess electrons are more likely to exist. We then performed over 40 DFT simulations targeting those sites. All calculations were done using VASP on System B. VASP was chosen here, because it is implemented with plane wave DFT, and it is known to have high parallel efficiency. For exchange-correlation functional, PBE+U was used, which was confirmed by our previous work to sufficiently describe defect state in TiO_2 [4]. The surface was described using slab model with 649 atoms (Fig. 1). Different slab models were compared including larger slab models. Also, stability of slab models with different localization sites of excess electrons

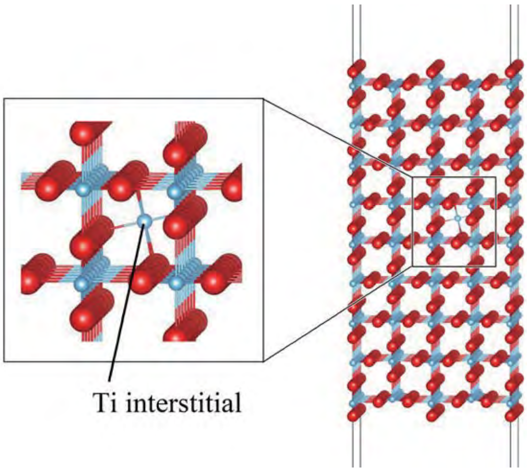

Figure 1: (right) Image of one calculation cell in a slab model, large (small) sphere is oxygen (Titanium) and (left) image enlarged near Ti interstitial

was compared.

As a result, excess electrons introduced by Ti interstitial were more stable near the surface compared to sites near Ti interstitial. This indicates that, Ti interstitials can provide excess electrons to the surface. This result is in agreement with the experimental result by Wendt et al.

References

[1] S. Wendt, P. T. Sprunger, E. Lira, G. K. H. Madsen, Z. Li, J. Ø. Hansen, J. Matthiesen, A. Blekinge-Rassmussen, E. Lægsgaard, B. Hammer, and F. Besenbacher: Science **320** (2008) 1755.

[2] E. Finazzi, C. D. Valentin, and G. Pacchioni: J. Phys. Chem. C. **113** (2009) 3382.

[3] H. Y. Lee, S. J. Clark, and J. Robertson: Phys. Rev. Lett. **86** (2012) 075209.

[4] T. Shibuya, K. Yasuoka, S. Mirbt, and B. Sanyal: J. Phys. Condens. Matt. **24** (2012) 435504.

Theoretical Analyses on Ionic Transport Properties, Electrical Properties and Interfacial Electronic States of Nanostructures

Satoshi WATANABE
Department of Materials Engineering, the University of Tokyo
7-3-1 Hongo, Bunkyo-ku, Tokyo, 113-8656

1 Introduction

Although the properties of nanostructures have been extensively investigated in the last few decades, our understanding on them is still insufficient to design and control novel nanoscale information and energy devices. In particular, further studies on complicated situations and phenomena, such as the effects of interface between novel two-dimensional materials and substrates and ionic transport at nanoscale in metal-oxide heterostructures, are strongly desired.

Keeping the above in minds, we have been investigating these topics using theoretical analyses based on atomic/electronic level simulations, taking various nanostructures as target systems. In the followings, some of our results in the fiscal year 2015 are described.

2 Interfacial electronic properties of graphene on Si-terminated SiC

The epitaxial growth of graphene on a SiC substrate has attracted much attention because of its potential for wafer-size high mobility graphene on a high-quality insulating substrate. However, the interface electronic structure of graphene on SiC is complicated due to the strong bonding between them.

We have examined the atom-specific interfacial electronic properties of the epitaxial graphene on Si-terminated SiC substrate using density functional theory (DFT) calculation with van der Waals interaction correction [1]. In doing so, we focused on the dependence of the local electronic state on the chemical environment. The band structure projected on the respective atomic orbitals reveals that the dangling bonds of the carbon atoms in the buffer layer and uppermost Si atoms form electronic states around the Fermi level. The contribution of each atom to the dangling bond states strongly depends on the presence/absence of the interlayer Si–C covalent bond. This affects the atom-specific local density of states of the top-layer graphene through its interaction with the substrate/buffer layer, which implies that the bias voltage dependence of the scanning tunneling spectroscopy mapping image reflects the presence of the dangling bonds of the buffer layer carbon or uppermost Si atom in the substrate.

3 Electronic structure of quasi-freestanding germanene on monolayer group III monochalcogenides

Germanene has high potential as a novel electronic device material owing to high intrinsic carrier mobility, large spin-orbital interaction and small electron-phonon coupling compared with graphene and silicene. However, germanene synthesized on a substrate often loses the Dirac-cone, which involves the loss of the above fascinating properties.

We have examined the stability and electronic structures of germanene on monolayer GaS, GaSe, GaTe and InSe using the DFT [2]. We have found that the germanene keeps its buckled-honeycomb structure on all the above substrates similar to the free-standing case. In addition, germanene preserves its Dirac-cone-like band structure on monolayer GaTe and InSe. In these two cases, a small bandgap of 0.14-0.16 eV opens at the Dirac point, and the effective masses are as small as 0.05-0.06 times the free-electron mass. The estimated carrier mobility is up to 2.2×10^5 cm^2 V^{-1} s^{-1}. These results suggest that the monolayer GaTe and InSe would be promising substrates for germanene devices.

4 Cu Diffusion in Amorphous Ta_2O_5

In some of novel information and energy devices such as the atomic switch, atom diffusion plays crucial role. Atomistic simulations using reliable method such as the DFT are powerful for understanding the atom diffusion behavior at nanoscale, but performing such simulations for amorphous materials is computationally very heavy.

Considering the above, we have constructed a simplified neural network (NN) interatomic potential to predict the diffusion behavior of Cu atom in amorphous Ta_2O_5 efficiently [3]. First, the amorphous Ta_2O_5 was generated by melt quenching method with ab-initio molecular dynamics. Then one Cu atom was inserted into the amorphous Ta_2O_5 randomly, and the structure was optimized. The NN potential was constructed using the method proposed by Behler and Parrinello [4].

After training using 540 samples, the mean absolute error of energy prediction is less than 0.1 eV. Using the NN potential combined with the nudged elastic band (NEB) method, the pathways and activation energy barriers for the Cu hopping were estimated. The results agree well with those obtained from the DFT+NEB method.

References

[1] M. Kajihara, T. Suzuki, S. M. F. Shahed, T. Komeda, E. Minamitani and S. Watanabe: Surf. Sci. **647** (2016) 39.

[2] Z. Ni, E. Minamitani, Y. Ando and S. Watanabe: Phys. Chem. Chem. Phys. **17** (2015) 19039.

[3] W. Li, Y. Ando and S. Watanabe: in preparation.

[4] J. Behler and M. Parrinello: Phys. Rev. Lett. **98** (2007) 146401.

First-Principles Study of Excited Electronic States and Dynamics of Nanostructures under External Fields

Kazuyuki WATANABE, Yasumitsu SUZUKI, Elena SILAEVA, Satoshi HAGIWARA,
Yoshihiro UEDA, Kazuki UCHIDA
Department of Physics, Tokyo University of Science
1-3 Kagurazaka, Shinjuku-ku, Tokyo 162-8601

In the project we investigated the following four topics this year. 1) Laser-assisted field evaporation of Si clusters by time-dependent density functional theory combined with molecular dynamics (TDDFT+MD), 2) dc-field enhanced photoexfoliation of bilayer benznene by TDDFT+MD, 3) development of first-principle non-adiabatic molecular dynamics simulation method based on the exact factorization of molecular wavefunction, and 4) spin-polarized annihilation lifetime of a positron in defective GaN by two-component DFT (TC-DFT).

1) *Laser-assisted field evaporation of Si clusters by TDDFT+MD*[**?**]: We studied laser-assisted field evaporation using the TDDFT+MD approach and including the laser as a time-dependent optical field. We have shown a drastic decrease of the HOMO-LOMO gap of a hydrogen molecule and a silicon cluster under high dc field, which is believed to be a common trend for different atomic systems and solids. The obtained photoabsorption spectra of the present systems also demonstrated strong changes with increasing the dc field. In particular, a pronounced redshift in the low-energy region was observed at high dc fields. The TDDFT+MD approach enabled monitoring the evaporation dynamics. The position and charge state of an atom evaporated from a hydrogen molecule and a silicon cluster as a function of time has been obtained under dc field without laser illumination and together with a laser field. The dc field and laser intensity conditions needed to generate the field evaporation have been analyzed and an agreement with experiments has been found. Evaporation was observed at lower dc fields when high-intensity laser is applied. The demonstrated field-induced changes in electronic and optical properties were shown to affect significantly laser-assisted field evaporation dynamics and are believed to play an important role also in other laser-assisted field emission techniques and nano-optoelectronics. The large scale TDDFT-MD calculations have been performed using System B.

2) *DC-field enhanced photoexfoliation of bilayer benznene by TDDFT+MD*[**?**]: We studied the exfoliation of bilayer benzene induced by intense laser pulse and external dc field by TDDFT+MD simulation. We showed that the dc field can accelerate the athermal photoexfoliation by dc-field induced force on one of benzene molecules in addition to the repulsive force between the benzene molecules caused by photoemission. Dc-field and photoemission lead to the increase in positive charge of benzene molecules that determines the dynamics of athermal exfoliation. The charge state of benzene is shown to be more important than absorbed laser energy during exfoliation process under given conditions of laser pulse and dc field parameters. Our theoretical study

thus demonstrated that a field-enhanced photoexfoliation can be an efficient technique for producing intact graphene sheets because dc field helps to avoid the laser-induced thermal melting and ablation of graphite. The present study also provides important insights on the field evaporation of graphite that can be an interesting and challenging problem for atom probe tomography experiments because evaporation not of individual atoms but entire monolayers of graphene is expected. The large scale TDDFT-MD calculations have been performed using System B.

3) *Development of first-principle non-adiabatic molecular dynamics simulation method based on the exact factorization of molecular wavefunction*: The exact factorization of the electron-nuclear wave function allows to define the time-dependent potential energy surfaces (TDPESs) responsible for the nuclear dynamics and electron dynamics. We are aiming to develop a novel first-principle non-adiabatic molecular dynamics simulation method based on this TDPES. To this end, we made a new algorithm that combines two methods; one is a coupled-trajectory mixed quantum-classical (CT-MQC) method, which is derived from the exact factorization and has been shown to reproduces quantum nuclear dynamics of small model systems very well, and the other is the linear response (LR) TDDFT, which is known as a very effective method to calculate the excitation energy, the nonadiabatic coupling (NAC) vectors, and the gradient of the excited state potential energy surfaces. We succeeded to formulate the algorithm, and then tested the efficiency and accuracy of LR-TDDFT calculation by our in-house code on System B. We also developed an algorithm that uses the wave-function theory instead of LR-TDDFT to calculate the excited-state properties, and made a code of it by implementing CT-MQC algorithm into SHARC code, which is a free program package of surface-hopping dynamics.

4) *Spin-polarized annihilation lifetime of a positron in defective GaN by TC-DFT*[**?**]: We determined the spin-polarized annihilation lifetime of a positron (SPALP) trapped by the Ga vacancies in GaN by TC-DFT with geometry optimization. SPALP clearly depends on the charged states of the Ga vacancies and the induced magnetization. The dependence is attributed to the overlap between the positron and electron densities at the defect. Thus, the present study proves the useful role of SPALP for probing and determining the mechanism of d^o ferromagnetism. The calculations have been performed using System B.

References

[1] E. P. Silaeva, K. Uchida, Y. Suzuki, K. Watanabe, Phys. Rev. B**92**, 155401 (2015).

[2] K. Uchida, E. P. Silaeva, and K. Watanabe, to appear in Appl. Phys. Express.

[3] S. Hagiwara, Y. Suzuki, and K. Watanabe, Appl. Phys. Express **9**, 041001 (2015).

Structural and magnetic anisotropy analyses in Fe/Cu ultra-thin films by first-principles calculation

Yasutomi TATETSU

The University of Tokyo, Hongo, Bunkyo, Tokyo 113-0033

Magnetic thin films have been studied due to its peculiar magnetic behaviors compared to their bulk systems. These behaviors can come from structural transitions depending on the temperature and growth conditions. Fe/Cu(001) magnetic thin films have been studied for the past decades, because of their uncertain magnetic structures [1, 2]. As is well know, the ground state of Fe has the bcc structure, but the fcc-Fe, which is stable above 1184 K in general, can epitaxially grow on a Cu(001) substrate even below room temperature, since the lattice parameters of Cu (3.615Å) and fcc Fe (3.58Å) are quite close to each other. Many kinds of studies for the systems have been reported, but its ground state is controversial.

We applied first-principles calculations to the fcc-Fe/Cu(001) system using a computational code OpenMX [3] for understanding its electronic and magnetic structures. Mainly, the system B super computer was used for all calculation. Our structure model is a slab model consisting of seven Cu layers and several Fe layers capped by a 10-Å vacuum layer. According to our collinear spin calculations, an antiferromagnetic structure is stable in the 4 to 7-ML systems and a ferromagnetic coupling at the top two layers can be obtained, which is in good agreement with experimental results (see Fig. 1). We also calculated the non-collinear spin configuration, which considers the spin-orbit interaction. This calculation indicates that the spin-orbit coupling in Fe sites can be ignored due to the weakness of the orbital moments of Fe.

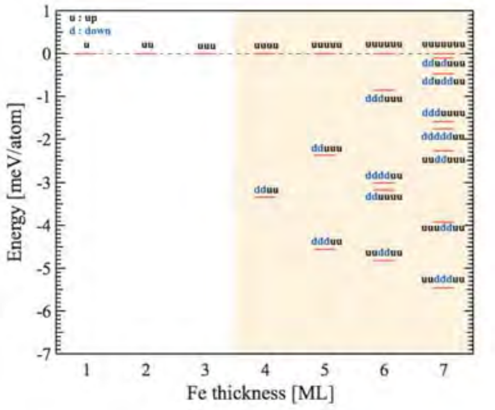

Figure 1: Energy differences of the collinear spin structures in each Fe/Cu system. Orange region indicates the antiferromagnetic states.

References

[1] H. Abe *et al.*: Phys. Rev. B **77** (2008) 054409.

[2] D. Pescia *et al.*: Phys. Rev. Lett. **58** (1987) 2126.

[3] http://www.openmx-square.org

[4] Z. Torbatian *et al.*: Appl. Phys. Lett. **104**, (2014) 242403.

Numerical studies on anharmonic phonon properties based on density functional theory

Terumasa TADANO
Department of Applied Physics, The University of Tokyo
Hongo, Bunkyo-ku, Tokyo 113-8656

Lattice anharmonicity has gained much attention in recent years because of its significant importance for characterizing various material properties. For example, SnSe is attracting strong interest because of its severe anharmonicity and ultralow thermal conductivity, which makes the thermoelectric figure-of-merit as high as ~2.7 [1]. Strong anharmonic effect is also suggested for a superconducting sulfur hydride H_3S [2], which is associated with the large zero-point motion of hydrogen atoms. Since anharmonic effects in these materials are quite large, they cannot be treated by perturbative methods.

To model anharmonic effects of phonons nonperturbatively, we have been developing an efficient numerical approach based on density functional theory (DFT). In our method, we first extract harmonic and anharmonic force constants (FCs) from displacement-force data sets sampled with accurate DFT calculations. Using the calculated FCs, we then solve the self-consistent phonon (SCPH) equation to obtain anharmonic phonon frequencies [3].

The validity of our approach has been demonstrated for the high-temperature phase of $SrTiO_3$ [3, 4] and sulfur hydrides H_3S and H_2S under pressure [5]. We also examined anharmonic phonon properties of the high-temperature *Cmcm* phase of SnSe. Here, the DFT calculations were conducted using the Quantum-ESPRESSO package [6], and FCs were estimated using *least absolute shrinkage and selection operator* (LASSO) implemented in the ALAMODE package [7]. Figure 1 shows the anharmonic phonon dispersion of SnSe calculated using the SCPH method. As can be seen in the figure, the phonon dispersion is strongly temperature-dependent, especially for the soft mode at Y point associated with the structural phase transition. We also calculated the lattice thermal conductivity of SnSe and obtained good agreements with experimental values at high temperatures.

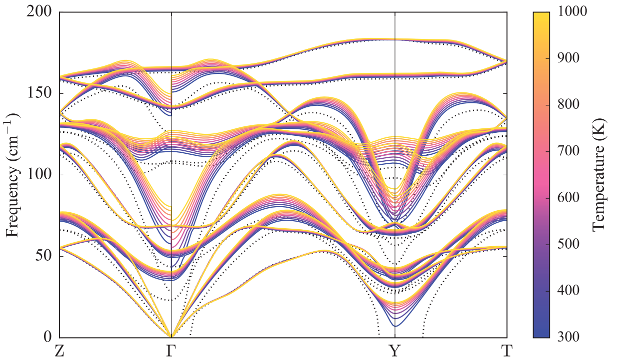

Figure 1: Calculated anharmonic phonon dispersion of SnSe (*Cmcm* structure)

References

[1] L.-D. Zhao *et al.*: Nature **508** (2014) 373.

[2] I. Errea *et al.*: Phys. Rev. Lett. **114** (2015) 157004.

[3] T. Tadano and S. Tsuneyuki: Phys. Rev. B **92** (2015) 054301.

[4] T. Tadano and S. Tsuneyuki: AIP Conf. Proc. **1702** (2015) 090063.

[5] W. Sano, T. Koretsune, T. Tadano, R. Akashi, and R. Arita: Phys. Rev. B **93** (2016) 094525.

[6] http://www.quantum-espresso.org

[7] https://github.com/ttadano/alamode

Ab initio GW calculation for low-dimensional metal $K_{0.3}MoO_3$

Kazuma NAKAMURA
Quantum Physics Section, Kyushu Institute of Technology
1-1 Sensui-cho, Tobata, Kitakyushu, Fukuoka, 804-8550

Using an *ab initio* GW calculation, we study quantitative accuracy of plasmon fluctuation in various materials. The quantum fluctuation is important in a metallic system, especially having isolated low-energy bands near the Fermi level. In the isolated-band materials, the plasma excitation can occur in this band, and then its energy scale is usually smaller than the bandwidth. In this case, the plasmon fluctuation can relevantly renormalize the bare band structure via the self-energy effect.

In this report, we present a study for the low-energy electronic structure of transition-metal oxide $K_{0.3}MoO_3$ which is a typical isolated low-energy band system. This is a typical low-dimensional metal and exhibits transition to the charge density wave state at the low temperature. In the metallic region, this material exhibits a large renormalization in the photoemission spectrum. From this observation and the quasi-one-dimensional nature, the origin of the renormalization has been discussed in view of the Tomonaga-Luttinger liquid. On the other hand, this material exhibits clear low-energy plasma edges around 0.1-1 eV in the reflectance spectra.

We study the low-energy electronic structure of $K_{0.3}MoO_3$ using our developed GW calculation code [1, 2]. We calculate density-functional band structure, maximally localized Wannier functions, reflectance spectra, and spectral functions. The crystal structure is centered monoclinic (a=9.880$\mathring{A}$, b=9.880$\mathring{A}$, c=9.894$\mathring{A}$, α=115.34°, β=115.34°, γ=45.01°) and contains 43 atoms in the unit cell. The developed code is massively parallelized, capable to treat large systems such as the present case. All calculations were done at Supercomputer center at Institute for Solid State Physics, University of Tokyo.

Figure 1(a) is our calculated density-functional band structure of $K_{0.3}MoO_3$. The isolated low-energy bands are drawn by blue dotted curves and its bandwidth is ∼1.5 eV. The panel (b) shows the maximally localized Wannier function for these isolated bands.

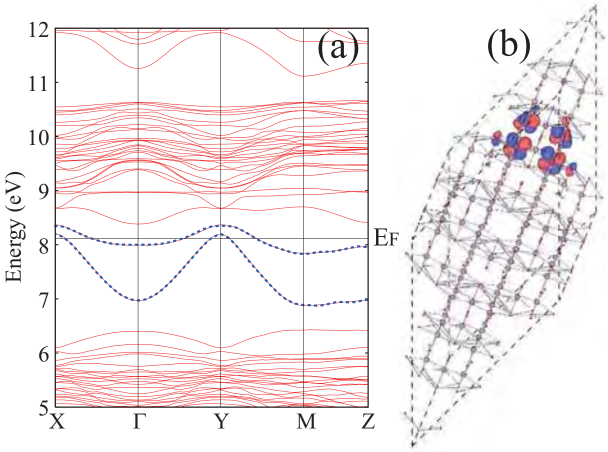

Figure 1: (a) Calculated band structure of $K_{0.3}MoO_3$, where the isolated low-energy bands are drawn by the blue dotted lines. (b) Calculated maximally localized Wannier function for the isolated bands.

Figure 2(a) compares the calculated reflectance spectra (solid curves) with the experimental data (open circles). The light-red and dark-blue colors specify the results in the light polarization of $E\|a$ and $E\|b'$, respectively, and the a axis is the one-dimensional conducting axis. The plasma edge is found to be $\sim$1 eV.

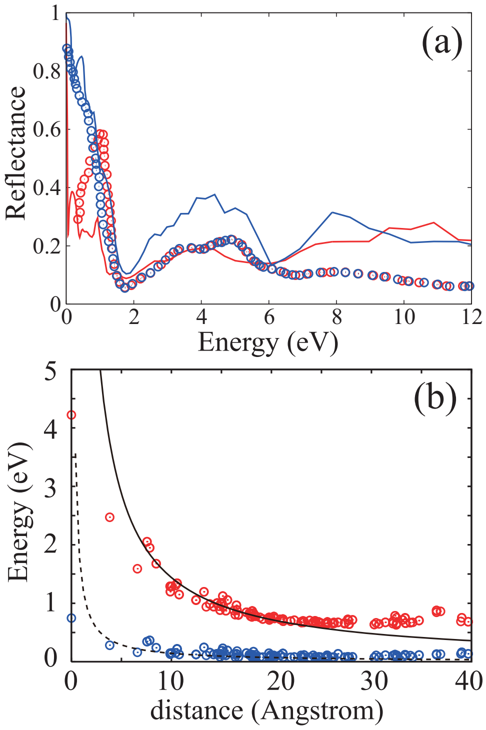

Figure 2: (a) Comparison between calculated reflectance spectra (solid curves) and experimental data (circles) of $K_{0.3}MoO_3$. (b) The calculated screened interaction with the constrained random phase approximation (dark-blue circles) compared with the bare interactions (light-red circles).

We show in Fig. 2(b) screened Coulomb interactions of $K_{0.3}MoO_3$, calculated with the constrained random phase approximation. The dark-blue and light-red circles describe effective and bare interactions, respectively. The effective onsite interaction $U - V$ is estimated as 0.59 eV which is smaller than the bandwidth and plasma excitation.

Figure 3(a) compare the calculated GW spectral function with the density-functional bands (blue solid curve). The GW spectra are basically similar to the density-functional one. We next in Fig. 3(b) the comparison among the GW (thick-red curve), density-functional theory (thin-black curve), and experiments (circles). The GW result is appreciably renormalized from the non-interacting one, thus resulting in a reasonable agreement with the experimental result.

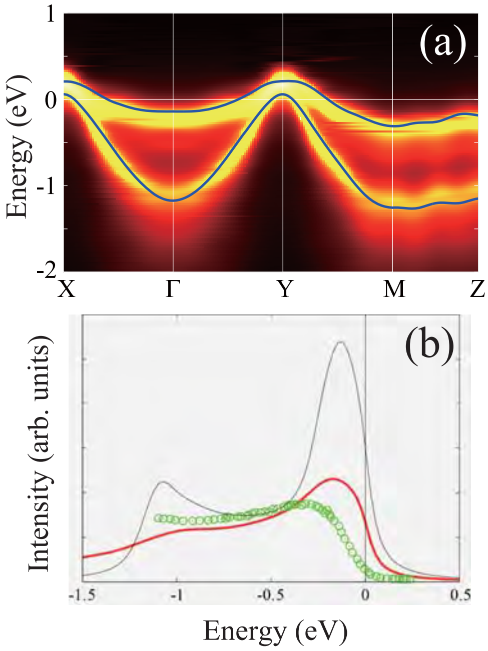

Figure 3: (a) Calculated GW spectral function of $K_{0.3}MoO_3$, where the isolated low-energy bands are superposed with blue solid curves. (b) Comparison of photoemission spectra among the GW, density-functional, and experimental ones.

In summary, we have studied low-energy plasmon fluctuation of low-dimensional metal $K_{0.3}MoO_3$. To investigate this effect on the electronic structure, we have calculated the GW spectral function, and compared it with the experimental data.

References

[1] K. Nakamura, S. Sakai, R. Arita, K. Kuroki, Phys. Rev. B 88, 125128 (2013)

[2] K. Nakamura, Y. Nohara, Y. Yoshimoto, Y. Nomura, Phys. Rev. B 93, 085124 (2016).

Parallelized ultra-large-scale electronic-structure theory based on first principle calculation and novel numerical method

Takeo Hoshi and Hiroto Imachi

Department of Applied Mathematics and Physics, Tottori University,

4-101 Koyama-Minami, Tottori 680-8550, Japan;

Large-scale electronic structure calculations were carried out by our original simulation code ELSES (http://www.elses.jp/) mainly for the structural and transport calculations of condensed organic polymers. Large-scale calculations are realized by novel massively parallel order-*N* algorithms. The transport calculations were carried out as a theoretical extension with the quantum wavepacket (QWP) dynamics simulation in which a dynamical equation ($i\,\partial_t\,\Psi = H_{\mathrm{eff}}\Psi$) is solved for a hole wavepacket based on *ab initio* based tight-binding formulations.

Figure 1 shows the preliminary result of the QWP dynamics [1][2]. The results of the organic polymer in Fig. 1(a) on calculated mobility are consistent to the experimental trend [3] in which the mobility of meta(zig-zag) type polymers is larger than that of para (linear) type polymers. Here single polymer simulations were carried out among different conditions and polymer lengths. The maximum length of polymer is 700nm or 1,000 monomer units. Figures 1(b), (c) (d) shows (b) pentacene thin film and (c)(d) a condensed organic polymer as a test calculation of condensed organic molecules. One can observe that the wavepacket progapagetes between molecules, as expected.

Related methodologies are also developed for *ab initio* transport calculation with non-equillibrium Green function theory [4] and optimal hybrid generalized eigenvalue solver for massively parallel computations [5][6].

References

[1] H. Imachi, S. Yokoyama, T. Kaji, Y. Abe, T. Tada, T. Hoshi, ‘One-hundred-nm-scale electronic structure and transport calculations of organic polymers on the K computer’, submitted, Preprint http://arxiv.org/abs/1603.09616

[2] (invited talk) T. Hoshi, ‘Massively parallel electronic structure calculations and transport property of organic materials’, Computational Chemistry Symposium of 12th International Conference of Computational Methods in Sciences and Engineering (ICCMSE 2016), 17-20, Mar., 2016, Athens, Greece.

[3] J. Terao, A. Wadahama, A. Matono, T. Tada, S. Watanabe, S. Seki, T. Fujihara and Y. Tsuji, ‘Design principle for increasing charge mobility of π -conjugated polymers using regularly localized molecular orbitals', Nat.

Commun. **4**, 1691 (2013).

[4] S. Iwase, T. Hoshi, T. Ono, 'Efficient numerical solver for first-principles transport calculation based on real-space finite-difference method', Phys. Rev. E 91, 063305, 9pp. (2015).

[5] H. Imachi and T. Hoshi, 'Hybrid numerical solvers for massively parallel eigenvalue computation and their benchmark with electronic structure calculations', J. Inf. Process. 24, pp. 164 -- 172 (2016).

[6] Eigenkernel:
https://github.com/eigenkernel/eigenkernel

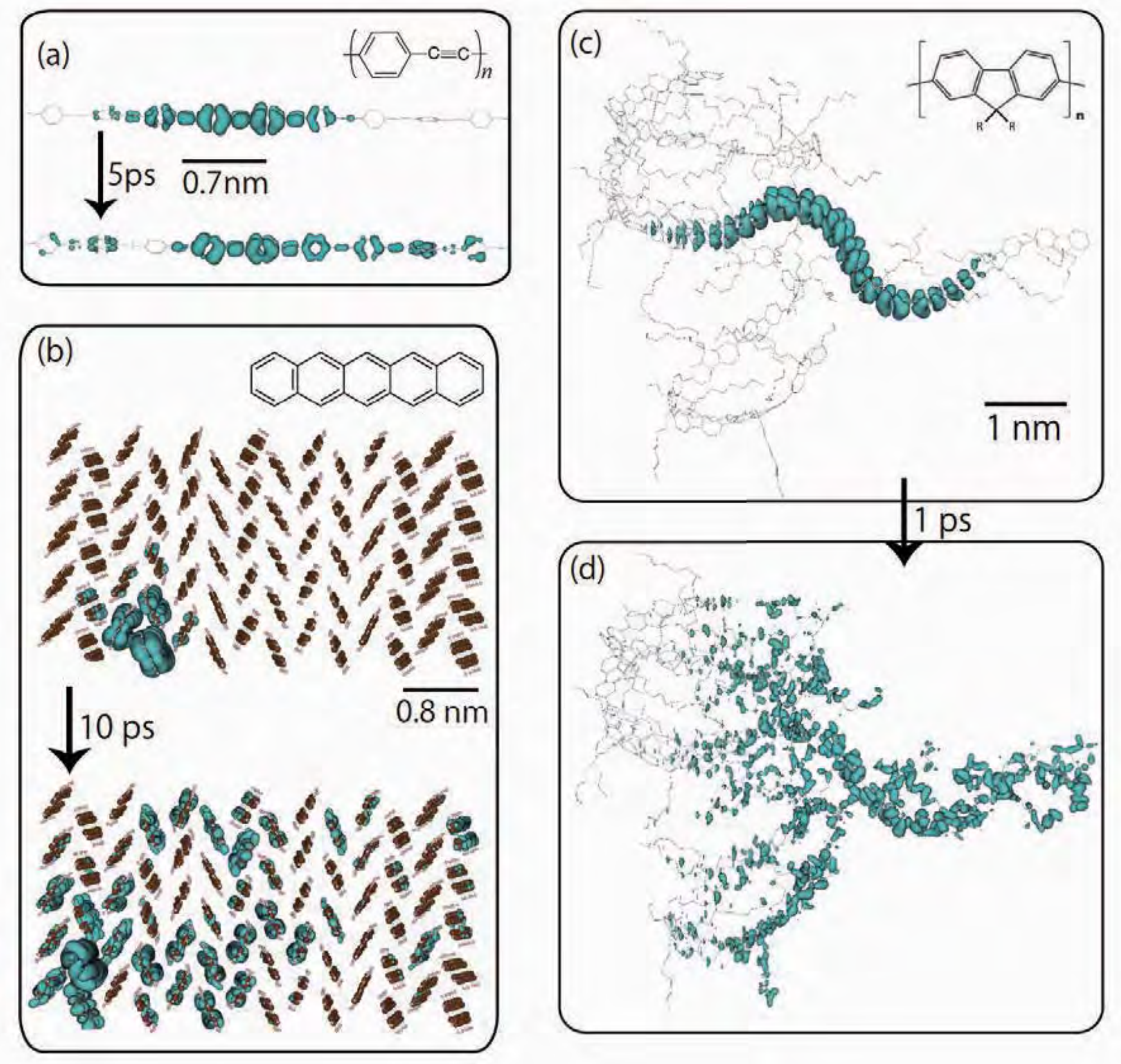

Fig. 1 Example of transport calculation of organic materials by the quantum wavepacket (QWP) dynamics[1][2]; (a) QWP dyanamics on a polymer of poly-(phenylene–ethynylene). The figre is a close-up. (b) QWP dyanamics on pentacene thin film with single layer. (c) QWP dyanamics on a condensed polymer of poly-((9,9)-dioctyl fluorene)(PFO). The three polymers in a periodic cell form an amourphous-like strcutures.

Ab-initio molecular dynamics study on organic molecules

Kazume NISHIDATE and Masayuki HASEGAWA
Faculty of Engineering, Iwate University
Ueda 4-3-5, Morioka, Iwate 020-8551

Graphene (GR) has attracted considerable attention due to its outstanding electronic, optical, thermal and mechanical properties. Recently, a particular attention has been paid to its transparency for a wide range of light frequencies since it can be used as a transparent electrode instead of the expensive tin-doped indium oxide (ITO) in the device applications. Organic semiconductors have also attracted considerable interest because of their favorable electrical properties in the development of flexible electronic devices such as the light emitting diode (LED) and the solar cells. Pentacene ($C_{22}H_{14}$, PEN) and perfluorinated pentacene ($C_{22}F_{14}$, PFP) molecules, in particular, are considered to be promising organic semiconductors due to their novel electronic properties. It has been suggested that the charge redistribution at the interfaces between the organic molecules and the substrate causes the changes in the electron energy levels and the carrier injection barrier. However, theoretical studies on the energetics of the organic molecules on GR have been a challenging subject due to the computational difficulties arising from a demand to use a large system. In this work, we investigate the energetics of the PEN and PFP molecules on GR using molecular dynamics simulation (MD) based on the density functional theory (DFT). We used the same methodology used in the DFT computation of collapsed armchair nanotube: the vdW interactions were supplemented either by the semi-empirical method (DFT-D2 and D3) or by the vdW DFT (optB86-DFT)[1].

Initially, three PEN or PFP molecules were placed on the GR in flat-laying orientation. Time step is 1 fs. We first evaluated the microcanonical ensemble of the MD system and confirmed its energy convergence. And then the temperature was controlled at 500 K by way of the Nose method. In the Figure 1, we show the snapshot of the PFP on the GR at the 3000 time step. The coverage of the molecules on GR corresponded to roughly 1.5 ML. In all cases, a PEN or PFP molecule started to stand up with respect to the other molecule. We believe that the T-type stacking formation will lead to the herringbone structure which is typical to the molecular crystals.

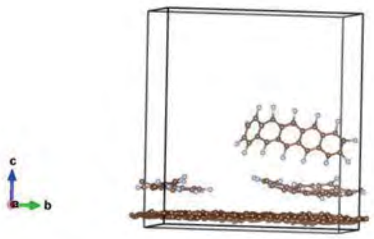

Figure 1: PFP molecules on GR.

References

[1] M. Hasegawa, K. Nishidate, and Y. Yoshimoto: Phys. Rev. B, **92** pp. 245429-1-13, 2015

Exploration of structure motifs characterizing "function" of metal oxides

Kazuto AKAGI

Advanced Institute for Materials Research,

Tohoku University, Katahira, Aoba-ku, Sendai, Miyagi 980-8577

We have explored the key motifs in metal oxides characterizing their "function" in this project. The brief summaries are as follows:

Li_2O_2 in a Li-Air battery

Li-Air battery is expected as one of the next generation batteries. In order to make it rechargeable, discharge product Li_2O_2 should be decomposed into Li^+ and O_2 during the charging process. It is known that TTF (Tetra thiafulvalene) promotes such decomposition of Li_2O_2 with the combination of DMSO solvent and nano-porous gold electrode, but its critical role was still unrevealed.

First, we performed a series of classical molecular dynamics (MD) simulations to see the formation and decomposition process of LiO_2 cluster in DMSO solvent. The parameters of force field were optimized using the information on total energies and atomic forces derived from a set of one-point first-principles calculations with rev-vdW-DF2 functional [1]. The obtained results showed a LiO_2 cluster is spontaneously decomposed under charging condition, *i.e.* at low $[O_2^-]$ condition [2].

Thus, we focused on the decomposition of Li_2O_2 into LiO_2. Since an excess electron given to a Li_2O_2 cluster was localized, it is considered this oxidation proceeds locally. We also checked O_2^- and TTF can be oxidized to O_2 and TTF^+ on a Au(111) surface, respectively, and prepared model systems containing a cluster of Li_2O_2 or $Li_3O_2^+$ (more stable form of Li_2O_2: Li_2O_2+Li^+) with O_2 or TTF^+ in DMSO solvent. The amount of charge transfer and free-energy profile were evaluated by the first-principles MD calculations performed at 400K using a 1.7 nm cubic cell with 20-23 DMSO molecules. Thermodynamic average was done over 100 ps time evolution.

The obtained results showed the special role of TTF as a redox mediator. While O_2 oxidized only the Li_2O_2 cluster, TTF^+ was able to oxidize both the Li_2O_2 or $Li_3O_2^+$ clusters. Since "$Li_3O_2^+$" is not only stable in DMSO but also exists as a key motif in a larger Li_2O_2, we cannot avoid the release of $Li_3O_2^+$ clusters with the decomposition of Li_2O_2. TTF^+ was suppressing their accumulation and formation of byproducts, which lead to improvement of the cycle lifetime as a rechargeable battery.

Electron trapping sites in a-HfO_2

Degradation phenomena in metal-insulator-semiconductor devices are often associated with unwanted charging of the insulating layers. This stimulated efforts to understand the nature of the charge traps in polycrystalline and amorphous oxide films of HfO_2 and Al_2O_3 grown on semiconducting and metal substrates. In order to identify the character of electron trapping sites, amorphous hafnium oxide (a-HfO_2) models were generated by classical MD simulation and structure optimization by first-principles calculation using hybrid functional HSE06 were performed with extra electrons. We choose 35 structures with density in the range of 9.2-9.9 g/cm^3 in order to investigate a possible trend of property changes as a function of density.

An extra electron can be spontaneously trapped on pre-existing structural precursors like longer Hf-O bonds or under-coordinated Hf atoms. About 90% of the electron spin density was localized predominantly on two or three Hf ions sharing a three coordinated oxygen atom. Electrons were trapped in deep states in the gap at ~2.0 eV ranging from 1.0 to 2.7 eV below the bottom of the conduction band in good agreement with experimental data. These results show that the behavior of electrons in crystalline and amorphous HfO_2 is radically different as no polaron trapping has been observed in crystalline HfO_2 so far. In the next step, extraction of structural characteristics of such trapping sites is planned.

Topological data analysis

Another important aspect of this project is application of the topological data analysis based on “persistent homology”, which helps us find hidden orders in a complex system [3]. The output is obtained as a two-dimensional “persistent diagram (PD)” in which birth and death of rings or cavities are plotted. Identification of local structures around the doped Co in rutile TiO_2 and precursor structures of electron trapping site in a-HfO_2 was tried as case studies, and some potential structural motifs were obtained by classification of the PDs. Finding correlation between such motifs and “function” is now in progress.

References

[1] I. Hamada: Phys. Rev. B **89** (2014) 121103.

[2] S. Jung, F. F. Canova and K. Akagi: J. Phys. Chem. A **120** (2016) 364.

[3] T. Nakamura, Y. Hiraoka, A. Hirata, E. G. Escolar and Y. Nishiura: Nanotechnology **26** (2015) 304001.

First-Principles Study of Coercivity in Hard Magnetic Materials

Daisuke HIRAI
The University of Tokyo
7-3-1 Hongo, Bunkyo, Tokyo 113-0033

Hard magnetic materials are widely used in applications such as permanent magnets, high-density magnetic recording media, and high-frequency electromagnetic wave absorbers. Until now, the high coercivity has been realized by using rare metals with large spin-orbit interactions. Recently, however, their shortage and price increase require us to design hard magnetic materials with no use of rare metals.

Keeping the above in minds, we investigated the magnetocrystalline anisotropy (MCA) of the rare-metal-free magnetic materials from first principles. In the following, some of our results in the fiscal year 2015 are described.

Understanding the MCA at each atom is crucial to identify weak parts for possible nucleation cores of magnetization reversal, which leads to the designing of hard magnetic materials. In general, however, the MCA is given for an entire phase of a material. To examine the local MCA, we developed the method to locally analyze the MCA on the basis of the second-order perturbation theory on spin-orbit interaction [1, 2].

Using this method, we calculated the MCA of ε-$\mathrm{Fe_2O_3}$ in terms of the effect of a single oxygen vacancy as an example [2]. As a result, we obtained an increase in the magnetocrystalline anisotropy energy (MAE) due to a single oxygen vacancy. Our local MAE analysis also showed that two Fe sites near the oxygen vacancy dominantly contribute to the change. In addtition, by decomposing the MAE contributions from respective orbital components for Fe atom nearest to the vacancy, we clarified that the spin-orbit coupling between occupied $3d^{\downarrow}_{x^2-y^2}$ orbital and unoccupied $3d^{\downarrow}_{xy}$ one gives the largest contribution to the MAE enhancement. This enhancement can be understood as follows. First, among the matrix elements related to the selection rule in the perturbation, $\langle d^{\downarrow}_{x^2-y^2}|V_{\mathrm{SO}}|d^{\downarrow}_{xy}\rangle = i\xi$, is largest, where ξ is the spin-orbit coupling constant. Second, a sharp peak as the dangling-bond state in occupied $3d^{\downarrow}_{x^2-y^2}$ states appears due to the vacancy, the appearance of which near the Fermi level is also significant to the MAE enhancement. Indeed, our Mulliken charge analysis confirmed the large increases in the number of states for $3d^{\mathrm{occ.}}_{x^2-y^2,\downarrow}$ and $3d^{\mathrm{unocc.}}_{xy,\downarrow}$ from 0.20 and 0.79 to 0.62 and 0.89, respectively. We also examined the effect of an interstitial hydrogen on the MAE, and showed that the contribution of Fe site nearest to the oxygen bonding with the hydrogen is dominant for the MAE enhancement. Moreover, our analysis has been applied to the relatively large-scale complicated system such as a $\mathrm{Nd_2Fe_{14}B/Nd_4O}$ interface model and we clarified the importance of the MCA of Fe atoms as well as that of Nd atoms [3].

References

[1] Z. Torbatian, T. Ozaki, S. Tsuneyuki, and Y. Gohda, Appl. Phys. Lett. **104**, 242403 (2014).

[2] D. Hirai, S. Tsuneyuki, and Y. Gohda, in preparation.

[3] Y. Tatetsu, private communication.

Theoretical analysis of electrochemical interfaces by first-principles calculation and statistical approach

Yasunobu ANDO
Department of Materials Engineering,
The University of Tokyo, 7-3-1 Hongo, Bunkyo-ku, Tokyo, 113-8656

A new, large family of atomic-layered materials found in 2011; called MXenes ($M_{n+1}X_n$) synthesized from MAX phases ($M_{n+1}A_nX_n$) have attracted increasing attention as promising candidates for new types of electrode materials in secondary batteries.

First of all, we studied basic properties of functinalized Ti_2C that is the simplest MXene compound by using first-principles simulations [1]. Our results reveals that oxygen terminated Ti_2C: Ti_2CO_2 is insulating with an indirect band gap of 0.44 eV. Upon atomic adsorption of H, Li, or Na, Ti_2CO_2 becomes metallic. This metal–insulator change may be used to produce switching devices with a high on/off ratio and low energy consumption by controlling ionic movement, as in ion batteries.

We also investigated the feature of the electric double-layer potential at the electrochemical interface models of functinalized Ti_2C shown in Fig. 1. We found that the depedence of the potential drop on the surface functionalizations.

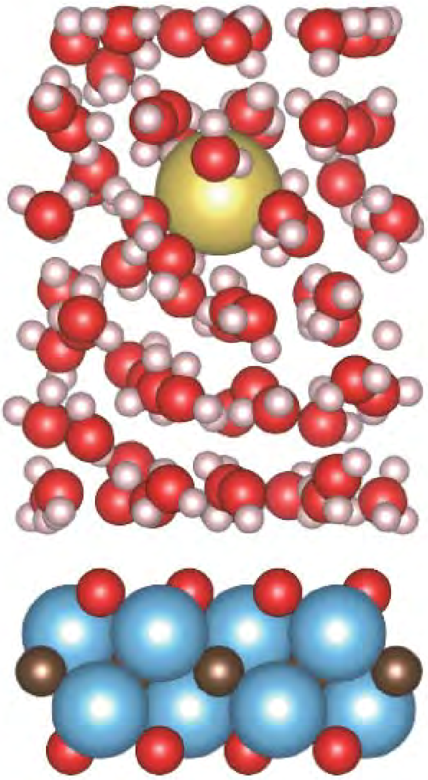
Fig. 1 Structure model of Ti2CO2-sodium solution interfaces

References

[1] 1. Y. Ando, and S. Watanabe, Appl. Phys. Express **9**, 015001 (2016).

Defect generation at metal/semiconductor interfaces: stability and ionization diffusion

Takashi NAKAYAMA
Department of Physics, Chiba University
1-33 Yayoi, Inage, Chiba 263-8522

Germanium (Ge) is expected as a promising material for post-Si high-speed devices because of its high carrier mobility. It was found very recently that metal/Ge interfaces have many defects; defect density around interface is 2-3 order larger than in bulk Ge, which promotes serious degradation of semiconducting properties. However, it has not been clarified why so many defects exist at metal/Ge interfaces. One purpose of the present project is to answer this question by the first-principles calculations. On the other hand, metal/semiconductor interface is not stable for a long time and changes its structure by metal-atom diffusion. The most serious case occurs at metal/SiO_2 interface; the application of voltage promotes meta-atom diffusion and induces large leakage currents. The other purpose is to clarify the effects of applied voltage on interface structure changes. In this report, we show some of the results.

We first consider the defect generation around metal/Ge interfaces, which is simulated by using repeated slab geometry as shown in Fig.1(a). Figure 1(b) shows calculated formation energies of Ge vacancy defect at Al/Ge interface as a function of distance from interface. The formation energy far from the interface, about 2.3eV, corresponds to values in bulk Ge. It is noted that the formation energy gradually increases with increasing the distance from interface to inner layers around 10Å, thus existing some transition region. Using these energies and assuming Boltzmann distribution, we can estimate the vacancy density as shown in the inset. The density increases and is 10^2-10^5 times larger around interface than in inner layers, which is in good agreement with recent experiments.

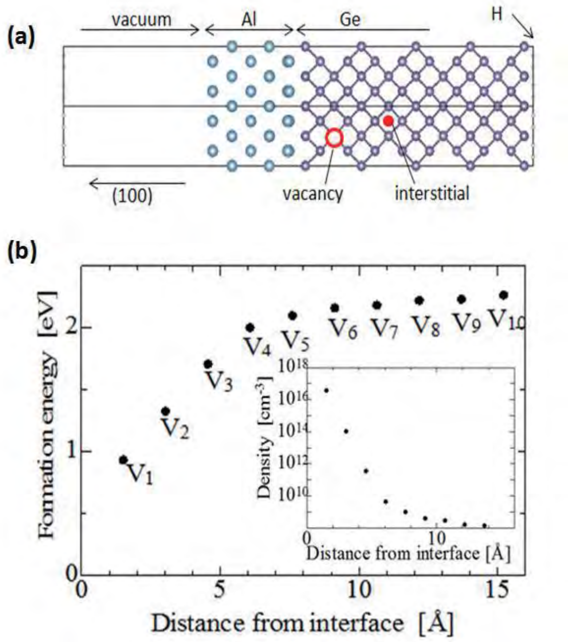

Fig.1. (a) Repeated slab model used in this study. (b) Calculated formation energies of Ge vacancy defect around Al/Ge interface as a function of distance from interface. Inset shows estimated vacancy density.

Then, we explain why defect density increases around interface. By analyzing electronic states, we found that the vacancy-related defect state is localized only around vacancy when the vacancy is located far from interface. On the other hand, when the vacancy is located near interface, we can see the hybridization between vacancy-related state and metal-induced gap states (MIGS), which correspond to evanescent states of metal Al. Owing to this hybridization, the formation energy of vacancy becomes smaller near the interface. We have also analyzed formation energies of various defects such as interstitials together with varying metal kinds and interface orientation and found that the same scenario is applicable; the defect density is large around the

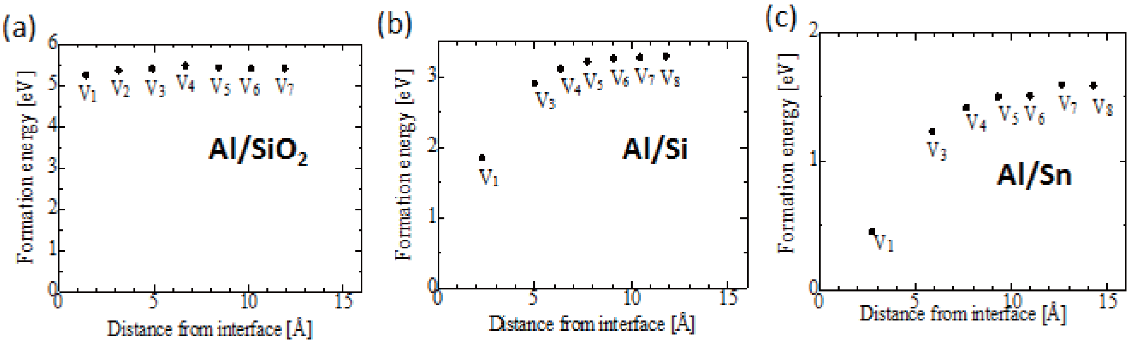

Fig.2. Calculated formation energies of vacancy defect as a function of distance from interface for (a) Al/SiO$_2$, (b) Al/Si, and Al/Sn (100) interfaces.

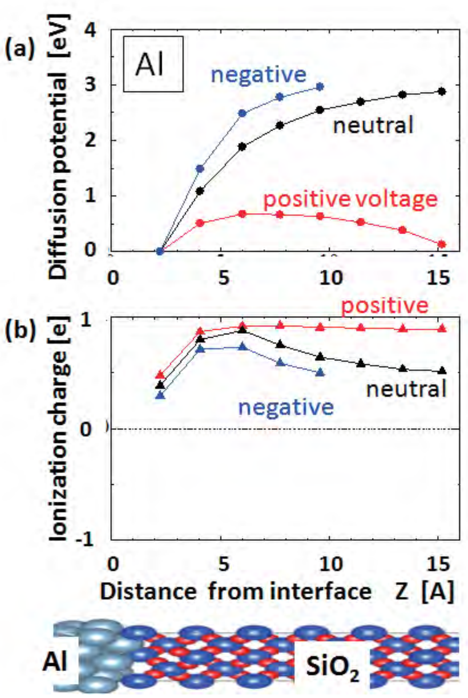

Fig.3. (a) Calculated potential of Al-atom diffusion from Al/SiO$_2$ interface into SiO2 layers and (b) ionic charge during the diffusion, for cases of neutral and positive/negative voltage applications. Bottom panel shows atom positions at Al/SiO$_2$ interface.

interface due to the hybridization of defect states with MIGS.

To demonstrate the important roles of MIGS, we calculated formation energies of vacancy for various Al/semiconductor (insulator) interfaces. The results are shown in Figs.2(a)-2(c). It is clearly seen that the width of transition region increases with going from SiO$_2$ having 9.0eV band gap to Sn with about 0eV gap. This is because the penetration length of MIGS into semiconductor layers is roughly proportional to the inverse of band-gap energy of semiconductor.

Finally, we consider the metal atom diffusion into SiO$_2$ under the electric field. Figure 3(a) and 3(b) show adiabatic potential and ionic charge of Al during the diffusion around Al/SiO$_2$ interface when neutral and positive/negative voltages are applied to Al layers. It is clearly seen that Al atom is positively ionized and the potential barrier into SiO$_2$ layers remarkably decreases in case of positive voltage application, which well explains observations. Even when negative voltage is applied, on the other hand, because Al atom is still positively ionized in SiO$_2$, the potential barrier increases and the diffusion into SiO$_2$ is remarkably suppressed.

All these calculations were performed using the xTAPP and VASP codes. In order to realize calculations for the present interface systems, because the system is made of a large number of atoms (200-500 atoms) and one has to consider a variety of atom configurations during metal-atom diffusion, the advanced computing facility having higher-speed CPU (more than 100G Flops), larger-size memory (around 100GB), larger-size strange (more than 1.0TB), and a multi-task operation is indispensable. These conditions are never prepared in personal research laboratory. Only the present super-computing system of the ISSP can realize these calculations.

First-principles analysis on the strain effect on the thermoelectric properties of nanomaterials

Junichiro SHIOMI

Department of Mechanical Engineering,

The University of Tokyo, 7-3-1, Hongo, Bunkyo-ku, Tokyo, 113-8656

Since interfacial thermal transport determines device performance, its analysis is of importance in the thermal management technology. While extremely high/low thermal boundary conductance is demanded for heat dissipation/thermal insulating device, thermal switching material, whose thermal conductivity can be tuned by an external force, is also required. Here an approach that has been recently paid attention is applied elastic strain in namomaterial. Different with bulk, it is known that one can apply large elastic strain to the nanomaterials without large lattice defect and dislocation. The impact of uniform elastic strain to heat conduction has been evaluated by molecular dynamics method, and it has been confirmed that an elastic strain as high as 20% can be applied [1]. In addition to this, recent theoretical study on local elastic strain in MoS_2 suggests that local elastic strain changes band structure of charge carrier locally, and it is possible to manipulate electric property of entire material [2].

In this work, in analogy to manipulation of electrical property of nanomaterial by local elastic strain, we have analyzed phonon transport in graphene under the presence of local and large elastic strain by means of the atomistic Green's function (AGF) method [3].

In order to locally apply elastic strain, we have considered the tapered graphene structures as shown in the inset figure in Fig. 1. For the structure, we have performed AGF method to calculate phonon transmission functions, $\zeta(\omega)$. Figure 1 shows frequency-dependent $\zeta(\omega)$ of tapered graphenes with different conditions. When comparing pristine (black line) and tapered structure (blue line), phonon transport is strongly suppressed by chocking structure, which results in the 50% reduction of thermal boundary conductance (G_{TBC}) at room temperature (G_{TBC}=3.5 and 1.8 W/m^{2}K for pristine and tapered structures, respectively). Next, we have calculated $\zeta(\omega)$ of tapered graphene with local strain (brown line). Here the local strain was introduced by pulling both ends of tapered graphene. After this process, it was found that 0.5% uniform strain leads to the 10% local elastic strain.

As seen in Fig. 1, high-frequency $\zeta(\omega)$ is suppressed, nevertheless, obtained G_{TBC} is as small as 1.2 W/m^{2}K because high-frequency phonons are not well excited at room temperature. In addition to this, by performing AGF calculation for the pristine with artificial strain (green line), it was found that low-frequency $\zeta(\omega)$ is not affected by large local strain. To summarize, we have investigated large local elastic strain to heat conduction in material for thermal switching device. Despite the local strain is as high as 10%, its impact to heat conduction is relatively small since the chocking structure is dominant in the reduction of thermal boundary conductance.

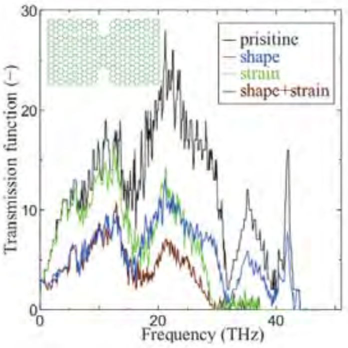

Fig. 1 Frequency-dependent phonon transmission functions, $\zeta(\omega)$, of graphenes with different conditions. Inset shows the tapered graphene structure.

References

[1] Z. Guo, *et al.*, *Appl. Phys. Lett.* **95** (2009).
[2] J. Feng, *et al.*, *Naature Photonics*, **6** (2012).
[3] W. Zhang, *et al.*, Numeriacal Heat Transfer, **51**, (2007).

First-Principles Study on Device Properties of Emerging Phase-Change Memory Devices

Masaaki Araidai

Institute of Materials and Systems for Sustainability, Nagoya University
Furo-cho, Chikusa-ku, Nagoya, 464-8603

Toward a realization of high-speed and low power non-volatile memory, a new type of phase change RAM (TRAM) has been examined intensively [1]. The high-resistive state (HRS) and low-resistive state (LRS) of TRAMs are switched by the movement of Ge atoms (Fig.1(a)). We showed that the movement of Ge atoms in TRAMs was enhanced by carrier injections [2]. Recently, it has been found that TRAMs consisting of Ge_xTe/Sb_2Te_3 superlattice with Ge deficiency have higher speed operation and lower switching power than stoichiometric $Ge_{1.0}Te/Sb_2Te_3$ superlattice TRAMs [3]. However, the conventional theoretical models for TRAMs [4] cannot rationalize the improvement in switching properties of Ge-deficient TRAMs.

In this study, we investigated on-off switching properties of Ge_xTe/Sb_2Te_3 superlattice TRAMs by first-principles molecular dynamics simulation. We prepared a stoichiometric $Ge_{1.0}Te/Sb_2Te_3$ superlattice and a Ge-deficient $Ge_{0.44}Te/Sb_2Te_3$ superlattice. The atomic and electronic structures were calculated by VASP code [5], which is based on the density-functional theory. The set operation was simulated by heating and hole injection. On the other hand, the reset operation was simulated by heating only (Fig. 2).

Our simulations showed that high-speed and low power switching operations can be realized in Ge-deficient TRAMs. Ge atoms at the interfaces between the GeTe and Sb_2Te_3 become the conduction channel (Fig.1(b)). Thus, the presence of Ge atoms at these interfaces determines the resistance of TRAMs. Moreover, we confirmed that Ge vacancies in the GeTe layer enhance the Ge mobility, leading to low power and high-speed memory operations of Ge-deficient TRAMs. We also found that the resistance of the LRS can be controlled by changing the number of injected holes during the set operation.

This work was performed in collaboration with LEAP. It was funded by the “Ultra-Low Voltage Device Project" and supported by METI and NEDO.

References

[1] M. Tai, et al., VLSI Technology (VLSIT), 2015 Symposium on, T96-T97 (2015).

[2] S. Kato, et al., Solid State Devices and Materials, A-3-1 (2013).

[3] N. Takaura, et al., 2014 IEEE International Electron Devices Meeting, 29.2.1-29.2.4 (2014).

[4] J. Tominaga, et al., Jpn. J. Appl. Phys. **48**, 03A053 (2009).

[5] G. Kresse and J. Hafner, Phys. Rev. B **47**, 558 (1993).

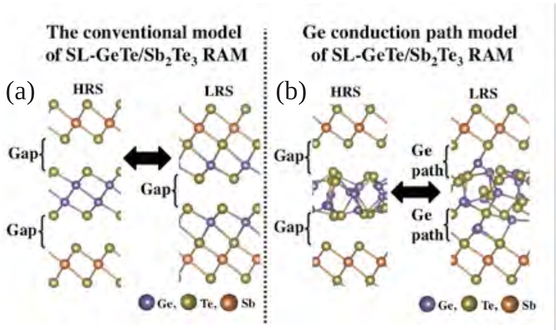

Figure 1: (a) Conventional HRS and LRS models of TRAM and (b) Ge-conduction channel models.

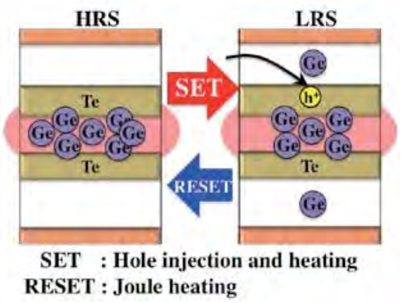

Figure 2: On-off switching is simulated by carrier injection and heating in first-principles molecular dynamics.

Magnetization in Twisted Bilayer Ribbons of Graphene

Kazuyuki Uchida
Department of Physics, Kyoto-Sangyo University

Magnetic structures in twisted bilayer ribbons of graphene have been explored by our first-principles calculations based on the density-functional theory (DFT) within the local-spin-density approximation (LSDA).

It has been known that peculiar electron states appear at zigzag edges of graphene ribbons [1]. The energy levels of the zigzag-edge states are located near the Fermi level. They are shown to be magnetized by LSDA calculations [2].

When two graphene ribbons are stacked, interactions between them lead to splitting of the energy levels of the zigzag-edge states, and the energy scale of the splitting depends on the stacking pattern of the ribbons [3]. This infers that magnetization of the edge states in twisted bilayer ribbons of graphene also reflects the stacking pattern of the bilayer.

To make this point clear, in this work, we have calculated magnetic structures in twisted bilayers ribbon of graphene with changing the twist angle between them. Thousands of atoms must be calculated for this purpose. We have used the real-space DFT (RSDFT [4]) code to perform such ultra-large-scale spin-density calculations.

A result of our calculations is shown in Fig.1, showing that the stacking pattern of the bilayer influences the magnetization: The magnetization is localized at the AB-stacking edge; The AA-stacking edge is not magnetized. Our results show that magnetic structures of systems can reflect Moiré patterns in the systems.

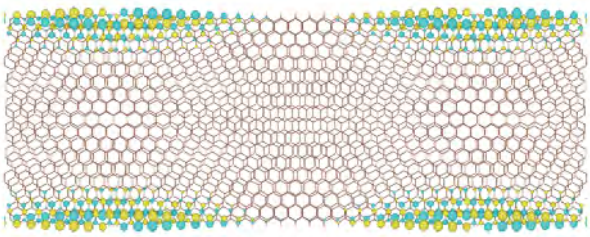

Figure 1: Magnetization in a twisted bilayer ribbon of graphene, reflecting the Moiré pattern in the system.

References

[1] M. Fujita, K. Wakabayashi, K. Nakada, and K. Kusakabe, J. Phys. Soc. Jpn. bf 65, 1920 (1996).Y. Miyamoto, K. Nakada, and M. Fujita, Phys. Rev. B 59, 9858 (1999). 10.1103/PhysRevB.59.9858.Y. Niimi, T. Matsui, H. Kambara, K. Tagami, M. Tsukada, and H. Fukuyama, Phys. Rev. B 73, 085421 (2006).

[2] S. Okada and A. Oshiyama, Phys. Rev. Lett. 87, 146803 (2001).

[3] E. S. Morell, R. Vergara, M. Pacheco, L. Brey, and L. Chico, Phys. Rev. B **89**, 205405 (2014).

[4] J.-I. Iwata, D. Takahashi, A. Oshiyama, B. Boku, K. Shiraishi, S. Okada, and K. Yabana, J. Comput. Phys. **229**, 2339 (2010).

Doping effects on Light Absorption of Light-harvesting Molecules: ab initio Molecular-Dynamics Study

Satoshi Ohmura
Research Center for Condensed Matter Physics,
Department of Civil Engineering and Urban Design,
Hiroshima Institute of Technology, 2-1-1 Miyake, Saeki-ku, Hiroshima 731-5193

Doping effect on optical response of a molecular graphene with covalently linked fullerene [the hexabenzocoronene (HBC)-triethylene glycol (TEG)–C_{60} molecule], a building block in a self-assembled supramolecular solar cell, has been explored by using *ab-initio* theoretical simulations. In HBC-TEG-C_{60} system, C_{60} attracts electron as electron transport layer whereas the HBC attracts hole as hole transport layer after irradiation of the light to the HBC.

We have evaluated HOMO/LUMO energy gaps and light absorption spectra of the HBC-TEG–C_{60} doped with B, N, O and F in the HBC. The substitutional doping affects the relative energies of the HBC significantly leading to broader spectrum of light absorption. Especially in O-doped case, maintaining the staggered structure of the HOMO/LUMO relationship between the HBC and C_{60} and narrow HBC gaps are identified. In order to investigate effects of the HOMO/LUMO levels modified by the O-doping on carrier dynamics, we have performed a nonadiabatic quantum-mechanical molecular-dynamics simulation that incorporates electronic transitions through a surface-hopping approach.

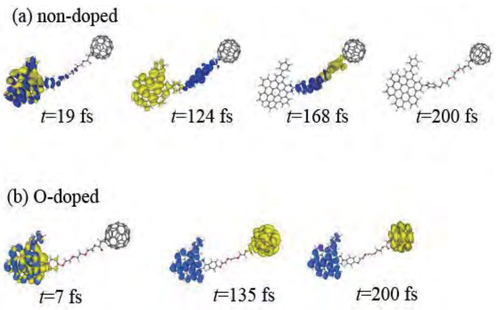

Fig. 1: Time evolution of the spatial distributions of the charge densities for quasi-excited electron and hole for non-doped (a) and O-doped (b) systems.

Figure 1 shows the time evolution of the spatial distributions of the charge densities for quasi-excited electron and hole for non-doped (a) and O-doped (b) systems obtained from the simulation. The simulation demonstrates that doping oxygen into HBC enhances the charge mobility after charge separation in HBC-TEG-C_{60} super molecule.

References

[1] S. Ohmura, K. Tsuruta, F. Shimojo, and A. Nakano: AIP advances **6** (2016) 015305

Large scale calculations on the fundamental processes of solar cells and their optimization in conversion efficiency

Koichi YAMASHITA
Department of Chemical System Engineering,
The University of Tokyo, Hongo, Bunkyo-ku, Tokyo 113-8656

Hydrogen production by splitting water with photo(electro)chemical system has been attracting many interest as it is sustainable way of solar energy. The oxygen evolution reaction (OER) is the key in water-splitting system because large part of overpotential is caused by OER. We studied electrocatalyst/water interfaces for OER by focusing on (i) pH and electrode potential dependent RuO_2/water interfacial structure, and (ii) electrode potential dependent Schottky-type barriers at n-type Ta_3N_5/water for efficient hole transfer.

First, interfacial structures of RuO_2/water under given electrode potential and pH are examined. As models for interfacial structures, RuO_2(110) is selected, and the formal valence of surface Ru atoms and orientations of water molecules are varied. In this manner a total of almost 100 configurations were modeled. All the calculations were performed using GPAW with the ASE simulation package. The GGA/RPBE functional and PAW method were employed with F4cpu and F36cpu queues. Based on the calculations of interfacial Gibbs energy as functions of both pH and electrode potential, surface Pourbaix diagram is generated. As a result, a significant structural difference is found between pH values of 0 and 14[1]. Next, interfacial band diagram on Ta3N5/water as a photoanode for photoelectrochemical water-splitting is discussed. For the examination of the interfacial Schottky barrier height under given electrode potential, Ta_3N_5 (6.5×1×1) supercell with explicitly introduced ice-like water molecules is employed with F36cpu, F18acc and F72acc queues. From the calculations of the position of valence band in bulk, position of valence band at the surface, and semiconductor barrier height at given electrode potentials, it is clearly shown that the interface of n-type Ta_3N_5/water shows the intermediate behavior between band edge pinning and Fermi level pinning. Consequently, the importance of surface modification is addressed from a viewpoint of utilizing the Schottky barrier height to get a driving force for charge separation.

References

[1] E. Watanabe, J. Rossmeisl, M. E. Björketun, H. Ushiyama, and K. Yamashita: *J. Phys. Chem. C*, **120** (2016) 8096-8103.

First principles calculation of point defects in electrodes of solid oxide fuel cells

Akihide Kuwabara

Nanostructures Research Laboratory,

Japan Fine Ceramics Center, Atsuta-ku, Nagoya, Aichi 456-8587

In complex oxides, considering the Gibbs' phase rule, more than one degree of freedom remain, even when the material is in a single phase at constant temperature and oxygen partial pressure. This means a variation of the cation composition leads to a variation of the oxygen nonstoichiometry, consequently material properties. In this study, we investigated how the cation nonstoichiometry influences the oxygen nonstoichiometry from theoretical points of view. For this purpose, perovskite-type oxide $SrFeO_{3-x}$ was chosen as a model oxide, and first principle calculations were performed on this oxide. Based on our preliminary calculations, $Sr_2Fe_2O_5$ (x = 0.167) was chosen as a target material.

Total energy calculations were carried out using VASP code. Plane wave cut-off energy was set to be 400 eV. We used the GGA-PBE type of an exchange-correlation potential. GGA+*U* approach was applied to 3*d* orbital of Fe and Hubbard *U* potential was set to be 5.4 eV. For calculations of point defects, supercell models of 2×1×2 unit cells of $Sr_2Fe_2O_5$ composed of 144 atoms were constructed. An oxide ion vacancy, an excess oxide ion, a cation vacancy were separately introduced into the supercell and defect formation energies were calculated according to the formalism reported by Zhang and Northrup [1]. In two-phase co-existing states, the chemical potentials of cations can be defined. Thus the chemical potentials of the components in Sr and Fe excess conditions can be determined, and consequently formation energies of defects can be calculated. From the calculated formation energies of defects together with the electrical neutrality conditions, the concentrations of defects in Sr and Fe excess conditions can be evaluated.

The calculated concentrations of oxygen vacancy [*V*o], interstitial oxygen [O_{int}] and electron hole [h] as a function of oxygen partial pressure at 900 K are given in Fig. 1. Interstitial oxygens are estimated as dominant defects. However there were no significant differences in the defect concentrations between Sr and Fe excess conditions, especially in relatively higher pO_2. This is inconsistent with the results observed in the measurements of the oxygen nonstoichiometry, that is, the oxygen content was relatively larger in Sr excess than Fe excess conditions [2]. The assumption used for the calculation must be reconsidered and improved to reveal the influence of the cation nonstoichiometry on the defect structure.

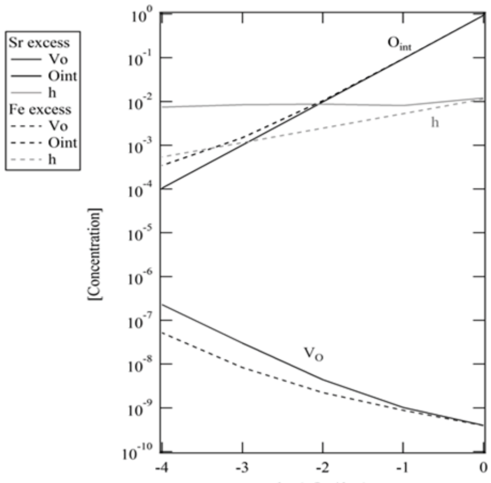

Fig. 1: Concentration of interstitial oxygen "O_{int}", oxygen vacancy "*V*o", and electron hole "h" in $Sr_2Fe_2O_5$ at 900 K.

References

[1] S. B. Zhang and J. E. Northrup, *Phys. Rev. Lett.*, **67** (1991) 2339.

[2] Y. Okamoto, *et al.*: *20th Int. Conf. Solid State Ionics (SSI-20)*, Keystone, USA, (2015)

First-Principles Molecular Dynamics Simulations of Water Dissociative Adsorption at Stepped Pt Surface and at SiC–Pt Interfaces

PHO VAN BUI, TAKUYA NISHITANI, HIDETOSHI KIZAKI, KOUJI INAGAKI, and
YOSHITADA MORIKAWA
Graduate School of Engineering,
Osaka University, 2-1, Yamada-oka, Suita, Osaka 565-0871

Water interaction with Pt surface plays important roles in many catalytic surface reactions, corrosion processes, and electrochemistry. Recently, intact adsorption and dissociation of water on flat Pt have been extensively studied by both experiments and simulations [1, 2]. A recent study on adsorption and dissociation of water at the edge of Pt(211) surface showed that the dissociation energy is about 0.5 eV for a monomer, 0.2 eV for a dimer, and nearly zero in the case of a trimer [3]. Moreover, water adsorption on a stepped Pt(111) surface, which is observed after deposition of Pt by X-ray diffraction [4] and commonly occurring in realistic situations, is not well understood.

Recently, Isohashi and co-workers [5] reported experimentally that silicon carbide (SiC) surface can be etched by just water with the presence of Platinum (Pt) as a catalyst. The results suggested that Pt plays an essential role in the catalytic reaction of water and SiC. To clarify the mechanism of the reaction and role of Pt as a catalyst, in this study, we use first-principles simulation tool for atom technology program package (STATE) to elucidate the adsorption and dissociation of water on a stepped Pt(111) surface and at Pt/SiC interface. The calculations are based on the density functional theory within a generalized gradient approximation of Perdew et al. Barrier height is evaluated by means of climbing image nudged elastic band method [6].

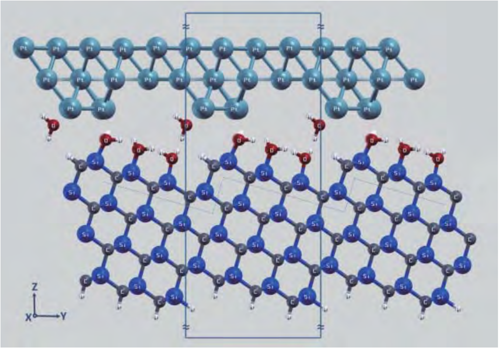

Fig. 1: 3C-SiC(111) and Pt(111) surfaces in the simulation model. The box showed a unit cell.

A stepped Pt(111) surface composed of 3-layer slab, in which the two topmost layers are kept fixed to mimic the bulk. A step-and-terrace 3C–SiC (111) surface was used as a model for the simulation as shown in Fig. 1. The model is periodically repeated unit cells of four bi-layers. During the simulations, the two topmost atomic layers with terminated surface atoms were allowed to fully relax, while the remaining atoms were kept fixed to maintain the substrate structure.

In this study, we focus on the reaction pathways and reaction barriers of the interaction between water molecules and OH-terminated step edge Si with the present of platinum (Pt) catalyst in the calculation model. The adsorption of water on a stepped Pt surface is preferentially at the step edge of Pt, stabilized by the effect of chemical bonds with Pt and hydrogen bonds. The atomic geometries at initial state (IS), metastable state (MS) & final state (FS), and energy profile of the water dissociative adsorption on the edge of the Pt (111) surface are shown in Figs. 2 and 3, respectively.

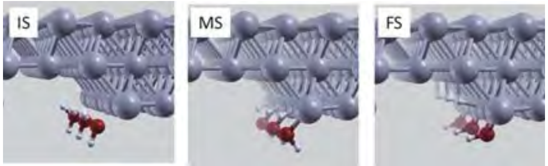

Fig. 2: Atomic geometries of the water dissociative adsorption on the edge of the Pt (111) surface at IS, MS, and FS.

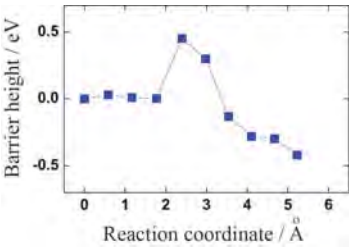

Fig. 3: Energy profile of the water dissociative adsorption on the edge of the Pt (111) surface

The results show that the barrier height of the water dissociation on the edge of Pt(111) surface is about 0.5 eV, which is about 0.3 eV lower than that on a terrace site [2].

With the presence of the SiC, the results show that the activation barrier of the water dissociation at the SiC–Pt interface affected by the distance of the Pt and SiC surfaces. The shorter distance between Pt and SiC surfaces, the smaller the barrier height. The adsorption and dissociation of water at Pt/SiC interface play important roles in etching of SiC in water.

After the water dissociative adsorption, the OH group may transfer to the topmost Si atom and break the Si–C bond. The activation energy and reaction pathway are now under investigation.

References

[1] A. Hodgson et al., Sur. Sci. Reports **64**, (2009) 381-451.

[2] J. L. Fajín, et al., J. Phys. Chem. A **118**, (2014) 5832-5840.

[3] D. Donadio et al., J. Am. Chem. Soc. **134**, (2012) 19217-19222.

[4] T. Aoltonen et al., Chem. Matter. **15**, (2003) 1924.

[5] Isohashi et al., Mater. Sci. Forum **778–780** (2014) 722.

[6] Henkelman et al., J. Chem. Phys. **113** (2000) 9901.

First-principles calculations of iron solid solution effects on the lattice thermal conductivity of lower mantle minerals

Haruhiko DEKURA

Geodynamics Research Center

Ehime University, 2-5 Bunkyo-cho, Matsuyama 790-8577, Japan

Iron-bearing Bridgmanite (Mg,Fe)SiO_3 is believed to be the most constituent mineral in the earth's lower mantle. Determination of the phonon transport property, *i.e.*, lattice thermal conductivity (κ), of the material should be therefore a key to understanding the dynamics and evolution of the earth's deep interior. Lattice anharmonicity owing to the phonon-phonon interaction strongly relates the phonon transport. The primary purpose of this project in this period is to determine the anharmonic properties of the iron-bearing system at deep mantle pressure conditions.

We have performed density-functional theoretic calculations combined with the LDA+U method [1] and have extracted the large number of anharmonic force constants (AFC) by higher order derivatives of the adiabatic potential surface [2]. All of the calculations were performed using the QUANTUM-ESPRESSO package [3]. The simulation cell of $(Mg_{0.9375},Fe^{2+}_{0.0625})SiO_3$ that includes totally 160 atoms was adopted in this study. The ferrous iron was treated in the high spin state ($S = 2$).

During this period, by the use of supercomputer (system B), we have almost finished the determination of the 3rd order AFC at 100 and 150 GPa relevant to the Earth's lowermost mantle conditions. Those obtained AFC will be analyzed and used for evaluation of the phonon lifetimes, combining with harmonic phonon properties determined also by the real-space method. The phonon lifetimes and thus κ are known to very sensitive to the choice of a mesh for the Brillouin zone integration, and we normally need a dense mesh for acceptable numerical accuracy. We will continue to promote this kind of analysis and perform anharmonic lattice dynamics simulation in other systems.

References

[1] T. Tsuchiya and X. Wang: J. Geophys. Res. **118** (2013) 83.

[2] K. Esfarjani and H. T. Stokes: Phys. Rev. B **77** (2008) 144112.

[3] http://www.quantum-espresso.org/

Ab initio calculation of superconducting pairing interactions in materials with complex Fermi surface

Ryosuke AKASHI
Department of Physics, University of Tokyo
Hongo, Bunkyo-ku, Tokyo 133-0033

In this project, we calculated the electron-phonon coupling strength in systems having complicated shapes of the Fermi surfaces. The recent development in the density functional theory has enabled us to calculate the superconducting transition temperature (T_c) in the conventional phonon-mediated superconductors [1, 2]. The accuracy of the present T_c-calculation method relies on that of the first-principles phonon calculation [3]. Although the Hermite-Gaussian broadening approximation [4] for describing the metallic occupation has been used as a standard treatment, this treatment in principle results in serious error in the systems with complicated Fermi surfaces. On the other hand, a recently developed tetrahedron-based method has been shown to yield quantitatively more reliable results [5].

We calculated the dynamical matrix and electron-phonon coupling strength in yttrium halogen-carbides and hydrogen sulfide using the tetrahedron-based method. These materials have been shown to exhibit the Fermi surfaces with complicated structures formed by multiple bands [6, 7]. QUANTUM ESPRESSO code package (5.0.3)(Ref. [8]) has been used for the calculations. The PBE-sol [9] and GGA-PBE [10] exchange-correlation potentials were used for the respective materials. Parallelization scheme with respect to **k** points (-*npool* option) as implemented in *ph.x* code was employed. The calculations were mainly done in System B (sekirei). In particular, the calculation for hydrogen sulfide with composition of $H_{31}S_{11}$ required $\lesssim$24 hour per **q** point with 32 nodes and -*npool 32*.

Table 1: Calculated factors representing the electron-phonon coupling strength and superconducting transition temperatures. The latter values were estimated using the strong-coupling-corrected McMillan-Allen-Dynes equation [12] with the empirical Coulomb-repulsion parameter $\mu^* = 0.13$

	YClC	YBrC	YIC	$H_{13}S_5$	$H_{31}S_{11}$
λ	0.527	0.650	0.831	1.301	1.481
$\omega_{\ln}$ (K)	283	248	218	1285	1351
ω_2 (K)	502	470	434	1569	1606
T_c (K)	2.7	5.4	9.5	124	153

The resulting Eliashberg function $\alpha^2F(\omega)$ (Ref.[11]) representing the electron-phonon coupling strength is shown in Fig. 1. The coupling strength λ and characteristic phonon moments $\omega_{\ln}$ and ω_2 (for their definitions, see Ref. [12]) are summarized in Table 1. The T_cs estimated from these values agree well with the experimental trends [13, 14, 15]. These results will be published in later papers.

References

[1] M. Lüders, M. A. L. Marques, N. N. Lathiotakis, A. Floris, G. Profeta, L. Fast, A. Continenza, S. Massidda, and E. K. U. Gross, Phys. Rev. B **72**, 024545 (2005).

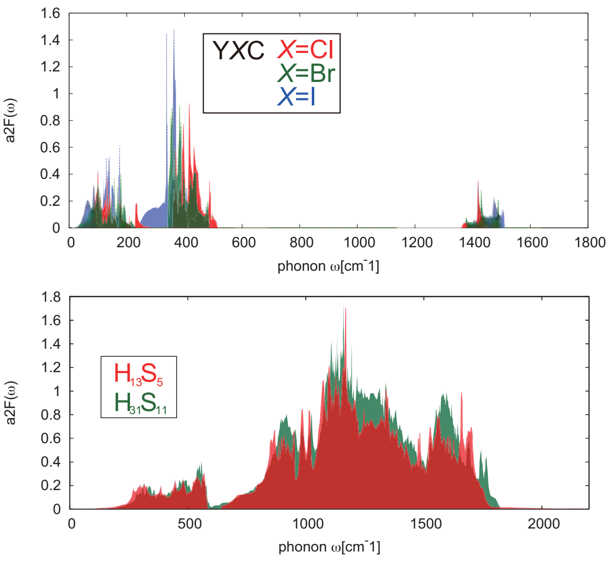

Figure 1: Calculated Eliashberg functions $\alpha^2F(\omega)$ for yttrium halogen carbides YXC ($X=$Cl, Br, I) and hydrogen sulfide H_xS. The pressures for the latter systems were set to be 190 ($H_{13}S_5$) and 200GPa ($H_{31}S_{11}$), respectively

[2] M. A. L. Marques, M. Lüders, N. N. Lathiotakis, G. Profeta, A. Floris, L. Fast, A. Continenza, E. K. U. Gross, and S. Massidda, Phys. Rev. B **72**, 024546 (2005).

[3] S. Baroni, S. de Gironcoli, A. Dal Corso, and P. Giannozzi, Rev. Mod. Phys. **73**, 515 (2001).

[4] M. Methfessel and A. T. Paxton, Phys. Rev. B **40**, 3616 (1989).

[5] M. Kawamura, Y. Gohda, and S. Tsuneyuki, Phys. Rev. B **89**, 094515 (2014).

[6] P. Puschnig, C. Ambrosch-Draxl, P. W. Henn, and A. Simon, Phys. Rev. B **64**, 024519 (2001).

[7] N. Bernstein, C. S. Hellberg, M. D. Johannes, I. I. Mazin, and M. J. Mehl, Phys. Rev. B **91**, 060511(R) (2015).

[8] P. Giannozzi *et al*, J. Phys.: Condens. Matter **21**, 395502 (2009); http://www.quantum-espresso.org/.

[9] J. P. Perdew, A. Ruzsinszky, G. I. Csonka, O. A. Vydrov, G. E. Scuseria, L. A. Constantin, X. Zhou, and K. Burke, Phys. Rev. Lett. **100**, 136406 (2008).

[10] J. P. Perdew, K. Burke, and M. Ernzerhof, Phys. Rev. Lett. **77**, 3865 (1996).

[11] D. J. Scalapino, in *Superconductivity* edited by R. D. Parks, (Marcel Dekker, New York, 1969) VOLUME 1.

[12] P. B. Allen and R. C. Dynes, Phys. Rev. B **12**, 905 (1975).

[13] A. Simon, A. Yoshiasa, M. Backer, R. W. Henn, C. Felser, R. K. Kremer and H. Mattausch, Z. anorg. allg. Chem. **622**, 123 (1996).

[14] R. W. Henn, W. Schnelle, R. K. Kremer, and A. Simon, Phys. Rev. Lett.**77**, 374 (1996).

[15] A. P. Drozdov, M. I. Eremets, and I. A. Troyan, V. Ksenofontov, and S. I. Shylin, Nature (London) **525**, 73 (2015).

Study on catalyst synthesis and surface reaction analysis for novel energy storage systems

Fumihiko KOSAKA and Junichiro OTOMO

Department of Environment Systems, Graduate School of Frontier Sciences,

The University of Tokyo, 5-1-5, Kashiwa-no-ha, Kashiwa, Chiba 277-8581, Japan

Redox reaction of metal oxides (MO) such as nickel oxide and iron oxide can be utilized for energy conversion and storage systems by using the energy gap between metals and metal oxides [1,2]. For example, a new energy storage system has been proposed utilizing the redox reaction of iron oxide with a solid oxide fuel cell (SOFC) using H_2–H_2O as a mediator [2]. In this system, electrical energy is converted to chemical energy of Fe during charging process. Reduction and oxidation of iron oxide by hydrogen and water proceed in charging and discharging processes, respectively. Therefore, investigation of the mechanisms that promote the redox reactions of metal oxides is of great importance and lead to highly efficient energy storage systems.

In this study, to discuss in a simple case, we focus on reduction process of NiO(111) by hydrogen. Hydrogen adsorbs on the surface of NiO, and then water desorbs and oxygen vacancy forms. The energy profile was investigated using the density functional theory (DFT). SIESTA code [3] was used for the DFT calculations. The generalized gradient approximation (GGA) using the RPBE functional [4] was used as the exchange correlation function. p(2×2) unit cell and vacuum layers of 10 Å was sampled with 2×2×1 k-point grid automatically generated using the Monkhorst-Pack method [5]. During relaxation, positions of atoms in bottom two layers were fixed. Crystal structures were visualized using VESTA software [6].

Fig. 1 shows the calculated energy profile and positions of Ni, H and O during the initial NiO reduction step by hydrogen. Hydrogen approached the surface of NiO and was stabilized by adsorption on the surface. Oxygen vacancy formed by desorption of water and

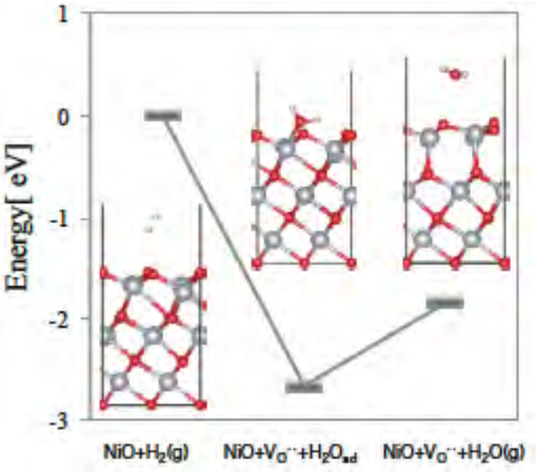

Fig. 1: Calculated energy profile of initial NiO reduction step by hydrogen. Red: O, white: H, grey: Ni.

surface relaxation occurred. Because of the oxygen vacancy formation, the total energy increased. In the future plan, we will calculate the reaction barrier using the nudged elastic band (NEB) method. Then, the investigation will be expanded to other materials such as iron oxide and ilmenite which will be used for the novel energy storage systems using redox cycles of the oxides.

References

[1] J. Adanez et al., *Prog. Energy Combust. Sci.*, **38** (2012) 215.

[2] N. Xu et al., *Energy Env. Sci.*, **4** (2011) 4942.

[3] J. M. Soler et al., *J. Phys.: Condens. Matter.*, **14** (2002) 2745.

[4] Y. Zhang et al., *Phys. Rev. Lett.*, **80** (1998) 890.

[5] H.J. Monkhorst et al., *Phys. Rev. B*, **13** (1976) 5188.

[6] K. Momma et al., *J. Appl. Crystallogor.,* **44** (2011) 1272.

Interface structure of β-FeSi$_2$(100) and Si(001)

Ken HATTORI
Graduate School of Materials Science, Nara Institute of Science and Technology
Takayama, Ikoma, Nara 630-0192

The authors' group found the formation of β-FeSi$_2$(100) on Si(001) prepared in ultra-high vacuum, using scanning tunneling microscopy (STM) and low-energy electron diffraction (LEED) [1]. Using Simulation Tool for Atom TEchnology (STATE)-Senri [2] in SCC-ISSP system A, the author calculated STM simulation images for β-FeSi$_2$(100)1×1 surface based on the LEED results, where the model consists of 1st-layer Si (8 atoms per β(100)1×1 unit-cell, corresponding to Si(001)2×2)/2nd-Fe (2 atoms)/3rd-Fe (2)/4th-Si (8)/5th-Fe (4)/6th-Si (8)/7th-Fe (2)/8th-Fe (2)/9th-Si (8)/10th-Fe (4)/11th-Si (8)/12th-H (8) (64 atoms in total)[1].

Recently the authors' group has confirmed such a slab structure using high-angle annular dark-field scanning transmission electron microscopy (HAADF-STEM) in atomic resolution. Furthermore, the STEM has revealed atomic interface structure of β-FeSi$_2$(100) and Si(001). Based on the experimental interface structure, the author calculated interface structures using STATE-Senri, from a small model ((Si (8)/Fe (2)/Fe (2)/Si (8)/Fe (4))/Si (8)/1st-Si-sub (4)/.../6th-Si-sub (4)/7th-H (8) (64 atoms)) to a certain large-scale moedel ((Si/Fe/Fe/Si/Fe)×3/Si/Si-sub×24/H (184 atoms), Fig. 1), step by step, under fixing the last three layers (Si/Si/H), within 0.3 eV/Å in residual force. The k-mesh gird was 4×4×1, and the spin polarization was not treated.

As shown in Fig. 1, the bottom Si atoms of β-FeSi$_2$ did not fully bond to the substrate Si atoms, suggesting loosely bonding at the interface. Indeed, the main residual force located at interface Si layers in calculated five models, implying interface stress. One of the interesting features of this system is nano-carpet formation; different β-FeSi$_2$(100) nano-film domains on different-height Si(001) terraces smoothly connected over the substrate steps, implying that the interface bonding is weaker than the lateral bonding inside the nano-film. The calculated interface stress might be a key point to reveal the nano-carpet growth.

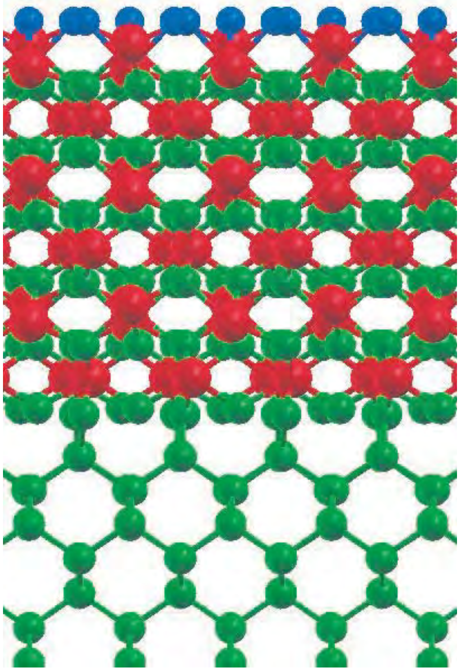

Figure 1: Calculated interface structure of β-FeSi$_2$(100) on Si(001). Red (blue and green) balls represent Fe (Si) atoms.

The author thank Prof. Morikawa in Osaka University, Dr. Yanagisawa in Ryukyu University, and Dr. Hamada in NIMS for their great support in STATE-Senri calculations.

References

[1] O. Romanyuk, K. Hattori, M. Someta, and H. Daimon: Phys. Rev. B **90** (2014) 155305.

[2] Y. Morikawa: Phys. Rev. B **63** (2001) 033405, and references therein.

Development of first-principles electronic structure calculation package xTAPP

Yoshihide YOSHIMOTO
Graduate School of Information Science and Technology, University of Tokyo
7-3-1 Hongo, Bunkyo-ku, Tokyo 113-0033

xTAPP is a first-principles electronic structure calculation package based on plane wave basis sets, pseudo potentials, and density functional theory. It has been opened for public under GNU General public license since April 2013 and it is acquiring users afterward.

One of the major request to xTAPP after its release was the calculation for spin-orbit interaction and relating non-collinear magnetism. The major aim of this project was to extend xTAPP to support these functions.

The developed version of xTAPP which supports these functions has been publicly available after 20th April 2016[1]. This release also contains a translated version of a pseudo potential library which takes the spin-orbit interaction into account by solving the Dirac equation instead of the Schrödinger equation in its generation processes. The library covers from H to Bi if they are not radioactive. In addition, stress calculations by the analytic expression is also available for the calculations with spin-orbit interaction and non-collinear magnetism in this new version. The developed code including the one for stress calculation supports up to f orbital.

Fig. 1 shows the simulated band structure of Au. The solid and the dotted lines correspond to the calculations with and without the spin-orbit interaction, respectively. The d-band splitting by the spin-orbit interaction at the Γ point is reproduced. Fig. 2 shows the stress of GaAs as a function of the lattice constant by using the analytic expression and by using numerical derivative of the total energy. We can not distinguish these two calculations.

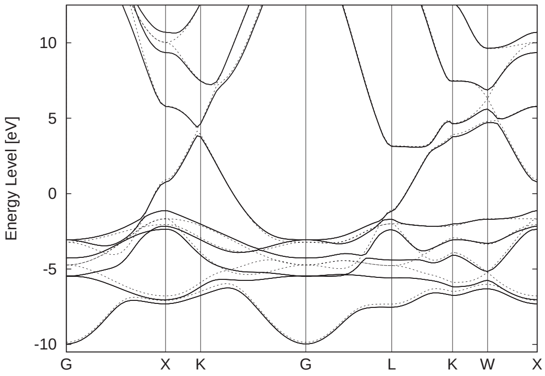

Fig. 1: calculated band structure of Au.

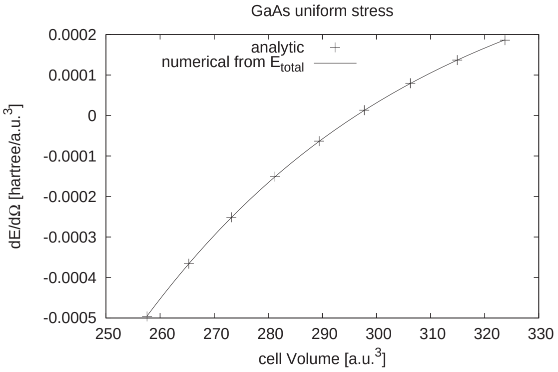

Fig. 2: calculated stress of GaAs.

References

[1] xTAPP web site: http://xtapp.cp.is.s.u-tokyo.ac.jp.

First-principles study of magnet materials and spin-orbit systems

Takashi MIYAKE
CD-FMat, National Institute of Advanced Industrial Science and Technology
Umezono, Tsukuba 305-8568

Synthesis of a $\mathrm{NdFe_{12}N}$ film [1], followed by a theoretical calculation [2], has attracted renewed interest in exploration of new magnet compounds having large saturation magnetization and strong magnetocrystalline anisotropy. Interstitial nitrogen enhances the magnetization and induces strong uniaxial magnetic anisotropy in $\mathrm{NdFe_{12}N}$, and both the magnetization and anisotropy field are superior to those of $\mathrm{Nd_2Fe_{14}B}$ over wide temperature range between the room temperature and Curie temperature [1].

One problem in $\mathrm{NdFe_{12}N}$ is that the compound is thermodynamically unstable. A third element, such as Ti, is necessary to stabilize the bulk phase. Another question is whether or not the magnetic properties can be improved further by changing the interstitial dopant. To address this problem, we have performed first-principles calculations of $\mathrm{NdFe_{11}Ti}X$, where X=B, C, N, O, F, using the QMAS code. The calculations are based on the density functional theory in the generalized gradient approximation. The Nd-4f electrons are treated as open-core states.

The magnetic moment is enhanced by doping X compared to $\mathrm{NdFe_{11}Ti}$ in all the five elements we have studied. The amount of the enhancement significantly depends on X, and is larger in $X=$ N, O, F than in $X =$ B, C. Analysis of the density of states clarified that the X dependence is associated with the anti-bonding states between Fe-3d and X-2p. The anti-bonding states appear above the Fermi level in the X=B system. As the atomic number increases, the X-2p energy level is shifted down. In the X=N system, the anti-binding states are partially filled in the majority spin channel, whereas the minority-spin anti-bonding states are not filled. This results in enhancement of the magnetization.

The magnetocrystalline anisotropy is evaluated based on the crystal field theory as

$$K_1 = -3J(J-1/2)\alpha_J \langle r^2\rangle A_2^0 n_R \ , \qquad (1)$$

where $J = 9/2$ is the total angular moment of the Nd ion, $\alpha_J = -7/1089$ is the Stevens factor, and n_R is the concentration of Nd atoms. The crystal-electric-field parameter $\langle r^2\rangle A_2^0$ is calculated as

$$\langle r^l\rangle A_l^m = F_l^m \int W_l^m(r)\phi^2(r)dr \ , \qquad (2)$$

where F_l^m is a prefactor of the real spherical harmonics Z_l^m, W_l^m is the Kohn-Sham effective potential expanded by Z_l^m, and ϕ is the radial function of the Nd-4f orbital. We have found that the $\langle r^2\rangle A_2^0$ is sensitive to X, and has the maximum for X=N. These results indicate that nitrogen is the best dopant among X=B, C, N, O and F in terms of magnetization and magnetocrystalline anisotropy.

References

[1] Y. Hirayama et al., Scr. Mater. **95** (2015) 70.

[2] T. Miyake et al., J. Phys. Soc. Jpn. **83** (2014) 043702.

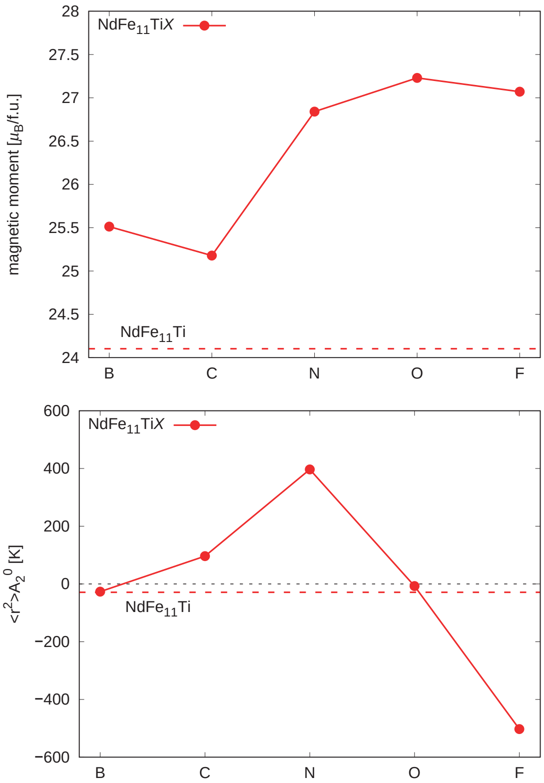

Figure 1: Magnetic moment and crystal electric field parameter of $\mathrm{NdFe_{11}Ti}X$ ($X=$ B, C, N, O, F).

[3] Y. Harashima et al., Phys. Rev. B **92** (2015) 184426.

Computational Simulation of the Hydrostatic Pressure Effect on the Néel Temperature in Corundum-type Cr_2O_3

Yohei KOTA
National Institute of Technology, Fukushima College
Nagao 30, Taira-Kamiarakawa, Iwaki, Fukushima 970-8034

Corundum-type Cr_2O_3 is an antiferromagnet with a Néel temperature of $T_N = 308$ [K]. The effect of lattice compression on the Néel temperature of Cr_2O_3 has been experimentally observed using hydrostatic pressure; and the variation of T_N was reported in the range from -16 to $+15$ K/GPa [1, 2, 3, 4]. However, these previous experimental studies could not reach a consensus, even with respect to the sign of the pressure dependence of T_N. To provide a theoretical perspective, the effect of hydrostatic pressure on the T_N of Cr_2O_3 is examined by first-principles calculations and Monte-Carlo simulations.

First-principles calculations of the electronic structure of corundum-type Cr_2O_3 [Fig. 1(a)] were performed using the Vienna *ab-initio* Simulation Package (VASP) [5, 6]. The exchange-correlation functional was described within the local spin-density functional approximation by considering the on-site Coulomb interaction correction. Note that the $U-J$ parameter [7] in the Cr 3d orbital was set to 3.2 eV [8], which was non-empirically determined by the unrestricted Hartree-Fock method. The cutoff energy of the plane wave basis was set to 520 eV and a Γ-point cenered 4×4×1 k-point grid was used. Structural optimization for ionic positions and cell shape was carried out with a fixed cell volume. the exchange coupling constants between Cr spins up to the fifth-nearest neighbors, J_1–J_5 [Fig. 1(b)], were evaluated by fitting the energy variation of the ground state and exited states with a noncollinear spin configuration. [9] Parallel computations were performed using 1 CPU (12×2 cores) of the System B.

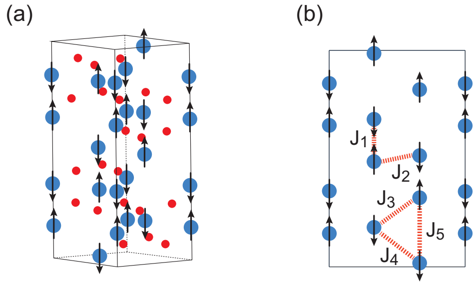

Figure 1: (a) Schematics of the hexagonal unit cell and spin configuration of corundum-type Cr_2O_3 (blue and red spheres are Cr and O, respectively). (b) The exchange coupling constants up to the fifth-nearest neighbors, J_1–J_5.

Figure 2 shows the pressure dependence of J_1–J_5. Note that the positive (negative) value indicates the antiferromagnetic (ferromagnetic) interaction. The first-nearest neighbor constant J_1, and the second-nearest neighbor constant J_2, linearly increase with increasing pressure, whereas the other constants, J_3, J_4, and J_5, are basically constant (although the J_3 and J_4 points seem to overlap, they are not equal; the $|J_3|$ values are approximately 0.2 meV smaller than the $|J_4|$ values over the entire region).

By substituting the J_1–J_5 values shown in Fig. 2(a) into the classical Heisenberg model,

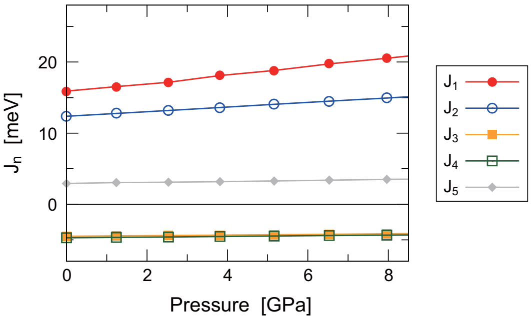

Figure 2: Pressure dependence of the exchange coupling constants up to the fifth-nearest neighbors, J_1–J_5.

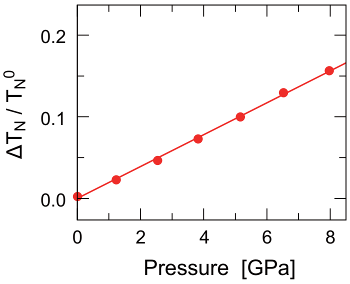

Figure 3: Néel temperature variation of Cr_2O_3 as a function of pressure, where T_N^0 denotes T_N at $P = 0$, and $\Delta T_N = T_N - T_N^0$.

the Néel temperature T_N for Cr_2O_3 is evaluated by Monte-Carlo simulation. The result is shown in Fig. 3, where T_N increases monotonically with pressure due to the increase in J_1 and J_2. Estimation of the slope of T_N with respect to P from Fig. 3 gives:

$$\frac{1}{T_N} \cdot \frac{dT_N}{dP} = +1.9 \times 10^{-2}\ [\mathrm{GPa}^{-1}].$$

In previous experiments on the effect of hydrostatic pressure, the obtained $(1/T_N)(dT_N/dP)$ values were -5.2×10^{-2} GPa^{-1} by Worlton *et al.* [1], $+4.9 \times 10^{-2}$ GPa^{-1} by Gorodetsky *et al.* [2], $+1.6 \times 10^{-2}$ GPa^{-1} by Alberts [3], and -0.3×10^{-2} GPa^{-1} by Bayarjargal and Winkler. [4]. Comparison of the results of the present calculation and previous experiments indicates that the absolute values of the slope are around the same. The sign of the slope for the calculated result is in agreement with the experimental results of Gorodetsky *et al.* and Alberts. In particular, the calculated result $+1.9 \times 10^{-2}$ GPa^{-1} is similar to an experimental value of $+1.6 \times 10^{-2}$ GPa^{-1}.

In summary, the effect of hydrostatic pressure on the Néel temperature T_N for Cr_2O_3 is studied by employing first-principles calculations and Monte-Carlo simulations. The obtained results indicate an increase in T_N with increasing pressure P, because the exchange coupling constants between Cr spins in the first and second nearest neighbors are enhanced. The calculated $(1/T_N)(dT_N/dP)$ is quantitatively comparable with an experimental value by Alberts [3].

This work was supported by ImPACT Program of Council for Science, Technology and Innovation (Cabinet Office, Government of Japan).

References

[1] T. Worlton, R. Brugger, and R. Bennion, J. Phys. Chem. Solids **29**, 435 (1968).

[2] G. Gorodetsky, R. M. Hornreich, and S. Shtrikman, Phys. Rev. Lett. **31**, 938 (1973).

[3] H. L. Alberts, J. Phys. Soc. Jpn. **38**, 1541 (1975).

[4] L. Bayarjargal and B. Winkler, Appl. Phys. Lett. **102**, 182403 (2013).

[5] G. Kresse and J. Hafner, Phys. Rev. B **47**, 558 (1993).

[6] G. Kresse and J. Furthmüller, Phys. Rev. B **54**, 11169 (1996).

[7] S. L. Dudarev, G. A. Botton, S. Y. Savrasov, C. J. Humphreys, and A. P. Sutton, Phys. Rev. B **57**, 1505 (1998).

[8] N. J. Mosey, P. Liao, and E. A. Carter, J. Chem. Phys. **129**, 014103 (2008).

[9] Y. Kota, H. Imamura, and M. Sasaki, J. Appl. Phys. **115**, 17D719 (2014).

Study on structure, formation, and physical properties of multiatomic vacancies and clusters of 2D semiconductors

Hiroyuki KAGESHIMA
Interdisciplinary Graduate School of Science and Engineering, Shimane University
Nishi-Kawatsucho, Matsue, Shimane 690-8504

Two dimensional (2D) semiconductors such as graphene, h-BN, and transition metal dichalcogenide (TMD) show very unique physical properties. In our project, we focus on the physical and structural properties of defects, surfaces and interfaces of them [1].

TMD recently attracts many researchers because of its two-dimensional feature as graphene. The field effect transistor based on TMD shows very high on/off ratio, which cannot be realized in that based on graphene [2]. TMD is also expected as a unique two-dimensional light emitting material because of its direct band gap nature [3]. Therefore, the crystal growth of TMD is studied widely. To obtain TMD crystal with high quality, it is important to know its growth mechanism. We focus on the very initial stage of the crystal growth of MoS_2, which is the most commonly studied material between the TMDs.

We have calculated Mo_xS_y clusters for the purpose. We put Mo and S atoms in different ways at the initial, optimize the atomic structures, and select the most stable one from each set of Mo and S complexes. The calculations were performed based on the first-principles calculation with the GGA density functional, plane wave bases, and pseudopotentials. Program package PHASE [4] was employed.

The results indicate that Mo atoms prefer direct bonding with each other (Fig. 1). We can obtain clusters with only Mo-S bonds and without any Mo-Mo bonds when the cluster contains more than 8 S atoms. This indicates that the ratio of Mo and S exceeds 1 and 2 of bulk MoS_2 crystal to obtain a good seed cluster. We can conclude that S rich condition is important in the crystal growth process to obtain crystal with high quality.

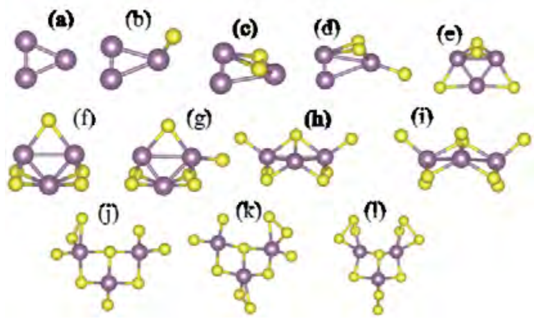

Figure 1: Optimized atomic structures for Mo_3S_y clusters.

References

[1] S. Urasaki and H. Kageshima, Extended Abstract of 2015 International Conference on Solid State Devices and Materials, PS-13-17 (2015).

[2] B. Radisavljevic, et al, Nature Nanotechnol. 6, 147 (2011).

[3] R. S. Sundaram, et al, Nano Lett. 13, 1416 (2013).

[4] https://azuma.nims.go.jp/cms1

First-principles simulation of electrolyte diffusion processes on constant-potential electrodes

Chunping HU[1,2]
[1]*Elements Strategy Initiative for Catalysts and Batteries (ESICB), Kyoto University,*
1-30 Goryo-Ohara, Nishikyo-ku, Kyoto 615-8245, Japan
[2]*Research Center for Computational Design of Advanced Functional Materials (CD-FMat),*
National Institute of Advanced Industrial Science and Technology (AIST),
Tsukuba, Ibaraki, 305-8565, Japan

In recent years, there have been much progress on the study of sodium-ion battery (SIB), which is a promising alternative to widely-used lithium-ion battery. To improve the efficiency of such second-battery systems, it is necessary to clarify the diffusion mechanism of electrolytes on electrodes. In the experimental condition, bias voltages are applied during charging or discharging, and thus electrode reactions (including diffusion) proceed at constant electrode potentials, as in the case of scanning tunneling microscope (STM). However, in theoretical research, especially in the study of reaction paths and energy barriers, it is traditionally assumed that the charge injected to the electrode is constant, without control on the potential.

In the present work, we aim to perform realistic first-principles simulation of electrolyte diffusion processes on constant-potential electrodes, using nudged elastic band (NEB) calculations at constant chemical potentials of electrons (constant μ_e). This method is realized by using the static version of the constant-μ_e scheme of Bonnet *et al.*, originally developed for molecular dynamics simulations [1]. In connection to a potentiostat, the system is automatically supplied with charges driven by the force arising from the difference of the instantaneous and the target μ_e. The constant-μ_e condition can be efficiently achieved by minimizing this force.

As a benchmark calculation, we have carried out simulations of bias-dependent diffusion of water on an Al(111) surface, using the above scheme. All calculations are carried out on System B and C, using the program package Quantum ESPRESSO [2]. Our results show that there are significant changes in diffusion barriers and paths under bias voltages. This serves to clarify the origin of experimental observations. Comparative studies also show that the conventional scheme with a constant charge cannot give a good description of bias-dependent molecular diffusion because of strong interaction between the molecular dipole and the electric field: To maintain a constant potential, the charge supplied by the potentiostat varies significantly along the pathway [3].

References

[1] N. Bonnet, T. Morishita, O. Sugino, and M. Otani, Phys. Rev. Lett. **109**, 266101 (2012).

[2] P. Giannozzi *et al.*, J. Phys.: Condens. Matter **21**, 395502 (2009).

[3] C. Hu and M. Otani, to be submitted to Phys. Rev. Lett.

Stabilities, structures, and electronic properties of atomic-layered materials

Yoshitaka FUJIMOTO
Depertment of Physics, Tokyo Institute of Technology
Oh-okayama, Meguro, Tokyo 152-8551

Since the discovery of graphene, hexagonal boron nitride (h-BN) atomic layers have received much attention because of the structural and mechanical properties similar to graphene. On the other hand, the electronic structure of the h-BN layers is quite different from that of graphene; h-BN layer is a gapped material and graphene is a gapless material. Hence, the h-BN layered materials are promising candidates for future semiconducting device materials in nano-electronics and opto-electronics applications.

We here report atomic structures and electronic properties of carbon defects in h-BN monolayer using a first-principles total-energy calculation within the density-functional theory. We show that the donor and acceptor states can be induced when carbon atoms are replaced with boron and nitrogen atoms, respectively. We also show that the ionization energies of the donor and acceptor states are controllable by applying tensile as well as compressive strains [1].

The pristine h-BN monolayer has a two-dimensional unit cell with the optimized lattice constant of 2.48 Å, and it is in good agreement with experimental result, 2.49 Å. Calculated band gap of pristine h-BN sheet is 4.64 eV, which is also in good agreement with other results. The calculated B-C bond and C-N bond lengths in the h-BN monolayers replaced with the C atom at the N site and the B site are 1.48 Å and 1.38 Å, respectively, and those are longer and shorter than the B-N bond length of 1.43 Å in the pristine h-BN monolayer. These structural behaviors are in agreement with other results.

The ionization energy of the acceptor state monotonically decreases as the tensile strain increases, and it increases as the compressive strain increases. For the donor state, on the other hand, the ionization energy shows the unique behavior: The ionization energy decreases as the tensile strain increases, and the ionization energy also decreases rapidly when h-BN monolayer is under the compressive strain of less than 1 %, being different from the case of the acceptor state. Interestingly, the ionization energies for the acceptor and the donor states show different behaviors, especially in the compressive region. The ionization energy increases for the acceptor state, while it rapidly diminishes for the donor state with increasing the compressive strain.

In order to study the behavior of ionization energies for the donor state under the strains, we exmaine the energy differences between the donor-state level and the conduction-band minima at the K and the Γ points. The value of the energy gap at the K point decreases as tensile strains increase. On the other hand, the energy-gap value at the Γ point diminishes when the h-BN monolayer is compressed, and it remains almost unchanged in the region of the tensile strains. It is thus found that conduction-band minimum changes from the K point to the Γ point at the compressive strain of around 1 %.

In summary, we have examined the relationship between the strains and the electronic properties of carbon defects in h-BN monolayers on the basis of the first-principles density-functional calculations. The donor and acceptor states can be induced when boron and nitrogen atoms are replaced with the carbon atom, respectively. The ionization energies are controllable for donor and acceptor states by applying tensile and compressive strains. For the donor state, the conduction-band minimum changes from the K point to the Γ point at the compressive strain of around 1 %.

References

[1] Y. Fujimoto and S. Saito, Phys. Rev. B **93**, 045402 (2016).

Electronic Structure of Rare Earth Magnets

Hisazumi AKAI
Institute for Solid State Physics, University of Tokyo
Kashiwa-no-ha, Kashiwa, Chiba 277-8581

We have pointed out in our previous study that the chemical bonding between N and Sm plays an important role in the magnetic anisotropy change of Sm_2Fe_{17} from in-plane to uniaxial ones caused by the introducing of N [1]. This effect of N insertion was discussed in terms of change in the electronic structure calculated in the framework of LDA+SIC. Now, the main issue is whether the 4f states are dealt with properly in SIC. In the present study, we examine the applicability of SIC for the evaluation of the magnetic anisotropy of rare-earth (RE) magnets by comparing the results with various methods, in particular, the optimized effective potential (OEP) method. In this study, OEP is applied only on the RE sites. Admittedly, this is a drawback from the viewpoint of performing a consistent treatment of uncertainly inherent in the so-called KLI (Krieger-Li-Iafrate) constants. Putting this aside for the moment, we have calculated the electronic structure of RE magnets $R_2Fe_{17}N_x$ and RCo_5 (R=light RE), by OEP with exact-exchange (EXX) energy combined with Colle-Salvetti correlation energy.

Figure 1 shows the total energy changes as functiona of the tile angle of the crystal calculated using SIC, 0° corresponding to the magnetization along the z direction, 90° to the xy direction. Three different curves are the result of self-consistent calculations, the band energy, and the total energy obtained using the potential for the zero tilt angle, respectively. The three curves are more or less the same, indicating that these results are reliable.

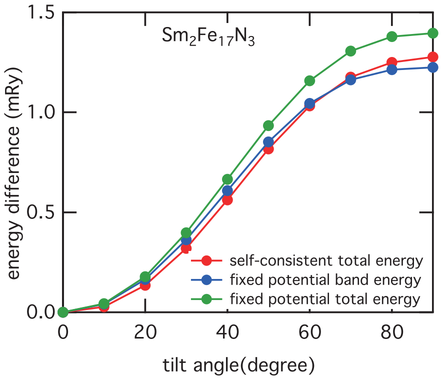

Figure 1: Total energy changes as functions of the tile angle of the crystal calculated using SIC

Unexpectedly, our preliminary results using OEP have shown considerable differences from the SIC results. There, the fixed potential total energy, which is supposed to be virtually the same as the self-consistent potential result, shows a considerably larger anisotropy energy than the result of the SIC calculations. Moreover the fixed potential band energy energy largely deviates from the behavior of total energy. These facts indicate that the OEP results are not reliable anymore for the calculation of the magnetic anisotropy. We are now analysing the origin of this inconsistency.

The calculations are performed using system B of the ISSP supercomputer systems and KKR-Green's function code (AkaiKKR).

References

[1] M. Ogura and H. Akai, J. Phys. Soc. Jpn 84, (2015) 084702.

First-principles study on the defects in semiconductors

Jun YAMAUCHI
Faculty of Science and Technology, Keio University
3-14-1 Hiyoshi, Kohoku-ku, Yokohama-shi, Kanagawa 223-8522

As the size of devices on integrated circuits decreases, the behavior of dopant atoms make relatively larger effect on the device performance. Especially, it is very important to understand the unfavorable defects including the dopant atoms. The experimental observations on each defect is extremely difficult. One of the major difficulties for detecting dopant configurations is the very weak signals from the defects of very low concentration comparing to those from the matrix semiconductors. However, recently, as a solution for the above problem, it is suggested to use powerful synchrotron radiation facilities to measure the X-ray photoelectron spectroscopy (XPS) signals of defects. On the other hand, there have been few reliable first-principles core-level XPS calculations for impurity defects in semiconductors, because the local potential boundary condition of defect model systems has not yet been sufficiently evaluated. To obtain reliable shifts in the XPS binding energy, it is necessary to take a sufficiently large supercell for a defect.

To investigate the dependence of the substrate semiconductors on the XPS binding energies, we carried out a comprehensive study on the B 1s core-level XPS binding energies for B defects in crystalline Si using a first-principles calculation with careful evaluation of the local potential boundary condition for the model system. We adopted cubic supercell corresponding to 1000 Si atoms and also considered the charged state and spin effect. The code used in this study is xTAPP, which is a hybrid paralleled density functional theory calculation program with plane-wave basis[1].

It is found that, while the spin polarization does not make large effect on the formation and XPS binding energy of defects, the charge state change those energies up to several tenth of eV in some cases. The electrically active clusters without any postannealing of ion-implanted Si were identified as icosahedral B_{12} clusters. The experimentally proposed threefold coordinated B was also identified as $\langle 001 \rangle$B-Si defects. For as-doped samples prepared by plasma doping, it is proposed that assuming that the XPS peak at 187.1 eV is due to substitutional B, the experimental XPS peaks at 187.9 and 186.7 eV in as-doped samples correspond to interstitial B at the H-site and $\langle 001 \rangle$B-Si defects, respectively.

References

[1] xTAPP (eXtended Tokyo Ab initio Program Package) (http://xtapp.cp.is.s.u-tokyo.ac.jp)

[2] J. Yamauchi, Y. Yoshimoto, and Y. Suwa: J. Appl. Phys. (in press).

Ab-initio DFT Calculations of Photocatalyst Material for Water Splitting

Kaoruho SAKATA, Takashi HISATOMI, Yosuke GOTO,
Taro YAMADA, Kazunari DOMEN
Artificial Photosynthetic Chemical Process Project,
The University of Tokyo, Kashiwa-no-ha, Kashiwa, Chiba 277-8581

Water splitting by photocatalyst under visible light irradiation is investigated keenly to reveal H_2 generation in practical use. Among the photocatalyst material, $La_5Ti_2CuS_5O_7$, and $La_5Ti_2Cu_{1-x}Ag_xS_5O_7$, which is partially substituted constituent elements from Cu to Ag, is one of candidate for photocatalyst of H_2 generation [1]. $La_5Ti_2CuS_5O_7$ has superior property having higher onset-potential compared with other materials when we used them as cathodic material, and also it is indicate to have one-dimensional conductive from experimental results [1]. However, it has not been clarified most of the material property yet, such as electric structures. This year, we focused on the assessment of band structure, especially its crystal orientation dependence of $La_5Ti_2CuS_5O_7$. Our group already studied Density of States of $La_5Ti_2CuS_5O_7$ and $La_5Ti_2AgS_5O_7$ using DFT calculation [2], therefore, we calculated the band structures of $La_5Ti_2Cu_{1-x}Ag_xS_5O_7$ (x= 0.08, 0.25, 0.5, 0.75), and assessed the correlation between its composition and calculated band gaps.

In this study, PW-DFT is used for all the calculation, which is implemented in VASP program. Structure of $La_5Ti_2CuS_5O_7$ is referred from Inorganic Crystal Structure Database (ICSD) [3], and $[La5Ti_2Cu_{1-x}Ag_xS_5O_7]_8$ or $[La_5Ti_2Cu_{1-x}Ag_xS_5O_7]_{12}$ was used as unit cell. DFT calculation is performed using PBE functional, and under GGA-level. Kinetic-energy cutoff was set to 300 eV, Monkhorst-pack set 4×12×4.

Fig. 1 shows the band structures including VBM and CBM of $La_5Ti_2CuS_5O_7$ in [100],

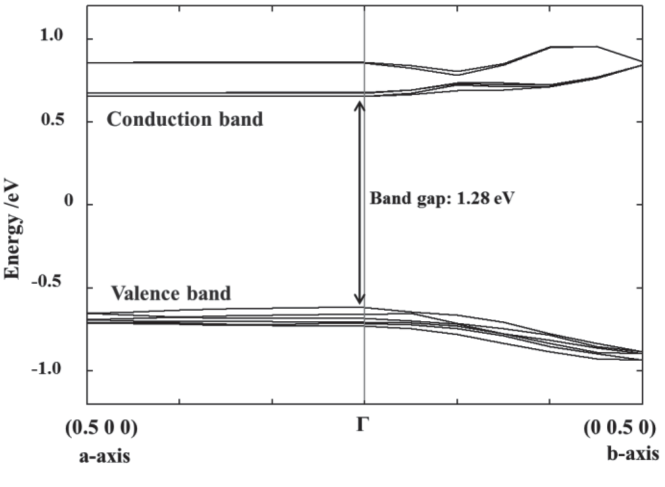

Fig. 1: Band structure of $La_5Ti_2CuS_5O_7$

obtained when $[La_5Ti_2Cu_{1-x}Ag_xS_5O_7]_8$ was used as an unit-cell. It is suggested that gradient of the band in [100] direction is flat compared with that in [010] direction. Previous experimental results [1] indicated that $La_5Ti_2CuS_5O_7$ has one-dimensional conductive, and our calculation results may have comparable to experimental tendency. In addition, band gap of $La_5Ti_2Cu_{1-x}Ag_xS_5O_7$ was calculated and it is indicated that band gap of $La_5Ti_2Cu_{0.5}Ag_{0.5}S_5O_7$ was smaller than that of $La_5Ti_2CuS_5O7$ and $La_5Ti_2AgS_5O_7$. This results is corresponds to the experimental results which is studied using ultraviolet-visible diffuse reflectance spectroscopy (DRS).

.

References

[1] T. Hisatomi, *et al.*, Energy Environ. Sci., **8** (2015) 3354.

[2] T. Suzuki, *et al.*, Phys. Chem. Chem. Phys., **14** (2012) 15475.

[3] V. Meignen, *et al.*, J. Solid State Chem., **177**, (2004) 2810.

Ab Initio Simulations of SiC Surface Reactions for Water Splitting and High-temperature Oxidation.

Kenji TSURUTA, Kazuhiro SHINIKE, Keiichi MITANI, and Atsushi ISHIKAWA

Graduate School of Natural Science and Technology, Okayama University, Okayama 700-8530

SiC surface provides versatile fields for catalytic reactions keeping the high chemical stability as well as its controllability of carrier injection as a wide-gap semiconductor. Using first-principles simulations, we have studied two types of reaction processes on SiC; H_2 production in the water splitting reaction and C-ring formation through high-temperature oxidation. All simulations are performed by using VASP, Vienna Ab-initio Simulation Package.

We have performed *ab-initio* molecular-dynamics (MD) simulations of H_2 production processes on 3C-SiC [001] surfaces. We first found that a Si-terminated (001) surface was more reactive than an O-terminated one against water adsorptions, and the reaction on the Si terminated surface was proceeded through the water dissociation as $2Si+H_2O \rightarrow Si\text{-}OH + Si\text{-}H$ or $Si+2H_2O \rightarrow Si\text{-}OH + H_3O^+$. For H_2 generation, we estimated reaction barriers of two reaction paths using Nudged Elastic Band (NEB) algorithm; (i) reaction between neighboring H atoms bonded to the Si's on the surface; (ii) reaction of H atoms between H_3O^+ molecule generated in the H_2O dissociation and Si-H. We find the process (ii), so called "Heyrovský process", has a lower barrier being approximately 0.55eV, while it's 2.4eV for the process (i). The process (ii) was also observed in the MD simulation at 900K (Fig. 1).

We have also investigated C-ring formation on [0001] surface of 4H-SiC via high-temperature oxidation. The C-ring formation is an incipient process of the graphene formation observed by high-resolution TEM measurement [2] and is proceeded through the desorption of Si atoms by oxidation on the SiC surface. We thus estimated the desorption energy from the energies required to remove Si atoms and create SiO_2 in bulk. Figure 2 depicts the Si desorption energy as a function of sequence of the removal from the terrace (atomically flat surface) and a $[11\bar{2}0]$ step[3]. We find that after the reaction reaches 7th removal, the process becomes unstable expediting the desorption and, in turn, the C-ring formation.

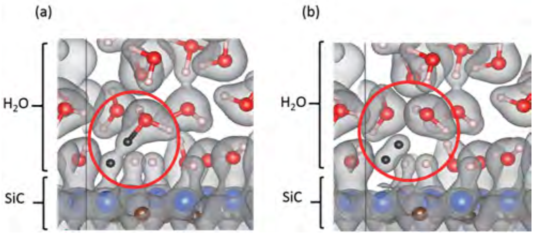

Fig. 1: Snapshots of surface reaction for (a) before and (b) after H_2 production.

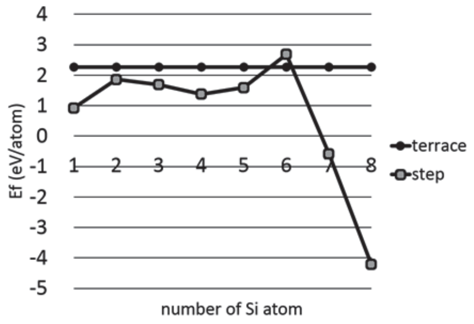

Fig. 2: Si desorption energy

References

[1] M. Kato *et al.*, Int. J. Hydrogen Energy **39**,4845(2014).

[2] W. Norimatsu *et al.*, Chem. Phys. Lett.**468**, 52(2009).

[3] T. Ohta *et al.*, Phys. Rev B **81**, 121411(R) (2010).

Calculation of Fe compounds Magnetism

Shuji OBATA
School of Science & Engineering, Tokyo Denki University
Ishizaka, Hatoyama, Hiki, Saitama 350-0394, Japan

The electronic binding energies J_{ij} of 3d electrons in Ni-Fe are induced from the tight binding interactions of the directed magnetic moments $\boldsymbol{\mu}_i$ bounded by the Hunts rule. These 3d and 4s electrons construct the eigenstates in external field environments. The magnetization processes are calculated by the Hamiltonian

$$\hat{H} = \sum_{i \le j} J_{ij} \hat{\boldsymbol{\mu}}_i \cdot \hat{\boldsymbol{\mu}}_j + \sum_{i \le j} W_{ij} + \sum_j \boldsymbol{\mu}_j \cdot \boldsymbol{H} \qquad (1)$$

including magnetic dipole moment interactions composed of spin magnetic fields

$$W_{ij} = \frac{1}{4\pi\mu_0 d_{ij}^3} \{(\boldsymbol{\mu}_i \cdot \boldsymbol{\mu}_j) - 3(\boldsymbol{\mu}_i \cdot \boldsymbol{e}_{ij})(\boldsymbol{\mu}_j \cdot \boldsymbol{e}_{ij})\}. \qquad (2)$$

The third term is magnetization energy in the external field $\boldsymbol{H}$. Distance vector is set as $\boldsymbol{d}_{ij}=\boldsymbol{e}_{ij}d_{ij}$ between the dipole moments at i and j.

Most of recent studies of the magnetizations are calculated with the quantum coulomb spin-spin interactions (Heisenberg model etc.) without the magnetic spin-spin interactions. However, one electron has the two fields as the static Coulomb field and the dynamic Ampere field. These fields are quantized with a Planck constant h. This Ampere field is called the Bohr magneton with the moment μ_B caused by the rotational motion of the spin. Thus, we must consider these two electron fields for the magnetization processes.

The well-known Hamiltonian excluding the second term cannot represent the Hysteresis magnetization curves in magnetic materials. The hysteresis loss in the magnetization processes are induced from the magnetic field energy, which do not include the coulomb energy J_{ij}. In this study, only the Hamiltonian composed of the second and the third terms are calculated for only clearing the hysteresis characteristics. The domain structures, the magnetization curves and the Barkhausen effects are investigated in these calculations.

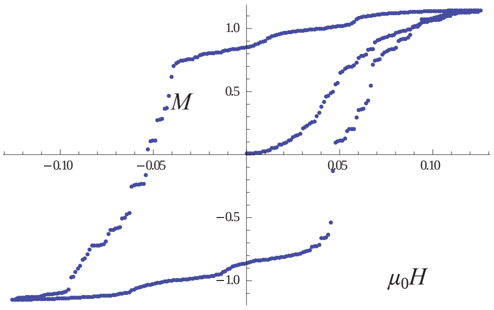

Fig.1. Ni_3Fe hysteresis curve of a 20×2×20 lattice point thin film.

Calculation processes of the energy in Eq. (2) require very much calculation resources, because the precise results are not obtained in restricted arias. The Barkhausen effects caused by the magnetic dipole moment interactions in FCC Ni_3Fe metal are cleared in this work. Using the ISSP system, the Fortran programs of the nano-Ni_3Fe magnetizations are executed by about 500 line programing. The used times are about 18 hours using PC cluster systems for drawing the Fig.1.

The dipole moment freedom is tentatively selected to 26 directions as not the energy minimum.[1][2] This limited condition may not fit with the real system. However now, it is not clear the existence of the quantized dipole moment directions instead of electromagnetic energy minimum states. The precise structures at the jump points of a circle in Fig. 2 are drawn in Fig. 3. Crystal Fe takes the BCC structure with the lattice constant a=2.86×10^{-10} [m] up to 911 ℃ and have the dipole moments of $2n_b\mu_0\mu_B$ per a lattice. The constants are n_b=2.22, permeability μ_0 and the Bohr magneton μ_B respectively. Through these results, the processes of the Barkhausen effects are clarified as the transitions of the dipole-moment arrangements in the magnetic domains.

1) S. Obata: Mater. Trans. **55** No 10 (2014) 1591-8.
2) S. Obata: IEEJ Trans. FM, **133** No 9 (2013) 489.

A First-principles study on magneto-crystalline anisotropy of ferromagnetic metal interfaces with spinel barrier

Yoshio MIURA

Kyoto Institute of Technology, Matsugasaki, Sakyo-ku, Kyoto 606-8585

In spintronics devices, required performance in magnetic tunnel junctions (MTJs) are a high tunneling magnetoresistance (TMR) ratio over 300% at 300K, low writing energy less than 1fJ/bit, and large thermal stability factor at room temperature. To this end, required properties for spintronic materials are the high spin polarization with low resistance, large perpendicular magnetic anisotropy with small magnetic damping constant α and a small saturation magnetization with large Curie temperature. Electric filed dependence of magneto-crystalline anisotropy of ferromagnetic materials is one of the crucial issue in the spintronics application, because of the suppression of energy consumption in the magnetization reversal. Control of magnetization reversal by voltage has been demonstrated in MgO-based magnetic tunnel junctions (MTJs), where the perpendicular magnetic anisotropies (PMA) of bcc-Fe interface had been changed, corresponding to the rate of 144fJ/Vm for the PMA enhancement [1]. Furthermore, the voltage control of the magnetic damping constant α of FM layer is also important in order to control the magnetization reversal with small energy consumption. Recent experiments show that the magnetic damping constant α of thin CoFeB layer in CoFeB/MgO/CoFeB MTJs strongly depends on the applied electric field when the CoFeB layer is less than 1.4nm[2].

In this study, we theoretically investigate the electric field (EF) modulation of magnetic damping constant of thin Fe-layer using the first-principles calculations. We calculated the magnetic damping constant of free-standing thin Fe-layer on the basis of the torque correlation model proposed by Kambersky[3] using the wave-function obtained by the first-principles calculations. We found that the magnetic damping constant α of free-standing thin Fe-layer increases with increasing the applied positive EF (Increase of electron accumulation at surface), which is opposite electric filed dependence as compared with the magneto-crystalline anisotropy, corresponding to 7% of damping constant α can be changed by EF=1[V/nm]. Furthermore, we found that EF dependence of magnetic damping of Fe surface can be attributed to the spin-conservation term of torque operator.

References

[1] D. Yoshikawa, *et al.*, APEX **7**, 113005 (2014).

[2] A. Okada, et al., APL **105**, 052415 (2014).

[3] V. Kambersky, CJPB **26**, 1366 (1976).

Search for new electronic properties of new nanoscale interfaces

Katsuyoshi KOBAYASHI
Department of Physics, Ochanomizu University
2-1-1 Otsuka, Bunkyo-ku, Tokyo 112-8610

In 2015 we studied IV-VI monolayers on alkaline-earth chalcogenide surfaces.

It is theoretically proposed that IV-VI monolayers are topological crystalline insulators (TCIs) in two dimensions (2D). Electronic states of insulators are classified according to topological numbers defined by point group symmetries of crystals. The first realistic materials of TCI are SnTe and its alloy with Pb. They are three-dimensional materials. Recently 2D materials of TCI are theoretically predicted, and their new applications were proposed [1]. However, they have not been materialized experimentally. We theoretically studied electronic states of 2D TCI thin films.

In 2014 we studied SnTe and PbTe monolayers as candidates of 2D TCIs [2]. Theoretical calculations show that isolated SnTe and PbTe monolayers are TCIs. However, planar structures of the monolayers are unstable, and TCI states are lost in buckled structures. For maintaining the planar structures of the monolayers we consider systems of the monolayers sandwiched between two alkali halide surfaces. We optimized atomic structures of the systems, and found that the planar structure of the monolayer maintains in SnTe monolayers sandwiched between NaBr surfaces. The electronic states of this system is TCI.

A problem is that the distorted-NaCl structure is energetically favorable than the single-layer structure for isolated IV-VI monolayers. The distorted-NaCl structure is formed by two single-layer structures. Total-energy calculations show that the interaction between a SnTe monolayer and a NaBr surface is weaker than that between SnTe monolayers. As a candidate of forming single-layer IV-VI monolayers on surfaces we consider alkaline-earth chalcogenide surfaces. The reason is that alkaline-earth chalcogenides are divalent ionic compounds, and the interaction with IV-VI monolayers is expected stronger.

Table 1: Calculated results.

	a (Å)	Δa (%)	ΔE (eV)
SnTe-NaBr	5.97324	−1.6	−0.463
SnTe-CaS	5.6903	−6.3	−0.380
SnTe-CaSe	5.91	−2.6	−0.152
SnTe-SrS	6.0198	−0.8	0.031
SnTe-SrSe	6.23	2.6	0.182
SnTe-CaTe	6.345	4.5	0.212
SnTe-BaS	6.3875	5.2	0.187

We computed total energy of IV-VI monolayers on various alkaline-earth chalcogenide surfaces. Some results for SnTe monolayers are listed in Table 1 as an example. a is the lattice constant of substrates. Δa is the difference of lattice constants between substrates and SnTe monolayers where the lattice constant of SnTe monolayers is 6.070 Å. ΔE is the difference of total energy per 1×1 2D unit cell between single-layer and double-layer structures of SnTe monolayers on substrates. Positive ΔE means that single-layer monolayers are favorable. This result suggests that single-layer monolayers may stably exist on some alkaline-earth chalcogenide substrates. Similar results are obtained for other IV-VI monolayers.

References

[1] J. Liu *et al.*: Nature Mat. **13** (2014) 178.

[2] K. Kobayashi: Surf. Sci. **639** (2015) 54.

Ab initio calculations for the silicon cluster superlattice

Nozomi ORITA, Yasushi IWATA
National Institute of Advanced Industrial Science and Technology
Tsukuba Central 2, Tsukuba, Ibaraki 305-8568

Recently, Iwata *et al.* found out the crystallographic coalescence of silicon (Si) clusters into a bcc superlattice structure with a lattice constant of 2.134 nm by direct deposition of a Si cluster beam on a graphene substrate[1]. The Si cluster superlattice have sp^3 structures in both the inside and the boundary of Si clusters. The size of the Si clusters composing the Si cluster superlattice and the electronic structure are unknown yet. Therefore, we have studied the crystal structure and the electronic structure of the silicon cluster superlattice using OpenMX[2] and obtained two suitable model structures constructed by Si_{211} and Si_{235} clusters as shown in Fig.1[3]. The lattice constants of the Si_{211} and Si_{235} cluster superlattices are 2.167 and 2.133 nm, respectively, and are in good agreement with the experimental value, 2.134nm.

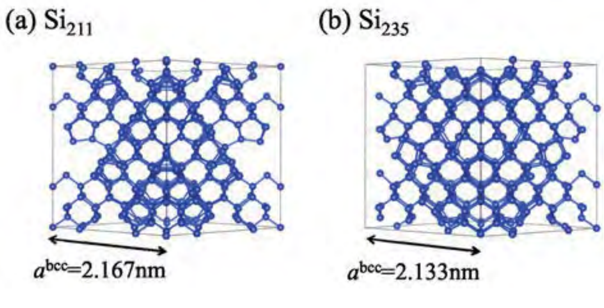

Figure 1: (a) Si_{211} and (b) Si_{235} cluster superlattices in the conventional bcc unit cells.

This year, we have performed *ab initio* calculation of the electron energy-loss spectra (EELS) of those Si cluster superlattices using QMAS code[4] on the ISSP supercomputer system B and the results are shown in Fig.2. The EELS of the Si_{211} cluster superlattice is more similar spectrum to that of the actual superlattice than that of the Si_{235} cluster superlattice.

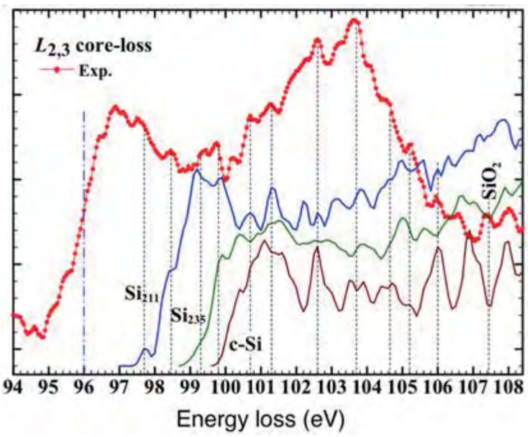

Figure 2: Si $L_{2,3}$ electron energy-loss spectra.

References

[1] Y. Iwata, K. Tomita, T. Uchida, and H. Matsuhata, Cryst. Growth Des. **15** (2015) 2119.

[2] T. Ozaki *et al.*, http://www.openmx-square.org/

[3] Y. Iwata, N. Orita, T. Uchida, and H. Matsuhata, Proc. Advanced Materials World Congress 2015, Chapter 10, p. 5.

[4] S. Ishibashi *et al.*, http://qmas.org/

Trapping of hydrogen isotopes in tungsten vacancy

Kazuhito Ohsawa
Institute for applied mechanics, Kyushu University
Kasuga-koen 6-1, Kasuga-shi, Fukuoka 816-85802

Tungsten (W) and its alloys are plausible candidates for plasma facing materials (PFMs) in fusion reactors due to their excellent properties, e.g. high melting point and low hydrogen solubility etc. However, a large amount of hydrogen isotopes (H, D, T) is retained in W specimens at lattice defects nucleated in irradiation circumstance. In particular, T inventory in W materials is an important issue for the safety of fusion reactors because T is a radioisotope whose half-life is about 12 years.

In the present study, the amounts of H isotopes trapped at monovacancies in the W materials are calculated in a thermodynamic model. Binding energies are estimated in terms of first-principle calculations on the basis of density functional theory. The isotope effect is derived from the difference of the zero-point energy of each H isotope.

The binding energies of H isotopes to a W monovacancy are shown in Fig. 1 as a function of the number of H isotopes. A maximum of 12 H atoms are accommodated in a vacancy. An important result is that the lighter H isotopes have the larger binding energies. H isotope retentions are shown in Fig. 2. In the present study, we assume that coexistence of two types of H isotopes, H and D or D and T, because the W materials will be exposed to the high fluxes of D and T particles in actual fusion reactors. The initial H isotope concentrations, (C_H, C_D, C_T) are assumed to be 5x10^{-5} and vacancy concentration is 10^{-5}. The lighter H isotopes are more trapped in the W vacancy than the heavier ones by reflecting the binding energies.

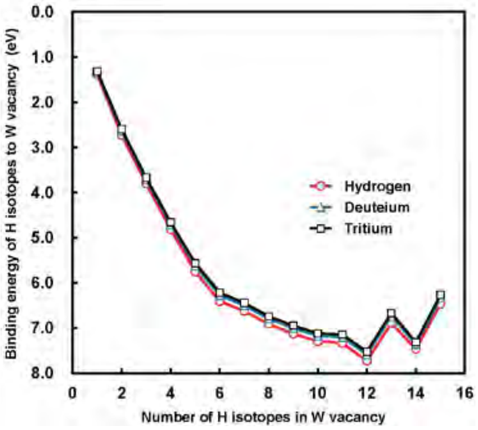

Fig. 1: Binding energy of each H isotope.

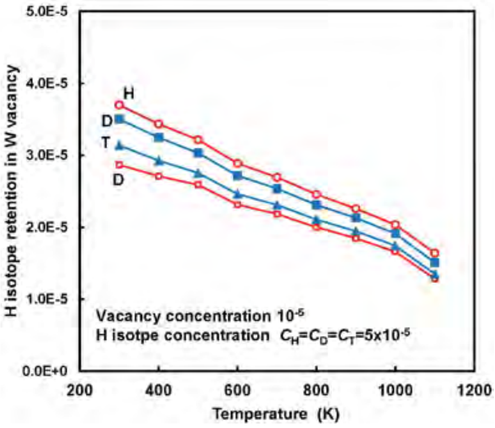

Fig. 2: H isotope retentions in W vacancy.

First principles calculations on electronic structures, magnetism, and electric field effects in transition-metal films and organometallic complexes

Kohji NAKAMURA
Department of Physics Engineering, Mie University
Tsu, Mie 514-8507

Symmetric and asymmetric exchange stiffnesses in transition-metal thin films — Controlling and designing spin-texture, which may be characterized by symmetric and asymmetric exchange stiffness, in transition-metal thin films have received much attention in fundamental and applied physics. Here, from first-principles calculations by using the full-potential linearized augmented plane wave (FLAPW) method, the exchange stiffnesses in a prototypical transition-metal thin films with perpendicular magnetic easy axis, a Co monolayer on Pt(111), were calculated. The formation energy as a function of the wave vector of the spin spirals, relative to that of the ferromagnetic state, were calculated. When the spin-orbit coupling is introduced, an asymmetry in the formation energy with respect to the spiral wave vector, so-called Dzyaloshinskii-Moriya interaction, appears. By fitting a liner curve in q^2 and q, the symmetric and asymmetric exchange stiffnesses were estimated to be 169.9 meVnm^2 and 6.5 meVnm, respectively.

Electron configurations in organic-metal complexes — In organometallic molecules, effective on-site Coulomb inter-actions (U$_{eff}$) and electron configurations of d electrons are essential aspects in magnetic properties but it is often difficult to analyze it. Here, by using FLAPW method based on the constraint density functional theory, we systematically investigated for prototypical molecules of metallocenes, TMCp$_2$ (TM=Cr, Mn, Fe, Co, Ni).[1] Moreover, using non-empirical values of U$_{eff}$ determined from the linear response theory, the predicted electron configurations are in agreement with the experiments; the $^3E_{2g}$, $^6A_{1g}$, $^1A_{1g}$, $^2E_{1g}$, and $^3A_{2g}$ states for the CrCp$_2$, MnCp$_2$, FeCp$_2$, CoCp$_2$, and NiCp$_2$, respectively.

Carrier tuning in transition-metal dichalcogenides by external fields — Two-dimensional thin films with no inversion symmetry have considerable attention due to their unique electronic, magnetic and optical properties. Here, spin-valley band structure and hole carriers in a prototypical transition-metal dichalcogenide monolayer of MoS$_2$ in external electric and magnetic (Zeeman) fields were systematically investigated by using FLAPW method. The calculated results predict that a negative electric field excites linearly the hole carriers while the spin-valleys are attainable even in the high field of more than -10 V/nm. With a magnetic field, further, an imbalance in the number of the hole carriers in the opposite spin states can be introduced so as to tailor the hole carriers with a spin-polarization.

References

[1] Nawa,Y. Kitaoka, K. Nakamura, T. Akiyama, T. Ito, JAP**117**, (2015) 17E131.

Exploring of low-dimensional honeycomb materials consisting of heavy elements

Noriaki TAKAGI[1], Ryuichi ARAFUNE[2], Naoya KAWAKAMI[1], and Emi MINAMITANI[3]

[1]*Department of Advanced Materials Science, University of Tokyo*
Kashiwa-no-ha, Kashiwa, Chiba 277-8561,
[2]*International Center for Materials Nanoarchitectonics, National Institute for Materials, Science, 1-1 Namiki, Ibaraki 304-0044,*
[3]*Department of Materials Engineering, The University of Tokyo, 7-3-1 Hongo, Bunkyo-ku, Tokyo 113-8656, Japan..*

The discovery of one-atom thick carbon honeycomb sheet, graphene, has triggered the competition to form exotic honeycomb materials and to uncover their hidden properties. Two-dimensional (2D) honeycomb sheets consisting of Bi, Si, Ge and Sn atoms have gathered lots of attention. Theoretically, these 2D materials are promising candidates of 2D topological insulator because these materials have an energy gap at the Dirac point due to the spin-orbit interaction [1, 2].

Recently, we have investigated the geometric and electronic structures of Bi thin films grown on Si(111) and Au(111) substrates mainly by using scanning tunneling microscopy and spectroscopy (STM/STS). We found that the Bi thin films have two types of step edges; One shows a regular step edge and the other exhibits a reconstruction. Interestingly, the latter edge hosts a localized 1D electronic state [3]. In order to reveal the origin of the electronic state, we carried out density functional theory (DFT) calculations.

The DFT calculations were carried out by the plane-wave-based Vienna Ab initio Simulation Package (VASP) [4, 5] with the projected augmented wave method [6]. We calculated the total energy and the electronic band structure for various structure models. Each model consists of 8 layers of Bi and a vacuum of 18 Å thick along the surface normal. The Bi layer consists of 2x10 lattices. Both surface layers possess the edges. The structure models we calculated did not reproduce the experimental results, but we will continue the DFT analysis.

Reference

[1] S. Murakami: Phys. Rev. Lett. **97**, 236805 (2006).

[2] M. Ezawa, Phys. Rev. Lett. **109**, 055502 (2012).

[3] N. Kawakami, C.-L. Lin, M. Kawai, R. Arafune and N. Takagi, Appl. Phys. Lett. **107**, 031602 (2015).

[4] G. Kresse and J. Furthmüller: Phys. Rev. B **56**, 11169 (1996).
[5] G. Kresse and J. Furthmüller: Comput. Mater. Sci. **6**, 15 (1996).
[6] P. E. Blöchl: Phys. Rev. B **24**, 17953 (1994) 17953.

Geometric and electronic structures of magnetic molecules at solid surfaces

Noriaki TAKAGI[1] and Emi MINAMITANI[2]
[1]*Department of Advanced Materials Science, University of Tokyo*
Kashiwa-no-ha, Kashiwa, Chiba 277-8561
[2]*Department of Materials Engineering, The University of Tokyo, 7-3-1 Hongo,*
Bunkyo-ku, Tokyo 113-8656, Japan.

Metal phthalocyanines (MPcs) and their derivatives have gathered considerable attention because they exhibit unique properties [1-3]. Among them, MnPc, FePc and CoPc are typical magnetic molecules and the adsorption of these molecules on solid surfaces have been intensively studied. Recently, we have investigated the magnetism of FePc on noble metal surfaces by using scanning tunneling microscopy/spectroscopy (STM/STS) and magnetic circular dichroism. The in-plane magnetic anisotropy (MA) of the bulk FePc changes to out-of-plane MA upon the adsorption on Cu(110) covered with a one-atom thick oxide layer [4] while the in-plane MA survives on Au(111) [5] and for FePc in the second layer on Ag(110).

In order to understand systematically the magnetic anisotropy of FePc and how the molecule-surface coupling impacts to the MA, we developed a theoretical approach. In this approach, we describe the electronic ground state as a linear combination of ^3E_g and $^3B_{2g}$ states. We calculated the eigenstates and eigenvalues by diagonalizing the molecular Hamiltonian with the linear combination. The molecular Hamiltonian includes the crystal field potential and the spin-orbit interaction at the Fe^{2+} ion. We used the deformations of molecular orbitals from the 3d atomic orbitals and the energy difference between the ^3E_g and $^3B_{2g}$ states. The deformations were evaluated by density functional theory (DFT) calculations. The DFT calculations were carried out by the plane-wave-based Vienna Ab initio Simulation Package (VASP) [6, 7] with the projected augmented wave method [8]. We found that the magnetism and MA of bulk FePc and the influence of the adsorption on solid surfaces can be understood reasonably with this approach.

Reference

[1] R. Bonnett: Chem. Soc. Rev. **24**, 19 (1995).

[2] C. C. Lanznoff and A. B. P. Lever: *Phthalocyanines, Properties and Applications* (Wiley, New York, 1996).

[3] K. Kadish, and R. Guillard: *Applications of Phthalocianines, The Porphrin Handbook* (Academic Press, San Diego, 2003).

[4] N. Tsukahara *et al.*: Phys. Rev. Lett.

102, 167203 (2009).
[5] E. Minamitani *et al.*: Phys. Rev. Lett. **109**, 086602 (2012).
[6] G. Kresse and J. Furthmüller: Phys. Rev. B **56**, 11169 (1996).
[7] G. Kresse and J. Furthmüller: Comput. Mater. Sci. **6**, 15 (1996) 15.
[8] P. E. Blöchl: Phys. Rev. B **24**, 17953 (1994).

Formation of C12A7 Surfaces and Work Function of C12A7:e$^-$

Yoichi KAMIHARA

Department of Applied Physics and Physico-Informatics, Keio University

3-14-1 Hiyoshi, Yokohama, Kanagawa 223-8522

1. Background

NH_3 is synthesized from N_2 and H_2 with an Fe-based double promoted catalyst for over 100 years[1]. In 21st century, it has been reported that Ru-loaded $[Ca_{24}Al_{28}O_{64}]^{4+}(e^-)^4$ (Ru/C12A7:e$^-$) works as an efficient catalyst for NH_3 synthesis[2] and characters of C12A7 surfaces are interested in. In this report, the forms of C12A7 surfaces are predicted and a work function of a C12A7:e- surface is derived by computation.

2. Method

All calculations were taken by Vienna *Ab-initio* Simulation Package (VASP)[3] with Projector Augmented Wave (PAW) method[4]. Perdew-Burke-Ernzerhof (PBE) functional[5] was adopted for exchange-correlation energy.

2.1 C12A7 surfaces identification

The forms of stoichiometric C12A7 surfaces should show several morphologies. Surfaces were formed by rupturing C12A7 crystal following to Sushko's work [6] in computation. A process of increasing lattice constant *c* and a process of structural optimization were repeated by turns.

2.2 Work function

A work function of C12A7:e$^-$ surface was derived from local potential distribution of a slab model optimized after self consistent calculations. The size of model is 1 × 1 × 3 crystal with a vacuum region of 7.193 nm.

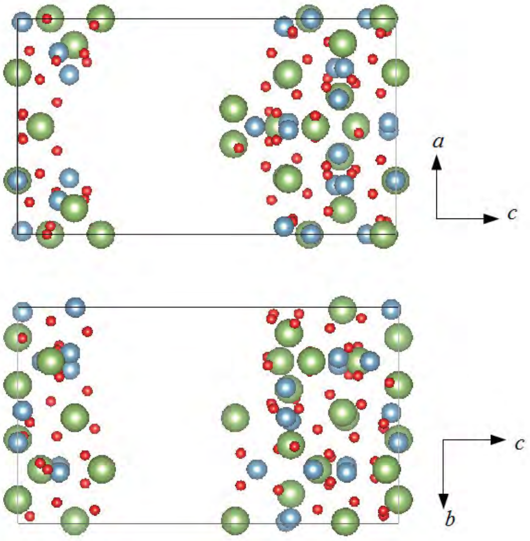

Fig. 1: Stoichiometric C12A7 model after rupturing process. Green, blue and red symbols represent Ca, Al and O ions, respectively.

3. Results

Figure 1 shows the ruptured C12A7 model. Obtained two surfaces have different forms. In the lower part, a nearly flat surface exists in the left and a rough surface exists in the right as literature [6]. On the other hand, both surfaces are rough in the upper view. Al-centered tetrahedrons also remain in ruptured surfaces.

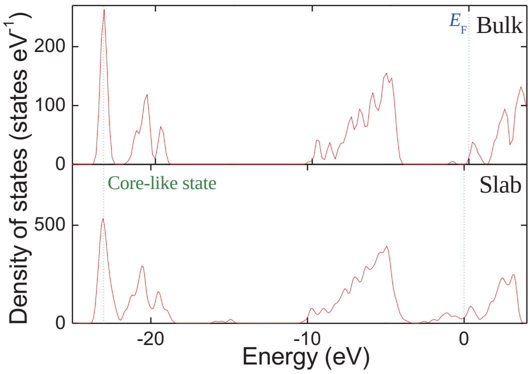

Fig. 2: Density of states of C12A7:e$^-$ bulk (upper) and slab (lower) models. A peak of core-like state lies at -23.0 eV and is defined as the standard.

Figure 2 shows density of states of C12A7:e$^-$ bulk and slab models. Since the Fermi level (E_F) of slab model does not correspond to that of bulk model, a core-like state of each is needed to be commonized to regard the E_F of bulk as real E_F. In Fig. 2, the E_F of bulk is 0.3 eV higher than that of slab. Considering E_F correction, the electronic potential distribution is plotted in Fig. 3. The periodic region in the left is the crystal and the constant region in the right is the vacuum. The work function of C12A7:e$^-$(001) surface was derived as 3.201(2) eV from the constant value of the vacuum region.

4. Conclusions

The form of C12A7 surfaces are predicted as two patterns. Besides, a work function of conducting C12A7:e$^-$ was derived as 3.201(2) eV by computation.

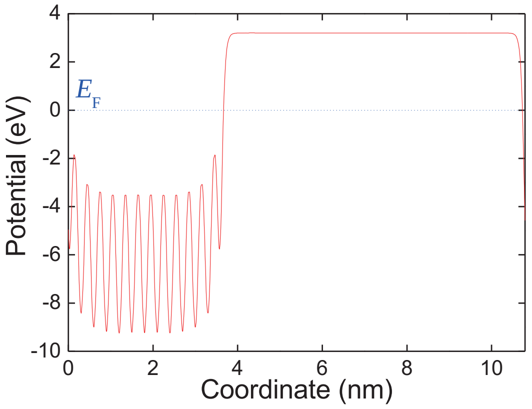

Fig. 3: Electronic potential distribution of C12A7:e$^-$(001) slab model. The horizontal axis is a coordinate perpendicular to the surface. The constant region in the right corresponds to the vacuum region.

References

[1] F. Haber: Z. Elktrochem. Angew. P. **16** (1910) 244.

[2] M. Kitano, *et al*.: Nature Chemistry **4** (2012) 934 .

[3] G. Kresse and J. Hafner: Phys. Rev. B **47** (1993) 558.

[4] P. E. Blöchl: Phys. Rev. B **50** (1994) 17953.

[5] J. P. Perdew, K. Burke and M. Ernzerhof: Phys. Rev. Lett. **77** (1996) 3865.

[6] P. V. Sushko, *et al*.: Proc. R. Soc. A **467** (2011) 2066.

First-principles calculation of electronic structure of thermoelectric material

Yukio SATO

Department of Materials Science and Engineering,

Kyushu University, 744 Motooka, Fukuoka, Fukuoka, 819-0395

Calcium cobalt oxide ($Ca_3Co_4O_9$: CCO) is known to exhibit excellent thermolelectric property mostly owing to its high Seebeck coefficient [1]. CCO has incommensurate layered misfit structure alternative stacking of CoO_2 and Ca_2CoO_3 layers (Fig.1) [2]. In particular, electronic state modulation of Co in the CoO2 layer is believed to be a key factor to obtain the high Seebeck coefficient. Thus, in order to understand the electronic structure of CCO, first-principles calculations were carried out in this study.

LSDA (local spin density approximation) calculations were carried out using the VASP code [4], where the effect of on-site Coulomb potential (*U*) was taken into account.

Figures 2 shows partial density of states (PDOS) of two particular Co sites in the CoO_2 layer for example. It is found that eighth and tenth Co sites from the left exhibit the magnetic moment of ~ 1.8 μ_B and slightly higher formal valence state from the others. Correspondingly, up-spin and down-spin PDOS is asymmetric with higher population in the energy range of 0 ~ 3 eV (Fig. 2(a)). Asymmetric PDOS but with smaller μ_B and is observed for the fourth, seventh, eleventh, and fourteenth Co from the left. On the other hand, in the case of other Co sites, symmetric PDOS and no magnetic moment is observed (Fig. 2(b)). It is thus considered that electronic structure of Co modulates in the CoO_2 layer.

References

[1] M. Shikano and R. Funahashi, Appl. Phys. Lett. **82** (2003) 1851.

[2] Y. Miyazaki, M. Onoda, T. Oku, M. Kikuchi, Y. Ishii, Y. Ono, Y. Morii, and T. Kajitani, J. Phys. Soc. Jpn. **71** (2002) 491.

[3] K. Momma and F. Izumi, J. Appl. Cryst. **44** (2011) 1272.

[4] G. Kresse and J. Hafner, Phys. Rev. B 47 , 558 (1993); ibid. 49 , 14 251 (1994).

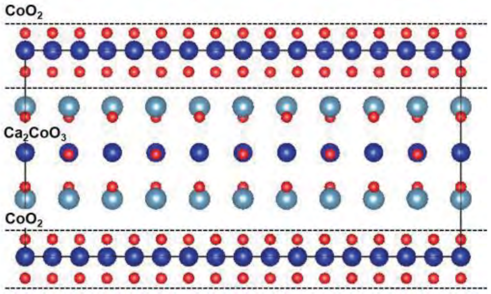

Fig. 1: Crystal structure of CCO. The figure is illustrated using VESTA [3]. The crystal structure is viewed along *a*-axis. Dark blue, light blue, and red circles represent Co, Ca, and O, respectively.

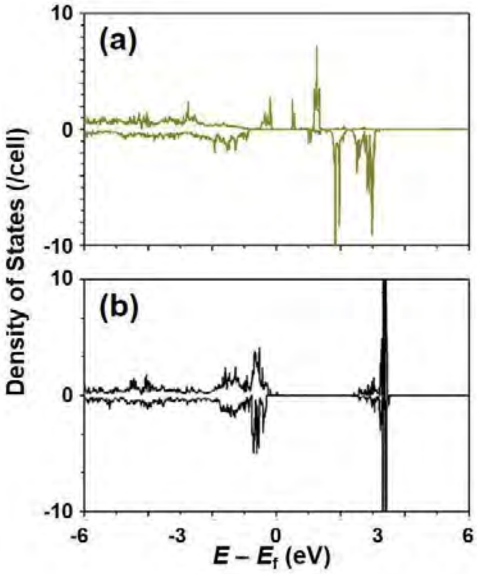

Fig. 2 PDOS of Co in the CoO_2 layer. Those of (a) eighth, (b) first Co site from the left.

Thermo-Chemical Wear Mechanism of Diamond Cutting Tool

Yutaka Uda, Shoichi Shimada
Osaka Electro-Communication University, Hatsu-cho, Neyagawa, Osaka 572-8530
Sakuro Honda
Technology Research Institute of Osaka Prefecture, Ayumino, Izumi, Osaka 594-1157

Demand has been increasing for highly durable molds of heat-resistant materials for the fabrication of complex and precise optical components with high aspect ratio. Diamond is the only ideal cutting tool material for high efficient ultraprecision metal cutting of complex three-dimensional metal works. However, it is well known that diamond cutting tool shows severe wear in cutting of heat-resistant materials such as steel. Preliminary ab-initio molecular orbital calculation by the authors showed that the essential mechanism of severe wear in cutting of steel is the dissociation of carbon atoms on diamond surface due to the chemical interaction with iron atoms in workpiece [1]. Therefore, to avoid chemical reactions between the carbon atoms of diamond and iron, modifying some chemical composition into steel for establishing a chemical bond between the iron atom and some other additional elements into iron is an effective method to suppress the tool wear. Nitrogen and carbon are the possible elements convenient for the purpose because they can easily diffuse into iron.

In this study, to understand the mechanisms of the initial stages of wear process of diamond cutting tool in machining of steel and effect of chemical modification of carbon and nitrogen, ab initio molecular dynamics calculations of chemical reaction on diamond surface in contact with Fe, Fe-C and Fe-N surfaces were carried out using double-grid method for real-space electronic-structure calculations developed by Professor T. Ono of University of Tsukuba [2].

At first step, the optimized atomic configuration of a $C_{10}H_{14}$ cluster was analyzed as the model of diamond (100) surface. And the thin Fe plate was analyzed as the models of Fe (100) surface. The dimensions of the plate, $x \times y \times z$, was $2a \times 2a \times a$, where a is lattice constant of Fe. The model has periodic boundaries in *x* and *y* directions and aperiodic boundary in *z* direction. Both models were successfully calculated.

References

[1] S. Shimada, H. Tanaka, M. Higuchi, T. Yamaguchi, S. Honda, K. Obata: 2004, Annals of the CIRP, **53**, 1 (2004) 57-60.

[2] T. Ono, K. Hirose: Physical Review Letters, **82** (1999) 5016.

First-Principles Momentum Dependent Local Ansatz Theory and Its Application to Fe Compounds

Yoshiro KAKEHASHI and Sumal CHANDRA
Department of Physics and Earth Sciences, Faculty of Science, University of the Ryukyus,
1 Senbaru, Nishihara, Okinawa, 903-0213, Japan

Although the band theory based on the density functional theory (DFT) is well-known to describe the properties of many metals and insulators, quantitative aspects of the theory become worse with increasing Coulomb interaction strength as found in ϵ-Fe, Fe-pnictides, cuprates, as well as heavyfermion system. We need alternative approaches to quantitative description of correlated electrons. We have developed the first-principles momentum dependent local ansatz (MLA) wavefunction theory on the basis of the tight-binding LDA+U Hamiltonian in order to describe the ground-state properties of correlated electrons quantitatively [1].

Introducing the three kinds of momentum dependent operators (,*i.e.*, the intra-orbital correlator $\tilde{O}^{(0)}_{imm}$, the inter-orbital charge-charge correlator $\tilde{O}^{(1)}_{imm'}$, and the inter-orbital spin-spin correlator $\tilde{O}^{(2)}_{imm'}$), we construct the first-principles MLA wavefunction $|\Psi_{\rm MLA}\rangle$ as

$$|\Psi_{\rm MLA}\rangle = \Big[\prod_i \Big(1-\sum_m \tilde{O}^{(0)}_{imm} - \sum_{m>m'} \tilde{O}^{(1)}_{imm'} - \sum_{m>m'} \tilde{O}^{(2)}_{imm'}\Big)\Big]\,|\phi\rangle. \quad (1)$$

The MLA takes into account all the two-particle excited states with the momentum-dependent amplitudes, so that it describes exactly the weak interaction limit, and describe well correlated electrons from the weak to strong Coulomb interaction regime.

In the implementation of the first-principles MLA, we first perform the Hartree-Fock band calculations for the LDA+U Hamiltonian. Using the energy eigenvalues and eigenvectors, we solve the self-consistent equations for the momentum-dependent variational parameters, correlation energy, and the Fermi level.

We performed the numerical calculations for the paramagnetic bcc Fe. Calculated Hund's rule correlation energy is found to be $\Delta\epsilon_{\rm H} \sim$ 3000 K, which explains the difference in magnetic energy between the LDA (5000K) and the DMFT, *i.e.*, DCPA (2000K). Calculated amplitude of local moment $\langle \boldsymbol{S}^2 \rangle = 2.58$ is in good agreement with the experimental value 2.56. We also found that the momentum distribution function bands along high-symmetry lines show a large deviation from the Fermi-Dirac function as shown in Fig. 1. Calculated mass enhancement factor 1.65 shows a good agreement with recent DMFT result 1.58 at finite temperatures as well as the experimental result 1.7 obtained by the ARPES.

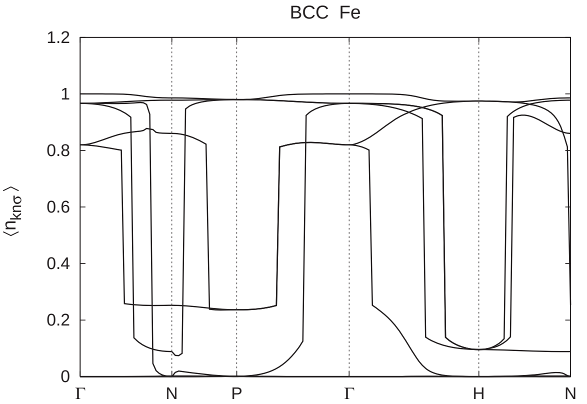

Figure 1: Momentum distribution functions along high-symmetry lines for bcc Fe

References

[1] Y. Kakehashi and S. Chandra, J. Phys. Soc. Jpn. **85**, 043707 1-5.

Electronic State and Proximity Effects around Interface in Layered Superlattices

Kunitomo HIRAI
Department of Physics, Nara Medical University
Kashihara, Nara 634–8521

The purpose of the present research is to elucidate characteristics of electronic state in superlattices with layered structures, in particular, to illustrate proximity effects of each layer on adjacent layers in the superlattices. This research of a first-principles electronic structure calculation is performed by means of the Korringa-Kohn-Rostoker (KKR) Green function method within the framework of the local spin density (LSD) functional formalism.

The calculation by means of the KKR method was so far carried out for superlattices of ferromagnetic layers with nonmagnetic spacer layers such as Fe/Cr, Fe/V, Fe/Cu, ... ones, with magnetizations of two successive Fe layers being aligned parallel or antiparallel. Oscillatory interlayer exchange coupling between ferromagnetic layers with respect to spacer thickness was investigated, and relation between bulk effects inherent in the spacer layer and the proximity effects due to the ferromagnetic layers was analyzed. In the calculation, every atom in a monolayer stacked in the superlattices is assumed to be equivalent, and there is one site in each monolayer. This assumption can be justified for the superlattices with ideal interfaces without structure, but not for those with realistic interfaces with structures like steps, islands, or such, and hence there are two or more sites in each monolayer for the superlattices with realistic interfaces.

A need of the calculation for superlattices with more sites in each monolayer arises also for layered superlattices of ordered alloys or compounds, which now attract broad interests particularly in viewpoint of spintronics. We then start preparation of the calculation for superlattices with more sites in each monolayer, which results in increase of the number of atoms in a unit cell and involves vast increase of computation times. In the preparation of the calculation, installation of parallelization with use of the OpenMP into program codes of the KKR methods is intended, together with parallelization with use of the MPI which was already achieved, that is, installation of hybrid parallelization is intended.

The installation of the OpenMP is in progress and will be achieved, and then the proximity effects in the superlattices with realistic interfaces will be investigated to elucidate the roles of the interfaces in the superlattices. The calculation will be carried out for Fe superlattices with steps, and magnetic frustration caused by the steps is investigated, in particular reference to possible mechanism of increase of total magnetization of the Fe layers, where fcc(001) or fcc(111) superlattices are considered together with usual bcc(001) ones and difference between those superlattices is to be analyzed. In addition, the calculation will be carried out for layered superlattices of ordered alloys, such as fcc(001) superlattices consisting of Fe and FePt layers, in particular reference to ferromagnetic or antiferromagnetic coupling between layers and within a monolayer.

Theory of magnetic alloys with octahedral frustration

Takashi UCHIDA
Hokkaido University of Science
4-1, 7-15, Maeda, Teine-ku, Sapporo 006-8585

Magnetic alloys with octahedral frustration such as Mn_3X (X=Pt, Rh, Ir) and Mn_3AN (A=Ga, Zn) have attracted attention because the competing and frustrated interactions in these systems give rise to temperature-driven magnetic phase transitions that accompany a peculiar magnetic structure (Mn_3Pt) or a large magnetovolume effects (Mn_3AN). Recently, we have applied the first-principles molecular spin dynamics (MSD) method to Mn_3X (X=Pt, Rh, Ir) and explained the magnetic phase transitions in terms of the temperature dependence of the electronic structure [1]. Although the obtained results are reasonable and consistent with experiment, they did not reproduce the details of the electronic structure because of using a small number of recursion levels in the local electronic structure calculations by the recursion method. In the present research, we have revised the calculation scheme of the MSD allowing for a large number of recursion levels in the recursion calculations. To test this scheme, we have calculated the electronic and magnetic structures of Mn_3X (X=Pt, Rh, Ir).

The MSD theory is formulated by incorporating the first-principles TB-LMTO Hamiltonian into the MSD approach for itinerant magnets on the basis of the functional integral method and the isothermal MSD technique [1]. The MSD approach allows us to determine automatically the magnetic structure of a large system with several hundred atoms in a unit cell at finite temperatures. In the present MSD analysis, we solved the isothermal MSD equations of motion by using site-dependent effective medium in order to treat the magnetic phase transition correctly. We used the recursion method to calculate the local electronic structure in determining the site-dependent effective medium and in calculating magnetic forces at each time step of the MSD equations of motion. Because the time-consuming recursion process consists of parallelizable loop calculations, we utilized the MPI parallel calculation scheme in the recursion calculation. In the calculations of the site-dependent effective medium, we embed the supercell with $4 \times 4 \times 4$ fcc lattice in a large cluster consisting of $5 \times 5 \times 5$ supercells, each of which are connected by the periodic boundary condition. By virtue of using the large cluster, we were able to calculate the local electronic structure up to recursion levels (7,9,19) for s, p, and d orbitals.

The calculated the d-electron densities of states (DOS) of Mn_3X (X=Pt, Rh, Ir) have a double-peak structure similar to those [1] obtained by the ground-state TB-LMTO calculations. With increasing temperature from 25 K, the Mn-Eg DOS of Mn_3Pt at the Fermi energy, which is located between the double peak, increases around 350 K, while those of Mn_3Rh and Mn_3Ir do not show appreciable increase. The results are consistent with the phase transitions of Mn_3X (X=Pt, Rh, Ir) [2].

References

[1] T. Uchida, N. Kimura, and Y. Kakehashi: J. Korean Phys. Soc. **62** (2013) 1748; Y. Kakehashi, S. Akbar, and N. Kimura, Phys. Rev. B**57** (1998) 8354.

[2] T. Uchida, Y. Kakehashi, and N. Kimura: J. Magn. Magn. Mater. **400** (2016) 103.

3.3 Strongly Correlated Quantum Systems

Numerical Studies on Low-Energy Effective Models for Thin Films of Cuprates by High-Precision Variational Wave Functions

Takahiro Misawa and Masatoshi Imada
Department of Applied Physics, University of Tokyo
Hongo 7-3-1, Bunkyo-ku, Tokyo 113-8656

Recently, in thin films or interfaces of high-T_c superconductors, many exotic phenomena have been found. For example, in recent experiments on interfaces of a cuprate superconductor, $\mathrm{La_2CuO_4/La_{2-x}Sr_xCuO_4}$ [1], unexpected pinning of the $T_c \sim 42\mathrm{K}$ has been found by systematically changing the doping rates of the metallic phase $\mathrm{La_{2-x}Sr_xCuO_4}$ between $x = 0.2$ and 0.5. This behavior is in marked contrast with the bulk system where the dome structures of T_c are established. The discovery has renewed interest in intrinsic nature of the purely two-dimensional $\mathrm{CuO_2}$ plane, because the superconductivity was shown to occur sharply at a single atomic layer located at the interface.

In this project, to clarify microscopic origin of unconventional pinning of critical temperatures of superconductivities observed at the interfaces of $\mathrm{La_2CuO_4/La_{2-x}Sr_xCuO_4}$, we study multi-layer Hubbard model as a realistic model for interfaces of the cuprates, which is defined by

$$\begin{aligned} H = &-t \sum_{\langle i,j\rangle,\sigma,\nu} (c^{\dagger}_{i\sigma\nu} c_{j\sigma\nu} + \text{h.c.}) \\ &- t_z \sum_{i,\sigma,\langle \nu,\nu'\rangle} (c^{\dagger}_{i\sigma\nu} c_{i\sigma\nu'} + \text{h.c.}) \\ &+ U \sum_{i,\nu} n_{i\uparrow} n_{i\downarrow} - \sum_{i\nu} \epsilon_{\nu} n_{i\nu}, \qquad (1) \end{aligned}$$

where $c^{\dagger}_{i\nu\sigma}$ ($c_{i\nu\sigma}$) is the creation (annihilation) operator of an electron at ith site on the νth layer with spin σ and $n_{i\nu\sigma} = c^{\dagger}_{i\nu\sigma} c_{i\nu\sigma}$ is the corresponding number operator. For simplicity, we consider only the nearest-neighbor pair for the intra-layer transfer t. For the inter-layer transfer we take $t_z = -0.05t$ and the onsite Coulomb interaction is set to $U = 8t$ as realistic values for the cuprates. The layer-dependent onsite hole level is represented by ϵ_{ν}, which simulates the effects of the inter-layer diffusion and exchange between La and Sr atoms around the interfaces [2].

For the multi-layer Hubbard model, we have performed high-accuracy many-variable variational Monte Carlo (mVMC) [3-4] calculations. The mVMC method is capable of describing quantum and spatial fluctuations allowing for an accurate estimate of the superconducting stability among competing orders present in strongly correlated systems.

As a result, we have found that carrier densities and superconducting correlations are pinned at the interfaces of the multi-layer Hubbard model in essential agreement with the experimental results. We have shown that the pinning emerges as a result of the inter-layer phase separation. Our result supports that the phase separation and associated enhanced uniform charge fluctuations hold the key to the understanding of the superconductivity in the cuprate superconductors.

References

[1] J. Wu *et al.*, Nat. Mat. 12, 877 (2013).

[2] G. Logvenov, A. Gozar, and I. Bozovic, Science 326, 699 (2009).

[3] D. Tahara and M. Imada, J. Phys. Soc. Jpn. 77, 114701 (2008).

[4] T. Misawa and M. Imada, Phys. Rev. B 90, 115137 (2014).

Theoretical study of novel physics by synergy between electron correlation and spin-orbit coupling

Yukitoshi MOTOME
Department of Applied Physics,
The University of Tokyo, Bunkyo, Tokyo 277-8581

We have theoretically studied the interplay between charge, spin, and orbital degrees of freedom through strong electron correlations and spin-orbit coupling. This year, we focused on the following three topics. We summarize the main achievements for each topic below.

(i) *Spin dynamics and phase transitions in Kitaev quantum spin liquids*: In some transition metal compounds, such as iridates and rhodates, the interplay between strong electron correlations and spin-orbit coupling brings about an anisotropic, bond-dependent exchange interaction in the Mott insulating state. The peculiar interaction is described by the so-called honeycomb Kitaev model, which has been extensively studied as it provides an exact spin liquid ground state. For clarifying fundamental physics related to the Kitaev model, we have studied the spin dynamics associated with the quantum spin liquid nature. Using the quantum Monte Carlo method and the cluster dynamical mean-field theory, we have calculated the magnetic susceptibility, dynamical spin structure factor, NMR relaxation rate T_1 [1], and Raman scattering spectrum [2]. The results provide the fingerprints of fractionalization of quantum spins into Majorana fermions. We have also studied the phase transitions from the quantum spin liquid to a long-range ordered state by adding the Ising interaction to the toric code in 2D and 3D (the 2D toric code is the anisotropic limit of the Kitaev model, and the 3D one is its extension to the higher dimension). We found that the system exhibits a peculiar bicritical phase diagram in 3D, while a quantum criticality in 2D [3]. We also published two review articles on the related topics [4,5].

(ii) *Noncoplanar spin configurations with chiral stripes in spin-charge coupled systems*: Noncoplanar spin textures, such as skyrmions, have attracted much attention, as they lead to unconventional transport phenomena through the spin Berry phase mechanism. We have investigated the possibility of new noncoplanar spin textures in itinerant magnets. Employing the Kondo lattice model with classical localized spins, we discovered two different types of noncoplanar spin textures. One is a double-Q state with scalar chirality stripes [5]. This finding has been validated by combination of large-scale numerical simulations, variational approach, and perturbative expansion. In this noncoplanar state, the chiral stripe gives rise to peculiar alternative helical currents along the stripes. The other is a multiple-Q state composed of a superposition of collinear up-up-down-down states [6]. Taking examples on the square and triangular lattices, we have showed that the multiple-Q states lead to topologically nontrivial states, such as the massless Dirac semimetals and Chern insulators.

(iii) *Charge-spin-orbital fluctuations in mixed valence spinels*: Mixed valence spinels provide a good playground for the interplay between charge, spin, and orbital degrees of freedom in strongly correlated electrons on a geometrically frustrated lattice. Among them, AlV_2O_4 and LiV_2O_4 exhibit contrasting and puzzling behavior: self-organization of seven-site clusters and heavy fermion behavior. We have performed a comparative study of charge-spin-orbital fluctuations in these two compounds, on the basis of the multiband Hubbard models constructed from the *ab initio* band calculations [7]. Performing the eigenmode analysis of the generalized susceptibility within the random phase approximation, we have found that, in AlV_2O_4, the relevant fluctuation appears in the charge sector in σ-bonding type orbitals. In contrast, in LiV_2O_4, optical-type spin fluctuations in the a_{1g} orbital are enhanced at an incommensurate wave number at low temperature.

References

[1] J. Yoshitake, J. Nasu, and Y. Motome: preprint (arXiv:1602.05253).

[2] J. Nasu, J. Knolle, D. L. Kovrizhin, Y. Motome, and R. Moessner: preprint (arXiv:1602.05277).

[3] Y. Kamiya, Y. Kato, J. Nasu, and Y. Motome, Phys. Rev. B **92** (2015) 100403(R).

[4] 那須 譲治, 宇田川 将文, 求 幸年: 日本物理学会誌 **70** (2015) 776.

[5] 求 幸年: パリティ **31** (2016) 22.

[5] R. Ozawa, S. Hayami, K. Barros, G.-W. Chern, Y. Motome, and C. D. Batista: preprint (arXiv:1510.06830).

[6] S. Hayami, R. Ozawa, and Y. Motome, preprint (arXiv:1603.06646).

[7] A. Uehara, H. Shinaoka, and Y. Motome: Phys. Rev. **92** (2015) 195150.

Analysis of an effective model with valence skipping effect using dynamical mean field theory

Akihisa Koga
Department of Physics, Tokyo Institute of Technology
Ookayama, Meguro, Tokyo 152-8551

Colossal negative thermal expansion in the nickel oxide $\mathrm{BiNiO_3}$ is recently found [1]. This phenomenon is considered to originate from the "valence skipping" nature of Bi ions and strong electron correlations intrinsic in Ni ions. Due to the valence slipping effect, at low temperature, the material is the insulator showing the characteristic valence as $\mathrm{Bi}^{3+}_{0.5}\mathrm{Bi}^{5+}_{0.5}\mathrm{Ni}^{2+}\mathrm{O}_3$. By applying pressure, it changes to $\mathrm{Bi}^{3+}\mathrm{Ni}^{3+}\mathrm{O}_3$, which is accompanied by a discontinuous volume shrinkage. In order to clarify the relation between the thermal expansion and valence skipping nature, an effective model with Coulomb interactions was analyzed by Hartree-Fock approximation [2].

In the present study, we address the Hubbard model, where the valence skipping nature in Bi ions and orbital degeneracy in Ni ions are taken into account. The schematic picture of this model is presented in Fig. 1. By applying dynamical mean-field theory and the continuous quantum Monte Carlo simulation to the model, we systematically examine the effect of the electron correlation in this model. In the Monte Carlo simulation, we use the ALPS library preinstalled in System B of the ISSP supercomputer system [3]. This library provides us with efficient parallelization in the Monte Carlo sampling.

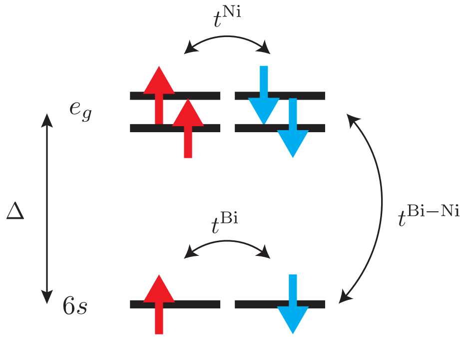

Figure 1: Schematic picture of the Hubbard model that we addressed.

Using the above technique, we newly find ferromagnetic and antiferro-orbital ordered phases due to the existence of the orbital degeneracy [4], in addition to charge ordered and antiferromagnetic phases discussed in the previous study [2]. The states that we find are stabilized in the case with the strong Coulomb interaction. We expect that the ferromagnetic and orbital ordered states could be experimentally observed at low temperatures.

References

[1] M. Azuma, W. Chen, H. Seki, M. Czapski, S. Olga, K. Oka, M. Mizumaki, T. Watanuki, N. Ishimatsu, N. Kawamura, S. Ishiwata, M. G. Tucker, Y. Shimakawa, and J. P. Attfield: Nat. Comm. **2** (2011) 347.

[2] M. Naka, H. Seo, and Y. Motome: Phys. Rev. Lett. **116**, (2016) 056402.

[3] B. Bauer *et al.*: J. Stat. Mech. **2011** (2011) P05001.

[4] S. Kojima, J. Nasu, and A. Koga: arXiv:1602.07831.

Photoinduced phase transitions in strongly correlated superconductors

Hideo AOKI
Department of Physics, University of Tokyo
Hongo, Tokyo 113-0033

FLEX+DMFT approach to the d-wave superconductivity[1]

The two-dimensional repulsive Hubbard model still harbours fundamental questions, among which is how the "Tc dome" in the phase diagram against the band filling can be understood. We have combined the dynamical mean field theory (DMFT) with the fluctuation exchange approximation (FLEX) to investigate strongly correlated systems, especially to obtain a phase diagram for d-wave superconductors[1]. The DMFT+FLEX method, which can also be viewed as a proposal for a new Luttinger-Ward functional, incorporates the momentum-dependent pairing interaction treated in FLEX into DMFT which can describe Mott's insulator, so that the method can describe anisotropic pairings along with the local correlation effects (Mott physics). We have applied the formalism to the two-dimensional repulsive Hubbard model to obtaine a phase diagram. The result does indeed exhibit a superconducting Tc-dome against band filling, both in the absence and presence of the Fermi surface warping (t'). We have traced back the origin of the dome to the local vertex correction from DMFT that gives a filling-dependence in the FLEX self-energy.

Light-induced collective Higgs mode in superconductors[2]

A superconductor illuminated by an ac electric field with frequency Ω poses an interesting problem. We have theoretically found that the ac modulation generates a collective precession of Anderson's pseudospins, hence a coherent amplitude oscillation of the order parameter, in the BCS state with a doubled frequency 2Ω through a nonlinear light-matter coupling[2]. We have formulated the problem in a mean-field to show that the induced pseudospin precession resonates with the Higgs amplitude mode of the superconductor at $2\Omega = 2\Delta$ with 2Δ being the superconducting gap. The resonant precession is accompanied by an enhancement of the third-harmonic generation. We have further explored the effect of electron-electron scattering on the pseudospin reso-

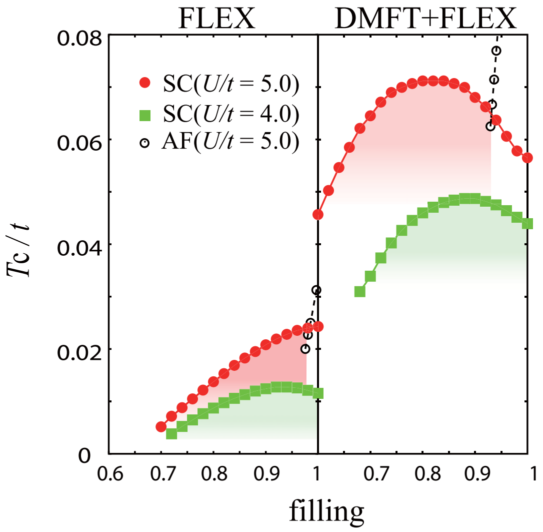

Figure 1: T_c vs band filling in FLEX (left panel) and in DMFT+FLEX (right) for different values of the Hubbard U. [1].

nance by applying the nonequilibrium dynamical mean-field theory (DMFT) to the attractive Hubbard model driven by ac electric fields. The result indicates that the pseudospin resonance is robust, although the resonance width is broadened due to electron scattering, which determines the lifetime of the Higgs mode.

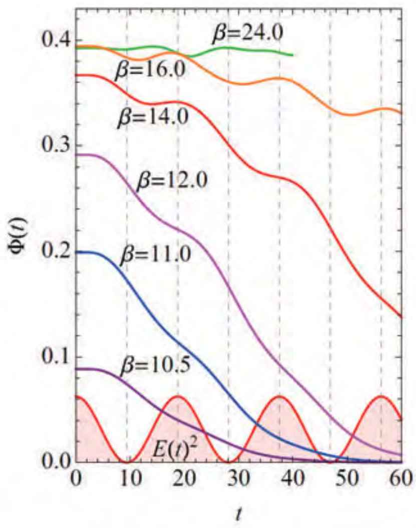

Figure 2: Temporal evolution of the superconducting order parameter $\Phi(t)$ calculated with the nonequilibrium DMFT for the attractive Hubbard model at half filling driven by the ac field with the infinite-dimensional density of states, $U = 2.25, A = 0.2$, and $\Omega = 2\pi/37.5$, for several temperatures (β^{-1}) for the initial states. The sinusoidal curve represents $E(t)^2 \propto \cos^2\Omega t$.[2].

Collective amplitude modes in strongly-coupled superconductors[3]

We have studied collective amplitude modes of the superconducting order parameter in strongly-coupled electron-phonon systems described by the Holstein model using the nonequilibrium DMFT with the self-consistent Migdal approximation as an impurity solver[3]. The frequency of the Higgs amplitude mode is found to coincide with the superconducting gap even in the strongly-coupled (beyond BCS) regime. Besides the Higgs mode, we find another collective mode involving the dynamics of both the phonon and the superconducting order parameter, which reflects a strong *electron-mediated phonon-phonon interaction.* We predict that these should be observed in time-resolved photoemission spectra.

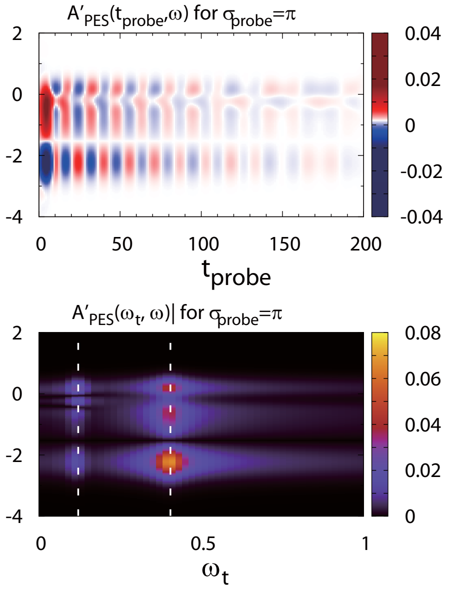

Figure 3: The spectral function $A(t, \omega)$ against t and ω and its Fourier transform. White vertical lines indicate the frequencies, ω_H and ω_{H2}, of the two collective modes.[3]

References

[1] M. Kitatani, N. Tsuji, H. Aoki: FLEX+DMFT approach to the d-wave superconducting phase diagram of the two-dimensional Hubbard model, *Phys. Rev. B* **92**, 085104 (2015).

[2] Naoto Tsuji and Hideo Aoki: Theory of Anderson pseudospin resonance with Higgs mode in a superconductor, *Phys. Rev. B* **92**, 064508 (2015).

[3] Yuta Murakami, Philipp Werner, Naoto Tsuji and Hideo Aoki: Multiple amplitude modes in strongly coupled phonon-mediated superconductors, *Phys. Rev. B* **93**, 094509 (2016).

Topological insulators in heavy-fermion systems

Tsuneya Yoshida
Department of Physics, Kyoto University, Kyoto 606-8502, Japan
Sakyo-ku, Kyoto 606-8502, Japan

Topological insulators attract much interest[1]. The electronic state of this system has nontrivial topology which predicts gapless excitations at the edge/surface. These gapless excitations are source of interesting phenomena; e.g., topological magnetoelectric effects and emergence of Majorana fermions. So far topological insulators are studied as free fermion systems. Recently, however, it has been pointed out that topological insulators can be realized in heavy-fermion systems where electron correlations are strong. In these systems, electron correlations and topology are expected to induce novel phenomena, and thus, understanding correlation effects on topological insulators is one of the important issues of this field.

In our study, we have analyzed heavy fermion systems having nontrivial topology. In particular, we have addressed temperature effects on topological Kondo insulators. Firstly, we have performed model calculation[2] by using real-space dynamical mean field theory (r-DMFT) combined with numerical renormalization group method. After that we addressed more detailed analysis[3]; LDA+DMFT is applied to SmB_6 which is a promising candidate for the topological Kondo insulator. In order to perform the large-scale numerical calculation, we have fully made used of the supercomputer resource at ISSP.

In Ref. [2], we have analyzed the Kane-Mele-Kondo lattice which is two-dimensional. With this method, we can study wide range of temperature[4], from $T \sim 10^{-4}t$ to $T \sim 10^{-1}t$. Here the bandwidth of the conduction electron is approximately $6t$.

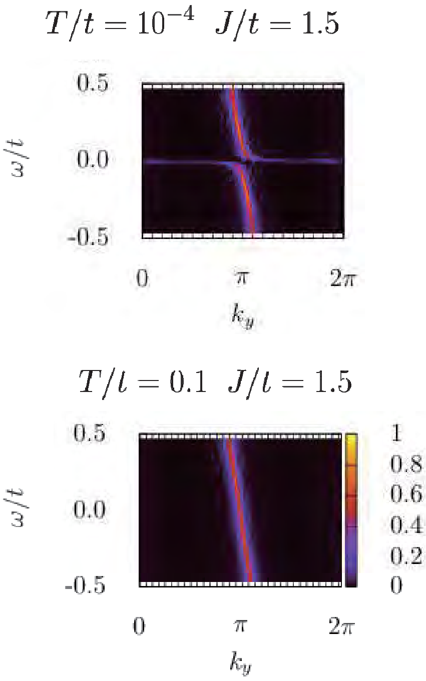

Figure 1: Gapless edge modes appearing at finite temperatures. Top and bottom panels represent data for $T = 0.1t$

As the result of the detailed analysis, we have found that gapless edge modes are restored by temperature effects. Around zero temperature, the Kondo effect is dominant and destroys topological structure. Correspondingly edge modes are gapped. With increasing temperature, however, the Kondo effect is suppressed and gapless edge modes are restored. We have observed this behavior by direct calculation of edge modes as well as the calculation of topological response in the bulk.

The restoration of gapless edge modes in finite temperature region is observed in Fig. 1. In this figure, we can see that edge modes are destroyed for $T = 10^{-4}t$, while the gapless modes are restored $T = 10^{-4}t$ and $T = 10^{-1}t$, respectively.

Furthermore, we have applied LDA+DMFT to SmB$_6$ [3]. Concerning the group velocity of this compound, two different experiments have reported different values; according to a transport measurement, the group velocity is $v \sim 200$meVÅ, while it is $v \sim 4$meVÅ according to an ARPES measurement. We have addressed this puzzle. Our study has elucidated that interplay between the Kondo effect and temperature drastically changes the group velocity (or, the renormalization factor) in gapless edge modes in the topological Kondo insulator SmB$_6$. We conclude that this interplay explains the puzzle of the above two experiment since transport and ARPES measurement have been carried out at $T = 3$K and $T = 17$K, respectively. This resutls is consistent with the slave-boson analysis in Ref. [5].

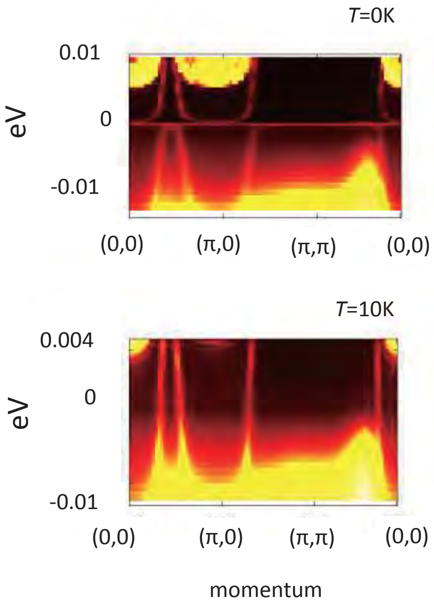

Figure 2: Surface state of SmB$_6$.

References

[1] M. Z. Hasan *et al.*, Rev. Mod. Phys. **82**, (2010) 3045-3067.;X. L. Qi *et al.*, Rev. Mod. Phys. **83**, (2011) 1057.

[2] T. Yoshida, R. Peters, and N. Kawakami: Phys. Rev. B **93**, (2016) 045138.

[3] R. Peters, T. Yoshida, H. Sakakibara, and N. Kawakami: arXiv:1510.06476

[4] R. Peters and N. Kawakami: Phys. Rev. B **92**, (2015) 075103.

[5] V. Alexandrov, *et al.*: Phys. Rev. Lett. **114**, (2015) 177202.

Effect of apical oxygen phonon on *d*-wave superconductivity

Takahiro OHGOE

Department of Applied Physics, The University of Tokyo,
7-3-1 Hongo, Bunkyo-ku, Tokyo 113-0033

Despite intensive studies on high-T_c cuprate, its mechanism of the superconductivity is still controversial. ARPES experiments [1] demonstrated indications of strong electron-phonon interactions. Motivated by these results, some theoretical works proposed scenarios that electron-phonon interactions enhance *d*-wave superconductivity[2,3]. However, the role of electron-phonon interactions in cuprates remains unclear.

In this work, we studied *d*-wave superconductivity in the Holstein-Hubbard model by using the many-variable variational Monte Carlo method[4,5]. We performed simulations in system B by using a flat MPI or OpenMP+MPI parallelization. The Holstein phonon can be viewed as a simplified electron-phonon interaction of apical oxygen in cuprates. Our simulation results showed that physical quantities are insensitive to Holstein phonons [Fig.1(a)]. In the next step, we considered the effect of the off-site part of the electron-phonon interaction *g'* which introduces phonon-mediated off-site attractions between electrons. As a result, we found that the off-site electron-phonon interaction increases the condensation energy [Fig.(b)], and thus a *d*-wave superconducting state becomes more stable energetically.

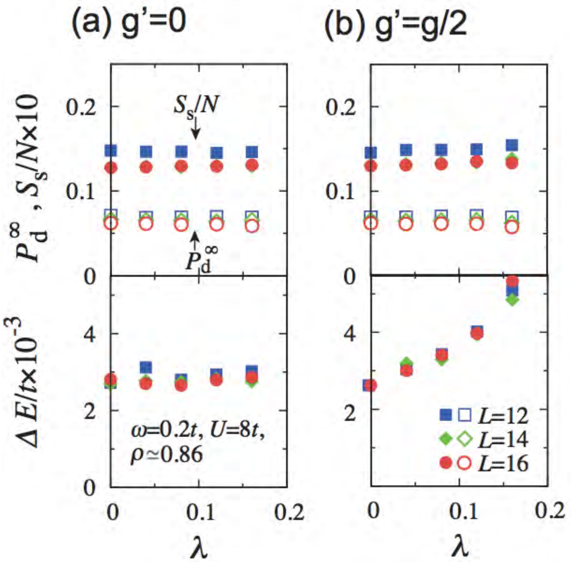

Fig. 1: Physical quantities (long-range part of *d*-wave superconducting correlation function P_d^∞, spin structure factor $S_s(\pi,\pi)$, and the condensation energy ΔE) as functions of the dimensionless electron phonon interaction λ.

References

[1] A. Lanzara *et. al*, Nature **412**, 510 (2001)

[2] S. Ishihara and N. Nagaosa, Phys. Rev. B **69**, 144520 (2004)

[3] Z. B. Huang *et. al*, PRB **68**, 220507 (2003)

[4] D. Tahara and M. Imada, J. Phys. Soc. Jpn. **77**, 1140701 (2008)

[5] T. Ohgoe and M. Imada, Phys. Rev. B **89**, 195139(2014)

Improvement of many-variable variational Monte Carlo method and its application to iron-based superconductors

Takahiro Misawa
Institute for Solid State Physics, The University of Tokyo
Kashiwa, Chiba 277-8581, Japan

In this project, to improve the accuracy of the many-variable Monte Carlo method (mVMC), we implement the backflow wave function based on the Pfaffian wave function and the multi-Pfaffian method, which superposes the many-body wave functions. We have also analyzed low-energy effective models for iron-based superconductors FeTe and FeSe by using the mVMC.

Before explaining the details of the backflow wave functions, we briefly explain the wavefunctions used in the mVMC method. Our wave function is defined as

$$|\psi\rangle = \mathcal{P}|\phi_{\mathrm{pair}}\rangle, \tag{1}$$

$$|\phi_{\mathrm{pair}}\rangle = \left(f_{ij}c^{\dagger}_{i\uparrow}c^{\dagger}_{j\downarrow}\right)^{N_{\mathrm{e}}/2}|0\rangle, \tag{2}$$

where f_{ij} is variational parameter and $c^{\dagger}_{i\sigma}(c_{i\sigma})$ is a creation (annihilation) operator of an electron with spin σ on the ith site. N_{e} represents the number of electrons. By properly optimizing the variational parameter f_{ij}, we can describe several different states such as antiferromagnetic orders, charge-ordered states, correlated paramagnetic metals, and superconducting phases. To include the many-body correlations, we introduce correlation factors $\mathcal{P}$ such as Gutzwiller of Jastrow factors. Details of mVMC method are explained in the literature [1, 2].

L. Tocchio and co-workers introduce the backflow wavefunctions in the conventional Slater-type wave function as follows [3]

$$|\phi_{\mathrm{bf}}\rangle = \prod_{\sigma,n=1}^{N_{\mathrm{e}}/2}(\sum_{i}\tilde{\Phi}_{in\sigma}c^{\dagger}_{i\sigma})|0\rangle, \tag{3}$$

$$\tilde{\Phi}_{in\sigma} = \Phi_{in\sigma} + \sum_{k}\eta_{k}(D,H)\Phi_{k\sigma}, \tag{4}$$

where $\Phi_{in\sigma}$ is the coefficient of the Slater-type wave function and $\eta_{k}(D,H)$ is the variational parameter that depends on the number of doublon (D) and holon (H). It is shown that backflow correlations improve the accuracy of the wave functions [3].

We extend this Slater-type backflow wavefunctions to Pfaffian-type wave functions as follows [4, 5]

$$|\psi_{\mathrm{pair-bf}}\rangle = \left(\tilde{f}_{ij}c^{\dagger}_{i\uparrow}c^{\dagger}_{j\downarrow}\right)^{N_{\mathrm{e}}/2}|0\rangle, \tag{5}$$

$$\tilde{f}_{ij} = \sum_{n}\tilde{\Phi}_{in\uparrow}\tilde{\Phi}_{jn\downarrow}. \tag{6}$$

We have also shown that wavefunctions are systematically improved by superposing the many-body wavefunctions (multi-Pfaffian method) as follows [5]

$$|\psi\rangle = \sum_{n=1}^{N_{\mathrm{Pf}}}\mathcal{P}_{n}|\phi_{n}\rangle, \tag{7}$$

where N_{Pf} is the number of independent many-body wavefunctions.

By using the improved wave functions, we have shown that the accurate finite-temperature calculation based on the imaginary time evolution is possible in the mVMC method [5].

In the analysis of the iron-based superconductors [6], we first derive the low-energy effective model by using the ab initio downfolding method. In this method, we evaluate the transfer integrals and interaction parameters based on the ab initio band calculations. To eliminate the double counting of the correlation effects the exists in the conventional ab initio downfolding scheme, we perform the constrained GW calculations. By solving the low-energy effective model, we show that elimination of the double counting plays an essential role in stabilizing the bicollinear magnetic order in FeTe. We also solve the low-energy effective model for FeSe and find the peculiar degeneracy of the several magnetic orders occurs in FeSe. We have pointed out that this peculiar degeneracy may be the origin of the exotic phenomena found in FeSe. Further analysis of the low-energy effective models by using the improved wavefunctions such as backflow wavefunction is intriguing issue but left for future study.

References

[1] D. Tahara and M. Imada, J. Phys. Soc. Jpn. **77**, 114701 (2008).

[2] T. Misawa and M. Imada, Phys. Rev. B **90**, 115137 (2014).

[3] L. F. Tocchio, F. Becca, and C. Gros, Phys. Rev. B **83**, 195138 (2011).

[4] K. Ido, T. Ohgoe, and M. Imada, Phys. Rev. B **92**, 245106 (2015).

[5] K. Takai, K. Ido, T. Misawa, Y. Yamaji, and M. Imada, J. Phys. Soc. Jpn. **85**, 034601 (2016).

[6] M. Hirayama, T. Misawa, K. Miyake, and M. Imada, J. Phys. Soc. Jpn. **84**, 093703 (2015).

Numerical study of critical phenomena in strongly correlated Dirac electrons

Yuichi OTSUKA
RIKEN Advanced Institute for Computational Science
Kobe, Hyogo 650-0047

Dirac electrons offer suitable test beds where we can study interaction-driven phase transitions by means of unbiased numerical methods. In our previous studies [1, 2], we have elucidated the quantum critical behavior of the Mott transition occurred in the Hubbard model on the honeycomb lattice and on the square lattice with π flux penetrating each plaquette, both of which constitute the massless Dirac dispersions in the non-interacting limit. These works were initially motivated by the possible Mott metal-insulator transition expected to occur in graphene-like materials. However, it has been recently recognized that the interaction-driven transitions in the Dirac fermions have more general and universal aspects, which can be interpreted in terms of the Gross-Neveu (GN) model, a model extensively studied in quantum field theory [3].

The semimetal (SM) to Mott insulator transition accompanied by the antiferromagnetic (AF) transition, which we have studied in the Hubbard model on the honeycomb lattice and the square lattice with π-flux, corresponds to the breaking of the chiral-$SU(2)$ symmetry in the context of the GN model. On the other hand, the transition from SM to the charge-density-wave phase, which has been recently investigated in the spinless t-V model on the same lattices [4], is categorized as the chiral-Z_2 symmetry breaking. The purpose of this project is to clarify the critical phenomena in the strongly correlated Dirac fermions classified with the chiral-XY symmetry, which is the one remaining class out of the known three categories in the GN model.

We have performed large-scale quantum Monte Carlo (QMC) simulations for the attractive Hubbard model on the triangular lattice, to which the staggered π-flux is added to constitute the Dirac dispersion in the non-interacting limit as shown in Fig. 1. In this model, since the lattice structure is not bipartite, we expect the only $U(1)$ symmetry is broken even at half-filling. In addition, the QMC simulation is not vexed by the negative-sign problem in the case of the attractive (negative U) model. We have utilized the QMC code that we have highly optimized on the K computer and the FX10 system. The simulations for small to intermediate clusters with linear system size $L \leq 24$ were done on the system B, and those with $L = 32, 40$ were performed on the system C.

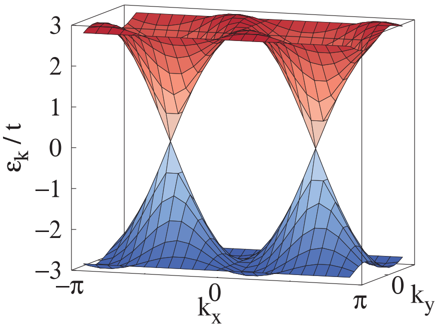

Figure 1: Non-interacting energy dispersion of triangular lattice with staggered π-flux.

We have calculated the pairing correlation function on each finite-size cluster, $P_s(L) = \frac{1}{N}\sum_{ij}\langle\Delta_i^\dagger\Delta_j + \Delta_i\Delta_j^\dagger\rangle$, where $\Delta_i^\dagger = c_{i\uparrow}^\dagger c_{i\downarrow}^\dagger$, and extrapolated them to the thermodynamic-limit to obtain the superconducting (SC)order parameters, $\Delta = \lim_{L\to\infty} P_s(L)$. In addition, the quasiparticle weight Z is estimated from jump of the momentum distribution function at the Fermi level. Both of these observables show that the SM to SC transition occurs at $U_c/t = 7.0 \pm 0.1$ as shown in Fig. 2. More detailed analysis on evaluation of the critical exponents is ongoing.

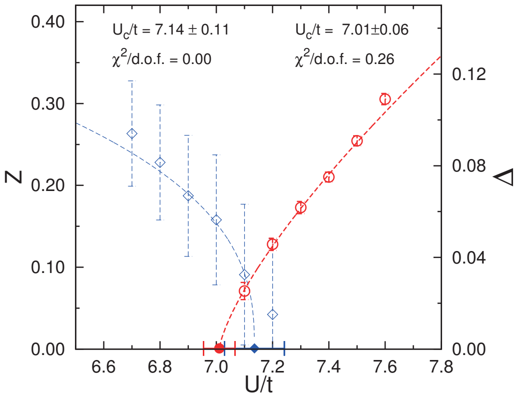

Figure 2: $|U|/t$-dependence of quasiparticle weight Z and superconducting order parameter Δ.

References

[1] S. Sorella, Y. Otsuka, and S. Yunoki: Sci. Rep. **2** (2012) 992.

[2] Y. Otsuka, S. Yunoki, and S. Sorella: Phys. Rev. X. **6** (2016) 011029.

[3] D. Gross and A. Neveu: Phys. Rev. D. **10** (1974) 3235.

[4] L. Wang, P. Corboz, and M. Troyer: N. J. Phys. **16** (2014) 103008.

Density-matrix renormalization group method for quantum impurity models

Tomonori SHIRAKAWA
RIKEN Center for Emergent Matter Science (CEMS)
Wako, Saitama 351-0198, Japan

We have introduced the density matrix renormalization group method (DMRG) as a solver for quantum impurity models, such as Anderson impurity models and Kondo impurity models [1]. The DMRG is advantageous for other impurity solvers when applied to quantum impurity models. First of all, unlike the quantum Monte Carlo methods, the DMRG is able to obtain directly the full spectral function in real frequency without analytical continuation. Secondly, the DMRG can readily calculate the entanglement properties.

Here, to demonstrate the power of the method, we apply it to the single-impurity Anderson model on the honeycomb lattice [2]. Our result shows that the phase diagram contains two distinct phases, the local moment phase (LM) and the asymmetric strong coupling (ASC) phase (See Fig. 1 (a)). We compare the results with those for the low-energy effective pseudogap Anderson model. We find that the ground state phase diagram and the asymptotically low-energy excitations for these two models are found to be in excellent quantitative agreement, thus providing a quantitative justification for the previous studies based on low-energy approximate approaches.

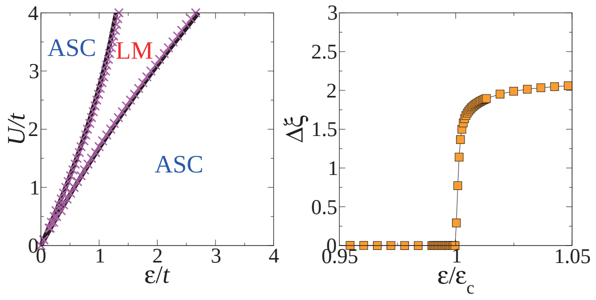

Figure 1: (a) Ground state phase diagram for the single-impurity Anderson model on the honeycomb lattice (symbol) and the pseudogap Anderson model (solid line). ε and U correspond to the on-site potential and Coulomb interaction at impurity site, respectively. (b) Gap of the entanglement spectrum, $\Delta\xi = \xi_2 - \xi_1$. ε_c is determined from (a).

Futhermore, we find that the lowest entanglement level ξ_i ($\xi_1 \leq \xi_2 \leq \cdots$) is doubly degenerate for the LM phase, whereas it is singlet for the ASC phase. Because of this qualitatively different behavior, we can consider the gap of the entanglement spectrum, $\Delta\xi = \xi_2 - \xi_1$, as an order parameter to distinguish the different phases. Indeed, the phase boundary determined from $\Delta\xi$ is the same as the one determined from the local quantities at the impurity site. This clearly demonstrates that $\Delta\xi$ serves as a quantity to determine the phase boundary of the impurity quantum phase transition.

References

[1] T. Shirakawa and S. Yunoki: Phys. Rev. B **90** (2014) 195109.

[2] T. Shirakawa and S. Yunoki: arXiv:1604.00721.

First-principles study of the iron-based ladder compound $BaFe_2S_3$

Ryotaro ARITA
RIKEN Center for Emergent Matter Science
Wako, Saitama, 351-0198

Recently, it has been reported that the two-leg ladder compound $BaFe_2S_3$ (Fig.1) becomes a superconductor under high pressure[1, 2]. Motivated by this discovery, we performed a first-principle calculation and investigated the electronic and magnetic properties of this compound[3]. We found that the magnetic alignment in which the spins are coupled ferromagnetically along the rung and antiferromagnetically along the leg is the most stable in the possible magnetic structure. This result is consistent with the experiment.

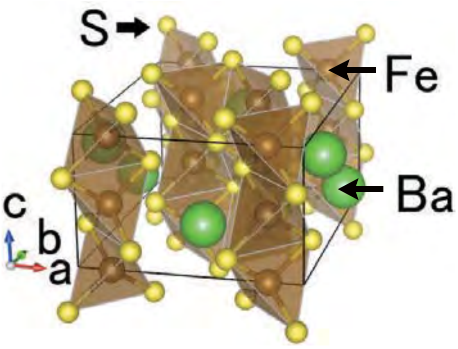

Figure 1: Crystal Structure of $BaFe_2S_3$.

We then derived an effective low-energy model[4] by means of the *ab initio* downfolding method. We found that the complex band structure around the Fermi level is represented only by the Fe $3d_{xz}$ (mixed with $3d_{xy}$) and $3d_{x^2-y^2}$ orbitals. The characteristic band degeneracy (at $k_z = \pi$ in the original BZ) allows us to construct a simple four-band model with the band unfolding approach (Fig.2). We also estimate the interaction parameters and found that the system is more correlated than the 1111 family of iron-based superconductors. Provided the superconductivity is mediated by spin fluctuations, the $3d_{xz}$-like band should play an essential role, and the gap function changes its sign between the Fermi surfaces around the Γ point.

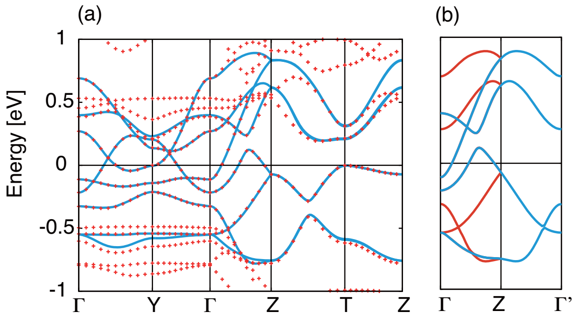

Figure 2: (a) Band dispersion of the effective two-orbital model. (b) Band dispersion in the extended Brillouin zone.

References

[1] H. Takahashi et al., Nature Materials **14**, (2015) 1008.

[2] T. Yamauchi, Y. Hirata, Y. Ueda, and K. Ohgushi, Phys. Rev. Lett. **115**, (2015) 246402.

[3] M-T. Suzuki, R. Arita and H. Ikeda, Phys. Rev. B **92**, (2015) 085116.

[4] R. Arita, H. Ikeda, S. Sakai and M-T. Suzuki, Phys. Rev. B **92**, (2015) 054515.

Numerical simulation of ^{4}He adsorbed on substrates

Yuichi MOTOYAMA
Institute for Solid State Physics, University of Tokyo
Kashiwa-no-ha, Kashiwa, Chiba 277-8581

^{4}He atoms adsorbed on a substrate such as graphite form a layer structure and a layer is an ideal two dimensional interacting bosonic system. Greywall and Busch [1] measured the heat capacity of the first layer of ^{4}He atoms on a graphite and found that a single phase transition occurs at temperature $T \simeq 1$K below areal density $\rho = 0.4\text{Å}^{-2}$. They concluded that KT and condensation (gas-liquid separation) transitions occur simultaneously as a single transition. However, they also pointed out that a problem still remains; at densities near the upper end of coexisting region, KT transition should occur at higher temperature than the condensation does.

For a preliminary simulation to examine this transition, I performed two grand-canonical path-integral Monte Carlo simulations with different initial condition of ^{4}He atoms; one is vacuum phase and the other is commensurate solid phase (C 1/3 phase) with respect to the below carbons. Other simulation parameters are as following: The simulation cell is of $44.28\text{Å}(x) \times 42.61\text{Å}(y) \times 9\text{Å}(z)$, the boundary condition is periodic along x and y direction, parallel to graphite surface, and is open along z direction. The imaginary time step $d\tau$ is 0.005K^{-1}. The potentials that a ^{4}He atom feels from another ^{4}He atom and the graphite are the Aziz potential [2] and the Carlos-Cole potential [3], respectively. Figure 1 shows the difference of areal density of the first layer of ^{4}He between the two simulations. The average over 100,000 Monte Calro steps after discarded 500,000 (1,000,000) steps is shown in the left (right) panel. From this figure, it is concluded that a line of first order phase transition exists at about $\mu = -143.2$K and ends at $T \simeq 0.9$K.

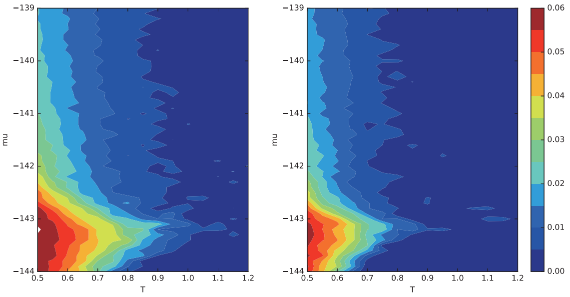

Figure 1: Difference of areal density of ^{4}He on a graphite between two simulations with different initial condition; one is vacuum and the other is commensurate solid with respect to the carbon atoms of graphite. The numbers of discarded Monte Carlo steps are 500,000 for the left panel and 1,000,000 for the right.

References

[1] D. S. Greywall and P. A. Busch, Phys. Rev. Lett. **67**, 3535 (1991).

[2] R. A. Aziz, V. P. S. Nain, J. S. Carley, W. L. Taylor, and G. T. McConville, J. Chem. Phys. **70**, 4330 (1979).

[3] W. E. Carlos and M. W. Cole, Surface Science **91**, 339 (1980).

[4] I used ALPS/parapack library [5] for embarrassingly parallelization and job scheduling.

[5] B. Bauer et al. (ALPS collaboration), J. Stat. Mech. P05001 (2011).

Quantum Monte Carlo simulation and electronic state calculations in correlated electron systems

Takashi YANAGISAWA
Electronics and Photonics Research Institute
National Institute of Advanced Industrial Science and Technology (AIST)
AIST Central 2, 1-1-1 Umezono, Tsukuba 305-8568

High-temperature superconductors have been studied intensively since the discovery of high-temperature cuprates. The electron correlation between electrons is important because parent compounds without carriers are insulators. It is primarily important to clarify electronic states in the CuO_2 plane contained in cuprate high-temperature superconductors. The mechanism of superconductivity has been investigated, but it remains unresolved. It is obvious that interaction with large energy scale is necessary and responsible for realization of high-temperature superconductivity. The Coulomb interaction has obviously a large characteristic energy scale and is a candidate of interaction that induces high-temperature superconductivity.

We have carried out numerical computations by using a Monte Carlo procedure to calculate expectation values of physical quantities. We performed parallel computing with 192 cores mainly on the system B.

The single-band Hubbard model is given by

$$H = \sum_{ij\sigma} t_{ij} c^{\dagger}_{i\sigma} c_{j\sigma} + U \sum_i n_{i\uparrow} n_{i\downarrow}, \qquad (1)$$

where t_{ij} are transfer integrals and U is the on-site Coulomb energy. The transfer integral t_{ij} is non-zero $t_{ij} = -t$ for nearest-neighbor pair $\langle ij \rangle$ and $t_{ij} = -t'$ for next-nearest neighbor $\langle\langle ij \rangle\rangle$. Otherwise t_{ij} vanishes. We denote the number of sites as N and the number of electrons as N_e. The energy unit is given by t.

The wave function should include correlation between electrons. The well-known Gutzwiller wave function is given by $\psi_G = P_G \psi_0$ where P_G is the Gutzwiller operator defined by $P_G = \prod_j (1 - (1-g) n_{j\uparrow} n_{j\downarrow})$ with the variational parameter g in the range of $0 \leq g \leq 1$. It is necessary to improve the Gutzwiller wave function because only the on-site correlation is considered in the Gutzwiller ansatz. The one way to improve the wave function is to take account of nearest-neighbor doublon-holon correlation: $\psi_{d-h} = P_{d-h} P_G \psi_0$. We can take into account inter-site correlations by multiplying P_J such as $P_J P_{d-h} P_G \psi_0$.

In the other way, we can take account of inter-site correlation by multiplying the kinetic operator to the Gutzwiller function in order to improve the wave function. A typical wave function of this type is written as[1]

$$\psi_\lambda \equiv \psi^{(2)} = e^{-\lambda K} P_G \psi_0, \qquad (2)$$

where K is the kinetic term in the Hamiltonian: $K = \sum_{ij\sigma} t_{ij} c^{\dagger}_{i\sigma} c_{j\sigma}$ and λ is a variational parameter to be optimized to lower the energy. This wave function is further improved by multiplying the Gutzwiller operator again:

$$\psi^{(3)} \equiv P_G \psi_\lambda = P_G e^{-\lambda K} P_G \psi_0. \qquad (3)$$

The expectation values for these wave functions are evaluated by using the variational Monte Carlo method.

It is seen that the energy is not so improved only by multiplying the doublon-holon correlation factor P_{d-h} to the Gutzwiller function. The trial wave function $P_{d-h} P_G \psi_0$ was used to develop the physics of Mott transition following the suggestion that the Mott transition occurs due to doublon-holon binding. We before examined the Mott transition with the wave function $e^{-\lambda K} P_G \psi_0$[4] because the variational energy by this wave function is much lower than that of the doublon-holon wave function.

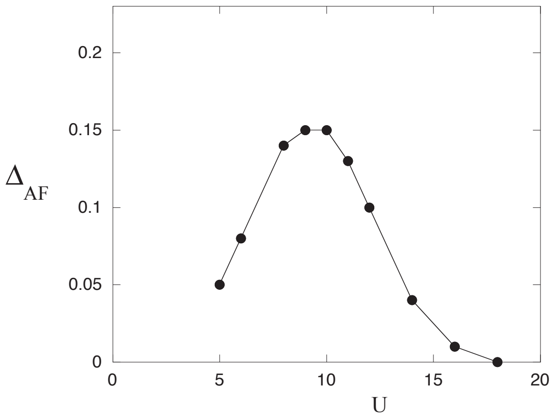

Figure 1: Antiferromagnetic order parameter Δ_{AF} as a function of U in units of t on 10×10 lattice. The number of electrons is $N_e = 84$ and we set $t' = -0.2t$. We used the periodic boundary condition in both directions.

We show the antiferromagnetic (AF) order parameter Δ_{AF} as a function of U in Fig.1[5]. This is a typical behavior of Δ_{AF} and the AF energy gain ΔE_{AF} also shows a similar behavior. The calculation was carried out, by employing the wave function ψ_λ, on a 10×10 lattice. When U is small, Δ_{AF} increases with the increase of U and has a maximum at $U_m \simeq 8t - 10t$ that is of the order of the bandwidth. When U is larger than U_m, the Δ_{AF} is decreased as U is increased. This indicates that AF correlation is suppressed for extremely large U and diminishes. In the region $U > U_m$, there is a competition between AF correlation and charge fluctuation; this means that we must have the AF energy gain or kinetic energy gain to lower the ground-state energy. The Δ_{AF} is reduced gradually as U is increased ($U > U_m$) since the energy gain ΔE_{AF} is presumably proportional to the AF exchange coupling $J \propto t^2/U$. The AF correlation should be suppressed to get the kinetic energy gain for large U. Thus we have weak AF correlation in the strongly correlated region with $U \geq U_m$. This indicates that there is a large AF fluctuation in this region, brought about by charge fluctuation, where the charge fluctuation is driven by the kinetic operator K in the exponential factor $\exp(-\lambda K)$. This charge fluctuation is properly called the kinetic charge fluctuation.

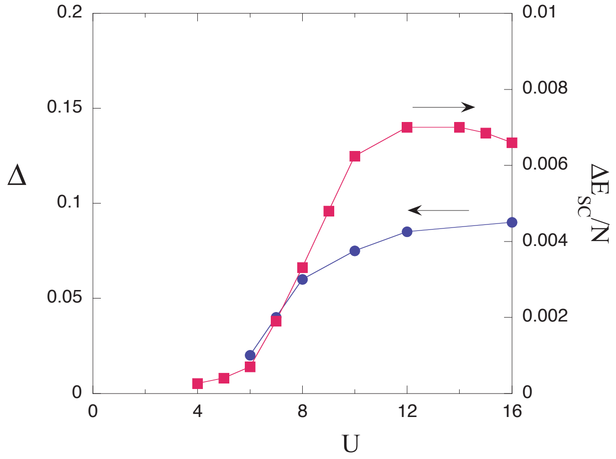

Figure 2: Superconducting order parameter Δ and superconducting condensation energy ΔE_{SC} per site as a function of U in units of t on 10×10 lattice. The number of electrons is $N_e = 84$ and $t' = -0.2t$. The boundary condition is periodic in one direction and antiperiodic in the other direction.

It has turned out that there is large spin fluctuation being driven by kinetic charge fluctuation. We expect that a pairing interaction is inspired by this kind of large spin fluctuation. In fact, the optimized superconducting order parameter increases as U is increased and has a maximum at some U being greater than U_m. This is shown in Fig.2 where the superconducting order parameter Δ and the condensation energy ΔE_{SC} are shown as a function of U. ΔE_{SC} has a maximum at $U \sim 12t$. This result was obtained by using the Gutzwiller-BCS function $P_{N_e} P_G \psi_{BCS}$. It indicates that the superconducting state becomes more stable in the strongly correlated region.

References

[1] T. Yanagisawa et al., J. Phys. Soc. Jpn. 67, 3867 (1998).

[2] T. Yanagisawa and M. Miyazaki, EPL 107, 27004 (2014).

[3] T. Yanagisawa and I. Hase, Physica C (2016).

The correlation between the real space hoppings and T_c in the iron-based superconductors

KAZUHIKO KUROKI
Department of Physics, Osaka University
1-1 Machikaneyama, Toyonaka, Osaka, 560-0043, Japan

HYDROGEN DOPED IRON-BASED SUPERCONDUCTORS

In the hydrogen doped 1111 iron pnictides $LaFeAsO_{1-x}H_x$, electron doping rate can exceed 50 percent, and the T_c against the doping rate x exhibits a double dome structure, where the second dome with higher doping concentration has the higher T_c[1]. In a rigid band picture, such a large amount of electron doping would wipe out the hole Fermi surfaces, so that the Fermi surface nesting would no longer be good in the higher T_c second dome.

EVOLUTION OF THE FERMI SURFACE

First principles band calculation that takes into account the band structure variation with chemical substitution reveals that the band structure rapidly changes with doping, and the rigid band picture is not valid[2–4]. In momentum space, the $d_{xz/yz}$ hole Fermi surfaces around (0,0) shrink monotonically and are eventually lost with sufficient electron doping, and in turn an electron Fermi surface appears. On the other hand, an interesting point is that the d_{xy} hole Fermi surface around (π, π) is barely changed with the doping rate x, which is clearly a non-rigid band feature.

REAL SPACE HOPPINGS

Analyzing the tightbinding model derived based on the first principles band and exploiting the maximally localized Wannier orbitals, it is revealed that the insensitivity of the d_{xy} Fermi surface is due to a rapid decrease of t_1 within the d_{xy} orbital upon increasing x, which pushes up the d_{xy} band top at (π, π), so that it follows the increase of the Fermi level. It should be noted that reduction of t_1 is largely due to the increase of the positive charge within the blocking layer by O(2-)→H(1-) substitution, which in turn reduces the As $4p$ electronic level and leads to the suppression of the indirect component of t_1[4]. We have found that a similar situation can occur when pressure is applied to some of the iron-based superconductors.

CORRELATION BETWEEN HOPPINGS, SPIN FLUCTUATION AND SUPERCONDUCTIVITY

The d_{xy} hole Fermi surface remains even at large electron doping rate, while the $d_{xz/yz}$ hole Fermi surfaces are lost, so that the importance of the d_{xy} orbital increases with doping. Our fluctuation exchange study of these non-rigid band models show that the spin fluctuation and the s ± pairing are both enhanced in this largely doped regime, exhibiting a double dome feature of the superconducting T_c as a function of doping. Moreover, the two domes are merged into a single dome when the Pn-Fe-Pn bond angle is reduced (a change that takes place when the rare earth is varied as La→Ce→Sm→Gd), in agreement with the experimental observations. Although the d_{xy} hole Fermi surface remains unchanged in the highly doped regime, the Fermi surface nesting in its original sense is monotonically degraded because the volume of the electron Fermi surfaces increases. Hence, the origin of the second dome in $LaFeAsO_{1-x}H_x$ cannot be attributed to a good Fermi surface nesting.

s ± pairing is a next nearest neighbor pairing, which is favored by the relation between nearest and next nearest neighbor antiferromagnetic interactions $J_2 > J_1$, corresponding to $t_2 > t_1$. In fact, as mentioned above, t_2 dominating over t_1 is what is happening in the second T_c dome regime. Hence, intuitively, $t_2 > t_1$ can be considered as the origin of the T_c enhancement in the largely doped regime. To be precise, however, the fluctuation exchange approximation is a weak coupling method based on the itinerant spin model, so using the $J_1 - J_2$ term of the localized spin model is not conceptually correct. In reality, the entire d_{xy} portion of the band structure is strongly modified in a manner that it favors the second nearest neighbor pairing. To see in more detail the effect of this modified band structure, we have further analyzed the correlation between the real space hoppings and the energy dependence of the spin fluctuation by calculating the imaginary part of the dynamical spin susceptibility. We find that as the Fermi surface nesting is degraded upon electron doping, the low energy spin fluctuation is suppressed, and the weight is shifted in the high energy regime. This is natural since the Fermi surface nesting in its original sense should enhance zero energy spin fluctuation. The enhancement of $s\pm$ spin fluctuation in the heavily electron doped regime can then be attributed to the enhancement of finite energy spin fluctuation. It is important to note that this behavior is peculiar to systems with disconnected Fermi surfaces, where the nesting vector itself is barely varied even when the degree of the nesting is degraded.

[1] S. Iimura, S. Matsuishi, H. Sato, T. Hanna, Y. Muraba, S.W. Kim, J. E. Kim, M. Takata and H. Hosono, Nat. Commun. 3, 943 (2012).

[2] S. Iimura, S. Matsuishi, M. Miyakawa, T. Taniguchi, K. Suzuki, H. Usui,K. Kuroki, R. Kajimoto, M. Nakamura, Y. Inamura, K. Ikeuchi, S. Ji, and H. Hosono, Phys. Rev. B, 060501(R) (2013).

[3] K. Suzuki, H. Usui, K. Kuroki, S. Iimura, Y. Sato, S.Matsuishi, and H. Hosono, J. Phys. Soc. Jpn. 82, 083702 (2013).

[4] K. Suzuki, H.Usui, S. Iimura, Y. Sato, S. Matsuishi, H. Hosono, and K. Kuroki Phys. Rev. Lett. 113, 027002 (2014)

Monte Carlo Study of Itinerant and Localized Chiral Helimagnets

Shintaro HOSHINO
Department of Basic Science, The University of Tokyo, Meguro, Tokyo 153-8902, Japan

Chiral magnets with the asymmetric Dzyaloshinkii-Moriya interaction show intriguing behaviors beyond simple magnetic strctures such as ferro- and antiferromagnetism. In $CrNb_3S_6$, the helical magnetic structure is realized at zero field. With increasing external field it changes into the chiral soliton lattice where the quasi-local magnetic kinks are aligned periodically [1, 2, 3]. The localized spins of the Cr ions are responsible for the magnetism and are coupled with each other through the Ruderman-Kittel-Kasuya-Yoshida interaction mediated by conduction electrons.

Since the characteristic length scale for the magnetic structure is much larger than the lattice constant in $CrNb_3S_6$, the low-energy behaviors are not sensitive to the fine structure of the system. Hence we choose the simplest classical spin model that can describe helical magnet and chiral soliton lattice structure. The explicit form of Hamiltonian is written as

$$\mathscr{H} = \sum_{ij} (J_{ij} \boldsymbol{S}_i \cdot \boldsymbol{S}_j + \boldsymbol{D}_{ij} \cdot \boldsymbol{S}_i \times \boldsymbol{S}_j) - \sum_i \boldsymbol{H} \cdot \boldsymbol{S}_i \qquad (1)$$

The vector $\boldsymbol{D}_{ij}$ is along the helical axis. The interaction parameter J_{ij} for the helical axis is much smaller than the one perpendicular . This strong anisotropy originates from quasi-two-dimensional electronic structure.

We have analyzed this model by using the mean-field theory [4]. Under the external magnetic field, the system has many metastable states characterized by the winding number. More specifically, if we use the initial condition with the form

$$\langle \boldsymbol{S}_i \rangle = S(\cos(2\pi i_{\parallel} w/N_{\parallel}), \sin(2\pi i_{\parallel} w/N_{\parallel}), 0) \qquad (2)$$

we obtain the different solution for each winding number w. Here $i_{\parallel}$ and N are the site index and the number of sites, respectively, along the helical axis. At each parameter we calculate solutions for all the possble w, and determine the most appropriate solution by comparing the value of free energy. The numerical computation has been effeciently perfomed by parallelization of the calcualtions at each w using supercomputer in ISSP. The realistic Dzyaloshinskii-Moriya interaction parameter for $CrNb_3S_6$ is given by $D = 0.16J$ which means the long periodicity of the helical structure. Hence our mean-field calculation requires a large system size. We take typically $N = 4000$ for the numerical simulation.

As one of the exemplary results of our study, we shown in Fig. 1 the free energy profile near the transition temperature under magnetic field [4]. The free energy has a double-minimum structure and thus we have identified first-order transition character. This behavior

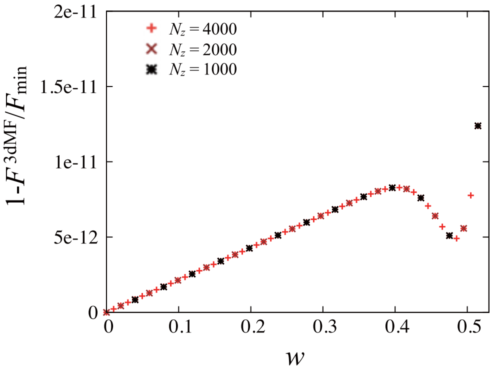

Figure 1: Free energy profile as a function of widing number w. The size (N_z) dependence is shown.

appears at finite temperatures and finite external fields, and is not observed in the zero-temperature nor zero-field limit. The change of the order of phase transition along the phase boundary was also discussed recently by two groups [5, 6]. The systematic studies is necessary to clarify the nature of phase transitions.

References

[1] I. E. Dzyaloshinskii, Sov. Phys. JETP 20, 665 (1965).

[2] T. Moriya and T. Miyadai, Solid State Commun. **42**, 209 (1982).

[3] J. Kishine, K. Inoue, and Y. Yoshida, Prog. Theor. Phys. Suppl. **159**, 82 (2005).

[4] M. Shinozaki, S. Hoshino, Y. Masaki, J. Kishine and Y. Kato, arXiv1512.00235 (2015).

[5] Y. Nishikawa, K. Hukushima, arXiv:1603.04200 (2016).

[6] V. Laliena, J. Campo, Y. Kousaka, and K. Inoue, arXiv:1603.06362 (2016).

Novel Charge Dynamics in Correlated Electron Systems

Sumio ISHIHARA
Department of Physics, Tohoku University
Sendai 980-8578

Electronic charge degree of freedom plays essential roles in dielectric, transport and optical properties in correlated electron systems, such as transition-metal oxides, and low dimensional organic salts. In the projects (H27-Ba-0014 and H27-Bb-0028), we have studied numerically the novel charge dynamics in correlated systems with multi degree of freedom. The following are the list of the obtained results.

1) Transient dynamics of the frustrated interacting charge systems coupled with the lattice degree of freedm are examined numerically. Real-time dynamics in the triangular-lattice spinless fermion model with lattice vibration are analyzed by the exact diagonalization method based on the Lanczos algorithm combined with the equation of motion. A photoinduced phase transition from the horizontal stripe-type charge order to the 3-fold charge order occurs through a characteristic intermediate time domain (Fig. 1). By analyzing the time evolution, we find that these characteristic dynamics are seen when the electron and lattice sectors are not complementary to each other but show cooperative time evolutions. [1].

2) Charge dynamics in a frustrated system are studied in wide ranges of energy, momentum, and temperature. As a typical frustrated charge system, we adopt an interacting spinless fermion model on a paired-triangular lattice which was proposed as an electronic model of the layered iron oxide $\mathrm{LuFe_2O_4}$ a candidate material for the electronic ferroelectricity. In particular, we focus on the charge dynamics in the three-fold charge order and the two-fold charge order. The optical conductivity spectra in the three-fold charge order show multiple components and their low-energy weights survive even below the charge order temperature. These are related to the stability of the three-fold charge order and are in sharp contrast to the spectra in the two-fold charge order. The change in the dynamical charge correlation below the charge ordering temperature is weakly momentum-dependent in the three-fold charge order, and an abrupt reduction is observed in the two-fold charge order. These results are attributable to the charge frustration effects, and explain some aspects of the results of recent optical and resonant inelastic x-ray scattering experiments [2, 3].

3) A possible way to realize the magneto-electric (ME) effect in the dimer-type organic molecular solids is studied. We show a symmetrical considerations in a simple one-dimensional model (Fig. 2). Next, we have carried out the numerical calculations in a two-dimensional lattice model for the κ-(BEDT-TTF) type organic molecular solids. We find that the linear ME effect emerges in a long-range ordered state of spins and electric dipoles owing to the electronic degree of freedom inside the molecular dimers. The essence of this ME effect is attributed to a ferroic order of the spin-charge composite object. The ME effect is also realized in the spin and charge disordered

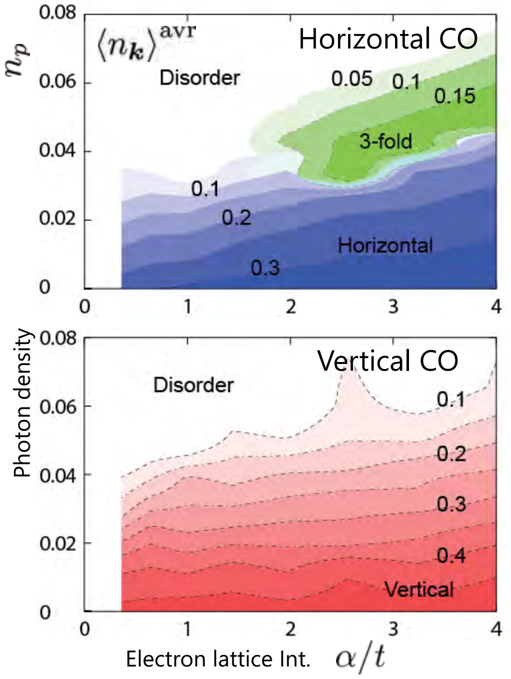

Figure 1: Phase diagrams in the excited states for the horizontal and vertical charge ordered states. Horizontal and vertical axes represent the electron lattice interaction and the photon density, respectively. Colors represent amplitudes of the order parameters. [1].

state, in which the spin-charge composite order emerges. [4]

The present researches has been collaborated with J. Nasu (Tokyo Institute of Technology), M. Naka (Tohoku University), H. Hashimoto (Tohoku University), H. Matsueda (Sendai National College of Technology) and H. Seo (RIKEN, CEMS). Some parts of the computation in the present works has been done using the facilities of the Supercomputer Center, the Institute for Solid State Physics, the University of Tokyo.

References

[1] H. Hashimoto, H. Matsueda, H. Seo, and S. Ishihara, J. Phys. Soc. Jpn. **84**, (2015) 113702.

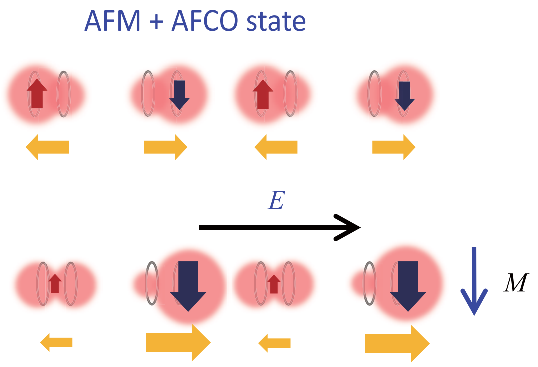

Figure 2: (top): A schematic view of the antiferromagnetic and antiferroelectric charge ordered state in the dimer-Mott insulating system. (bottom): Magnetoelectric effect in the system. [4].

[2] M. Naka and S. Ishihara, J. Phys. Soc. Jpn. **84**, (2015) 023703.

[3] M. Yoshida, K. Ishii, M. Naka, S. Ishihara, I. Jarrige, K. Ikeuchi, Y. Murakami, K. Kudo, Y. Koike, T. Nagata, Y. Fukada, N. Ikeda and J. Mizuki, Scientific Report **6**, (2015) 23611.

[4] M. Naka and S. Ishihara, Scientific Report **6**, (2015) 20781.

Magnetic properties in the Hubbard model on the Honeycomb Lattice by variational cluster approximation

Atsushi Yamada
Department of Physics, Chiba University
Chiba 263-8522, Japana, Chiba 277-8581

A spin liquid state, which is a purely non-magnetic Mott insulator without spontaneously broken spatial or spin symmetry, has attracted a lot of interest. This state is realized in geometrically frustrated systems like the charge organic transfer salts κ-(BEDT-TTF)$_2$X[1] and Cs$_2$CuCl$_4$.[2] A simple theoretical model of these compounds is the Hubbard model on the an-isotropic triangular lattice, and spin liquid state is in fact found in this model.[3] A spin liquid could arise also in the intermediate coupling region of strongly correlated systems between a semi-metal and ordered state, because in this case a correlation-driven insulating gap might open before the system becomes ordered. This possibility might be realized in the half-filled Hubbard model on the honeycomb lattice.

We have studied the magnetic and metal-to-insulator transitions by variational cluster approximation using 10-site cluster as a reference system. Parts of numerical calculations were done using the computer facilities of the ISSP. We found that $U_{\mathrm{AF}} = 2.7$ and $U_{\mathrm{MI}} = 3.0$. This result also rules out the existence of the spin liquid in this model. Both the magnetic and non-magnetic metal-to-insulator transitions are of the second order. Our results agree with recent large scale Quantum Monte Carlo simulations.[4]

We plan to continue this study using larger reference cluster to see the cluster size dependence of the results.[5]

References

[1] Y. Shimizu, K. Miyagawa, K. Kanoda, M. Maesato, and G. Saito, Phys. Rev. Lett. **91**, 107001 (2003); Y. Kurosaki, Y. Shimizu, K. Miyagawa, K. Kanoda, and G. Saito, Phys. Rev. Lett. **95**, 177001 (2005).

[2] R. Coldea, D.A. Tennant, A.M. Tsvelik, and Z. Tylczynski, Phys. Rev. Lett. **86**, 1335 (2001); R. Coldea, D.A. Tennant, and Z. Tylczynski, Phys. Rev. Lett. **68**, 134424 (2003).

[3] T. Yoshioka, A. Koga, and N. Kawakami, Phys. Rev. Lett. **103**, 036401 (2009); P. Sahebsara and D. Sénéchal, Phys. Rev. Lett. **100**, 136402 (2008); L.F. Tocchio, H. Feldner, F. Becca, R. Valenti, and C. Gros, Phys. Rev. B **87**, 035143 (2013); A. Yamada, Phys. Rev. B **89**, 195108 (2014); L.F. Tocchio, C. Gros, R. Valentí, F. Becca, Phys. Rev. B **89**, 235107 (2014); A. Yamada, Phys. Rev. B **90**, 235138 (2014).

[4] S. Sorella, Y. Otsuka, and S. Yunoki, Sci. Rep. **2**, 992 (2012); F. F. Assaad and I. F. Herbut, Phys. Rev. X **3**, 031010 (2013); F. Parisen Toldin, M. Hohenadler, F. F. Assaad, and I. F. Herbut, Phys. Rev. B **91**, 165108 (2015).

[5] A. Yamada, in preparation.

Optical conductivity near antiferromagnetic transition in the square-lattice Hubbard model

Toshihiro SATO
Computational Condensed Matter Physics Laboratory, RIKEN
Wako, Saitama 351-0198, Japan

A cluster dynamical mean field theory (CDMFT) [1] has advanced our understanding of electronic properties in strongly correlated electronic systems described by the Hubbard model such as metal-insulator Mott transition, pseudogap state, and superconductivity. Recently, the focus has stated to move onto transport properties. Optical conductivity is one of the most fundamental transport coefficient and provides useful information on charge dynamics, particularly effective mass and transport scattering process as well as electric structure.

The main purpose of this study is to derive a new formula of optical conductivity on the antiferromagnetic phase based on our previous one for the paramagnetic phase [2]. To take into account both strong short-range electronic correlations and magnetic fluctuations, we employ the CDMFT using a four-site square cluster and calculate optical conductivity with including the vertex corrections near the antiferromagnetic transition in a square-lattice Hubbard model at half filling, $H = -t\sum_{\langle i,j\rangle,\sigma} c^{\dagger}_{i\sigma}c_{j\sigma} + U\sum_i n_{i\uparrow}n_{i\downarrow} - \mu\sum_{i,\sigma} n_{i\sigma}$. Here, t is the nearest-neighbor hopping amplitude, U is the on-site Coulomb repulsion and μ is the chemical potential. $c_{i\sigma}$ is the electron annihilation operator at site i with spin σ and $n_{i\sigma}$=$c^{\dagger}_{i\sigma}c_{i\sigma}$. The numerical solver is the continuous-time quantum Monte Carlo method based on the strong coupling expansion [3]. This is performed by the large-scale numerical computations using facilities at Supercomputer Center in ISSP.

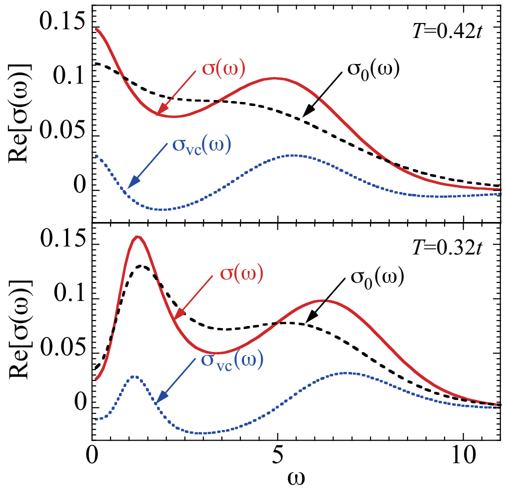

Figure 1: Effects of vertex corrections on optical conductivity $\sigma(\omega)$ in the paramagnetic phase ($T = 0.42t$) and the antiferromagnetic phase ($T = 0.32t$). $\sigma(\omega)$ is the result with vertex corrections, $\sigma_0(\omega)$ is the result without vertex corrections, and the contribution of vertex corrections is $\sigma_{\rm vc}(\omega)$.

We calculate temperature-dependence of optical conductivity $\sigma(\omega)$ at $U = 6.5t$ fixed and investigate the effects of the vertex corrections. Figure 1 presents the contributions of vertex corrections: $\sigma(\omega)$ is the result with vertex corrections, $\sigma_0(\omega)$ is the result without vertex corrections, and the contribution of vertex corrections is $\sigma_{\rm vc}(\omega)$. The most important finding is that vertex corrections change various important details in temperature and frequency dependence of conductivity. In the paramagnetic phase, the vertex corrections enhance both the Drude peak and the broad incoherent peak related to the Hubbard band and the two peaks become sharper. In the antiferromagnetic phase, the dip of $\sigma(\omega)$ at $\omega = 0$ is suppressed by the vertex corrections, in addition to the sharply enhancement of the low-energy peak around $\omega = 1$. Moreover, we demonstrate that in a temperature region just above the antiferromagnetic transition temperature with including the vertex corrections, dc conductivity shows an insulating behavior, whereas the Drude peak is stable. We also investigate the momentum dependence of the vertex function and find that there exists very different fluctuations in the vertex corrections between quasiparticles at different positions in the Brillouin zone both in the paramagnetic and antiferromagnetic phases [4].

This work is done in collaboration with Prof. Hirokazu Tsunetsugu (ISSP, The University of Tokyo).

References

[1] G. Kotliar, S. Y. Savrasov, G. Pálsson, and G. Biroli: Phys. Rev. Lett. **87** (2001) 186401.

[2] T. Sato, K. Hattori, and H. Tsunetsugu: Phys. Rev. B **86** (2012) 235137.

[3] P. Werner, A. Comanac, L. de ¡ Ç Medici, M. Troyer, and A. J. Millis: Phys. Rev. Lett. **97** (2006) 076405.

[4] T. Sato and H. Tsunetsugu: submitted to Phys. Rev. B.

Research of Kondo effect in f^7-electron systems by numerical renormalization group method

Takashi HOTTA
Department of Physics, Tokyo Metropolitan University
1-1 Minami-Osawa, Hachioji, Tokyo 192-0397

In order to promote our basic understanding of the Kondo behavior recently observed in europium compounds [1, 2, 3, 4], we analyze an impurity Anderson model with seven f electrons at an impurity site by employing a numerical renormalization group method [5].

The model is given by

$$\begin{aligned} H &= \sum_{\boldsymbol{k},m,\sigma} \varepsilon_{\boldsymbol{k}m} c^{\dagger}_{\boldsymbol{k}m\sigma} c_{\boldsymbol{k}m\sigma} \\ &+ \sum_{\boldsymbol{k},m,\sigma} (V_m c^{\dagger}_{\boldsymbol{k}m\sigma} f_{m\sigma} + \text{h.c.}) \\ &+ \lambda \sum_{m,\sigma,m',\sigma'} \zeta_{m,\sigma;m',\sigma'} f^{\dagger}_{m\sigma} f_{m'\sigma'} \\ &+ \sum_{m,m',\sigma} B_{m,m'} f^{\dagger}_{m\sigma} f_{m'\sigma} \\ &+ \sum_{\substack{m_1 \sim m_4 \\ \sigma,\sigma'}} I_{m_1 m_2, m_3 m_4} f^{\dagger}_{m_1\sigma} f^{\dagger}_{m_2\sigma'} f_{m_3\sigma'} f_{m_4\sigma}, \end{aligned} \quad (1)$$

where $\varepsilon_{\boldsymbol{k}m}$ is the dispersion of conduction electron with the z-component m of angular momentum $\ell = 3$, $c_{\boldsymbol{k}m\sigma}$ is an annihilation operator of conduction electron with momentum $\boldsymbol{k}$, angular momentum m, and spin σ, $\sigma = +1$ (-1) for up (down) spin, $f_{m\sigma}$ denotes the annihilation operator for local f electron, V_m is the hybridization between conduction and localized electrons, $I_{m_1 m_2, m_3 m_4}$ indicates the Coulomb interaction, λ is the spin-orbit coupling, and $B_{m,m'}$ denotes the crystalline electric field (CEF) potential.

The Coulomb interaction I is known to be expressed by the Slater-Condon parameters, F^0, F^2, F^4, and F^6. Although these should be determined for the material from the experimental results, here we assume the ratio among the Slater-Condon parameters as $F^0 = 10U$, $F^2 = 5U$, $F^4 = 3U$, and $F^6 = U$, where U is the Hund's rule interaction among f orbitals. Each matrix element of ζ for the spin-orbit coupling is given by $\zeta_{m,\sigma;m,\sigma} = m\sigma/2$, $\zeta_{m+\sigma,-\sigma;m,\sigma} = \sqrt{\ell(\ell+1) - m(m+\sigma)}/2$, and zero for other cases. The CEF potentials for f electrons from the ligand ions is given in the table of Hutchings for $\ell = 3$. For cubic structure with $O_{\rm h}$ symmetry, $B_{m,m'}$ is expressed by a couple of CEF parameters, B_4^0 and B_6^0, which are given by $B_4^0 = Wx/F(4)$ and $B_6^0 = W(1 - |x|)/F(6)$. Here x indicates the CEF scheme for the $O_{\rm h}$ point group, while W determines the energy scale for the CEF potentials. We choose $F(4) = 15$ and $F(6) = 180$ for $\ell = 3$.

Here we consider a single $a_{\rm u}$ conduction band, since the local $a_{\rm u}$ state is non-degenerate even under a high-symmetry ligand field such as the cubic CEF potential. Note that the local $a_{\rm u}$ state is described as $(f^{\dagger}_{m=2,\sigma} - f^{\dagger}_{m=-2,\sigma})|0\rangle/\sqrt{2}$, where $|0\rangle$ denotes the vacuum. Thus, V_m is given by $V_{m=2} = -V_{m=-2} = V$ and is zero for other components. The energy unit is half of the $a_{\rm u}$ conduction bandwidth, which is set as 1 eV throughout this paper, as mentioned above.

For the diagonalization of the impurity Anderson model, we employ a numerical renormalization group (NRG) method [6, 7], in which we logarithmically discretize the momentum space so as to include efficiently the

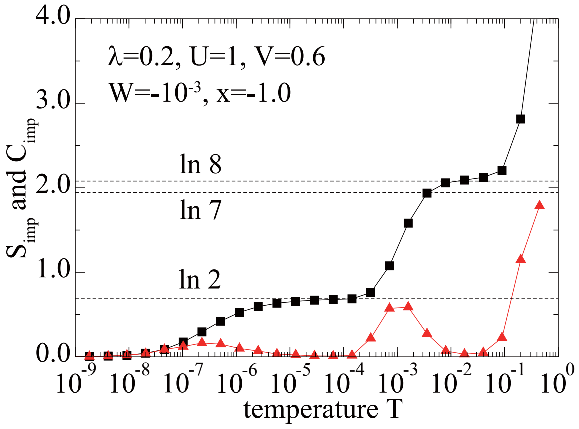

Figure 1: Entropy $S_{\rm imp}$ (solid squares) and specific heat $C_{\rm imp}$ (solid triangles) for $\lambda = 0.2$, $U = 1$, $W = -10^{-3}$, $x = -1.0$, and $V = 0.6$.

conduction electrons near the Fermi energy. The conduction electron states are characterized by "shell" labeled by N and the shell of $N = 0$ denotes an impurity site described by the local Hamiltonian.

For $\lambda = 0$, we observe underscreening Kondo behavior for appropriate values of V, characterized by an entropy change from $\ln 8$ to $\ln 7$, in which one of the seven f electrons is screened by conduction electrons. When λ is increased, we obtain two types of behavior depending on the value of V. For large V, we find an entropy release of $\ln 7$ at low temperatures, determined by the level splitting energy due to the hybridization. For small V, we also observe an entropy change from $\ln 8$ to $\ln 2$ by the level splitting due to the hybridization, but at low temperatures, $\ln 2$ entropy is found to be released, leading to the Kondo effect. We emphasize that the Kondo behavior for small V is observed for realistic values of λ on the order of 0.1 eV.

In Fig. 1, we depict the temperature dependence of the entropy $S_{\rm imp}$ and specific heat $C_{\rm imp}$ for $\lambda = 0.2$, $U = 1$, $W = -10^{-3}$, $x = -1.0$, and $V = 0.6$. We find a plateau of $\ln 8$ around at $T = 10^{-2}$ originating from the local octet of $J = 7/2$. For the case of $\lambda = 0$, only one electron spin is screened by one conduction band, leading to the entropy changing from $\ln 8$ to $\ln 7$, but in the present case with $\lambda = 0.2$, first we find that the entropy changes from $\ln 8$ to $\ln 2$ by the level splitting due to the hybridization with conduction electrons. Then, the entropy of $\ln 2$ is eventually released at around $T = 10^{-7}$, leading to the Kondo temperature $T_{\rm K}$. The behavior of the entropy and specific heat is essentially the same as those without the CEF potentials. This is not surprising, since the level splitting due to the hybridization plays the same role as that in the case of the CEF potentials.

References

[1] A. Mitsuda, S. Hamano, N. Araoka, H. Yayama, and H.Wada, J. Phys. Soc. Jpn. **81**, 023709 (2012).

[2] Y. Hiranaka, A. Nakamura, M. Hedo, T. Takeuchi, A. Mori, Y. Hirose, K. Mitamura, K. Sugiyama, M. Hagiwara, T. Nakama, and Y. Ōnuki, J. Phys. Soc. Jpn. **82**, 083708 (2013).

[3] A. Nakamura, T. Takeuchi, H. Harima, M. Hedo, T. Nakama, and Y. Ōnuki, J. Phys. Soc. Jpn. **83**, 053708 (2014).

[4] A. Nakamura, T. Okazaki, M. Nakashima, Y. Amako, K. Matsubayashi, Y. Uwatoko, S. Kayama, T. Kagayama, K. Shimizu, T. Uejo, H. Akamine, M. Hedo, T. Nakama, Y. Ōnuki, and H. Shiba, J. Phys. Soc. Jpn. **84**, 053701 (2015).

[5] T. Hotta, J. Phys. Soc. Jpn. **84**, 114707 (2015).

[6] K. G. Wilson, Rev. Mod. Phys. **47**, 773 (1975).

[7] H. R. Krishna-murthy, J. W. Wilkins, and K. G. Wilson, Phys. Rev. B **21**, 1003 (1980).

General formalism for the anomalous-Hall or spin-Hall effects of interacting multiorbital metals

Naoya ARAKAWA
Center for Emergent Matter Science, RIKEN
Wako, Saitama 351-0198

Theoretical research about transport phenomena still need further development. One of the well known transport phenomena is the usual-Hall effect. The important development for the usual-Hall effect was obtained in the theoretical research [1] of a single-orbital Hubbard model on a square lattice: in this model near an antiferromagnetic quantum-critical point, the Hall coefficient showed the Curie-Weiss-like temperature dependence due to the strong antiferromagnetic spin fluctuation. This research showed the importance of the electron-electron interaction in the usual-Hall effect in a strongly correlated metal. Although the electron-electron interaction may be important even in another Hall effect such as the anomalous-Hall effect or the spin-Hall effect, our understanding of its effects is less developed than that for the usual-Hall effect.

About the effects of the electron-electron interaction in the anomalous-Hall or spin-Hall effect in metals, we have two important issues. One is about the roles of the Fermi-surface term and Fermi-sea term of the anomalous-Hall or spin-Hall conductivity in the presence of the electron-electron interaction. The theoretical research [2] neglecting the electron-electron interaction showed that the anomalous-Hall or spin-Hall conductivity at $T = 0$K without impurities was given by part of the Fermi-sea term, the Berry-curvature term, which was proportional to the Fermi distribution function, and that with increasing the nonmagnetic impurity concentration the dominant term of the anomalous-Hall or spin-Hall conductivity changed from the Berry-curvature term to the Fermi-surface term, which was proportional to the energy derivative of the Fermi distribution function. The other issue is about the spin-Colomb drag [3]. If the electron-electron interaction causes the scattering between different-spin electrons with finite momentum transfer in the presence of the onsite spin-orbit coupling, the total momentum of spin-up or spin-down electrons is not separatetly (but totally) consereved. This violation of the conservation law causes a characteristic friction of the spin current, the spin-Coulomb drag. Although the spin-Coulomb drag may affect the spin-Hall effect in metals and the effects may result in a characteristic property of the spin transports, the effects have not studied yet.

To develop our understanding of the electron-electron interaction in the anomalous-Hall and spin-Hall effects in metals, I construct the general formalism by using the linear-response theory with the approximations appropriate for metals, and clarify a new mechanism of the temperature dependence of the anomalous-Hall or spin-Hall conductivity at high or intermediate temperature even without impurities and the existence of the correction term of the spin-Hall conductivity due to the spin-Coulomb drag [4]. After deriving the exact expression of the anomalous-Hall or spin-Hall conductivity for a multiorbital Hubbard model with the onsite spin-

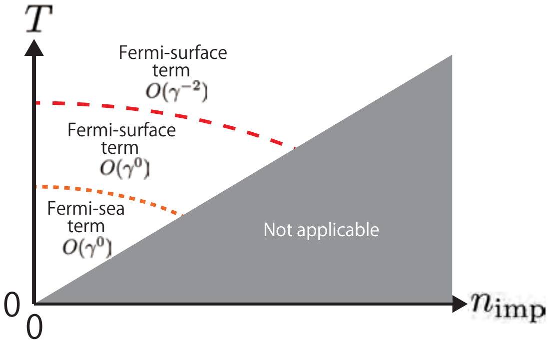

Figure 1: Schematic diagram about the dominant term and damping dependence of the anomalous-Hall or spin-Hall conductivity.

orbit coupling and the onsite weak-scattering potential of nonmagnetic impurities, I derive an approximate expression in Éliashberg's approximation, which is often used for the resistivity and the Hall coefficient in metals in the presence of the electron-electron interaction [5], and show that this approximation is applicable in the high-temperature and intermedite-temperature region in Fig. 1. As the result, I find that the dominant term of the anomalous-Hall or spin-Hall conductivity is the Fermi-surface term, resulting in the temperature depencence in the high-temperature region in Fig. 1 due to the dependence on the interaction-induced quasiparticle damping and the spin-Coulomb-drag-induced correction of the spin-Hall conductivity. Then, I construct an approximation beyond Éliashberg's approximation in order to describe the anomalous-Hall and spin-Hall effects in the low-temperature region of Fig. 1, and find that in this region the Fermi-sea term becomes dominant. In contrast to the Fermi-surface term, the Fermi-sea term is independent of the quasiparticle damping and is not affected by the spin-Coulomb drag.

The above theoretical research is the first step towards our thoroughly understanding of the electron-electron itneraction in the anomalous-Hall or spin-Hall effect in metals. In particular, by combining the general formalism with the first-principle calculation, we can analyze the anomalous-Hall or spin-Hall effect in metals in a realistic way.

References

[1] H. Kontani *et al.*: Phys. Rev. B **59** (1999) 14723.

[2] H. Kontani *et al.*: Phys. Rev. B **75** (2007) 184416; H. Kontani *et al.*: Phys. Rev. B **77** (2008) 165117.

[3] E. M. Hankiewicz and G. Vignale: J.Phys.:Condens.Matter **21** (2009) 253202.

[4] N. Arakawa: arXiv:1510.03988.

[5] N. Arakawa: arXiv:1505.05274.

Charge-density wave and exciton condensation induced by Coulomb interaction and electron-lattice interaction

Hiroshi WATANABE
RIKEN CEMS
2-1, Hirosawa, Wako-shi, Saitama 351-0198

The charge-density wave (CDW) is widely observed in low-dimensional solids and has been extensively studied for a long time. Transition metal dichalcogenides (TMDC) MX_2 (M = transition metal, X = S, Se, Te) are one of the typical CDW materials with a layered triangular lattice structure. $1T$-$TiSe_2$ shows commensurate $2 \times 2 \times 2$ CDW below T_c=200K and also shows superconductivity (SC) by applying pressure or intercalation of Cu atoms. The origin of the CDW and SC is still controversial and two different mechanism are proposed: exciton condensation and band Jahn-Teller effect. Although the former is originated from the Coulomb interaction and the latter is originated from the elctron-lattice interaction, they are not separable and closely related with each other.

In this project, we have studied the two-band Hubbard model in a two-dimensional triangular lattice including Coulomb and electron-lattice interactions to clarify the mechanism of CDW and possibility of exciton condensation in $1T$-$TiSe_2$ [1]. The ground state property is investigated by variational Monte Carlo (VMC) method. The Gutzwiller-Jastrow type wave function is used for electronic part and the Gaussian type wave function is used for lattice part of the VMC trial function. The system sizes for calculation are from 12×12×2 to 24×24×2.

We have shown that the Coulomb and electron-lattice interactions cooperately induce the CDW phase (Fig. 1). We have also shown that “pure” exciton condensation without lattice distortion is difficult (not realistic) in $1T$-$TiSe_2$. This is in contrast to the case of two-dimensional square lattice, where the pure exciton condensation is widely observed using the same calculation method [2]. Our result suggests that the stability of exciton condensation greatly depends on the nesting condition of the Fermi surface in the normal state. We conclude that in $1T$-$TiSe_2$ with poor nesting conditon, both electronic and lattice degrees of freedom are crucial for the understanding of the quantum phases.

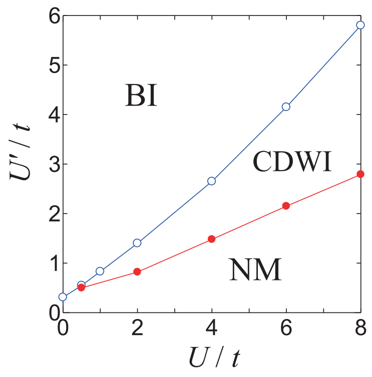

Figure 1: Ground state phase diagram for intraband (U) and interband (U') Coulomb interactions with electron-lattice coupling $g/t = 0.19$ [1]. NM, CDWI, and BI denote normal metal, charge-density wave insulator, and band insulator.

References

[1] H. Watanabe, K. Seki, and S. Yunoki: Phys. Rev. B **91** (2015) 205135.

[2] H. Watanabe, K. Seki, and S. Yunoki: J. Phys.: Conf. Ser. **592** (2015) 012097.

Chiral Magnetic Effect in Condensed Matter Systems

Hiroyuki FUJITA and Masaki OSHIKAWA
Institute for Solid State Physics, University of Tokyo
Kashiwa-no-ha, Kashiwa, Chiba 277-8581

Interface between quantum field theory and condensed matter physics has been a source of many important developments. Weyl fermions and accompanying chiral anomaly is a particularly notable example. Chiral Magnetic Effect (CME), namely an induction of electric current parallel to the applied magnetic field, was predicted as one of the consequences of chiral anomaly. With the prediction and subsequent experimental confirmations of Weyl fermions realized in actual materials ("Weyl semimetals"), there has been a strong interest in observing the CME in these materials. However, there are several subtle issues to be addressed carefully, for the possible observation of the CME. One of them is that, it is shown rigorously that the electric current vanishes under a static magnetic field in the equilibrium. This still leaves the possibility that the CME can be observed at a non-vanishing frequency. Even if this is the case, another subtlety is that the electric and magnetic fields, and electric charge and current densities have to obey the laws of electrodynamics.

By solving the Maxwell-Chern-Simons (MCS) equations, we demonstrated that CME will qualitatively change transport properties of matter in rather unexpected ways [1]. We showed that the physically observed admittance is not simply proportional to the chiral magnetic conductivity $\sigma_{\mathrm{ch}}(\omega)$ as it has been expected, even when it is governed by the CME. Furthermore, we found that the CME-induced AC current is resonantly enhanced when the cross section matches the "chiral magnetic length". Our results imply that the electromagnetism is fundamental for actual transports in Weyl semimetals and that proposals for their applications to future electronics need careful considerations on this issue.

As a concrete setup, we considered the CME-capable Weyl semimetal in the solenoid as shown in Fig. 1. We focused on the CME-dominant regime and discuss the leading order in the small-δ expansion, where

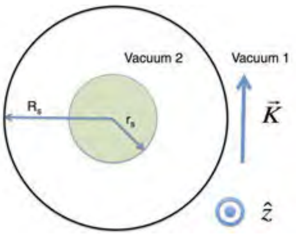

Figure 1: Schematic picture of our setup. A solenoid (radius R_{s}) is represented as a surface current $\boldsymbol{K}$ between the two vacua. Inside them, a cylindrical sample (radius r_{s}) is placed.

$$\delta = \frac{\omega\sigma}{\mu\sigma_{\mathrm{ch}}^2}. \tag{1}$$

The admittance G of a cylinder with length L was determined as $G = -i\omega C$, where

$$C = \frac{iI_z^{\mathrm{tot}}}{\omega L E_z} \simeq \frac{2\pi}{\mu_0\omega^2 L \log\left[\frac{c}{\omega r_s}\right]}. \tag{2}$$

Namely, the admittance is universal and does not depend on material parameters.

Furthermore, the total current I_z^{tot} as a function of the external magnetic field $\sim K$ was obtained as

$$I_z^{\rm tot} = \frac{\pi r_{\rm s} J_0(\mu\sigma_{\rm ch} r_{\rm s})}{\mu_0 J_1(\mu\sigma_{\rm ch} r_{\rm s}) \log\left[\frac{c}{\omega r_s}\right]} K + {\rm O}\left(\frac{r_s}{R_s}\right). \tag{3}$$

This shows a resonant enhancement when $J_1(\mu\sigma_{\rm ch} r_{\rm s}) \sim 0$. In FIG. 2, we show $I_z^{\rm tot}$ for the following parameters: $\mu\sigma_{\rm ch} = 1\,[{\rm mm}^{-1}]$, $\omega = 100\,[{\rm Hz}]$, $B = 1\,[{\rm Gauss}]$ assuming $r_s/R_s \simeq 0$.

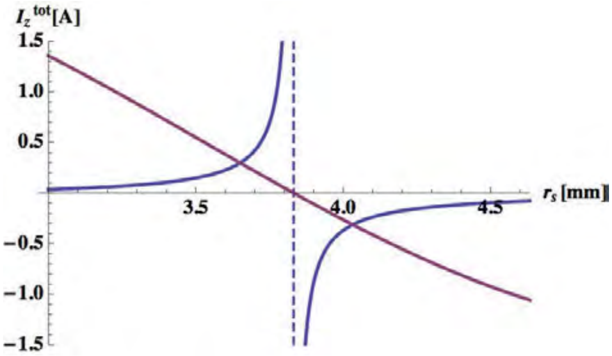

Figure 2: Blue line: Total current $I_z^{\rm tot}$[A] for parameters $\mu\sigma_{\rm ch} = 1\,[{\rm mm}^{-1}], \omega = 100\,[{\rm Hz}], B = 1\,[{\rm Gauss}]$. Red: $J_1(\mu\sigma_{\rm ch} r_{\rm s})$ in an arbitrary unit. The current is resonantly enhanced for $r_{\rm s}$ satisfying $J_1(\mu\sigma_{\rm ch} r_{\rm s}) = 0$ represented by a dashed line.

While these results have been obtained analytically, we are now studying various aspects of the CME in more detail based on numerical calculations partially using the ISSP supercomputers.

References

[1] H. Fujita and M. Oshikawa, arXiv:1602.00687.

3.4 Cooperative Phenomena in Complex Macroscopic Systems

Super-solidity in 2D Bose Systems

Yoshihiko HIRANO, Yuichi MOTOYAMA, and Naoki KAWASHIMA
Institute for Solid State Physics,
The University of Tokyo, Kashiwa-no-ha, Kashiwa, Chiba 277-8581

Motivated by recent experiments on the He-4 atoms adsorbed on graphite surfaces, we studied Bosonic models in two dimensions. We considered two models: (i) a simple model (the hard-core Bose gas on a honeycomb lattice with nearest-neighbor repulsion), and (ii) a realistic model (the Bose particles interacting with each other by Aziz potential in the periodic potential mimicking the effect of the graphite substrate). Using the computational resources allocated to the present proposal, we mainly carried out calculations of (i), for which we summarize in the following what we achieved in the project. For calculations of (ii), one of the present authors (Y.M.) writes a separate report.

We considered the hard-core boson system on the honeycomb lattice with the nearest neighbor repulsion and the periodic potential that forms triangular super-lattice. Specifically, the model is described by the following Hamiltonian:

$$H = -t\sum_{(ij)}\left(a_i^{+}a_j + \mathrm{h.c.}\right) + V\sum_{(ij)} n_i n_j - \mu\sum_i n_i + \sum_i \varepsilon_i n_i . \quad \left(\varepsilon_i = 0, \varepsilon\right)$$

This Hamiltonian naturally interpolates between the honeycomb lattice ($\varepsilon = 0$) and the triangular lattice ($\varepsilon = \infty$). In the former case, the model is equivalent to the $S = 1/2$ ferromagnetic Heisenberg model showing with uniform magnetic field and show only uniformly ordered states.

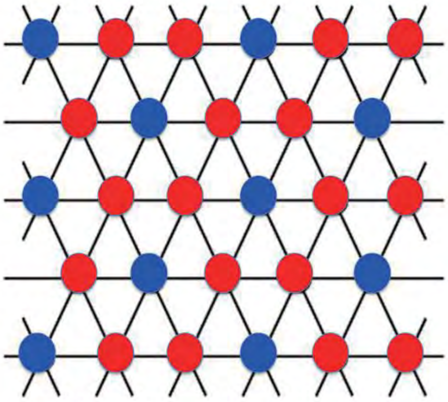

Fig. 1: The honeycomb lattice with periodic potential. ($\varepsilon_i = 0$ on the red sites whereas $\varepsilon_i = \varepsilon > 0$ on the blue.)

For the computation, we used our own code based on DSQSS, the program package based on the worm algorithm for the world-line quantum Monte Carlo simulation. The package is an open-source software, available through GitHub under the GPU license.

For the present model, we computed three quantities: the density, the superfluid density and the static structure factor, as functions of the chemical potential. In these calculations, we fixed the value of t/V as $t/V = 0.1$, and varied ε/V as $\varepsilon/V =$ 0.0, 0.1, 0.2, 0.5 and 1.0.

Our calculation revealed the following. Near $\mu/V = 3$, and at all values of ε/V, the system is in the super fluid phase where the super current is carried by particles that mainly reside easy sites (red sites in Fig.1). Increase in the chemical potential brings the system into the 2/3-filling incompressible solid state through a second order phase transition. In this solid state, nearly all easy sites are occupied and red ones are mostly empty. The superfluid density is negligibly small. Further increase of the chemical potential does not change the system until it reaches a discontinuous phase transition to the second superfluid phase. This phase persists up to the final phase transition to the fully occupied state.

Our results are still in the preliminary stage, and will need further investigation before we report our results in full details. However, our aim is to systematically modify the discrete lattice model to closer proximity to the realistic model for the helium-on-graphite system that is defined in continuous space, thereby obtaining information complementary to the continuous space simulation.

Novel phases in frustrated spin systems

Tsuyoshi OKUBO
Institute for Solid State Physics, University of Tokyo
Kashiwa-no-ha, Kashiwa, Chiba 277-8581

The kagome lattice Heisenberg antiferromagnet is a typical example of the two-dimensional frustrated spin systems. Due to strong quantum fluctuations, the ground state of the $S = 1/2$ quantum spin kagome lattice Heisenberg model is expected to be a spin-liquid state without any magnetic long-range orders. Under magnetic fields, it has been proposed that several magnetization plateaus at $1/9, 1/3, 5/9$, and $7/9$ of the saturation magnetization appear in the magnetization curve based on a density matrix renormalization group (DMRG) calculation [1]. Recently, a tensor network calculation has also shown the existence of these magnetization plateaus [2]. On the other hand, based on the exact diagonalization (ED) up to 42 sites, Nakano and Sakai proposed that the expected $1/3$ plateau has peculiar critical exponents compared to other two-dimensional systems such as the triangular lattice Heisenberg antiferromagnets [3, 4].

In this year project, we have investigated the ground state properties of $S = 1/2$ kagome lattice Heisenberg antiferromagnet under external magnetic fields using a infinite Projected Entangled Pair State (iPEPS) tensor network method. In this iPEPS method, we represent the ground state wave-function as the two-dimensional network of tensors (Fig. 1). By optimizing each tensor so as to minimize the energy, we obtained wave-functions close to the ground state under magnetic fields. The magnetization curve obtained by iPEPS contains clear $1/9, 1/3, 5/9$ and $7/9$ plateaus that are consistent with the previous calculations. We also investigated effects of the Dzyaloshinskii-Moriya (DM) interaction, which exists in real kagome lattice compounds. Our calculation shows that the plateau width becomes smaller when we increase the amplitude of the DM interaction and the plateaus disappear for $D_z/J \gtrsim 0.1$.

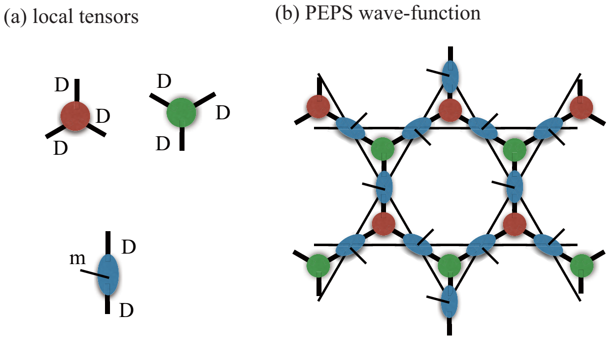

Figure 1: Tensor network representation of the ground state wave-function for the kagome lattice Heisenberg antiferromagnet.

References

[1] S. Nishimoto, N. Shibata, and C. Hotta, Nat. Commun. **4**, 2287 (2013).

[2] T. Picot, M. Ziegler, R. Orus, and D. Poilblanc, arXiv:1508.07189.

[3] H. Nakano and T. Sakai, J.Phys.Soc.Jpn. **79**, 053707 (2010).

[4] H. Nakano and T. Sakai, J.Phys.Soc.Jpn. **83**, 104710 (2014).

Structure formation of biomembranes

Koh M. NAKAGAWA[a], Hayato SHIBA[a,b], J.-B. FOURNIER[c], and Hiroshi NOGUCHI[a]
[a] *Institute for Solid State Physics, University of Tokyo, Kashiwa, Chiba 277-8581*
[b] *Institute for Materials Research, Tohoku University 2-1-1 Sendai 980-8577*
[c] *Laboratoire Matière et Systèmes Complexes (MSC), UMR 7057 CNRS,*
Université Paris, Diderot, F-75205, Paris, France

We have studied the following three phenomena using ISSP super computer this year.

1 Vesicle dynamics induced by chemical reaction

Some softmatter systems exhibit various shape transformations induced by chemical reactions, for example, self-beating gel, self-reproducing vesicle, and cell-division. Recently we studied shape transformations of an oil droplet induced by dehydrocondensation reaction using dissipative particle dynamics simulations [1]. Various types of shape transformations are found such as a spherical oil to a tubular vesicle and toroidal vesicle. Multiple daughter vesicles generation from the oil droplet is found during the shape transformation, and this process is also found in the experimental observations.

To investigate chemical-reaction-induced shape transformations further, we examine shape transformations of vesicle induced by hydrolysis reaction. The hydrolysis reaction are modeled as a stochastic process. A forward chemical reaction (bond breaking) and inverse chemical reaction (bond binding) are included in this chemical reaction model. Hydrolysis reaction changes the number difference of amphiphile molecules between two monolayers of the vesicle, resulting in various shape transformations such as budding and bilayer protrusion into inside of the vesicle (Fig. 1 (a) bilayer protrusions and (b) budding). We also found that these shape transformation pathways strongly depend on a spatial inhomogeneity of reaction products and stress relaxation time scale, which depends on the bilayer elastic modulus and solvent shear viscosity.

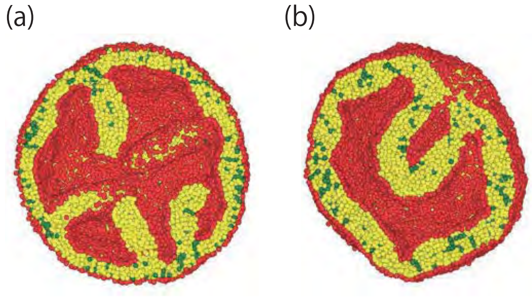

Figure 1: Two snapshots of typical shape transformations. (a) bilayer protrusions and (b) budding.

2 Relation between three membrane surface tensions

Three types of the surface tensions can be defined for lipid membranes: internal tension σ conjugated to real membrane area, mechanical frame tension τ conjugated to the projected area, and "fluctuation tension", r, obtained from the fluctuation spectrum of the membrane height. We studied the relation of these surface tensions using the Monte-Carlo simulation technique for a lattice membrane defined by a Monge gauge, where the membrane surface is described as a function of height [2]. It involves the exact, nonlinear, Helfrich Hamiltonian and a measure correction for excess entropy of the Monge gauge.

Our results for tor the relation between σ and τ corresponds very well to the previous theoretical prediction based on a Gaussian approximation. The fluctuation tension r coin-sides with the frame tension with an accuracy of our simulation. We checked that our conclusions are valid for an different ensemble in which the membrane area is controlled.

3 Shape transformation induced by banana-shaped proteins

In living cells, membrane morphology is regulated by various proteins. Many membrane reshaping proteins contain a Bin/Amphiphysin/Rvs (BAR) domain, which consists of a banana-shaped rod. The BAR domain bends the biomembrane along the rod axis and the features of this anisotropic bending have recently been studied. We study as to how such a local anisotropic curvature induces effective interaction between proteins and changes the global shape of vesicles and membrane tubes using meshless membrane simulations. The proteins are modeled as banana-shaped rods strongly adhered to the membrane.

As reported last year, the rod assembly occurs separately in parallel and perpendicular directions with coupled membrane shape deformation at low rod density. This year, we revealed that polyhedral vesicles and polygonal tubes are stabilized at high rod densities [3]. The discrete shape transition between triangular and buckled discoidal tubes and between polyhedral shapes are obtained. As line tension of the membrane edge is reduced, the protein adhesion induces membrane rupture leading to high-genus vesicle formation and vesicle inversion [4]. These shape transformations and assemblies are not obtained by isotropic inclusions.

We also studied the effects of the spontaneous (side) curvature perpendicular to the rod, which can be generated by protein-protein and membrane-protein interactions [5]. We revealed that the perpendicular curvature can drastically alter the tubulation dynamics from a flat membrane at high protein density whereas no significant difference is obtained at low density. A percolated network is intermediately formed depending on the perpendicular curvature (see Fig.2). This network suppresses tubule protrusion. The stability of network structures can be explained by a simple geometric model. Positive surface tensions and the vesicle membrane curvature can stabilize this network structure by suppressing the tubulation. It is known that tubulation dynamics can be different even for proteins consisting of the same BAR domains. Our finding suggests that the interactions between the rest parts of the proteins can give significant effects.

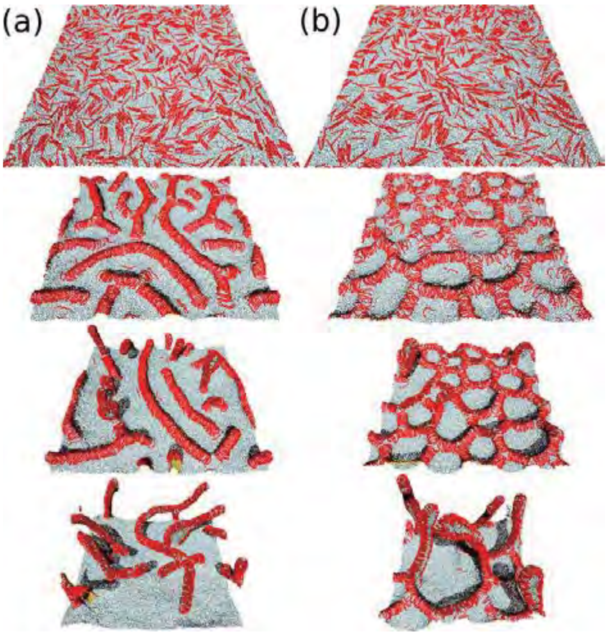

Figure 2: Sequential snapshots of tabulation from a flat membrane induced by protein rods. (a) Positive perpendicular rod curvature. (b) Negative perpendicular rod curvature.

References

[1] K. M. Nakagawa and H. Noguchi: Soft Matter **11**, 1403 (2015).

[2] H. Shiba, H. Noguchi, and J.-B. Fournier: Soft Matter **12**, 2373 (2016).

[3] Noguchi: J. Chem. Phys. **143**, 243109 (2015).

[4] Noguchi: Phys. Rev. E **93**, 052404 (2016).

[5] Noguchi: Sci. Rep. **6**, 20935 (2016).

Dynamical properties and thermal properties of Kitaev-Heisenberg models on a honeycomb lattice

Takafumi SUZUKI
Graduate school of Engineering,
University of Hyogo, Shosha 2167, Himeji, Hyogo 670-2520

In this project, we studied dynamical properties and thermal properties of Kitaev-Heisenberg models on a honeycomb lattice.

Magnetic properties of 4d and 5d transition metal compounds have attracted much attention in condensed matter physics. In some materials, the energy scales of spin-orbit interactions, on-site coulomb interactions, and crystal fields compete with each other and such competition can produce an interesting phase, namely the Kitaev's spin liquid. Na_2IrO_3, for instance, is considered as a candidate for realization of the Kitaev's spin liquid. In Na_2IrO_3, each Ir^{4+} ion constituting the honeycomb-lattice network carries a total angular momentum J_{eff} =1/2. Since IrO_6 octahedrons are connected by sharing the oxygen atoms on the edges making the Ir-O-Ir bond angle nearly 90^o, three kinds of anisotropic interactions are expected between the transition metal ions depending on the bonding direction. Thus, considering the direct interactions via overlap of 5d orbits, Na_2IrO_3 is expected to be described by the Kitaev-Heisenberg model [1] on the honeycomb lattice.

Na_2IrO_3 shows an antiferromagnetic zigzag order below T_N~15 [K]. In a typical Kitaev-Heisenberg model, where ferromagnetic Kitaev and antiferromagnetic Heisenberg interactions are summed for nearest neighbor pairs, the zigzag order is not stabilized. Thus, several magnetic effective models have been proposed to explain the zigzag order.

In order to discuss the proper model for Na_2IrO_3, we evaluated the dynamical properties of five models proposed in Refs. [2-6]. By using exact diagonalization method, we calculated dynamical structure factor (DSF) up to N=32 site cluster. First, we compared the numerical results for the candidate models [2-6] and the inelastic neutron scattering results [2]. We found that the model model proposed in the Ref. [5] can explain the experimental results well. Next, we calculated the linearized spin-wave dispersion to discuss the characteristics of the low-lying magnetic excitations. The obtained results indicated that the spin-wave excitations in the magnetic ordered phases fail to explain the low-lying excitations of the DSFs, when the system is located in the vicinity of the Kitaev's spin liquid phase. In contrast, if the system is placed in the depth of the magnetic ordered phase, the low-lying excitation can be successfully explained by the spin-wave excitation. We also studied the temperature dependence of the specific heat. If the system is located in the vicinity of the Kitaev's spin liquid phase, where the spin-wave picture for the low-lying magnetic excitations is broken down, we observe a clear two-peak structure in the temperature dependence of the specific heat that is also observed in the Kitaev's spin liquid phase. The origin of the two-peak structure in the specific heat is associated with the fractionalization of quantum spins, emergence of two Majorana fermions. Therefore, the obtained result implies that the two-peak structure of the specific heat becomes a good indicator for the closeness to the Kitaev's spin liquid phase [8].

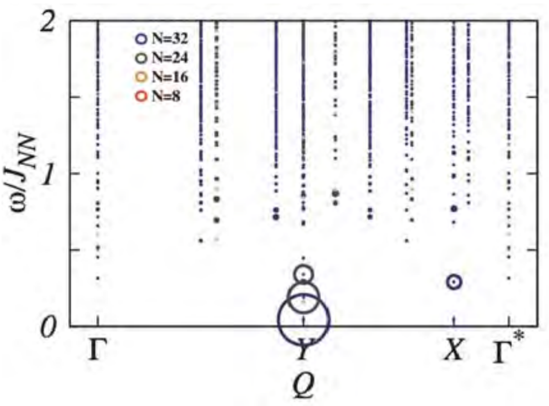

Fig 1. Dynamical structure factor of the effective model for Na_2IrO_3 proposed in Ref. [5]. Area of circles corresponds to the scattering intensity. $J_{\rm NN}$ the nearest-neighbor Heisenberg interaction and $J_{\rm NN} \sim 4.17$ [meV].

References

[1] G. Jackeli and G. Khaliullin, Phys. Rev. Lett. **102**, 017205 (2009).

[2] S. K. Choi, R. Coldea, A. N. Kolomogorov, T. Lancaster, I. I. Mazin, S. J. Blundell, P. G. Radealli, Y. Singh, P. Gegenwart, K. R. Choi, et al., Phys. Rev. Lett. **108**, 127204 (2012).

[3] J. Chaloupka, G. Jackeli, and G. Khaliullin, Phys. Rev. Lett. **110**, 097204 (2013).

[4] V. M. Katukuri, S. Nishimoto, V. Yushankhai, A. Stroyanova, H. Kandpal, S. Choi, R. Coldea, I. Rousochatzakis, L. Hozoi, and J. van den Brik, New J. Phys. **16**, 013056 (2014).

[5] Y. Yamaji, Y. Nomura, M. Kurita, R. Arita, and M. Imada, Phys. Rev. Lett. **113**, 107201 (2014).

[6] Y. Sizyuk, C. Price, P. Wolfe, and N. B. Perkins, Phys. Rev. B **90**, 155126 (2014).

[7] T. Suzuki, Y. Takuto, Y. Yamaji, and S. Suga, Phys. Rev. B **92**, 184411 (2015).

[8] Y. Yamaji, T. Suzuki, Y. Yamada, S. Suga, N. Kawashima, and M. Imada, arXiv:1601.

Development of Quantum Monte Carlo Algorithm and Application to Hardcore Bose System

Akiko Masaki-Kato

Riken,

Hirosawa, Wako, Saitama 351-0105

The worm algorithm for quantum Monte Carlo methods based on the Feynman's path integral is capable of global updates of the worldline configuration and has a broader range of applicability for quantum lattice model without the negative sign problem. However parallelization of the worm algorithm is nontrivial because of the event-driven process of updates by single moving-worm. We have developed the parallelized multi-worm algorithm (PMWA) and, in last year, we presented the numerical recipe of this algorithm which is described to be applicable for general quantum lattice model in Ref. [1]. PMWA is implemented on the directed loop algorithm (DLA) [2], a kind of the worm algorithm. In PMWA we execute to measure physical quantities in configuration space including many worms introduced by the additional source field to the Hamiltonian. After the simulation, we extrapolate the source field to 0 to obtain values without the source field.

This year, we developed the method of measuring various physical quantities, especially G-sector measurement i.e. off-diagonal quantities. Besides we investigated extrapolation rules of the various quantities. To give practical arguments, we focus on hardcore boson model. We first determined the 3D phase diagram of the ground state of this model under the source field (Fig.1) in order to make use of extrapolation. This phase diagram can be mapped to S=1/2 spin model under the both transvers and longitudinal field as shown in Fig. 1. We accurately explored the phase boundary by finite size scaling with the different system size up to L=576 and the inverse temperature β = L/2. To calculate large size we impose the nontrivial parallelization with domain decomposition of the configuration space and the trivial parallelization to calculate statistical error with 1728 cores of F144 queue. Then we measure the various quantities of hardcore boson with/without random potential. We find that integrated quantities, e.g. the compressibility and the xx-susceptibility, rapidly change by small source field, therefore it is difficult to extrapolate. To improve this problem we use the modified definition of these quantities. The modified quantities coincide the original quantities at 0 limit of the source field and change relatively slow for the source field[3].

Moreover, this year, we have opened our

source codes on a github repository[4] as an application named “DSQSS” which consist of not only DLA for serial or trivial-parallel simulations but also PMWA for nontrivial parallel simulation. We prepare the manual and tutorial for calculating Heisenberg models. For a future work we are planning to unify the DLA code and the PMWA cod and provide various tutorials.

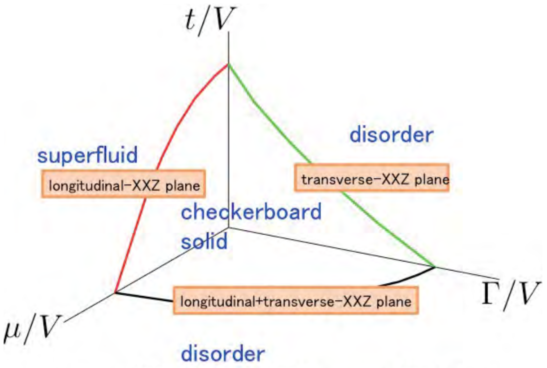

$$\mathcal{H} = -t \sum_{<i,j>} b_i^\dagger b_j + V \sum_i n_i n_j - \Gamma \sum_i (b_i^\dagger + b_j)$$

Fig. 1:The phase diagram of the ground state of the hardcore boson.

References

[1] A. Masaki-Kato, T. Suzuki, K. Harada, S. Todo, N. Kawashima, Phys. Rev. Lett., 112, 140603 (2014).

[3] A. Masaki-Kato and N. Kawashima, in preparation.

[4] https://github.com/qmc/dsqss/wiki.

Equilibrium and dynamical properties in glassy systems

Koji Hukushima
Department of Basic Science, University of Tokyo
3-8-1 Komaba, Meguro-ku, Tokyo 153-8902

Frustration is a key concept in condensed matter physics. In particular, the frustration in classical magnetism caused by competing interactions provides us novel critical and ordering phenomena such as re-entrant transition. In many-particle systems, a competition between local-packing patterns and global crystallization can lead to frustration. Such frustration plays also an important role in structural glass transition.

In this project, we studied an effect of geometrical constraints in a lattice glass model. More specifically, hard rigid rods with k successive occupied sites are put on a three-dimensional lattice. This system has no interaction except for hard-core repulsion and a possible phase transition is entropy driven. This rigid-rods system in two dimensions has been studied by Ghosh and Dhar. They found that an orientational long range order occurs at finite mean coverage of rods in the system for $k \geq 7$. The transition of the orientational transition is of second order and its universality class depending on the lattice structure belongs to two-dimensional Ising model for a square lattice. In our work, we use the exchange MC method for accelerating equilibrium process, which allows us to achieve equilibration of the system for large sizes. It is found that, in contrast to the two dimensions, the system even with $k = 6$ in a simple cubic lattice exhibits the second-order orientational phase transition. No explicit interaction between any two layers is there in the system. Therefore, the order-parameter distribution has a different structure between the systems with $k = 6$ and $k \geq 7$. However, finite-size scaling analysis reveals that the systems share a common universality class, independent of the value of k, which belongs to three-dimensional three-state antiferromagnetic Potts model.

Another topic is a development of Markov-chain Monte Carlo (MCMC) algorithms. Some simple algorithms with local updates including the original Metropolis algorithm frequently suffer from difficulties of slow relaxation The cluster algorithms are one of the promising ways for overcoming the slow relaxation, but unfortunately they do not work in frustrated spin systems. Recently, another type of algorithms has attracted great interests, which does not rely on the detailed balance condition. The event-chain Monte Carlo (ECMC) algorithm is one of such algorithms breaking the detailed balance condition. ECMC is proposed originally for hard-sphere systems and is subsequently generalized for more general particle systems such as soft-sphere and Lennard–Jones particles and continuous spin systems such as XY and Heisenberg spin models[1]. We applied ECMC to a Heisenberg ferromagnetic model in three dimensions and found that it enables to reduce the dynamical exponent from a conventional value $z = 2$[1]. Furthermore, using a large scale simulation with ECMC, phase transitions in a Heisenberg spin model of a chiral helimagnet with the Dzyaloshinskii–Moriya interaction in three dimensions are studied. In the presence of a magnetic field perpendicular to the axis of the helical structure, it is found that there exists a critical point on the temperature and magnetic-field phase diagram and that above the critical point the system exhibits a phase transition with strong divergence of the specific heat and the uniform magnetic susceptibility[2].

[1] Y. Nishikawa, M. Michel, W. Krauth, K. Hukushima: Phys. Rev. E**92**, 063306 (2015).
[2] Y Nishikawa, K Hukushima: arXiv preprint arXiv:1603.04200

Entanglement and Quantum Phase Transition in Quantum Spin Systems

Synge Todo
Department of Physics, University of Tokyo, Tokyo 113-0033, Japan
Institute for Solid State Physics, University of Tokyo, Kashiwa, 277-8581, Japan

Quantum phase transitions are phase transitions between two different ground states that are triggered by quantum fluctuations at absolute zero temperature. We develop various novel and powerful techniques to tackle various exotic quantum critical phenomena observed in quantum spin systems and performed large-scale and high-precision simulations on the ISSP supercomputer system.

Critical Phenomena of quantum systems with strong spatial and temporal anisotropy: we have developed a generic method that can automatically optimize the aspect ratio of the system by the combination of the quantum Monte Carlo method and the machine learning technique, and applied to the two-dimensional Bose-Hubbard model with dynamical exponent $z > 1$ [1]. We also extended our method to systems with quenched randomness and studied the dynamical property of the Superfluid-Bose-Glass transition.

Analysis of quantum phases and quantum phase transitions by local Z_N Berry phase: we have developed a new quantum Monte Carlo technique for calculating the overlap of two wave functions (including phase factor), and applied it to the local Z_N Berry phase that is a topological order parameter for low-dimensional quantum magnets.

Critical phenomena of long-range interacting spin model: using the $O(N)$ cluster algorithm, we have precisely studied the critical exponents and critical amplitudes of the long-range interacting spin model on the square lattice, and established the non-trivial dependence of the critical exponents on the exponent of interaction σ.

QMC level spectroscopy: It is hard to estimate the gap precisely in the quantum Monte Carlo simulations because it is not simply expressed by an average with respect to the Boltzmann distribution. We devised an unbiased and reliable gap-estimation method in the worldline quantum Monte Carlo simulations [2]. It was shown that the criticality of the spin-phonon model is described by the Wess-Zumino-Witten model and the quantum nature of the lattice degrees of freedom is essential to the one-dimensional quantum spin or spinless fermion systems.

The programs used in the present research projects have been developed based on the open-source libraries: ALPS [3], ALPS/looper [4], BCL [5], worms [6], etc.

References

[1] S. Yasuda, H. Suwa, and S. Todo: Phys. Rev. B **92** (2015) 104411.

[2] H. Suwa and S. Todo: Phys. Rev. Lett. **115** (2015) 080601.

[3] http://alps.comp-phys.org/.

[4] http://wistaria.comp-phys.org/alps-looper/.

[5] http://github.com/cmsi/bcl.

[6] http://github.com/wistaria/worms.

Estimation of spin-spin interactions from magnetization process by Bayesian inference

Ryo TAMURA
Computational Materials Science Unit, National Institute for Materials Science,
1-1 Namiki, Tsukuba, Ibaraki, 305-0044

The importance of data-driven technique using the machine learning has been well recognized in both academic and industrial fields. By using the machine leaning, we can estimate an appropriate governing equation by finite observable data sets. In the condensed matter physics, the machine learning techniques have been used for such as interpolating Density Functional Theory (DFT)[1] and Dynamical Mean-Field Theory (DMFT)[2] calculations, and for model selection of strongly correlated systems[3] and the Ginzburg-Landau equation[4].

We developed a method for estimating spin-spin interactions in the Hamiltonian from a given magnetization process by the machine learning based on the Bayesian statistics[5]. In the estimation method, plausible spin-spin interactions that explain the given magnetization process are determined by maximizing the posterior distribution. It is obtained as the conditional probability of the spin-spin interactions for a given magnetization process with observation noise.

The efficiency of the estimation method was tested for a case of synthetic magnetization process data obtained by the classical Heisenberg model. In this research, we used the Markov chain Monte Carlo (MC) method and the exchange MC method to analyze the posterior distribution. The combination of Markov chain MC and exchange MC methods makes a significant contribution to finding the global maximum of the posterior distribution in systems where many local maxima exist. Results showed that the developed estimation method enables estimation of the spin-spin interactions with high accuracy and, in particular, the relevant terms of the spin-spin interactions are successfully selected from among redundant interaction candidates by using l_1 regularization in the prior distribution:

$$P(\mathbf{x}) \propto \exp\left(-\lambda \sum_{k=1}^{K} |x_k|\right), \tag{1}$$

where $\{x_k\}$ denotes the set of spin-spin interactions and K is the number of spin-spin interactions we consider. The inference scheme using the prior distribution is called Least Absolute Shrinkage and Selection Operator (LASSO)[6] and the value of λ controls the strength of regularization. We would like to emphasize that the framework of our estimation method can be used not only for magnetization processes but also for any measured data as the input data.

This work was done in collaboration with Koji Hukushima (The University of Tokyo).

References

[1] Z. Li, J. R. Kermode, and A. D. Vita, Phys. Rev. Lett. **114** (2015) 096405.

[2] L.-F. Arsenault, A. Lopez-Bezanilla, O. A. Lilienfeld, and A. J. Millis: Phys. Rev. B **90** (2014) 155136.

[3] H. Takenaka, K. Nagata, T. Mizokawa, and M. Okada: J. Phys. Soc. Jpn. **83** (2014) 124706.

[4] S. Taverniers, T. S. Haut, K. Barros, F. J. Alexander, and T. Lookman: Phys. Rev. E **92** (2015) 053301.

[5] R. Tamura and K. Hukushima: in preparation.

[6] R. Tibshirani: J. Royal. Statist. Soc. B. **58** (1996) 267.

Impurity effect on magnetocaloric effect in Gadolinium alloy

Ryo TAMURA
Computational Materials Science Unit, National Institute for Materials Science,
1-1 Namiki, Tsukuba, Ibaraki, 305-0044

Cooling phenomena are widely used in everyday applications, such as food storage and medical treatment, and also in technology for next-generation electronics, such as hydrogen-fuel cells and quantum information processing. Thus, high-performance cooling technology has been actively developed for many fields. Magnetic refrigeration is a promising candidate for next-generation cooling technology that can solve environmental and noise problems. The key to the magnetic refrigeration is the change of magnetic entropy in magnetic materials under different magnetic fields, which is known as the magnetocaloric effect[1, 2, 3].

The Active Magnetic Regeneration Refrigeration (AMRR) cycle is a typical cycle to perform magnetic refrigeration. In this cycle, the multiple magnetic materials are used. In each magnetic material, the temperature exhibiting the maximum magnetic entropy change is different. Then, to change the temperature at which the magnetic entropy change becomes maximum is important for practical applications of magnetic refrigeration with various temperature range. In order to control this temperature, the impurity effect has been often considered. In general, the maximum magnetic entropy change is realized around the phase transition temperature in each magnetic material. Thus, using the impurity effect, the phase transition temperature can be changed. We studied the impurity effect on the magnetocaloric effect for the Gadolinium alloy [4].

Gadolinium alloy is a ferromagnetic material with the Curie temperature which is around the room temperature and is a typical magnetocaloric material. In order to clarify the impurity effect in Gadolinium alloy, we considered that some of the Gd ions are substituted for non-magnetic ions. By using Monte Carlo simulations, we calculated, depending on the concentration of non-magnetic ions, specific heat and magnetic entropy change of the $S = 7/2$ Ising model as an effective model of Gadolinium alloys. The obtained results were compared with experimental results in the Gd-R alloy (R = Y, Zr). The results showed that the Curie temperature linearly decreases with the concentration of non-magnetic ions in the effective model, which was observed in the Gd-R alloy.

This work was done in collaboration with R. Arai (Chiba University), H. Fukuda (Chiba University), J. Li (Chiba University), A. T. Saito (Toshiba Corporation), S. Kaji (Toshiba Corporation), H. Nakagome (Chiba University), and T. Numazawa (NIMS).

References

[1] R. Tamura, T. Ohno, and H. Kitazawa: Appl. Phys. Lett. **104** (2014) 052415.

[2] R. Tamura, S. Tanaka, T. Ohno, and H. Kitazawa: J. Appl. Phys. **116** (2014) 053908.

[3] S. Toyoizumi, H. Kitazawa, Y. Kawamura, H. Mamiya, N. Terada, R. Tamura, A. Dönni, K. Morita, and A. Tamaki: J. Appl. Phys. **117** (2015) 17D101.

[4] R. Arai, R. Tamura, H. Fukuda, J. Li, A. T. Saito, S. Kaji. H. Nakagome, and T. Numazawa: IOP Conf. Ser.: Materials Science and Engineering **101** (2015) 012118.

Randomness-induced quantum spin-liquid behaviors in the frustrated spin-*1/2* Heisenberg antiferromagnets on two-dimensional lattices

Hikaru Kawamura, Kazuki Uematsu and Tokuro Shimokawa
Graduate School of Science, Osaka University, Toyonaka 560-0043

The quantum spin-liquid (QSL) state possibly realized in certain $S=1/2$ frustrated magnets has attracted interest of researchers. After a long experimental quest, several candidate materials were recently reported in certain geometrically frustrated magnets, including both the triangular-lattice and the kagome-lattice antiferromagnets (AFs).

In our 2013 and 2014's project, with examples of triangular-lattice $S=1/2$ organic salts such as κ-(ET)$_2$Cu$_2$(CN)$_3$ and EtMe$_3$Sb[Pd(dmit)$_2$]$_2$ and the kagome-lattice AF herbertsmithite CuZn$_3$(OH)$_6$Cl$_2$ in mind, we investigated the properties of the bond-random $S=1/2$ AF Heisenberg model on the triangular and the kagome lattices by means of an exact diagonalization (ED) method. The Hamiltonian is given by $\Sigma_{<ij>} J_{ij} S_i S_j$ where the nearest-neighbor exchange coupling J_{ij} is assumed to obey the bond-independent uniform distribution between $[(1-\Delta)J, (1+\Delta)J]$ with the mean J. The parameter Δ represents the extent of the randomness.

We then found that the model exhibited a randomness-induced gapless QSL behavior at low temperatures [1,2]. This "random singlet" state explains many of the experimental features observed in the triangular organic salts and the kagome herbertsmithite.

In this year's project, we extend these calculations for the AF bond-random $S=1/2$ Heisenberg models in three directions. First, in order to get further detailed information on the nature of spin correlations in the random-singlet state, we newly compute static and dynamical spin structure factors $S(q)$ and $S(q, \omega)$ by the ED method both for the triangular and the kagome models [3]. As an example, we show in Fig.1 the computed static spin structure factor $S(q)$ of the random kagome-lattice model of $\Delta=1$.

Second, we newly computed several finite-temperature properties of both the random triangular and kagome models by means of the TPQ (thermal pure quantum state) method for lattices considerably larger than those obtained by the standard ED method. The obtained new data have confirmed and strengthened our earlier conclusions about the gapless nature of the random-singlet state, including the T–linear low-T specific heat and the gapless behavior of the susceptibility with a Curie tail, also revealing some new features [4].

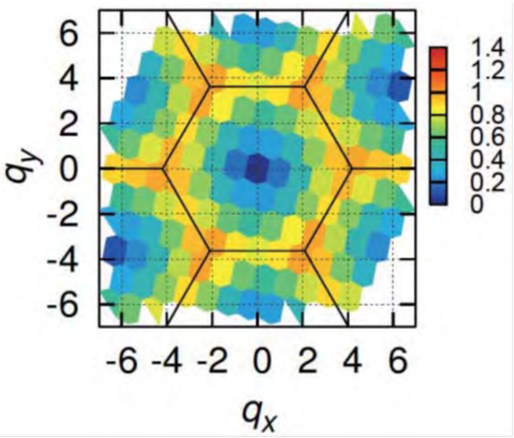

Fig. 1: The ground-state spin structure factor $S(q)$ in the (q_x,q_y) plane in the random singlet state of the random kagome model with ⊿=1. The system size is N=30.

Third, in order to get a wider view on the generality of the random-singlet state, and especially, to understand how frustration and randomness cooperate to realize the phase, we also studied the properties of the S=1/2 random Heisenberg model on the *honeycomb lattice* with the next-nearest-neighbor interaction (J_1-J_2 model) in comparison with those of the triangular and the kagome lattices [5]. Honeycomb lattice might be interesting because of its potential to sustain enhanced fluctuations originating from the weak connectivity of the lattice (small number of nearest neighbors, $z=3$). We draw a $T=0$ phase diagram in the plane of frustration (J_2) and randomness (⊿) plane by means of the ED method, and the result is shown in Fig.2. One sees that the random-singlet phase appears in a wide region of the phase diagram.

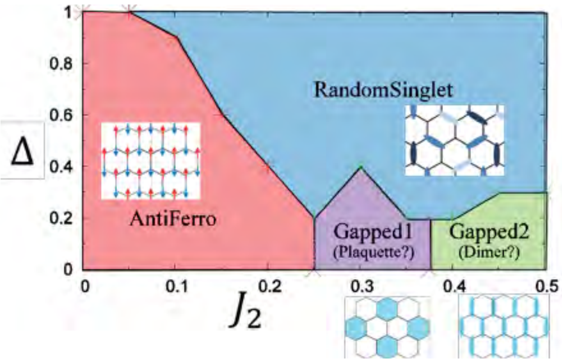

Fig. 2: The ground-state phase diagram of the J_1-J_2 random kagome model in the frustration (J_2) vs. randomness (⊿) plane.

[1] K. Watanabe, H. Kawamura, H. Nakano and T. Sakai, J. Phys. Soc. Jpn. **83**, 034714 (2014).

[2] H. Kawamura, K. Watanabe, and T. Shimokawa, J. Phys. Soc. Jpn. **83**, 103704 (2014)

[3] T. Shimokawa and H. Kawamura, Phys. Rev. B **92**, 134407 (2015).

[4] T. Shimokawa and H. Kawamura, in preparation.

[5] K. Uematsu and H. Kawamura, in preparation.

Effects of inhomogeneity in the one-dimensional Burridge-Knopoff model of earthquakes

Hikaru Kawamura and Jun Akutagawa

Graduate School of Science, Osaka University, Toyonaka, Osaka 560-0043

An earthquake is a stick-slip dynamical instability of a pre-existing fault driven by the motion of a tectonic plate. Numerical simulations of earthquakes based on a simplified statistical model, the so-called Burridge-Knopoff (BK) model, has been popular in statistical physics and provided much information about statistical properties of earthquakes. Some of the properties of the BK model was reviewed in Ref.[1].

Earthquake, not doubt, is quite a complex phenomenon. One fundamental question is where its complexity is originated from. In one view, complexity of earthquakes is originated from the complexity or the heterogeneity of the fault, including the complexity of material properties such as the elastic and the frictional properties, or the complexity of the shape and geometry of the fault, *etc*. In the other view, the apparent complexity of earthquakes is self-generated even from simple uniform parameters via its nonlinear dynamics. It would be very important to understand which of these two contrasting views is appropriate or dominant in real earthquakes. In this year's project, we take the first step toward the understanding of the role of inhomogeneity in earthquake occurrence.

The model studied is the one-dimensional BK model under the rate-and-state friction law, where the step-type inhomogeneity is assumed in the frictional parameter b, i.e., the b parameter in the left half is taken smaller than that in the right half, $b_{left} < b_{right}$. In Fig.1, we show the probability that a given block becoming an epicenter for each type of events including 1) small events, 2) large unilateral events propagating left, 3) those propagating right, and 4) large events propagating to both sides. One sees that seismicity here is quite anisotropic.

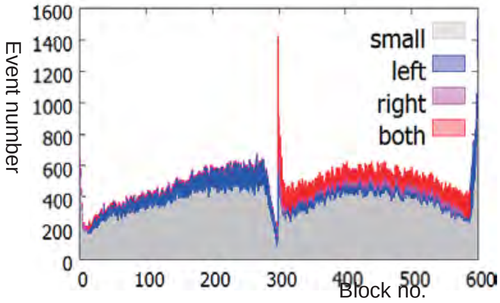

Fig.1 The number of events plotted versus the epicenter-block number of the event.

References

[1] For review, see, H. Kawamura, T. Hatano, N. Kato, S. Biswas and B.K. Chakrabarti, Rev. Mod. Phys. 84, 839-884 (2012).

Entanglement in A Solvable Quantum System – A Generalized Cluster-Ising Model –

Shu TANAKA
Waseda Institute for Advanced Study, Waseda University
1-6-1, Nishi-Waseda, Shinjuku-ku, Tokyo, 169-8050 Japan

Entanglement is an important concept in quantum information science, statistical physics, and condensed matter physics. Entanglement can be quantified by the entanglement entropy and entanglement spectrum. The entanglement entropy is obtained by the reduced density matrix which is calculated by tracing out the degree of freedom in a part of a system we consider. The entanglement entropy diverges logarithmically with the system size when the system is a one-dimensional critical system. On the contrary, the entanglement entropy converges to a particular value when the system is gapped. The entanglement spectrum is also obtained by the reduced density matrix, which characterizes topological properties of quantum systems.

We proposed a new one-dimensional topological model called a generalized cluster-Ising model [1] whose Hamiltonian is given by

$$\begin{aligned}\mathcal{H} = \quad & -J^{XZX}\sum_i \sigma_i^x\sigma_{i+1}^z\sigma_{i+2}^x \\ & -J^{YY}\sum_i \sigma_i^y\sigma_{i+1}^y \\ & -J^{YZY}\sum_i \sigma_i^y\sigma_{i+1}^z\sigma_{i+2}^y. \qquad (1)\end{aligned}$$

In this model, topological phase transitions appear depending on the parameters. The phase boundaries can be determined analytically since the above model can be transformed into a free fermion model[1, 2]. We identified each phase by some order parameters obtained by the time-evolving block decimation method for infinite systems (iTEBD). Entanglement properties of the model were also investigated by the exact diagonalization method. We found that the number of degenerated ground states corresponds to the number of the lowest eigenvalues of the reduced density matrix.

Next, we studied the dynamic behavior of the model under the sweep dynamics in which an interaction parameter changes with a finite speed. We found that the topological blocking phenomenon occurs at the topological phase transition point.

We expected that the obtained results are related to the quantum information processing based on the Ising model.

This work was done in collaboration with Takumi Ohta (YITP, Kyoto University), Ippei Danshita (YITP, Kyoto University), and Keisuke Totsuka (YITP, Kyoto University).

References

[1] T. Ohta, S. Tanaka, I. Danshita, and K. Totsuka: J. Phys. Soc. Jpn. **84** (2015) 063001.

[2] T. Ohta, S. Tanaka, I. Danshita, and K. Totsuka: Phys. Rev. B **93** (2016) 165423.

Quantum Phase Transition of the Spin Nanotubes

Tôru SAKAI[1,2,3], Hiroki NAKANO[1,2], and Tokuro SHIMOKAWA[3],
[1] *Graduate School of Material Science, University of Hyogo,*
Kouto, Kamigori, Hyogo 678-1297, Japan
[2] *Research Center for New Functional Materials, University of Hyogo,*
Kouto, Kamigori, Hyogo 678-1297, Japan
[3] *Synchrotron Radiation Research Center, Kansai Photon Science Institute,*
Quantum Beam Science Research Directorate,
National Institute for Quantum and Radiological Science and Technology (QST)
SPring-8, Kouto, Sayo, Hyogo 679-5148, Japan
[4] *Department of Physics, Osaka University, Toyanaka, Osaka 560-0043, Japan*

Recently some quantum spin systems on tube lattices, to called spin nanotubes, have been synthesized. They are expected to be interesting low-dimensional systems like the carbon nanotubes. As the first step of thoretical study on the spin nanotube, we investigate the S=1/2 three-leg spin tube, which is the simplest one, using the density matrix renormalization group (DMRG) and the numerical exact diagonalization (ED), conbined with a precise finite-size scaling analysis named level spectroscopy[1]. The spin gap, which is one of the most interesting macroscopic quantum effects, was revealed to be open due to frustration for sufficiently strong rung exchange couplings, in contrast to the three-leg spin ladder system which is gapless. The critical point of a quantum phase transition between the gapped and gapless phases was estimated. It is consistent with the previous effective Hamiltonian approach[1]. We also found a new quantum phase transition to another spin-gap phase caused by the ring exchange interaction. In addition we theoretically predicted some new field-induced quantum phase transitions. A chirality-mediated novel superconductivity mechanism is also proposed[2, 3].

The recent numerical diagonalization and finite size scaling analyses on the S=1/2 three-leg spin tube indicated a new quantum phase transition between the 1/3 magnetization phase and the plateauless one, with respect to the coupling anisotropy. The phase diagram at 1/3 of the saturation magnetization was presented[4].

References

[1] T. Sakai et al., Phys. Rev. B 78 (2008) 184415.

[2] T. Sakai et al., J. Phys.: Condens. Matter 22 (2010) 403201.

[3] K. Okunishi et al., Phys. Rev. B 85 (2012) 054416.

[4] T. Sakai and H. Nakano, Physics Procedia 75 (2015) 369.

Field-Induced Quantum Phase Transition in the Kagome-Lattice Antiferromagnet

Tôru SAKAI[1,2,3], Hiroki NAKANO[1,2], and Tokuro SHIMOKAWA[3],
[1] *Graduate School of Material Science, University of Hyogo,*
Kouto, Kamigori, Hyogo 678-1297, Japan
[2] *Research Center for New Functional Materials, University of Hyogo,*
Kouto, Kamigori, Hyogo 678-1297, Japan
[3] *Synchrotron Radiation Research Center, Kansai Photon Science Institute,*
Quantum Beam Science Research Directorate,
National Institute for Quantum and Radiological Science and Technology (QST)
SPring-8, Kouto, Sayo, Hyogo 679-5148, Japan
[4] *Department of Physics, Osaka University, Toyanaka, Osaka 560-0043, Japan*

The kagome-lattice antiferromagnets have attracted a lot of interest in the field of the low-temperature physics. It exhibits some exotic field-induced phenomena, like a magnetization plateau, jump etc. Our previous large-scale yumerical exact diagonalization study on the S=1/2 kagome-lattice antiferromagnet revealed that a novel field-induced phenomenon, "the magnetization ramp", occurs at 1/3 of the saturation magnetization[1]. It is characterized by different critical exponents between the lower-field and higher-field sides of the magnetization curve[2]. In order to clarify unconventional properties around the 1/3 magnetization, we considered some extended lattice models; a distorted kagome lattice and distorted triangular lattice etc[3]. The ground-state magnetization curve recently obtained by the numerical exact diagonalization up to 42-spin clusters is also presented to estimate the shape in the thermodynamic limit. Our numerical exact diagonalization study also indicates that the ground state of the kagome-lattice antiferromagnet is gapless quantum spin liquid.

The recent critical exponent analysis up to 42-spin cluster still confirmed the unconventional magnetization behavior around the 1/3 magnetization plateau-like anomaly; the field derivative is infinite at the low-field side, while it is zero at the high-field side[4].

References

[1] H. Nakano and T. Sakai, J. Phys. Soc. Jpn. 79 (2010) 053707.

[2] T. Sakai and H. Nakano, Phys. Rev. B 83 (2011) 100405(R).

[3] H. Nakano and T. Sakai, J. Phys. Soc. Jpn. 83 (2014) 104710.

[4] T. Sakai and H. Nakano, Physics Procedia 75 (2015) 821.

Protein-folding Simulations by Efficient Sampling Algorithms

Yasuteru Shigeta
Center for Computational Sciences,
University of Tsukuba, 1-1-1 Tennodai, Tsukuba, Ibaraki 305-8577

In recent progress in protein-folding simulations, force fields for the all-atom model have been updated extensively. Although further refinements might still be needed to improve accuracy, most current force fields are capable of folding proteins in good agreement with experimental data, indicating that semiempirical atomic force fields are accurate enough to simulate protein folding. However, it is expensive computationally to produce statistically reliable trajectories of protein folding to reach a typical folding time scale, i.e., milliseconds, because the time step for MD is typically 1 fs, so that 10^{12} iterations of the integration are required. Generally, the accessible time scale traced by the laboratory-level computer resources might be several hundreds of nanoseconds, which is far from the timescale for protein folding.

For this problem, We have recently proposed a series of methods as simple yet powerful conformational resampling methods [1]. In these methods, initial structures of the conformational resampling are selected as seeds by referring to several measures, and then short-time MD simulations from the selected seeds with different initial velocities from a previous run are performed. Cycles of the above selection and resampling are repeated until convergence of predefined criteria is reached. For rare event searches, a key point is how to select appropriate seeds with sufficiently high potential to make structural transitions, where measures should be given *a priori* so as to characterize the structural transitions of interest. We further performed applications of our methods to several biological systems, such as domain motions of proteins with large-amplitude fluctuations, conformational transitions upon ligand binding, and protein-folding/refolding [2]. We have also proposed an automatic detection of relevant reaction coordinates for protein folding on the basis of the algorithm used in our method [3].

References

[1] R. Harada, T. Baba, Y. Takano, Y. Shigeta: Phys. Chem. Chem. Phys. **17** (2015) 6155.

[2] R. Harada, T. Nakamura, Y. Takano, Y. Shigeta, J. Comp. Chem. **36** (2015) 763.

[3] R. Harada, T. Nakamura, Y. Shigeta, Chem. Phys. Lett. **639** (2015) 269.

Efficient Sampling Simulation of the Soft Modes Significantly Contribute to Protein Properties

Jacob SWADLING, Kazuhiro TAKEMURA, Yasutaka NISHIHARA,
Hisham DOKAINISH, Duy TRAN, Chika SATO, and Akio KITAO
Institute of Molecular and Cellular Biosciences, University of Tokyo

We will report our findings about hairpin loops using Replica Exchange Molecular Dynamics (REMD)[1] this year.

Hairpin loops are one of the most common secondary structural motifs found in RNA.[2] DNA hairpins, on the other hand, rarely occur in nature and as a consequence are far less studied. Our current work represents an in-depth computational comparison of the thermodynamics, structure formation and kinetics of these important secondary structures. We have used REMD to elucidate the free energy landscapes of single-stranded RNA and DNA, of sequence:

5'-UUUAACC(U)$_{18}$GGUU-3'
5'-TTTAACC(T)$_{18}$GGTT-3'

Each model consisted of 108 replicas of 32,522 atoms, simulated at temperatures ranging from 270 - 500 K for 1 μs.

REMD is a state-of-the-art method for the study of protein and RNA folding. REMD consists of M noninteracting replicas of the original system in the canonical ensemble at M different temperatures T_m ($m = 0,\ldots,M$). The trajectory of each independent replica is computed using MD. Adjacent replicas exchange temperatures according to a Boltzmann probability distribution. REMD essentially runs N copies of the system, randomly initialised, at different temperatures. Then, on the basis of the Metropolis criterion, configurations are exchanged at different temperatures. The idea of this method is to make configurations at higher temperatures available to the simulations at lower temperatures and vice versa. This results in a very robust ensemble that is able to sample both low- and high-energy configurations. REMD produces enhanced sampling over single trajectory MD because fixed-temperature conformations are much more easily trapped in local energy minima.

Our simulations have successfully reproduced many findings from single-molecule fluorescence experiments. Our simulations have added new insight and predictions to experiment, such as the complete structural distribution of folded, unfolded and misfolded conformations, that were previously unknown.

Melting temperatures visible in figure 1 show a difference of approximately 15 K between

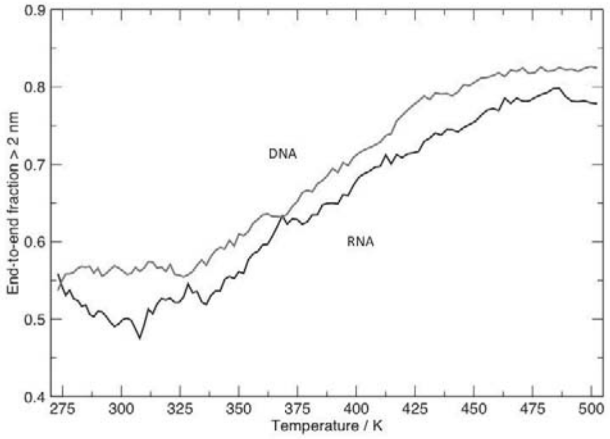

Fig 1 Melting curves based on average fraction of end-to-end distances greater than 2 nm, for RNA and DNA.

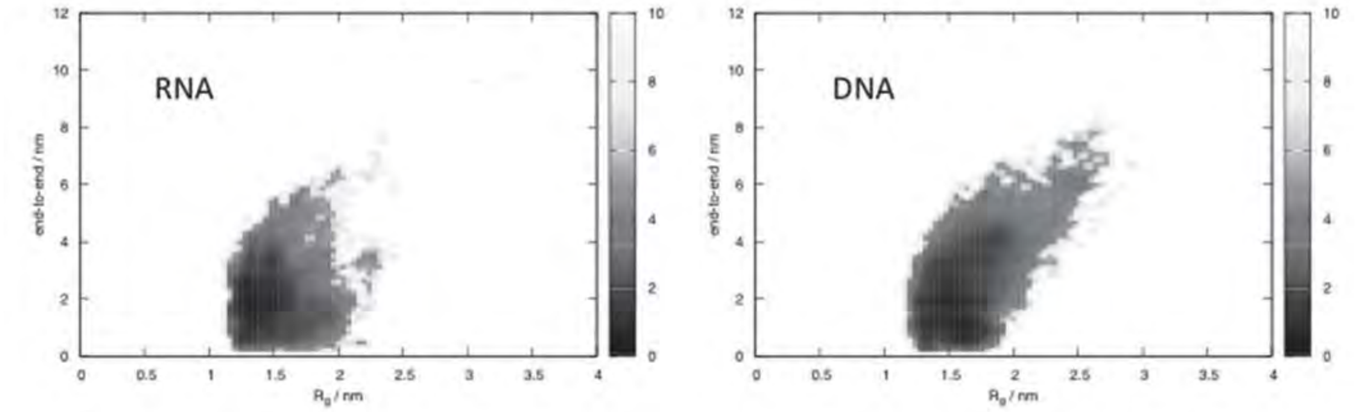

Fig 2 Free energy surface for RNA and DNA, shown as radii of gyration and end-to-end distances. The shading shows the relative population of that area of conformational space, with the darker area being more populated.

RNA and DNA, which corroborates with the values taken from single-molecule fluorescence experiments.

The free energy surfaces shown in figure 2 show the different areas of conformational space that RNA and DNA occupy. RNA structures occupy a smaller area of conformational space than DNA, corresponding to structures that have shorter end-to-end distances and smaller radius of gyration – indicating that RNA favours a more compact folded conformation over DNA. In comparison DNA conformations display a broad distribution occupying more space in the unfolded regime.

The distribution of persistence lengths (a basic mechanical property quantifying the stiffness of a polymer) show DNA is much stiffer than RNA and occupies a narrower distribution of lengths. This data agrees with the accessible conformational space of the two nucleic acid strands. The stiffness of the sequence plays a significant role in differences between the melting temperatures of the two nucleic acid analogues.

Folded DNAs are much less studied than RNAs but have been found to play an important role in replication, transcription regulation, and recognition. More recently, they were shown to be used as recombination sites. The structural diversity of RNA also contains information about biological processes that regulate biological functions.[3] Characterisation of the structural diversity and kinetics of folding will help our understanding of the fundamental role of RNA in biology. By comparing with a DNA analogue, we can realise the origins of unique RNA folding process.

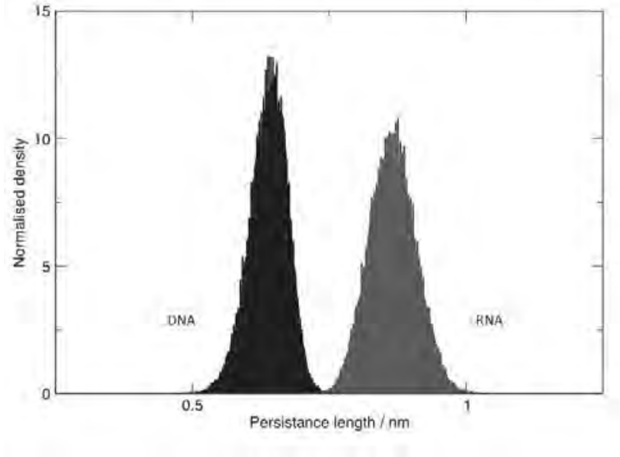

Fig 3 Distribution of Persistence lengths for DNA and RNA at 300 K.

References

[1] Y. Sugita and Y. Okamoto. *Chem. Phys. Lett.* 1999, 314, 141-151

[2] Bernat, V. ,and Disney, D., Neuron. 2015, **87**, 28-46.

[3] Donahue, C.P., Muratore, C., Wu, J.Y., Kosik, K.S., and Wolfe, M.S., J. Biol. Chem. 2006, **281**, 23302–23306.

Tensor network calculation on two-dimensional quantum spin models

Kenji HARADA
Graduate School of Informatics, Kyoto University, Kyoto 606-8501, Japan

Recently, the development of tensor network algorithm is very active. However, if we use the tensor network for applying the interesting problem in the condensed matter physics, we need high computational resources. To resolve this issue, we need to develop the parallel library for general tensor network computations.

In this year, we mainly focus on building a library of parallel tensor computations for general tensor network algorithms. If we define two composite indices by splitting the tensor indices into two groups, we can always regard a tensor as a matrix. Thus, most operations of tensors can be rewritten as matrix computations temporarily derived from original tensors. For example, the basics calculation of tensors is a tensor contraction. It can be rewritten as a matrix multiplication of temporal matrices. Based on a transformation between tensor and matrix, we often use various matrix algorithms in a tensor network algorithm: singular value decomposition, QR decomposition, and so on. Therefore, we can build our parallel library of tensor calculations on a parallel computational library for large-scale matrix calculations.

ScaLAPACK[1] is a library of high-performance linear algebra routines for parallel distributed memory machines. There are many implementations on large-scale distributed-memory machines as the system B on ISSP. Thus, we choose ScaLAPACK as the basics parallel matrix library for our tensor library. In detail, ScaLAPACK is built on PBLAS (Parallel BLAS)[2] library for distributed matrices. We define a distributed tensor as a distributed matrix of PBLAS. To calculate a tensor contraction, we first prepare two distributed matrices by using data transformations based on MPI routines, and we call a PBLAS Level 3 routine to a matrix multiplication on a distributed-memory machine. Since PBLAS Level 3 routines are highly optimized by vendors of supercomputers, the performance except for data transformations is good. Even if we consider the data transformation time, the use of PBLAS Level 3 is a good solution.

We have a plan to open our library with APIs similar to NumPy library of Python language in near future.

References

[1] J. Choi, J. Dongarra, S. Ostrouchov, A. Petitet, D. Walker, and R. C. Whaley, in Applied Parallel Computing Computations in Physics, Chemistry and Engineering Science, edited by J. Dongarra, K. Madsen, and J. Waniewski (Springer Berlin Heidelberg, Berlin, Heidelberg, 1995), pp. 107–114.

[2] J. Choi, J. Demmel, I. Dhillon, J. Dongarra, S. Ostrouchov, A. Petitet, K. Stanley, D. Walker, and R. C. Whaley, in Applied Parallel Computing Computations in Physics, Chemistry and Engineering Science, edited by J. Dongarra, K. Madsen, and J. Waniewski (Springer Berlin Heidelberg, Berlin, Heidelberg, 1995), pp. 95–106.

Numerical study on low-energy states of quantum spin systems

Hiroki NAKANO
Graduate School of Material Science, University of Hyogo
3-2-1 Kouto, Kamigori-cho, Ako-gun, Hyogo 678-1297, Japan

Since it is often difficult to estimate presicely physical quantities in systems of many-body problems in condensed matter physics, numerical approaches become more important. Under circumstances, computational studies have contributed much to our deeper understanding of such quantum systems. When quantum spin systems in spatial dimensions larger than one include frustrations, unfortunately, numerical studies are still difficult. The reason for this difficulty is that such systems cannot be treated by the density matrix renormalization group (DMRG) calculations and the quantum Monte Carlo simulations. Only the numerical diagonalization method based on the Lanczos algorithm is generally valid for such frustrated quantum spin systems in dimensions larger than one. This method, however, has a weak point. In this method, only very small system sizes can be treated. In order to overcome this disadvantage, we successfully developed a hybrid-type parallelized code of Lanczos diagonalization[1]. We study quantum spin systems using this Lanczos-diagonalization code we developed as a primary approach. Some quantum spin systems are examined from various points of view.

The primary study of this year in the present project examines the magnetization jump in the magnetization processes in the $S = 1/2$ Heisenberg antiferromagnet on the square-kagome lattice with a distortion[2]. The magnetization jump was originally observed in the case without the distortion[3]. Within the study of [3] examining the finite-size systems up to 36 sites, however, the skip of the jump δM in a finite-size system is detected up to $\delta M = 2$. Only the skip $\delta M = 2$ cannot deny the possibility that this jump appears owing to the formation of the spin-nematic state because this state is a two-magnon bound state. Then, we attack calculations for a system with larger size of 42 sites and successfully obtain the magnetization processes of the cases without and with a distortion. Our result for the undistorted system of 42 sites shows the same skip of $\delta M = 2$. When we introduce small distortion into the square-kagome lattice, on the other hand, we successfully observe the skip of $\delta M = 3$ in the 42-site system. This result indicates the exclusion of the possibility that this jump appears owing to the formation of a two-magnon bound state. This result also suggests that the magnetization jump is a macroscopic phenomenon which survives in the thermodynamic limit. The same behaviors of the jump are observed in the Heisenberg antiferromagnets on the Cairo-pentagon-lattice[4, 5], the $\sqrt{3} \times \sqrt{3}$-distorted kagome lattice[6, 7], and the *Shuriken*-bonded honeycomb lattice[6]. In these systems, however, only the finite-size jump of $\delta M = 2$ are detected. Further studies by calculations of larger sizes on these lattices will be required to clarify the behavior of the magnetization jump in the thermodynamic limit. Such studies will contribute to our understandings of this magnetization jump and the nontrivial effect of frustration in magnetic materials.

References

[1] H. Nakano and A. Terai: J. Phys. Soc. Jpn. **78** (2009) 014003.

[2] H. Nakano and T. Sakai: J. Phys. Soc. Jpn. **84** (2015) 063705.

[3] H. Nakano and T. Sakai: J. Phys. Soc. Jpn. **82** (2013) 083709.

[4] H. Nakano, M. Isoda, and T. Sakai: J. Phys. Soc. Jpn. **83** (2014) 053702.

[5] M. Isoda, H. Nakano, and T. Sakai: J. Phys. Soc. Jpn. **83** (2014) 084710.

[6] H. Nakano, Y. Hasegawa, and T. Sakai: J. Phys. Soc. Jpn. **83** (2014) 084709.

[7] H. Nakano and T. Sakai: J. Phys. Soc. Jpn. **83** (2014) 104710.

Numerical study of the low-lying excited state in low-dimensional frustrated magnetism

Tokuro SHIMOKAWA and Hikaru KAWAMURA

Faculty of Science, Osaka University

Machikane-yama, Toyonaka Osaka 560-0043

Recent theoretical studies have suggested that the effect of bond randomness could be the origin of the observed quantum spin liquid behaviors. Such a randomness-induced QSL is called "random-singlet (RS) state". It has been reported that the RS state might be realized in the S=1/2 random-bond antiferromagnetic (AF) Heisenberg models on the triangular and kagome lattices [1][2][3], and the possible importance of quenched randomness has been pointed out for understanding the observed QSL-like behaviors in herbertsmithite $ZnCu_3(OH)_6Cl_2$ and some organic salts such as κ-$(ET)_2Cu_2(CN)_3$ and $EtMe_3Sb[Pd(dmit)_2]_2$.

In this study, we have investigated the low-lying excited properties from RS state by using thermal pure quantum (TPQ) state method [4]. This TPQ method enables us to treat larger finite-size clusters than those treated with the exact diagonalization (ED) method. More concretely, the total number of spins N we treated is N= 18, 24, 30.

Previous ED calculation results [1][2] with small size ($N\leqq 18$) clusters exhibited the T-linear specific heat and gapless magnetic susceptibility with Curie like behavior in the RS state. In this study, we have computed the specific heat and magnetic susceptibility in larger size ($N\geqq 18$) systems. Figs. 1 show the calculation results of the specific heat (a) and the magnetic suscep-tibility (b) of the S=1/2 random-bond AF Heisenberg model on the triangular lattice. Here, Δ means the randomness parameter: Δ=0 and Δ=1 cases correspond to the regular and maximally random cases, respectively. (Details are shown ref. [1][2][3].) We can see clearly T-linear specific heat at low-temperature region and gapless magnetic susceptibility with Curie-like behavior in stronger randomness system even in N>18 size systems. We can also confirm these behaviors in Fig.2 (a) and Fig. 2 (b) exhibiting the numerical results of

S=1/2 random-bond AF Heisenberg model on kagome lattice.

Our TPQ calculations have been performed by using CPU and FAT nodes of system B. The parallel computing technique with OpenMP has been employed.

References

[1] K. Watanabe, H. Kawamura, H. Nakano, and T. Sakai: J. Phys. Soc. Jpn. **83** (2014) 034714.

[2] H. Kawamura, K. Watanabe, and T. Shimokawa: J. Phys. Soc. Jpn. **83** (2014) 103704.

[3] T. Shimokawa, K. Watanabe, and H. Kawamura: Phys. Rev. B **92** (2015) 134407.

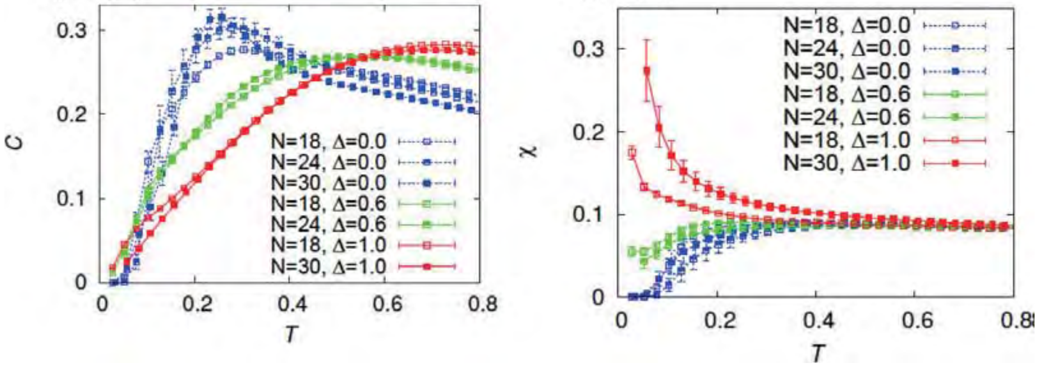

Fig. 1(a) Fig. 1(b)

Figure 1: Temperature dependence of specific heat (a) and magnetic susceptibility (b) of the triangular-lattice Heisenberg antiferromagnet for several values of the randomness *Δ*=0, 0.6, 1.0.

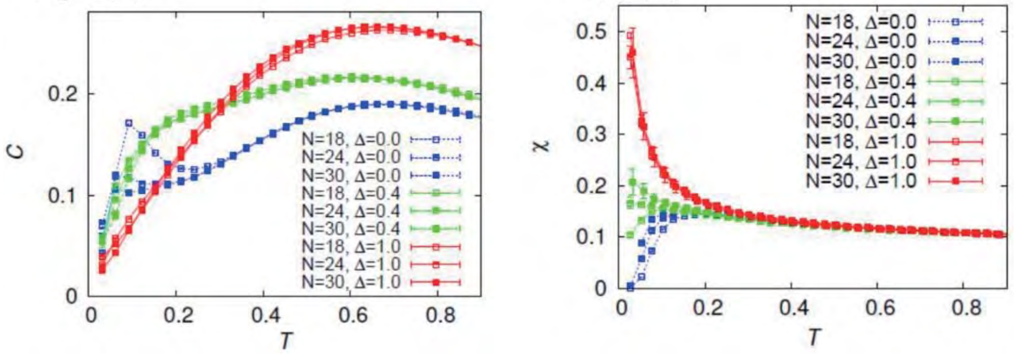

Fig. 2(a) Fig. 2(b)

Figure 1: Temperature dependence of specific heat (a) and magnetic susceptibility (b) of the kagome-lattice Heisenberg antiferromagnet for several values of the randomness *Δ*=0, 0.4, 1.0.

Numerical study of the novel magnetic phenomenon on the honeycomb magnetism

Tokuro SHIMOKAWA, Hikaru KAWAMURA and Kazuki UEMATSU
Faculty of Science, Osaka University
Machikane-yama, Toyonaka Osaka 560-0043

Motivated recent theoretical study [1] that the classical triangular-lattice Heisenberg model exhibit several types of multiple-q states including the triple-q state corresponding to skyrmion-lattice state, we here investigate the possibility of the realization of multiple-q state in the J_1-J_2 classical honeycomb-lattice Heisenberg model.

The Hamiltonian of the honeycomb-lattice Heisenberg model is given by,

$$\begin{aligned}\mathcal{H} &= J_1 \sum_{\langle i,j\rangle} \mathbf{S}_i \cdot \mathbf{S}_j + J_2 \sum_{\langle\langle i,j\rangle\rangle} \mathbf{S}_i \cdot \mathbf{S}_j \\ &- H \sum_i S_i^z, \end{aligned} \tag{1}$$

where $\sum_{\langle i,j\rangle}$ and $\sum_{\langle\langle i,j\rangle\rangle}$ mean the sum over the nearest-neighbor and the second-neighbor pairs, respectively. Here, J_1 and J_2 are both antiferromagnetic interactions and H is the magnetic field intensity. By using monte carlo (MC) method based on the heat-bath method combined with the over-relaxation and replica exchange methods, we have revealed the realization of several multiple-q orders on the honeycomb lattice under the magnetic field. In this study, we have focused on the region of $1/6 < J_2/J_1 \leq 0.3$.

In the case of $J_2/J_1 = 0.3$, we have confirmed clearly several types of mutiple-q states including single-q, double-q and triple-q states. We have found the appearance of two types of single-q states characterized by different directions of q-vector. According to our calculation results of static spin structure factor, we have found that the direction of single-q state appearing at lower (higher) magnetic field is the nearest (second-nearest) neighbor one. Previous study by the low-temperature expansion and monte carlo methods reported that the nearest neighbor direction is selected by thermal fluctuation under zero magnetic field in the case of $J_2/J_1 = 0.3$ [2]. The direction of q-vector is switched from the nearest-neighbor direction to the second-nearest direction by the thermal fluctuation under the high magnetic field. This switching behavior could be understood qualitatively by our results of the low-temperature expansion under magnetic field.

In contrast to the result of triangular-lattice Heisenberg model, our triple-q state in the honeycomb-lattice model does not correspond to the skyrmion state. The spin configuration of the triple-q state in this honeycomb model forms meron-like structure. The difference between the honeycomb and triangular model are understood qualitatively within a mean-field analysis.

Our computational results were obtained by using CPU node of system B. Our MC code are executed in parallel by using OpenMP.

References

[1] T. Okubo, S. Chung, and H. Kawamura : Phys. Rev. Lett. **108** (2012) 017206.

[2] S. Okumura, H. Kawamura, T. Okubo, and Y. Motome : J. Phys. Soc. Jpn. **79** (2010) 114705.

Study of Quantum Phases in Triangular Kitaev-Heisenberg Model

Takami TOHYAMA
Department of Applied Physics, Tokyo University of Science, Tokyo 125-8585

The Kitaev-Heisenberg (KH) model on honeycomb lattice is suggested as an effective model for $(\mathrm{Na,Li})_2\mathrm{IrO}_3$. Not only honeycomb lattice but also triangular lattice has attracted much attention from both the theoretical and experimental viewpoints. From the experimental side, $\mathrm{Ba_3IrTi_2O_9}$ has been suggested as a possible candidate of a spin-liquid material with the triangular-lattice structure. Theoretically, because the KH model on the triangular lattice has both geometrical frustration and Kitaev-type frustration that breaks SU(2) spin symmetry, the quantum effect on the model is expected to be highly non-trivial and interesting.

Motivated by these, we examine the KH model on the triangular lattice by using the two-dimensional density-matrix renormalization group (2D-DMRG) method for a 12×6-site lattice [1]. We used the System B in the Supercomputer Center, the Institute for Solid State Physics, the University of Tokyo, and the K-computer. The 2D-DMRG code has been developed by our group. To perform DMRG, we map the original system to a snake-like one-dimensional chain, and combine the chain with long-range interactions. We keep 1300∼1800 states in the DMRG block and performed more than 10 sweeps, resulting in a typical truncation error 10^{-5} or smaller.

Calculating the ground-state energy and spin structure factors, we obtain the ground state phase diagram of the Kitaev-Heisenberg model. As suggested by previous studies, we find a 120° antiferromagnetic (AFM) phase, a Z_2-vortex crystal phase, a nematic phase, a dual Z_2-vortex crystal phase (dual counterpart of Z_2-vortex crystal phase), a Z_6 ferromagnetic phase, and a dual ferromagnetic phase (dual counterpart of Z_6 ferromagnetic phase). Spin correlations discontinuously change at the phase boundaries because of first-order phase transitions. In the (dual) Z_6 ferromagnetic phase, we find that the dominant spin component of the spin structure factors is different on either side of the SU(2) symmetric point, although there is no phase transition.

Furthermore, we study the relation among von Neumann entanglement entropy, entanglement spectrum, and phase transitions. As in the case of the spin structure factors, the entanglement entropy also discontinuously changes at all the phase boundaries. We find that the Schmidt gap defined by the energy difference between the ground state and the first-excited state in the entanglement Hamiltonian is much larger than the other gaps among entanglement levels. At the phase transition points, the Schmidt gap is closing. This is in contrast with the extended KH model on honeycomb lattice, where the Schmidt gap is not necessarily a measure of phase transition [2].

References

[1] K. Shinjo, S. Sota, S. Yunoki, K. Totsuka, and T. Tohyama: arXiv:1512.02334.

[2] K. Shinjo, S. Sota, and T. Tohyama: Phys. Rev. B **91** 054401 (2015).

Quantum Phase Transitions of One-Dimensional Spin Systems Coupling with Lattice Degrees of Freedom

Hidemaro SUWA
Department of Physics, The University of Tokyo
7-3-1 Hongo, Bunkyo, Tokyo 113-0033

The interplay between the spin and the lattice degrees of freedom can bring about a non-trivial structural phase transition and its criticality. In particular, the dimerization occurs when the energy decrease of the quantum spins exceeds the energy increase of the lattice. Many materials called the spin-Peierls system show the dimerization transition experimentally. The recently proposed quantum simulator of trapped ions can realize even the quantum spin-Peierls transition. In the meantime, the quantum nature of the lattice degrees of freedom has been often ignored in the theoretical analysis for the spin-Peierls systems. Such an approximation will be appropriate in the adiabatic limit where the energy scale of lattice is much smaller than the that of spins. However, the inorganic spin-Peierls material $CuGeO_3$ has the comparable energy scales between the spin and the lattice. Then the quantum lattice fluctuation is expected to be important to the material and its phase transition. Nevertheless, the understanding of the quantum lattice effect has been lacking.

We have investigated the one-dimensional quantum spin system coupling the quantum phonons by means of the worldline quantum Monte Carlo method without any approximation [1]. The unbiased gap-estimation method is devised and the energy gaps are precisely calculated. While the adiabatic approximation concludes that the infinitesimal spin-lattice coupling drives the ground state into the dimer phase from the Tomonaga-Luttinger liquid phase, we have unambiguously shown that the Kosterlitz-Thouless-type quantum phase transition occurs between the dimer and liquid phases at a *finite* spin-phonon coupling as a result of the quantum phonon effect (Fig. 1). We have established that the quantum lattice fluctuation is essential to the one-dimensional spin, or spinless fermion, system and the transition point is described by the $k = 1$ SU(2) Wess-Zumino-Witten model.

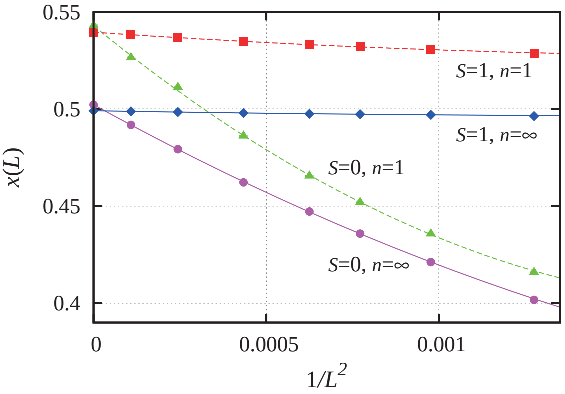

Figure 1: Scaling dimensions corresponding to the singlet and the triplet-exciting operators at the liquid-dimer transition point. The developed higher-order estimations successfully converges to 1/2, which shows the transition point is described by the Wess-Zumino-Witten model, while the conventional second moment estimators ($n = 1$) fails to converge to 1/2. This figure was taken from Ref.[1]

As for the computation, we used the system B as the class C (project ID:H27-Cb-0051). Independent worldline quantum Monte Carlo simulations with the worm (directed-loop) algorithm were efficiently run by the MPI parallelization.

References

[1] H. Suwa and S. Todo: Phys. Rev. Lett. **115** (2015) 080601

Spectral Analysis of Quantum Phase Transition between Competitive Magnetic Order and Lattice Order Phases

Hidemaro SUWA
Department of Physics, The University of Tokyo
7-3-1 Hongo, Bunkyo, Tokyo 113-0033

The Landau-Ginzburg-Wilson (LGW) paradigm is a powerful theoretical framework of general continuous phase transitions. The key concept of the paradigm is that the action of a physical system can be expanded in an order parameter and a phase transition can be described by the spontaneous symmetry breaking. Although this framework works very well in many phase transitions, it has been recently challenged by a new type of transition triggered by the so-called deconfined criticality [1]. As an example of the deconfinement, the phase transition between a spin-symmetry broken phase and a lattice-symmetry broken (and spin-symmetry unbroken) phase is predicted to be continuous, which must be first-order according to the LGW paradigm. The deconfined criticality is expected to appear in frustrated quantum spin systems, doped superconductors, heavy-fermion systems, and so on. Many of these systems, however, are not easy to study their phase transitions owing to the complex interaction and the sign problem. In the meantime, as a spin model amenable to the quantum Monte Carlo simulation, the J-Q model was proposed [2] and extensively studied. Nevertheless, the criticality of the model has not been conclusive because of the unconventional finite-size effect. To understand the non-trivial physics of the deconfined criticality, the spectral analysis that could catch the deconfinement of the fractional (spinon) excitation is strongly needed.

We have calculated the excitation gaps of the SU(2) J-Q model on the square lattice. The level-cross analysis was tested for locating the phase transition point between the Néel phase and the valence-bond-solid (VBS) phase. While the triplet at wavenumber (π, π) is the lowest excitation in the Néel phase for a finite-size system, the singlet at $(\pi, 0)$ and $(0, \pi)$ are the lowest excitation in the VBS phase. Then the crossing coupling between the two gaps should converge to the transition point in the thermodynamic limit. We have obtained the crossing coupling is remarkably well scaled in a power-law form. Combining the scaling of the crossing gap value, we have estimated the exponent relating to the spinon-deconfinement length. Also the triplet gap at $(\pi, 0)$ was calculated, which must become zero if the phase transition is continuous. We have observed the gap approximately scales in $1/L$, and the system has the multiple gapless modes only at the critical point. A paper to sum up these results is under preparation.

As for the computation, we used the system B as the class C (project ID:H27-Ca-0090). Independent worldline quantum Monte Carlo simulations with the loop algorithm were efficiently run by the MPI parallelization.

References

[1] T. Senthil *et al.*, Science **303** (2004) 1490.

[2] A.W. Sandvik, Phys. Rev. Lett. **98** (2007) 227202.

Estimating Kinetic Equation from Bubble Dynamics

Hiroshi Watanabe
Institute for Solid State Physics, University of Tokyo
Kashiwa-no-ha, Kashiwa, Chiba 277-8581

The coarsening phenomena can be described by the classical Lifshitz-Slyozov-Wagner (LSW) theory [2, 3]. The only input of the theory is the kinetic equation which describes the growth rate of a droplet. However, it was difficult to observe the kinetic equation directly. Therefore, one has to infer the kinetic equation from macroscopic behaviors, such as the power-law behavior of the average volume of the droplets. Recently, it was shown that the LSW theory works well for bubble coarsening [1]. Assuming that the dynamics is reaction-limited in low temperature and diffusion-limited in high temperature, the time evolution of the average volume of bubbles were well explained. However, the kinetic equation of bubbles are still in mystery. Therefore, we estimate the kinetic equation directly from the dynamics of bubbles [4]. We performed molecular dynamics simulation with the truncated Lennard-Jones (LJ) potential. The simulation involves up to 680 million atoms. From the snapshots of the simulation, we calculate the kinetic equation, *i.e.*, growth or shrinkage rates of bubbles. While confirmed that the form of the kinetic equation in low temperature is well described by the LSW theory assuming the reaction-limited dynamics, the kinetic equation were found to be multivalued function for higher temperature regime, and therefore, the mean-field like treatment may fail in this regime.

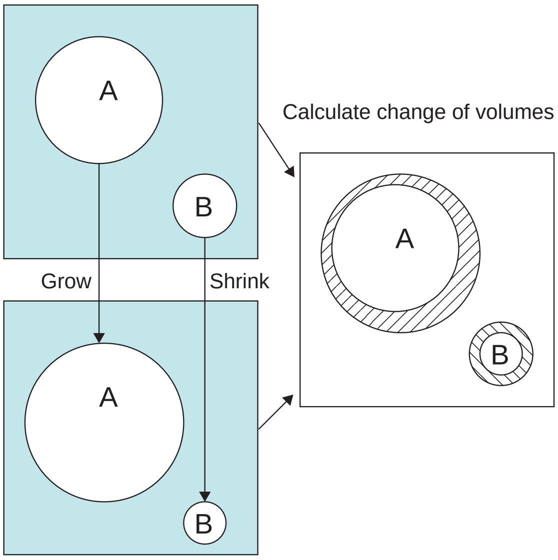

Figure 1: A schematic illustration of the calculation of the kinetic equation. We calculate the growth or shrinkage rates of bubbles from two successive snapshots.

References

[1] H. Watanabe, M. Suzuki, H. Inaoka, and N. Ito; J. Chem. Phys. **141**, 234703 (2014).

[2] I. Lifshitz and V. Slyozov. *J. Phys. Chem. Solids*, 19:35–50, 1961.

[3] C. Wagner. *Z. Elektrochem.*, 65:581 – 591, 1961.

[4] H. Watanabe, H. Inaoka, and N. Ito; arXiv:1603.04181

Improvement of dynamical scaling and accurate analysis of nonequilibrium relaxation data

Y. Ozeki

Graduate School of Informatics and Engineering, The University of Electro-Communications

We investigate the efficiency of the corrections to scaling to the dynamical scaling analysis in the nonequilibrium relaxation (NER) method [1] by the use of the Bayesian inference and the kernel method [2, 3]. Previously, we have applied the method to the 2D Ising model and obtained an improvement for the estimation of the transition temperature [4]. In the present study, we will check this improvement carefully by the use of the the bootstrap method. Furthermore, we apply the method for the general S Ising model to check the accuracy of the estimated critical exponents.

In the dynamical scaling analysis for the NER method, a general scaling form is examined;

$$m(t,T) = \tau^{-\lambda}\Psi(t/\tau), \quad (1)$$

where $m(t,T)$ is the relaxation of magnetization from the all aligned state. $\tau(T)$ is the relaxation time, which is expected to diverge as

$$\tau(T) \sim |T - T_c|^{-z\nu}$$

in $T > T_\mathrm{c}$ or $T < T_\mathrm{c}$. To estimate T_x, one may calculate $m(t,T)$ for several values of T, and fit the data to the above formula. Recently, the corrections to scaling are included to the kernel method in the static case. [5] We apply this idea to the dynamical scaling analysis of NER data. The scaling form

$$m(t,T) = t^{-\lambda}\Psi(t/\tau, t^{-c}),$$

is applied instead of eq.(1).

Previously [4], we demonstrated the method for the data on the square lattice with 1501×1500 up to 10000 MCS for 1024 samples in the temperature $2.27 \leq T \leq 2.279$. In the case without corrections, we had an estimation $T_c = 2.2692301$, while, in the present study, we obtained $T_c = 2.2691851$, which shows more accurate by comparing the exact value $T_c = 2.2691853\cdots$.

To obtain a precise estimation and a reliable error bar, here, we apply the bootstrap method. We perform multiple times dynamical scaling analysis for the data sampled at random, and take statistics. The relaxation data used in the above work is used. We prepare a sample by randomly choosing 100 points for each temperature identically along $\log t$ axis, then perform the dynamical scaling for each sample. In the case without corrections, we had an estimation $T_c = 2.269232(8)$, while, with corrections to scaling, we obtained $T_c = 2.269184(9)$. which shows more accurate by Comparing with the exact value $T_c = 2.2691853\cdots$, we understand that the latter estimation gives a precise result with a reliable error bar, while the former shows a little deviation from it. Note that the estimated errors by the bootstrap method in the present study is not a confidential interval which is usually shown in the NER analysis, but a interval as highly reliable as one can estimate from the prepared data.

Next we check the efficiency for estimations of critical exponents. In the table, we show the result for the 2D Ising model with $S = 1, 3/2, 5, 50$, For each S case, estimations obtained with corrections give good values compared with the expected ones, $z\nu \sim 2.15$ and $\beta \sim 0.125$.

	$z\nu$	β
$S = 1$ (no corrections)	2.0852	0.1261
$S = 1$ (with corrections)	2.1084	0.1246
$S = 3/2$ (no corrections)	2.0773	0.1279
$S = 3/2$ (with corrections)	2.1148	0.1253
$S = 5$ (no corrections)	2.0178	0.1306
$S = 5$ (with corrections)	2.1227	0.1214
$S = 50$ (no corrections)	2.0160	0.1371
$S = 50$ (with corrections)	2.1434	0.1236

[C class; 5000K (B), 0K (C)]

References

[1] Y. Ozeki and N. Ito, J. Phys. A: Math. Theor. **40** R149 (2007);

[2] K. Harada, Phys. Rev. E **84** 056704 (2011).

[3] Y. Ozeki and Y. Echinaka, Activity Report 2012 (Supercomputer Center, ISSP, 2013)

[4] Y. Ozeki and Y. Echinaka, Activity Report 2013 (Supercomputer Center, ISSP, 2014)

[5] K. Harada, cond-mat, stat-mech, arxiv: 1410.3622 (2014)

Dynamical ordering of biomolecular systems by molecular dynamics simulations

Satoru G. Itoh and Hisashi Okumura

Research Center for Computational Science,

Institute for Molecular Science, Okazaki, Aichi 444-8585

We are interested in amyloid fibrils, which are insoluble aggregates of misfolded fibrous proteins and associated with more than 30 human neurodegenerative diseases. For example, Alzheimer’s disease is related to amyloid-β (Aβ) peptides. To overcome these diseases, it is essential to understand amyloid fibril formation. We have performed such molecular dynamics (MD) simulations of amyloid fibrils [1,2].

This year, we focused on dimerization process and conformations of Aβ(1-40), which consist of 40 amino acids. For this purpose, we applied the Hamiltonian replica-permutation method [3], which is a better alternative to the Hamiltonian replica-exchange method, to two Aβ(1-40) molecules in explicit water solvent. The number of replicas is 18. We finished so far about 30ns per replica and about 550 ns in total.

At the first step of the dimerization process, two Aβ(1-40) molecules came close to each other and had intermolecular sidechain contacts. When two molecules had the intermolecular sidechain contacts, the Aβ(1-40) tended to have intramolecular secondary structures, especially β-hairpin structures as in Fig. 1. The two molecules had intermolecular β-bridge structures by coming much closer at the second step of the dimerization process.

To obtain enough statistics, more MD simulations should be performed. We plan to continue the MD simulations and to analyze the data in more detail.

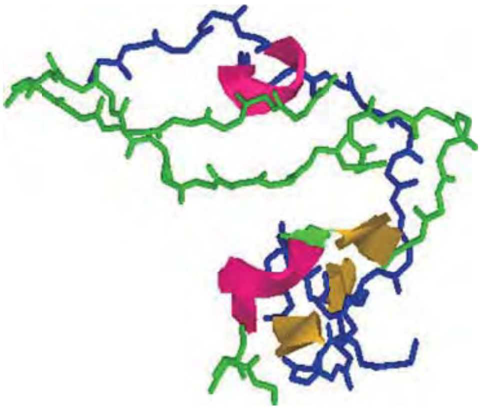

Fig. 1: Snapshot obtained by the Hamiltonian replica-permutation MD simulations.

References

[1] H. Okumura and S. G. Itoh: J. Am. Chem. Soc. **136** (2014) 10549.

[2] S. G. Itoh and H. Okumura: J. Phys. Chem. B **118** (2014) 11428.

[3] S. G. Itoh and H. Okumura: J. Comput. Chem. **34** (2013) 2493.

Simulation studies of (i) the role of hydrodynamics on colloidal gelation and (ii) the essential difference in the dynamics between strong and fragile liquids

Akira Furukawa
Institute of Industrial Science, University of Tokyo
Komaba 4-6-1, Meguro-ku, Tokyo 153-8505

(i) Using a fluid-particle dynamics (FPD) method [1], which is a hybrid simulation method for the dynamics of complex colloidal suspensions, we numerically studied the effects of hydrodynamic interactions on the collective gelation dynamics in model colloidal suspensions.

Colloidal gels are out-of-equilibrium structures, made up of a rarefied network of colloidal particles. With simulations which properly include hydrodynamics, we confirmed that hydrodynamic interactions suppress the formation of larger local equilibrium structures of closed shapes, and instead leads to the formation of highly anisotropic threads, which is crucial for making up the open gel network. We found a strong difference in the gelation dynamics between systems with and without hydrodynamics, quantifying the role of hydrodynamics [2].

(ii) Through molecular dynamics simulations, we revealed an essential difference in the dynamics between strong and fragile glass-formers [3]: In strong glass-formers, the relaxation dynamics of density fluctuations is non-conservative, whereas that of fragile glass-formers exhibits conservative (diffusive) behavior. We demonstrate that this distinction is a direct consequence of the fundamental difference in the underlying elementary process between these two dynamical classes of glass-formers. For fragile glass-formers, a density-exchange process proceedes the density relaxation, which locally takes place in normal states, but is increasingly cooperative and non-local as the temperature is lowered in supercooled states. On the other hand, in strong glass-formers such an exchange process is absent. Our finding provides a novel insight into the Angell's classification scheme from a hydrodynamic perspective.

These simulations (i) and (ii) were partially performed at the ISSP Supercomputer Center. The programs are parallelized with a combination of OpenMP and MPI techniques.

References

[1] H. Tanaka and T. Araki, Phys. Rev. Lett. **85**, 1338 (2000).

[2] C. P. Royall, J. Eggers, A. Furukawa, and H. Tanaka, Phys. Rev. Lett. 114, 258302 (2015).

[3] A. Furukawa and H. Tanaka, submitted.

Dynamical phase transitions under time dependent external fields

Seiji MIYASHITA
Department of Physics, University of Tokyo
7-3-1Hongo, Bunkyo-ku, Tokyo 113-0033

We have studied various novel types of ordering processes, dynamics, and also related cooperative phenomena using massive computer simulations.

We developed Landau-Lifshitz-Gilbert equation for systems consisting of various amplitudes of spins at finite temperatures with stochastic noise. There we pointed out that within the condition of the fluctuation dissipation relation, there are several ways to realize the equilibrium states. We confirmed that the system reaches to the equilibrium state, but we pointed out that the relaxation depends on the choice largely. [1]

We have studied the effect of lattice distortion on the ordering processes of bistable systems. The distortion causes an effective long-range ferromagnetic interaction. Competition between the long-range ferromagnetic interaction and short range interaction of the system provides various new types of phase transition. In this fiscal year, we studied this competition in the Mekata model (triangular antiferromagnetic model with next nearest neighbor ferromagnetic interaction), and found the long-range ferromagnetic interaction causes a modification on the dual Kosterlitz-Thouless transition to be a new type of second order phase transition. [2]

In antiferromagnetic systems without frustration, the long-range ferromagnetic interaction does not relevant effect at zero magnetic field. However in finite magnetic field, we found a new type gas-liquid type phase diagram.[3]

We have pointed out that high-spin low-spin transtion of an spin-crossover material SCO material $[\mathrm{Fe}^{\mathrm{II}}\mathrm{H}_2\mathrm{L}^{2-\mathrm{Me}}][\mathrm{PF}_6]_2$ is well described by a modified ANNNI model.[4]

We have developed method to obtain ESR spectrum from microscopic Hamiltonian. In this fiscal year, we investigated time domain methods in which we study time evolution of autocorrelation function and obtain the spectrum by Fourier transform. Besides the method making use of the autocorrelation function (AC method), we introduced a new method by making use of the Wiener-Khinchin relation (WK method). We found the WK method is less suffered by the Gibbs oscillation, but we also found that the Gibbs oscillation is suppressed in large systems even in AC method. We obtain the spectrum up to 26 spin systems.[5]

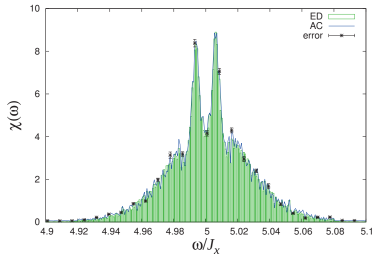

Figure 1: ESR Spectrum obtained by a new numerical method (Wiener-Khinchine method) of a XXZ chain. See the recernce [5]

We also studied collapse of metastable state in quantum systems. In particular, we investigated the quantum version of the Stoner-Wahlfarth model which consists of a single spin with uni-axial anisotropy in a magnetic field. The magnetization can stay in the opposite direction to the magnetic field due to the anisotropy. The metastable state disappears at a point which is a kind of spinodal point and is called Stoner-Wahlfarth point. We studied how a large S spin in quantum system behaves in this situation. We found that the energy gap distribution due to an quantum mixing term (in the present case the transverse field) has a singularity described by a classical spinodal decomposition. We also found that a nontrivial beating phenomena appears after the Stoner-Wahlfarth point.[6]

We have also studied mechanisms of coercive force in permanent magnets. In particular, we studied the nucleation and domain wall pinning at the grain boundary of magnets. In particular, we obtained the temperature dependence of the threshold field of the phenomena and we analyzed the dependence from the view point of temperature dependence of the anisotropy energy.[7]

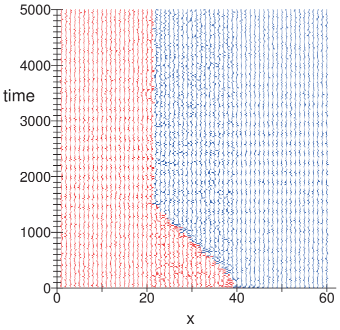

Figure 2: Domain-wall de-pinning. The horizontal axis denotes the space and the vertical axis denotes the time. The center part (20-40) is drain boundary consisting of a soft magnets. Initially, the right side of hard magnet is reversed. See the recernce [7]

References

[1] M. Nishino and S. Miyashita, Realization of thermal equilibrium in inhomogeneous magnetic systems by the Landau-Lifshitz-Gilbert equation with stochastic noise, and its dynamical aspects, Phys. Rev. B 91, 134411(1-13) (2015).

[2] M. Nishino, S. Miyashita, Termination of the Berezinskii-Kosterlitz-Thouless phase with a new critical universality in spin-crossover systems, Phys. Rev. B 92, 184404 (1-7) (2015).

[3] P.A. Rikvold, G. Brown, S. Miyashita, C. Omand and M. Nishino, Equilibrium, metastability, and hysteresis in a model spin-crossover material with nearest-neighbor antiferromagnetic-like and long-range ferromagnetic-like interactions, Phys. Rev. B. 93, 064109, (1-13) (2016).

[4] H. Watanabe, K. Tanaka, N. Brefuel, H. Cailleau, J. F. Letard, S. Ravy, P. Fertey, M. Nishino, S. Miyashita and E. Collet, Ordering phenomena of high-spin/low-spin states in stepwise spin-crossover materials described by the ANNNI model, Phys. Rev. B. 93, 014419, (1-12) (2016).

[5] H. Ikeuchi, H. De Raedt, S. Bertaina, S. Miyashita, Computation of ESR spectra from the time evolution of the magnetization: Comparison of autocorrelation and Wiener-Khinchin-relation-based methods, Phys. Rev. B 92, 214431 (1-15) (2015).

[6] T. Hatomura, B. Barbara and S. Miyashita, Quantum Stoner-Wohlfarth Model, Phys. Rev. Lett. 116, 037203, (1-5) (2016).

[7] S. Mohakud, Sergio Andraus, M. Nishino, A. Sakuma and S. Miyashita, Temperature dependence of the threshold magnetic field for nucleation and domain wall propagation in an inhomogeneous structure with grain boundary, http://arxiv.org/abs/1602.03285.

Scaling theory of disordered topological insulators

TOMI OHTSUKI[1]
TOHRU KAWARABAYASHI[2]
KEITH SLEVIN[3]
KOJI KOBAYASHI[1]
1) Dept. Phys., Sophia University, Chiyoda-ku, Tokyo 102-8554, Japan
2) Dept. Phys., Toho University, Miyama 2-2-1, Funabashi 274-8510, Japan
3) Dept. Phys., Osaka University, Toyonaka, Osaka 560-0043, Japan

Recent discoveries of two-dimensional quantum spin Hall states and three-dimensional (3D) topological insulators (TIs) have inspired extensive research for these novel materials. In the impurity free systems where the translational invariance exists, the topological insulator is characterized by the non-zero topological numbers, which are defined via integral over the Brillouin zone. This definition is no longer valid once the translational invariance is broken due to disorder. In this case, we usually use edge/surface states to characterize TIs.

Here we studied the transport properties of the thin disordered three-dimensional topological insulators [1]. We stacked N layers of two dimensional systems, and determined the TI and OI (ordinary insulator) phases, which subtly depends on N, but robust against certain amount of disorder. In addition, we have analyzed the density of states and the transport properties of bulk 3D TI's where only the surface of the systems are disordered [2].

Recently, we have proposed the density of state scaling for Dirac semi-metal phase and described the novel semi-metal to metal transitions [3] . We have extended this idea to the case of 3D Weyl semi-metals which is realized by stacking two dimensional Chern insulators. We have determined the phase diagram and analyzed the scaling of density of states as well as the conductivity scaling [3] via numerical and self-consistent Born calculation.

References

1.K. Kobayashi, Y. Yoshimura, K.-I. Imura, T Ohtsuki: Physical Review B **92**, 235407 (2015)

2. V. Sacksteder, T. Ohtsuki, K. Kobayashi: Physical Review Applied **3**, 064006 (2015)

3. K. Kobayashi, T. Ohtsuki, K.-I. Imura, I. Herbut: PRL **112**, 016402 (2014)

4. S. Liu, T. Ohtsuki, R. Shindou: Physical Review Letters **116**, 066401 (2016)

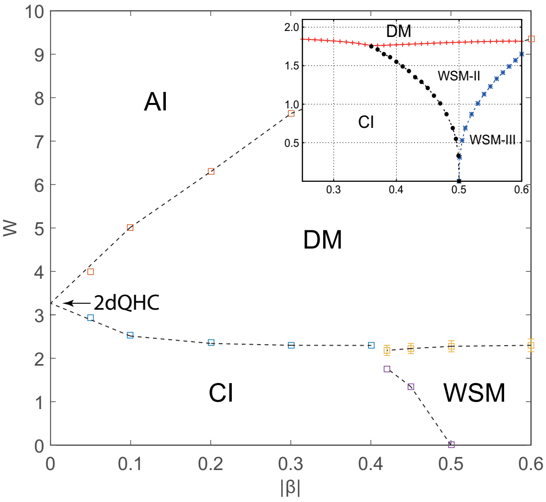

Figure 1: Phase diagram of layered Chern insulator subtended by disorder strength W and the interlayer coupling strength β. WSM, DM, CI, AI and 2dQHC stand for renomarlized Weyl semimetal, diffusive metal, Chern insulator, ordinary Anderson insulator and 2D QH quantum critical point, respectively. (inset) Phase diagram obtained from the self-consistent Born analysis. The region-II WSM phase (WSM-II) has two pairs of the Weyl points, while the region-III WSM phase (WSM-III) has three pairs of the Weyl points.

Developing microscopic simulation method of superconductors

Ryo IGARASHI
Information Technology Center, The University of Tokyo
Yayoi, Bunkyo, Tokyo 113-8658 JAPAN

This project aims to account for physical properties and microscopic mechanism of various superconducting materials such as high-temperature cuprate superconductors and recently discovered iron pnictide superconductors. In this purpose, we need to develop highly accurate simulation method for quantum lattice model. The density matrix renormalization group (DMRG) method is widely used to obtain the ground state of large quantum lattice models. Since the DMRG method has been originally developed for one-dimensional models, we have implemented the direct extension DMRG (dex-DMRG) method as shown in Fig. 1 to simulate two-dimensional model using MPS framework. However, this extension requires a large CPU time and a huge memory usage. Thus, we parallelized this method for massively parallel computer.

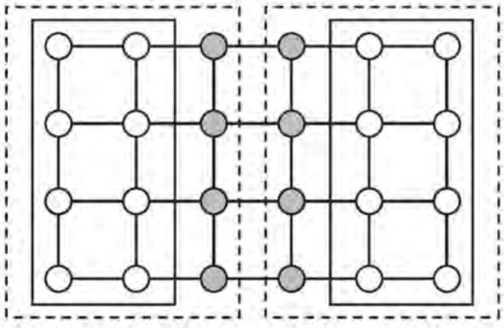

Figure 1: A schematic superblock configuration of direct extension DMRG method for a 4-leg model.

In order to check the validity of the dex-DMRG method further, we first decided to compare to the ALPS exact diagonalization [1]. We used the ISSP supercomputer system B and C for systematic comparison between the dex-DMRG method and the ALPS diagonalization.

References

[1] B. Bauer *et. al.* (ALPS collaboration): J. Stat. Mech. (2011) P05001.

Dipolar Spin Systems on Kagomé Lattice

Yusuke TOMITA
Shibaura Institute of Technology
307 Fukasaku, Minuma-ku, Saitama-City, Saitama 337-8570

The effect of the dipolar interaction depends on a positional relation between interacting sites; it is ferroic when their moments are parallel to the displacement vector while it is anti-ferroic when they are perpendicular to the vector. The dependence on a positional relation brings about various order formations which depend on lattice forms, and their nontrivial ordered states and critical phenomena are attracting much interest from fundamental and applied sciences. Dipolar systems on kagomé lattice are fine instances which show nontrivial orders and critical phenomena. In the previous work, the author implied a part of moments on a kagomé lattice are disordered even in the ordered state [1], while recent studies advocate the order is a ferrimagnetic [2, 3]. Furthermore, Maksymenko and colleagues also studied the kagomé system with exchange interactions, and an unidentified ordered phase is found between the ferrimagnetic (Ferri) and an antiferromagnetic (AFM) phases.

The Hamiltonian of the dipolar systems are given by

$$\begin{aligned}\mathcal{H} =& J\sum_{\langle i,j\rangle} \boldsymbol{S}_i\cdot\boldsymbol{S}_j \\ &+ D\sum_{i<j}\left[\frac{\boldsymbol{S}_i\cdot\boldsymbol{S}_j}{r_{ij}^3} - 3\frac{(\boldsymbol{S}_i\cdot\boldsymbol{r}_{ij})(\boldsymbol{S}_j\cdot\boldsymbol{r}_{ij})}{r_{ij}^5}\right],\end{aligned}$$

where $\boldsymbol{S}_i$ represents a Heisenberg spin at site i. Coefficients J and D are parametrized by a single variable θ,

$$J = \sin\theta, \quad D = \cos\theta.$$

In order to update dipolar spins efficiently, I employed O(N) Monte Carlo method [4]. By observing the structure factor, the existence of the ferrimagnetic ground state is confirmed at the pure dipolar interaction point, $\theta = 0$, which has been pointed out by Maksymenko *et al.* and Holden *et al* [2, 3]. When J is large enough, the antiferromagnetic order is observed at low temperatures. Using a finite-size scaling analysis, as Maksymenko *et al.* have reported, I confirmed that the universality class of the paramagnetic (P) to the AFM phase transition belongs to the two-dimensional ferromagnetic Ising model. In the intermediate region ($1^\circ \le \theta \le 10^\circ$), three types of phase transitions, P-AFM, P-Ferri, and AFM-Ferri, are observed. In a region ($5^\circ < \theta \le 10^\circ$), successive phase transitions, P-AFM-Ferri, are observed. The P to AFM phase transition is continuous while the AFM to Ferri phase transition is discontinuous. Figure 1 shows the specific heat at $\theta = 7.5^\circ$. The specific heat data indicate the successive phase transition at $T \sim 0.44$ and 0.26. While I expect the triple point resides $\theta \lesssim 5^\circ$, a strong crossover from the first order transition line between the AFM and the Ferri phases hinders from determining the precise position. Further computational efforts are needed to identify the triple point and to clarify the critical phenomena at the triple point.

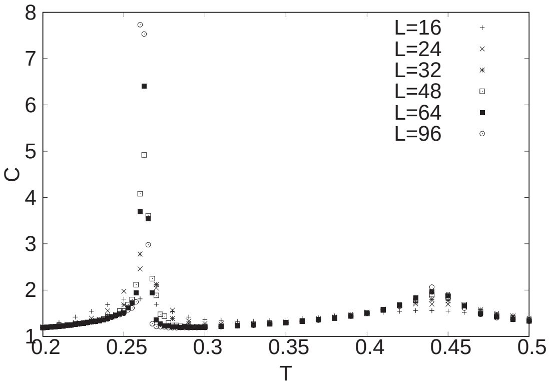

Figure 1: Specific heat at $\theta = 7.5^\circ$.

References

[1] Y. Tomita, J. Phys. Soc. Jpn. **78**, 114004 (2009).

[2] M. Maksymenko, V. R. Chandra, and R. Moessner, Phys. Rev. B **91**, 184407 (2015).

[3] M. S. Holden, M. L. Plumer, I. Saika-Voivod, and B. W. Southern, Phys. Rev. B **91**, 224425 (2015).

[4] K. Fukui and S. Todo, J. Comput. Phys. **228**, 2629 (2009).

Variety of bulk-edge correspondence by numerical methods

Y. Hatsugai
Division of Physics
Faculty of Pure and Applied Sciences, University of Tsukuba
1-1-1 Tennodai, Tsukuba 305-8571, Ibaraki, Japan

Topological phases are surely one of the recent focuses of the condensed matter society. Without relying on the symmetry breaking, many of the interesting phases have been identified as non trivial. The class includes the integer/fractional quantum Hall states, the quantized spin Hall states as the topological insulators, graphene and so on. The common feature is that there exist localized modes near the system boundaries or geometrically localized defects. This emergence of the edge states itself characterizes the bulk before making the boudary. Then the edge state is a sort of order parmeter for the topological phases. This is a physical obeservable. Except this emergence of the edge states, the bulk is featureless for the topological state. Now we have many exampeles. Some of them are surface Dirac cones of the topological insulators, Majorana/Andreev bound states of unconventional superconductors and the Fujita state of zigzag boundary of graphene. Although the edge states characterize the bulk, the reverse is also true. The emergence of the edge states is predicted by bulk without making the boudary using topological invariants of the bulk. This topological invariant is usually hidden in the sence that the direct experimental measurement is difficult. As for a model hamiltonian, it is not the case and one may calculate the invariants/quantized quatities numerically. This is an advangtage of the numerical works. These invariants are mostly constructed by the Berry connection of the quantum mechanical state as the quantized Berry phases and the Chern numbers.

This inter-relation is the bulk-edge correspondence. The bulk and the edges are closely related. In the project, we have tried to get another important realization of the bulk-edge correspondence to confirm its variety and universality using several numerical methods.

The validity of the bulk-edge correspondence is not limited to the quantum mechanics. It is also justified and quite productive for the photonic systems as a world governed by the classical Maxwell equation and even for the clasical mechanics where the classical Newton equation determines everything. We have justified the bulk-edge correspondence for the mechanical graphene that is a sping-mass model on the honeycomb lattice[1](Fig.1). This bulk-edge correspondence is generically discussed by using the classic analogue of the Berry phase, that is, the Hannay angle[2]. Also more than the well established quantization of the Berry phase into π, anomalous/fractional quantization is also investigated in the project and used to identify several interesting phases in quantum spins in a magnetic field[3]. Another important result obtained in the project is that we have successfully reproduced the phase diagram of the Kane-Mele model that is a standard model of the topological insulator in 2D using the entanglement Chern number (EC)[4](Fig.2). The EC is a new topological tool proposed recently and here, in the project, we have demonstrated its validity.

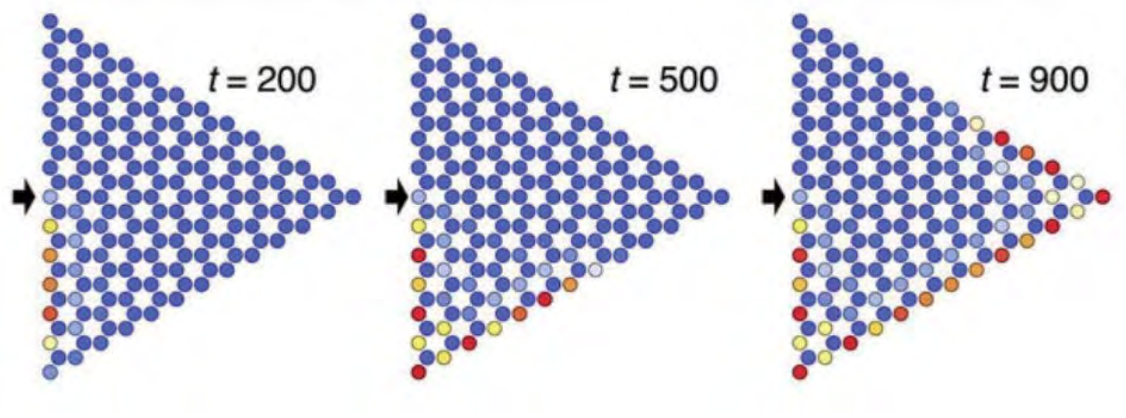

Figure 1: Classical analogue of the edge states: a localized chiral propagating mode of the Newton equation (a spring mass model) on a honeycomb lattice[1].

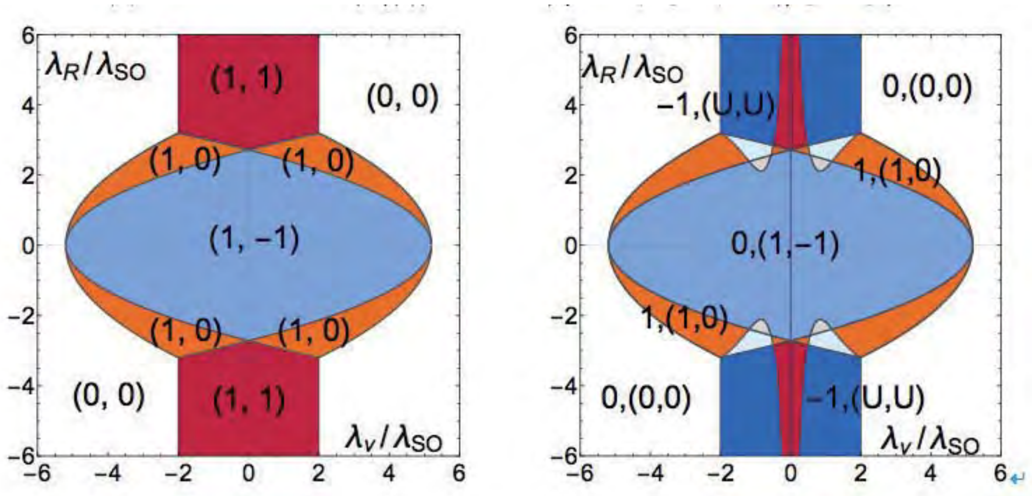

Figure 2: Various phases of the extendex Kane-Mele model with the Zeeman term. (Entanglement) Chern numbers are effective to characterize the phases[4].

References

[1] “Manipulation of Dirac Cones in Mechanical Graphene”, Toshikaze Kariyado, Yasuhiro Hatsugai, Scientific Reports **5**, 18107 (2015).

[2] “Hannay Angle: Yet Another Symmetry-Protected Topological Order Parameter in Classical Mechanics”, Toshikaze Kariyado, Yasuhiro Hatsugai, Journal of the Physical Society of Japan, **85**, 043001 (2016).

[3] ”Topological Order Parameters of the Spin-1/2 Dimerized Heisenberg Ladder in Magnetic Field”, Toshikaze Kariyado, Yasuhiro Hatsugai, Phys. Rev. B**91** 214410 (2015).

[4] “Entanglement Chern Number of the Kane-Mele Model with Ferromagnetism”, Hiromu Araki, Toshikaze Kariyado, Takahiro Fukui, Yasuhiro Hatsugai, Journal of the Physical Society of Japan, **85**, 043706 (2016), selected as ”Editor’s choice”.

Characterization of thermal transport at nanostructure interface

Junichiro SHIOMI

Department of Mechanical Engineering,

The University of Tokyo, 7-3-1, Hongo, Bunkyo-ku, Tokyo, 113-8656

Desirable thermal boundary conductance (TBC), which is a measure of interfacial thermal transport, is dependent on thermal management applications. For instance, high TBC and low TBC are respectively demanded in thermal dissipation and thermal insulation devices. At the interface between two dissimilar semiconducting materials, TBC is mainly dominated by phonons (quanta of lattice vibration). Since the TBC is determined by not only spectral mismatch of phonons in two composed materials, but also an interfacial state (local atomic configuration, bond, etc.), in order to achieve high (low) TBC value, large (small) spectral mismatch between phonons in bulk and coherent (incoherent) atomic configuration at interface are required.

On the other hand, a manipulation of TBC value has been also required in thermoelectrics that is capable of converting wasted heat to electricity. Thermoelectric energy conversion efficiency is here determined by the figure of merit, Z, which is expressed as $Z=S^2\sigma/\kappa$ in terms of electrical conductivity σ, Seebeck coefficient S, and thermal conductivity κ of material [1]. As seen, since the Z is inversely proportional to an inverse of κ, thermal conductivity reduction is one of effective approaches that enhance thermoelectric performance. Therefore several approaches including nanostructuring and alloying have been utilized in experiment.

Among several approaches, it has been demonstrated that poly-nanocrystalline can largely reduce thermal conductivity without significantly altering electrical properties of material [2]. The reduction of thermal conductivity by poly-nanocrystalline is mainly attributed to boundary scattering of phonons due to increment of specific interfacial area. However, the investigation to measure exact TBC value between nanoparticles in the poly-nanocrystal is limited due to the difficulty of measurement. Therefore we have recently proposed a new approach to isolate an actual nanoparticle-interface and measure its TBC value by means of time-domain thermoreflectance (TDTR) technique (M. Sakata, *et al.* [3]).

In this method, we can measure the TBC at silicon-silicon smooth interface and also evaluate an influence of surface contamination and mirror index difference of sintered Si-Si interface to TBC value. These knowledge can lead to tailoring interfacial structure and manipulation of interfacial phonon transport.

In order to get insight into phonon transport at such well established interface structure, we have numerically calculated TBC value of same structure observed in experiment. In this calculation, firstly, by applying the image analysis technique to high-resolution TEM image, we have extracted atomic configurations at interface (Fig. 1(a)). Next we have performed molecular dynamics simulations to obtain the interface structure similar with TEM image (Fig. 1(b)). Finally, by performing independently non-equilibrium molecular dynamics and Green's function method, we have evaluated the correlation between actual interface structure and phonon-mode-dependent TBC (L. Feng, *et al.* [4]) (Fig. 1(c)).

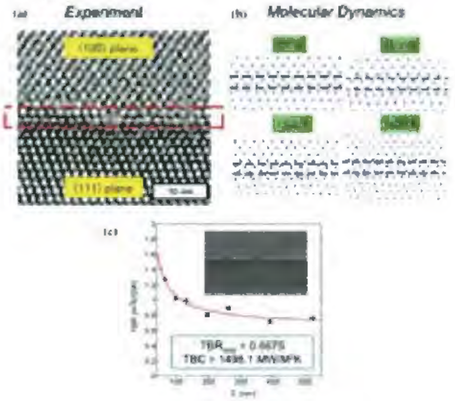

Fig. 1 (a) High-resolution transmission electron microscopy (TEM) image of Si(100)-Si(111) interface [3]. (b) Si(100)-Si(111) interfaces obtained by molecular dynamics simulations with different conditions. (c) Length-dependent thermal boundary resistance (inverse of TBC) at 300 K [4].

As described above, in order to effectively suppress phonon conduction in material, structural manipulation by means of nanostructuring is effective. Here a key challenge to further reduce thermal conductivity and improve thermoelectric performance is to predict the relation between thermal conductivity reduction and the representative length scales of nanostructure, however, that requires the knowledge in mode-dependent contribution to thermal conductivity, i.e., thermal conductivity spectrum.

Here a difficulty arises: unlike electrical conductivity that can be attributed to electrons and holes around Fermi surface, distribution of phonons contributing to heat conduction is wide in energy space. For instance, in single-crystal silicon, phonons with frequency up to 16 THz and mean free paths (MFPs) up to 10 μm noticeably contribute to heat conduction [5], which indicates that single kind nanostructure cannot cover with overall phonons contributing to heat conduction.

For the calculation of thermal conductivity spectrum of material, the first-principles-based anharmonic lattice dynamics (FP-ALD) method ([5], J. Shiomi, *et al.*, [6]) has recently become accessible, which enables us not only to quantitatively calculate thermal conductivity, but also to microscopically evaluate an influence of specific phonon-phonon scattering on heat conduction. Indeed, by performing the FP-ALD methods to several thermoelectric materials, we have revealed that large lattice anharmonicity yields intrinsically low thermal conductivity of lead chalcogenides (T. Shiga, *et al.*, [7]). Furthermore, by combining the FP-ALD method with first-principles-based molecular dynamics, we have succeeded in the thermal conductivity calculation of perovskite $SrTiO_3$ that is the phase-transition material, and showed wide adoptability of FP-ALD scheme (L. Feng, *et al.*, [8]).

In principles, one can apply FP-ALD method to any materials. However, due to its high computational cost, it is hard to apply the FP-ALD method to numerous materials in order to obtain thermal conductivity spectrum. Therefore we have developed new empirical model that describes thermal conductivity spectrum of a crystal in terms only of harmonic phonon properties and bulk thermal conductivity.

In the model, while harmonic phonon properties (heat capacity and group velocity) are accurately calculated by first-principles-based (harmonic) lattice dynamics, relaxation time, which is caused by lattice anharmonicity, is modelled by the scattering phase space (momentum-conserving two phonon density of states) and Klemens model at the classical model. By validating the model against the FP-ALD results, we have confirmed the current model reproduces the overall profiles of thermal conductivity spectra of several materials with different structural complexities and thermal conductivities (Fig. 2) (T. Shiga, *et al.*, [9]).

Since interfacial phonon transport depends on both bulk phonon property and interface structure, we have independently conducted atomistic simulations in order to calculate thermal boundary conductance (TBC) and phonon conduction in bulk. For the interfacial phonon transport, by performing molecular dynamics and Green's function method, we have calculated the TBC at Si-Si interface whose atomic configurations can be comparable with experimental ones. As for phonon transport in bulk material, we have proposed new empirical method that describes mode-dependent thermal conductivity in terms only of harmonic phonon properties and bulk thermal conductivity. Combination of these two approaches leads to comprehensive understanding of thermal transport at and around interface.

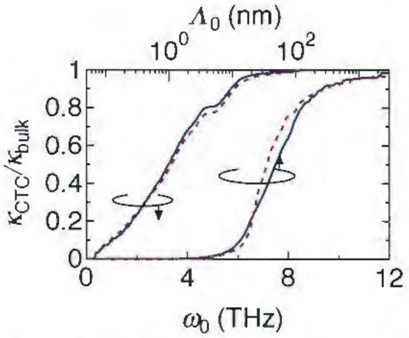

Fig. 2 Cumulative thermal conductivities of half-Heusler ZrCoSb at frequency and MFP spaces calculated from FP-ALD and the current model.

References

[1] H. J. Goldsmid, *Introduction to Thermoelectricity* (2009).

[2] B. Poudel, *et al.*, *Science* **320**, 634 (2008).

[3] M. Sakata, T. Hori, T. Oyake, J. Maire, M. Nomura, J. Shiomi, *Nano energy, Rapid communication*, **13**, 601 (2015).

[4] L. Feng, M. Ohnishi, T. Shiga, and J. Shiomi, **In preparing.**

[5] K. Esfarjani, *et al.*, *Phys. Rev. B* **84**, 085204 (2011).

[6] J. Shiomi, K. Esfarjnani, G. Chen, *Phys. Rev. B* **84**, 104302 (2011).

[7] T. Shiga, J. Shiomi, J. Ma, O. Delaire, T. Radzyunski, A. Lusakowski, K. Esfarjani, and G. Chen, *Phys. Rev. B* **85**, 155203 (2012).

[8] L. Feng, T. Shiga, and J. Shiomi, *Appl. Phys. Express* **8**, 071501(2015).

[9] T. Shiga, D. Aketo, L. Feng, and J. Shiomi, **submitted**

Computational study of the mechanism of voltage sensing proteins

Yu TAKANO,[1] Yasushige YONEZAWA,[2] and Hiroko KONDO[1]

[1]*Graduate School of Information Sciences, Hiroshima City University, 3-4-1 Ozuka-Higashi, Asa-Minami-Ku, Hiroshima 731-3194*

[2]*High Pressure Protein Research Center, Institute of Advanced Technology, Kindai University, 930 Nishimitani Kinokawa, Wakayama 649-6493*

The voltage-gated proton channel, VSOP, [1,2] consisting of the four-transmembrane domain homologous to the voltage sensor in the voltage-gated potassium channel is activated by both the membrane potential and the pH gradient. Unlike other voltage-gated ion channels, the voltage-sensor domain of VSOP has a function as a pore. Though the X-ray crystallographic structure of VSOP with zinc ions in the resting state was obtained [3], the mechanism of proton permeation still remains unclear. Here we aim to clarify the effect of zinc ion on the activation of VSOP and a mechanism of proton permeation by using the molecular dynamics (MD) simulation.

We performed the simulations of wild-type (WT) VSOP with and without a zinc ion, and mutant proteins (E115S, D119S, and E115S/D119S) with a zinc ion. Zinc ions prevent the activation of VSOP, but the E115S/D119S mutant is known to be less sensitive to zinc ions. The differences in the tertiary structure and its fluctuation were analyzed. We also created model structures of the activated state by using a homologous protein as a template, and performed the MD simulations for different protonation states. All simulations were carried out with GROMACS software package.

The results showed no large differences in the conformational fluctuations between WT and mutant proteins, suggesting that zinc ions physically prevent the conformational transition from the resting to the activated states. The simulations of model structures of the activated state also showed that two arginine residues formed salt-bridges with E115 and D119 that also interact with a zinc ion

References

[1] M. Sasaki et al., *Science* **312**, 589-592 (2006)

[2] I. S. Ramsey et al., *Nature* **440**, 1213-1216 (2006)

[3] K. Takeshita et al., *Nature Struct. Mol. Biol.* **21**, 352-357 (2014)

Molecular Dynamics Simulation Study of Growth Promotion Mechanism of Ice Basal Plane by Antifreeze Protein

Hiroki NADA
National Institute of Advanced Industrial Science and Technology (AIST)
Onogawa16-1, Tsukuba, Ibaraki 305-8569

Antifreeze proteins (AFPs), which are dissolved in the bodily fluids of organisms that lived in cold areas, function as inhibitors of ice crystal growth [1]. Studies on AFPs are important in regard to not only ice but also other materials. For example, elucidation of the mechanism of the ice crystal growth inhibition by AFPs provides insight into the control of crystal morphology and the design of functional composite materials in material technology.

In this project, we carried out a molecular dynamics (MD) simulation study on the mechanism of ice crystal growth in the presence of a winter flounder AFP. It is known that the AFP inhibits ice crystal growth on $(20\bar{2}1)$ pyramidal planes and, therefore, the growth shape of ice crystals in the presence of the AFP is hexagonal bipyramid containing 12 equivalent flat $(20\bar{2}1)$ planes [2].

Interestingly, when the hexagonal bipyramidal ice crystals are grown in the presence of the AFP, ice crystal growth on (0001) basal planes is ”promoted”. However, the mechanism of ice crystal growth promotion has not yet been elucidated. Therefore, in this project, we specially focused on the mechanism of ice crystal growth promotion on the basal plane in the presence of the AFP.

MD simulations were performed using a rectangular-parallelepiped system in which an ice crystal was sandwiched by two liquid water phases. The number of H_2O molecules in the system was 9720. A six-site model of H_2O [3] was used to estimate the intermolecular interaction between a pair of H_2O molecules. Temperature and pressure were maintained at 270 K and 1 atm, respectively.

Owing to the facillities of ISSP supercomputer center (system B), slow ice crystal growth on the basal plane due to the growth mechanism of a layer-by-layer mode in real systems was successfully reproduced. MD simulations in the presence of the AFP have also been performed. The AFP did not bind to the basal plane stably. This result is consistent with the fact that ice crystal growth inhibition does not occur on the basal plane. Further simulations with a much longer run than in this study are needed to elucidate the mechanism of ice crystal growth promotion on the basal plane.

References

[1] H. Nada and Y. Furukawa: Polym. J. **44** (2012) 690.

[2] H. Nada and Y. Furukawa: J. Phys. Chem. B **112** (2008) 7111.

[3] H. Nada and J.P.J.M. van der Eerden, J. Chem. Phys., **118** (2003) 7401.

Simulation of collective migrations induced by the cell-cell adhesion and the cell polarity

Katsuyoshi Matsushita
Cybermedia Center, Osaka University
Machikaneyama, Toyonaka 560-0043

We have investigated the collective cell migration of Dictyostelium discoideum (Dicty). Here, collective cell migration is a collective motion of cells, in which the cells mechanically contact with each other and they form a order state in cell polarity related to their motion[1]. The collective migration is indispensable for the development of the fruiting body formation of Dicty.

In collective cell migration, Dicty exhibits various styles of intercellular contact when the effect of an adhesion molecule is inhibited. Therefore, the style of intercellular contact strongly reflects intercellular interaction through cell-cell adhesion with adhesion molecule. The style of side-by-side contact is observed in the case of inhibition of DdCad1[2]. Here side-by-side contact is intercellular contact in the direction perpendicular to the cell polarity as shown in Fig.1(a). Since this protein is known to have high concentration in the direction of cell polarity, we can expect that the intercellular contact in the direction of the cell polarity as shown in Fig. 1(b). Thus, the formation of side-by-side contact is seemingly peculiar observation.

The clarification of the relation between the style of intercellular contact in collective cell migration and cell-cell adhesion is important to promote our understanding of collective cell migration. To clarify this, we carried out a simulation using cellular Potts model [3] where the concentration of cell-cell adhesion protein is correlated with the direction of cell polarity. Through this simulation, although the concentration is in the direction of cell polarity, we observe the formation of side-by-side contact. Namely, we show that the concentration of DdCad1 is consistent with the experimental observation of side-by-side contact [4]. This result imply that the side-by-side contact is a cooperation effect between the cell-cell adhesion and cell motility.

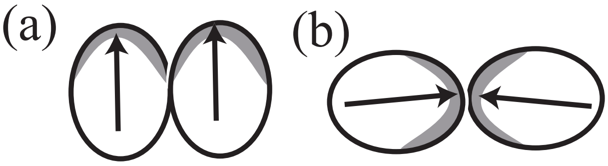

Figure 1: (a) side-by-side contact and (b) expected contact on the basis of the concentration of adhesion protein. Gray region indicates the high concentration of adhesion protein. Arrow indicate the direction of cell polarity.

References

[1] M. H. Köpf, Phys. Rev. E 91, 012712 (2015).

[2] H. Beug, F. E. Katz, and G. Gerisch, J. Cell Biol. 56,

[3] F. Graner and J. A. Glazier, Phys. Rev. Lett. 69, 2013 (1992).

[4] K. Matsushita, submitted.

Heat Transfer Characteristics of Condensate Film Flow along Vertical Plates with Microscopic Grooves

Takahiro ADACHI
Department of Mechanical Engineering, Akita University
Tegata-Gakuen 1-1, Akita, Akita 010-8502

The characteristics of thin, falling liquid films due to condensation along a vertical plate have been of interest to engineers, for example, in plate-type absorber, plate-type condenser and so on. In order to enhance the heat transfer, fluted parts along the streamwise direction have been established on the plate. This is because the liquid film spreads as thinly as possible over the plate surface since strong surface tension aids in the removal of film from the top to bottom of the fluted parts, thereby producing a very thin liquid film. This is called a drainage effect[1].

On the other hand, little research was done on the film flow along a plate with a grooved part setting perpendicular to the streamwise direction due to some mathematical difficulties. Therefore, our objective in this study is to clarify how the grooved part affects the flow patterns and heat transfer.

We consider a liquid film flow along a plate with a rectangular groove setting perpendicular to the stream-wise direction on its surface. Figure 1 shows a geometry of the problem and the coordinate system. The x-axis is taken to be parallel to the vertical direction and the y-axis to be perpendicular to it. Nondimensional parameters to characterize the plate configuration, height h of the groove, width of the groove w_b, inlet length w_i and outlet length w_o are, using δ_0^* at the inlet as a characteristic length, defined as

$$h = \frac{h^*}{\delta_0^*}, \quad w_b = \frac{w_b^*}{\delta_0^*}, \quad w_i = \frac{w_i}{\delta_0^*}, \quad w_o = \frac{w_o}{\delta_0^*} \qquad (1)$$

where we represent physical quantities with their dimensions by attaching a superscript $*$ to them, and the total plate length is $L = w_i + w_b + w_o$. The characteristic length δ_0^* can be derived from Nusselt's film theory such as

$$\delta_0^* = \left(\frac{3\nu_l^* Q^*}{g^*}\right)^{1/3}, \qquad (2)$$

where ν_l^*, g^* and Q^* are dynamic viscosity of the fluid, gravitational acceleration and flow rate, respectively.

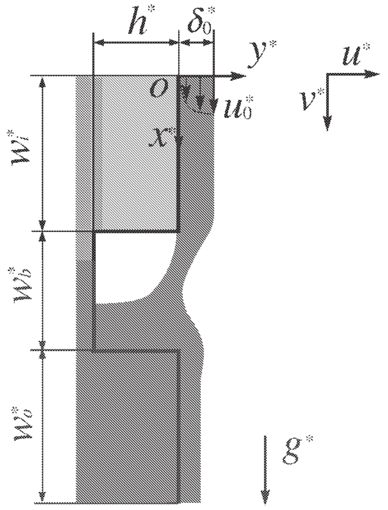

Fig.1 Geometry and coordinates.

We assume that the flow is two-dimensional because the film flow is thin and the depth in the spanwise direction of plate is large enough. Moreover, the fluid is assumed to be incompressible and the shear stress from the gas phase side can be negligible. Then we make non-dimensional the following quantities, by using characteristic length δ_0^* and surface velocity at the reference point as $u_0^* = \rho_l^* g^* \delta_0^2/(2\mu_l^*)$ which is also derive from Nusselt's film theory, as

$$\boldsymbol{x} = \frac{\boldsymbol{x}}{\delta_0^*}, \quad \boldsymbol{u} = \frac{\boldsymbol{u}}{u_0^*}, \quad t = \frac{t^* u_0^*}{\delta_0^*}, \quad p = \frac{p^*}{\rho_l^* \ u_0^{*2}},$$

$$\rho = \frac{\rho^*}{\rho_l^*}, \quad \mu = \frac{\mu^*}{\mu_l^*}. \tag{3}$$

This time, we proceed our calculations not only for liquid phase but also for gas phase. Then, the governing equations for the velocities and pressure are written in nondimensional forms as

$$\nabla \cdot \boldsymbol{u} = 0, \tag{4}$$

$$\rho \left\{ \frac{\partial \boldsymbol{u}}{\partial t} + (\boldsymbol{u} \cdot \nabla)\boldsymbol{u} \right\} = \rho Fr \boldsymbol{e}_x - \nabla p - \frac{Fr}{Bo}\kappa \nabla H + \frac{1}{Re}\nabla \left[\mu \{ \nabla \cdot \boldsymbol{u} + (\nabla \cdot \boldsymbol{u})^T \} \right], \tag{5}$$

Nondimensional parameters in the equations are the Reynolds number, Flude number and Bond number respectively defined as

$$Re = \frac{u_0^* \delta_0^*}{\nu^*}, \quad Fr = \frac{\delta_0^* g^*}{u_0^{*2}}, Bo = \frac{\delta_0^{*2} \rho^* g^*}{\sigma^*}. \tag{6}$$

First, we solve the governing equations Eq. (4) and (5) for velocity and pressure fields numerically by Highly Simplified Marker and Cell (HSMAC) method using staggered grid system. In addition to HSMAC method for the velocity and pressure fields, we have used a Coupled Level-Set and Volume Of Fluid (CLSVOF) method[2,3] to determine the free surface between gas and liquid phases, wehre we have been dealing with a new approach to impose surface tension effect and discontinuous changes of physical quantities between liquid and gas phases. Namely, Ghost Fluid Method(GFM)[4] are examined as well as CLSVOF Mmethod in our program.

Before, we used CSF(Continuum Surface Force) model proposed by Brackbill et al.[5] in order to express the surface tension effect. In such model, a continuous Heaviside function was used. However in this study, we have used a discontinuous Heaviside function in the Ghost Fluid method defned as

$$\begin{aligned} H(\phi) &= 1, & \text{if } \phi \geq 0, \\ &= 0, & \text{if } \phi \leq 0. \end{aligned} \tag{7}$$

Therefore, we can express the discontinuous changes of density and viscousity between the liquid and gas phased as

$$\rho = \frac{\rho_g^*}{\rho_l^*}(1 - H(\phi)) + H(\phi), \tag{8}$$

$$\mu = \frac{\mu_g^*}{\mu_l^*}(1 - H(\phi)) + H(\phi). \tag{9}$$

This leads to the more realistic calculation results in our study.

However, the treatment of condensation is very difficult. In addition, iteration process in HSMAC spends much time of about 80% to total time in our code. So we are now trying to parallelize the part by using MPI.

References

[1] R. Gregorig, Z. Angew. Math. Phys., Vol. 5, (1954) 36.

[2] M. Sussman, E. G. Puckett. J. Comput. Phys., Vol. 162, (200) 301.

[3] G. Son, and N, Hur. Numer. Heat Transf., Part B, Vol. 42, (2002) 523.

[4] G. Son, and V. K. Dhir. Numer. Heat Transf., PArt B, Vol. 52, (2007) 153.

[5] U. J. Brackbill, D. B. Kothe, and C. Zemach. J. Comput. Phys., Vol. 100, (1992) 335.

Study on numerical method to solve n-beam Takagi-Taupin equation for not coplanar n-beam cases.

Kouhei OKITSU
Institute of Engineering Innovation, University of Tokyo
2-11-16 Yayoi, Bunkyo-ku, Tokyo 113-8656

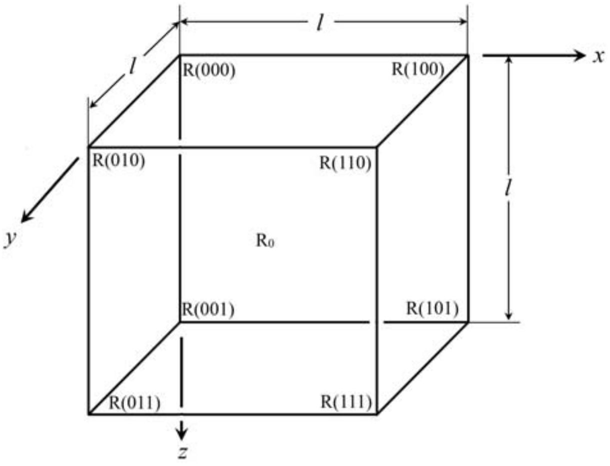

Figure 1: A small cube whose center is R_0 and corners are $\mathrm{R}(n_x n_y n_z)$, where $n_x, n_y, n_z \in \{0, 1\}$.

The present author has derived n-beam Takagi-Taupin equation that describes X-ray wavefields when n X-ray beams ($n \in \{3, 4, 5, 6, 8, 12\}$) are simultaneously strong [1, 2] and has verified it by comparing experimentally obtained pinhole topograph images and computer-simulated ones obtained by numerically solving the equation. Excellent agreements were found between them [3, 4, 5]. This equation can be applied for coplanar n-beam cases in which n reciprocal lattice nodes are on a circle in reciprocal space.

However, the ultimate purpose of the study on n-beam cases is solving the phase problem of protein crystal structure analysis. In cases of proteins, many (>12) reciprocal lattice nodes always exist in the vicinity of surface of the Ewald sphere since reciprocal lattice node density is extremely large as compared with cases of small molecular-weight crystals. Therefore, an n-beam equation applicable for not coplanar n-beam cases is necessary. The equation that the present author derived is given by

$$\begin{aligned}
&\frac{\partial}{\partial s_i} D_i^{(l)}(\mathbf{r}) + \frac{\mathrm{i}}{4\pi K} \nabla^2 D_i^{(l)}(\mathbf{r}) \\
&= -\mathrm{i}2\pi K \sum_{m=0}^{1} S_{i,0}^{(m)} \gamma_i^{(m)} D_i^{(l)}(\mathbf{r}) \\
&- \mathrm{i}\pi K \sum_{j=0}^{n-1} \sum_{m=0}^{1} C_{i,j}^{(l,m)} \chi_{h_i - h_j} D_j^{(m)}(\mathbf{r}), \qquad (1) \\
&\text{where } \ i, j \in \{0, 1, \cdots, n-1\}, \\
&\qquad\quad l, m \in \{0, 1\}.
\end{aligned}$$

Here, $\partial/\partial s_i$ is $\mathbf{s}_i \cdot \mathrm{grad}$, D is X-ray amplitude, i and j ($i, j \in \{0, 1, 2, \cdots, n-1\}$; n is number of waves) are ordinal number of the X-ray beams, l and m ($l, m \in \{0, 1\}$) are polarization states and K is wavenumber ($1/\lambda$) of X-rays in vacuum. $S_{i,0}^{(m)}$ and $C_{i,0}^{(l,m)}$ are polarization factors defined such that $\mathbf{e}_j = S_{i,j}^{(m)} \mathbf{s}_i + C_{i,j}^{(0,m)} \mathbf{e}_i^{(0)} + C_{i,j}^{(1,m)} \mathbf{e}_i^{(1)}$. Here, $\mathbf{s}_i$ is a unit vector parallel to the wavevector of the ith X-ray beam and $\mathbf{e}_i^{(0)}$ and $\mathbf{e}_i^{(1)}$ are unit vectors taken such that $\mathbf{s}_i$, $\mathbf{e}_i^{(0)}$ and $\mathbf{e}_i^{(1)}$ construct a right-handed orthogonal system. $\gamma_i^{(m)}$ is angular deviation in the direction of $\mathbf{e}_i^{(m)}$ of the ith numbered Laue point La_i from 0th numbered Laue point La_0.

When dealing with a lattice displacement field $\mathbf{u}(\mathbf{r})$, $\chi_{h_i-h_j}$ can be replaced with $\chi_{h_i-h_j}\exp[\mathrm{i}2\pi(\mathbf{h}_i-\mathbf{h}_j)\cdot\mathbf{u}(\mathbf{r})]$. Except for the case of grazing incidence, the second term of the left-hand side of (1) $\nabla^2 D_i^{(l)}(\mathbf{r})$ is negligible small.

A method that the present author recently developed numerically to solve (1) is as follows, which can be read by referring to Fig. 1. At first, $\partial/\partial s_i$ can also be described as follows,

$$\frac{\partial}{\partial s_i} = s_{i_x}\frac{\partial}{\partial x} + s_{i_y}\frac{\partial}{\partial y} + s_{i_z}\frac{\partial}{\partial z}. \tag{2}$$

Here, s_{i_x}, s_{i_y} and s_{i_z} are x-, y- and z-components of $\mathbf{s}_i$, respectively. In Fig. 1, when the size of the cube l is sufficiently small, $\partial D_i^{(l)}(\mathrm{R}_0)/\partial x$ at the center of cube R_0 can be approximated in the following two ways,

$$\begin{aligned}\frac{\partial D_i^{(l)}(\mathrm{R}_0)}{\partial x} &= D_i^{(l)}(\mathrm{R}(100))/2l \\ &- D_i^{(l)}(\mathrm{R}(000))/2l \\ &+ D_i^{(l)}(\mathrm{R}(111))/2l \\ &- D_i^{(l)}(\mathrm{R}(011))/2l. \qquad (3)\end{aligned}$$

$$\begin{aligned}\frac{\partial D_i^{(l)}(\mathrm{R}_0)}{\partial x} &= D_i^{(l)}(\mathrm{R}(110))/2l \\ &- D_i^{(l)}(\mathrm{R}(010))/2l \\ &+ D_i^{(l)}(\mathrm{R}(101))/2l \\ &- D_i^{(l)}(\mathrm{R}(001))/2l. \qquad (4)\end{aligned}$$

$\partial D_i^{(l)}(\mathrm{R}_0)/\partial y$ and $\partial D_i^{(l)}(\mathrm{R}_0)/\partial z$ can also be approximated in two ways, respectively, similarly to (3) and (4). Therefore, there are eight independent equations to approximate $\partial D_i^{(l)}(\mathrm{R}_0)/\partial s_i$. On the other hand, $D_i^{(l)}(\mathrm{R}_0)$ can be approximated in one way as follows,

$$D_i^{(l)}(\mathrm{R}_0) = \sum_{n_x=0}^{1}\sum_{n_y=0}^{1}\sum_{n_z=0}^{1} D_i^{(l)}[R(n_x n_y n_z)]/8. \tag{5}$$

Therefore, there are $16n$ independent difference equations described with $D_i^{(l)}(R_{n_x}R_{n_y}R_{n_z})$ and $D_j^{(m)}(R_{n_x}R_{n_y}R_{n_z})$ $(i,j \in \{0,1,2,\cdots,n-1\},\ l,m \in \{0,1\},\ n_x,n_y,n_z \in \{0,1\})$ that approximate (1).

When a crystal is divided by orthogonal N_m meshes whose size is sufficiently small, X-ray amplitudes at nodes whose number is less than $16 \times n \times N_m$ can be obtained by solving $16 \times n \times N_m$ simultaneous linear equations by least-square fitting.

This problem turns out to be a least square problem that can be solved by using for example lapack routine 'ZGels'. The present author is now coding a program to solve (1) based on the method described above.

References

[1] K. Okitsu: Acta Cryst A **59** (2003) 235-244.

[2] K. Okitsu, Y. Yoda, Y. Imai, Y. Ueji, Y. Urano and X.-W. Zhang: Acta Cryst A **62** (2006) 237-247.

[3] K. Okitsu, Y. Imai, Y. Ueji and Y. Yoda: Acta Cryst A **59** (2003) 311-316.

[4] K. Okitsu, Y. Yoda, Y. Imai and Y. Ueji: Acta Cryst A **67** (2011) 557-558.

[5] K. Okitsu, Y. Imai and Y. Yoda: In-Tech *Recent Advances in Crystallography* (2012) 67-86 [Invited].

Some trials of predicting thermodynamic properties using the modified Lennard-Jones system

Kazuhiro Fuchizaki, Kazuma Okamoto, and Takahiro Sakagami
Department of Physics, Ehime University, Matsuyama 790-8577
Yuta Asano
Department of Applied Chemistry, Nagoya University, Nagoya, 464-8603

We have been trying to "standardize" the modified Lennard-Jones (mLJ) system as a substitute for the ordinary LJ system [1]. In FY 2015, we used the mLJ system to discuss melting. The melting curve of the mLJ system could be satisfactorily predicted from the melting equation. The condition for Simon's equation to be valid was identified in the course of derivation. This aspect is sketched in the following. We are now trying to find the equilibrium melting point using a one-phase approach, which is mentioned subsequently. The third topic concerns a recent trial for predicting density of a liquid mLJ system from its structural information. In the following all the quantities are expressed in reduced units, which are standard for the (m)LJ system.

Melting curve of the mLJ system

With the one-phase approach, a melting curve is then given by the solution to the following thermodynamic identity.

$$\frac{\mathrm{d}\ln T_\mathrm{m}}{\mathrm{d}p} = \frac{\Gamma_\mathrm{m}}{K_\mathrm{m}}, \tag{1}$$

where K_m is the bulk modulus at the melting point T_m for a pressure p, and Γ_m is defined by

$$\Gamma_\mathrm{m} = -\frac{\mathrm{d}\ln T_\mathrm{m}}{\mathrm{d}\ln v_\mathrm{m}}. \tag{2}$$

Note here that T_m represents not the equilibrium melting point but rather a stability limit of solid state. v_m is the specific volume at T_m. An important step in the derivation of the melting curve was the evaluation of Γ_m, defined by Eq. (2), and K_m separately as functions of p. Various solutions, including Simon's and Kechin's curves, are obtainable depending on the degree of "Padé's approximation" on the RHS of Eq. (1).

Our strategy in solving Eq. (1) does not take any versions of Lindemann's law into account, but does reexpress Eq. (2) as

$$\Gamma_\mathrm{m} = \frac{\mathrm{d}\ln T_\mathrm{m}/\mathrm{d}p}{-\mathrm{d}\ln v_\mathrm{m}/\mathrm{d}p}, \tag{2$'$}$$

noting that p is the only independent variable along a melting curve.

Isothermal–isobaric molecular simulation for the mLJ system with 6912 particles was extensively carried out to establish the equation of state (EOS) of the solid phase. A preliminary result was described in 2014 activity report. The accurate EOS was reported in Ref. [2], and was assumed to be valid until melting. The EOS then could give K_m and its first pressure derivative at the reference state. Our simulation data allowed us to evaluate the p-dependence of $\ln T_\mathrm{m}$ and $\ln v_\mathrm{m}$ in Eq. (2$'$), from which Γ_m and its first pressure derivative at the reference state could be obtained. The Padé series converged at an intermediate stage to give Simon's melting curve

$$T_\mathrm{m} = T_{\mathrm{m}0}\left(1 + \frac{\Delta p}{\pi_0}\right)^{1/c_\mathrm{S}}, \tag{3}$$

where $\Delta p = p - p_0$ with $p_0 = 2.417 \times 10^{-3}$ and $T_{\mathrm{m}0} = T_\mathrm{m}|_{p_0} = 0.752$, as the solution to

Eq. (1). The predicted values for the parameters were $\pi_0 = 6.50(8)$ and $c_S = 1.44(20)$, which are almost comparable with those obtained by the direct fit of the melting points to Eq. (3). We have explicitly shown that Simon's equation becomes exact when $\Gamma'_m|_{p_0} = 0$ [3]. This criterion was found to be fulfilled for the melting curve of the mLJ solid. We have thus arrived at the significant conclusion that the melting curve of the mLJ solid is exactly captured by Simon's equation [4].

A trial implementation of the nonequilibrium relaxation (NER) method

The equilibrium solid–liquid phase boundary of the mLJ system has been already reported [5]. The boundary was determined using a costly two-phase approach. The situation motivated us to look for a costless method to determine the boundary with comparative accuracy. The NER was employed to this end.

Two mLJ systems, one is in solid state and the other in liquid state, with different densities were combined together to form a rectangular parallelepiped composite system, in which the solid–liquid boundary is to be moved freely under isobaric and isothermal conditions. The Parrinello–Rahman barostat and Nosé–Hoover thermostat were used to control pressure and temperature, respectively. The shape of the combined system was kept unchanged. Figure 1 shows time variations in density of the composite system consisting of 20512 particles (in which 6912 particles were initially on the solid side) at temperatures indicated under $p = 1.0$. The density approaches that of the solid phase at $T = 0.71$ whereas it approaches the liquid density at $T = 0.72$, implying that the melting point is located between the two temperatures. However, the expecting $T_m \simeq 0.715$ is somewhat higher than the accurate result of 0.693. Examining the difference is now in progress.

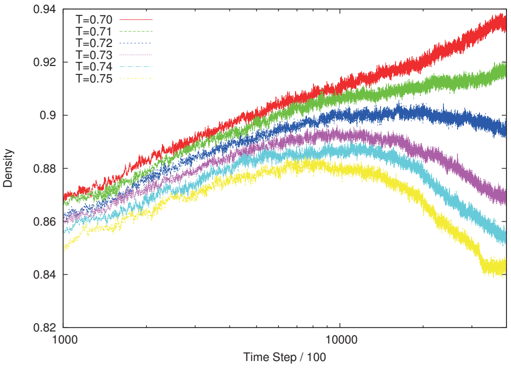

Figure 1: Time variation in density of the combined system kept at temperature indicated under $p = 1.0$.

A new approach for estimating the density of noncrystalline substances

A new trial for estimation of density from structure factors of noncrystalline systems was examined based on the working ansatz: noncrystalline substances would be structurally similar provided that they are under thermodynamically similar circumstances. By rescaling the length of the reference structure with the known density, the structures expected to be realized at nearby thermodynamic conditions were simulated, thereby allowing us to compare the actual density of the realized state with the predicted density. The ansatz was inspected by simulating the structures along an isothermal or an isobaric path emanating from the reference state. We thus arrived at a conjecture that a liquid takes a more similar structure when varied along rather than away from the melting curve [6].

References

[1] K. Fuchizaki: Read at 4th CCMS, ISSP, November 12–14, 2014.

[2] K. Fuchizaki, K. Okamoto, and S. Doi: J. Phys. Soc. Jpn. **84** (2015) 085002.

[3] K. Fuchizaki and Y. Asano: J. Phys. Soc. Jpn. **84** (2015) 064601.

[4] K. Fuchizaki and K. Okamoto: Phys. Lett. A **380** (2016) 293.

[5] Y. Asano and K. Fuchizaki: J. Chem. Phys. **137** (2012) 174502.

[6] T. Sakagami, K. Fuchizaki, and K. Ohara: submitted to J. Phys.: Condens. Matter.

Ground-State Phase Diagram of an Anisotropic $S=1/2$ Two-Leg Ladder with Different Leg Interactions

Takashi Tonegawa

Professor Emeritus, Kobe Univ. and Visiting Professor, Osaka Prefecture Univ.

The purpose of this report is to explore the ground-state phase diagram of an anisotropic $S=1/2$ two-leg ladder with different leg interactions by using mainly numerical methods. We express the Hamiltonian which describes this system as

$$\begin{aligned}\mathcal{H} = J_{\rm leg,a} &\sum\nolimits_{j=1}^{L} \vec{S}_{j,a}\cdot\vec{S}_{j+1,a}\\ &+J_{\rm leg,b}\sum\nolimits_{j=1}^{L} \vec{S}_{j,b}\cdot\vec{S}_{j+1,b} \qquad (1)\\ &+J_{\rm rung}\sum\nolimits_{j=1}^{L}[\vec{S}_{j,a},\,\vec{S}_{j,b}]_{\Delta}\end{aligned}$$

with

$$[\vec{S}_{j,a},\,\vec{S}_{j,b}]_{\Delta} \equiv S^x_{j,a}S^x_{j,b}+S^y_{j,a}S^y_{j,b}+\Delta S^z_{j,a}S^z_{j,b}\,. \quad (2)$$

Here, $\vec{S}_{j,\ell}=\bigl(S^x_{j,\ell},\,S^y_{j,\ell},\,S^z_{j,\ell}\bigr)$ is the $S=1/2$ operator acting at the (j,ℓ) site assigned by rung j and leg $\ell(=a$ or $b)$; $J_{{\rm leg},a}$ and $J_{{\rm leg},b}$ denote, respectively, the magnitudes of the isotropic leg a and leg b interactions; $J_{\rm rung}$ denotes that of the anisotropic rung interaction, the XXZ-type anisotropy being controlled by the parameter Δ; L is the total number of rungs, which is assumed to be even. It should be noted that this system has a frustration when $J_{{\rm leg},a}J_{{\rm leg},b}<0$ irrespective of the sign of $J_{\rm rung}$ [1].

The most striking feature of the present system is the fact that, if the condition $J_{{\rm leg},a}+J_{{\rm leg},b}=0$ is satisfied, the following three states are the *exact eigenstates* of the Hamiltonian (1) [2]:

1) The state in which all rungs form the singlet-dimer $\bigl((\alpha_{j,a}\beta_{j,b}-\beta_{j,a}\alpha_{j,b})/\sqrt{2}\bigr)$ pair. This state is the direct-product singlet-dimer state.
2) The state in which all rungs form the triplet-dimer $\bigl((\alpha_{j,a}\beta_{j,b}+\beta_{j,a}\alpha_{j,b})/\sqrt{2}\bigr)$ pair. This state is the direct-product triplet-dimer state.
3) The state in which all rungs are in the state given by a linear combination of two ferromagnetic states, $\cos\phi\,\alpha_{j,a}\alpha_{j,b}+\sin\phi\,\beta_{j,a}\beta_{j,b}$, where ϕ is an arbitrary phase. This state is the nematic state with ϕ.

Here, $\alpha_{j,l}$ denotes the $S^z_{j,l}=+1/2$ state and $\beta_{j,l}$ the $S^z_{j,l}=-1/2$ state. Furthermore, it can be analytically shown that, when $J_{{\rm leg},a}+J_{{\rm leg},b}=0$, $J_{\rm rung}<0$, and the XY-type anisotropy of rung interactions is sufficiently strong $\Bigl(1-\frac{2|J_{{\rm leg},a}|}{|J_{\rm rung}|}\gg\Delta\geq 0\Bigr)$, the direct-product triplet-dimer state is the *exact ground state* of the system, and that, when $J_{{\rm leg},a}+J_{{\rm leg},b}=0$ and $J_{\rm rung}(>0)$ is sufficiently large, the direct-product singlet-dimer state is the *exact ground state* of the system. It is noted that the above result concerning with the direct-product singlet-dimer state has been already shown by Tsukano and Takahshi [3]. We also note that all of the above results including the nematic state with ϕ as well as the direct-product triplet-dimer and singlet-dimer states are applicable to systems in higher dimensions, in which units of two $S=1/2$ spins form lattices [2].

When $J_{\rm rung}<0$ and $|J_{{\rm leg},\ell}|\ll|J_{\rm rung}|$, by the use of the degenerate perturbation theory, we can map the present spin-1/2 ladder onto the one-dimensional spin-1 chain governed by the effective Hamiltonian $\mathcal{H}_{\rm eff}$; in the lowest-order of $|J_{{\rm leg},\ell}|/|J_{\rm rung}|$, it is given by

$$\mathcal{H}_{\rm eff}=\sum\nolimits_{j=1}^{L}\Bigl\{J_{\rm eff}\;\vec{T}_j\cdot\vec{T}_{j+1}+D_{\rm eff}\;(T^z_j)^2\Bigr\} \quad (3)$$

with

$$J_{\rm eff}=\frac{1}{4}\bigl(J_{\rm leg,a}+J_{\rm leg,b}\bigr)\,,\quad D_{\rm eff}=\frac{1}{2}J_{\rm rung}\;(\Delta-1)\,, \quad (4)$$

where $\vec{T}_j$ is the pseudo $S=1$ operator at the jth site, and T^z_j is its z-component. It is apparent that the above $\mathcal{H}_{\rm eff}$ is not applicable to the frustrated region of the original Hamiltonian (1), which includes the case where $J_{{\rm leg},a}+J_{{\rm leg},b}=0$. In order to improve this point, higher-order perturbation calculations are indispensable. Chen *et al.* [4] have determined the ground-state phase diagram of this spin-1 chain, and showed, for example, that when $J_{\rm eff}=-1$, the phase transition from the XY phase to the large-D phase takes place at $D_{\rm eff}\simeq 1$, as the value of $D_{\rm eff}$ increases from zero. From this result, we may conclude that in our spin-1/2 ladder with $J_{\rm rung}=-1$, the phase transition between the XY phase and the triplet-dimer phase occurs at $J_{\rm leg,a}+J_{\rm leg,b}\simeq 2(\Delta-1)$ when $J_{\rm leg,a}+J_{\rm leg,b}<0$ (or, equivalently, when $\Delta<1$). It is noted that the large-D phase in the spin-1 chain corresponds to the triplet-dimer phase in the present spin-1/2 ladder.

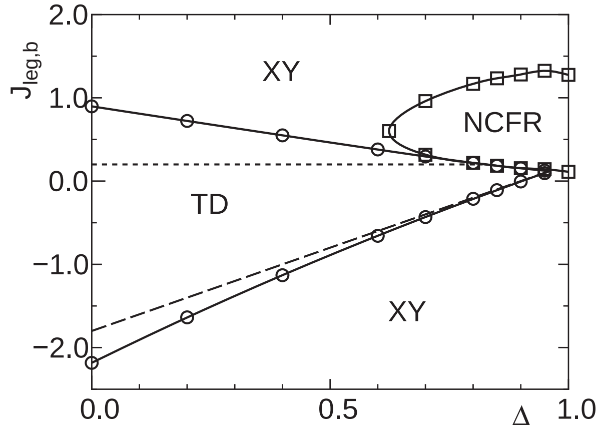

Figure 1: Ground-state phase diagram on the Δ versus $J_{\mathrm{leg,b}}$ plane for $J_{\mathrm{leg,a}}=-0.2$ and $J_{\mathrm{rung}}=-1$. Here, TD and NCFR stand, respectively, for triplet-dimer and the non-collinear ferrimagnet.

Choosing the values of $J_{\mathrm{leg,a}}$ and J_{rung} as $J_{\mathrm{leg,a}}=-0.2$ and $J_{\mathrm{rung}}=-1$, respectively, we have numerically determined the ground-state phase diagram on the Δ versus $J_{\mathrm{leg,b}}$ plane, where $0\leq\Delta\leq 1$. The obtained result is shown in Fig.1. This phase diagram consists of the triplet-dimer (TD) phase, the XY phase and the non-collinear ferrimagnetic (NCFR) phase [3,5] which has an incommensurate character. The solid lines with open circles shows the TD-XY transition lines, while that with open squares the NCFR-XY or the NCFR-TD transition line. On the broken line, where $J_{\mathrm{leg},b}=0.2\,(=-J_{\mathrm{leg},a})$, the direct-product TD state is the *exact ground state*. Furthermore, the dashed line shows the result of the degenerate perturbation calculation for the TD-XY transition line; it is in excellent agreement with the numerical result at least when $|J_{\mathrm{leg,b}}|$ is not too large.

Since the phase transition between the TD and XY phases is of the Berezinskii-Kosterlitz-Thouless type [6], the phase transition line can be very accurately estimated by using the level spectroscopy method developed by Nomura and Kitazawa [7] in the following way. First, we calculate the finite-size critical value $J_{\mathrm{leg},b}^{(\mathrm{cr})}(L)$ of $J_{\mathrm{leg},b}$ for given Δ by solving numerically the equation,

$$E_0^{(\mathrm{pbc})}(L,2)=E_0^{(\mathrm{tbc})}(L,0,+1)\,. \tag{5}$$

Here, $E_0^{(\mathrm{pbc})}(L,M)$ is the lowest energy eigenvalue of the Hamiltonian (1) under periodic boundary conditions within the subspace characterized by both L and the total magnetization M defined by $M=\sum_{j=1}^{L}(S_{j,a}^z+S_{j,b}^z)$, and $E_0^{(\mathrm{tbc})}(L,M,P)$ is that under twisted boundary conditions within the subspace characterized by L, M and $P(=+1$ or $-1)$ which is the eigenvalue of the space inversion operator with respect to the twisted bond. Then, we estimate the phase transition point $J_{\mathrm{leg},b}^{(\mathrm{cr})}$ of the infinite system by extrapolating $J_{\mathrm{leg},b}^{(\mathrm{cr})}(L)$ to $L\to\infty$. In practical calculations, we have extrapolated $J_{\mathrm{leg},b}^{(\mathrm{cr})}(L)$'s for $L=8$, 10, 12, and 14 to $L\to\infty$ by assuming that $J_{\mathrm{leg},b}^{(\mathrm{cr})}(L)$ is a quadratic function of $(1/L)^2$. The results of the least-square fitting, for example, for $\Delta=0.6$ are given by $J_{\mathrm{leg},b}^{(\mathrm{cr})}=-0.6570(1)$ and $0.3787(1)$.

In order to estimate the phase transition line between the NCFR phase and one of the XY and TD phases, we have calculated, for various values of $J_{\mathrm{leg},b}$ and Δ, the ground-state magnetization M_{g} by performing density-matrix renormalization-group (DMRG) calculations mainly for the finite-size system with $2L=72$ spins. (In a few cases, we have made sure that the results obtained for $2L=96$ and 120 agree with those for $2L=72$ within the numerical error.) In the NCFR region M_{g} is finite, while $M_{\mathrm{g}}=0$ in the TD and XY regions; for example, the phase transition points for $\Delta=0.8$ are $J_{\mathrm{leg},b}^{(\mathrm{cr})}=0.2185(5)$ and $1.1675(5)$. The value of M_{g} depends on Δ and $J_{\mathrm{leg},b}$ in the NCFR region. It is difficult, however, to clarify the order of this transition only by the DMRG method. We have also calculated the ground-state site-magnetization $m_{j,a,\mathrm{g}}$ by the DMRG method, and shown that the NCFR state has an incommensurate character by examining the Fourier transform of this quantity.

This work has been done in collaboration with T. Hikihara, K. Okamoto and T. Sakai.

[1] Vert recently, we [T. Tonegawa, K. Okamoto, T. Hikihara and T. Sakai: J. Phys.: Conf. Series **683** (2016) 012039] have discussed the ground-state phase diagram of an anisotropic $S=1/2$ ladder, in which leg interactions are antiferromagnetically uniform and isotropic, while rung interactions are ferromagnetically-antiferromagnetically alternating and have a common Ising-type anisotropy. This system is another example of the frustrated $S=1/2$ two-leg ladder.

[2] T. Hikihara, T. Tonegawa, K. Okamoto, T. Sakai and T. Momoi: in preparation.

[3] M. Tsukano and M. Takahashi: J. Phys. Soc. Jpn. **66** (1997) 1153.

[4] W. Chen, K. Hida and B. C. Sanctuary: Phys. Rev. B **67** (2003) 104401.

[5] S. Yoshikawa and S. Miyashita: J. Phys. Soc. Jpn. **74** (2005) Suppl. 71.

[6] Z. L. Berezinskii: Sov. Phys.-JETP **34** (1971) 610; J. M. Kosterlitz and D. J. Thouless: J. Phys. C: Solid State Phys. **6** (1973) 1181.

[7] K. Nomura and A. Kitazawa: J. Phys. A: Math. Gen. **31** (1998) 7341.

Molecular Dynamics Simulation of Ferroelectrics Using a Shell Model

T. Hashimoto
Research Center for Computational Design of Advanced Functional Materials (CD-FMat),
National Institute of Advanced Industrial Science and Technology (AIST),
Tsukuba Central 2, 1-1-1 Umezono, Tsukuba, Ibaraki 305-8568, Japan

$KNbO_3$ is an ABO_3 type perovskite whose solid solution with other A site atoms could be a potential candidate for Pb free piezoelectric materials. $KNbO_3$ undergoes phase transitions among, listing from high temperature to low temperature, cubic (C), tetragonal (T), orthorhombic (O), and rhombohedral (R) phases. Despite its importance, the number of the experimental reports on the piezoelectric constants of $KNbO_3$ is small due to experimental difficulties. Molecular dynamics (MD) simulations using a shell model were performed that focus on room temperature piezoelectric properties of $Li_xK_{1-x}NbO_3$[1]. In this study, we also performed MD simulations using the shell model[2, 3, 4], but we focused on the temperature dependence of the piezoelectric properties of the mother material $KNbO_3$[5].

The piezoelectric constants were calculated by[6] $d_{kij} = \frac{1}{k_BT} \langle \Delta M_k \Delta \eta_{ij} \rangle$. Here, $\eta_{ij} = \frac{1}{2} \left(H_0^{t-1} G H_0^{-1} - 1 \right)$ is the strain tensor, where $G = H^t H$ with $H = \{\mathbf{a}, \mathbf{b}, \mathbf{c}\}$ representing the MD cell, and H_0 is the reference state of H. $\mathbf{M}$ is the total dipole moment of the MD cell. ΔX represents $X - \langle X \rangle$, where X is M_k or η_{ij}.

The temperature dependences of piezoelectric constants were similar to those obtained by the Landau-Ginzburg-Devonshire (LGD) theory[7, 8]. The shear and some of the longitudinal piezoelectric constants changed by 200–300 % depending on the temperature. This arises from the temperature dependence of the dipole moment and the strain fluctuations. We also calculated the temperature dependences of the longitudinal piezoelectric surface d^*_{33} of $KNbO_3$. Due to the large temperature dependence of the piezoelectric constants, the $d^*_{33\ \mathrm{max}}$ surface changes significantly with temperatures[5].

References

[1] R. Machado, M. Sepliarsky, and M. G. Stachiotti, Appl. Phys. Lett. **103** (2013) 242901.

[2] M. Sepliarsky, S. R. Phillpot, D. Wolf, M. G. Stachiotti, and R. L. Migoni, Appl. Phys. Lett. **76** (2000) 3986.

[3] T. Hashimoto and H. Moriwake, Mol. Simul. **41** (2015) 1074.

[4] T. Hashimoto and H. Moriwake, Physica B **485** (2016) 110.

[5] T. Hashimoto and H. Moriwake, J. Phys. Soc. Jpn. **85** (2016) 034702.

[6] A. García and D. Vanderbilt, Appl. Phys. Lett. **72** (1998) 2981.

[7] M. Budimir, D. Damjanovic, and N. Setter, J. Appl. Phys. **94** (2003) 6753.

[8] L. Liang, Y. L. Li, S. Y. Hu, L.-Q. Chen, and G.-H. Lu, J. Appl. Phys. **108** (2010) 094111.

Large-scale simulations of semiconductor nanocrystals

Takamichi TERAO

Department of Electrical, Electronic and Computer Engineering,

Gifu University, Yanagido 1-1, Gifu 501-1193

Recently, glassy dynamics in interacting electron systems with geometrical frustration have attracted much attention. For example, an organic conductor with a triangular lattice was experimentally studied, and it was observed that the electronic system in the clean organic conductors freezes on cooling and a charge-cluster glass is formed [1]. Despite these studies, the behavior of electronic systems with geometrical frustration is still not fully understood, requiring further investigations of this problem.

It has been pointed out that these frustrated electron systems may show a non-equilibrium relaxation behavior similar to that found in Coulomb glass systems where both many-body electron–electron interactions and randomness of the system are present. The relaxational dynamics of the Coulomb glass model were investigated, and a transition from stationary to non-stationary dynamics at the equilibrium glass transition temperature of the system was observed. At low temperatures, the system exhibits glassy dynamics, and the two-time autocorrelation function shows aging owing to the lack of time translation invariance. The behavior of electronic systems with geometrical frustration is still not fully understood, requiring further investigations of this problem, and it is interesting to clarify their glassy behavior.

In this study, the hopping electron model on the Kagome lattice was investigated by kinetic Monte Carlo simulations and the non-equilibrium nature of the system has been elucidated. We have numerically confirmed the presence of aging phenomena in the autocorrelation function $C(t,t_W)$ obtained in the electron system of the geometrically frustrated lattice without any disorder. We have also studied the waiting-time distribution $p(\tau)$ of hopping electrons of the system, and it was confirmed that the $p(\tau)$ profile at lower temperatures obeys the power-law behavior. The power law dependence is a characteristic feature of the continuous time random walk (CTRW) behavior of the electrons in different systems such as the system on the Kagome lattice and that of the Coulomb glass, while the obtained $p(\tau)$ profiles at higher temperatures differ between these two systems.

[1] T. Sato *et al.*, J. Phys. Soc. Jpn. 83, 083602 (2014).

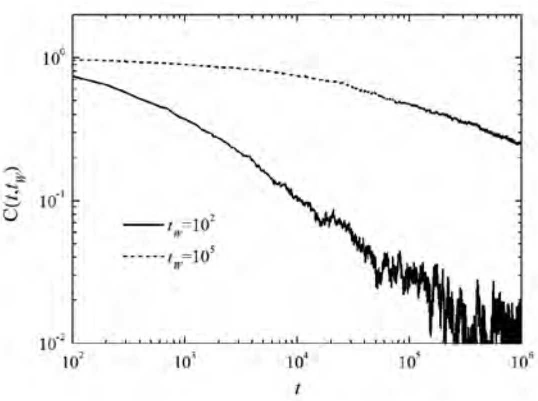

Fig. 1: Autocorrelation function $C(t,t_W)$ on Kagome lattice

Spin dynamics of frustrated quantum spin chain in magnetic field

Hiroaki ONISHI
Advanced Science Research Center, Japan Atomic Energy Agency,
Tokai, Ibaraki 319-1195

The spin nematic state, which is a quantum spin analogue of the nematic liquid crystal, has been of great interest as a novel spin state. In this project, we have studied the spin nematic state in a spin-$\frac{1}{2}$ frustrated J_1-J_2 chain with ferromagnetic J_1 and antiferromagnetic J_2 in a magnetic field [1, 2, 3]. In the J_1-J_2 chain, a spin nematic state occurs at high fields, while a vector chiral state appears at low fields [4]. Here, we investigate the influence of an added Dzyaloshinskii-Moriya (DM) interaction.

To clarify the properties of the spin nematic state from the dynamical aspect, we analyze the dynamical spin structure factor, $S^{\alpha}(q,\omega)$, at zero temperature by exploiting a dynamical DMRG method [5]. Note that we calculate the spectral weight at q and ω after one DMRG run with fixed q and ω, so that we need to perform many runs according to the number of meshes to obtain a full spectrum in a wide range of the q-ω space. The computations are accelerated by parallel simulations utilizing the system B of the ISSP supercomputer.

In Fig. 1, we show results of $S^{-}(q,\omega)$ in the spin nematic regime. We find a lowest-energy peak around $q=\pi/2$ at a finite energy, which corresponds to the binding energy of a magnon pair. The overall spectral shape looks similar even if we consider the DM interaction, but the peak position shifts toward low energy, i.e., the gap decreases, indicating that the spin nematic state is suppressed due to the DM interaction, since it induces a helical spin state. Detailed analyses will be reported elsewhere [3].

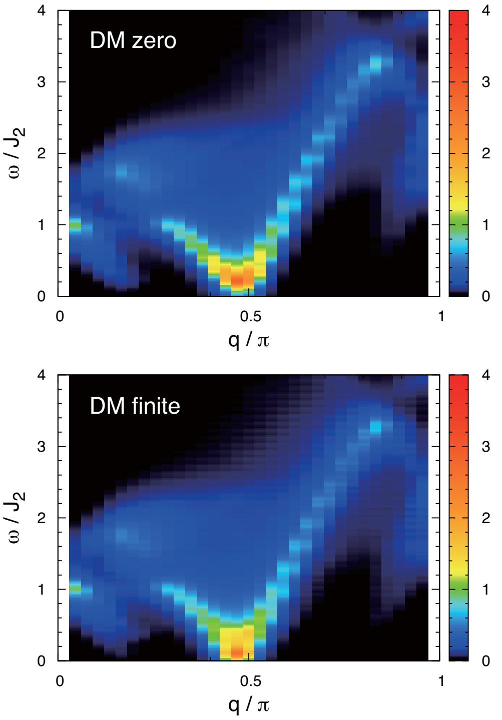

Figure 1: $S^{-}(q,\omega)$ without and with the DM interaction.

References

[1] H. Onishi, J. Phys.: Conf. Ser. **592**, 012109 (2015).

[2] H. Onishi, J. Phys.Soc. Jpn. **84**, 083702 (2015).

[3] H. Onishi, in preparation.

[4] T. Hikihara, L. Kecke, T. Momoi, and A. Furusaki, Phys. Rev. B **78**, 144404 (2008).

[5] E. Jeckelmann, Phys. Rev. B **66**, 045114 (2002).

Simulation of quantum response of graphene quantum devices

Koichi KUSAKABE
Graduate School of Engineering Science, Osaka University
1-3 Machikaneyama, Toyonaka, Osaka 560-8531

1. Introduction

The topological zero mode is known to appear at a tri-hydrogenated vacancy of graphene, V_{111}.[1, 2] Since one-body hybridization between the zero-energy eigen mode and Dirac modes is cut, relevant hybridization between the zero mode and Dirac modes of graphene is given by two-body interactions, which is given by super processes.[3] We have shown that the Coulomb interaction chooses the singlet ground state, which causes various characteristic low-energy phenomena including the Kondo effect.[4]

2. A new approach to nanographene molecular device

For a proof of the singlet ground state, the vacancy-centered armchair-edged nanographene[5] provides us a firm ground. On this network, when we consider a Hubbard model of the π electrons, the singlet ground state is exactly concluded. The degenerate single-particle levels of the quasi-localized zero mode (QLZM) and the $\sqrt{3} \times \sqrt{3}$ zero mode (S3ZM) have vanishing first-order perturbation by the on-site Hubbard interaction letting the higher-order anti-ferromagnetic exchange relevant. There are various derivatives of VANG, where the edge states may appear at edge boundaries of the molecule. Thus, quantum dynamics may be designed to show correlation of QLZM and the edge states in their response to external electro-magnetic fields.

3. Kondo screening in graphene as a zero-gap-insulator

The VANG molecules may have a large size limit, where the inter-level spacing Δ vanishes faster than the on-site effective interaction U_0 in QLZM. This picture defined by VANG provides us a novel Kondo effect, where low-lying modes in the Dirac cone screen the s=1/2 spin of QLZM. This may be a prototype of the zero-gap Kondo effect.

4. Hydrogen reaction processes relevant for hydrogen storage devices

The V_{111} structure and relating several hydrogenated vacancy structures of graphene can be used to strengthen chemical functions of graphene drastically. After providing control methods of charge transfer rates at various atomic sites of hydrogenated graphene,[6] we evaluated potential energy surfaces relevant for hydrogenation processes of a graphene vacancy.[7] The result strongly suggests a possible enhancement method of hydrogen storage ability of graphene by creation of the vacancy.

[1] M. Ziatodinov, *et al.*: Phys. Rev. B **89** (2014) 155405. [2] S. Fujii, *et al.*: Faraday Discuss., **173** (2014) 10. [3] K. Kusakabe and I. Maruyam: Japanese patent No. 5447674. [4] N. Morishita, *et al.*: arXiv:1412.8589. [5] N. Morishita, *et al.*: arXiv:1604.06841. [6] G.K. Sunnardianto, *et al.*: J. Comput. Thero. Nanosci., in print. [7] G.K. Sunnardianto, *et al.*: J. Adv. Sci. Eng. Med., in print.

Novel properties of low-dimensional electron systems at solid surfaces and finite electron systems in nanoparticles

Takeshi INAOKA
Department of Physics and Earth Sciences, Faculty of Science,
University of the Ryukyus, 1 Senbaru, Nishihara, Okinawa 903-0213

Strain engineering is expected to achieve higher operation performance of Si devices through modification of the band structure, since the conventional downsizing approach is showing its limitations. We investigated the strain effect on electronic structure of the Si(001) surface and on bulk electronic structure of Ge.

Graphene (GPN) is a promising candidate for high speed electronic devices owing to its extremely high electron mobility. However, to realize effective switching performance, we need to introduce a band gap at the Dirac point. On the other hand, hexagonal boron nitride (h-BN) is a suitable template for creating an atomic-layer structure with GPN. We examined the gap opening in atomic-layer systems of GPN and h-BN.

To perform the above calculations, we used the program package 'Vienna ab initio Simulation Package' (VASP) [1,2] on the systems B and C.

(1) Tensile strain effect on the electronic structure of the Si(001)- 2x1 surface [3]

By forming a Si layer on a $Si_{1-x}Ge_x$ buffer layer, we can apply biaxial tensile strain to the Si layer. We analyzed the electronic structure of the Si(001)-2x1 surface under biaxial tensile strain. No normal stress is a reasonable condition for the Si layer extended biaxially on the buffer layer. We assume a slab system of 30 atomic layers, and terminate dangling bonds on the other side by H atoms. Our thick slab enables us to identify the surface-resonance states extending into a deeper region. We employ the generalized gradient approximation (GGA). By minimizing the total energy, we optimize the structure in a unit cell under the condition of given biaxial extension of the unit cell.

Figure 1 shows the valence-band dispersion on the $\bar{\Gamma}-\bar{J}'$ line under (a) no strain and (b) 1.1 % biaxial tensility. This surface has an asymmetric surface dimer due to stabilization. The band S is the lower one of the surface-band pair that has its electron density concentrated on the up atom of the dimer. We can locate the surface states and the surface-resonance states by analyzing the electron-density distribution of each eigenstate. These states are indicated by squares in this figure. In the absence of

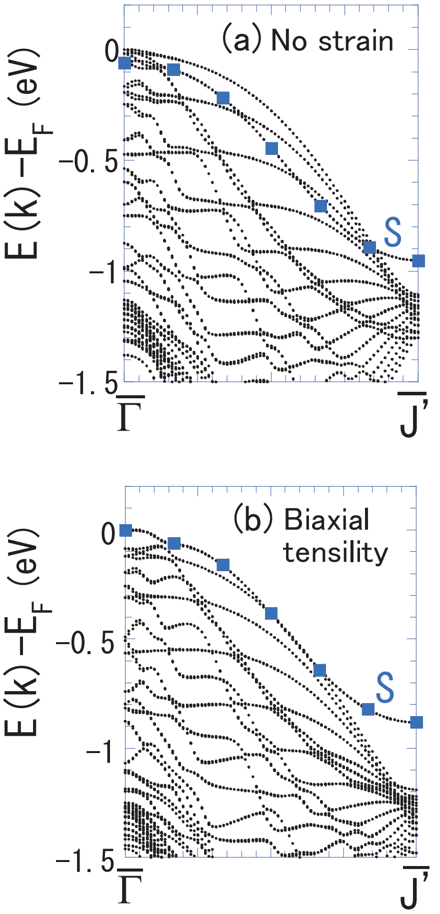

Fig. 1 Valence-band dispersion of the Si(001)-2x1 surface under (a) no strain and (b) 1.1% biaxial tensile strain. As for details, see the text.

strain, these states lie below the upper boundary of the valence band of the semi-infinite system (thick slab in this calculation) except near the $\bar{J}'$ point. However, when biaxial tensile strain is applied, these states shift to the upper boundary of the valence band. To be exact, tensile strain lowers energies of the surface or surface-resonance states less effectively than those of the valence-band states. Though we can expect that the surface-localized states are more sensitive to biaxial tensility, we can recognize that the in-plane tensile strain increases the apex angle of backbonds of the up atom of the dimer, and therefore, we can ascribe the above smaller energy fall of the surface-localized states under strain to weakening of the buckling stabilization.

(2) Strain effect on the valence band of bulk Ge [4]

By means of combination of the hybrid density functional method and the first-principles-optimized **k・p** method, we started to examine the strain effect on the valence band of bulk Ge. Assuming no normal stress and minimizing the total energy, we determined the normal and internal strain for each applied strain. The internal strain means the relative displacement of two atoms in a primitive unit cell. We considered [111] uniaxial and (111) biaxial strain, and paid special attention to the angle dependence of the hole effective-mass ratio m^*/m_e. Here, the angle was varied from the [111] direction to the [11$\bar{2}$] direction.

In 1% [111] uniaxial compression, the ratio m^*/m_e takes the smallest value 0.032 in the [111] direction, while, in 1% [111] uniaxial tensility, this value assumes the lowest value 0.038 in the [11$\bar{2}$] direction.

In (111) biaxial tensility, the ratio m^*/m_e takes the smallest value 0.022 in the [111] direction, while, in 1% (111) biaxial compression, this value assumes the lowest value 0.052 in the [11$\bar{2}$] direction.

We can obtain remarkably small effective masses in the strain direction of uniaxial compression, and in the normal direction to the biaxial tensility plane.

(3) Electronic structure of atomic-layer systems of GPN and h-BN [5]

By means of the GGA combined with a recent revised version of the van-der-Waals (vdW) density functional (rev-vdW-DF2) [6], we examined the electronic structure of atomic-layer systems of GPN and h-BN.

First, we considered a GPN layer adsorbed on the h-BN substrate (6 layer slab). We took a Γ-centered 16x16x1 k-point grid and a cutoff energy of 1200 eV. As the LDA calculation predicted [7], the most stable stacking type is the one where one of the two C atoms in a primitive unit cell of GPN sits just above a B atom and the other of the two C atoms above the center of a hexagonal BN ring. The binding energy per unit cell of the GPN layer with the BN substrate was found to be 125 meV, which is significantly larger than the LDA value of 62 meV. This difference originates from the vdW interaction included in our calculation. We obtained a band gap of 51 meV at the Dirac point.

Next, we considered a periodic arrangement of one GPN layer and three h-BN layers with the above stacking type. We chose a 16x16x8 k-point mesh. Our calculation indicated that a gap opens along the dispersion line from the K to the H point in the Brillouin zone. The gap energy varies only slightly from 97 to 103 meV as we move from the K to the H point. This gap is about twice that of the above adsorbed GPN layer.

References

[1] G. Kresse and J. Hafner. Phys. Rev. B **47** (1993) 558-561.

[2] G. Kresse and J. Furthmüller. Comput. Mat. Sci. **6** (1996) 15-50.

[3] T. Inaoka, S. N. Takeda, and T. Shirasawa: to be prepared.

[4] T. Inaoka, T. Tsuda, and S. Yanagisawa: unpublished.

[5] T. Inaoka, M. Kaminuma, and S. Yanagisawa: unpublished.

[6] I. Hamada: Phys. Rev. B **89** (2014) 121103 (R) .

[7] G. Giovannetti et al.: Phys. Rev. B **76** (2007) 073103.

Development of parallelized codes for tensor network methods

Satoshi MORITA
Institute for Solid State Physics, The University of Tokyo,
Kashiwa-no-ha, Kashiwa, Chiba 277-8581

Tensor network method is one of numerical methods for quantum and classical many-body systems. To achieve high accuracy simulation for interesting problems, one needs to increase bond dimensions of tensors. Unfortunately, the computational cost and the amount of necessary memory rapidly increase. Therefore we need to develop parallelized codes for tensor network methods.

The main operations in tensor network methods are “contraction” and “decomposition”. The former operation, which combines some tensors into one tensor, can be implemented using matrix-matrix product. With GPGPU porting support by ISSP, we developed MPI-parallelized CUDA codes of matrix-matrix product routines, pdgemm and pzgemm, in ScaLAPACK[1]. Our code of pdgemm[2] is 4.3 times faster than the original one for 65536×65536 matrices on 72 nodes with 144 GPUs in ISSP supercomputer System B.

For the latter operation, singular value decomposition (SVD) and QR decomposition are typical. In the most case, however, the exact decomposition is not necessary. For example, one 4-rank tensor with bond dimension χ is decomposed into two 3-rank tensors connected by a χ-dim bond, in which only $O(\chi)$ singular values are necessary. For such a problem, we developed parallelized codes of the randomized algorithms for the low-rank approximation, which was recently proposed[3]. Its computational cost is $O(\chi^5)$ for the previous example in contrast to the $O(\chi^6)$ cost of the exact decomposition. We applied the randomized algorithm to the Tensor Network Renormalization method (TNR), and succeeded in reducing its computational cost from $O(\chi^6)$ to $O(\chi^5)$ by avoiding a creation of 4-rank tensors.

References

[1] http://www.netlib.org/scalapack/

[2] https://github.com/smorita/cuscalapack/

[3] N. Halko, P. G. Martinsonn, J. A. Tropp, SIAM Review **53**, 217 (2011).

Numerical research of many-body effects on phonon transport by a quantum Monte Carlo method

Takeo KATO
Institute for Solid State Physics, University of Tokyo
Kashiwa-no-ha, Kashiwa, Chiba 277-8581

Heat and electric transport have several similarities as well as dissimilarities. For example, ballistic transport of electrons leads to the quantization of conductance, whereas ballistic transport of phonons to the quantization of thermal conductance. Recently, the signature of the Kondo effect, which is a typical many-body effect in electronic transport via a quantum dot, has been discussed theoretically in heat transport via a local two-state system coupled with ohmic reservoirs [1].

In order to obtain the whole feature in heat transport via a local two-state system, we have studied heat transport via a local two-state system coupled with *non-ohmic* reservoirs. We have expressed a thermal conductance by a correlation function of the two-state system based on the linear response theory. The correlation function has been evaluated along the imaginary time by a Monte Carlo calculation using a mapping to a Ising model with a long-range exchange interaction. To obtain the real-frequency correlation function, we have performed analytic continuation from data of the imaginary-frequency correlation function. To obtain reasonable results, one has to calculate the correlation function very accurately. We have employed the Wolff algorithm, and have performed typically 50,000,000 Monte Carlo steps for one parameter set.

In Figure 1, we show a calculated thermal conductance for the super-ohmic case of $s = 2$, where s is an exponent of the spectral function ($s = 1$ corresponds to the ohmic case). The solid curves show analytic results for sequential tunneling and cotunneling. At high temperatures, the calculated conductance agrees with the result of the sequential tunneling, whereas at low temperatures, it agrees with the one of the cotunneling. We have shown that the thermal conductance is proportional to T^{2s+1} by using the generalized Shiba relation. We have also studied the sub-ohmic case, and fount a drastic change at low temperatures due to a quantum phase transition [2].

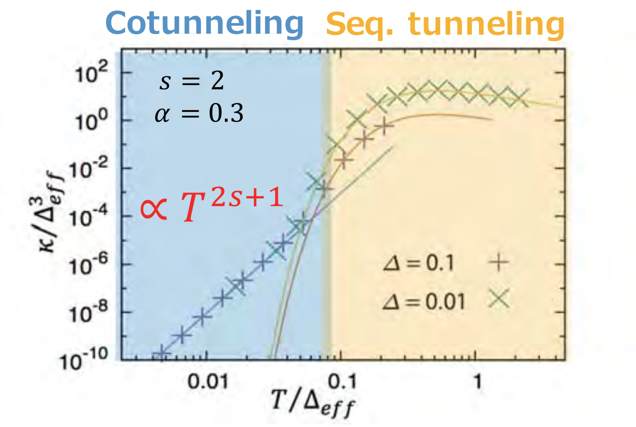

Figure 1: A calculated thermal conductance as a function of a temperature.

References

[1] K. Saito and T. Kato, Phys. Rev. Lett. **111**, 214301 (2013).

[2] M. Kato, T. Kato, and K. Saito, in preparation.

Study of Heisenberg-Kitaev model by exact diagonalization package "Rokko"

Tatsuya Sakashita
Institute for Solid State Physics, University of Tokyo
7-1-26-R501 Port Island South, Kobe 650-0047

To establish universal exact diagonalization package for quantum lattice models including the Heisenberg-Kitaev model, we focused on developing integrated interfaces for eigensolvers, "Rokko" [1].

In Rokko, we implemented the integrated interfaces for the following types:

- Serial solvers for dense matrices (Eigen3, LAPACK)
- MPI parallelized solvers for dense matrices (EigenExa[2], ELPA[3], Elemental[4], ScaLAPACK)
- MPI parallelized solvers for sparse matrices (Anasazi in Trilinos[5], SLEPc[6]) to cover matrix representations below:
  - CRS (Compressed Row Storage)
  - Matrix-free method (the method to give matrix-vector product routines to solvers)

Rokko has the following features:

- Integrated interfaces for eigensolvers and matrices, independent of individual eigensolver libraries
- Rokko's interfaces are implemented by utilizing factory. It enables the user to dynamically select a solver.
- C, Fortran, and Python bindings of Rokko
- Automatically detecting libraries by using CMake in building Rokko
- The install scripts of eigensolvers for various architectures

We prepare a paper to report design policy, software structure, and usage examples of Rokko.

References

[1] T. Sakashita, R. Igarashi, Y. Motoyama, T. Okubo, and S. Todo. Repository of Rokko. `https://github.com/t-sakashita/rokko.git`, 2012.

[2] T. Imamura, T. Hirota, and T. Fukaya. EigenExa web page. `http://www.aics.riken.jp/labs/lpnctrt/EigenExa_e.html`, 2013.

[3] ELPA Consortium. ELPA (Eigenvalue soLvers for Petaflop Applications web page). `http://elpa.rzg.mpg.de`, 2013.

[4] J. Poulson, M. Petschow, and P. Bientinesi. Distributed-memory dense linear algebra Elemental web page. `http://libelemental.org/`, 2013.

[5] M. A. Heroux, R. A. Bartlett, V. E. Howle, R. J. Hoekstra, J. J. Hu, T. G. Kolda, R. B. Lehoucq, K. R. Long, R. P. Pawlowski, E. T. Phipps, A. G. Salinger, H. K. Thornquist, R. S. Tuminaro, J. M. Willenbring, A. Williams, and K. S. Stanley. Trilinos Project web page. `http://trilinos.org`, 2003.

[6] V. Hernandez, J. E. Roman, and V. Vidal. SLEPc web page. `http://www.grycap.upv.es/slepc/`, 2002.

Search of close packing states of multicomponent hard-sphere systems by the parallelized Wang-Landau sampling

Tomoaki NOGAWA
Faculty of Medicine, Toho University
5-21-16, Omori-Nishi, Ota-ku, Tokyo, 143-8540

We have been studied a numerical method to search the densest packing of hardcore particle. We use the Wang-Landau sampling [1] for grandcanonical ensemble which is expected to be efficient because it leads to frequent global reconfiguration of particles owing to the repeat of packing and thinning. It have been found, however, that the conversion of the learning step of the Wang-Landau sampling cannot be achieved even in very small size systems if we include the densest packing state. It seems to be an essential difficulty for the optimization of the systems with continuous variable. In this work, we employ a system with discrete variables and take the continuous limit. For simplicity we treat one dimensional system: hardcore particles which occupy serial D lattice point of one dimensional chain.

When we aim to realize the flat probability distribution with respect to a single state variable, that is the number of particle N, it is actually impossible to visit the all possible value of the state variable. The number of the state which has not been visited decreases slower than any power-low decaying function of time, i.e., Monte-Calro step. By employing two state variables, N and the number of contacts of two particles C, we obtain exponential decay of the unvisited states. However, the characteristic time of the decay grows as an exponential function of particle length D to diverge in the continuous limit.

Such a slowing down of convergence is presumably due to the bottle neck effect; most of the trial of state change toward higher density state is forbidden in the high density region of state-variable space. We next try to improve the efficiency by using the method proposed by Jaster [2] that is rejection free in the case that N is fixed and C is not observed. Even though we change N and observe C, it actually reduced the bottle-neck. Furthermore, we also modify the method of adding a particle. When we randomly choose the place of setting particle, the place is occupied by another particle with large probability. We integrate the moving and adding of particles. After one particle moves by the Jaster's method, we add a particle so that it contacts on the back of the particle moved. It also raises the acceptance probability of particle adding. The total performance is, however, not improved as we expected. Unfortunately, we have not been able to find the reason, but inverse process to decrease N becomes the next bottleneck. Now we consider the possibility of a state variable, instead the contact number, which avoid the divergence of convergence time in the continuous limit.

References

[1] D. P. Landau, Shan-Ho Tsai1 and M. Exler: Am. J. Phys. **72** (2004) 1294.

[2] Jaster, Physica A **264** (1999) 134.

Self-propelled motion of a Janus particle in periodically phase separating mixtures

Takeaki ARAKI and Shintaro FUKAI
Department of Physics, Kyoto University
Kitashirakawa-oiwake-cho, Sakyo-ku, Kyoto 606-8502

Recently, the developments of science and technology enabled us to product high performance particles such as Janus particles. Janus particles are a kind of colloidal particles whose surface is divided into two hemispheres having different chemical and physical properties. The asymmetry of Janus particles causes a variety of phenomena which do not appear in normal colloidal systems. For example, strange properties are observed in their aggregated structures and electrical field responses. Also, self-propelled motions of Janus particles have been attracting attention of many researchers studying biological and non-equilibrium physics. The mechanism of the self-propelled motion of Janus particles is very interesting. Even when Janus particles are in symmetrical environments, they make asymmetry in their neighboring environment to move by themselves.

In this study, we investigated the dynamics of amphiphilic Janus particles in binary liquid (oil-water) system with numerical simulations. We used fluid particle dynamics simulation method. In this scheme, we treat a colloidal particle as a fluid particle of high viscosity to deal with hydrodynamic interactions efficiently. We have focused on two cases. In the first case, we studied many-particles dynamics in phase-separating mixtures and their aggregated structures. Through the phase separation dynamics, the particles behave as surfactant and the resultant phase-separated pattern depends on the particle concentration. In an equilibrium state, the particles' positions and directions are fixed at interfaces between the two phases (see Fig. 1). In the second case, we studied the self-propelled motion of a single particle in binary mixtures where the temperature is repeatedly changed around the phase transition temperature. The temporal change in the temperature leads to a cycle of phase separation and mixing in the water and oil mixtures. We observed some patterns of self-propelled motions which depend on the volume fraction of the binary mixture and the frequency of the temperature change. Roles of hydrodynamic interaction are asymmetric in the periods of the phase separation and mixing. This asymmetry causes a directional motion of the Janus particle. We propose an optimum condition of the self-propelled motion.[1]

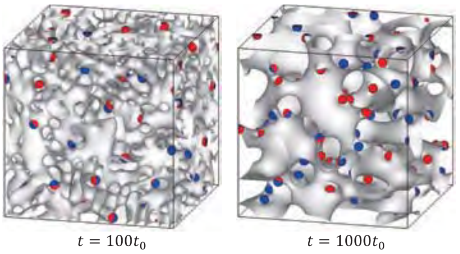

Figure 1: Snapshots of Janus particles in a phase-separated binary mixture. At $t = 0$, the system is quenched from a mixing state to a two-phase state.

References

[1] T. Araki and S. Fukai: Soft Matter **11** (2015), 3470.

Spin-lattice coupling effects in Heisenberg antiferromagnets on pyrochlore lattices

Kazushi AOYAMA
Department of Earth and Space Science, Graduate School of Science, Osaka University
Machikaneyama-cho, Toyonaka-shi, Osaka 560-0043

1 Introduction

Geometrical frustration plays an important role in magnetism. One typical example of frustrated systems is antiferromagnets on a pyrochlore lattice which is a three dimensional network of corner-sharing tetrahedra. With the nearest-neighbor (NN) antiferromagnetic interaction alone, classical Heisenberg spins on the tetrahedra do not order at any finite temperatures.

The spinel oxides ACr_2O_4 (A=Zn, Cd, Hg, Mg) are well-known pyrochlore antiferromagnets with spin-3/2. The common feature of ACr_2O_4 is that the system undergoes a first order Neel transition together with a simultaneous structural transition, which suggests strong spin-lattice coupling (SLC) in this class of antiferromagnets. Similar magnetostructural orderings have been also observed in the antiferromagnets on "breathing pyrochlore" lattices consisting of alternating array of small and large tetrahedra, $LiInCr_4O_4$ and $LiGaCr_4O_4$. In spite of the SLC commonly seen in the chromium oxides, ordering patterns of the Neel states vary material to material, and the origin of the long-range magnetic orders has not been well understood. In view of such a situation, we theoretically investigate SLC effects on the spin ordering in the antiferromagnetic classical Heisenberg model on the pyrochlore lattice. This year, we examined effects of *local* lattice distortions based on the so-called site-phonon model.

2 Model and numerical method

The effecitve spin Hamiltonian in the site-phonon model has been derived elsewhere and is given by $\mathcal{H}_{\rm eff} = \mathcal{H}_0 + \mathcal{H}_{\rm SL}$,

$$\begin{aligned}\mathcal{H}_0 &= J \sum_{\langle i,j\rangle_s} \mathbf{S}_i \cdot \mathbf{S}_j, \\ \mathcal{H}_{\rm SL} &= -J\, b \sum_{\langle i,j\rangle} (\mathbf{S}_i \cdot \mathbf{S}_j)^2 \\ &- \frac{J\, b}{2} \sum_i \sum_{j\neq k \in N(i)} \mathbf{e}_{ij} \cdot \mathbf{e}_{ik}\, (\mathbf{S}_i \cdot \mathbf{S}_j)(\mathbf{S}_i \cdot \mathbf{S}_k),\end{aligned}$$

where J is the antiferromagnetic exchange interaction between NN classical Heisenberg spins $\mathbf{S}_i$ and $\mathbf{S}_j$, the parameter b measures the strength of the SLC, and $\mathbf{e}_{ij}$ is a unit vector connecting NN sites i and j. In $\mathcal{H}_{\rm SL}$, the first term favors collinear spin state and the second term includes effective further neighbor interactions. In a collinear spin state, due to the effective further neighbor interactions, three neighboring spins on a straight line cannot be up-up-up nor down-down-down. This local constraint in the collinear state is called "bending rule". The question is whether or not these inter-tetrahedral interactions may drive a long-range spin order, and if so, what type.

In this work, we determined a zero-field phase diagram of the site phonon model based on Monte Carlo (MC) simulations. In our MC simulation, we perform 10^6 Metropolis sweeps under periodic boundary conditions at each temperature, where the first half is discarded for thermalization. Our single spin flip at each site consists of the conventional local update and a successive over-relaxation process in which we try to rotate a spin by the angle π around the local mean field. Observations are done in every 5 MC steps and the statistical average is taken over $8-10$ independent runs. Since the cubic unit cell includes 16 sites, a total number of spins N is $N = 16L^3$ for a system size L. In this study, we take $L = 4$ and 8. In the present model, the transitions into ordered phases are of first order and a large hysteresis can be seen. The results shown below are obtained in warming runs. We note that on cooling, the first order transition temperatures at $b = 0.2$ and $b = 0.35$ are lower than the corresponding warming results by 10% and 20%, respectively, but the low-temperature spin structures themselves are basically unchanged.

3 Result and Discussion

Our results are shown in Fig.1. We find two different types of collinear long-range magnetic orders, each accompanied by periodic local lattice distortions. For stronger SLC (larger b), the ordered phase is made of $\uparrow\uparrow\downarrow\downarrow$ spin chains running along all the six [110] directions showing the multiple Bragg peaks at the $(\frac{1}{2}, \frac{1}{2}, \frac{1}{2})$ family in the spin structure factor (see Fig.1(c)). This spin state and the associated local lattice distortion are cubic-symmetric. For weaker SLC (smaller b), the ordered state consists of the $\uparrow\downarrow\uparrow\downarrow$ and $\uparrow\uparrow\downarrow\downarrow$ spin chains running along the two facing tetrahedral bonds and the rest four, respectively (see Fig.1(b)). This spin configuration is tetragonal-symmetric characterized by the $(1, 1, 0)$-type magnetic Bragg reflections and the associated local lattice distortion is two dimensional [1].

From neutron diffraction experiments, it has been known that the ordered states in most of the spinel chromium oxides basically involve the $(1, 1, 0)$ magnetic patterns as observed in the weak SLC regime in the present model. The $(\frac{1}{2}, \frac{1}{2}, \frac{1}{2})$ Bragg reflections observed in the strong SLC regime in the site phonon model have been reported as a magnetic domain in $ZnCr_2O_4$, although the experimentally proposed spin structure looks different from ours. These results suggest that the SLC originating from the site phonons may be relevant to the magnetic ordering in these materials.

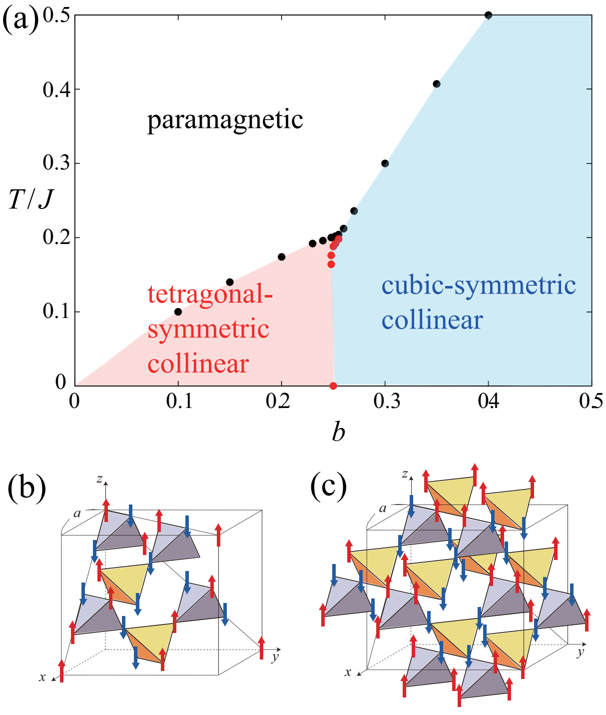

Figure 1: (a) The b-T phase diagram of pyrochlore antiferromagnets with local lattice distortions. (b) and (c) Real space spin configurations for the weaker and stronger SLC, respectively. A box represents the cubic unit cell.

References

[1] K. Aoyama and H. Kawamura, submitted.

Molecular Simulation Study of Micellar Shape Transition in Amphiphilic Solution

Susumu FUJIWARA
Graduate School of Science and Technology, Kyoto Institute of Technology
Matsugasaki, Sakyo-ku, Kyoto 606-8585

Amphiphilic molecules such as lipids and surfactants comprise both a hydrophilic group and a hydrophobic group. In solutions, they spontaneously self-assemble into various structures such as micelles, lamellar structures, and bicontinuous structures [1-3]. Self-assembling properties of amphiphilic molecules have been intensively studied because they are of great importance in many biological and industrial processes. Although several computer simulations have been performed on the micelle formation, few simulation studies have been conducted on the micellar shape transition. The purpose of this study is to determine the effect of hydrophilicity on the micellar shapes in amphiphilic solutions. With a view to investigating the micellar shape transition in amphiphilic solutions at the molecular level, we perform the molecular dynamics (MD) simulations of coarse-grained rigid amphiphilic molecules with explicit solvent molecules and analyze the micellar shape transitions.

The computational model used is the same as that used in the previous work [4]. An amphiphilic molecule is modeled as a rigid rod which is composed of one hydrophilic head particle and two hydrophobic tail particles. A solvent molecule is modeled as a hydrophilic particle. These particles interact via the non-bonded potentials. The interaction between a hydrophilic particle and a hydrophobic particle is modeled by a repulsive soft core potential and all other interactions are modeled by a Lennard-Jones (LJ) potential. Let me note that the LJ interaction parameter $\varepsilon_{\mathrm{hs}}^*$ between the hydrophilic head particles and the solvent particles represents the intensity of the hydrophilic interaction.

The equations of motion for all particles are solved numerically using the leap-frog algorithm at constant temperature with a time step of $\Delta t^* = 0.0025$ and the temperature is controlled at every 10 time steps by *ad hoc* velocity scaling [5]. We apply periodic boundary conditions and the number density ρ^* is set to $\rho^* = 0.75$. Initially, we prepare an isolated micelle of 97 amphiphilic molecules with $\varepsilon_{\mathrm{hs}}^* = 1.0$ in solutions. The number of solvent particles is 5541, which leads to the amphiphilic concentration of 0.05. The

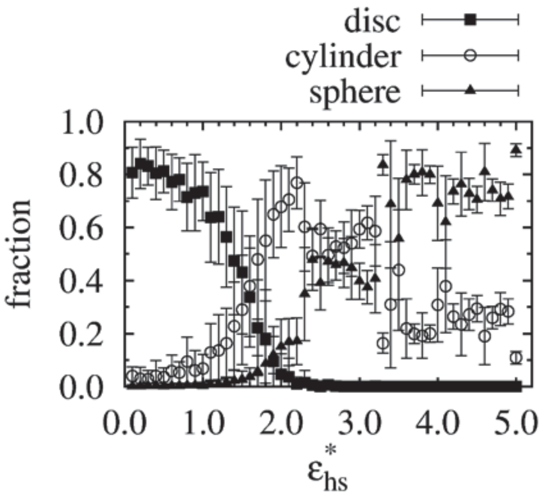

Fig. 1: The fraction of various micellar shapes versus the intensity of the hydrophilic interaction $\varepsilon^*_{\mathrm{hs}}$.

intensity of the hydrophilic interaction $\varepsilon^*_{\mathrm{hs}}$ is then varied ($0.1 \le \varepsilon^*_{\mathrm{hs}} \le 5.0$) and MD simulations of $t^* = 2.0 \times 10^4$ (8.0×10^6 time steps) are carried out for each simulation run.

Figure 1 shows the fraction of various micellar shapes as a function of the intensity of the hydrophilic interaction $\varepsilon^*_{\mathrm{hs}}$. We use the orientational order parameters along three principal axes of inertia of the micelle as indices to characterize the micellar shapes [4]. This figure tells us that the dominant micellar shape is disc-like for $\varepsilon^*_{\mathrm{hs}} < 1.6$, cylindrical for $1.6 < \varepsilon^*_{\mathrm{hs}} \le 2.2$, and spherical for $\varepsilon^*_{\mathrm{hs}} \ge 3.3$. It is also ascertained that there exists a wide coexistence region in the intensity of the hydrophilic interaction between the cylinder and the sphere for $2.3 \le \varepsilon^*_{\mathrm{hs}} \le 3.2$. In contrast, there exists a narrow coexistence region between the cylinder and the disc, which is located around $\varepsilon^*_{\mathrm{hs}} \approx 1.6$. It is worth noting that the micellar shapes are clearly distinguishable even in the coexistence region, that is, two types of micellar shapes (cylindrical and spherical, or cylindrical and disc-like) coexist dynamically.

References

[1] J. N. Israelachvili: *Intermolecular and Surface Forces*, 2nd ed. (Academic Press, London, 1992).

[2] *Micelles, Membranes, Microemulsions, and Monolayers*, edited by W. M. Gelbart, A. Ben-Shaul and D. Roux (Springer-Verlag, New York, 1994), pp. 1-104.

[3] I. W. Hamley: *Introduction to Soft Matter*, Rev. ed. (J. Wiley, ChichSester, 2007).

[4] S. Fujiwara, T. Itoh, M. Hashimoto and R. Horiuchi: J. Chem. Phys. **130** (2009) 144901.

[5] M. P. Allen and D. J. Tildesley: *Computer Simulation of Liquids*, 2nd ed. (Clarendon, Oxford, 1987).

Analysis of deterministic Monte Carlo algorithms

Hideyuki SUZUKI and Takaaki MIMURA
Graduate School of Information Science and Technology, University of Tokyo
Hongo, Bunkyo-ku, Tokyo 113-8656

In the fields of statistical physics and machine learning, efficient sampling from spin systems is crucial for achieving better analysis of a model and better learning of data. Recently, deterministic Monte Carlo algorithms such as chaotic Boltzmann machines [1–3] and herded Gibbs sampling [4] have been proposed. These algorithms can generate samples from spin systems without any use of random numbers. Furthermore, such algorithms may possibly exhibit better performance than conventional (stochastic) Monte Carlo algorithms.

Although it has been shown [2] that chaotic Boltzmann machines can be applied to estimate statistics of spin systems, dynamical behavior of deterministic Monte Carlo algorithms has not been investigated well.

Therefore, in this project, we focused on dynamical aspects of deterministic Monte Carlo algorithms when applied to spin systems. More specifically, we estimated dynamical critical exponents of deterministic algorithms. We also developed cluster algorithms for chaotic Boltzmann machines and analyzed their correlation time.

(1) Dynamical critical exponents. The dynamical critical exponent z of a sampling algorithm characterizes its dynamical behavior at the critical temperature. In this experiment, we employed four Monte Carlo sampling algorithms: Gibbs sampling, the Sakaguchi model [5], the chaotic Boltzmann machine, and herded Gibbs sampling. We applied these algorithms to the Ising model on two-dimensional square lattices, and estimated dynamical critical exponents. First, we confirmed that the results for Gibbs sampling and the Sakaguchi model are consistent with the previous study [6]. Then, we obtained the following estimates for dynamical critical exponents of deterministic algorithms: 2.01 ± 0.05 (chaotic Boltzmann machine) and 1.90 ± 0.03 (herded Gibbs).

(2) Cluster algorithms for chaotic Boltzmann machines. We developed two types of cluster algorithms for chaotic Boltzmann machines. One is multi-grid chaotic Boltzmann machines, in which multi-grid algorithm [7] and chaotic Boltzmann machines are combined. The other is parallelized chaotic Boltzmann machines, in which chaotic Boltzmann machines for multiple layers run in parallel. We applied these algorithms to XY model on two-dimensional square lattices and showed that correlation time is reduced significantly.

Throughout this project, a massive amount of samples are required to obtain reliable estimates of correlation time, for which the ISSP supercomputer system played an important role.

References

[1] H. Suzuki, J. Imura, Y. Horio, and K. Aihara: Sci. Rep. **3** (2013) 1610.

[2] H. Suzuki: Phys. Rev. E **88** (2013) 052144.

[3] H. Suzuki: arXiv:1501.07039 (2015).

[4] L. Bornn, Y. Chen, N. de Freitas, M. Eskelin, J. Fang, and M. Welling: arXiv:1301.4168 (2013).

[5] H. Sakaguchi: Prog. Theor. Phys. **80** (1988) 7.

[6] P. Marcq and H. Chaté: Phys. Rev. E **57** (1998) 1591.

[7] J. Goodman and A. D. Sokal: Phys. Rev. D **40** (1989) 2035.

Absorbing phase transition and viscoelasticity of Non-Brownian suspension in Low Reynolds number fluid

Masaki Sano, Kotaro Otomura
Department of Physics, Graduate School of Science,
The University of Tokyo, 7-3-1 Hongo, Bunkyo-ku, Tokyo, 113-033

We have studied about the rheology of the non Brownian suspension, composed of low Reynolds number fluid and athermal particles. Such suspensions typically exhibit elasticity and change of viscosity, which is expected to have something to do with absorbing phase transition.

The numerical simulation method adopted in this thesis is Smoothed Profile Method, which is a optimized method for computational fluid dynamics of suspensions[1]. In this method, the boundaries of particles are not solid but diffusive, which enable us to reduce the meshing cost drastically. Using this method, it is investigated that the relevance of rheology and internal structure of suspensions numerically and theoretically, finding that internal structure of suspension develops into various type of structure by shear induced diffusion under a large amplitude oscillatory shear.

In addition, both linear and nonlinear rheological properties have been changed by development of the structure.

In detail, qualitative behaviors are drastically changed by volume fraction of suspension. It is found that shear induced diffusion causes elasticity and strain thickening with relatively low volume fraction, and their typical nonlinearity evaluated by Chebyshev rheology are strain-softening

and shear-thickening. In this case, internal structure tends to be organized with moderate strain amplitudes, but eventually broken down with large strain amplitude with anisotropy in shear plane. A phenomenological model to describe rheology of suspensions with relatively low volume fraction is proposed, based on these results. This model provides us how short ranged interparticle interaction contributes to the rheology In particular, it is in agreement with numerical results in elasticity and strain thickening, which indicates their source is interparticle interaction.

Increase of volume fraction suppresses shear induced diffusion even with large strain amplitude.

Suppression of shear induced diffusion leads to slow down of development of structure, which causes

the locally organized structure. As a result, suspension becomes much stiffer compared with fully organized structure since confinement of particles motion. However, once after fully organized structure is created, such structure becomes quite robust, and the suspension exhibits strain softening in elasticity and quasi Newtonian behavior in viscosity.

These results provide us many insights about the relationship between rheology, structure, and dynamics of suspensions. It is indicated that the contribution of short ranged interparticle interaction to them is significant, which was not fully investigated quantitatively. Especially the phenomenological proposed in this thesis is the first minimal model to describe the contribution of short ranged interparticle interaction to bulk rheology of non Brownian suspension with low Reynolds number fluid[2].

References

[1] J. Molina, K. Otomura, H. Shiba, M. Sano, and R. Yamamoto. JFM, **792** (2016) 590.

[2] K. Otomura: Doctoral Thesis (2016)

Phase Transition in Quantum Spin Systems Coupled to Lattice Degrees of Freedom

Chitoshi YASUDA and Shota MIYARA
Department of Physics and Earth Sciences, Faculty of Science,
University of the Ryukyus, Nishihara, Okinawa 903-0213, Japan

In the spin-Peierls (SP) compound $CuGeO_3$, positions of magnetic atoms are distorted alternately at low temperatures and two nearest magnetic atoms form a spin singlet state. An antiferromagnetic long-range ordered phase is induced when nonmagnetic impurities are doped in the SP compound. The mechanism is understood in terms of effective spins near impurities [1]. By substituting a magnetic atom of a singlet pair for a nonmagnetic atom, an effective spin is induced around the other magnetic atom. Since the effective spins interact through a sea of spin-singlet pairs, the antiferromagnetic long-range order is induced. However, an experimental result contradictory to this interpretation has been reported: the effective spins are not induced near diluted sites. We need to take into account of the lattice degrees of freedom to investigate positions of effective spins induced.

In the present work, we investigated bond-randomness effects of a ground state of low-dimensional systems with the lattice degrees of freedom, and how position of effective spins change depending on parameters. A spin interaction coupled to adiabatic lattice displacements is written as a Hamiltonian $H_{\rm sl} = J\sum_i(1+\Delta_i)\boldsymbol{S}_i\cdot\boldsymbol{S}_{i+1}$. In order to numerically calculate a stable spin configuration and a stable lattice displacement, we use Lanczos diagonalizations and the quantum Monte Carlo simulations with the continuous-imaginary-time loop algorithm. An iterative procedure is used to determine the displacements $\{\Delta_i\}$ by solving a set of coupled nonlinear equations. At first, we select an initial set of the lattice displacements and calculate spin correlation functions under the fixed lattice displacement. Next, we solve a set of coupled nonlinear equations described by the spin correlation functions and obtain a next set of the lattice displacements. By performing the iterative procedure, we can obtain solutions within a certain accuracy. There is one problem with this method: poor accuracy of correlation functions leads to an incorrect solution depending on the initial set. In order to avoid this problem, we performed the procedure under various initial sets and compared the energies.

As the result, it is found that there are two types of the lattice displacement. One is the bond-alternating displacement with strong and weak bonds (type A). The lattice displacement of type A is always realized in pure systems. The other is the strong-bond displacement with strong bonds near impurities (type B). In the case of type B, the effective spins are not induced near impurities. We performed simulations in two-dimensional systems in addition to one-dimensional systems. In impure systems, the type B is realized in wide regions of parameters. On account of difficulty of the iterative procedure, however, we have not done calculations for small concentration of impurities. It is a future problem.

References

[1] C. Yasuda, *et al.*: Phys. Rev. B **64** (2001) 092405; J. Phys. Soc. Jpn. **75** (2006) 124704.

Phase transition on scale-free networks 2

Masanori SHIRO
HTRI, National Institute of Advanced Industrial Science and Technology
Umezono1-1-1 Central 2, Tsukuba, Ibaraki 305-8568

A purposes of our project is to clarify the phase transition temperature of the ising model on some types of scale-free network by using Monte Carlo method.

Pure ising model is based on grid network, which express a strong proximal interaction and well studied. But changes of transitions on a scall-free network of it, are not well known. We checked it on this project.

In the solid stat physics, these conditions express time evolutionary systems as growth of a paracrystal. Or some types of heavy fermions included long-term interaction may be related to the system.

Example of results is as follows. Fig. 1 shows the specific heat on normal ising model. Fig.2 shows the specific heat on B-A model.

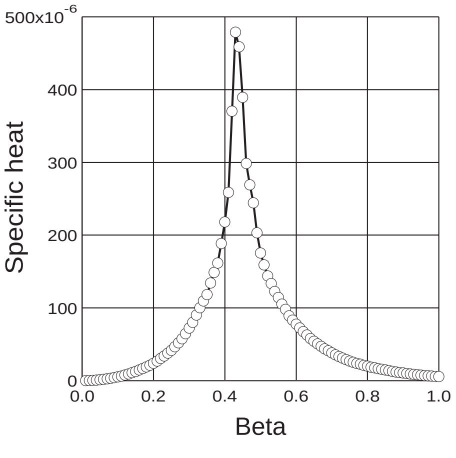

Fig.1 Pure ising model transition

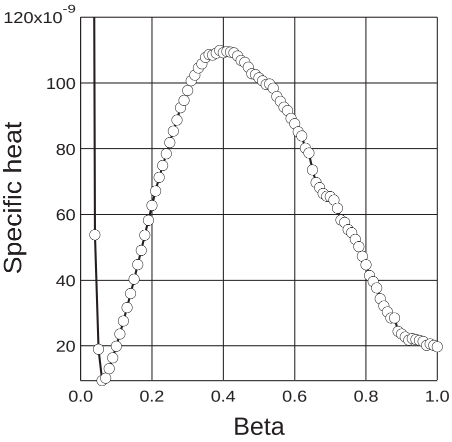

Fig.2 B-A model transition

In Figs, connection rate is assumed 0.2 and 1000 nodes, network topology is B-A model. Program is written in C++ and used Boost libraries. Results of larger scaled network are under analysis now.

The most important of facts is that proximal interactions are important for phase transition because the long range interactions homogenize the system. Hence in the B-A model, transition curve is doodling and we cannot find peak.

Nonequilibrium phase transition in the large scale dense hard sphere molecular dynamics simulation

Masaharu ISOBE
Nagoya Institute of Technology
Gokiso-cho, Showa-ku, Nagoya, 466-8555

The hard disk/sphere systems are one of the crucial models to investigate fundamental problems in the field of both equilibrium and non-equilibrium statistical physics. In this project, we investigated non-equilibrium phase transition in the hard disk/sphre model system with modern algorithms, especially for Event-Chain Monte Carlo(ECMC) [1] and Event-Driven Molecular Dynamics(EDMD) [2], where we propose the “Hybrid Scheme”, namely, ECMC for equilibration and EDMD for calculation of dynamical properties [3, 4].

(i) *Hard-sphere melting and crystallization with Event-Chain Monte Carlo*: Crystallization and melting have been investigated as central subjects in statistical physics. The hard-sphere system is simple to describe, however, equilibration in the whole particle systems is a quite slow due to the large activation free energy for crystallization. Timescales are also quite long especially in the fluid-solid coexistence regime due to the surface tension between coexisting phases. In this study, we simulate crystallization and melting with three algorithms, local Monte Carlo (LMC), ECMC [1], and with EDMD [2], in systems with up to one million three-dimensional hard spheres. We confirmed that our implementations of the three algorithms rigorously coincide in their equilibrium properties. We then study nucleation from the fcc crystal into the homogeneous liquid phase and from the liquid into the homogeneous crystal. We concluded that both ECMC and EDMD approached equilibrium orders of magnitude faster than LMC. ECMC is also notably faster than EDMD, especially for the equilibration into a crystal from an initially disordered condition at high density [5].

(ii) *Dynamic Facilitation in Binary Hard Disk Systems*: In a couple of decades, it has been highly debated to describe the theoretical approaches regarding relaxational dynamics of glass formers such as supercooled liquids. Dynamic facilitation (DF) theory [6, 7, 8] provides one of perspective which is constructed on the idealized kinetically constrained models (KCMs). The central predictions of the DF approach are as follows: (i) In the supercooled regime, relaxation originates from localized excitation distributed randomly with an equilibrium concentration which decreases exponentially with inverse temperature. The kinetics of localized excitation is facilitated such that the relaxation of excitations occurs in the vicinity of excitations, which cause heterogeneous dynamics. (ii) Relaxation is “hierarchical” cause the increasing relaxation time as a “parabolic” law with no finite temperature singularity. The super-Arrhenius behavior is distinct from the empirical Vögel-Fulcher-Tammann (VFT) law. (iii) The origin of glassy slowing down is a non-equilibrium “space-time” transition, i.e. a transition in the space of trajectories between a dynamically active equilibrium liquid phase and a dynamically inactive non-equilibrium glass phase. In this study, we investigate numerically the applicability of DF theory for glass-forming binary hard disk systems where supercompression is controlled by "pressure". The modern, efficient algorithms [1, 2, 3] for hard disks generate successfully the regions of the supercompressed equilibrium states with the model of the additive non-equimolar binary mixture, where micro-crystallization and size segregation do not emerge at the highly packing fraction. Above the onset pressure, the kinetically constraint facilitated and hierarchical collective motion, a parabolic form of structural relaxation, the exponential decay of excitation concentration and logarithmic growth of excitation-free energy emerge as in the soft sphere system below onset temperature. These observations are fairly consistent with the predictions of DF generalized to systems controlled by pressure instead of inverse temperature [9].

References

[1] E. P. Bernard, W. Krauth, and D. B. Wilson: Phys. Rev. E **80** (2009) 056704.

[2] M. Isobe: Int. J. Mod. Phys. C **10** (1999) 1281.

[3] M. Isobe: Mol. Sim. (2016) in press.

[4] M. Isobe: Proceedings Book of Berni Alder's 90th Birthday Symposium. (2016) in press.

[5] M. Isobe and W. Krauth: J. Chem. Phys. **143** (2015) 084509.

[6] D. Chandler and J. P. Garrahan, Annu. Rev. Phys. Chem. **61** (2010) 191

[7] L. O. Hedges, R. L. Jack, J. P. Garrahan and D. Chandler, Science **323** (2009) 1309.

[8] A. S. Keys, L. O. Hedges, J. P. Garrahan, S. C. Glotzer, and D. Chandler, Phys. Rev. X, **1** (2011) 021013.

[9] M. Isobe, A. S. Keys, J. P. Garrahan, and D. Chandler: arXiv:1604.02621.

Numerical Study of One Dimensional Frustrated Quantum Spin Systems

Kazuo HIDA and Hiroshi SHINAOKA
Division of Material Science, Graduate School of Science and Engineering
Saitama, Saitama 338-8570

1 Topological Phases in Zigzag Heisenberg Ladder with Ferromagnetc Legs

Ground-state phases of the spin-1/2 zigzag ladder with unequal ferromagnetic legs

$$\mathcal{H} = \sum_{l=1}^{L} [J_{\rm F}\boldsymbol{S}_{2l-1}\boldsymbol{S}_{2l} + J_{\rm A}\boldsymbol{S}_{2l}\boldsymbol{S}_{2l+1} + J_{\rm L}(1+\delta)\boldsymbol{S}_{2l-1}\boldsymbol{S}_{2l+1} + J_{\rm L}(1-\delta)\boldsymbol{S}_{2l}\boldsymbol{S}_{2l+2}] \quad (1)$$

are investigated based on the iDMRG calculation of the entanglement spectrum (ES). We consider the case of $J_{\rm L} < 0$, $J_{\rm F} < 0$,$J_{\rm A} > 0$, $0 \leq \delta \leq 1$. This model tends to the spin-1 chain in the limit of $J_{\rm F} \to -\infty$.

For $\delta = 0$, a series of topologically distinct spin-gap phases have been found from the analysis of the edge spin[1, 2]. For $\delta = 1$, this model reduces to the Δ-chain with ferromagnetic main chain. Although similar series of spin-gap phases are known in this model[3], their nature remained unclarified so far. However, the phase diagram obtained in [3] redrawn with the present parametrization turned out to be almost identical with that for $\delta = 0$. We carried out the iDMRG calculation of the ES with divisions A and B depicted in Fig. 1 for $\delta = 0, 0.5$ and 1 with $J_{\rm L}/J_{\rm A} = -2.5$. It is found that the behaviors of ES are insensitive to δ as shown in Fig. 2.

The results are consistent with the exact solution on the ferromagnetic-nonmagnetic phase boundary[4] and the nonlinear sigma model analysis[5] for large $J_{\rm L}$.

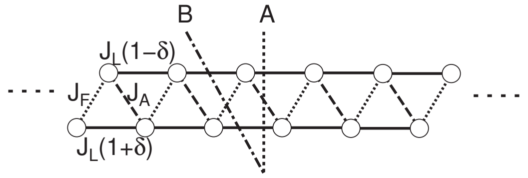

Figure 1: Lattice structure of the present system. Two types of divisions for the calculation of ES are also shown.

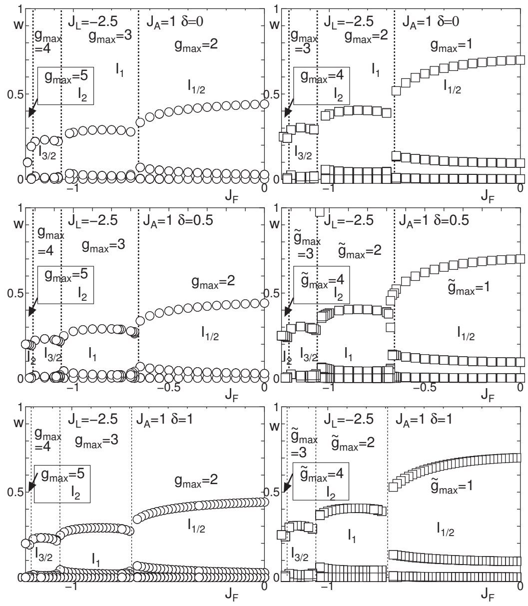

Figure 2: $J_{\rm F}$-dependence of ES. The degeneracy of largest eigenvalues are $g_{\rm max}$ for division A and $\tilde{g}_{\rm max}$ for division B.

This work is supported by KAKENHI (C) (No. 25400389) from JSPS.

2 Finite-temperature phase diagram of the single-band Hubbard model on the pyrochlore lattice

Itinerant electronic systems on the pyrochlore lattice are one of the most frustrated three-dimensional systems. Such models may be relevant for understanding the electronic and magnetic properties of pyrochlore oxides and spinel oxides where transition metal atoms comprise the pyrochlore lattice.

In the recent years, extensive numerical studies have been carried for two-dimensional frustrated itinerant systems such as the Hubbard model on the triangular lattice. In particular, the dynamical mean-field theory (DMFT) and its cluster extensions have been used to investigate finite-temperature properties of the models. However, so far, no DMFT studies have been reported for the pyrochlore Hubbard model, which may be due to a severe sign problem coming from the geometrical frustration in solving an impurity problem by continuous-time quantum Monte Carlo (QMC) methods.

Recently, we systematically investigated the dependence of the sign problem on the single-particle basis [6]. We explored both the hybridization-expansion and the interaction-expansion variants of continuous-time QMC for three-site and four-site impurity models with baths that are diagonal in the orbital degrees of freedom. We found that the sign problem in these models can be substantially reduced by using a non-trivial single-particle basis.

In this study, we applied this non-trivial single-particle basis “dimer basis” to four-site cluster DMFT calculations to map out its finite-temperature phase diagram. We consider the single-band Hubbard model only with nearest-neighbor hopping ($t = 1$) at half filling. We employed the interaction-expansion QMC algorithm. We plot the quasi-particle weight computed at $\beta = 20$ in Fig. 3. We used a metallic solution or an insulating solution as the initial state of the DMFT self-consistent procedure. We assumed paramagnetic solutions. There is hysteric behavior around $U/t \simeq 9$, indicating the existence of a first-order transition. The critical value $U/t \simeq 9$ is almost twice larger than the estimate by the unrestricted Hartree-Fock approximation [7].

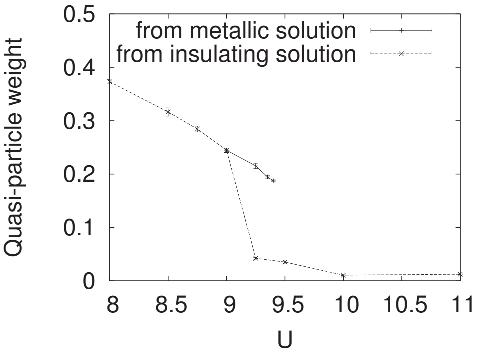

Figure 3: U dependence of the quasi-particle weight. We used a metallic solution or an insulating solution as the initial state of the DMFT self-consistent procedure. The data of the self-consistent solutions are shown by the solid line (from metallic initial state) and the broken line (from insulating initial state), respectively.

This work was done in collaboration with Yusuke Nomura.

References

[1] K. Hida, K. Takano and H. Suzuki : J. Phys. Soc. Jpn. **82** 064703 (2013).

[2] K. Hida : J. Phys. Soc. Jpn. **85** 024705 (2015).

[3] K. Hida : J. Phys. Soc. Jpn. **77** 044707 (2008), [Errata **79** 028001 (2010)].

[4] H. Suzuki and K. Takano: J. Phys. Soc. Jpn. **77** 113701(2008).

[5] S. C. Furuya : private communication.

[6] H. Shinaoka, Y. Nomura, S. Biermann, M. Troyer, P. Werner, Phys. Rev. B **92**, 195125 (2015).

[7] N. Swain, R. Tiwari and P. Majumdar, arXiv:1505.03502v1.

3.5 CMSI projects

Nonadiabatic electron dynamics and many-body nuclear dynamics in molecules

Satoshi TAKAHASHI and Kazuo TAKATSUKA
Department of Basic Science, Graduate School of Arts and Sciences, University of Tokyo
Komaba, Meguro, Tokyo 153-8902

To understand the quantum effects of nuclei in chemical reactions, it is necessary to track the wavepacket dynamics during the reactions. However, even with the modern massive parallel computers, it is still prohibitive to perform a primitive fully-quantum wavepacket dynamics simulations, because the required amount of calculation grows exponentially with the number of degrees of freedom. To overcome such a situation, we have been continuing researches based on the action decomposed function (ADF) [1, 2].

In the theoretical framework of ADF, wavepacket dynamics is described in terms of an ensemble of classical trajectories. Starting from the fundamental equation of ADF, it is found that dynamics is decomposed into two terms. One is proved to represent geometry of small spatial region around the reference trajectory, and the other is the “diffusion operator” with a pure imaginary diffusion constant.

Our preliminary numerical studies have already shown that the geometrical change around the reference path is described well with the nearby running ones, and also that quantum effects are able to be well incorporated thereby. These facts provide a significant advantage for the calculations of real systems with many degrees of freedom, because a reference trajectory, on which a volume element propagation is monitored, is reused as a nearby trajectory for some other nearby ones. Although we have not embarked on practical massive parallel computations based on this theoretical formalism, we are going to make a start of many-body nuclear dynamics simulation, further proceeding to the connection to nonadiabatic electron dynamics.

Besides the advantage of describing multidimensional wavepacket dynamics, because of its structure, ADF theory also possesses an ability to reveal the quantum-classical correspondence in detail. Our previous study has made it clear that energy quantization is performed with action integrals and the so-called Maslov phases in the semiclassical regime [3]. However, such semiclassical phase quantization can yield a small deviation in the energy values, which becomes non-negligible when the Planck constant is large. Numerical tests based on the ADF has so far revealed the following facts: (i) It is the finiteness rather than being infinitesimal of the tiny volume element that allows to take the finite value of the Planck constant into account. (ii) Interference among propagated volume elements with initially different size also appears to be essential to reproduce quantum energy eigenvalues.

References

[1] S. Takahashi and K. Takatsuka: Phys. Rev. A **89** (2014) 012108.

[2] K. Takatsuka and S. Takahashi: Phys. Rev. A **89** (2014) 012109.

[3] S. Takahashi and K. Takatsuka: J. Chem. Phys. **127**, (2007) 084112.

Ab Initio Calculation of High-Temperature Superconducting Mechanism – Comparison between Cuprates and Iron-Based Superconductors

Takahiro Misawa, Motoaki Hirayama, Takahiro Ohgoe, Terumasa Tadano,
Youhei Yamaji, Kota Ido and Masatoshi Imada
Department of Applied Physics, University of Tokyo
Hongo 7-3-1, Bunkyo-ku, Tokyo 113-8656

A hierarchical method [1] (multi-scale *ab initio* scheme for strongly correlated electrons, MACE) developed by integration of the density functional theory (DFT) and the precise model calculation for strongly correlated electrons has been established a decade ago and is a promising way for treatments of electronic correlations beyond the standard DFT. In MACE, we first obtain the global band structures based on the DFT and evaluate the interaction parameters in the low-energy effective models by using constrained random-phase approximation following the idea of the renormalization group. Then, we solve the derived low-energy effective models by using precise low-energy solvers such as the many-variable variational Monte Carlo (mVMC) method. By using this scheme, we have successfully reproduced the electronic structures including the high-T_c superconductivity of the iron-based superconductors [2].

However, in this scheme, there is a fundamental problem that the electronic correlations are doubly counted, i.e., the electronic correlations are included in both the DFT and the model calculations. Although this double counting is likely to be small in the MACE, in the strong coupling region where copper oxide high-T_c superconductors are believed to be located, eliminating of the double counting offers more reliable estimate for correctly reproducing the electronic structures.

In this project, to examine the effects of the double counting, we perform constrained GW (cGW) calculations [3]. In the cGW calculations, we first subtract the exchange-correlation energy in the LDA calculations and replace it with the GW self-energy that comes from only the high-energy degrees of freedom. In this procedure, since we do not consider the low-energy part of the GW self-energy in deriving the low-energy effective model, the double counting of exchange correlations does not occur. By performing cGW calculations for the cuprates, we find that the elimination of the double counting is quantitatively important to reproduce the realistic electronic structures of the cuprates.

Furthermore, in the cuprates, because the several bands entangle around the Fermi level, it is not clear what is the low-energy degrees of freedom. To identify the essential low-energy degrees of freedom, we have derived and solved single- and two-band models for two different cuprates ($\mathrm{HgBa_2CuO_4}$ and $\mathrm{La_2CuO_4}$). As a result, we find that the single-orbital ($d_{x^2-y^2}$ orbital) model can be justified for $\mathrm{HgBa_2CuO_4}$. In contrast to this, for $\mathrm{La_2CuO_4}$, in addition to the $d_{x^2-y^2}$ orbital, another orbital (d_{z^2} orbital) degrees of freedom play substantial roles. Our detailed analysis on the low-energy effective models for the cuprates will provide a firm theoretical basis for understanding the origin of the high-T_c superconductivity in the cuprates. The role of electron-phonon interactions can also be studied on unified grounds [4] and the detailed studies will be reported elsewhere.

Acknowledgements
We thank Kosuke Miyatani for collaborations at the initial stage of this project and useful discussions.

References

[1] For a review, see M. Imada and T. Miyake, J. Phys. Soc. Jpn. **79**, 112001 (2010).

[2] T. Misawa and M. Imada, Nat. Commun **5**, 5738 (2014).

[3] M. Hirayama, T. Misawa, T. Miyake, and M. Imada, J. Phys. Soc. Jpn. **84**, 093703 (2015).

[4] T. Ohgoe, and M. Imada, Phys. Rev. B. **89** 195139 (2014).

DMRG Study of Kitaev-Heisenberg Model: from Honeycomb to Triangular Lattice

Takami TOHYAMA
Department of Applied Physics, Tokyo University of Science, Tokyo 125-8585

The Kitaev-Heisenberg (KH) model is suggested as an effective model for $(\mathrm{Na,Li})_2\mathrm{IrO}_3$ that has a honeycomb lattice structure. The number of the bonds from each site on the honeycomb lattice is three. The same number appears on triangular lattice. Therefore, one can define a KH model on the triangular lattice. Furthermore, the triangular lattice is formed by putting a site at the center of the hexagonal unit of the honeycomb lattice. This leads to a motivation to study the models changing the interaction strength on the bonds connecting the central site and surrounding sites. It is also interesting how phases in the honeycomb lattices are connected to phases in the triangular lattice when the parameter values of the KH model are the same. For example, the honeycomb Kitaev model show a spin-liquid phase, while the triangular Kitaev model gives a nematic phase. The change of the two phases is an interesting issue to be studied theoretically. We ote that our group has already studied the KH model on both lattices [1, 2].

We examine the KH model by changing the interaction connecting the both lattices by the two-dimensional density-matrix renormalization group (2D-DMRG) method for a 12×6-site lattice. We used the System C in the Supercomputer Center, the Institute for Solid State Physics, the University of Tokyo, and the K-computer. The 2D-DMRG code has been developed by our group. To perform DMRG, we map the original system to a snake-like one-dimensional chain, and combine the chain with long-range interactions. We keep nearly 1000 states in the DMRG block and performed nearly 10 sweeps, resulting in a typical truncation error with the order of 10^{-5}. Calculating the ground-state energy, spin structure factors, and entanglement properties, we preliminarily obtain the ground state phase diagram of the Kitaev-Heisenberg model as a function of the strength of the connecting interaction.

We focus on the Kitaev model without the Heisenberg terms, since the end points exhibit interesting phases: a nematic phase and a spin-liquid phase for the triangular and honeycomb lattice, respectively. Since the Kitaev spin-liquid phase is week against additional interaction, it is destroyed as soon as the connecting interaction is turned on. The same is for the other end where the nematic phase exists. These weakness means the presence of another phase between the honeycomb and triangular Kitaev models, which is a stripy phase. A detailed examination is now in progress together with the construction of the detailed phase diagram with full parameter region.

This work was done in collaboration with Shigetoshi Sota.

References

[1] K. Shinjo, S. Sota, and T. Tohyama: Phys. Rev. B **91** 054401 (2015).

[2] K. Shinjo, S. Sota, S. Yunoki, K. Totsuka, and T. Tohyama: arXiv:1512.02334.

Study of Novel Quantum Phases and Critical Phenomena by Monte Carlo Method and Tensor Network --- SU(*N*) Heisenberg Model with Multicolumn Representations

Tsuyoshi Okubo[1], Kenji Harada[2], Jie Lou[3], and Naoki KAWASHIMA[1]

[1]*Institute for Solid State Physics, The University of Tokyo, Kashiwa-no-ha, Kashiwa, Chiba 277-8581,*

[2]*Graduate School of Informatics, Kyoto University, Kyoto 606-8501, Japan,*

[3]*Department of Physics, Fudan University, Shanghai 200433, China*

Quantum spin liquid states and topological states are among the most intensively investigated subjects in the recent condensed matter theory. In our project, we consider several quantum spin systems as characteristic examples for studying these novel states and related quantum phase transitions. We also develop computer programs specialized for large scale parallelization aiming at the K-computer. In particular, we investigate the SU(*N*) *J*-*Q* model, to clarify the nature of the deconfined critical phenomena. In general, our model is the Heisenberg generalized in two ways: the spin operators are generators of SU(*N*) (*N*=2,3,4,...) algebra instead of the conventional SU(2) spins, and the model has 4 or 6-spin interactions in addition to the conventional 2-spin nearest neighbor interactions.

However, in the present report, we concentrate on the effect of representations and only discuss the case with no multi-spin interactions. To be specific, our Hamiltonian is

$$H = \frac{J}{N}\sum_{(ij)}\sum_{\alpha,\beta=1}^{N} S_i^{\alpha\beta}\bar{S}_j^{\beta\alpha} ,$$

where *i* runs over lattice points of one of the two sublattices of square lattice. The symbol $S_i^{\alpha\beta}$ represent an SU(*N*) spin in *n*-column and single-raw representation whereas $\bar{S}_i^{\beta\alpha}$ in the conjugate representation, i.e., *n*-column and (*N*-1)-raw representation.

We used an original code developed based on the ALPS/Looper, a program package based on the loop algorithm of the world-line

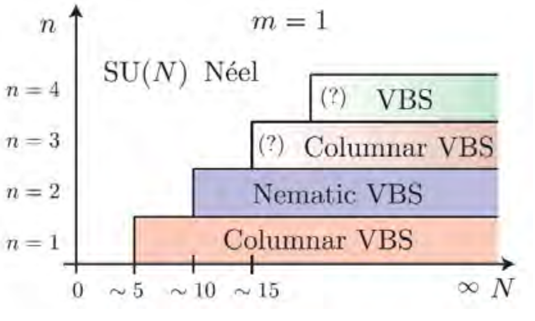

Fig. 1 Schematic phase diagraom of the SU(*N*) Heisenberg model on the square lattice with single-row representations. (Adapted from Ref.[1].)

quantum Monte Carlo simulation.

In this report, the central question is whether the intermediate spin-liquid state exist or not in the *n*-*N* phase diagram of the generalized Heisenberg model. For n=1 (fundamental representation), it had been established [2] that the transition occurs from the magnetic state (Néel state) for $N \leq 4$ to the non-magnetic state for $N \geq 5$, where the latter non-magnetic phase is the valence bond solid (VBS) state with spontaneously broken lattice-rotational symmetry.

We carried out calculation for *n*=2 and 3 for $N \leq 25$. The system size studied was $L = J/T \leq 128$. From our calculation, we found no evidence for the intermediate spin liquid state. To be more specific, for *n*=2, we found that the ground state is the Néel state for $N \leq 9$ and the VBS state for $N \geq 10$. For *n*=3, we found that the ground state is the Néel state for $N \leq 14$ and that the magnetic order is absent for $N \geq 15$. Unlike the case of *n*=2, we could not detect any other order for $N \geq 15$. However, we do not take this observation as an evidence for the intermediate spin-liquid state because our estimate of the amplitude of the VBS order parameter based on the field theory suggests that it could well be too small for the present precision to detect.

References

[1] Tsuyoshi Okubo, Kenji Harada, Jie Lou, Naoki Kawashima, Phys. Rev. B **92** (2015) 134404(1-5).

[2] N. Kawashima and Y. Tanabe, Phys. Rev. Lett. 98, (2007) 057202

Multi-scale simulation of nano-structured devices from electronic structures to mechanical properties

Shuji OGATA
Nagoya Institute of Technology
Gokiso-cho, Showa-ku, Nagoya 466-8555, Japan

In the fiscal year of 2015, we have mainly treated three subjects. The first one is the hybrid quantum-classical (QM-CL) simulation study of the thermal diffusion of correlated Li-ions in graphite. The second one is the classical molecular-dynamics (MD) simulation study of the heat transfer through alumina/epoxy/alumina system. The third one is the hybrid QM-CL simulation stidy of Si-O bond breaking in silica glass. Those are described briefly as follows.

Subject 1: The hybrid QM-CL simulation of the thermal diffusion of Li-ions in graphite [1]. Diffusion of Li-ions in graphite is an essential elementary process in the current lithium-ion battery. The C-layers of graphite deform with Li due to relatively large size of Li-ion, which acts to confine the Li-ions and thereby create correlation between them. We address theoretically the thermal diffusivity of such correlated Li-ions in graphite by the hybrid quantum-classical simulation method. In this method, the quantum-region composed of the Li-ions and surrounding C atoms is treated by the density-functional theory, while it is embedded dynamically in the total system described with an empirical inter-atomic interaction potential. We thereby take into account the long-ranged deformation field in graphite in simulating the Li-ion dynamics.

We perform the hybrid simulation run with 14 Li-ions inserted, 7 by 7, to two inter-layer spaces of graphite (ten C-layers). The stacking structures of the C-layers that sandwich Li-ions are the AA-stacking. The largest QM-region contains 625 C-atoms and 11 Li-ions; it takes about 9 minutes per time step using about 100 CPU's of Fujitsu FX10 at ISSP with the domain decomposition 2×2×1, the spatial decomposition of each domain 5×5×3, the band parallelization 2, and the OpenMP parallelization 4 set in the divide-and-conquer-type O(N)-RGDFT (named DC-RGDFT) code.

Subject 2: The MD simulation of the heat transfer through alumina/epoxy/alumina system [2]. The composite of epoxy polymers and a-alumina fillers is used as a heat dissipation material. The fillers often agglomerate with nanometer-depth polymers sandwiched in between. We address theoretically the effective thermal conductivity of such a filler-polymer-filler system (see Fig. 1). The non-equilibrium MD simulation is performed to obtain the effective thermal conductivity of the system, in which bisphenol-A (bisA) epoxy polymer sub-system with depth 14–70 Å is inserted between two a-alumina slabs. Effects of surface-coupling (SC) agent are also investigated by adding model molecules to the polymer sub-system.

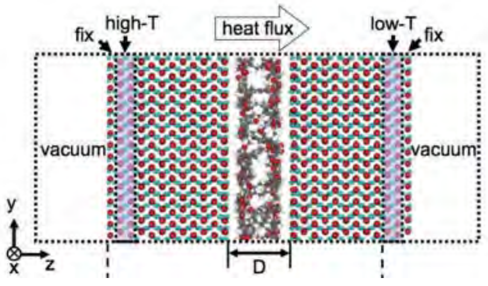

Figure 1: Atomic configuration of a typical system for the NEMD simulation with D = 14 Å without the SC molecules. Large red spheres are O's; medium cyan, Al's; medium grey, C's; small white, H's.

For smaller polymer-depth cases, the effective thermal conductivity is determined essentially by the interfacial thermal conductance that relates to the temperature-gaps at the interfaces. We find for the interfacial thermal conductance that: (i) it is decreased by decreasing the polymer depth toward the chain length of a single bisA molecule, and (ii) it is increased by adding the SC molecules to the polymer sub-system. Combining separate simulation analyses, we show that the (i) results from effectively weakened interaction between a bisA molecule and two a-alumina slabs due to the orientation constraint on the bisA molecule by the slabs. Reasons of the (ii) are enhancement of the following three quantities by addition of the SC molecules: the phonon population of the bisA molecules at those frequencies corresponding to that of acoustic phonons of a-alumina, the phonon transmission coefficient from the a-alumina slab to the polymer sub-system for the transverse acoustic phonon, and the group velocity of the transverse acoustic phonon in the polymer sub-system.

Subject 3: The hybrid QM-CL simulation of Si-O bond breaking in silica glass [3]. We perform a hybrid QM-CL simulation of a 4,608-atom silica glass at a temperature of 400 K with either a water monomer or dimer inserted in a void (see Fig. 2). The quantum region that includes the water and the surrounding atoms is treated by the DFT. During a simulation, the silica glass is gradually compressed or expanded. No Si-O bond breaking occurs with a water monomer until the silica glass collapses. With a water dimer, we find that Si-O bond breaking occurs through three steps in 3 out of 24 compression cases: (i) H-transfer as $2H_2O \rightarrow OH^- + H_3O^+$ accompanied by the adsorption of OH^- at a strained Si to make it five-coordinated, (ii) breaking of a Si-O bond that originates from the five-coordinated Si, and (iii) H-transfer from H_3O^+ to the O of the broken Si-O bond. A separate DFT calculation confirms that the barrier energy of the bond breaking with a water dimer under compression is smaller than that with a water monomer and that the barrier energy decreases significantly when the silica glass is compressed further.

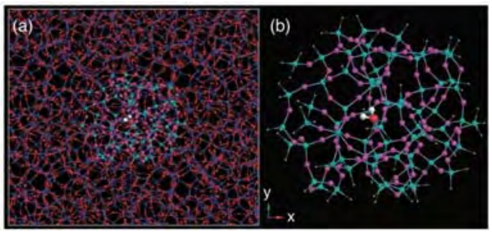

Figure 2: (a) Present silica glass with a water molecule in a void. The red and blue spheres are CL O and Si, respectively. The magenta and cyan spheres are QM O and Si, respectively. The large red and white spheres are respectively QM O and H of a water molecule. (b) Atomic cluster used for the QM calculation.

References

[1] N. Ohba, S. Ogata, T. Kouno, and R. Asahi, Comp. Mater. Sci. **108** (2015) 250-257.
[2] K. Tanaka, S. Ogata, R. Kobayashi, T. Tamura, and T. Kouno, Int. J. Heat and Mass Transfer **89** (2015) 714-723.
[3] T. Kouno, S. Ogata, T. Shimada, T. Tamura, and R. Kobayashi, J. Phys. Soc. Jpn. **85** (2016), in press.

Highly accurate calculation of impurity hydrogen in oxides

Shinji TSUNEYUKI
Department of Physics, School of Science, The University of Tokyo
7-3-1 Hongo, Bunkyo-ku, Tokyo 113-0033
Institute for Solid State Physics, The University of Tokyo
Kashiwa-no-ha, Kashiwa, Chiba 277-8581

Impurity hydrogen is known to play a crucial role for electronic properties of semiconductors. It does not only terminate dangling bonds of defects or surface of semiconductors but also passivate carriers in both p-type and n-type semiconductors by changing its charge state to a cation (H^+) or an anion (H^-), respectively. Impurity hydrogen is also attracting much attention as a carrier dopant in oxide semiconductors and superconductors.

Direct observation of the existence and charge state of impurity hydrogen is so difficult that there have been a lot of theoretical studies with the first-principles calculation based on the density functional theory (DFT). However, the accuracy of the total energy calculated by DFT is considered to be insufficient for conclusive prediction of the stable charge state of impurity hydrogen. In this project, we used the diffusion Monte Carlo method, a state-of-the-art first-principles total-energy calculation method, to clarify the most stable charge state of impurity hydrogen in crystalline SiO_2,

Neutral H^0 does not exist in SiO_2 by ESR study except when the sample is irradiated by an electron beam, meaning that H^0 is not a stable state of impurity hydrogen. On the other hand, in μSR study, it is known that a large portion of muon impinged in low-quartz, a typical polymorph of SiO_2, turns into a muonium (Mu), a bound state of a muon and an electron. It suggests the stability of H^0. Mu is also observed in stishovite, a high-pressure polymorph of SiO_2. From the DFT calculation of low-quartz and stishovite, a typical polymorph of SiO_2, the stable charge state of impurity hydrogen is either H^+ or H^- depending on the electron chemical potential and H^0 is unstable in any condition. Here we calculated the total energy of impurity hydrogen in low-quartz and stishovite changing its position and charge states by DMC to find that the DFT results are qualitatively reproduced, that is, H^0 is energetically unstable in thermal equilibrium.

From the present calculation we conclude that the Mu observed in μSR experiments are realized only as a metastable state. To confirm the metastability of Mu (or H^0), we developed a method to find activation barrier for the diffusion of an impurity considering the change in its charge state. The method is based on the nudged elastic band (NEB) method but potential energy hypersurfaces for different charge states are considered. With the method, we investigated the stability of hydrogen impurity (H^0, H^+, H^-) in SiO_2 to find the neutral state can be actually realized by large activation energy barriers [1].

References

[1] Y. Yamamoto, R. Akashi and S. Tsuneyuki, in preparation.

Materials design for spintronics/multiferroics applications

Mineo SAITO, Tasuki, ODA and Fumiyuki ISHII
Division of Mathematical and Physical Science, Institute of Science and Technology,
Kanazawa University, Kakuma, Kanazawa, 920-1192 Japan

In this project, we have developed codes which enable the study of spintronics and multiferroics materials. We have developed a program code of newly parallelized density functional electronic structure calculations (CPVO). We also make a program that enables drawing spin textures by using numerical results which are calculated by using the OpenMX code.

We have performed the first-principles density functional calculation for the slab systems; single interface MgO/Fe, magnetic junction Fe/MgO/Fe, the double interface MgO/Fe/MgO, and Fe/TiO_2/SrO/TiO_2 [1]. To clarify the origin of electric field (EF) effect on the magnetic anisotropy energy (MAE), we discussed the electronic structure of interface Fe with using the calculated results. In these studies, we found that the EF-induced modulation sign of MAE is reversed when the dielectric material is changed to $SrTiO_2$(STO) from MgO. In the STO systems, the MAE decreases as the electron depletion condition (positive EF) is induced in the interface using the external EF. However, as shown in Fig. 1, the number of electrons (NOE) slightly increases as the EF, associated with the decrease of spin magnetic moment (SM) on the interface Fe. This decrease of SM is consistent with an increase of NOE assuming a usual simple exchange-splitting band model. In Fig. 1, however, the increasing ratio on NOE is not so high (rather small), compared with the absolute of decreasing ratio on SM. This situation may be understand by considering that under the EF the 3d electron increases and other 4s electron decreases on the interface Fe. When assuming the decrease of 3d electron, the decrease of MAE may be explained by the general property in the Fe thin film, so that the MAE decreases as number of electrons.

The partial density of states projected to the Fe atom at interface was calculated Fe/TiO_2/SrO/TiO_2, for shown in Fig. 2. In these PDOSs, the minority spin states of 3d orbitals are located around the Fermi level (E_F). When compared with the corresponding quantities of Fe/MgO systems, the Fermi level is located at the lower energy. This energy is far from the interface resonance states (IRS) which are observed as spiky peaks just above the Fermi level in the PDOS. Although such property may be one of the circumstantial evidences which deduce the decreasing behavior in MAE with respect to EF, no adequate mechanism has been proposed yet. Further investigations are required.

We have been studying ZnO and found the possibility of its application to spintronics devices [2-3]. In this study [4], we find that metallic spin-split surface bands can be achieved on hydrogenated ZnO (10-10) surface (Fig. 3). We clarify that the hydrogenation plays an important role in spin-orbit interaction and the spin-split bands induce strongly anisotropic Rashba-type spin textures, which are expected to be useful for device applications.

References

[1] D. Yoshikawa et al., ICM2015, Barcelona (Spain), July 2015.

[2] M. A. U. Absor et al, Appl. Phys. Express 7, 053002 (2014).

[3] M. A. U. Absor et al, Appl. Phys. Express 8, 073006 (2015).

[4] M. A. U, Absor et al, AIP Advances 6, 025309 (2016).

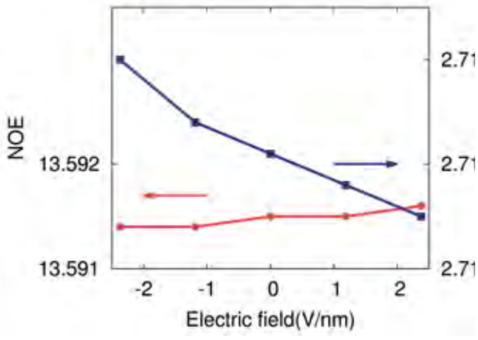

Fig 1. Number of electron (NOE) and spin magnetic moment as a function of electric field.

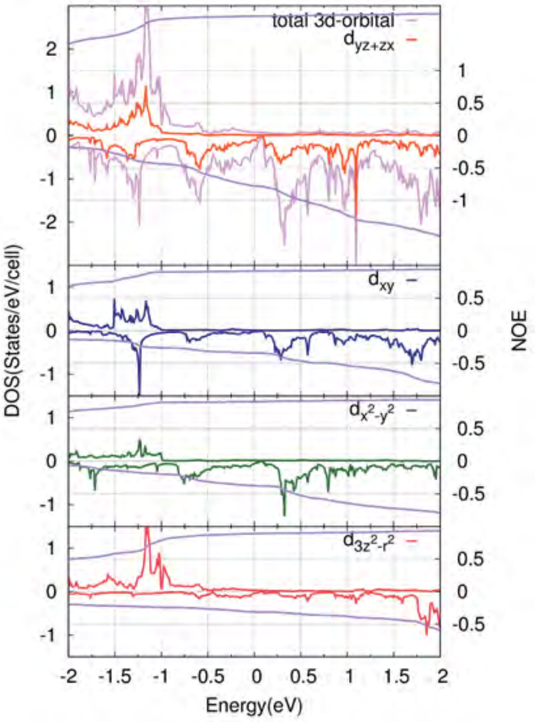

Fig 2. Partial density of states (PDOS) on the Fe atom at the interface Fe/TiO_2/SrO/TiO_2.

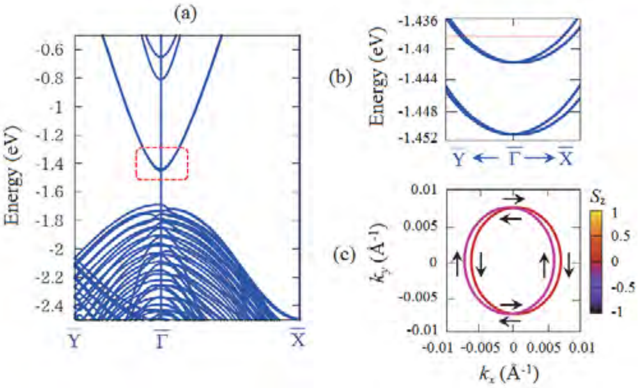

Fig 3. Electronic band structure (a), (b) and spin-resolved isoenergy line at -1.4eV (c) of hydrogen terminated ZnO (10-10).

Photo-induced electron dynamics in nanostructures and development of quantum devices with optical and electronic functionality

Katsuyuki NOBUSADA
Institute for Molecular Science,
Myodaiji, Okazaki, Aichi 444-8585

An optical near-field (ONF) is a nonpropagating light localized in proximity to a surface or, more precisely, an interface region between materials, such as nanoparticles in the air, dopants or holes embedded in solids, and interfaces between different dielectrics. ONFs have been discussed very frequently in the context of electric field enhancement in nanometer regions far beyond the diffraction limit. The field enhancement due to plasmon excitation in metals such as precious metal clusters is a major topic in the field of plasmonics. However, a more intrinsic feature of ONFs, which causes qualitatively different electron excitation from that of a far-field light, is the nonuniformity of the electric field [1]. Since an ONF rapidly decays with increasing distance from ONF source, the electric field gradient plays an important role in the ONF and matter interaction. In such an interaction, matter experiences a nonuniform electric field that is qualitatively different from the uniform far-field propagating light. Thus, the conventional theoretical treatment of a light-matter interaction based on a dipole approximation does not work well.

We have illustrated an unusual dynamical interaction effect between an ONF and electrons. This dynamical ONF effect was introduced in our studies [1], in which we showed that the ONF excitation inherently includes a second-harmonic electric field component, derived from the dynamical interaction between the ONF and the electron. As an example, we demonstrated the ONF induced two-photon absorption in a real nanostructure of a metal-organic-framework (MOF). More specifically, an acetylene molecule is efficiently two-photon excited by the ONF generated in the MOF. The MOF is highly ordered and large nanostructures. Our originally developed computational program called GCEED [2] allows us to perform massively parallelized calculations of such ONF excitation dynamics in the MOF.

We also started first-principles molecular dynamics simulations of metal cluster catalysts supported on solid surfaces. Catalytic CO oxidation on a gold or platinum supported cluster has proved to occur through Langmuir-

Hinshelwood mechanism [3,4].

References

[1] M. Yamaguchi, K. Nobusada and T. Yatsui, *Phys. Rev. A*, **92**, 043809 (2015).

[2] M. Noda, K. Ishimura, K. Nobusada, K. Yabana and T. Boku, *J. Comp. Phys.*, **265**, 145 (2014).

[3] K. Koizumi, K. Nobusada and M. Boero, Chem. Eur. J. 22, 5181 (2016).

[4] K. Koizumi, K. Nobusada and M. Boero, J. Phys. Chem. C 119, 15421 (2015).

Molecular Science of Virus by All-Atom Simulation

Susumu Okazaki
Department of Applied Chemistry, Nagoya University
Furo-cho, Chikusa-ku, Nagoya, 444-0868

In fiscal 2015, our group used the system-B in the second half year and the system-C throughout the year. We carried out the molecular dynamics (MD) calculation with respect to the stability of poliovirus empty capsids in electrolyte solution[1] and the interaction between poliovirus capsids and its receptor CD155. These systems contain $10^6 - 10^7$ charged atoms. Electrostatic interactions among the charges were calculated under the three dimensional periodic boundary condition based on the fast multipole method. Further, the machine time was used to analyze trajectories of production runs of poliovirus systems generated on the K computer.

Analyses were carried out using parallelized programs by MPI and OpenMP, and partially OpenACC, combined with MODYLAS[2]. Interactions between the capsid and D1 domain of CD155 was evaluated calculating the free energy profile as a function of radial distance between the two. The attractive forces do act between the capsid and receptor. Further, analysis on the electric field around poliovirus capsids was conducted, which provided valuable information to understand the origin of a specific interaction between poliovirus capsid and CD155-D1. MD calculation studies on physical properties of lipid bilayers modeling hepatocyte plasma membranes[3] were carried out, too. This contributes to understanding of the physico-chemical properties of the envelope of Hepatitis B viruses.

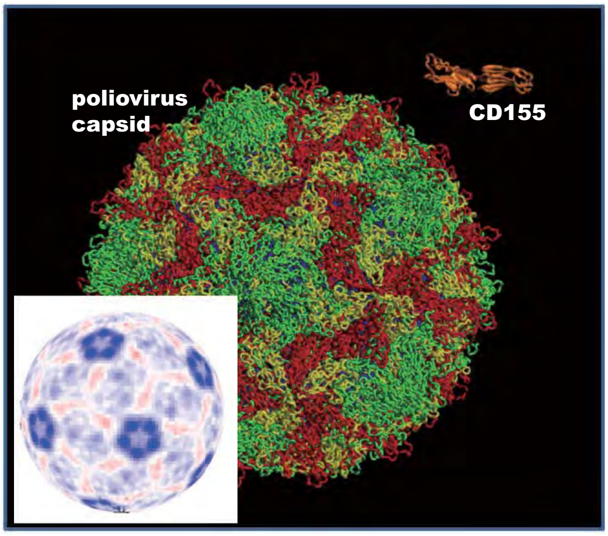

Figure 1: Poliovirus capsid and poliovirus receptor CD155. Ions and waters are not shown. Inserted figure is an example of the calculated electric field around the capsid.

References

[1] Y. Andoh, et al. : J. Chem. Phys., **141** (2014) 165101.

[2] Y. Andoh, et al. : J. Chem. Theory Comput. **9** (2013) 3201.

[3] Y. Andoh, et al. : J. Chem. Phys., **144** (2016) 085104.

Large scale ab initio calculations on the fundamental processes of energy convergence devices and on their optimization for high conversion efficiency

Koichi YAMASHITA
Department of Chemical System Engineering,
The University of Tokyo, Hongo, Bunkyo-ku, Tokyo 113-8656

Organic photovoltaic (OPV) cells are being eagerly researched and developed. In particular, bulk heterojunction (BHJ) photovoltaic cells have many attractive properties. Exciton dissociation that leads to generation of free electron and hole has been considered as a key factor in photo-conversion process of OPVs. However, the fine mechanism of the exciton dissociation against Coulomb interaction between the electrons and holes has not been fully revealed yet. Then, we studied (1) charge recombination which depress the power conversion efficiency of OPVs [1] and (2) short-circuit currents which is determined by competition of the charge dissociation and charge recombination [2, 3]. In both studies, we used our original code named as MolDS that is implemented for massive parallel computing of semiempirical quantum calculations, especially electronic excites states calculations, by using hybrid (openMPMPI) parallelization technique. In the first part, the electronic structures of P3HT at the interface and in the bulk phase were investigated to elucidate the charge separation process in the P3HT/SWNT blends. We found energy difference between the HOMO levels at the interface and those in the bulk phase, which explains observations in a previous experiment where long-lived charge carriers were only observed in blends containing excess P3HT. In the second part, we found that a pair of donor and acceptor exhibits the largest charge-bridging upon photo-absorption, which leads to the highest IQE and PCE. This later finding should be a unique guiding principle to synthesize new molecular materials for OPVs.

References

[1] K. Nishimra, M. Fujii, R. Jono, and K. Yamashita: J. Phys. Chem. C **119**, 26258-26265 (2015)

[2] M. Fujii, W. Shin, T. Yasuda, and K. Yamashita: Phys Chem Chem Phys. **18**, 9514-9523, (2016)

[3] S. Koda, M. Fujii, S. Hatamiya, K. Yamashita: Theor. Chem. Acc. **135**, 115-124, (2016)

[4] M. Fujii, K. Nishimra, M. Okuyama, MolDS URL: https:// en.osdn.jp/projects/molds/

Surface/Interface Science of Energy Conversion

Osamu SUGINO
Institute for Solid State Physics, University of Tokyo
Kashiwa-no-ha, Kashiwa, Chiba 277-8581

This article reports work done by members of the priority project of CMSI[1], aiming at establishing a first-principles approach to the electrochemical interface. The target consists of the two; the electrocatalyst-solution interface typical of the fuel-cell study and the solid-electrolyte interface typical of the battery study. The former study is mainly based on the package called STATE which has been developed by Morikawa group, and the latter is based on stat-CPMD developed by Tateyama group. Both codes have been specialized to the interface study and are able to obtain equilibrium structures of the interface and free-energy of the electrochemical reactions: The codes are parallelized not only w.r.t. the typical parallelization axes[2] but also w.r.t. the reaction coordinates, by which the free-energy landscape can be obtained by a single run. Major problem encountered therein is that the reaction coordinate needs to be assumed before the simulation but the reaction does not always proceed as assumed[3], reflecting a number of competing reaction sites appearing in the simulation cell. This means the method developed in quantum chemistry cannot be applied to the complex interface, requiring us to develop a distinct one. In this context, we have focused on a method developed by Morishita[4], which allows us to correct the reaction coordinate on the fly, and implemented the method to STATE. Our test calculation shows a promise in applying to realistic electrocatalytic reactions to predict a current voltage curve from first-principles.

In the study of battery, the relevant process is often the bias-induced shift of equilibrium between the solid and the electrolyte, where the simulation is demanding compared with that for the electrocatalytic reaction. The required spatial and time scales exceed achievable by the first-principles simulation. In this context, we have developed a procedure to construct a force field model on the basis of first-principles calculation using a modern statistical technique with which to perform a larger-scale (ten thousands of molecules and sub-micro second long) simulation. The simulation on $2\mathrm{Li}+\mathrm{O}_2 \rightleftarrows \mathrm{Li}_2\mathrm{O}_2$ revealed that the oxide nucleates differently in the ionic liquid (EMI-TFSI) and in the organic solvent (DMSO) when discharging, and that the oxide dissolves only partially and remains as $\mathrm{Li}_3\mathrm{O}_2^+$ when charging [5]. The experimental study is still difficult for this lithium-air battery system, and our theoretical prediction is expected to provide particularly useful information.

Group IV oxides, such as $\mathrm{Ta}_2\mathrm{O}_5$ or ZrO_2, are regarded as a next-generation fuel-cell electrocatalyst because of its better durability than that of Pt. The oxide catalysts have long been the target of electrochemistry but the microscopic process is still unknown. In this context, we started the study of a monoclinic ZrO_2 surface by investigating if the pristine surface would be active enough or needs modification to be reactive. We have investigated how the activity can be improved by introducing oxygen vacancies together with nitrogen impurities, as suggested by experimentalists. We have not yet successful in explaining the experimentally observed activity and thus there will be a room for improving the modeling.

References

[1] The project members are Y. Morikawa (Osaka University), K. Inagaki (Osaka University), H. Kizaki (Osaka University), Y. Tateyama (NIMS), K. Sodeyama (NIMS), K. Akagi (Tohoku University), M. Otani (AIST), O. Sugino (ISSP) and S. Kasamatsu (ISSP).

[2] The band axis, the G-point axis, and the k-point axis. Through parallelization w.r.t. these axes, we have achieved good parallel efficiency at least up to a few thousand of atoms. The average CPU usage is $\sim 20\%$.

[3] I. Hamada and O. Sugino, Hyomen Kagaku **34**, 638 (2013).

[4] T. Morishita, S. G. Ito, H. Okumura and M. Mikami, J. Compt. Chem. **34**, 1375 (2013). The method developed herein is based on logarithmic mean force dynamics (log-MFD); Morishita et al., Phys. Rev. **E 85**, 066702 (2012).

[5] K. Akagi et al. (submitted)

Role of calcium ion in molecular recognition process of calcium-dependent carbohydrate-binding module

Norio YOSHIDA

Department of Chemistry, Graduate School of Science

Kyushu University, 744 Motooka, Nishi-ku, Fukuoka 809-0395

The enzymatic degradation of polysaccharides is an important process in the cell wall biomass creation. The carbohydrate-active enzymes have a module to recognize the carbohydrate chain, called carbohydrate-binding module (CBM). The carbohydrate binding by a CBM is the initial process of carbohydrate degradation and also the rate-determining process of the reaction. CBMs are classified into numerous families, and each family has different mechanism of the selective recognition of carbohydrates. Xylanase 43 from *Paenibacilus polymyxa* is a three-module protein that has Ca^{2+}-dependent xylan binding module (CBM36).[1]

The mechanism of xylan binding of CBM36 and the role of Ca^{2+} ion were investigated by the combinational use of the molecular dynamics (MD) simulation and the three-dimensional reference interaction site model (3D-RISM) method.[2]

The Ca^{2+}-bound CBM36 showed xylan affinity, while the Mg^{2+}-bound CBM36 showed no affinity. The free energy component analysis for the xylan binding process revealed that the major factor of the xylan affinity is the electrostatic interaction between the Ca^{2+} ion and the hydroxyl oxygens of xylan. The van der Waals interaction between the hydrophobic side chain and the xylan also contributes to the stabilization. The dehydration by the complex formation has the opposite effect on those interactions. In the case of the Ca^{2+}-bound CBM these interactions are well balanced, while in the case of the Mg^{2+}-bound CBM the dehydration penalty is too large.

The details of the xylan binding of CBM36 are revealed at the molecular level by this study. It is expected that the results of this study contribute to the design of highly efficient CBM or the control of the selectivity of polysaccharides.

References

[1] S. Jamal-Talabani, A.B. Boraston, J.P. Turkenburg, N. Tarbouriech, V.M. Ducros, G.J. Davies, *Structure* 12 (2004) 1177.

[2] S. Tanimoto, M. Higashi, N. Yoshida, H. Nakano, Submitted.

First Principles Calculation of Properties of MXene Electrode Materials under Bias

Minoru OTANI[1,2], Chunping HU[1,2]
[1]*Research Center for Computational Design of Advanced Functional Materials (CD-FMat),*
National Institute of Advanced Industrial Science and Technology (AIST),
Tsukuba, Ibaraki, 305-8565, Japan
[2]*Elements Strategy Initiative for Catalysts and Batteries (ESICB), Kyoto University,*
1-30 Goryo-Ohara, Nishikyo-ku, Kyoto 615-8245, Japan

Sodium ion batteries (SIBs) have been rapidly developed since 2010, on the basis of research and development of lithium ion batteries (LIBs) [1]. In order to improve the battery performance, it is an urgent task to develop new hardly-degraded electrode materials for SIBs, as Na intercalation/extraction process would incur much larger volume expansion/shrinkage if using existing electrode materials for LIBs. Very recently a new type of negative electrode materials – MXene – has been developed for SIBs and found to be very stable during the charging-discharging cycles in which the inter-layer distance of MXene can be kept constant [2]. Great interests have been aroused for the theoretical investigation of properties of MXene, however, first principles study considering the effect of bias voltages has not been carried out yet.

In the present work, we use the effective screening medium (ESM) method developed by Otani and Sugino [3] to study the effect of bias voltages on the properties of MXene with or without ion adsorption, within the planewave pseudopotential framework of density functional theory. The *ab initio* program package QUANTUM ESPRESSO [4] was used and numerical calculations were done in System B and C. In order to achieve the experimental condition of constant bias voltages, the chemical potential of electrons in the electrode is kept constant by adjusting the charge of the system [5].

First, we carried out extensive studies on the surface termination of MXene under bias using mono-, bi- and tri-layer models either terminated by F, O, or OH atoms. All these atoms are founed to be bonded to Ti_2C on the Ti site with or without bias voltages. Next, as a comparative study, we calculated Li adsorption and diffusion on a (3×3) supercell of monolayer Ti_2CO_2. Upon a bias of ±2 V, the Li adsorption sites do not change, but the Li diffusion barrier was found to be varied by more than 50 meV. This shows that although the bias voltage has little effect on ion adsorption, it significantly affect ion diffusion on MXene.

References

[1] K. Kubota and S. Komaba, J. Electrochem. Soc. **162**, A2538 (2015).

[2] X. Wang *et al.*, Nat. Commun. **6**, 6544 (2015).

[3] M. Otani and O. Sugino, Phys. Rev. B **73**, 115407 (2006).

[4] P. Giannozzi *et al.*, J. Phys.: Condens. Matter **21**, 395502 (2009).

[5] C. Hu and M. Otani, to be submitted to Phys. Rev. Lett.

All electron spectra and dynamics of functional materials from nanoclusters to crystals

Kaoru Ohno

Department of Physics, Faculty of Engineering Science,

Yokohama National University, Tokiwadai, Hodogaya-ku, Yokohama 240-8501

To obtain all-electron spectra and dynamics of functional materials from nanoclusters to crystals, a versatile program TOMBO Ver.2 is developed using the all-electron mixed basis approach, which removes weak points of the preexisting first-principles methods. Ground- and excited-state chemical reactions can be treated within the DFT, TDDFT, and TDGW formalisms. UPS or XPS spectra are calculated by the GW approximation (GWA), which well reproduces the energy gap and band structures. This year, we have mainly focused on the program tuning of TOMBO using fortran90, MPI and openMP on the system B (SGI) and the system C (FX10) of ISSP. As an application of TOMBO, we have calculated the band structure of TiO_2 and ZnO by using the GWA [1,2]. For example, Fig. 1 represents the resulting band structure of rutile TiO_2 with Nb impurities ($Ti_{0.75}Nb_{0.25}O_2$) [1]. Dots and curves represent the GWA and the LDA results, respectively, and energy zero is set at the top of the valence band. There is an occupied impurity level in the middle of the band gap and an empty impurity level just below the conduction band. The result well agrees with the experiment [3].

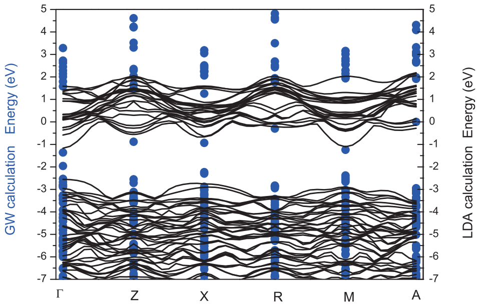

Fig.1 GW band structure of $Ti_{0.75}Nb_{0.25}O_2$ [1].

In this year, we opened source code of LDA part as well as WINDOWS executable of the TOMBO program from our home page [4,5].

References

[1] M. Zhang, S. Ono, and K. Ohno, Phys. Rev. B **92**, 035205 (2015).

[2] M. Zhang, S. Ono, N. Nagatsuka, and K. Ohno, Phys. Rev. B **93**, 155116 (2016).

[3] D. Morris, Y. Dou, J. Rebane, C. E. J. Mitchell, R. G. Egdell, D. S. L. Law, A. Vittadini, and M. Casarin, Phys. Rev. B **61**, 13445 (2000).

[4] S. Ono, Y. Noguchi, R. Sahara, Y. Kawazoe, and K. Ohno, Comp. Phys. Comm. **189**, 20-30 (2015).

[5] http://www.ohno.ynu.ac.jp/tombo/index.html

Computational-Science Study of Frustrated Magnets

Hiroki NAKANO
Graduate School of Material Science, University of Hyogo
3-2-1 Kouto, Kamigori-cho, Ako-gun, Hyogo 678-1297, Japan

It is well known that to study quantum spin systems is generally difficult because they are typical many-body problems. For such studies, therefore, computational approaches become more important. Each method among the computational ones, however, has not only merits but also demerits. Quantum Monte Carlo method faces with a so-called negative sign problem when a system includes frustrations in it although this method can treat large systems if they do not include frustrations. Density matrix renormalization group (DMRG) method can treat frustrated systems. This method, however, is powerful to a one-dimensional system; the extention of this method to systems in dimensions larger than one is now developing. Numerical-diagonalization method, on the other hand, is a reliable way irrespect of the point whether or not a target system is frustrated and irrespect of spational shape of the system. The most serious weak point of this method is that this method can treat only very small systems. To overcome this weak point, we developed an MPI-parallelized code of numerical diagonalizations based on the Lanczos algorithm[1]. This code can treat systems with its sizes that are larger than those determined by computer resources when calculations are carried out in a single node.

The primary study of the present project is to clarify the behavior of the magnetization process of the spin-S Heisenberg antiferromagnet on the kagome lattice by means of the Lanczos-diagonalization code mentioned in the above[2]. The magnetization process for the $S = 1/2$ case has been extensively studied[3, 4, 5, 6]; however, there are few studies for the cases of larger S. For $S = 1$, the magnetization process was reported in Ref. 3. When S is large, the increase of the dimension of the Hamiltonian matrix for the increase of the system sizes becomes more rapid. Therefore, the weak point of the numerical-diagonalization method becomes more serious; there are no reports for $S > 1$ to the best of our knowledge. Under circumstances, we clarify the behavior of the magnetization processes for various spin-S cases from $S = 1$ up to $S = 5/2$. We successfully observed the existence of the magnetization plateau at one-third of the height of the saturation in the magnetization process. The existence is irrespective of S. We discuss the S dependences of the edge fields and the width of the plateau and find a significant difference between our numerical-diagonalization results and results obtained by real-space perturbation theory[7].

Our result of a quantum spin system by large-scale parallelized calculations of Lanczos diagonalization make the true behavior of the system. Our large-scale Lanczos-diagonalization study contributes much to our understandings of these systems.

References

[1] H. Nakano and A. Terai: J. Phys. Soc. Jpn. **78**, 014003 (2009).

[2] H. Nakano and T. Sakai: J. Phys. Soc. Jpn. **84** (2015) 063705.

[3] K. Hida: J. Phys. Soc. Jpn. **70** (2001) 3673.

[4] H. Nakano and T. Sakai: J. Phys. Soc. Jpn. **79** (2010) 053707.

[5] T. Sakai and H. Nakano: Phys. Rev. B **83** (2011) 100405(R).

[6] H. Nakano and T. Sakai: J. Phys. Soc. Jpn. **83** (2014) 104710.

[7] M. E. Zhitomirsky: J. Phys.: Conf. Ser. **592** (2015) 012110.

Ordering of topological excitations of the frustrated magnets

Tsuyoshi OKUBO
Institute for Solid State Physics, University of Tokyo
Kashiwa-no-ha, Kashiwa, Chiba 277-8581

Frustrated spin systems have attracted much recent interest because of their novel orderings. In two-dimensional frustrated Heisenberg spin systems, a topologically stable point defect, a Z_2 vortex, often plays an important role. A possible topological phase transition driven by binding-unbinding of the Z_2 vortices was proposed by Kawamura and Miyashita about 30 years ago [1]. In this Z_2 vortex transition, the spin correlation length keeps finite. At the Z_2-vortex transition temperature $T = T_v$, only the vortex correlation length characterizing the typical separation of the free vortices diverges. This is a sharp contrast to the case of the Kosterlitz-Thouless transition in two dimensional XY spin systems, where the spin correlation length diverges together with the vortex correlation length below the transition temperature.

The nature of the possible Z_2-vortex transition has been investigated typically on the triangular-lattice Heisenberg antiferromagnet. Recent Monte Carlo simulation up to $L = 1536$ suggested the occurrence of Z_2-vortex transition at a finite temperature $T_v/J \simeq 0.285$ with a finite spin-correlation length $\xi \simeq 2000$ [2]. However, the existence of topological phase transition has not been fully resolved because the observed spin correlation length is larger than the maximum system size. In order to clarify the true nature of the Z_2-vortex transition, we need larger systems beyond the spin-correlation length at the transition temperature.

In order to perform such larger scale Monte Carlo simulations, we consider an effective model of two-dimensional frustrated Heisenberg magnets. The Hamiltonian of the model is give by

$$\mathcal{H} = -\frac{J}{4}\sum_{\langle i,j\rangle} \mathrm{Tr} R_i R_j^t \qquad (J > 0), \qquad (1)$$

where R_i is a $SO(3)$ rotation matrix on the site i, and $\sum_{\langle i,j\rangle}$ means the sum over the nearest-neighbor pairs on the square lattice. This effective model does not have explicit frustrated interactions. However, it has topological Z_2 vortices, and therefore we expect the Z_2-vortex binding-unbinding transition at a finite temperature as similar to the frustrated Heisenberg spin systems. For the Monte Carlo simulation of this unfrustrated model, we can use Wolff-Swendsen-Wang type cluster algorithm, which is not efficient for the frustrated interactions. We have implemented MPI parallelized cluster algorithm for this model and investigated nature of possible Z_2-vortex transition by extensive Monte Carlo simulation of the model. The lattice is a $L \times L$ square lattice with periodic boundary conditions.

In this year project, we performed Monte Carlo simulation for $L \leq 16384$ on the ISSP system B and the kei computer. In order to investigate the Z_2-vortex transition, we consider the free-energy cost against vortex formation, $\Delta V(L)$. The free-energy cost is expected to be proportional to the logarithm of the system size L as

$$\Delta V(L) \sim C + v \log L, \tag{2}$$

where the coefficient v is called “vorticity modulus”. The vorticity modulus is an order parameter of the Z_2 vortex transition: it takes a finite value for $T < T_v$, while $v = 0$ for $T > T_v$. In Fig.1, we show the temperature dependence of the vorticity modulus calculated from two sizes $(L_1, L_2 = L_1/2)$ as

$$v(L_1, L_2) \equiv \frac{\Delta V(L_1) - \Delta V(L_2)}{\log L_1/L_2}. \tag{3}$$

We see that the vorticity modulus increases around $T/J \simeq 0.28$, indicating a finite-temperature phase transition. We define the effective transition temperature as the temperature where vorticity modulus across $v = 0$. A preliminary extrapolation assuming the existence of Z_2-vortex transition leads $T_v/J \simeq 0.27$, which is considered as the upper bound of T_v. On the other hand, the spin correlation length at this temperature is estimated at least $\xi \simeq 20000$ lattice spacings. Because the present system is limited $L \leq 16384$, which is comparable with the correlation length at the estimated T_v, we need a careful analysis to conclude the existence of the finite-temperature topological phase transition.

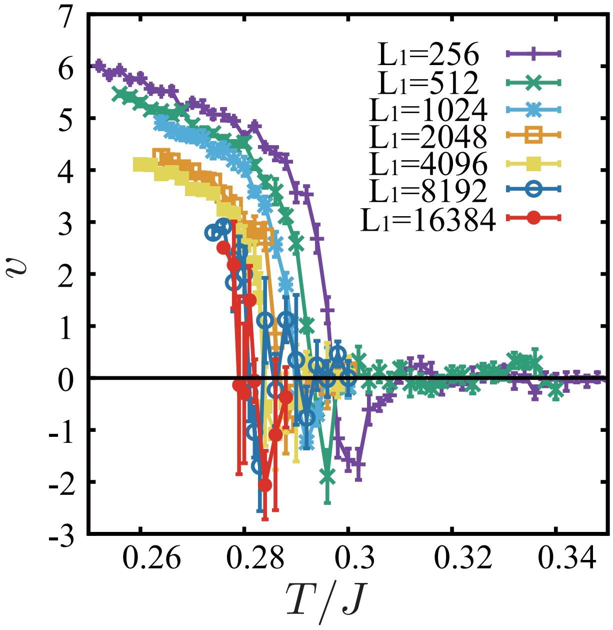

Figure 1: Vorticity modulus as a function of the temperature for various systems sizes $128 \leq L \leq 16384$.

References

[1] H. Kawamura and S. Miyashita: J. Phys. Soc. Jpn. **53** (1984) 4138.

[2] H. Kawamura, A. Yamamoto, and T. Okubo: J. Phys. Soc. Jpn. **79** (2010) 023701.

Large-scale computational simulations of non-equilibrium transport phenomena

Yoshihiro ASAI, Marius BÜRKLE, Jun-ichi OZAKI
Research Center for Computational Design of Advanced Functional Materials National Institute of Advanced Industrial Science and Technology (AIST),
Central 2, Umezono 1-1-1, Tsukuba, Ibaraki 305-8568

We have studied the following subjects in the context of non-equilibrium transport in terms of large-scale computational simulations:

1) The effect of short-range strong correlation on the electric conductance and the electric current at finite bias voltage.
2) Electric conductance and electric current calculations based on an order-N DFT method for large channel materials.
3) Phonon transport calculation based on the first-principles DFT theory.
4) Thermopower calculation for materials in the hopping transport regime.
5) Phonon effects on the electric current noise including shot noise and temperature noise.
6) First-principles non-equilibrium Green’s function (NEGF) calculations of the I-V characteristics of non-volatile memory materials.
7) Comparisons of first-principles transport calculations with scanning tunneling microscope break junction experiments.

In the following we outline these subjects and give the main:

1) Calculations were made in terms of the time dependent DMRG method. The Hubbard chain model was adopted for the channel. Firstly, we focused our attention to the length dependence of the conductance and found a damped oscillatory behavior, which indicates the inelastic contribution from the strong onsite repulsion U on the conductance. 【submitted to PRL: 1】
2) The non-equilibrium Green’s function (NEGF) method based transport code was combined with the CONQUEST code for order-N calculation of large systems. It was tested for some hundred nm length channel materials for the conductance. Finite voltage calculation code has been also implemented.【unpublished: 2】
3) Phonon transport calculations without and with phonon-phonon scattering were made for two terminal devices with a single molecule as a channel material. 【PRB: 3, unpublished: 4】

4) The Seebeck coefficient was calculated in terms of the self-consistent theory of electron and phonon currents (PRB 78, 045434 (2008)) using the extended Su-Schrieffer-Heeger model. The result was used to discuss the base alignment dependence of the Seebeck coefficient for DNA.【Nature Commun.: 5】
5) The phonon transport and the electronphonon coupling effects on the electric current noise including shot noise and temperature noise was discussed using a full counting statistics approach.【PRB, Rapid Commun.: 6】
6) The I-V characteristic and the material dependence of the ON/OFF ratio of the current were investigated using the first-principles NEGF transport calculation results on the resistive random access memory cells【PCCP: 7 and 8】and the interfacial phase change memory cells【unpublished: 9】. A lowest order expansion method was used to discuss the phonon effect in the former case.
7) Our first-principles NEGF calculation results were compared with scanning tunneling microscope (STM) break junction experiments showing fair agreement with each other.

References

[1] J. Ozaki and Y. Asai, submitted to Phys. Rev. Lett.

[2] Unpublished.

[3] M. Bürkle, T.J. Hellmuth, F. Pauly, and Y. Asai: Phys. Rev. B, **91**, 165419 (2015).

[4] Unpublished.

[5] Y. Li, Limin X. J. L. Palma, Y. Asai and N. J. Tao: Nature Communications, **7**, 11294-1-8 (2016).

[6] Y. Asai: Phys. Rev. B, **91**, 161402 (R) (2015).

[7] H. Nakamura and Y. Asai: Phys. Chem. Chem. Phys. **18**, 8820 (2016).

[8] X. Zhong, I. Rungger, P. Zapol, H. Nakamura, Y. Asai and O. Heinonen: Phys. Chem. Chem. Phys. **18**, 7502 (2016).

[9] Unpublished.

[10] S. –K. Lee, M. Buerkle, R. Yamada, Y. Asai and H. Tada, Nanoscale, 7, 20497 (2015).

[11] D. Miguel, L.Á. de Cienfuegos, A. Martín-Lasanta, S.P. Morcillo, L.A. Zotti, E. Leary, M. Bürkle, Y. Asai, R. Jurado, D.J. Cárdenas, G. Rubio-Bollinger, N. Agraït, J.M. Cuerva, and M.T. González: J. Am. Chem. Soc. **137**, 13818 (2015).

[12] R. García, M.Á. Herranz, E. Leary, M.T. González, G. Rubio-Bollinger, M. Bürkle, L.A. Zotti, Y. Asai, F. Pauly, J. C. Cuevas, N. Agraït and N. Martín, Beilstein: J. Org. Chem. **11**, 1068 (2015).

3.6 Software Advancement Projects

Project for advancement of software usability in materials science

Mitsuaki Kawamura, Kazuyoshi Yoshimi
Institute for Solid State Physics, University of Tokyo
Kashiwa-no-ha, Kashiwa, Chiba 277-8581

1 Overview

From the 2015 fiscal year, the supercomputer center (SCC) has started “Project for advancement of software usability in materials science” [1]. In this project, for enhancing the usability of the supercomputer system in ISSP, we perform some software-advancement activity such as implementing a new function to an existing code, releasing a private code on Web, writing manuals. Target programs are publicly offered in December and selected in the review by the Steering Committee of SCC. The projects are carried out by the software development team composed of three members in ISSP.

In the 2015 fiscal year, since it is the first time to start the project, the public offering was announced in March 2015 and the following two projects were selected in April 2015: One is adding new functions to compute eigenchannels and the real space current density into the first-principles program package OpenMX [2]. The other is releasing a numerical solver package for a wide range of quantum lattice models $\mathcal{H}\Phi$ [3]. In this package, the Lanczos algorithm for finding ground states and newly developed Lanczos-based algorithm for finite-temperature properties [4] are implemented for parallel computing. In the following sections, we report the details of the contents of these projects, respectively.

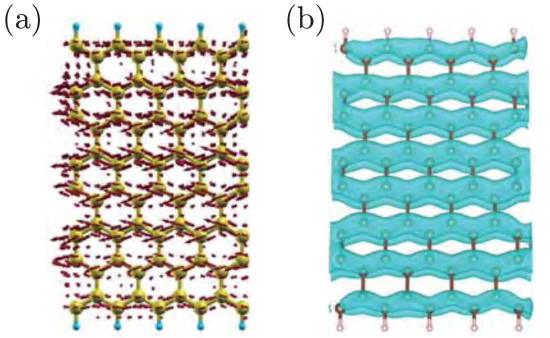

Figure 1: (a) Current density in 8-zigzag graphene nanoribbon with an antiferromagnetic junction under a finite bias voltage of 0.3 V. (b) Isosurfaces of the **a**-compontent of that.

2 Eigenchannel and real space current density in OpenMX

In a nanoscale electronic transmission phenomena, it is important to realize the path of transmitting electrons. Transmission eigenchannel analysis is suitable to obtain real space microscopic picture of that phenomena; this channel is represented as a special transmission wavefunction which maximizes the transmission probability. On the other hand, when we scope the spatial variation of the direction of transmission, the real space current density analysis is preferred. A program package which can perform easily these calculation have been required.

OpenMX (Open source package for Material eXplorer) [2] is a software package for nano-scale material simulations based on density functional theories (DFT); it uses norm-conserving pseudopotentials and pseudo-atomic localized basis functions [5]. This program package supports the simulation of the electronic conduction phenomena in a nanoscale device; this simulation is performed by using the *ab initio* nonequilibrium Green's function (NEGF) theorem. We implemented functions to compute the transmission eigenchannels [6] and the real space current density [7] in the framework of the NEGF theory; this calculation is performed as a post process of the calculation of NEGF.

As an example, we apply these functions to 8-zigzag graphene nanoribbon with an antiferromagnetic junction; the spin polarization at the edge of this system and the dual spin filter effect are predicted by previous first-principles study [8]. We show the currentdensity in 8-zigzag graphene nanoribbon with an antiferromagnetic junction under a finite bias voltage of 0.3 V in Fig. 1. Figure 2 shows eigenchannels of this system under a finite bias voltage of ± 0.3 V besides the spin dependent transmission probability at each energy.

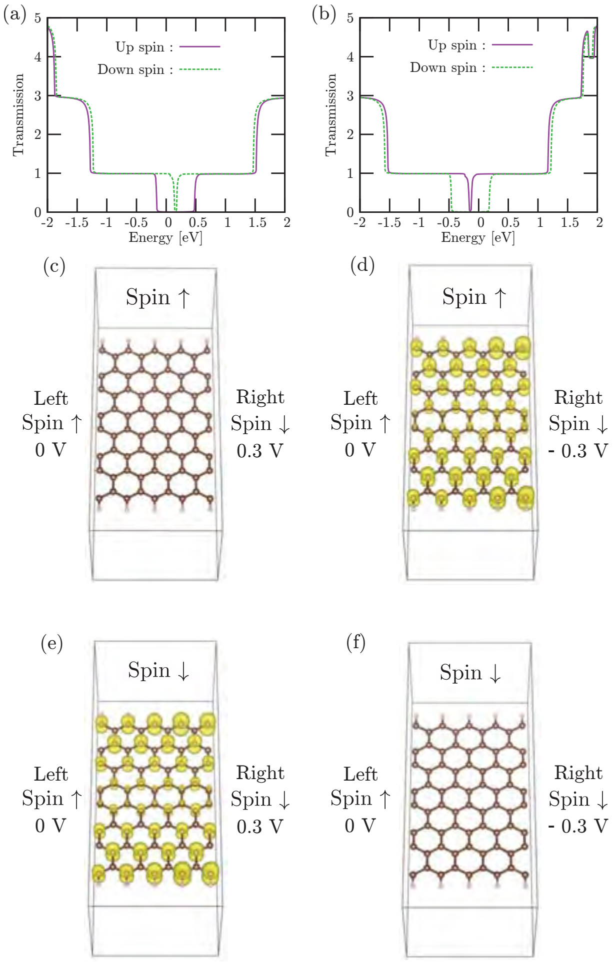

Figure 2: (a) Spin dependent transmission under a bias voltage of 0.3 V, (b) Spin dependent transmission under a bias voltage of -0.3 V, (c) An eigenchannel at a energy of 0 eV, spin ↑, and 0.3 V as a bias voltage, (d) An eigenchannel at a energy of 0 eV, spin ↑, and - 0.3 V as a bias voltage, (e) An eigenchannel at a energy of 0 eV, spin ↓, and 0.3 V as a bias voltage, and (f) An eigenchannel at a energy of 0 eV, spin ↓, and - 0.3 V as a bias voltage in 8-zigzag graphene nanoribbon with an antiferromagnetic junction (The spin is ↑ in the left region and it is ↓ in the right region.) are depicted. The level of isosurfaces are identical in these figures; when the transmission is small, the eigenchannel itself is also small.

3 $\mathcal{H}\Phi$: Solver for general quantum lattice models

For the quantitative comparison with experimental data, the numerical exact diagonalization of a quantum lattice system [9] is one of the most reliable tools without any approximation for small systems. This method can be used also for benchmarks of other numerical methods (such as DMRG, DMFT, VMC, QMC, tensor network, etc.). In addition, recent advances in quantum statistical mechanics [4, 10, 11, 12] enable us to calculate finite-temperature properties of quantum many-body systems without an ensemble average. This method enables us to compare theoretical results for temperature dependence of, for example, specific heat and magnetic susceptibility with experimental results quantitatively [13]. To utilize the parallel computing infrastructure with narrow bandwidth and distributed-memory architectures, an efficient, user-friendly, and highly parallelized diagonalization packages are highly desirable.

In this project, we released a flexible diagonalization package $\mathcal{H}\Phi$[3] for solving quantum

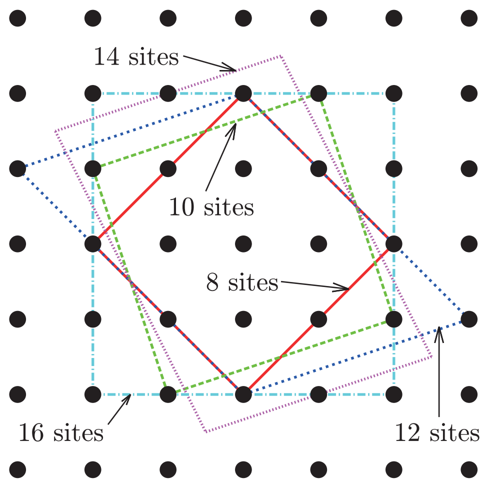

Figure 3: Shapes of numerical cells having 8, 10, 12, 14, 16 sites.

lattice hamiltonians; the Lanczos method for calculations of the ground state and a few excited states properties, and finite temperature calculations based on thermal pure quantum (TPQ) states [4] are implemented in this program package. We designed its user-interface to use easily by theoretical/experimental researchers and students. By using $\mathcal{H}\Phi$, a wide range of quantum lattice hamiltonians including simple Hubbard and Heisenberg models, multi-band extensions of the Hubbard model, exchange couplings that break SU(2) symmetry of quantum spins such as Dzyaloshinskii-Moriya and Kitaev interactions, and Kondo lattice models describing itinerant electrons coupled with quantum spins can be analized. $\mathcal{H}\Phi$ calculates a variety of physical quantities such as internal energy at zero temperature or finite temperatures, temperature dependence of specific heat, charge/spin structure factors, and so on. A broad spectrum of users including experimental scientists is cordially welcome.

As an example of using $\mathcal{H}\Phi$, we compute the temperature dependence of the doublon density in a Hubbard model ($U/t = 8$) for 8, 10, 12, 14, 16 sites; the shape of the numerical cell is depicted in Fig. 3. We can easily construct these Hamiltonian by using $\mathcal{H}\Phi$.

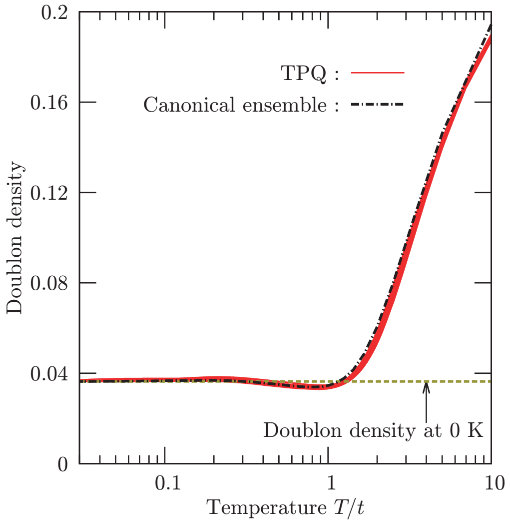

Figure 4: Temperature dependence of the doublon density calculated from the TPQ state and the canonical ensemble obtained by the full diagonalization method on 8 sites Hubbard model. We perform the TPQ calculation 20 times and depict each results. The yellow horizontal line indicates the doublon density at 0 K, which is calculated with the Lanczos method.

Figure 4 shows the temperature dependence of the doublon density calculated from the TPQ state and the canonical ensemble obtained by the full diagonalization method on Hubbard model with 8 sites; we perform the TPQ calculation 20 times and depict each results. These two results show a good agreement. In Fig. 5, we show the doublon density calculated from TPQ states on Hubbard model with 8, 10, 12, 14, 16 sites; we performed the TPQ calculation 20 times in each size and found that the result almost converges about the number of sites.

In the project for advancement of software usability in materials science for 2016 fiscal year, we are planning to implement a function to compute an optical spectrum of the quantum lattice system in $\mathcal{H}\Phi$. With this function, we will be able to compare the theoretical results and data of some spectroscopic experiments such as ARPES, the neutron scattering, and so on.

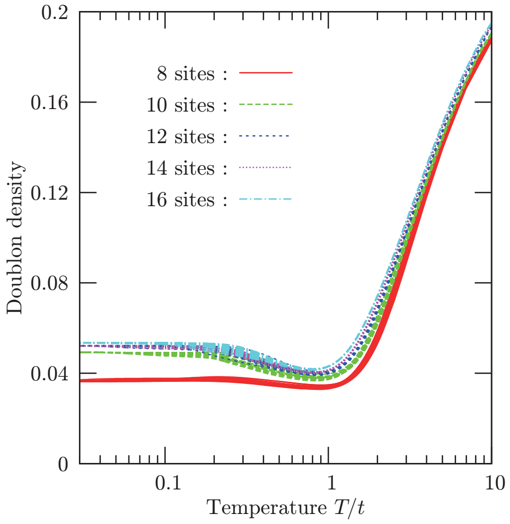

Figure 5: The doublon density calculated from TPQ states on Hubbard model with 8, 10, 12, 14, 16 sites; we perform the TPQ calculation 20 times in each size and plot all of them.

References

[1] http://www.issp.u-tokyo.ac.jp/supercom/rsayh2/softwea-dev

[2] http://www.openmx-square.org/

[3] http://ma.cms-initiative.jp/ja/listapps/hphi/hphi

[4] S. Sugiura and A. Shimizu, Phys. Rev. Lett. **108**, 240401 (2012).

[5] T. Ozaki, Phys. Rev. B. **67**, 155108, (2003); T. Ozaki and H. Kino, Phys. Rev. B **69**, 195113 (2004).

[6] M. Paulsson and M. Brandbyge, Phys. Rev. B **76**, 115117 (2007).

[7] C. Li, L. Wan, Y. Wei, and J. Wang, Nanotechnology **19**, 155401 (2008).

[8] T. Ozaki, K. Nishio, H. Weng, and H. Kino, Phys. Rev. B. **81**, 075422, (2010).

[9] E. Dagotto, Rev. Mod. Phys. **66**, 763 (1994).

[10] M. Imada and M. Takahashi, J. Phys. Soc. Jpn. **55**, 3354 (1986).

[11] J. Jaklič, P. Prelovšek, Phys. Rev. B **49**, 5065 (1994).

[12] A. Hams and H. De Raedt, Phys. Rev. E **62**, 4365 (2000).

[13] Y. Yamaji, Y. Nomura, M. Kurita, R. Arita, and M. Imada, Phys. Rev. Lett. **113**, 107201 (2014).

4 PUBLICATION LIST

Example:

LASTNAME, Firstname [project class; # points (B), # points (C)] (Page #)
Project title
1. First paper
   Names of Authors, etc.
2. Second paper
   ...

□ ISSP Joint Research Projects

ADACHI, Takahiro [C class; 2500 (B), 300 (C)] (230)
— *Heat Transfer Characteristics of Condensate Film Flow along Vertical Plates with Microscopic Grooves*

AKAGI, Kazuto [B,C class; 4600 (B), 0 (C)] (91)
— *Local structure analysis around impurity atoms in a metal oxide*
— *Exploration of structure motifs characterizing the behavior of metal oxides*
1. The chemistry of simple alkene molecules on Si(100)c(4 × 2): The mechanism of cycloaddition and their selectivities
   K. Akagi and J. Yoshinobu: Surf. Sci. in press
2. Theoretical investigation on oxidation of lithium peroxide by tetrathiafulvalene in non-aqueous Li-O_2 battery
   S. Jung and K. Akagi: submitted to J. Phys. Chem. Lett.

AKAI, Hisazumi [B class; 300 (B), 700 (C)] (121)
— *Electronic structure of rare earth magnets*
1. Role of N in the Permanent Magnet Materials $Sm_2Fe_{17}N_x$
   M. Ogura and H. Akai: J. Phys. Soc. Jpn. **84** (2015) 084702.
2. Near-field correction in the first-principles calculations by the exact two-center expansion for the inverse of the distance
   M. Ogura, C. Zecha, M. Offenberger, H. Ebert, and H. Akai: J. Phys: Condens. Matter. **27** (2015) 485201
3. Schottky junctions studied by KKR non-equilibrium Green's function method
   M. Ogura and H. Akai: submitted to Phys. Rev. B.

AKASHI, Ryosuke [C class; 1500 (B), 200 (C)] (107)
— *Ab initio calculation of superconducting pairing interactions in materials with complex Fermi surface*

ANDO, Yasunobu [C class; 2000 (B), 2200 (C)] (95)
— *Theoretical analysis of electrochemical interfaces by first-principles calculation and statistical approach*
1. First-principles study of metal–insulator control by ion adsorption on Ti_2C MXene dioxide monolayers
   Y. Ando, and S. Watanabe: Appl. Phys. Express **9**, (2016) 015001.

AOKI, Hideo [C class; 4000 (B), 2400 (C)] (149)
— *Photoinduced phase transitions in strongly correlated superconductors*
1. FLEX+DMFT approach to the d-wave superconducting phase diagram of the two-dimensional Hubbard model

M. Kitatani, N. Tsuji, H. Aoki: Phys. Rev. B **92**, 085104 (2015).
2. Theory of Anderson pseudospin resonance with Higgs mode in a superconductor
   Naoto Tsuji and Hideo Aoki: Phys. Rev. B **92**, 064508 (2015).
3. Multiple amplitude modes in strongly coupled phonon-mediated superconductors
   Yuta Murakami, Philipp Werner, Naoto Tsuji and Hideo Aoki: Phys. Rev. B **93**, 094509 (2016).

AOYAMA, Kazushi [B class; 700 (B), 0 (C)] (249)
— *Spin-lattice coupling effects in Heisenberg antiferromagnets on breathing pyrochlore lattices*

ARAIDAI, Masaaki [C class; 2500 (B), 800 (C)] (99)
— *First-Principles Study on Device Properties of Emerging Phase-Change Memory Devices*

ARAKAWA, Naoya [B class; 400 (B), 0 (C)] (174)
— *Theoretical study of many-body effects on spin transports in a multiorbital system*
1. Spin-orbital-coupled vector chirality in a non-frustrated Mott insulator with the strong spin-orbit coupling without *ab*-plane's inversion symmetry
   N. Arakawa: arXiv:1604.05867.
2. Microscropic theory on charge transports of a correlated multiorbital system
   N. Arakawa: arXiv:1505.05274.
3. Many-body effects on the resistivity of a multiorbital system beyond Landau's Fermi-liquid theory
   N. Arakawa: Mod. Phys. Lett. B **29** (2015) 1530005.
4. Interaction-driven temperature dependence and spin-Coulomb-drag-induced correction in intrinsis anomalous-Hall and spin-Hall effects on multiorbital metals
   N. Arakawa: arXiv:1510.03988
5. Controlling spin Hall effect by using a band anticrossing and nonmagnetic impurity scattering
   T. Mizoguchi and N. Arakawa: Phys. Rev. B **93** (2016) 041304(R).

ARAKI, Takeaki [B class; 700 (B), 0 (C)] (248)
— *Self-propelled motion of a Janus particle in periodically phase separating mixtures*
1. Controlled motion of Janus particles in periodically phase-separating binary fluids
   T. Araki and S. Fukai: Soft Matter **11** (2015), 3470.

ARITA, Ryotaro [C class; 3500 (B), 0 (C)] (159)
— *First-principles study of multi-orbital correlated materials*
1. Ab initio downfolding study of the iron-based ladder superconductor $BaFe_2S_3$
   R. Arita, H. Ikeda, S. Sakai and M-T. Suzuki, Phys. Rev. B **92**, (2015) 054515.
2. First-Principles study of magnetic properties in Fe-ladder compounds $BaFe_2S_3$
   M-T. Suzuki, R. Arita and H. Ikeda: Phys. Rev. B **92**, (2015) 085116.

DEKURA, Haruhiko [C class; 2000 (B), 0 (C)] (106)
— *First-principles calculations of iron solid solution effects on the lattice thermal conductivity of lower mantle minerals*

EGAMI, Yoshiyuki [C class; 2500 (B), 3300 (C)] (74)
— *Development and application of first-principles electron-transport simulator based on time-dependent density functional theory*
1. First-principles calculation method for electron transport based on grid Lippmann-Schwinger equation
   Y. Egami, S. Iwase, S. Tsukamoto, T. Ono and K. Hirose: Phys. Rev. E **92** (2015) 033301.

FUCHIZAKI, Kazuhiro [C class; 2500 (B), 0 (C)] (234)
— *Melting phenomena and polyamorphism*
1. Accurate Equation of State for the Modified Lennard-Jones Solid
   K. Fuchizaki, K. Okamoto, and S. Doi: J. Phys. Soc. Jpn. **84** (2015) 085002.
2. Nonequilibrium Effects on Macromolecules Immersed in a Solvent

K. Fuchizaki: JPSJ News and Comments 12 (2015) 13.

3. Determination of a melting curve using the one-phase approach
   K. Fuchizaki and K. Okamoto: Phys. Lett. A **380** (2016) 293.
4. ヨウ化錫系に期待される第二臨界現象
   渕崎員弘: 日本結晶学会誌 **58** (2016) 42.

FUJIMOTO, Yoshitaka [C class; 1000 (B), 0 (C)] (119)
— *Stabilities, structures, and electronic properties of atomic-layered materials*

1. Electronic structures and stabilities of bilayer graphene doped with boron and nitrogen
   Y. Fujimoto and S. Saito: Surface Science **634**, 57 (2015).
2. Atomic geometries and electronic structures of hexagonal boron-nitride bilayers under strain
   Y. Fujimoto and S. Saito: Journal of the Ceramic Society of Japan **123**, 576 (2015).
3. Formation, energetics, and electronic properties of graphene monolayer and bilayer doped with boron and nitrogen
   Y. Fujimoto: Advances in Condensed Matter Physics **2015**, 571490 (2015).
4. First-Principles Computational Design of Graphene for Gas Detection
   Y. Fujimoto: Smart Materials for Waste Water Application, Wiley-Scrivener Publishers, Chapter 6 (2016).
5. Effects of strain on Carbon Donors and Acceptors in Hexagonal Boron-Nitride Monoalyers
   Y. Fujimoto and S. Saito: Physical Review B **93**, 045402 (2016).
6. Energetics and scanning tunneling microscopy images of B and N defects in graphene bilayer
   Y. Fujimoto and S. Saito: submitted.
7. Gas adsorption, energetics and electronic properties of boron- and nitrogen-doped bilayer graphenes
   Y. Fujimoto and S. Saito: submitted.
8. Interlayer distances and band-gap tuning of hexagonal boron-nitride bilayers
   Y. Fujimoto and S. Saito: Journal of the Ceramic Society of Japan, accepted.

FUJIWARA, Susumu [B class; 600 (B), 0 (C)] (251)
— *Molecular Simulation Study of Micellar Shape Transition in Amphiphilic Solution*

1. Molecular Dynamics Simulation of Phase Behavior in a Bolaamphiphilic Solution
   S. Fujiwara, T. Miyata, M. Hashimoto, Y. Tamura, H. Nakamura and R. Horiuchi: Plasma Fusion Res. **10** (2015) 3401029.
2. Melt memory of a spherulite nucleus formed through a seeding process in the crystal growth of isotactic polystyrene
   M. Hashimoto, J. O'ishi, S. Moriya and S. Fujiwara: Polymer J. **47** (2015) 481-486.
3. Dissipative Particle Dynamics Simulation of Self-Assembly in a Bolaamphiphilic Solution
   S. Fujiwara, Y. Takahashi, H. Ikebe, T. Mizuguchi, M. Hashimoto, Y. Tamura, H. Nakamura and R. Horiuchi: Plasma Fusion Res. in press.
4. Intuitive interface for visualizing numerical data using gesture recognition
   Y. Tamura, H. Nakamura and S. Fujiwara: Plasma Fusion Res. in press.

FUKUI, Ken-Ichi [C class; 5500 (B), 3800 (C)] (64)
— *Microscopic Investigations of Solid / Liquid Interfaces Using First-Principles and Classical Molecular Dynamics*
— *First-Principles and Classical Molecular Dynamics Investigations of Electrolyte Solution / Electrode Interfaces: Potential Dependence*

1. Density Functional Theory Investigations of Ferrocene-Terminated Self-Assembled Monolayers: Electronic State Changes Induced by Electric Dipole Field of Coadsorbed Species
   Y. Yokota, S. Akiyama, Y. Kaneda, A. Imanishi, K. Inagaki, Y. Morikawa and K. Fukui:J. Phys. Chem. C, in press.

FURUKAWA, Akira [C class; 5000 (B), 0 (C)] (217)
— *Rheology of Glassy Materials*

1. Probing colloidal gels at multiple length scales: The role of hydrodynamics
   C. P. Royall, J. Eggers, A. Furukawa, and H. Tanaka: Physical Review Letters

2. Essential Difference in the Dynamics between Strong and Fragile Glass-formers
   A. Furukawa and H. Tanka: submitted

GOHDA, Yoshihiro [C class; 3500 (B), 2200 (C)] ()
— *Doping effects of heavy elements for multiferroic materials*

HAMAMOTO, Yuji [C class; 3500 (B), 2900 (C)] (72)
— *First principles study of catalytic properties of Pt cluster supported on graphene*

HARADA, Kenji [C class; 7500 (B), 0 (C)] (205)
— *Tensor network calculation on two-dimensional quantum spin models*

1. SU(N) Heisenberg model with multicolumn representations
   T. Okubo, K. Harada, J. Lou, and N. Kawashima: Phys Rev B **92**, 134404 (2015).
2. Kernel method for corrections to scaling
   K. Harada: Phys Rev E **92**, 012106 (2015).

HASHIMOTO, Tamotsu [C class; 2000 (B), 0 (C)] (238)
— *Molecular dynamics simulation of ferroelectrics using a shell model*

1. Dielectric Properties of $BaTiO_3$ by Molecular Dynamics Simulations Using a Shell Model
   T. Hashimoto and H. Moriwake: Mol. Simul. **41** (2015) 1074.
2. Electrical Susceptibilities of $KNbO_3$ by Molecular Dynamics Simulations Using a Shell Model
   T. Hashimoto and H. Moriwake: Physica B **485** (2016) 110.
3. Piezoelectric Anisotropy of $KNbO_3$ by Molecular Dynamics Simulations Using a Shell Model
   T. Hashimoto and H. Moriwake: J. Phys. Soc. Jpn. **85** (2016) 034702.

HATSUGAI, Yasuhiro [C class; 3000 (B), 800 (C)] (223)
— *Variety of bulk-edge correspondence by numerical methods*

1. Entanglement Chern Number of the Kane-Mele Model with Ferromagnetism
   Hiromu Araki, Toshikaze Kariyado, Takahiro Fukui, Yasuhiro Hatsugai, Journal of the Physical Society of Japan, **85**, 043706 (2016), selected as ”Editor’s choice”.
2. Hannay Angle: Yet Another Symmetry-Protected Topological Order Parameter in Classical Mechanics
   Toshikaze Kariyado, Yasuhiro Hatsugai, Journal of the Physical Society of Japan, **85**, 043001 (2016).
3. Topological order parameters of the spin- 1/2 dimerized Heisenberg ladder in magnetic field
   Toshikaze Kariyado, Yasuhiro Hatsugai, Phys. Rev. B**91** 214410 (2015).
4. Manipulation of Dirac Cones in Mechanical Graphene
   Toshikaze Kariyado, Yasuhiro Hatsugai, Scientific Reports 5, 18107 (2015).

HATTORI, Ken [B class; 600 (B), 500 (C)] (111)
— *Model calculations in Si surfaces with adsorbates*

1. Surface structure and electronic states of epitaxial β-$FeSi_2$(100)/Si(001) thin films: Combined quantitative LEED, *ab initio* DFT, and STM study
   O. Romanyuk, K. Hattori, M. Someta, H. Daimon: Phys. Rev. B **90** (2014) 155305.

HIDA, Kazuo [B class; 400 (B), 0 (C)] (260)
— *Numerical Study of One Dimensional Frustrated Quantum Spin Systems*

1. K. Hida: Characterization of Topological Phases of Spin-1/2 Frustrated Ferromagnetic-Antiferromagnetic Alternating Heisenberg Chains by Entanglement Spectrum
   K. Hida: J. Phys. Soc. Jpn. 85 024705 (2016).

HIRAI, Daisuke [C class; 2500 (B), 1800 (C)] (93)
— *First-Principles Study of Coercivity in Hard Magnetic Materials*

HIRAI, Kunitomo [B class; 100 (B), 50 (C)] (141)
— *Electronic State and Proximity Effects around Interface in Layered Superlattices*

HOSHI, Takeo [C class; 3000 (B), 2000 (C)] (88)
— *Parallelized ultra-large-scale electronic-structure theory based on first principle calculation and novel numerical method*

1. Efficient numerical solver for first-principles transport calculation based on real-space finite-difference method
   S. Iwase, T. Hoshi, T. Ono, Phys. Rev. E 91, 063305, 9pp. (2015)
2. Hybrid numerical solvers for massively parallel eigenvalue computation and their benchmark with electronic structure calculations
   H. Imachi and T. Hoshi, J. Inf. Process. 24, pp. 164 – 172 (2016)
3. One-hundred-nm-scale electronic structure and transport calculations of organic polymers on the K computer
   H. Imachi, S. Yokoyama, T. Kaji, Y. Abe, T. Tada, submitted; Preprint http://arxiv.org/abs/1603.09616

HOSHINO, Shintaro [C class; 1500 (B), 0 (C)] (165)
— *Monte Carlo Study of Itinerant and Localized Chiral Helimagnets*

1. Superconductivity from Emerging Magnetic Moments
   Shintaro Hoshino and Philipp Werner: Phys. Rev. Lett. **115**, 247001 (2015).
2. Anisotropic Magnetic Response in Kondo Lattice with Antiferromagnetic Order
   M. Shinozaki, S. Hoshino, Y. Masaki, J. Kishine and Y. Kato: arXiv1512.00235 (2015).
3. Electronic orders in multi-orbital models with lifted orbital degeneracy
   Shintaro Hoshino and Philipp Werner: Phys. Rev. B **93**, 155161 (2016).

HOTTA, Takashi [C class; 500 (B), 0 (C)] (172)
— *Research for multipole ordering and superconductivity induced by multipole fluctuations in seven-orbital Hubbard model with spin-orbit coupling*

1. Key Role of Rutile Structure for Layered Magnetism in Chromium Compounds
   Yasuhiro Kondo and Takashi Hotta: Phys. Procedia **75** (2015) 671-678.
2. Quantum Interference of Surface-Induced Friedel Oscillations Enhanced by Fermi-Surface Nesting in Layered Manganites
   Ryosuke Yamamura and Takashi Hotta: Phys. Procedia **75** (2015) 902-910.
3. Effect of Spin-Orbit Coupling on Kondo Phenomena in f^7-Electron Systems
   Takashi Hotta: J. Phys. Soc. Jpn. **84** (2015) 114707-1-12.
4. Fermi-Surface Topology and Pairing Symmetry in BiS_2-Based Layered Superconductors
   Tomoaki Agatsuma and Takashi Hotta: J. Magn. Magn. Mater. **400** (2016) 73-80.
5. Valence Imbalance of Manganese Ions between Surface and Bulk Enhanced by Fermi-Surface Structure in Layered Manganites
   Ryosuke Yamamura and Takashi Hotta: J. Phys.: Conf. Ser. **683** (2016) 012042.

HU, Chunping [B class; 600 (B), 400 (C)] (118)
— *First-principles simulation of electrolyte diffusion process on constant-potential electrodes*

1. Bias-dependent molecular diffusion on a metal surface: H_2O on Al(111)
   C. Hu and M. Otani: to be submitted to Phys. Rev. Lett.

HUKUSHIMA, Koji [C class; 9000 (B), 2000 (C)] (190)
— *Equilibrium and dynamical properties in glassy systems*

1. Minimum vertex cover problems on random hypergraphs: Replica symmetric solution and a leaf removal algorithm
   S.Takabe and K. Hukushima: Phys. Rev. E **89** (2014) 043801/1-4
2. Evidence of one-step replica symmetry breaking in a three-dimensional Potts glass model
   T.Takahashi and K. Hukushima: Phys. Rev. E **91** (2015) 020102(R)/1-4
3. Extracting nonlinear spatiotemporal dynamics in active dendrites using data-driven statistical approach

T. Omori and K. Hukushima: J. of Phys.: Conf. Seri. **699** (2016) 012011/1-8

4. Event-chain algorithm for the Heisenberg model: Evidence for z 1 dynamic scaling
   Y. Nishikawa, M. Michel, W. Krauth, and K.Hukushima: Phys. Rev. E **92** (2015) 063306/1-5
5. Free-energy landscape and nucleation pathway of polymorphic minerals from solution in a Potts lattice-gas model
   A. Okamoto, T. Kuwatani, T. Omori and K. Hukushima: Phys. Rev. E **92** (2015) 042130/1-9
6. Eigenvalue analysis of an irreversible random walk with skew detailed balance conditions
   Y. Sakai and K. Hukushima: Phys. Rev. E **93** (2016) 043318/1-13.

IGARASHI, Ryo [C class; 2500 (B), 2000 (C)] (221)
— *Development of parallelized MPS algorithm and its application to various frustrated systems*
— *GPU parallelization of MPS algorithm and its application to various frustrated systems*

IKUHARA, Yuichi [C class; 4500 (B), 2700 (C)] (69)
— *Study of atomic structure and electronic states of interfaces and dislocations*
— *First-Principles Study of Atomic and Electronic Structure of Grain Boundaries*

1. Atomic-Scale Structure and Local Chemistry of CoFeB-MgO Magnetic Tunnel Junctions
   Z.C. Wang, M. Saito, K.P. McKenna, S. Fukami, H. Sato, S. Ikeda, H. Ohno, and Y. Ikuhara: Nano Lett. **16** (2016) 1530-1536.

IMADA, Masatoshi [C class; 9000 (B), 4400 (C)] (144)
— *Numerical studies on ab initio low-energy effective models for thin films of cuprates by high-precision variational wave functions*
— *Numerical studies on photoinduced superconductivity in two dimensional doped Hubbard model by high-precision variational wave functions*

1. *Ab initio* Studies on Magnetism in the Iron Chalcogenides FeTe and FeSe
   Motoaki Hirayama, Takahiro Misawa, Takashi Miyake, Masatoshi Imada: J. Phys. Soc. Jpn. **84** (2015) 093703.
2. Hidden fermionic excitation in the superconductivity of the strongly attractive Hubbard model
   Shiro Sakai, Marcello Civelli, Yusuke Nomura, and Masatoshi Imada: Phys. Rev. B **92** (2015) 180503.
3. Exciton Lifetime Paradoxically Enhanced by Dissipation and Decoherence: Toward Efficient Energy Conversion of a Solar Cell
   Yasuhiro Yamada, Youhei Yamaji, and Masatoshi Imada: Phys. Rev. Lett. **115** (2015) 197701.
4. Time-dependent many-variable variational Monte Carlo method for nonequilibrium strongly correlated electron systems
   Kota Ido, Takahiro Ohgoe, and Masatoshi Imada: Phys. Rev. B **92** (2015) 245106.
5. Hidden Fermionic Excitation Boosting High-Temperature Superconductivity in Cuprates
   Shiro Sakai, Marcello Civelli, Yusuke Nomura, and Masatoshi Imada: Phys. Rev. Lett. **116** (2016) 057003.
6. Finite-Temperature Variational Monte Carlo Method for Strongly Correlated Electron Systems
   Kensaku Takai, Kota Ido, Takahiro Misawa, Youhei Yamaji, and Masatoshi Imada: J. Phys. Soc. Jpn. 85 (2016) 034601.
7. Tensor network algorithm by coarse-graining tensor renormalization on finite periodic lattices
   Hui-Hai Zhao, Zhi-Yuan Xie, Tao Xiang, and Masatoshi Imada: Phys. Rev. B **93** (2016) 125115.
8. Real-space renormalized dynamical mean field theory
   Dai Kubota, Shiro Sakai, Masatoshi Imada: to appear in Phys. Rev. B.
9. Clues and criteria for designing Kitaev spin liquid revealed by thermal and spin excitations of honeycomb iridates Na_2IrO_3
   Youhei Yamaji, Takafumi Suzuki, Takuto Yamada, Sei-ichiro Suga, Naoki Kawashima, and Masatoshi Imada: submitted to Phys. Rev. B.
10. Modulated Helical Metals at Magnetic Domain Walls of Pyrochlore Iridium Oxides
    Youhei Yamaji, Masatoshi Imada: submitted to Phys. Rev. B.
11. Stabilization of Topological Insulator Emerging from Electron Correlations on Honeycomb Lattice and Its Possible Relevance in Twisted Bilayer Graphene

Moyuru Kurita, Youhei Yamaji, Masatoshi Imada: submitted to Phys. Rev. B.

12. Clues and criteria for designing Kitaev spin liquid revealed by thermal and spin excitations of honeycomb iridates Na_2IrO_3
    Youhei Yamaji, Takafumi Suzuki, Takuto Yamada, Sei-ichiro Suga, Naoki Kawashima, and Masatoshi Imada : submitted to Phys. Rev. B.

INAGAKI, Kouji [C class; 8000 (B), 3700 (C)] (54)

— *First-principles meta-dynamics analysis of Catalytic Referred Etching method (Analysis of atom removal process)*

1. Study on the mechanism of platinum-assisted hydrofluoric acid etching of SiC using density functional theory calculations
   P. V. Bui, A. Isohashi, H. Kizaki, Y. Sano, K. Yamauchi, Y. Morikawa, and K. Inagaki: Appl. Phys. Lett. **107** (2015) 201601.

INAOKA, Takeshi [B class; 600 (B), 500 (C)] (242)

— *Novel properties of low-dimensional electron systems at solid surfaces and finite electron systems in nanoparticles*

1. Tensile-strain effect of inducing the indirect-to-direct band-gap transition and reducing the band-gap energy of Ge
   T. Inaoka, T. Furukawa, R. Toma, and S. Yanagisawa: J. Appl. Phys. **118** (2015) 105704 (11 pages).
2. Recent progress in predicting structural and electronic properties of organic solids with the van der Waals density functional
   S. Yanagisawa, K. Okuma, T. Inaoka, and I. Hamada: J. Electron Spectrosc. Relat. Phenom. **204** (2015) 159-167.

ISHIHARA, Sumio [B class; 1200 (B), 0 (C)] (167)

— *Novel quantum phase and real time dynamics in correlated electron systems*

— *Numerical analyses of nonequilibrium state in electron-lattice correlated systems*

1. Charge Dynamics in a Correlated Fermion System on a Geometrically Frustrated Lattice
   M. Naka and S. Ishihara, J. Phys. Soc. Jpn. **84**, (2015) 023703.
2. Emergence of charge degrees of freedom under high pressure in the organic dimer-Mott insulator β'-$(BEDT\text{-}TTF)_2ICl_2$
   K. Hashimoto, R. Kobayashi, H. Okamura, H. Taniguchi, Y. Ikemoto, T. Moriwaki, S. Iguchi, M. Naka, S. Ishihara, and T. Sasaki, Phys. Rev. B **92**, (2015) 085149.
3. Photo-Induced Phase Transition in Charge Order Systems –Charge Frustration and Interplay with Lattice–
   H. Hashimoto, H. Matsueda, H. Seo, and S. Ishihara, J. Phys. Soc. Jpn. **84**, (2015) 113702.
4. Magnetoelectric effect in organic molecular solids
   M. Naka and S. Ishihara, Scientific Report **6**, (2015) 20781.
5. Ultrafast electronic state conversion at room temperature utilizing hidden state in cuprate ladder system
   R. Fukaya, Y. Okimoto, M. Kunitomo, K. Onda, T. Ishikawa, S. Koshihara, H. Hashimoto, S. Ishihara, A. Isayama, H. Yui and T. Sasagawa, Nat. Comm. **6**, (2015) 8519.
6. Observation of momentum-resolved charge fluctuations proximate to the charge-order phase using resonant inelastic x-ray scattering
   M. Yoshida, K. Ishii, M. Naka, S. Ishihara, I. Jarrige, K. Ikeuchi, Y. Murakami, K. Kudo, Y. Koike, T. Nagata, Y. Fukada, N. Ikeda and J. Mizuki, Scientific Report **6**, (2015) 23611.

ISHII, Fumiyuki [C class; 5000 (B), 4100 (C)] (65, 66)

— *First-Principles Calculation of Spin-Orbit Field and Thermopower*

— *Spin-orbit coupling parameters at surfaces and interfaces of semiconductors: first-principles study*

1. Large Anomalous Nernst Effect in a Skyrmion Crystal
   Y. P. Mizuta and F. Ishii, arXiv:1601.03510, submitted.
2. Spin-split bands of metallic hydrogenated ZnO (10-10) surface: First-principles study

M. A. Absor, F. Ishii, H. Kotaka, nd M. Saito, AIP Advances 6, 025309 (2016).

3. First-principles study on cubic pyrochlore iridates Y2Ir2O7 and Pr2Ir2O7
   F. Ishii, Y. P. Mizuta, T. Kato, T. Ozaki, H. Weng, and S. Onoda, J. Phys. Soc. Jpn. 84, 073703 (2015).
4. Persistent spin helix on a wurtzite ZnO (10-10) surface: First-principles density-functional study
   M. A. Absor, F. Ishii, H. Kotaka, and M. Saito, Applied Physics Express 8, 073006 (2015).

ISOBE, Masaharu [B class; 400 (B), 0 (C)] (258)

— *Nonequilibirum phase transition in the large scale dense hard sphere molecular dynamics simulation*

1. Hard-Sphere Melting and Crystallization with Event-Chain Monte Carlo
   M. Isobe and W. Krauth: J. Chem. Phys. **143** (2015) 084509.
2. Hard Sphere Simulation in Statistical Physics —Methodologies and Applications—
   M. Isobe: Molecular Simulation, — A special issue on nonequilibrium systems —, (2016) in press.
3. Hard Sphere Simulation by Event-Driven Molecular Dynamics : Breakthrough, Numerical Difficulty and Overcoming the Issues
   M. Isobe: Proceedings Book of Berni Alder's 90th Birthday Symposium. in press.

KAGESHIMA, Hiroyuki [C class; 1000 (B), 0 (C)] (117)

— *Study on formation and property mechanism of semiconductor surfaces/interfaces/defects*

KAKEHASHI, Yoshiro [B class; 200 (B), 0 (C)] (140)

— *First-Principles Momentum Dependent Local Ansatz Theory and Its Application to Fe Compounds*

1. First-Principles Theory of Momentum-Dependent Local Ansatz for Correlated Electron System
   S. Chandra and Y. Kakehashi : Physics Procedia **75** (2015) 41-48.
2. Molecular Spin Dynamics Analysis of Complex Magnetic Structure on the FCC Lattice in Itinerant Electron System
   Y. Kakehashi, S. Chandra, and T. Uchida: Physics Procedia **75** (2015) 625-633.
3. First-Principles Molecular Spin Dynamics Study on the Magnetic Structure of Mn-Based Alloys with Cu_3Au-Type Crystal Structure
   T. Uchida, Y. Kakehashi, and N. Kimura : J. Magn. Magn. Mater. **400C** (2016) 103-106.
4. First-Principles Momentum-Dependent Local Ansatz Wavefunction and Momentum Distribution Function Bands of Iron
   Y. Kakehashi and S. Chandra : J. Phys. Soc. Jpn. **85** (2016) 043707/1-5.

KAMIHARA, Yoichi [B class; 400 (B), 0 (C)] (136)

— *Theoretical research on dissociation of N2 and H2 for designing new ammonia synthesis catalysts*

KASAI, Hideaki [C class; 7500 (B), 3900 (C)] (56)

— *Quantum Effects of Hydrogen and Oxygen Reactions on Solid Surfaces.*

— *Investigations of hydrogen and oxygen reactions on oxide surfaces and interfaces*

1. Quantum states of hydrogen atom on Pd(110) surface
   Allan Abraham B. Padama, Hiroshi Nakanishi, Hideaki Kasai: App. Surf. Sci. **359** (2015) 687-691.
2. A computational study on the effect of local curvature on the adsorption of oxygen on single-walled carbon nanotubes
   Joaquin Moreno, Susan Aspera, Melanie David, Hideaki Kasai: Carbon, **94** (2015) 936-941.
3. A theoretical study of how C2-substitution affects alkaline stability in imidazolium-based anion exchange membranes
   Ryo Tsuchitani, Hiroshi Nakanishi, Hideyuki Shishitani, Susumu Yamaguchi, Hirohisa Tanaka, Hideaki Kasai: Solid State Inonics, **278** (2015) 5-10.
4. Surface magnetism in α PbO induced by Fe interstitials
   Elvis Arguelles, Shuichi Amino, Susan Aspera, Hiroshi Nakanishi, Hideaki Kasai: J. Phys. Soc. Jpn. **84** (2015) 45002/1-2.
5. Effect of oxygen vacancy on the adsorption of O2 on anatase TiO2(001): a DFT-based study
   Nguyen Hoang Linh, Tien Quang Nguyen, Wilson Agerico Di ño, Hideaki Kasai: Surf. Sci. **633**

(2015) 38-45.

6. Oxygen reduction reaction on neighboring Fe-N4 and quaternary-N sites of pyrolized Fe/N/C catalyst
   Adhitya Gandaryus Saputro, Hideaki Kasai: Phys. Chem. Chem. Phys. **17** (2015) 3059-3071.
7. A Theoretical Study on the Adsorption of CO2 on CuO(110) Surface
   Joaquin Lorenzo Valmoria Moreno, Ryan Lacdao Arevalo, Mary Clare Sison Escaño, Allan Abraham Bustria Padama, Hideaki Kasai: J. Phys. Soc. Jpn. **84** (2015) 015003/1-2.
8. Mechanism of dopachrome tautomerization into 5,6-dihydroxyindole-2-carboxylic acid catalyzed by Cu(II) based on quantum chemical calculations
   Ryo Kishida, Adhitya Gandaryus Saputro, Hideaki Kasai: Biochim. Biophys. Acta **1850** (2015) 281-286.
9. First-Principles Study of Nitric Oxide Oxidation on Pt(111) versus Pt Overlayer on 3d Transition Metals
   Ryan Lacdao Arevalo, Mary Clare Sison Escano, Hideaki Kasai: J. Vac. Sci. Technol. A **33** (2015) 021402/1-8.
10. Interstitial impurity-induced in α-PbO surface
    Elvis Arguelles, Shuichi Amino, Susan Aspera, Hiroshi Nakanishi, Hideaki Kasai: J. Phys.: Condens. Matter **27** (2015) 016002/1-7.
11. First principles study of N and H atoms adsorption and NH formation on Pd(111) and Pd3Ag(111) surfaces
    Bhume Chantaramolee, Allan Abraham Bastria Padama, Hideaki Kasai, Yogi Wibisono Budhi: J. Membr. Sci. **474** (2015) 57-63.

KASAMATSU, Shusuke [C class; 2500 (B), 0 (C)] (15)
— *First-principles analysis of the dielectric response at metal/oxide interfaces*

1. First-principles calculation of charged capacitors under open-circuit conditions using the orbital-separation approach
   S. Kasamatsu, S. Watanabe, and S. Han: Phys. Rev. B **92** (2015) 115124.
2. Emergence of Negative Capacitance in Multidomain Ferroelectric-Paraelectric Nanocapacitors at Finite Bias
   S. Kasamatsu, S. Watanabe, C. S. Hwang, and S. Han: Adv. Mater. **28** (2016) 335.

KATO, Takeo [B class; 800 (B), 0 (C)] (245)
— *Numerical research of many-body effects on phonon transport by a quantum Monte Carlo method*

KAWAKAMI, Norio [C class; 5000 (B), 800 (C)] (27)
— *Correlation Effects in Nonequilibrium/Inhomogeneous Cold Atom Systems*
— *Topologically nontrivial phases and nonequilibrium phenomena in strongly correlated superlattice and quasiperiodic systems*

1. Drag dynamics in one-dimensional Fermi systems
   Jun'ichi Ozaki, Masaki Tezuka and Norio Kawakami: Phy. Rev. A **92** (2015) 023607.
2. Large and small Fermi-surface spin density waves in the Kondo lattice model
   R. Peters and N. Kawakami: Phys. Rev. B **92** (2015) 075103.
3. Restoration of topological properties at finite temperatures in a heavy-fermion system
   Tsuneya Yoshida, Robert Peters, and Norio Kawakami: Phy. Rev. B **93** (2016) 045138.
4. Unveiling hidden topological phases of a one-dimensional Hadamard quantum walk
   Hideaki Obuse, Janos K. Asboth, Yuki Nishimura, and Norio Kawakami: Phys. Rev. B **92** (2015) 045424.
5. Laser-induced Kondo effect in ultracold alkaline-earth fermions
   Masaya Nakagawa and Norio Kawakami: Phys. Rev. Lett. 115 (2015) 165303.

KAWAMURA, Hikaru [B,C class; 10100 (B), 0 (C)] (196, 198)
— *Numerical simulations on statistical models of earthquakes*
— *Novel order in frustrated magnets*

1. Static and dynamical spin correlations of the S =1/2 random-bond antiferromagnetic Heisenberg

model on the triangular and kagome lattices
T. Shimokawa, K. Watanabe and H. Kawamura: Phys. Rev. B 92, 134407/1-12 (2015).

2. Low-temperature magnetic properties of the Kondo lattice model in one dimension
   S. Minami and H. Kawamura: J. Phys. Sco. Jpn. 84, 044702/1-8 (2015).
3. Dynamics of earthquake nucleation process represented by the Burridge -Knopoff model
   Y. Ueda, S. Morimoto, S. Kakui, T. Yamamoto and H. Kawamura: Euro. Phys. J. B 88, 235/1-24 (2015).

KAWASHIMA, Naoki [C,E class; 20500 (B), 4400 (C)] (181)
— *Possibility of Supersolid in Helium 4 Adsorbed on Graphite Surface*

1. SU(N) Heisenberg model with multicolumn representations
   Tsuyoshi Okubo, Kenji Harada, Jie Lou, Naoki Kawashima: Phys. Rev. B **92** (2015) 134404/1-5.
2. Scaling relation for dangerously irrelevant symmetry-breaking fields
   Tsuyoshi Okubo, Kosei Oshikawa, Hiroshi Watanabe, Naoki Kawashima : Phys. Rev. B **91** (2015) 174417/1-4.

KITAO, Akio [C class; 5000 (B), 2500 (C)] (203)
— *Efficient sampling simulation of the soft modes significantly contribute to protein properties*

1. Nontargeted Parallel Cascade Selection Molecular Dynamics for Enhancing the Conformational Sampling of Proteins.
   R. Harada and A. Kitao: J. Chem. Theory Comput.Nature Comm. **11** (2015) 5493.
2. Monte Carlo Sampling with Linear Inverse Kinematics for Simulation of Protein Flexible Regions.
   S. Hayward and A. Kitao: J. Chem. Theory Comput. **11** (2015) 3895.
3. Gate-controlled proton diffusion and protonation-induced ratchet motion in the stator of the bacterial flagellar motor.
   Y. Nishihara and A. Kitao: Proc. Natl. Acad. Sci. **112** (2015) 7737.

KIZAKI, Hidetoshi [C class; 2000 (B), 0 (C)] (104)
— *Pt stepped structure dependence for oxygen reduction reaction in fuel cell*

1. Study on the mechanism of platinum-assisted hydrofluoric acid etching of SiC using density functional theory calculations
   P. V. Bui, A. Isohashi, H. Kizaki, Y. Sano, K. Yamauchi, Y. Morikawa and K. Inagaki: Applied Physics Letters **107** (2015) 201601/1 − 3

KOBAYASHI, Katsuyoshi [B class; 400 (B), 200 (C)] (128)
— *Search for electronic properties of new nanoscale interfaces*

1. Electronic states of SnTe and PbTe (001) monolayers with supports
   K. Kobayashi: Surf. Sci. **639** (2015) 54.

KOBAYASHI, Nobuhiko [C class; 9500 (B), 2400 (C)] (52)
— *First-principles study of quantum transport in nanostructures*

1. Correlation between thermal fluctuation effects and phase coherence factor in carrier transport of single-crystal organic semiconductors
   T. Fukami, H. Ishii, N. Kobayashi, T. Uemura, K. Sakai, Y. Okada, J. Takeya, and K. Hirose: Appl. Phys. Lett. **106** (2015) 143302.
2. Electronic Band Structure of Various TiN/MgO Superlattices
   K. Kobayashi, H. Takaki, N. Kobayashi, and K. Hirose: JPS Conf. Proc. **5** (2015) 011013.
3. Wave Packet Dynamical Calculations for Charge Transport of Organic Semiconductors: Role of Molecular Vibrations and Trap Potentials
   H. Ishii, N. Kobayashi, K. Hirose, Mol. Cryst. Liq. Cryst. **620** (2015) 2-9.
4. First-principles calculations of thermoelectric properties of TiN/MgO superlattices: The route for an enhancement of thermoelectric effects in artificial nanostructures
   H. Takaki, K. Kobayashi, M. Shimono, N. Kobayashi, and K. Hirose, J. Appl. Phys. **119**, 014302 (2016).
5. Confinement of the Pt(111) Surface State in Graphene Nanoislands

H. W. Kim, S. Takemoto, E. Minamitani, T. Okada, T. Takami, K. Motobayashi, M. Trenary, M. Kawai, N. Kobayashi, and Y. Kim, J. Phys. Chem. C **120**, 345-349 (2016).

6. Emergence of charge coherence in soft molecular organic semiconductors by suppressing thermal fluctuations
   K. Sakai, Y. Okada, T. Uemura, J. Tsurumi, R. Hausermann, H. Matsui, T. Fukami, H. Ishii, N. Kobayashi, K. Hirose and J. Takeya, NPG Asia Materials, **8**, e252 (2016).

KOGA, Akihisa [C class; 7500 (B), 0 (C)] (148)

— *Superconductivity and ordered phases in correlated fermion systems with internal degree of freedom*

— *Spin-orbit coupling in strongly correlated electron systems with orbital degeneracy*

1. Phase transitions in the Hubbard model for the bismuth nickelate
   S. Kojima, J. Nasu, A. Koga: arXiv:1604.05916.
2. Finite Temperature Phase Transitions in the SU(N) Hubbard model
   H. Yanatori and A. Koga: arXiv:1603.02647.
3. Phase diagram and collective excitation in excitonic insulator: from the orbital physics viewpoint
   J. Nasu, T. Watanabe, M. Naka, S. Ishihara: arXiv:1602.07831.
4. Fermionic response from fractionalization in an insulating two-dimensional magnet
   J. Nasu, J. Knolle, D. L. Kovrizhin, Y. Motome, R. Moessner: arXiv:1602.05277.
5. Fractional Spin Fluctuation as a Precursor of Quantum Spin Liquids: Majorana Dynamical Mean-Field Study for the Kitaev Model
   J. Yoshitake, J. Nasu, Y. Motome, arXiv:1602.05253.
6. Finite Temperature Properties of Three-Component Fermion Systems in Optical Lattice
   H. Yanatori and A. Koga: J. Phys. Soc. Jpn. **85** (2016) 014002.
7. Magnetic Three States of Matter: A Quantum Monte Carlo Study of Spin Liquids
   Y. Kamiya, Y. Kato, J. Nasu, Y. Motome: Phys. Rev. B **92** (2015) 100403.
8. Thermal fractionalization of quantum spins in a Kitaev model: Temperature-linear specific heat and coherent transport of Majorana fermions
   J. Nasu, M. Udagawa, Y. Motome: Phys. Rev. B **92** (2015) 115122.
9. Thermodynamics of Chiral Spin Liquids with Abelian and Non-Abelian Anyons
   J. Nasu, Y. Motome: Phys. Rev. Lett. **115** (2015) 087203.
10. Transport properties for a quantum dot coupled to normal leads with pseudogap
    B. Hara, A. Koga, and T. Aono: Phys. Rev. B **92** (2015) 081103.
11. DMFT Study for Valence Fluctuations in the Extended Periodic Anderson Model
    R. Shinzaki, J. Nasu, and A. Koga: J. Phys.: Conf. Ser. **683** (2016) 012041.
12. Intersite electron correlations in a Hubbard model on inhomogeneous lattices
    N. Takemori, A. Koga, and H. Hafermann: J. Phys.: Conf. Ser. **683** (2016) 012040.
13. Spin correlation and Majorana spectrum in chiral spin liquids in a decorated-honeycomb Kitaev model
    J. Nasu and Y. Motome: J. Phys.: Conf. Ser. **683** (2016) 012037.
14. Phase Diagram of the Kitaev-type Model on a Decorated Honeycomb Lattice in the Isolated Dimer Limit
    J. Nasu and Y. Motome: Physics Procedia **75** (2015) 755-762.
15. Low-energy Majorana states in spin liquid transitions in a three-dimensional Kitaev model
    J. Nasu, M. Udagawa, Y. Motome: J. Phys.: Conf. Ser. **592** (2015) 012115.
16. DMFT study of the local correlation effects in quasi-periodic system
    N. Takemori and A. Koga, J. Phys.: Conf. Ser. **592** (2015) 012038.

KOTA, Yohei [B class; 600 (B), 400 (C)] (115)

— *Analysis of magnetic anisotropy energy in corundum-type Cr2O3 and Fe2O3*

1. Theoretical Simulation of the Hydrostatic Pressure Effect on the Néel Temperature in Corundum-Type Cr_2O_3
   Y. Kota: J. Phys. Soc. Jpn. (submitted)

KOURA, Akihide [C class; 1500 (B), 1600 (C)] ()

— *Ab initio molecular dynamics study for the static structure of the network forming glass*

KUNISADA, Yuji [C class; 5500 (B), 0 (C)] (76)
— *Development of Oxygen Storage Materials and Analysis of Hydrogen Embrittlement Properties of Steel*
— *Development of Measurement Technique of Local Optical Property and Analysis of Hydrogen Embrittlement Properties of Steel*

1. Hindered Rotational Physisorption States of H_2 on Ag(111) Surfaces
   Y. Kunisada, H. Kasai: Phys. Chem. Chem. Phys. **17** (2015) 19625.
2. Salt-assisted combustion synthesis of Ca-α-SiAlON: Eu^{2+} phosphors
   G. Saito, J. Niu, X. Yi, Y. Kunisada, N. Sakaguchi, T. Akiyama: J. Alloy. Compd. in press.
3. fcc 鉄 (111) 表面近傍での空孔形成における水素原子の影響
   國貞雄治，坂口紀史: 金属学会誌 **79** (2015) 447.

KUROKI, Kazuhiko [C class; 1500 (B), 0 (C)] (163)
— *Study on the enhanced pairing due to peculiar hoppings in the iron-based superconductors*

1. Asymmetry of superconductivity in hole- and electron-doped cuprates: explanation within two-particle self-consistent analysis for the three-band Model
   D. Ogura, K. Kuroki, Phys. Rev. B **92** (2015) 144511/1-5.
2. Minimal electronic model for a layered nitride halide superconductor β-ZrNCl
   H. Tanaka, K. Suzuki, H.Usui, K. Kuroki, J. Phys. Soc. Jpn. **84** (2015) 124706/1-7.
3. Origin of the non-monotonic variance of T_c in the 1111 iron based superconductors with isovalent doping
   H. Usui, K. Suzuki, K. Kuroki, Scientific Reports **5** (2015) 11399/1-8.
4. Theoretical aspects of the study of the new bismuth chalcogenide based superconductors
   H. Usui, K. Kuroki, Nov. Supercond. Mater. **1** (2015) 50-63 (invited review)
5. Iron-Based Superconductors: current status of materials and pairing mechanism
   H. Hosono, K. Kuroki, Physica C **514** (2015) 399-422 (invited review)

KUSAKABE, Koichi [C class; 1500 (B), 0 (C)] (241)
— *Simulation of quantum response of graphene quantum devices*

1. Theoretical Analysis on Pseudo-Degenerate Zero-Energy Modes in Vacancy-Centered Hexagonal Armchair Nanographene
   Naoki Morishita, Gagus Ketut Sunnardianto, Satoaki Miyao, Koichi Kusakabe: submitted to J. Phys. Soc. Jpn.: preprint arXiv:1604.06841
2. Systematic study of the effect of H adsorption on the rate of electron transfer in graphene
   Gagus Ketut Sunnardianto, Isao Maruyama, Koichi Kusakabe: Journal of Computational and Theoretical Nanoscience, in press.
3. Dissociation-chemisorption pathways of H2 molecule on graphene activated by a hydrogenated mono-vacancy V11
   Gagus Ketut Sunnardianto, Isao Maruyama, Koichi Kusakabe: Journal of Advanced Science, Engineering and Medicine, in press.

KUWABARA, Akihide [C class; 2000 (B), 0 (C)] (103)
— *First principles calculation of point defects in electrodes of solid oxide fuel cells*

MASAKI-KATO, Akiko [C class; 8000 (B), 4100 (C)] (188)
— *Quantum Monte Carlo Simulations of Interacting Bosons on Kagome lattices with the Parallelized Multi-Worm Algorithm*
— *Development and Application of the Quantum Monte Carlo Method for Critical Phenomena of Random Bosonic Systems*

MATSUKAWA, Hiroshi [C class; 2500 (B), 0 (C)] ()
— *Physics of Friction*

MATSUSHITA, Katsuyoshi [C class; 3000 (B), 0 (C)] (229)
— *Simulation of collective migrations induced by the cell-cell adhesion and the cell polarity*
— *Simulation of Cell-Cell Adhesion control of Collective Cell Motion*

1. Collective Migration of Repulsively Interacting Cells
   Katsuyoshi Matsushita: Proceedings of the 21th symposium on simulations of traffic flow, pp

MISAWA, Takahiro [C class; 3500 (B), 2200 (C)] (154)
— *Improvement of many-variable variational Monte Carlo method and its application to iron-based superconductors*

1. Finite-Temperature Variational Monte Carlo Method for Strongly Correlated Electron Systems
   K. Takai, K. Ido, T. Misawa, Y. Yamaji, and M. Imada, J. Phys. Soc. Jpn. **85** (2016) 034601.
2. Ab initio Studies of Magnetism in the Iron Chalcogenides FeTe and FeSe
   M. Hirayama, T. Misawa, K. Miyake, and M. Imada, J. Phys. Soc. Jpn. **84** (2015) 093703.

MIURA, Yoshio [B class; 600 (B), 0 (C)] (127)
— *A first-principles study on magneto-crystalline anisotropy of ferromagnetic metal interfaces with spinel barrier*

MIYAKE, Takashi [C class; 1000 (B), 0 (C)] (113)
— *First-principles study of magnet materials and spin-orbit systems*

1. Weyl node and spin texture in trigonal tellurium and selenium
   M. Hirayama, R. Okugawa, S. Ishibashi, S. Murakami and T. Miyake: Phys. Rev. Lett. **114** (2015) 206401.
2. Nitrogen as the best interstitial dopant among X = B, C, N, O, and F for strong permanent magnet $\mathrm{NdFe}_{11}\mathrm{Ti}X$: First-principles study
   Y. Harashima, K. Terakura, H. Kino, S. Ishibashi and T. Miyake: Phys. Rev. B **92** (2015) 184426.

MIYASHITA, Seiji [C class; 3000 (B), 1800 (C)] (218)
— *Dynamical phase transitions under time dependent external fields*

1. Realization of thermal equilibrium in inhomogeneous magnetic systems by the Landau-Lifshitz-Gilbert equation with stochastic noise, and its dynamical aspects
   M. Nishino and S. Miyashita: Phys. Rev. B **91**, 134411/1-13 (2015).
2. Termination of the Berezinskii-Kosterlitz-Thouless phase with a new critical universality in spin-crossover systems
   M. Nishino, S. Miyashita: Phys. Rev. B **92**, 184404/1-7 (2015).
3. Computation of ESR spectra from the time evolution of the magnetization: Comparison of auto-correlation and Wiener-Khinchin-relation-based methods
   H. Ikeuchi, H. De Raedt, S. Bertaina, S. Miyashita: Phys. Rev. B **92**, 214431/1-15 (2015).
4. Ordering phenomena of high-spin/low-spin states in stepwise spin-crossover materials described by the ANNNI model
   H. Watanabe, K. Tanaka, N. Brefuel, H. Cailleau, J. F. Letard, S. Ravy, P. Fertey, M. Nishino, S. Miyashita and E. Collet: Phys. Rev. B. **93**, 014419/1-12 (2016).
5. Quantum Stoner-Wohlfarth Model
   T. Hatomura, B. Barbara and S. Miyashita: Phys. Rev. Lett. **116**, 037203/1-5 (2016).
6. Equilibrium, metastability, and hysteresis in a model spin-crossover material with nearest-neighbor antiferromagnetic-like and long-range ferromagnetic-like interactions
   P.A. Rikvold, G. Brown, S. Miyashita, C. Omand and M. Nishino: Phys. Rev. B. **93**, 064109/1-13 (2016).

MORIKAWA, Yoshitada [C,E class; 21500 (B), 4200 (C)] (47)
— *First-principles statistical thermodynamics simulations on the structure and reactivity of heterogeneous catalysts*

1. First-principles investigation of the GaN growth process in carbon-added Na-flux method
   T. Kawamura, H. Imabayashi, M. Maruyama, M. Imade, M. Yoshimura, Y. Mori, and Y. Morikawa: Phys. Status Solidi B **252** (2015) 1084-1088.

2. Study on the mechanism of platinum-assisted hydrofluoric acid etching of SiC using density functional theory calculations
   P.V. Bui, A. Isohashi, H. Kizaki, Y. Sano, K. Yamauchi, Y. Morikawa, and K. Inagaki: Appl. Phys. Lett. **107** (2015) 201601.
3. Mechanism for enhanced single-crystal GaN growth in the C-assisted Na-flux method
   T. Kawamura, H. Imabayashi, M. Maruyama, M. Imade, M. Yoshimura, Y. Mori, and Y. Morikawa: Appl. Phys. Express **9** (2015) 015601.
4. Density Functional Theory Investigationsj of Ferrocene-Terminated Self-Assembled Monolayers: Electronic State Changes Induced by Electric Dipole Field of Coadsorbed Species
   Y. Yokota, S. Akiyama, Y. Kaneda, A. Imanishi, K. Inagaki, Y. Morikawa, and K. Fukui: J. Phys. Chem. C **120** (2016) 8684-8692.
5. Theoretical Study on Electronic Structure of Bathocuproine: Renormalization of the Band Gap in the Crystalline State and the Large Exciton Binding Energy
   S. Yanagisawa, S. Hatada, and Y. Morikawa: J. Chin. Chem. Soc. **63**, in press.
6. Self-consistent van der Waals density functional study of benzene adsorption on Si(100)
   Y. Hamamoto, I. Hamada, K. Inagaki, and Y. Morikawa: Phys. Rev. B, submitted.

MORITA, Satoshi [B class; 400 (B), 400 (C)] (129, 244)
— *Parallelization of tensor network method*

1. Variational Monte Carlo method in the presence of spin-orbit interaction and its application to Kitaev and Kitaev-Heisenberg models
   M. Kurita, Y. Yamaji, S. Morita, and M. Imada: Phys. Rev. B **92**, 035122 (2015).

MOTOME, Yukitoshi [C class; 9000 (B), 0 (C)] (146)
— *New physics opened by charge-spin-orbital coupling in strongly correlated electron systems*
— *Theoretical study of novel physics by synergy between electron correlation and spin-orbit coupling*

1. Spontaneous formation of kagome network and Dirac half-semimetal on a triangular lattice
   Y. Akagi and Y. Motome: Phys. Rev. B **91** (2015) 155132.
2. Spontaneous Multipole Ordering by Local Parity Mixing
   S. Hayami, H. Kusunose, and Y. Motome: J. Phys. Soc. Jpn. **84** (2015) 064717.
3. Strong coupling theory for electron-mediated interactions in double-exchange models
   H. Ishizuka and Y. Motome: Phys. Rev. B **92** (2015) 024415.
4. Thermodynamics of Chiral Spin Liquids with Abelian and Non-Abelian Anyons
   J. Nasu and Y. Motome: Phys. Rev. Lett. **115** (2015) 087203.
5. Thermal fractionalization of quantum spins in a Kitaev model: Temperature-linear specific heat and coherent transport of Majorana fermions
   J. Nasu, M. Udagawa, and Y. Motome: Phys. Rev. B **92** (2015) 115122.
6. Magnetic three states of matter: A quantum Monte Carlo study of spin liquids
   Y. Kamiya, Y. Kato, J. Nasu, and Y. Motome: Phys. Rev. B **92** (2015) 100403(R).
7. Charge-spin-orbital fluctuations in mixed valence spinels: Comparative study of AlV2O4 and LiV2O4
   A. Uehara, H. Shinaoka, and Y. Motome: Phys. Rev. B **92** (2015) 195150.
8. Theory of Valence Transition in BiNiO3
   M. Naka, H. Seo, and Y. Motome: Phys. Rev. Lett. **116** (2016) 056402.
9. 量子スピン液体を計算機で温める：新しい磁気相転移の発見
   求幸年: パリティ **30(10)** (2015) 36.
10. キタエフ量子スピン液体の”気液”相転移
    那須譲治, 宇田川将文, 求幸年: 日本物理學會誌 **70(10)** (2015) 776.
11. 計算機で見る磁性体の新しい相転移
    求幸年: パリティ **31(1)** (2016) 22.
12. Asymmetric Magnon Excitation by Spontaneous Toroidal Ordering
    S. Hayami, H. Kusunose, and Y. Motome: accepted for publication in J. Phys. Soc. Jpn.
13. Vortex Crystals with Chiral Stripes in Itinerant Magnets
    R. Ozawa, S. Hayami, K. Barros, G-W. Chern, Y. Motome, C. D. Batista: submitted to Europhys. Lett.

14. Fractional Spin Fluctuation as a Precursor of Quantum Spin Liquids: Majorana Dynamical Mean-Field Study for the Kitaev Model
    J. Yoshitake, J. Nasu, and Y. Motome: submitted to Phys. Rev. Lett.
15. Fermionic response from fractionalization in an insulating two-dimensional magnet
    J. Nasu, J. Knolle, D. L. Kovrizhin, Y. Motome, and R. Moessner: submitted to Nature Phys.
16. Engineering chiral density waves and topological band structures by multiple-Q superpositions of collinear up-up-down-down orders
    S. Hayami, R. Ozawa, and Y. Motome: submitted to Phys. Rev. B

MOTOYAMA, Yuichi [B,C class; 2800 (B), 600 (C)] (160)
— *Numerical simulation of* ^{4}*He adsorbed on substrates*

MURASHIMA, Takahiro [C class; 3500 (B), 2200 (C)] (35)
— *Viscoelastic analysis on soft matter systems (polymer, liquid crystal, micelle) and multiscale simulation*

NADA, Hiroki [C class; 3000 (B), 0 (C)] (228)
— *Molecular Dynamics Simulation Study of Growth Promotion Mechanism of Ice Basal Plane by Antifreeze Protein*
1. Anisotropy in Conformation and Dynamics of a Glycolate Ion Near the Surface of a TiO_2 Rutile Crystal Between Its 001 and 110 Planes: A Molecular Dynamics Study
   H. Nada, M. Kobayashi and M. Kakihana: J. Phys. Chem. C, **120** (2016) 6502.
2. Heterogeneous Growth of Calcite at Aragonite 001- and Vaterite 001-Melt Interfaces: A Molecular Dynamics Simulation Study
   H. Nada, T. Nishimura, T. Sakamoto and T. Kato: submitted to J. Cryst. Growth

NAKAMURA, Kazuma [C class; 5000 (B), 0 (C)] (86)
— *Temperature dependence of low-energy plasmaron states of materials: Ab initio GW analysis*
— *Ab initio GW+cumulant study for spectral function of low-dimensional system*
1. GW calculation of plasmon excitations in the quasi-one-dimensional organic compound (TMTSF)2PF6
   Kazuma Nakamura, Shiro Sakai, Ryotaro Arita, and Kazuhiko Kuroki: Physical Review B **88** (2013) 125128.
2. Effect of Electron-Phonon Interactions on Orbital Fluctuations in Iron-Based Superconductors
   Yusuke Nomura, Kazuma Nakamura, and Ryotaro Arita: Phys. Rev. Lett. **112** (2014) 027002.
3. Ab initio GW plus cumulant calculation for isolated band systems: Application to organic conductor (TMTSF)2PF6 and transition-metal oxide
   Kazuma Nakamura, Yoshiro Nohara, Yoshihide Yoshimoto, and Yusuke Nomura: Phys. Rev. B **93** (2016) 085124.

NAKAMURA, Kohji [C class; 500 (B), 0 (C)] (131)
— *First principles calculations on electronic structures, magnetism, and electric field effects in transition-metal films and organometallic complexes*
1. Electronic configurations and magnetic anisotropy in organometallic metallocenes
   K. Nawa, Y. Kitaoka, K. Nakamura, T. Akiyama and T. Ito,: JAP **117** (2015) 17E131.
2. Search for the ground state electronic confgurations of correlated organometallic metallocenes from constraint density functional theory
   K. Nawa, Y. Kitaoka, K. Nakamura, H. Imamura, T. Akiyama, T. Ito and M. Weinert: submitted.

NAKANO, Hiroki [C class; 4000 (B), 2200 (C)] (206)
— *Numerical study on low-energy states of quantum spin systems*
1. Magnetization Process of the Spin-S Kagome-Lattice Heisenberg Antiferromagnet
   H. Nakano and T. Sakai: J. Phys. Soc. Jpn. **84** (2015) 063705.
2. Magnetization Jump in the Magnetization Process of the Spin-1/2 Heisenberg Antiferromagnet on a Distorted Square-Kagome Lattice
   H. Nakano, Y. Hasegawa, and T. Sakai: J. Phys. Soc. Jpn. **84** (2015) 114703.

3. Novel Quantum Phase Transition in the Frustrated Spin Nanotube
   T. Sakai and H. Nakano: Physics Procedia **75** (2015) 369.
4. Exotic Field Induced Quantum Phase Transition of the Kagome Lattice Antiferromagnet
   T. Sakai and H. Nakano: Physics Procedia **75** (2015) 821.

NAKAYAMA, Takashi [C class; 3000 (B), 1000 (C)] (96)
— *Defect generation at metal/semiconductor interfaces: stability and ionization diffusion*

1. First-Principles Calculation of Electronic Properties of Isoelectronic Impurity Complexes in Si
   S. Iizuka, T. Nakayama: Appl. Phys. Express **8** (2015) 081301.
2. Tunneling Desorption of Atomic Hydrogen on the Surface of Titanium Dioxide
   T. Minato, S. Kajita, C-L. Pang, N. Asao, Y. Yamamoto, T. Nakayama, M. Kawai, and Y. Kim: ACS Nano. **9** (2015) 6837.
3. Quantum process of exciton dissociation at organic semiconductor interfaces; Effects of interface roughness and hot exciton
   H. Iizuka, T. Nakayama: Jpn. J. Appl. Phys. **55** (2016) 021601.

NISHIDATE, Kazume [C class; 3000 (B), 1600 (C)] (90)
— *Theoretical investigation of growing process of organic semiconductors*

1. Collapsed armchair single-walled carbon nanotubes as an analog of closed-edged bilayer graphene nanoribbons
   M. Hasegawa, K. Nishidate, and Y. Yoshimoto: Phys. Rev. B, **92** (2015) 245429/1-13.

NOGAWA, Tomoaki [B class; 700 (B), 0 (C)] (247)
— *Search of close packing states of multicomponent hard-sphere systems by the parallelized Wang-Landau sampling*

NOGUCHI, Hiroshi [C class; 10500 (B), 4700 (C)] (184)
— *Shape transformation of lipid membranes induced by protein adsorption and chemical reaction*
— *Structure formation of biomembranes*

1. Formation of polyhedral vesicles and polygonal membrane tubes induced by banana-shaped proteins
   H. Noguchi: J. Chem. Phys. **143** (2015) 243109.
2. Shape transitions of high-genus fluid vesicles
   H. Noguchi: EPL **112** (2015) 58004.
3. Membrane tubule formation by banana-shaped proteins with or without transient network structure
   H. Noguchi: Sci. Rep. **6** (2016) 20935.
4. Monte Carlo study of the frame, fluctuation and internal tensions of fluctuating membranes with fixed area
   H. Shiba, H. Noguchi, and J.-B. Fournier: Soft Matter **12** (2016) 2373.
5. Rheological evaluation of colloidal dispersions using smoothed profile method - formulation and applications
   J. J. Molina, K. Otomura, H. Shiba, H. Kobayashi, M. Sano, and R. Yamamoto: J. Fluid Mech. **792** (2016) 590.
6. Shape deformation of lipid membranes by banana-shaped protein rods: comparison with isotropic inclusions and membrane rupture
   H. Noguchi: Phys. Rev. E **93** (2016) 052404.

NOGUCHI, Yoshifumi [C class; 4500 (B), 2400 (C)] (70)
— *First-principles GW+Bethe-Salpeter calculations of core electron excitations*

1. Vibronic Structures in Absorption and Fluorescence Spectra of Firefly Oxyluciferin in Aqueous Solutions
   M. Hiyama, Y. Noguchi, H. Akiyama, K. Yamada, and N. Koga: Photochem. Photobio. **91** (2015) 819.
2. TOMBO: All-electron mixed-basis approach to condensed matter physics

S. Ono, Y. Noguchi, R. Sahara, Y. Kawazoe, and K. Ohno: Compt. Phys. Comm. **189** (2015) 20

3. All-electron GW+Bethe-Salpeter calculations on small molecules
   D. Hirose, Y. Noguchi, and O. Sugino: Phys. Rev. B. **91** (2015) 205111.

OBATA, Shuji [C class; 500 (B), 100 (C)] (126)
— *Calculations of Fe compounds Magnetism*

1. Duality and control theory in spin Josephson junction
   Morishige Yoneda, Shuji Obata, and Masaaki Niwa and Mitsuya Motohashi: Trans. Mat. Res. Soc. Japan, 40 [2] (2015) 115-118
2. Simulation of the Magnetic Hysteresis Loop in Ferrimagnetizm
   Morishige Yoneda, Shuji Obata, and Masaaki Niwa: Materials Transactions. 56 No 9. (2015) 1488-1490

ODA, Tatsuki [C class; 6500 (B), 4200 (C)] (57)
— *Analyses on atomic structure, magnetism, and electronic structure in spintronics materials and molecular magnets*

1. First principles study on solid oxygen using van der Waals density functional
   M. Obata, I. Hamada, and T. Oda: Physics Procedia, **75** (2015) 771.
2. Density functional study on positively charged six-coordinate FeO_2 porphyrin complex for a trigger of O_2 dissociation
   N. Kitagawa, M. Obata, T. Oda: Chem. Phys. Lett. **643** (2016) 119.
3. Superconducting H_5S_2 phase in sulfur-hydrogen system under high-pressure
   T. Ishikawa, A. Nakanishi, K. Shimizu, H. Katayama-Yoshida, T. Oda, and Naoshi Suzuki: Scientific Reports, **6** (2016) 23160; doi:10.1038/srep23160.

OGUCHI, Tamio [C class; 3500 (B), 1800 (C)] (77)
— *First-Principles Calculations of Transition Metals and Their Alloys and Compounds*

1. Impact of Ferroelectric Distortion on Thermopower in $BaTiO_3$
   H. Saijo, K. Yamauchi, K. Shirai, and T. Oguchi, J. Phys. Soc. Jpn. **84**, 054701/1-5 (2015).
2. First-Principles Investigation on a Phase Transition in $Na_xC_6O_6$ as an Organic Cathode Material for Na-ion Batteries: Role of Inter-molecule Bonding of C_6O_6
   T. Yamashita, H. Momida, and T. Oguchi, J. Phys. Soc. Jpn. **84**, 074703/1-7 (2015).
3. Superexchange interaction in the A-site ordered pervskite $YMn_3Al_4O_{12}$
   M. Toyoda, T. Saito, K. Yamauchi, Y. Shimakawa, and T. Oguchi, Phys. Rev. B **92**, 014420/1-7 (2015).
4. Discharge Reaction Mechanism in Na/FeS_2 Batteries: First-Principles Calculations
   H. Momida, A. Kitajou, S. Okada, T. Yamashita, and T. Oguchi, J. Phys. Soc. Jpn. **84**, 124709/1-7 (2015).
5. Crystal structure predictions of $Na_xC_6O_6$ for sodium-ion batteries: First-principles calculations with an evolutionary algorithm
   T. Yamashita, H. Momida, and T. Oguchi, Electrochimica Acta **195**, 1-8 (2016).
6. Comparative ARPES study on iron-platinum-arsenide superconductor $Ca_{10}(Pt_4As_8)(Fe_{2-x}Pt_xAs_2)_5$ ($x = 0.25$ and 0.42)
   M. Sunagawa, R. Yoshida, T. Ishiga, K. Tsubota, T. Jabuchi, J. Sonoyama, S. Kakiya, D. Mitsuoka, K. Kudo, M. Nohara, K. Ono, H. Kumigashira, T. Oguchi, T. Wakita, Y. Muraoka, and T. Yokoya, J. Phys. Soc. Jpn. **84**, 055001/1-2 (2015).
7. *A*-site driven ferroelectricity in strained ferromagnetic La_2NiMnO_6 thin film
   R. Takahashi, I. Ohkubo, K. Yamauchi, M. Kitamura, Y. Sakurai, M. Oshima, T. Oguchi, Y. Cho, and M. Lippmaa, Phys. Rev. B **91**, 134107/1-9 (2015).
8. Quasi-One-Dimensional Nature of the Rashba States of Au Wires on Si(557) Surface
   T. Oguchi, J. Electron Spectrosc. Relat. Phenom. **201**, 18-22 (2015).
9. Local electronic states of Fe_4N films revealed by x-ray absorption spectroscopy and x- ray magnetic circular dichroism
   K. Ito, K. Toko, Y. Takeda, Y. Saitoh, T. Oguchi, T. Suemasu, and A. Kimura, J. Appl. Phys. **117**, 193906/1-6 (2015).

10. Superconductivity and the electronic phase diagram of $\mathrm{LaPt}_{2-x}\mathrm{Ge}_{2+x}$
    S. Maeda, K. Matano, R. Yatagai, T. Oguchi, and Guo-qing Zheng, Phys. Rev. B **91**, 174516/1-7 (2015).
11. Coupling Ferroelectricity with Spin-Valley Physics in Oxide-Based Heterostructures
    K. Yamauchi, P. Barone, T. Shishidou, T. Oguchi, and S. Picozzi, Phys. Rev. Lett. **115**, 037602/1-5 (2015).
12. Tetrahedral tilting and ferroelectricity in $\mathrm{Bi}_2\mathrm{AO}_5$ (A=Si, Ge) from first principles calculations
    J. Park, B. G. Kim, S. Mori, and T. Oguchi, J. Solid State Chem. **235**, 68-75 (2016).

OHGOE, Takahiro [C class; 6000 (B), 0 (C)] (153)
— *Multi-variable variational Monte Carlo study of the Hubbard model with electron-phonon interactions*
— *Numerical study of an ab-initio effective model for an iron-based superconductor with electron-phonon interactions*

OHMURA, Satoshi [C class; 2500 (B), 0 (C)] (101)
— *Doping effects on Light Absorption of Light-harvesting Molecules: ab initio Molecular-Dynamics Study*

1. Structural Changes of Short- and Intermediate-Range Order in Liquid Arsenic under Pressure
   S. Ohmura, A. Chiba, Y. Yanagawa, A. Koura, K. Tsuji, and F. Shimojo: J. Phys. Soc. Jpn. **84** (2015) 094602.
2. Doping effect on photoabsorption and charge-separation dynamics in light- harvesting organic molecule
   S. Ohmura, K. Tsuruta, F. Shimojo, and A. Nakano: AIP Advances **6** (2016) 015305
3. Crystalline anisotropy of shock-induced phenomena: omni-directional multiscale shock technique
   K. Shimamura, M. Misawa, S. Ohmura, F. Shimojo, R. K. Kalia, A. Nakano, and P. Vashishta: Appl. Phys. Lett. **108** (2016) 071901
4. Dissociation Dynamics of Ethylene Molecules on a Ni Cluster Using Ab Initio Molecular Dynamics Simulationse
   K. Shimamura, Y. Shibuta, S. Ohmura, Rizal Arifin, F. Shimojo: J. Phys. Condens. Matter **28** (2016) 145001
5. Intermolecular correlations of racemic mixtures – comparison between liquid $\mathrm{S}_2\mathrm{Cl}_2$ and $\mathrm{Se}_2\mathrm{Br}_2$
   H. Shimakura, Y. Kawakita, S. Ohmura, K. Ohara, S. Takeda, S. Ohno: Mol. Phys. **114** (2015) 297
6. Charge and Nuclear Dynamics Induced by Deep Inner-Shell Multiphoton Ionization of CH3I Molecules by Intense X-ray Free-Electron Laser Pulses
   K. Motomura, E. Kukk, H. Fukuzawa, S. Wada, K. Nagaya, S. Ohmura, S. Mondal, T. Tachibana, Y. Ito, R. Koga, T. Sakai, K. Matsunami, A. Rudenko, C. Nicolas, Xiao-Jing Liu, C. Miron, Y. Zhang, Y. Jiang, J. Chen, M. Anand, D. E. Kim, K. Tono, M. Yabashi, M. Yao, and K. Ueda: J. Phys. Chem. Lett. **6** (2015) 2944

OHSAWA, Kazuhito [C class; 500 (B), 0 (C)] (130)
— *Study of interaction between radiation damage and interstitial atom*

OHTSUKI, Tomi [C class; 3500 (B), 1000 (C)] (220)
— *Scaling theory of disordered topological insulators*

1. Modification and Control of Topological Insulator Surface States Using Surface Disorder
   V. Sacksteder, T. Ohtsuki, K. Kobayashi: Physical Review Applied **3** (2015), 064006
2. Dimensional crossover of transport characteristics in topological insulator nanofilms
   K. Kobayashi, K.-I. Imura, Y. Yoshimura, T. Ohtsuki: Physical Review B **92** (2015), 235407
3. Effect of disorder in a three dimensional layered Chern insulator
   S. Liu, T. Ohtsuki, R. Shindou: Physical Review Letters 116 (2016), 066401

OKADA, Susumu [C class; 500 (B), 0 (C)] ()
— *Electronic structures of carbon nanomaterials*

OKITSU, Kouhei [C class; 2000 (B), 500 (C)] (232)
— *Study on protein crystal structure analysis using X-ray n-beam dynamical diffraction theory*
— *Study on numerical mathod to solve n-beam Takagi equation*

OKUBO, Tsuyoshi [C class; 11000 (B), 4700 (C)] (183)
— *Novel phases in frustrated magnets*

1. Scaling Relation for Dangerously Irrelevant Symmetry-Breaking Fields
T. Okubo, K. Oshikawa, H. Watanabe, and N. Kawashima: Phys. Rev. B **91** (2015) 174417.
2. $SU(N)$ Heisenberg model with multi-column representations
T. Okubo, K. Harada, J. Lou, and N. Kawashima: Phys. Rev. B **92** (2015) 134404.
3. Experimental Realization of a Quantum Pentagonal Lattice
H. Yamaguchi, T. Okubo, S. Kittaka, T. Sakakibara, K. Araki, K. Iwase, N. Amaya, T. Ono, and Y. Hosokoshi: Scientific Reports, **5** (2015) 15327.

OKUMURA, Hisashi [C class; 5000 (B), 0 (C)] (216)
— *Dynamical ordering of biomolecular systems by molecular dynamics simulations*

ONISHI, Hiroaki [C class; 1500 (B), 0 (C)] (240)
— *Spin dynamics of frustrated quantum spin chain in magnetic field*

1. Magnetic Excitations of Spin Nematic State in Frustrated Ferromagnetic Chain
H. Onishi, J. Phys. Soc. Jpn. **84**, 083702 (2015).

ONO, Tomoya [C class; 8500 (B), 4200 (C)] (50)
— *Development of first-principles electronic-structure and transport calculation method based on real-space finite-difference approach*

1. Real-space method for first-principles electron transport calculations: Self-energy terms of electrodes for large systems
T. Ono and S. Tsukamoto: Phys. Rev. B **93** (2016) 045421.
2. First-principles study on interlayer states at the 4H-SiC/SiO_2 interface and the effect of oxygen-related defects
C. Kirkham and T. Ono: J. Phys. Soc. Jpn. **85** (2016) 024701.
3. Numerical solver for first-principles transport calculation based on real-space finite-difference method
S. Iwase, T. Hoshi, and T. Ono: Phys. Rev. E **91** (2015) 063305.
4. Ballistic electron transport through nanostructure junctions from a real-space finite-difference approach
S. Tsukamoto, T. Ono, and Y. Egami: Quantum Matter **4** (2015) 403.
5. 実空間差分法に基づく第一原理輸送特性計算によるナノ構造体の電子輸送特性
小野倫也: シミュレーション **34** (2015) 18.
6. 実空間差分法を用いた第一原理電気伝導特性計算の高速化
小野倫也, 塚本茂, 江上喜幸, 岩瀬滋: アンサンブル, in press.
7. First-principles study on oxidation of Ge and its interface electronic structures
T. Ono, S. Saito, and S. Iwase: Jpn. J. Appl. Phys. in press.
8. Importance of SiC Stacking to Interlayer States at the SiC/SiO_2 Interface
C. Kirkham and T. Ono: Materials Science Forum, in press.

ORITA, Nozomi [C class; 500 (B), 0 (C)] ()
— *Ab initio calculations for the silicon cluster superlattice*

OSHIKAWA, Masaki [B class; 300 (B), 0 (C)] (178)
— *Theoretical study of chiral magnetic effect in materials*

1. Distinct Trivial Phases Protected by a Point-Group Symmetry in Quantum Spin Chains
Y. Fuji, F. Pollmann, and M. Oshikawa: Phys. Rev. Lett. **114** (2015) 177204.
2. Flux quench in a system of interacting spinless fermions in one dimension
Y. O. Nakagawa, G. Misguich, and M. Oshikawa: preprint arXiv:1601.06167

3. Universal transport and resonant current from chiral magnetic effect
   H. Fujita and M. Oshikawa: preprint arXiv:1602.00687

OSHIYAMA, Atsushi [C,E class; 24500 (B), 4600 (C)] (45)
— *Atomic Structures and Electronic Properties of Hard- and Soft-Nanomaterials*
1. Structural Stability and Energy-Gap Modulation through Atomic Protrusion in Freestanding Bilayer Silicene
   Y. Sakai and A. Oshiyama: Phys. Rev. B **91** (2015) 201405(R) (2015)
2. Origin of Repulsive Interactions between Bunched Steps on Vicinal Solid Surfaces
   K. Sawada, J.-I. Iwata and A. Oshiyama: e-Journal of Surf. Sci Technol. **13** (2015) 231-234.
3. Crossover between silicene and ultra-thin Si atomic layers on Ag (111) surfaces
   Z.-X. Guo and A. Oshiyama: New J. Phys. **17** (2015) 045028.
4. Electron and Hole Confinement in Hetero-Crystalline SiC Superlattice
   Y. Sugihara, K. Uchida and A. Oshiyama: J. Phys. Soc. Jpn. **84** (2015) 084709.
5. Electron doping through lithium intercalation to interstitial channels in tetrahedrally bonded SiC
   Y. Sakai and A. Oshiyama: J. Appl. Phys. **118** (2015) 175704.
6. Structural evolution and optoelectronic applications of multilayer silicene
   Z.-X. Guo, Y.-Y. Zhang, H. Xiang, X.-G. Gong and A. Oshiyama: Phys. Rev. B, **92** (2015) 201413(R).
7. Density-Functional Study of Atomic and Electronic Structures of Multivacancies in Silicon Carbide
   J.-I. Iwata, C. Shinei and A. Oshiyama: Phys. Rev. B **93** (2016) 125202.

OTANI, Minoru [C class; 4000 (B), 2400 (C)] ()
— *Simulation of an operando soft x-ray spectroscopy using the ESM method*

OTOMO, Junichiro [C class; 500 (B), 600 (C)] (109)
— *Study on catalyst synthesis and surface reaction analysis for novel energy storage systems*

OTSUKA, Yuichi [C class; 3500 (B), 1600 (C)] (156)
— *Numerical study of critical phenomena in strongly correlated Dirac electrons*

OZEKI, Yukiyasu [C class; 5000 (B), 0 (C)] (215)
— *Improvement of dynamical scaling and accurate analysis of nonequilibrium relaxation data*

RAEBIGER, Hannes [C class; 3000 (B), 0 (C)] ()
— *Theory of self-organized nano-interfaces for electronic devices*

SAITO, Mineo [C class; 6500 (B), 0 (C)] (71)
— *First-principles calculation for device application of wide gap semiconductors*
1. Spin-split bands of metallic hydrogenated ZnO $(10\bar{1}0)$ surface: First-principles study
   Moh. Adhib Ulil Absor, Fumiyuki Ishii, Hiroki Kotaka, and Mineo Saito, AIP Advances, **6** (2016) 025309.
2. First-principles calculations of multivacancies in germanium
   Sholihun, Fumiyuki Ishii, and Mineo Saito: Jpn. J. Appl. Phys. **55** (2016) 011301.

SAKAI, Toru [C class; 6000 (B), 3300 (C)] (200, 201)
— *Quantum Phase Transition of the Spin Nanotubes*
— *Field-Induced Quantum Phase Transition in the Kagome-Lattice Antiferromagnet*
1. Instability of a ferromagnetic state of a frustrated S=1/2 Heisenberg antiferromagnet in two dimensions
   H. Nakano and T. Sakai: Jpn. J. Appl. Phys. **54** (2015) 030305.
2. Magnetization Process of the Spin-S Kagome-Lattice Heisenberg Antiferromagnet
   H. Nakano and T. Sakai: J. Phys. Soc. Jpn. **84** (2015) 063705.
3. Spin nanotubes with the ring exchange interactions
   T. Sakai, T. Kasahara, K. Hijii, H. Ohta, H. Nakano: Synthetic Metals **208** (2015) 26.

4. Possible Singlet-Triplet Transition of ESR in the Kagome-Lattice Antiferromagnet
   T. Sakai, K. Hijii, S. Okubo, H. Ohta, H. Nakano, S. Miyashita: Applied Magnetic Resonance **46** (2015) 997
5. Magnetization jump in the Magnetization Process of the spin-1/2 Heisenberg Antiferromagnet on a Distorted Square-Kagome Lattice
   H. Nakano, Y. Hasegawa and T. Sakai: J. Phys. Soc. Jpn. **84** (2015) 114703.
6. Evolution of the filamentary 3-Kelvin phase in Pb-Ru-Sr_2RuO_4 Josephson junction
   H. Kaneyasu, S. B. Etter, T. Sakai and M. Sigrist: Phys. Rev. B **92** (2015) 134515.
7. Quantum Phase Transition in the Three-Leg Spin Tube
   T. Sakai and H. Nakano: Physics Procedia **75** (2015) 369.
8. Exotic Field Induced Quantum Phase Transition of the Kagome Lattice Antiferromagnet
   T. Sakai and H. Nakano: Physics Procedia **75** (2015) 821.a
9. Ground-state phase diagram of an anisotropic S=1/2 ladder with alternating rung interactions
   T. Tonegawa, K. Okamoto, T. Hikihara and T. Sakai: J. Phys.: Conf. Ser. **683** (2016) 012039.
10. Effect of monomer-monomer interactions on the phase diagrams of the S=1/2 distorted diamond type quantum spin chain
    K. Okamoto, T. Tonegawa and T. Sakai: J. Phys.: Conf. Ser. **683** (2016) 012038.a
11. Quantum Spin Liquid in the Kagome-Lattice Antiferromagnet and Related Systems
    T. Sakai and H. Nakano: to appear in J. Phys.: Conf. Ser.

SAKAKIBARA, Hirofumi [B class; 800 (B), 500 (C)] ()
— *Derivation of effective model in transition metal compounds by first-principles calculation and its analysis from the view point of many body effect*

SAKASHITA, Tatsuya [B class; 700 (B), 0 (C)] (246)
— *Study of Heisenberg-Kitaev model by exact diagonalization package Rokko*

SAKATA, Kaoruho [B class; 400 (B), 300 (C)] (123)
— *Ab-initio DFT Calculations of Photocatalyst Material for Water Splitting*

SANO, Masaki [B class; 500 (B), 0 (C)] (254)
— *Absorbing phase transition and viscoleasticity of Non-Brownian suspension in Low Reynolds number fluid*

1. Rheological evaluation of colloidal dispersions using the smoothed profile method: formulation and applications
   J. Molina, K. Otomura, H. Shiba, M. Sano, and R. Yamamoto:Journal of Fluid Mechanics, **792** (2016) 590-619

SATO, Tetsuya [C class; 3000 (B), 0 (C)] ()
— *Change in magnetism of Pd(100) ultrathin films due to the modulation in the interface electric states*

SATO, Toshihiro [C class; 1000 (B), 0 (C)] (170)
— *Optical conductivity near the magnetic transition in a square-lattice Hubbard model*

1. A CDMFT study of antiferromagnetic transition in the square-lattice Hubbard model: optical conductivity and electronic structure
   Toshihiro Sato and Hirokazu Tsunetsugu: submitted to Phys. Rev. B

SATO, Yukio [B class; 300 (B), 0 (C)] (138)
— *First-principles calculation on electronic structure of thermoelectric material*

1. Grain Boundary Plane Effect on Pr Segregation Site in ZnO S13 [0001] Symmetric Tilt Grain Boundaries
   J.-Y. Roh, Y. Sato, and Y. Ikuhara, Journal of the American Ceramic Society, 98, 1932 (2015).
2. Amphoteric doping of praseodymium Pr3+ in SrTiO3 grain boundaries
   H. Yang, H. S. Lee, P. G. Kotula, Y. Sato, Y. Ikuhara, and N. D. Browning, Applied Physics Letters, 106 121904 (2015).

SHIGETA, Yasuteru [C class; 6500 (B), 1500 (C)] (202)
— *First-principles analyses on protein folding processes*
— *Theoretical Design of Heat Resistivity of Nyl C*

1. Enhanced Conformational Sampling Method for Proteins Based on the TaBoo SeArch (TBSA) Algorithm: Application to the Folding of a Mini-protein, Chignolin
   R. Harada, Y. Takano, Y. Shigeta: J. Comp. Chem. **36** (2015) 763.
2. Automatic detection of hidden dimension in Outlier FLOODing (OFLOOD) method
   R. Harada, T. Nakamura, Y. Shigeta: Chem. Phys. Lett. **639** (2015) 269.

SHIMOJO, Fuyuki [C class; 3000 (B), 2000 (C)] ()
— *First-Principles Molecular-Dynamics Study of Structural and Electronic Properties of Covalent Liquids under Pressure*

SHIMOKAWA, Tokuro [B,C class; 3500 (B), 2500 (C)] (208, 210)
— *Numerical study of the novel magnetic phenomenon on the honeycomb magnetism*
— *Numerical study of the low-lying excited state in low-dimensional frustrated magnetism*

1. Static and dynamical spin correlations of the S=1/2 random-bond antiferromagnetic Heisenberg model on the triangular and kagome lattices
   T. Shimokawa, K. Watanabe, and H. Kawamura: Phys. Rev. B **92** (2015) 134407.

SHIOMI, Junichiro [B,C class; 3200 (B), 500 (C)] (98, 225)
— *First-principles analysis on the strain effect on the thermoelectric properties of nanomaterials*
— *Characterization of thermal transport at nanostructure interface*

1. Phonon transport in perovskite SrTiO3 from first principles
   Lei Feng, Takuma Shiga, Junichiro Shiomi: Applied Physics Express Vol. 8, 071501 (2015).

SHIRAISHI, Kenji [C class; 3500 (B), 2200 (C)] (75)
— *Computational Design of SiC-Based Future Power Devices*

1. First-principles calculations for initial oxidation processes of SiC surfaces: Effect of crystalline surface orientations
   A. Ito, T. Akiyama, K. Nakamura, T. Ito, H. Kageshima, M. Uematsu, and K. Shiraishi: Jpn. J. Appl. Phys. **54**, (2015)101301.
2. 4H-SiC/SiO2 interface and its orientation dependence
   T. Akiyama, A. Ito, K. Nakamura, T. Ito, H. Kageshima, M. Uematsu, and K. Shiraishi: Surf. Sci. **641**, (2015) 174.
3. First-principles study on the origin of the unidentied positive mobile ions causing the negative bias temperature instability on SiC-MOSFET and their diffusion process
   H. Shirakawa, M. Araidai, K. Kamiya, H. Watanabe, and K. Shiraishi: Appl. Phys. Exp. in press.

SHIRAKAWA, Tomonori [C class; 4000 (B), 0 (C)] (158)
— *Density-matrix renormalization group method for quantum impurity models*

1. Density matrix renormalization group study in energy space for a single-impurity Anderson model and an impurity quantum phase transition
   T. Shirakawa and S. Yunoki: to appear in Phys. Rev. B.

SHIRO, Masanori [B class; 400 (B), 0 (C)] (257)
— *Phase transition on scale-free networks*
— *Phase transition on scale-free networks 2*

SHISHIDOU, Tatsuya [D class; 7000 (B), 1500 (C)] ()
— *First-principles study of chiral magnet Cr(NbS2)3*

SUGINO, Osamu [C class; 4000 (B), 1000 (C)] ()
— *Constant-potential simulation of electrode interfaces*

SUWA, Hidemaro [C class; 5500 (B), 0 (C)] (212, 213)
— *Spectral Analysis of Quantum Phase Transition between Competitive Magnetic Order and Lattice Order Phases*
— *Quantum Phase Transitions of One-Dimensional Spin Systems Coupling with Lattice Degrees of Freedom*

1. Generalized Moment Method for Gap Estimation and Quantum Monte Carlo Level Spectroscopy
   H. Suwa, S. Todo: Phys. Rev. Lett. **115** (2015) 080601

SUZUKI, Hideyuki [B class; 500 (B), 0 (C)] (253)
— *Analysis of deterministic Monte Carlo algorithms*

SUZUKI, Takafumi [C,D class; 10500 (B), 3200 (C)] (186)
— *Dynamical properties of honeybomb lattice magnets*
— *Mangetic excitations of the Heisenberg-Kitaev model on a honeycomb lattice*

1. Dynamical properties of Honeycomb-Lattice Iridates Na_2IrO_3
   Takafumi Suzuki, Takuto Yamada, Youhei Yamaji, and Sei-ichiro Suga: Phys. Rev. B **92**, 184411 (2015).

TADANO, Terumasa [C class; 5000 (B), 0 (C)] (85)
— *Numerical studies on anharmonic phonon properties based on density functional theory*

1. Self-consistent phonon calculations of lattice dynamical properties in cubic $SrTiO_3$ with first-principles anharmonic force constants
   T. Tadano and S. Tsuneyuki: Phys. Rev. B **92** (2015) 054301.
2. First-principles analysis of anharmonic nuclear motion and thermal transport in thermoelectric materials
   T. Tadano and S. Tsuneyuki: AIP Conf. Proc. **1702** (2015) 090063.
3. Effect of Van Hove singularities on high-T_c superconductivity in H_3S
   W. Sano, T. Koretsune, T. Tadano, R. Akashi, and R. Arita: Phys. Rev. B **93** (2016) 094525.

TAKAGI, Noriaki [B class; 400 (B), 0 (C)] (132, 134)
— *Geometric and electronic structures of honeycomb materials of heavy atoms*

1. Spectroscopic identification of Ag-terminated “multilayer silicene” grown on Ag(111)
   C.-L. Lin, T. Hagino, Y. Ito, K. Kawahara, R. Nagao, M. Aoki, S. Masuda, R. Arafune, M. Kawai and N. Takagi: J. Phys. Chem. C **120** (2016) 6689.
2. Surface phonon excitation on clean metal surfaces in scanning tunneling microscopy
   E. Minamitani, R. Arafune, N. Tsukahara, Y. Ohda, S. Watanabe, M. Kawai, H. Ueba and N. Takagi: Phys. Rev. B **93** (2016) 085411.
3. Comparison between Electronic structures of monolayer silicenes on Ag(111)
   C.-L. Lin, R. Arafune, M. Kawai and N. Takagi: Chin. Phys. B **24** (2015) 087307.

TAKANO, Yu [C class; 3500 (B), 0 (C)] (227)
— *Computational study of the mechanism of voltage sensing proteins*

TAMURA, Ryo [C class; 6500 (B), 3700 (C)] (192, 194)
— *Study on Relation between Impurity Doping and Magnetic Refrigeration Efficiency*
— *Development of a method to estimate a model Hamiltonian from observed data*

1. Estimation of magnetocaloric properties by using Monte Carlo method for AMRR cycle
   R. Arai, R. Tamura, H. Fukuda, J. Li, A. T. Saito, S. Kaji. H. Nakagome, and T. Numazawa: IOP Conference Series: Materials Science and Engineering **101** (2015) 012118.
2. Magnetic Structure of the Spin − 1/2 Frustrated Quasi-One-Dimensional Antiferromagnet Cu3Mo2O9: Appearance of a Partially Disordered State
   M. Hase, H. Kuroe, V. Yu. Pomjakushin, L. Keller, R. Tamura, N. Terada, Y. Matsushita,

A. Dönni, and T. Sekine: Physical Review B **92** (2015) 054425.

3. Phase Diagram and Sweep Dynamics of a One-Dimensional Generalized Cluster Model
   T. Ohta, S. Tanaka, I. Danshita, and K. Totsuka: Journal of the Physical Society of Japan **84** (2015) 063001.
4. Topological and dynamical properties of a generalized cluster model in one dimension
   T. Ohta, S. Tanaka, I. Danshita, and K. Totsuka: Physical Review B **93** (2015) 165423.

TANAKA, Hajime [B class; 800 (B), 500 (C)] ()
— *Hydrodynamic effects on phase ordering 3*

TANAKA, Shu [C class; 6000 (B), 3500 (C)] (199)
— *Quantum Information Processing Based on the Ising Models*
— *Study on entanglement properties in exactly solvable models*

1. Phase Diagram and Sweep Dynamics of a One-Dimensional Generalized Cluster Model
   Takumi Ohta, Shu Tanaka, Ippei Danshita, and Keisuke Totsuka: Journal of the Physical Society of Japan **84** (2015) 063001.
2. Magnetic Structure of the Spin − 1/2 Frustrated Quasi-One-Dimensional Antiferromagnet $Cu_3Mo_2O_9$: Appearance of a Partially Disordered State
   Masashi Hase, Haruhiko Kuroe, Vladimir Yu. Pomjakushin, Lukas Keller, Ryo Tamura, Noriki Terada, Yoshitaka Matsushita, Andreas Dnni, and Tomoyuki Sekine: Physical Review B **92** (2015) 054425.
3. Estimation of magnetocaloric properties by using Monte Carlo method for AMRR cycle
   R. Arai, R. Tamura, H. Fukuda, J. Li, A. T. Saito, S. Kaji. H. Nakagome, and T. Numazawa: IOP Conference Series: Materials Science and Engineering **101** (2015) 012118.
4. Topological and Dynamical Properties of a Generalized Cluster Model in One Dimension
   Takumi Ohta, Shu Tanaka, Ippei Danshita, and Keisuke Totsuka: Physical Review B **93** (2016) 165423.

TATENO, Masaru [C class; 7000 (B), 0 (C)] ()
— *Hybrid ab initio QM/MM simulations of biological macromolecular systems*

TATETSU, Yasutomi [C class; 3000 (B), 2000 (C)] (84)
— *Structural and magnetic anisotropy analyses in Fe/Cu ultra-thin films by first-principles calculation*

TATEYAMA, Yoshitaka [C class; 8500 (B), 2000 (C)] (59)
— *DFT study on electron transfer and ionic transport at solid-liquid and solid-solid interfaces*

1. First-Principles Study of Ion Diffusion In Perovskite Solar Cell Sensitizers
   Jun Haruyama, Keitaro Sodeyama, Liyuan Han, Yoshitaka Tateyama: J. Am. Chem. Soc. **137**, 10048-10051 (2015).
2. A method to calculate redox potentials relative to the normal hydrogen electrode in nonaqueous solution by using density functional theory-based molecular dynamics
   Ryota Jono, Yoshitaka Tateyama, Koichi Yamashita: Phys. Chem. Chem. Phys. **17**, 27103-27108 (2015).
3. Near-Shore Aggregation Mechanism of Electrolyte Decomposition Products to Explain Solid Electrolyte Interphase Formation
   Keisuke Ushirogata, Keitaro Sodeyama, Zdenek Futera, Yoshitaka Tateyama, Yukihiro Okuno: J. Electrochem. Soc. **162**, A2670-A2678 (2015).
4. Investigating crystalline-polarity-dependent electronic structures of GaN by hard x-ray photoemission and ab-initio calculations
   Takeo Ohsawa, Shigenori Ueda, Motohiro Suzuki, Yoshitaka Tateyama, Jesse R. Williams, Naoki Ohashi: Appl. Phys. Lett. **107**, 171604 (2015).
5. Corrosion Prevention Mechanism of Aluminum Metal in Superconcentrated Electrolytes
   Yuki Yamada, Ching Hua Chiang, Keitaro Sodeyama, Jianhui Wang, Yoshitaka Tateyama, Atsuo Yamada: ChemElectroChem. **2**, 1687-1694 (2015).
6. Conservation of the pure adiabatic state in Ehrenfest dynamics of the photoisomerization of

molecules
Yoshiyuki Miyamoto, Yoshitaka Tateyama, Norihisa Oyama, Takahisa Ohno: Sci. Rep. **5**, 18220 (2015).

7. First-principles study on the cosensitization effects of Ru and squaraine dyes on a TiO2 surface
   Yusuke Ootani, Keitaro Sodeyama, Liyuan Han, Yoshitaka Tateyama: Surf. Sci. **649**, 66-71 (2016).
8. Sodium-Ion Intercalation Mechanism in MXene Nanosheets
   Satoshi Kajiyama, Lucie Szabova, Keitaro Sodeyama, Hiroki Iinuma, Ryohei Morita, Kazuma Gotoh, Yoshitaka Tateyama, Masashi Okubo, Atsuo Yamada: ACS Nano **10**, 3334-3341 (2016).
9. Life of superoxide in aprotic Li–O2 battery electrolytes: simulated solvent and counter-ion effects
   Johan Scheers, D. Lidberg, Keitaro Sodeyama, Zdenek Futera, Yoshitaka Tateyama: Phys. Chem. Chem. Phys. **18**, 9961-9968 (2016).
10. Decomposition of the fluoroethylene carbonate additive and the glue effect of lithium fluoride products for the solid electrolyte interphase: an ab initio study
    Yukihiro Okuno, Keisuke Ushirogata, Keitaro Sodeyama, Yoshitaka Tateyama: Phys. Chem. Chem. Phys. **18**, 8643-8653 (2016).

TERAO, Takamichi [B class; 1100 (B), 800 (C)] (239)
— *Numerical study of semiconductor nanocrystals*

1. Vibrational properties of acoustic metamaterial multilayers
   T. Terao and Y. Ohnishi: J. Appl. Phys. **117** (2015) 134305.
2. Structural formation of dendritic polymer brushes: analysis using an explicit solvent model
   T. Terao: Chem. Lett. **44** (2015) 1092.

TODO, Synge [C class; 8500 (B), 1800 (C)] (191)
— *Entanglement and Quantum Phase Transition in Quantum Spin Systems*

1. Generalized Moment Method for Gap Estimation and Quantum Monte Carlo Level Spectroscopy
   H. Suwa, S. Todo, Phys. Rev. Lett. **115**, 080601 (2015)
2. Stochastic approximation of dynamical exponent at quantum critical point
   S. Yasuda, H. Suwa, S. Todo, Phys. Rev. B **92**, 104411 (2015)

TOHYAMA, Takami [C class; 3500 (B), 2200 (C)] (211)
— *Study of Quantum Phases in Triangular Kitaev-Heisenberg Model*

1. Photoinduced In-Gap States in the One-Dimensional Extended Hubbard Model
   H. Lu, C. Shao, J. Bonca, D. Manske and T. Tohyama: Phys. Rev. B **91**, (2015) 245117.
2. Orbital-selective electronic excitations in iron arsenides revealed by simulated nonresonant inelastic x-ray scattering
   K. Tsutsui, E. Kaneshita, and T. Tohyama: Phys. Rev. B **92**, (2015) 195103.
3. Quasi-Spin Correlations in a Frustrated Quantum Spin Ladder
   T. Sugimoto, M. Mori, T. Tohyama, and S. Maekawa: Physics Procedia **75**, (2015) 861.
4. Density-matrix renormalization group study of Kitaev-Heisenberg model on the triangular lattice
   K. Shinjo, S. Sota, S. Yunoki, K. Totsuka, and T. Tohyama: submitted to Phys. Rev. B.

TOMITA, Yusuke [C class; 4000 (B), 0 (C)] (222)
— *Numerical study of dynamics in spin glass models with long-range interactions*

TONEGAWA, Takashi [B,C class; 2000 (B), 0 (C)] (236)
— *Numerical Study of the One-Dimensional Quantum Spin Systems with Spatial Structures*

1. Effect of Monomer-Monomer Interactions on the Phase Diagrams of the $S = 1/2$ Distorted Diamond Type Quantum Spin Chain
   K. Okamoto, T. Tonegawa, and T. Sakai: J. Phys.: Conf. Series **683** (2016) 012038.
2. Ground-State Phase Diagram of an Anisotropic $S = 1/2$ Ladder with Alternating Rung Interactions
   T. Tonegawa, K. Okamoto, T. Hikihara, and T. Sakai: J. Phys.: Conf. Series **683** (2016) 012039.
3. Ground-State Phase Diagram of the Bond-Alternating $S = 2$ Quantum Spin Chain with the XXZ

and On-Site Anisotropies —Symmetry Protected Topological Phase versus Trivial Phase—
K. Okamoto, T. Tonegawa, and T. Sakai: submitted to J. Phys. Soc. Jpn.; arXiv:1604.00452

TSUNEYUKI, Shinji [C class; 5000 (B), 2500 (C)] (67)
— *Development and Application of First-Principles Simulation of Material Structure and Electronic Properties*

1. Iterative diagonalization of the non-Hermitian transcorrelated Hamiltonian using a plane-wave basis set: Application to sp-electron systems with deep core states
   M. Ochi, Y. Yamamoto, R. Arita, and S. Tsuneyuki, J. Chem. Phys. **144**, 104109 (2016).
2. Self-consistent phonon calculations of lattice dynamical properties in cubic $SrTiO_3$ with first-principles anharmonic force constants
   T. Tadano and S. Tsuneyuki, Phys. Rev. B **92**, 054301 (2015).
3. Second-order Møller-Plesset perturbation theory for the transcorrelated Hamiltonian applied to solid-state calculations
   M. Ochi and S. Tsuneyuki, Chem. Phys. Lett. **621**, 177 (2015). (selected as Editor's Choice)
4. Impact of Rattlers on Thermal Conductivity of a Thermoelectric Clathrate: A First-Principles Study
   T. Tadano, Y. Gohda, and S. Tsuneyuki, Phys. Rev. Lett. **114**, 095501 (2015).

TSURUTA, Kenji [B class; 600 (B), 0 (C)] (125)
— *Ab Initio Simulation of SiC Nanocluster for High-temperature Oxidation and Water Splitting*

UCHIDA, Kazuyuki [C class; 1000 (B), 2200 (C)] (100)
— *First-Principles Study of Moire Patterns in Atomic Layers*

UCHIDA, Takashi [B class; 100 (B), 0 (C)] (142)
— *Theory of magnetic alloys with octahedral frustration*

1. First-principles molecular spin dynamics study on the magnetic structure of Mn-based alloys with Cu_3Au-type crystal structure
   T. Uchida, Y. Kakehashi, and N. Kimura: J. Magn. Magn. Mater. **400** (2016) 103.

UDA, Yutaka [B class; 200 (B), 0 (C)] (139)
— *Wear mechanism of diamond tool*

WATANABE, Hiroshi [C class; 3000 (B), 2000 (C)] (214)
— *Molecular dynamics study on polymer drag reduction effect*

1. Direct Observation of Kinetic Equation in Bubble Coarsening
   Hiroshi Watanabe, Hajime Inaoka, and Nobuyasu Ito: submitted to J. Chem. Phys.

WATANABE, Hiroshi [B class; 300 (B), 0 (C)] (176)
— *Exciton condensation, CDW, and superconductivity induced by cooperation and competition between Coulomb interaction and electron-lattice interaction*

1. A variational Monte Carlo study of exciton condensation
   H. Watanabe, K. Seki, and S. Yunoki: J. Phys.: Conf. Ser. **592** (2015) 012097.
2. Charge-density wave induced by combined electron-electron and electron-phonon interactions in $1T$-$TiSe_2$: A variational Monte Carlo study
   H. Watanabe, K. Seki, and S. Yunoki: Phys. Rev. B **91** (2015) 205135.

WATANABE, Kazuyuki [C class; 5000 (B), 0 (C)] (82)
— *First-Principles Study of Excited Electronic States and Dynamics of Nanostructures under External Fields*

1. Energetics and dynamics of laser-assisted field evaporation: Time-dependent density functional theory simulations
   Elena P. Silaeva, K. Uchida, Y. Suzuki, K. Watanabe, Phys. Rev. B **92**, 155401 (2015).
2. Spin-polarized annihilation lifetime of positron of d0 ferromagnetism in gallium nitride: A twocom-

ponent density functional theory simulation
S. Hagiwara, Y. Suzuki, and K. Watanabe, Appl. Phys. Express **9**, 041001 (2016).
3. Electrostatic-field enhancement photoexfoliation of bilayer benzene: a first-principles study
K. Uchida, E. P. Silaeva, and K. Watanabe, to appear in Appl. Phys. Express.

WATANABE, Satoshi [C class; 3000 (B), 2000 (C)] (80)
— *Theoretical Analyses on Ionic Transport Properties Electrical Properties, and Interfacial Electronic States of Nanostructures*

1. The electronic structure of quasi-free-standing germanene on monolayer MX (M = Ga, In; X = S, Se, Te)
Z. Ni, E. Minamitani, Y. Ando and S. Watanabe: Phys. Chem. Chem. Phys. **17** (2015) 19039.
2. Electronic and magnetic effects of a stacking fault in cobalt nanoscale islands on the Ag(111) surface
K. Doi, E. Minamitani, S. Yamamoto, R. Arafune, Y. Yoshida, S. Watanabe and Y. Hasegawa: Phys. Rev. B **92** (2015) 064421.
3. Spatially extended underscreened Kondo state from collective molecular spin
E. Minamitani, Y.-S. Fu, Q.-K. Xue, Y. Kim and S. Watanabe: Phys. Rev. B 92 (2015) 075144.
4. First-principles calculation of charged capacitors under open-circuit conditions using the orbital-separation approach
S. Kasamatsu, S. Watanabe and S. Han: Phys. Rev. B **92** (2015) 115124.
5. Materials Search of Perovskite Cathode in SOFC by Statistical Analysis
J. Hwang, Y. Ando and S. Watanabe: ECS Trans.**68** (2015) 549.
6. Emergence of Negative Capacitance in Multidomain Ferroelectric-Paraelectric Nanocapacitors at Finite Bias
S. Kasamatsu, S. Watanabe, C. S. Hwang and S. Han: Adv. Mater. **28** (2016) 335.
7. DFT calculations on atom-specific electronic properties of G/SiC (0001)
M. Kajihara, T. Suzuki, S. M. F. Shahed, T. Komeda, E. Minamitani and S. Watanabe: Surf. Sci. **647** (2016) 39.
8. First-principles study of metal insulator control by ion adsorption on Ti_2C MXene dioxide monolayers
Y. Ando and S. Watanabe: Appl. Phys. Express **9** (2016) 015001.
9. Surface phonon excitation on clean metal surfaces in scanning tunneling microscopy
E. Minamitani, R. Arafune, N. Tsukahara, Y. Ohda, S. Watanabe, M. Kawai, H. Ueba and N. Takagi: Phys. Rev. B **93** (2016) 085411.
10. マテリアルズ・インフォマティクスによる分子電気伝導シミュレーション解析の試み
安藤 康伸, 藤掛 壮 and 渡邉 聡: 表面科学 **36** (2015) 515.
11. スパースモデリングによるナノデバイスシミュレーション解析
安藤康伸, 藤掛 壮, W. Li and 渡邉 聡: 電子情報通信学会誌, 印刷中.

YABANA, Kazuhiro [C,E class; 24500 (B), 0 (C)] (49)
— *First-principles calculation of interactions between extreme pulse light and matter*

1. Controlling ultrafast currents by the non-linear photogalvanic effect
G. Wachter, S.A. Sato, C. Lemell, X.M. Tong, K. Yabana, J. Burgdoerfer: New J. Phys. **17** (2015) 123026.
2. Protocol for observing molecular dipole excitations by attosecond self-streaking
G. Wachter, S. Nagele, S.A. Sato, R. Pazourek, M. Wais, C. Lemell, X.-M. Tong, K. Yabana, J. Burgdoerfer: Phys. Rev. **A92** (2015) 061403.
3. Nonlinear electronic excitations in crystalline solids using meta-generalized gradient approximation and hybrid functional in time-dependent density functional theory
S.A. Sato, Y. Taniguchi, Y. Shinohara, K. Yabana: J. Chem. Phys. **143** (2015) 224116.

YAMADA, Atsushi [C class; 1000 (B), 0 (C)] (169)
— *Magnetic properties and spin liquids in the strongly correlated electron systems*

1. Magnetic properties and Mott transition of the Hubbard model for weakly coupled chains on the anisotropic triangular lattice

A. Yamada: Phys. Rev. B**90** (2014) 235138.

2. Magnetic phase diagram and Mott transition of the half-filled 1/5-depleted Hubbard model with frustration
   A. Yamada: Phys. Rev. B**90** (2014) 245139.

YAMASHITA, Koichi [C class; 2000 (B), 0 (C)] (102)
— *Large scale ab initio calculations on the fundamental processes of energy convergence devices and on their optimization for high conversion efficiency*

1. The Mechanism of Slow Hot-Hole Cooling in Lead-Iodide Perovskite: First-Principles Calculation on Carrier Lifetime from Electron—Phonon Interaction
   H. Kawai, G. Giorgi, A. Marini, and K. Yamashita: Nano Lett. **15** (2015) 3103.
2. Alternative, lead-free, hybrid organic-inorganic perovskites for solar applications: a DFT analysis
   G. Giorgi, K. Yamashita: Chem. Lett. **44** (2015) 826.
3. A Density Functional Tight Binding Study of Acetic Acid Adsorption on Crystalline and Amorphous Surfaces of Titania
   S. Manzhos, G. Giorgi, K. Yamashita: Molecules **20** (2015) 3371.
4. Theoretical studies on the mechanism of oxygen reduction reaction on clean and O-substituted Ta3N5(100) surfaces
   E. Watanabe, H. Ushiyama and K. Yamashita: Catal. Sci. Technol. **5** (2015) 2769.
5. Theoretical studies on the absorption spectra of cis-[Ru(4,4´ -COO-2,2´ -bpy)2(X)2]4 −, (X = NCS, Cl) and panchromatic trans-terpyridyl Ru complexes including strong spin—orbit coupling
   K. Mishima, T. Kinoshita, M. Hayashi, R. Jono, H. Segawa, K. Yamashita, and S. H. Lin de: Phys. Chem. Chem. Phys. **20** (2015) 9732.
6. Theoretical Verification of Photoelectrochemical Water Oxidation Using Nanocrystalline TiO2 Electrodes
   S. Yanagida, S. Yanagisawa, K. Yamashita, R. Jono, and H. Segawa: Molecules **20** (2015) 9732.
7. A Method to Calculate Redox Potentials Relative to the Normal Hydrogen Electrode in Nonaqueous Solution by using Density Functional Theory-Based Molecular Dynamics
   R. Jono, Yoshitaka Tateyama, and K. Yamashita: Phys. Chem. Chem. Phys. **17** (2015) 27103.
8. Energy Alignment of Frontier Orbitals and Suppression of Charge Recombinations in P3HT/SWNT
   K. Nishimra, M. Fujii, R. Jono, and K. Yamashita: J. Phys. Chem. C **119** (2015) 26258.
9. Remarkable Dependence of the Final Charge Separation Efficiency on the Donor—Acceptor Interaction in Photoinduced Electron Transfer
   T. Higashino, T. Yamada, M. Yamamoto, A. Furube, N. V. Tkachenko, T. Miura, Y. Kobori, R. Jono, K. Yamashita and H. Imahori: Angew. Chem. Int. Ed. **54** (2015) 629.
10. Quantum-classical correspondence in steady states of nonadiabatic systems
    M. Fujii and K. Yamashita: AIP Conf. Proc. **1702** (090051) 2015.
11. Theoretical investigation of [Ru(tpy)2]2+, [Ru(tpy)(bpy)(H2O)]2+, and [Ru(tpy)(bpy)(Cl)]+ complexes in acetone revisited: Inclusion of strong spin-orbit couplings to quantum chemistry calculations
    K. Mishima, T. Kinoshita, M. Hayashi, R. Jono, H. Segawa, and K. Yamashita: J. Theor. Comput. Chem. **15** (2016) 1650001.
12. Dipole Analyses for Short-Circuit Current in Organic Photovoltaic Devices of Diketopyrrolopyrrole-Based Donor and PCBM
    Shohei Koda, M. Fujii, Shintaro Hatamiya, K. Yamashita: Theor. Chem. Acc. **135** (2016) 115.
13. Photon-absorbing charge-bridging states in organic bulk heterojunctions consisting of diketopyrrolopyrrole derivatives and PCBM
    M. Fujii, Woong Shin, Takuma Yasuda, and K. Yamashita: Phys. Chem. Chem. Phys. **18** (2016) 9514.
14. Atomic-Scale Analysis of the RuO2/Water Interface under Electrochemical Conditions
    E. Watanabe, J. Rossmeisl, M. E. Björketun, H. Ushiyama, and K. Yamashita: J. Phys. Chem. C **120** (2016) 8096.

YAMAUCHI, Jun [B class; 600 (B), 100 (C)] (122)
— *First-principles study on the defects in semiconductors*

1. X-ray photoelectron spectroscopy analysis of boron defects in silicon crystal: a first-principles study
   J. Yamauchi, Y. Yoshimoto, and Y. Suwa: J. Appl. Phys. in press.

YAMAUCHI, Kunihiko [C class; 7000 (B), 3300 (C)] (61)
— *Materials design toward spin-valleytronics by using ferroelectric oxides*

1. Coupling Ferroelectricity with Spin-Valley Physics in Oxide-Based Heterostructures
   Kunihiko Yamauchi, Paolo Barone, Tatsuya Shishidou, Tamio Oguchi, and Silvia Picozzi: Phys. Rev. Lett. 115, 037602/1-5 (2015).
2. Superexchange interaction in the A-site ordered perovskite YMn3Al4O12
   Masayuki Toyoda, Takashi Saito, Kunihiko Yamauchi, Yuichi Shimakawa, and Tamio Oguchi: Phys. Rev. B 92, 014420/1-7 (2015).
3. Jahn-Teller distortions as a novel source of multiferroicity
   Paolo Barone, Kunihiko Yamauchi, and Silvia Picozzi: Phys. Rev. B 92, 014116/1-6 (2015).
4. A-site-driven ferroelectricity in strained ferromagnetic La2NiMnO6 thin film
   R. Takahashi, I. Ohkubo, K. Yamauchi, M. Kitamura, Y. Sakurai, M. Oshima, T. Oguchi, Y. Cho, and M. Lippmaa: Phys. Rev. B 91, 134107/1-9 (2015).

YANAGISAWA, Susumu [B,C class; 7600 (B), 2200 (C)] (62)
— *Theoretical investigation of spin polarization induced at the organic-metal interfaces*
— *Theoretical investigation on electronic properties of organic solids*

1. Recent progress in predicting structural and electronic properties of organic solids with the van der Waals density functional
   S. Yanagisawa, K. Okuma, T. Inaoka and I. Hamada: J. Electron Spectrosc. Relat. Phenom. **204** (2015) 159
2. Theoretical Study on Electronic Structure of Bathocuproine: Renormalization of the Band Gap in the Crystalline State and the Large Exciton Binding Energy
   S. Yanagisawa, S. Hatada and Y. Morikawa: J. Chin. Chem. Soc. *in press*
3. Charge transfer states appear in the π-conjugated pure hydrocarbon molecule on Cu(111)
   K. Yonezawa, Y. Suda, S. Yanagisawa, T. Hosokai, K. Kato, T. Yamaguchi, H. Yoshida, N. Ueno and S. Kera: Appl. Phys. Express **9** (2016) 045201

YANAGISAWA, Takashi [B class; 800 (B), 700 (C)] (161)
— *Numerical study of correlated electron systems by quantum Monte Carlo and first-principles calculations*
— *Quantum Monte Carlo study of strongly correlated electron systems*

1. High Temperature Superconductivity from Strong Correlation
   T. Yanagisawa: Physics Procedia 65 (2015) 5.
2. The Absence of CDW order in PbSb, and its unexpected softness
   I. Hase, K. Yasutomi, T. Yanagisawa, K. Odagiri and T. Nishio: Physics Procedia 65 (2015) 36.
3. Dirac fermions and Kondo effect
   T. Yanagisawa: JPS Conference Ser. 603 (2015) 012014.
4. Kondo effect in Dirac systems
   T. Yanagisawa: Journal of the Physical Society of Japan 84 (2015) 074705.
5. Superconductivity from strong correlation in high-temperature superconductors
   T. Yanagisawa, M. Miyazaki and K. Yamaji: J. Superconductivity Novel Magnetism 29 (2015) 655.
6. Superconductivity, antiferromagnetism and kinetic correlation in strongly correlated electron systems
   T. Yanagisawa: Adv. Cond. Matt. Phys. 2015 (2015) 141263.
7. Chiral sine-Gordon model
   T. Yanagisawa: EPL 113 (2016) 41001.
8. Electronic Structure of $\mathrm{SnF_3}$: An Example of Valence Skipper which Forms Charge-Density Wave
   I. Hase, T. Yanagisawa and K. Kawashima: Physica C521 (2016) in press.
9. Duality in Spin Fluctuations in Correlated Electron Systems

T. Yanagisawa and I. Hase: Physica C521 (2016) in press.

YASUDA, Chitoshi [B class; 400 (B), 0 (C)] (256)
— *Phase Transition in Quantum Spin Systems Coupled to Lattice Degrees of Freedom*

YASUNO, Satoshi [E class; 6000 (B), 0 (C)] ()
— *First-Principles Study of the Structure of a-*$InGaZnO_4$

YASUOKA, Kenji [C class; 5000 (B), 0 (C)] (78)
— *The role of the negatively charged oxygen vacancy in the chemisorption process of oxygen molecules on TiO2 (110)*

YOSHIDA, Tsuneya [C class; 6000 (B), 0 (C)] (151)
— *Study of correlation effects on topological phases*

1. Local origin of the pseudogap in the attractive Hubbard model.
   Robert Peters and Johannes Bauer: Phys. Rev. B **92**, (2015) 014511.
2. Large and small Fermi-surface spin density waves in the Kondo lattice model
   Robert Peters and Norio Kawakami: Phys. Rev. B **92**, (2015) 075103.
3. Large and small Fermi-surface spin density waves in the Kondo lattice model
   Robert Peters and Norio Kawakami: Phys. Rev. B **92**, (2015) 075103.
4. Coexistence of light and heavy surface states in the topological Kondo insulator SmB_6
   Tsuneya Yoshida, Robert Peters, Hirohumi Sakakibara, and Norio Kawakami: arXiv:1510.06476.

YOSHIMOTO, Yoshihide [B class; 800 (B), 200 (C)] (112)
— *Development of first-principles electronic structure calculation package xTAPP*

1. X-ray photoelectron spectroscopy analysis of boron defects in silicon crystal: a first-principles study
   Jun Yamauchi, Yoshihide Yoshimoto, and Yuji Suwa: J. Appl. Phys. accepted.

ZHONGCHANG, Wang [C class; 2000 (B), 1000 (C)] ()
— *First-principles investigation of functional interfaces in metallic oxides*

□ CMSI Projects

ASAI, Yoshihiro [R class; 10000 (B), 0 (C)] (287)

— *Large scale computational simulations of non-equilibrium transport phenomena*

1. Thermoelectric effect and its dependence on molecular length and sequence in single DNA molecules
   Y. Li, L. Xiang, J.L. Palma, Y. Asai and NJ Tao: Nature Communications, **7** (2016) 11294.
2. Competitive effects of oxygen vacancy formation and interfacial oxidation on an ultra-thin HfO2-based resistive switching memory: beyond filament and charge hopping models
   H. Nakamura and Y. Asai: Phys. Chem. Chem. Phys., **18** (2016) 8820.
3. The effect of a Ta oxygen scavenger layer on HfO2-based resistive switching behavior: thermodynamic stability, electronic structure, and low-bias transport
   X. Zhong, I. Rungger, P. Zapol, H. Nakamura, Y. Asai and O. Heinonen: Phys. Chem. Chem. Phys., **18** (2016) 7502.
4. Thermoelectricity at the molecular scale: a large Seebeck effect in endohedral metallofullerenes
   S.-K. Lee, M. Bürkle, R. Yamada, Y. Asai and H. Tada: Nanoscale, **7** (2015) 20497.
5. Towards multiple conductance pathways with heterocycle-based oligo (phenyleneethynylene) derivatives
   D. Miguel, L. Á. de Cienfuegos, A. Martín-Lasanta, S.P. Morcillo, L.A. Zotti, E. Leary, M. Bürkle, Y. Asai, R. Jurado, D.J. Cárdenas, G. Rubio-Bollinger, N. Agraït, J.M. Cuerva, and M.T. González: J. Am. Chem. Soc., **137** (2015) 13818.
6. Single-molecule conductance of a chemically modified, π-extended tetrathiafulvalene and its charge-transfer complex with F_4TCNQ
   R. García, M. Á. Herranz, E. Leary, M.T. González, G. Rubio- Bollinger, M. Bürkle, L.A. Zotti, Y. Asai, F. Pauly, J.C. Cuevas, N. Agraït and N. Martín: Beilstein J. Org. Chem., **11** (2015) 1068.
7. First-principles calculation of the thermoelectric figure of merit for [2,2] paracyclophane-based single-molecule junctions
   M. Bürkle, T.J. Hellmuth, and Y. Asai: Phys. Rev. B, **91** (2015) 165419.
8. Vibronic spectroscopy using current noise
   Y. Asai: Phys. Rev. B, **91** (2015) 165402(R).

IMADA, Masatoshi [R class; 10000 (B), 10000 (C)] (264)

— *Superconducting Mechanism Driven by Both Electron-Phonon and Strong Electron Correlations*

1. *Ab initio* Studies on Magnetism in the Iron Chalcogenides FeTe and FeSe
   Motoaki Hirayama, Takahiro Misawa, Takashi Miyake, Masatoshi Imada: J. Phys. Soc. Jpn. **84** (2015) 093703.
2. Hidden fermionic excitation in the superconductivity of the strongly attractive Hubbard model
   Shiro Sakai, Marcello Civelli, Yusuke Nomura, and Masatoshi Imada: Phys. Rev. B **92** (2015) 180503.
3. Exciton Lifetime Paradoxically Enhanced by Dissipation and Decoherence: Toward Efficient Energy Conversion of a Solar Cell
   Yasuhiro Yamada, Youhei Yamaji, and Masatoshi Imada: Phys. Rev. Lett. **115** (2015) 197701.
4. Time-dependent many-variable variational Monte Carlo method for nonequilibrium strongly correlated electron systems
   Kota Ido, Takahiro Ohgoe, and Masatoshi Imada: Phys. Rev. B **92** (2015) 245106.
5. Hidden Fermionic Excitation Boosting High-Temperature Superconductivity in Cuprates
   Shiro Sakai, Marcello Civelli, Yusuke Nomura, and Masatoshi Imada: Phys. Rev. Lett. **116** (2016) 057003.
6. Finite-Temperature Variational Monte Carlo Method for Strongly Correlated Electron Systems
   Kensaku Takai, Kota Ido, Takahiro Misawa, Youhei Yamaji, and Masatoshi Imada: J. Phys. Soc. Jpn. 85 (2016) 034601.
7. Tensor network algorithm by coarse-graining tensor renormalization on finite periodic lattices
   Hui-Hai Zhao, Zhi-Yuan Xie, Tao Xiang, and Masatoshi Imada: Phys. Rev. B **93** (2016) 125115.

8. Real-space renormalized dynamical mean field theory
   Dai Kubota, Shiro Sakai, Masatoshi Imada: to appear in Phys. Rev. B.
9. Clues and criteria for designing Kitaev spin liquid revealed by thermal and spin excitations of honeycomb iridates Na_2IrO_3
   Youhei Yamaji, Takafumi Suzuki, Takuto Yamada, Sei-ichiro Suga, Naoki Kawashima, and Masatoshi Imada: submitted to Phys. Rev. B.
10. Modulated Helical Metals at Magnetic Domain Walls of Pyrochlore Iridium Oxides
    Youhei Yamaji, Masatoshi Imada: submitted to Phys. Rev. B.
11. Stabilization of Topological Insulator Emerging from Electron Correlations on Honeycomb Lattice and Its Possible Relevance in Twisted Bilayer Graphene
    Moyuru Kurita, Youhei Yamaji, Masatoshi Imada: submitted to Phys. Rev. B.
12. Clues and criteria for designing Kitaev spin liquid revealed by thermal and spin excitations of honeycomb iridates Na_2IrO_3
    Youhei Yamaji, Takafumi Suzuki, Takuto Yamada, Sei-ichiro Suga, Naoki Kawashima, and Masatoshi Imada : submitted to Phys. Rev. B.

KAWASHIMA, Naoki [R class; 10000 (B), 10000 (C)] (267)
— *Monte Carlo Study of Novel Quantum Phases and Critical Phenomena*
— *Study of Novel Quantum Phases and Critical Phenomena by Monte Carlo Method and Tensor Network*

1. SU(N) Heisenberg model with multicolumn representations
   Tsuyoshi Okubo, Kenji Harada, Jie Lou, Naoki Kawashima: Phys. Rev. B **92** (2015) 134404/1-5.
2. Scaling relation for dangerously irrelevant symmetry-breaking fields
   Tsuyoshi Okubo, Kosei Oshikawa, Hiroshi Watanabe, Naoki Kawashima : Phys. Rev. B **91** (2015) 174417/1-4.

NAKANO, Hiroki [R class; 5000 (B), 4000 (C)] (283)
— *Computational-Science Study of Frustrated Magnets*

1. Magnetization Process of the Spin-S Kagome-Lattice Heisenberg Antiferromagnet
   H. Nakano and T. Sakai: J. Phys. Soc. Jpn. **84** (2015) 063705.
2. Magnetization Jump in the Magnetization Process of the Spin-1/2 Heisenberg Antiferromagnet on a Distorted Square-Kagome Lattice
   H. Nakano, Y. Hasegawa, and T. Sakai: J. Phys. Soc. Jpn. **84** (2015) 114703.
3. Novel Quantum Phase Transition in the Frustrated Spin Nanotube
   T. Sakai and H. Nakano: Physics Procedia **75** (2015) 369.
4. Exotic Field Induced Quantum Phase Transition of the Kagome Lattice Antiferromagnet
   T. Sakai and H. Nakano: Physics Procedia **75** (2015) 821.

NOBUSADA, Katsuyuki [R class; 10000 (B), 10000 (C)] (274)
— *Prediction of electronic properties in spatiotemporal nano-field based on the density functional theory*

1. Reducing the Cost and Preserving the Reactivity in Noble-Metal-Based Catalysts: Oxidation of CO by Pt and Al–Pt Alloy Clusters Supported on Graphene
   K. Koizumi, K. Nobusada and M. Boero: Chem. Eur. J. **22**, 5181–5188 (2016).
2. Reaction Pathway and Free Energy Landscape of Catalytic Oxidation of Carbon Monoxide Operated by a Novel Supported Gold–Copper Alloy Cluster
   K. Koizumi, K. Nobusada and M. Boero: J. Phys. Chem. C **119**, 15421–15427 (2015).

OGATA, Shuji [R class; 5000 (B), 6000 (C)] (269)
— *Multi-scale simulation of nano-structured materials from electronic to mechanical properties*

1. A Molecular Dynamics Study on Thermal Conductivity of Thin Epoxy Polymer Sandwiched Between Alumina Fillers in Heat-dissipation Composite Material
   K. Tanaka, S. Ogata, R. Kobayashi, T. Tamura, and T. Kouno: Int. J. Heat and Mass Transfer **89** (2015) 714-723.
2. Thermal Diffusion of Correlated Li-ions in Graphite: A Hybrid Quantum-Classical Simulation Study
   N. Ohba, S. Ogata, T. Kouno, and R. Asahi: Comp. Mater. Sci. **108** (2015) 250-257.

3. Enhanced Si-O Bond Breaking in Silica Glass by Water Dimer: A Hybrid Quantum-Classical Simulation Study
   T. Kouno, S. Ogata, T. Shimada, T. Tamura, and R. Kobayashi: J. Phys. Soc. Jpn., in press.

OHNO, Kaoru [R class; 10000 (B), 10000 (C)] (282)
— *All electron spectra and dynamics of functional materials from nanoclusters to crystals*

1. Phase Transition of $S = 1/2$ Heisenberg Antiferomagnet
   S. Ono, Y. Noguchi, R. Sahara, Y. Kawazoe, and K. Ohno: Comp. Phys. Comm. **189**, 20-30 (2015).
2. Geometry Dependence of Electronic and Energetic Properties of One-Dimensional Peanut-Shaped Fullerene Polymers
   Y. Noda, S. Ono, and K. Ohno: J. Phys. Chem. A **119**, 3048-3055 (2015).
3. Capped carbon nanotube photovoltaic cells: Influence of distribution of the five-membered rings on the efficiency
   S. Ono, K. Tanikawa, R. Kuwahara, and K. Ohno: Diamond Related Mater. **58**, 24-30 (2015).
4. All-electron GW calculation of rutile TiO_2 with and without Nb impurities
   M. Zhang, S. Ono, and K. Ohno: Phys. Rev. B **92**, 035205;1-7 (2015).
5. All-electron GW calculation of rutile TiO2 with and without Nb impurities
   S. Ono and K. Ohno: Phys. Rev. B **93**, 121301(R);1-5 (2016).
6. All-electron mixed basis GW calculations of TiO_2 and ZnO crystals
   M. Zhang, S. Ono, N. Nagatsuka, and K. Ohno: Phys. Rev. B **93**, 155116;1-9 (2016).
7. Ab initio molecular dynamics simulation study of successive hydrogenation reactions of carbon monoxide producing methanol
   T. N. Pham, S. Ono, and K. Ohno: J. Chem. Phys. **144**, 144309;1-6 (2016).
8. Tomonaga-Luttinger liquid theory for metallic fullerene polymers
   H. Yoshioka, H. Shima, Y. Noda, S. Ono, and K. Ohno: Phys. Rev. B **93**, 165431;1-10 (2016).

OKAZAKI, Susumu [R class; 10000 (B), 10000 (C)] (276)
— *Molecular Science of Virus by All-Atom Simulation*

1. A molecular dynamics study of intramolecular proton transfer reaction of malonaldehyde in solutions based upon mixed quantum-classical approximation. II. Proton transfer reaction in neon
   H. Kojima, A. Yamada, and S. Okazaki: J. Chem. Phys. **142**, 174502 (2015).
2. Free energy surface for rotamers of cis-enol malonaldehyde in aqueous solution studied by molecular dynamics calculations
   H. Kojima, A. Yamada, and S. Okazaki: Mol. Simul. **41**, 850–856 (2015).
3. Molecular dynamics study of changes in physic-chemical properties of DMPC lipid bilayers by addition of nonionic surfactant $C_{12}E_{10}$
   Y. Andoh, S. Muraoka and S. Okazaki: Mol. Simul. **41**, 955–960 (2015). @@
4. Molecular dynamics study of lipid bilayers modeling the plasma membranes of mouse hepatocytes and hepatomas
   Y Andoh, N Aoki, and S Okazaki: J. Chem. Phys. **144**, 085104 (2016).

OKUBO, Tsuyoshi [R class; 5000 (B), 4000 (C)] (285)
— *Ordering of topological excitations of the frustrated magnets*

1. Scaling Relation for Dangerously Irrelevant Symmetry-Breaking Fields
   T. Okubo, K. Oshikawa, H. Watanabe, and N. Kawashima: Phys. Rev. B **91** (2015) 174417.
2. $SU(N)$ Heisenberg model with multi-column representations
   T. Okubo, K. Harada, J. Lou, and N. Kawashima: Phys. Rev. B **92** (2015) 134404.
3. Experimental Realization of a Quantum Pentagonal Lattice
   H. Yamaguchi, T. Okubo, S. Kittaka, T. Sakakibara, K. Araki, K. Iwase, N. Amaya, T. Ono, and Y. Hosokoshi: Scientific Reports, **5** (2015) 15327.

OSHIYAMA, Atsushi [R class; 10000 (B), 10000 (C)] ()
— *Density-Functional Study on Prediction of Electronic Properties of Spatiotemporal Fields in Nanostructures*

OTANI, Minoru [R class; 5000 (B), 10000 (C)] (281)
— *First-principles simulations of electrode-electrolyte interfaces in secondary batteries with a bias-control technique*
— *First-principlemolecular dynamics study toward a high performance Li-ion battery*

SAITO, Mineo [R class; 10000 (B), 10000 (C)] (272)
— *Materials design for spintronics/multiferroics applications*

1. Spin-split bands of metallic hydrogenated ZnO (101¯0) surface: First-principles study
   Moh. Adhib Ulil Absor, Fumiyuki Ishii, Hiroki Kotaka, and Mineo Saito, AIP Advances, **6** (2016) 025309.
2. First-principles calculations of multivacancies in germanium
   Sholihun, Fumiyuki Ishii, and Mineo Saito: , Jpn. J. Appl. Phys., **55** (2016) 011301.
3. First principles study on solid oxygen using van der Waals density functional
   M. Obata, I. Hamada, and T. Oda: Physics Procedia, **75** (2015) 771.
4. Density functional study on positively charged six-coordinate FeO_2 porphyrin complex for a trigger of O_2 dissociation
   N. Kitagawa, M. Obata, T. Oda: , Chem. Phys. Lett., **643** (2016) 119.

SUGINO, Osamu [R class; 10000 (B), 5000 (C)] (278)
— *Interface science on energy conversion*
— *Structure and functionality of electrode-electrolyte interface in battery*

TAKATSUKA, Kazuo [R class; 0 (B), 5000 (C)] (263)
— *Nonadiabatic electron dynamics and many-body nuclear dynamics in molecules*

TOHYAMA, Takami [R class; 5000 (B), 5000 (C)] (266)
— *Study of Excitation Dynamics in Strongly Correlated Electron Systems*

1. Magnetization Plateaux by Reconstructed Quasi-spinons in a Frustrated Two-Leg Spin Ladder under a Magnetic Field
   T. Sugimoto, M. Mori, T. Tohyama, and S. Maekawa: Phys. Rev. B **92**, (2015) 125114.
2. Enhanced Charge Excitations in Electron-Doped Cuprates by Resonant Inelastic X-Ray Scattering
   T. Tohyama, K. Tsutsui, S. Sota, and S. Yunoki, Phys. Rev. B **92**, (2015) 014515.
3. Density-matrix renormalization group study of Kitaev-Heisenberg model on the triangular lattice
   K. Shinjo, S. Sota, S. Yunoki, K. Totsuka, and T. Tohyama: submitted to Phys. Rev. B.

TSUNEYUKI, Shinji [R class; 5000 (B), 10000 (C)] (271)
— *Development and Application of First-Principles Simulations for New Materials Exploration*

YAMASHITA, Koichi [R class; 0 (B), 10000 (C)] (277)
— *Large scale calculations on the fundamental processes of solar cells and their optimization in conversion efficiency*

1. The Mechanism of Slow Hot-Hole Cooling in Lead-Iodide Perovskite: First-Principles Calculation on Carrier Lifetime from Electron–Phonon Interaction
   H. Kawai, G. Giorgi, A. Marini, and K. Yamashita: Nano Lett. **15** (2015) 3103.
2. Alternative, lead-free, hybrid organic-inorganic perovskites for solar applications: a DFT analysis
   G. Giorgi, K. Yamashita: Chem. Lett. **44** (2015) 826.
3. A Method to Calculate Redox Potentials Relative to the Normal Hydrogen Electrode in Nonaqueous Solution by using Density Functional Theory-Based Molecular Dynamics
   R. Jono, Yoshitaka Tateyama, and K. Yamashita: Phys. Chem. Chem. Phys. **17** (2015) 27103.
4. Energy Alignment of Frontier Orbitals and Suppression of Charge Recombinations in P3HT/SWNT
   K. Nishimra, M. Fujii, R. Jono, and K. Yamashita: J. Phys. Chem. C **119** (2015) 26258.
5. Remarkable Dependence of the Final Charge Separation Efficiency on the Donor–Acceptor Interaction in Photoinduced Electron Transfer
   T. Higashino, T. Yamada, M. Yamamoto, A. Furube, N. V. Tkachenko, T. Miura, Y. Kobori, R.

Jono, K. Yamashita and H. Imahori: Angew. Chem. Int. Ed. **54** (2015) 629.

6. Dipole Analyses for Short-Circuit Current in Organic Photovoltaic Devices of Diketopyrrolopyrrole-Based Donor and PCBM
   Shohei Koda, M. Fujii, Shintaro Hatamiya, K. Yamashita: Theor. Chem. Acc. **135** (2016) 115.
7. Photon-absorbing charge-bridging states in organic bulk heterojunctions consisting of diketopyrrolopyrrole derivatives and PCBM
   M. Fujii, Woong Shin, Takuma Yasuda, and K. Yamashita: Phys. Chem. Chem. Phys. **18** (2016) 9514.

YOSHIDA, Norio [R class; 5000 (B), 10000 (C)] (280)
— *Analysis of enzymatic reaction for biomass energy creation*

1. Theoretical analysis of complex formation of p-carboxybenzeneboronic acid with a monosaccharide
   S. Seno, N. Yoshida, H. Nakano: J. Mol. Liquids, in press.
2. A 3D-RISM/RISM study of the oseltamivir binding efficiency with the wild-type and resistance-associated mutant forms of the viral influenza B neuraminidase
   J. Phanich, T. Rungrotmongkol, D. Sindhikara, S. Phongphanphanee, N. Yoshida, F. Hirata, N. Kungwan, S. Hannongbua: Protein Science **25** (2016) 147-158.
3. Hydrogen Bonding Structure at Zwitterionic Lipid/Water Interface
   T. Ishiyama, D. Terada and A. Morita: J. Phys. Chem. Lett. **7** (2016) 216-220.
4. Liquid/Liquid Interface Layering of 1-Butanol and [bmim]PF6 Ionic Liquid: A Nonlinear Vibrational Spectroscopy and Molecular Dynamics Simulation Study
   T. Iwahashi, T. Ishiyama, Y. Sakai, A. Morita, D. Kim and Y. Ouchi: Phys. Chem. Chem. Phys. **17** (2015) 24587-24597.
5. Construction of Exchange Repulsion in Terms of the Wave Functions at QM/MM Boundary Region
   H. Takahashi, S. Umino and A. Morita: J. Chem. Phys. **143** (2015) 084104/1-11.
6. Microscopic Barrier Mechanism of Ion Transport through Liquid-Liquid Interface
   N. Kikkawa, L.-j. Wang and A. Morita: J. Am. Chem. Soc. **137** (2015) 8022-8025.
7. Surface Structure of Methanol/Water Solutions via Sum-Frequency Orientational Analysis and Molecular Dynamics Simulation
   T. Ishihara, T. Ishiyama and A. Morita: J. Phys. Chem. C **119** (2015) 9879-9889.

□ Doctor theses

1. **IIZUKA, Hideyuki**
   Scattering processes of exciton at organic semiconductor interfaces: interface disorder and energy dissipation
   Chiba University, 2016-03

2. **IIZUKA, Shota**
   Electronic structures of impurity complexes and tunneling current properties at Si-p/n interfaces
   Chiba University, 2016-03

3. **KIKKAWA, Nobuaki**
   Theoretical and Computational Study of Ion Transport through Water–Oil Interface
   Tohoku University, 2016-03

4. **MORENO, Joaquin Lorenzo Valmoria**
   Density functional theory-based studies on precious metal-free surfaces as alternative catalysts for green energy applications : Carbon nanotubes and copper oxide
   Osaka University, 2015-09

5. **MUSA, Alaydrus**
   Theoretical investigation of ionic conduction in rare-earth oxide materials
   Osaka University, 2016-03

6. **NGUYEN, Hoang Linh**
   Theoretical Study on The Role of Oxygen Vacancy in The Improvement of Metal Oxides' Reactivity for Green Technology Applications
   Osaka University, 2015-09

7. **OTOMURA, Kotaro**
   Rheology and Structure of Non Brownian Suspension under Large Amplitude Oscillatory Shear Strain
   University of Tokyo, 2015-4

8. **SATO, Shunsuke**
   Time-dependent density functional theory for extremely nonlinear interactions of light with dielectrics
   University of Tsukuba, 2016-03

9. **SHIMIZU, Koji**
   Dissociative AdsorptionEAbsorption and DesorptionEScattering Dynamics of Atoms and Molecules on Solid Surfaces
   Osaka University, 2016-03

10. **SHINJO, Kazuya**
    Density-matirx renormalization group study of quantum spin systems with Kitaev-type anisotropic interaction
    Kyoto University, 2016-03

11. **SHIRAI, Tatsuhiko**
    Long-time asymptotic of periodically driven open quantum systems
    University of Tokyo, 2016-03

12. **TAKEMORI, Nayuta**
    Strong electron correlation effects in a quasiperiodic lattice
    Tokyo Institute of Technology, 2016-03

13. **WATANABE, Eriko**
    First principles study on electrocatalyst/water interfaces for oxygen reduction/evolution reactions
    University of Tokyo, 2016-03

14. **YAMAMOTO, Yoshiyuki**
    Ab initio quantum Monte Carlo study on hydrogen impurities in silica
    University of Tokyo, 2016-03

15. **YASUDA, Shinya**
    Study of quantum criticality with strong space-time anisotropy by quantum Monte Carlo
    University of Tokyo, 2016-03

□ Master Theses

1. **FUJITA, Hiroyuki**
   Chiral Magnetic Effect in Condensed Matter Systems
   University of Tokyo, 2016-03

2. **HATOMURA, Takuya**
   Quantum dynamics of nano-magnets under time-dependent fields
   University of Tokyo, 2016-03

3. **HWANG, Jaekyun**
   Theoretical investigation of the evaluation method for the SOFC cathodes performance by first-principles calculation
   University of Tokyo, 2016-03

4. **IKEUCHI, Hiroki**
   Study of the spectra of Electron-Spin-Resonance from the quantum time time evolution of magnetization
   University of Tokyo, 2016-03

5. **IMOTO, Fumihiro**
   Microscopic mechanisms of initial formation process of graphene on SiC(0001) surfaces based on the density functional theory
   University of Tokyo, 2016-03

6. **KAMBE, Hiroyuki**
   Calculation of solvation free energy using the QM/MM-ER approach which incorporates the first solvation shell in the QM region
   Tohoku University, 2016-03

7. **KAWANABE, Go**
   Theoretical study on the electronic structure of pentacene adsorbed on a graphite surface
   University of the Ryukyus, 2016-03

8. **KAWASAKI, Wataru**
   Theoretical study of negative ion production on solid surfaces
   Osaka University, 2016-03

9. **KITAGAWA, Naohiro**
   Ab initio study on dioxygen coordinated iron porphyrin complex considering hemoglobin environment
   Kanazawa University, 2016-03

10. **KOJIMA, Shoya**
    DMFT analysis for $BiNiO_3$
    Tokyo Institute of Technology, 2016-03

11. **KUROKAWA, Daiichi**
    Spin-Dependent O2 Binding to Hemoglobin
    Osaka University, 2016-03

12. **KUWABARA, Yuki**
    Time-Space analysis of nonlinear polarization by time-dependent density functional theory
    University of Tsukuba, 2016-03

13. **MASUGATA, Yoshimitsu**
    Scattering processes of exciton polarons at organic semiconductor interfaces
    Chiba University, 2015-03

14. **MIMURA, Takaaki**
    Analysis of spin models with deterministic Monte Carlo methods
    University of Tokyo, 2016-03

15. **MIYARA, Shota**
    Study of bond-randomness-induced magnetic moment in quantum spin systems with the degree of freedom of the lattice
    University of the Ryukyus, 2016-03

16. **MURAYAMA, Kaori**
    Ortho-para conversion of H2 on alpha-Fe2O3(0001) surface
    Osaka University, 2016-03

17. **NAKANO, Hiroto**
    First-principles study on electronic structure and anomalous Rashba effect in Tl-Pb alloy on Si(111) surface
    Kanazawa University, 2016-03

18. **OHBA, Koji**
    Calculation of thermal conductivity of silicon nanowires by density functional theory
    University of Tokyo, 2016-03

19. **ONDA, Yukiko**
    Stability of metal atoms in insulator films; first-principles study
    Chiba University, 2015-03

20. **OSUGA, Yuki**
    First-principles study of impurity, surface, and interface of BaSi2
    Chiba University, 2015-03

21. **SAKAGAWA, Yasuaki**
    Improvement of continuous-space path-integral Monte Carlo and search for novel quantum phase of He4
    University of Tokyo, 2016-03

22. **SASAKI, Shogo**
    Defects and Schottky barrier at metal/Ge interfaces; first-principles study
    Chiba University, 2015-03

23. **SHINOHARA, Yurie**
    Calculation of light absorption properties in nanoscale structures
    Ochanomizu University, 2016-03

24. **TANAKA, Shogo**
    Molecular dynamics study of the water bending mode in sum frequency generation spectroscopy
    Tohoku University, 2016-03

25. **UMINO, Satoru**
Construction of the exchange repulsion in QM/MM system based on the exchange hole function and its application to condensed phase
Tohoku University, 2016-03

26. **WANG, Lingjian**
Effects of hydration on ion transfer through liquid-liquid interface
Tohoku University, 2015-09

27. **YAMADA, Takuto**
Magnetic excitations of Kitaev-Heisenberg models
University of Hyogo, 2015-03

28. **YANATORI, Hiromasa**
Ordered phases of multi-component fermion systems in optical lattices
Tokyo Institute of Technology, 2016-03

29. **YOSHIKAWA, Daiki**
First-principles study on electronic structure and magnetic anisotropy variations by electric field in the Fe/oxide-insulator interfaces
Kanazawa University, 2015-09